The Gravity Field of Sundaland - Acquisition, Assessment and Interpretation

by

Robert Andrew Holt, B.Sc., M.Sc.

A thesis submitted for the degree of Doctor of Philosophy
at the University of London

Research School of Geological and Geophysical Sciences
Birkbeck College and University College London

1998

ABSTRACT

The 1995 Sandwell & Smith WGI7.2 satellite gravity map has been compared with high quality ship gravity data offshore Sabah. The standard deviation of the differences between gravity profiles interpolated from WGI7.2 and the ship survey was 5.7 mGal. Spectral analysis indicated that WGI7.2 resolves features with half-wavelengths greater than 10 km.

Three hundred new gravity stations, including ten base stations tied to IGSN71, were established during a survey of Sabah and were merged with two previous surveys to complete the gravity coverage of the state at reconnaissance level. New gravity maps of Sundaland, compiled from the Sabah and WGI7.2 gravity data sets have been interpreted. Subtraction from these data sets of the long wavelength GEM-T3 gravity anomaly field, which is dominated by the effects of the subducted proto-South China Sea and the ongoing subduction of the Australian, Indian and Philippine Sea Plates, achieved a simple 'regional-residual' separation and the isolation of crustal-scale anomalies.

5' × 5' maps of the depth to Moho, crustal thickness and β (crustal extension) factor beneath the Sunda Shelf and the South China Sea have been produced by 1-D geometric manipulation of the marine gravity field using sediment isopach and bathymetry control data. The average difference between the new Moho map and seismic refraction depth-to-Moho estimates at the south China margin was 0.2 ± 2.0 km. The Moho rises from an average depth of 29 km beneath the Sunda Shelf to a depth of about 16 km beneath the South China Sea oceanic basin. It is estimated that approximately 1100 km of oceanic crust of the proto-South China Sea was subducted at the northwest Borneo margin. Gravity modelling independently confirmed the average 35 mm/yr spreading rate prediction for the southwestern subbasin of the South China Sea oceanic basin from magnetic lineation interpretation.

Quantitative interpretation indicates that Sabah is underlain by thick continental crust, and gravity modelling of the Maliau Basin predicts a minimum sediment thickness of 8 km. The ophiolite bodies at Telupid and Darvel Bay are separated by a gravity low and there is no evidence that the two are related. The crustal root of the Crocker Ranges extends to a depth of ~ 49 km below sea level. In order to reach this present day crustal thickness, the turbiditic sediments forming the Crocker Ranges must have been compressed to less than half of their original lateral extent during the Sabah Orogeny.

CONTENTS

LIST OF FIGURES

Chapter 3

Chapter 4

Chapter 5

Chapter 6

Appendix 1

LIST OF PLATES

Chapter 5

LIST OF TABLES

ACKNOWLEDGEMENTS

I would firstly like to thank John Milsom who initiated and supervised this project. John provided assistance, encouragement and sage advice on all aspects of the study. The project was sponsored by the University of London Consortium for Geological Research in Southeast Asia and I am grateful to them for their financial support. Diane Cameron, Danuta Kaminski, Celine Murphy and Ron Dudman have consistently provided much appreciated help.

I am indebted to the friendship of my peers, notably Alex, Alison, Andy, Bart, Claire, Dave, Dave, Delphine, Elena, Emma, Emma, Emma, Gemma, Greg, Hannah, James, John, Jon, Kerry, Lee, Neil, Nicki, New Nigel, Ossie, Paul, Phil, Rhodri, Robin, Ruaraidh, Shawn, Simon, Steve, Wilson, and Zuwena. I thank those other people who remain nameless. I am sure that without these friends my time in London would have been a lot more productive and a lot less fun.

Funding for the 1995 Sabah gravity survey was provided by the University of London Consortium for Geological Research in Southeast Asia. I am very grateful to the Geological Survey of Malaysia for making the survey possible, by provision of a vehicle and driver and by allocating a geophysicist, Mr. Dzazali bin Ayub, to the survey. Mr. Chen Shick Pei (Deputy Director General, GSM) and Mr. Lim Peng Siong (Director, GSM, Sabah) were particularly helpful and supportive.

Much appreciated assistance was provided by Nigel Press Associates during the initial phase of this study, and I thank Nigel Press, Ross Smail and Andy Flemming for their help. Ship gravity data were kindly provided by Prof. K. Hinz of the Bundesanstalt für Geowissenschaften und Rohstoffe, Germany, and by Gilles Balma of the Bureau Gravimetrique International, France. Satellite gravity data were provided by the National Geophysical Data Center, USA. Delphine Roques and Jon Noad are thanked for providing geological insight during the final challenging stage of the project.

Finally, I would like to thank my family for their love and support.

CHAPTER 1

Introduction

CHAPTER 1. INTRODUCTION

This chapter gives an introduction to the project. First, an overview of the thesis is presented. This is followed by a discussion of the fundamental concepts of gravity surveying. In the final part of the chapter, the data and computer software used during the project are discussed. Included in this final part are sections on the display of gravity images and on data location using the internet.

1.1 Thesis Overview

This thesis is based on the study of the land and marine gravity anomalies of Sundaland, where Sundaland is defined as the promontory that extends south from the mainland of Asia that includes Borneo, western Java, Sumatra, Peninsula Malaysia and the shallow marine area in between. Sundaland lies at the heart of the collision zone between the Australian, Eurasian, Indian and Philippine Sea Plates (Chapter 2). The project is an extension of current research into the gravity field of Southeast Asia which has the support of the University of London Consortium for Geological Research in Southeast Asia. A project location map is given in Figure 1.1.

The main marine gravity data set used in the project was the Sandwell & Smith World Gravity Image V7.2 (WGI7.2). These gravity data were derived from satellite altimeter measurements of sea surface height which were transformed to gravity anomalies after correction for oceanographic disturbances such as currents and tides (Chapter 3). One of the primary aims of the project was to assess the accuracy and resolution of this data set, and this was achieved by comparison with a high resolution ship gravity survey (Chapter 4).

A new 300 station gravity survey collected in Sabah by the author in 1995 formed the major land gravity data set (Chapter 5). Using these new gravity data, two older gravity surveys were corrected to the IGSN71 datum. Combined, these data complete the gravity coverage of Sabah at a regional reconnaissance level.

Regional gravity interpretation was based on both free-air and Bouguer gravity anomaly maps (Chapter 6). The amount of quantitative information that it was possible to extract from these maps was highly dependent on the availability of geologic control data. Estimates of crustal thickness made in the South China Sea and on the northern Sunda Shelf permitted an examination of the crustal properties of these areas. Detailed analysis of the gravity anomaly field of Sundaland focused on a number of key areas, namely the Sunda Shelf edge, the South China Sea Oceanic Basin and Sabah.

1.1.2 Future Work

Given the finite time scale of this project, there were areas of research which could not be fully explored. Work has since been undertaken by T. Wright of UCL/MSSL to improve the quality of the marine gravity field (Section 3.5). This project is ongoing with additional work being carried out by J. Milsom, S. Laxon and D. McAdoo (J. Milsom, UCL, *pers. comm.*). Similarly, GM-SYS gravity modelling of the subducted slab of the proto-South China Sea constrained by the seismic tomography inversion results of Widiyantoro and van der Hilst (1996) has been carried out by V. Rocchi of UCL (unpub. M.Res. project, Physics Dept., 1998).

As noted in Chapter 6, there is also a great deal of additional work that could be carried out on the analysis and modelling of both the South China Sea shelf edge and South China Sea oceanic basin fossil spreading ridge anomalies. Both studies would also benefit greatly from comparison with similar features in other regions of the world, as discussed in Sections 6.4.1 and 6.4.3.5.

On Sabah there is an urgent need for the collection of paleomagnetic data and also for a regional seismic crustal transect. Well constrained paleo-latitude and basement composition control data would very significantly improve the Southeast Asian tectonic syntheses by removing two highly contentious issues which cause the present models to diverge greatly. Finally, the correlation between the Darvel Bay gravity high, which is caused by the Darvel Bay Ophiolite, and the outline of the bay should be the focus of additional study using the flexural rigidity modelling approach.

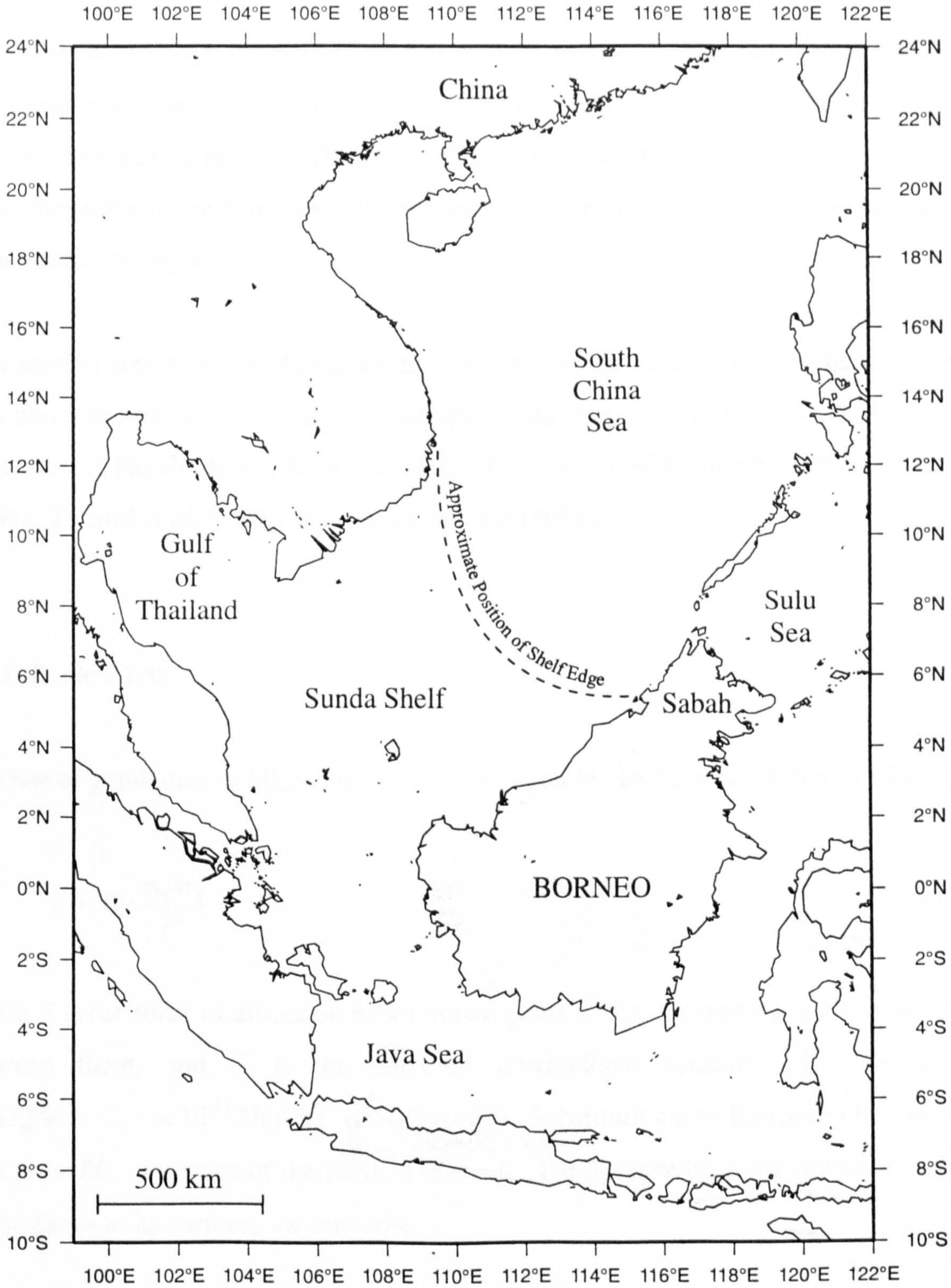

Figure 1.1. Project study area - areas labelled are referred to extensively throughout the thesis.

1.2 Fundamental Concepts of Gravity Surveying and their Practical Application

Gravity surveying was at one time the method of choice in oil exploration, and the characteristic bulls-eye pattern of negative gravity anomalies over salt diapirs revealed many profitable targets for the Texan oilmen of the twenties. Today, the gravity meter is capable of measuring gravity differences of 1 part in 100 million. Although the principles of gravity surveying remain essentially the same, the method still represents an important exploration technique.

This section describes the fundamental concepts of the Earth's gravity field, gravity measurement and reduction, and the complications that arise in the real world. This discussion is largely drawn from the work of Verma (1985), Sharma (1986), Strange (1991), Telford *et al.* (1990) and Kearey & Vine (1996).

1.2.1 Basic Facts

The law of gravitation published by Sir Isaac Newton in 1687 can be written as follows,

$$F = G \cdot \frac{m_1 m_2}{r^2} \tag{1.1}$$

where F is the force of attraction between two point masses m_1 and m_2, r is the distance between them, and G is the universal gravitational constant whose value is 6.6726 $\times 10^{-11}$ Nm^2/kg^2 (IUGG, 1967). Substituting into Equation (1.1) $m_1 = 1$ unit, $m_2 = M_E$ - the mass of the Earth, and $r = R$ - the distance from the centre of gravity of the Earth to its surface, we can write,

$$g = \frac{GM_E}{R^2} \tag{1.2}$$

where g is the acceleration due to gravity expressed in m/s^2. Geophysicists often use the unit of milligal (also known as mGal or mgal) which is defined as an acceleration of 1×10^{-5} m/s^2.

The shape of the Earth is approximately that of an oblate spheroid with the equatorial radius being greater than the polar radius. Variations in the value of g occur from place to place simply because the distance of a place at sea level from the centre of the Earth varies with latitude. In addition to distance from the centre of the Earth, the gravitational acceleration is affected by centripetal force acting on a body. In 1743 Clairaut obtained an expression for the acceleration due to gravity as a function of latitude, taking into account the flattening of the spheroid, as well as the angular velocity of rotation of the Earth, which takes the form,

$$g_{th} = g_0 [1 + b_1 \sin^2\phi - b_2 \sin^2 2\phi + \dots] \qquad (1.3)$$

where b_1 and b_2 are constants, ϕ is the latitude, g_0 is the value of g at the Equator at sea level and g_{th} is the theoretical value of gravity at the surface of the spheroidal Earth at that latitude.

The gravity field at the Earth's surface is also influenced by the underlying geology because different geological formations are characterised by different rock densities. The average density for the upper crustal rock may differ considerably from the nominal 2.67 $Mg.m^{-3}$ average density. Anomalous gravity highs or lows therefore arise, depending on whether the rock masses underlying an area have densities higher or lower than the average value. These variations reach a few hundred parts per million. Such 'gravity anomalies' are the targets of gravity surveys and their interpretation may yield significant geological information (e.g. Chapter 6).

1.2.2 Gravity Measurement

Gravity surveys are carried out with gravity meters that measure relative changes in the gravity field rather than the absolute value of gravity. During a gravity survey, the value of gravity at a field station is found by first taking a gravity measurement at a base station where the absolute value of gravity, *g*, is known. Next, the gravity measurement is made at the field station (or a series of field stations). A final gravity measurement is made at the base station. The absolute value of gravity at the field station(s) is found by adding the difference in gravity between the field and base stations to the absolute value of gravity at the base station. The gravity measurement is repeated at the base station to correct for instrument errors (Section 1.2.3.3).

A network of gravity base stations has been established throughout the world. The original base network was tied to the site of an absolute gravity measurement in Potsdam, East Germany, which was first made with six different pendulums in 1906. This datum is referred to as the Potsdam datum. Subsequent absolute measurements of gravity indicated that the Potsdam datum was about 14 milligals too high (e.g. van Blaricom, 1992). Correction for this error led to a second datum referred to as the International Gravity Standardisation Network 1971 or IGSN71. Further improvements have been made to the gravity datum (e.g. WGS84). However, the differences between these datums and IGSN71 are small, typically less than 1 mGal (J. Milsom, *pers. comm.*), and they are not yet in widespread use. Care should be exercised when using old gravity survey data as they are often tied to the Potsdam datum, and thus require correction. This was the case with the USAMS(FE) gravity survey data of Sabah used during this project, which were corrected with a -13.7 mGal datum shift (Chapter 5).

1.2.3 Reduction of Gravity Data

1.2.3.1 Reduction to the Reference Surface

The theoretical value of gravity is valid only at the surface of the Earth ellipsoid (also known as the reference spheroid). The Earth ellipsoid is a low-order approximation to the shape of the Earth, accounting for the effect of the Earth's rotation which has created the ~ 20 km equatorial bulge, and approximates mean sea-level with the land above it removed. Owing to the uneven density distribution within the Earth, the best-fitting ellipsoid is not simply the hydrostatic ellipsoid and parameters for several internationally recognised ellipsoids have been published. These have been refined with increasing accuracy due to the improved definition of the mass, volume and angular rotation of the Earth. Examples include the reference ellipsoids of the Geodetic Reference System 1967 (GRS67) (IAG, 1967), and the Geodetic Reference System 1980 (GRS80) (Moritz, 1980*a*).

The gravity anomaly is obtained by subtracting the theoretical value for the ideal Earth from the observed gravity value and reducing the measurement to the reference surface. Gravity measurements are taken all over the surface of the Earth and even under sea water. For practical purposes of gravity field computation the geoid is taken as a reference surface for the observed gravity rather than the Earth ellipsoid. The geoid is an equipotential surface of the Earth's gravitation and rotation and on average coincides with the mean sea level in the open sea. Mean sea level itself cannot be defined as an equipotential surface because in addition to variations caused by the local gravity field, it is affected by dynamic topography caused by currents, tides, etc. (Chapter 3). The simplified model of the Earth, upon which the perfect mathematical form of the ellipsoid of revolution is based, allows for increasing density with depth, but not for lateral variations, which are the objects of gravity exploration. Because of these lateral variations, the geoid and ellipsoid do not coincide. Local mass anomalies warp the geoid, so that the deviations between the two surfaces are as much as 100 m (Kahn, 1983). In practice, the effect of the mismatch between the geoid and the ellipsoid is

negligible because the gravitational difference is of the order of the gravity observation error (Heiskanen & Vening Meinesz, 1958).

Corrections that are normally made to gravity observations are the tidal correction, drift correction, latitude correction and the free-air correction. Supplemental corrections include the Bouguer correction, the terrain correction and the curvature correction. These corrections are discussed below.

1.2.3.2 Tidal Correction

Time dependent tidal accelerations are caused by the various lunar and solar gravitational forces acting on different parts of the rotating Earth. These are supplemented by the effects of the revolutions of the Moon about the Earth and the Earth about the Sun. The accelerations produce variations in the terrestrial gravity field which are of the order of 0.1 mGal. This temporal variation in the gravity field is removed with the tidal correction, which is evaluated in practice either from published tables of tidal correction data or with computer programs.

Besides the tides, the terrestrial gravity field is affected by a number of additional time dependent processes (Hotine, 1969; Torge, 1980). Changes in gravitation are caused by the shifting of mass in the atmosphere, in the oceans, on the solid surface of the Earth, and in its interior. However, these changes are generally at least an order of magnitude smaller than tidal effects and remain at the limit of present measurement capabilities. The same is true for any secular decline in gravitation which might be connected with an expansion of the Earth. The variations of centripetal acceleration caused both by polar motion and by the changes in the Earth's rotational velocity remain below the accuracy of measurement.

1.2.3.3 Drift Correction

The drift correction is determined empirically during a survey and corrects for the stretching of the gravity meter spring during the survey. The correction is calculated by comparing gravity measurements made at a common station over a period of time.

1.2.3.4 Latitude Correction

Latitude corrections are applied to reduce the observed gravity to the gravity anomaly. The latitude correction is usually made by subtracting the theoretical gravity, calculated from the international gravity formula (e.g. GRS80), from the observed absolute gravity.

The theoretical gravity, g_ϕ, calculated with GRS80 is:

$$g_\phi = 978031.8\,(\,1 + 0.0053024\,\sin^2\phi - 0.000005\,\sin^4 2\phi)\ \text{mGal} \qquad (1.4)$$

where ϕ is the geographic latitude of the point of observation.

For surveys not tied to the absolute reference system, local latitude corrections may be made by selecting an arbitrary base and using the theoretical north-south gradient, Δg_ϕ, (obtained by differentiating Equation (1.4)):

$$\Delta g_\phi = \frac{1}{R}\frac{dg}{d\phi} = 0.812 \sin 2\phi\ \text{mGal/km}\ \ (\text{north} - \text{south}) \qquad (1.5)$$

where R is the Earth's radius and ϕ the geographic latitude of the arbitrary base station. This correction must be subtracted from, or added to, the measured gravity difference, depending on whether the station is at a higher or lower latitude than the base station. At mid-latitudes the correction is about 0.08 mGal per 100 m.

1.2.3.5 Free-Air Correction

The free-air correction compensates for the decrease in gravity with increased distance from the centre of the Earth; in practice sea level is taken as the reference surface approximating to the geoid and the height of the stations above or below this level is used in the calculations. The effect of topographic masses is ignored and individual free-air anomalies are thus strongly correlated with elevation. However, if the topography is isostatically compensated, i.e. if there is no net mass excess or deficiency in the Earth's uppermost layers, the average free-air anomaly over a sufficiently large area is zero.

The decrease in gravity with increased distance from the centre of the Earth (R) may be quantified by differentiating Equation (1.2):

$$\frac{\partial g}{\partial R} = -\frac{2GM}{R^3} = -\frac{2g}{R} \approx -0.3086 \text{ mGal/m} \tag{1.6}$$

where h is the height at which the observation is made above sea level in metres. Using a value for the mean radius of the Earth (R_E) of 6.367×10^6 m, and the theoretical value of gravity at sea level at 45° latitude, $g = 980629$ mGal, then at sea level Equation (1.6) gives the vertical variation of gravity as -0.3086 mGal/m. For most purposes this value may be used anywhere on the Earth in the free-air correction. A more complete expression for the free-air correction, taking into account the Earth's spheroidal shape, is:

$$\frac{\partial g}{\partial R} = -0.30855 - 0.00022\cos 2\phi + 0.000144h \text{ mGal/m} \tag{1.7}$$

where ϕ is geographic latitude of the observation, and h is the height at which the observation is made above sea level in metres (Verma, 1985). The second order term is only important at high elevations and high latitudes. The magnitude of second order term at various elevations and latitudes is given in Table 1.1.

Table 1.1. Magnitude of second order term of Equation (1.7) (values in mGal at various elevations), from Verma (1985).

Latitude	Elevation in metres					
	0	1000	2000	3000	4000	5000
0°	0.0	-0.2	-0.2	0.0	+0.2	+0.6
10°	0.0	-0.2	-0.2	0.0	+0.3	+0.7
20°	0.0	-0.2	-0.1	0.0	+0.4	+0.8
30°	0.0	-0.1	0.0	+0.2	+0.6	+1.0
40°	0.0	0.0	+0.1	+0.5	+1.0	+1.5
50°	0.0	+0.1	+0.3	+0.7	+1.2	+1.8
60°	0.0	+0.1	+0.4	+0.9	+1.5	+2.2
70°	0.0	+0.2	+0.5	+1.1	+1.7	+2.5
80°	0.0	+0.2	+0.6	+1.2	+1.9	+2.7
90°	0.0	+0.2	+0.7	+1.3	+2.0	+2.8

1.2.3.6 Bouguer Correction

Land Gravity Measurements

The purpose of the Bouguer correction is to correct for topographic masses above the reference surface. Traditionally this has been done by correcting for an infinite horizontal slab, with a thickness equal to the station elevation, whose gravitational effect is given by:

$$g = 2\pi G\rho h \tag{1.8}$$

where ρ is the slab density, G is the universal gravitational constant, and h the station elevation in metres. This is known as the Bouguer correction, whose magnitude is $0.04192\ \rho h$ mGal. It is common practice to use the value of $\rho = 2.67$ Mg.m^{-3} as the average density for rocks above sea level. The Bouguer correction is subtracted from the free-air anomaly to give the Bouguer anomaly. In areas of subdued topography, the Bouguer correction is often sufficient to correct for the effect of the topographic masses above the reference surface. However, in mountainous areas, the topography can differ substantially from that approximated by the slab, and terrain corrections are made for deviations of the true topography from the slab (Section 1.2.3.7).

Marine Gravity Measurements

In the discussion above it has been assumed that the gravity observations are made on land. Gravity readings taken offshore are a lot easier to handle than those made on land, since, after instrumental and acceleration corrections have been made, the free-air anomaly is obtained directly by application of the latitude correction. In shallow water these free-air anomalies are critically dependent on bottom topography. The marine Bouguer reduction is applied to reduce this effect.

The marine Bouguer reduction involves 'infilling' the sea layer with an equivalent volume of rock of mean upper crustal rock density, 2.67 $Mg.m^{-3}$. The correction is calculated using the Bouguer slab correction, whose magnitude is 0.04192 $\Delta\rho.h$ mGal, where $\Delta\rho$ is the difference in density between the sea water (1.03 $Mg.m^{-3}$) and the upper crust (2.67 $Mg.m^{-3}$), and h is the water depth in metres.

1.2.3.7 Terrain Correction

When applying the Bouguer correction it is assumed that topography around the station is a horizontal plane of height equal to the elevation of the observation station. This situation is not normally encountered in the field. The correction for this discrepancy is known as the terrain correction.

In order to apply terrain corrections two cases are to be considered: (1) elevated areas above the Bouguer plate; and (2) areas depressed below the level of the Bouguer plate. When the attraction of the Bouguer plate ($2\pi G\rho h$) is subtracted from the observed gravity, too little mass is subtracted for case (1) and too much for case (2). The resulting Bouguer anomaly is therefore not free from topographic effects.

The terrain correction, when applied, removes these discrepancies and takes into account the gravitational effect of actual topography. The gravitational effect of masses above the Bouguer plate as well as of depressions is to reduce the value of observed gravity at the station. Since we assume that the topography around the station is flat and this effect

is subtracted from the observed gravity, the corrections for topographic effects are always positive.

Terrain corrections are usually obtained by dividing the region around a station into segments bounded by concentric rings at suitable angular intervals (Φ). The difference in mean elevation (Δh) between each segment and the gravity station is determined from a topographic map, without regard to its sign. The terrain correction due to the attraction of the material in such a segment is

$$\Delta g_T = G\rho\Phi(r_2 - r_1) + \sqrt{\left[r_1^2 + \Delta h^2\right]} - \sqrt{\left[r_2^2 + \Delta h^2\right]} \qquad (1.9)$$

where r_1 and r_2 are the radii of the inner and outer rings bounding the segment and ρ is the density of the terrain material. Tables of the bracketed expression in Equation (1.9) have been published by Hammer (1939) and Haalck (1953).

In order to calculate terrain corrections, therefore, detailed topographic maps are required. In many parts of the world access to these maps is restricted by the military, and it may not be possible to calculate terrain corrections. For regional surveys, this becomes a significant source of error in areas of rugged topography. For example, topographic maps were unavailable for the gravity data collected during this project in Sabah (Chapter 5). Terrain corrections were estimated only at stations acquired over the mountainous Crocker Ranges, and these estimates should be treated with caution. Elsewhere, the lack of terrain correction contributes an error of about 0.5 mGal to the station accuracy, and does not significantly affect the final gravity anomaly map which is contoured at 10 mGal intervals.

1.2.3.8 Curvature Correction

This correction is occasionally applied in order to take into consideration the curvature of the Earth's surface. When applying the Bouguer correction, the Bouguer slab is assumed to be a horizontal plane, infinite in two orthogonal directions. In reality the

surface of the Earth is curved. This factor is accounted for by the Bullard correction. The Bullard correction is positive up to an elevation of about 4000 m above sea level, and negative above this. The magnitude of this correction is given in Table 1.2.

Table 1.2. Magnitude of curvature correction for different elevations. From Verma (1985).

Elevation (m)	Correction (mGal)	Elevation (m)	Correction (mGal)
0	0.0	1000	1.2
100	0.2	1200	1.3
200	0.3	1500	1.5
300	0.4	2000	1.7
400	0.6	2500	1.7
500	0.7	3000	1.5
600	0.8	3500	1.1
700	0.9	4000	0.6
800	1.0	4500	-0.1
900	1.1	5000	-1.0

As with the terrain correction, the omission of a curvature correction to the gravity data collected during this project in Sabah (Chapter 5) does not significantly affect the final gravity anomaly map.

1.2.4 Free-Air and Bouguer Gravity Anomalies

The gravity anomaly is defined as the difference between the observed value of gravity at some point and the theoretical value of gravity for the same point. If only the free-air and tidal corrections have been applied, we define the free-air anomaly, g_{faa}, as:

$$g_{faa} = g_{obs} - g_{\phi} - \Delta g_{tc} + \Delta g_{fa} \tag{1.10}$$

where g_{obs} is the observed gravity, g_{ϕ} is the theoretical gravity, Δg_{tc} is the tidal correction and Δg_{fa} is the free-air correction. Occasionally gravity data are presented as a free-air anomaly map without taking into consideration the topography above sea level. This usually occurs when maps of oceans and continental shelves are drawn; as previously

mentioned, any free-air anomaly map of land gravity observations will show a strong correlation with local topography.

In the case of gravity observations on land, it is usual to apply the free-air correction, the tidal correction, the Bouguer correction (Δg_B) and the terrain correction (Δg_T) in order to reduce the observed gravity anomaly to the reference geoid. The Bouguer anomaly, g_{Ba}, is then expressed as:

$$g_{Ba} = g_{obs} - g_{\phi} - \Delta g_{tc} + \Delta g_{fa} - \Delta g_B + \Delta g_T \qquad (1.11)$$

This anomaly should be zero if there are no horizontal variations in the density of rocks below sea level. A Bouguer anomaly different from zero may represent the effect of lateral variations in the density of the rocks below sea level, or it may show that the actual density above sea level differs from that assumed in the calculation of the Bouguer and terrain corrections.

1.2.5 Isostasy

The phenomenon of isostasy concerns the response of the outer shell of the Earth to the imposition and removal of large loads. This layer, although relatively strong, is unable to support the large stresses generated by, for example, the positive weight of a mountain range or the relative lack of weight of an oceanic basin. For such features to exist on the Earth's surface, some form of compensating mechanism is required to avoid the large stresses that would otherwise be generated. The presence of subsurface compensation of surface loads is confirmed by the variation in the Earth's gravitational field over broad regions. Bouguer anomalies are generally negative over elevated continental areas and positive over oceans (Figure 1.2A). These observations confirm that the positive topography of continents and the negative topography of oceans are compensated by regions at depth with density contrasts which are, respectively, negative and positive.

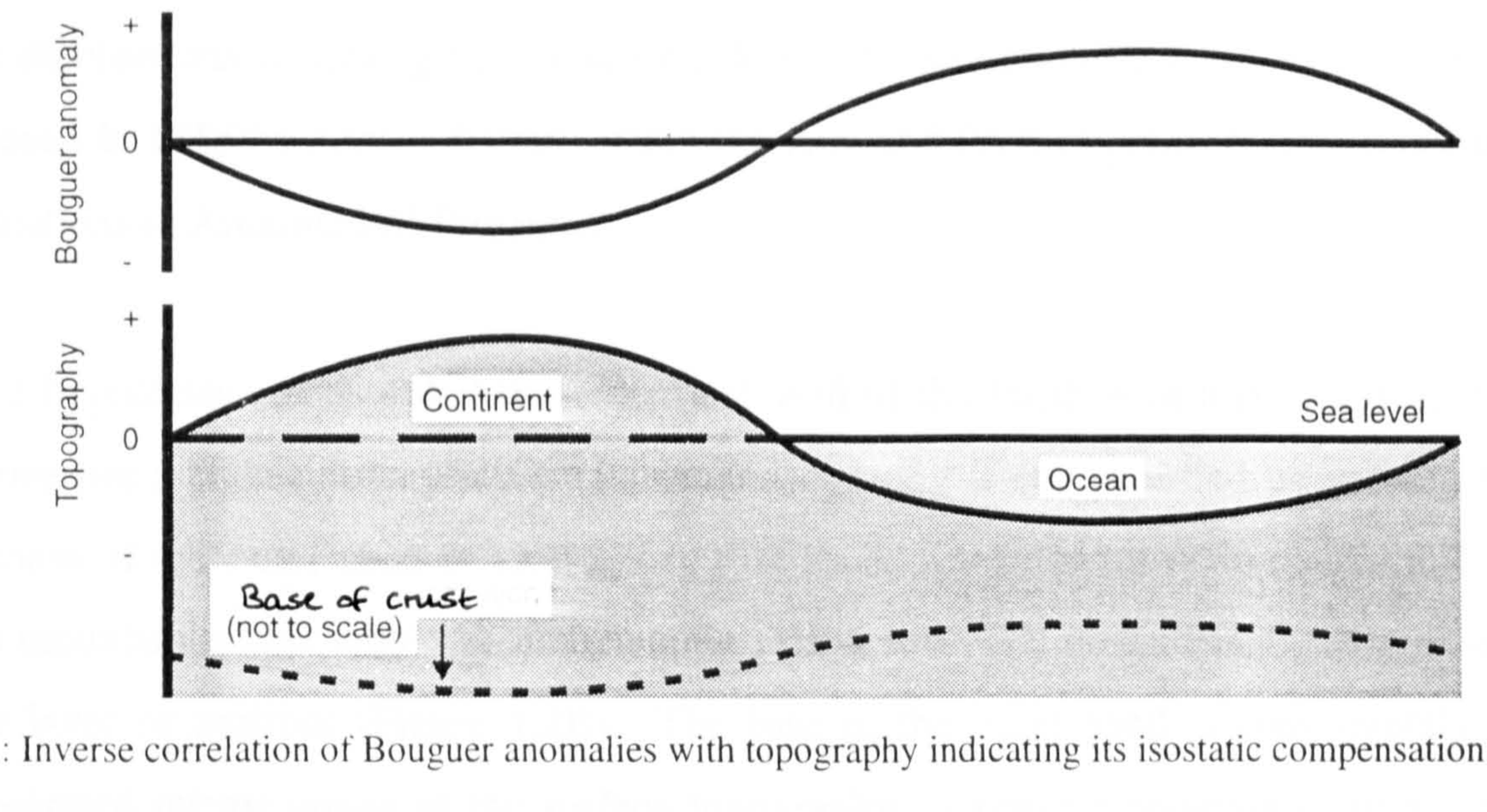

A: Inverse correlation of Bouguer anomalies with topography indicating its isostatic compensation.

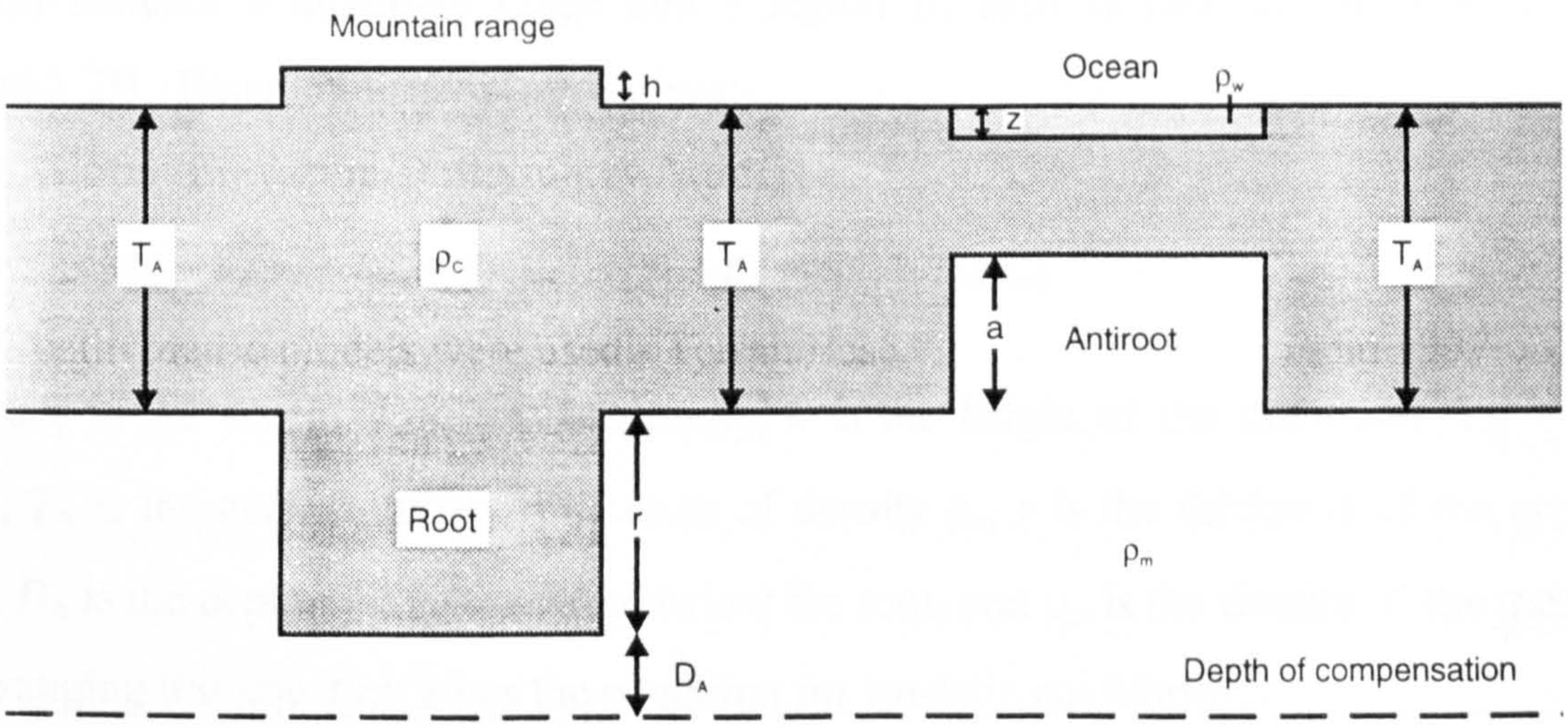

B: Airy mechanism of isostatic compensation. h, height of mountain above sea level; z, depth of water of density ρ_w; T_A, normal thickness of crust of density ρ_c; r, thickness of root; a, thickness of antiroot; D_A, depth of compensation below root; ρ_m, density of mantle.

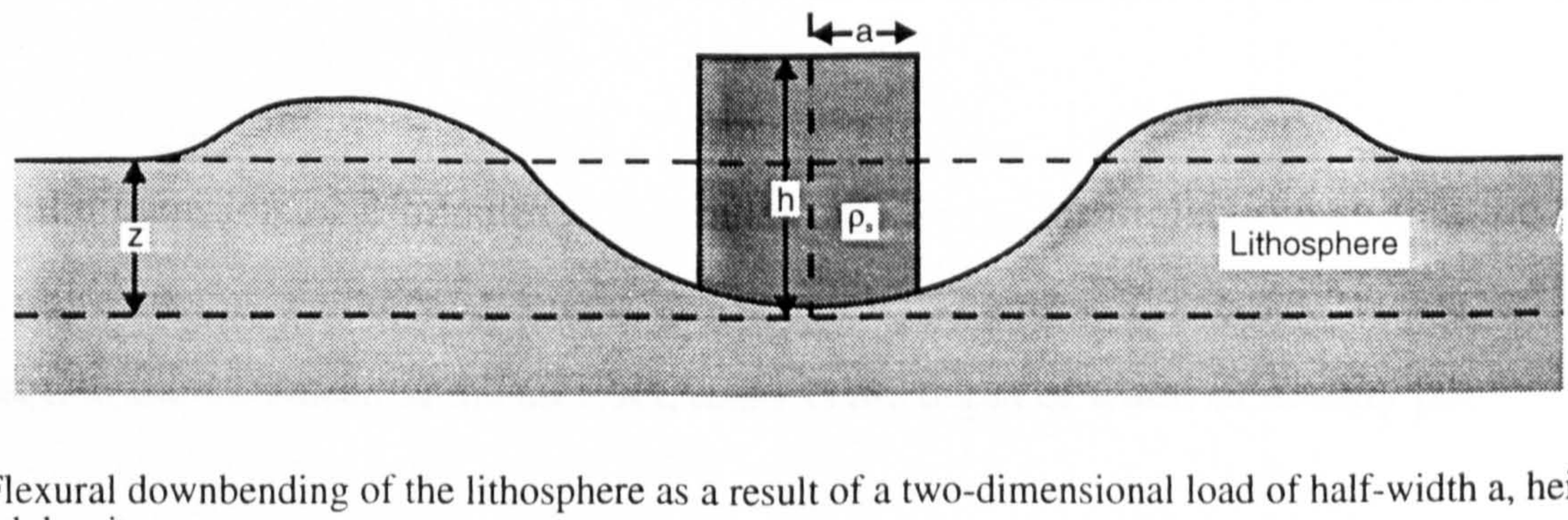

C: Flexural downbending of the lithosphere as a result of a two-dimensional load of half-width a, height h and density ρ_s.

Figure 1.2. Elements of Isostasy, after Kearey & Vine (1996).

Two mechanisms regarding the geometric form of local isostatic compensation were proposed in 1855 by Airy and Pratt. Both the Airy and Pratt hypotheses are essentially applications of Archimedes' Principle.

Airy's hypothesis assumes that the outermost shell of the Earth is of a constant density and overlies a higher density layer. Surface topography is compensated by varying the thickness of the outer shell in such a way that its buoyancy balances the surface load. Thus mountain ranges would be underlain by a thick root, and ocean basins by a thinned outer layer or antiroot (Figure 1.2B). The base of the outer shell is consequently an exaggerated mirror image of the surface topography. Consider columns of unit cross section beneath a mountain range and a region of zero surface elevation shown in Figure 1.2B. Equating their weights gives:

$$g[h\rho_c + T_A\rho_c + r\rho_c + D_A\rho_m] = g[T_A\rho_c + r\rho_m + D_A\rho_m] \tag{1.12}$$

where g is the acceleration due to gravity, h is the height of the mountain above sea level, T_A is the normal thickness of crust of density ρ_c, r is the thickness of the crustal root, D_A is the depth of compensation below the root, and ρ_m is the density of the mantle. Rearranging this equation gives the condition for isostatic equilibrium:

$$r = \frac{h\rho_c}{(\rho_m - \rho_c)} \tag{1.13}$$

A similar computation provides the condition for the compensation of an ocean basin:

$$a = \frac{z(\rho_c - \rho_w)}{(\rho_m - \rho_c)} \tag{1.14}$$

where a is the thickness of the antiroot, and z is the depth of water of density ρ_w.

Pratt's hypothesis assumes that the base of the Earth's upper layer (the 'isopiestic level') is horizontal and that isostatic equilibrium is achieved by allowing this upper layer to be composed of columns of constant density material. Compensation is achieved by

mountains consisting of and being underlain by material of low density, and by oceans being underlain by material of higher density.

Earlier this century, it was assumed that the outer shell of the Earth whose topography is compensated corresponded to the crust. Certainly the large density contrast existing across the Moho plays a major part in the compensation. It is now believed, however, that the compensating layer is rather thicker and includes part of the upper mantle. This strong outer layer of the Earth is known as the lithosphere. Further compensation may also occur deeper within the Earth.

These models of local isostatic compensation, although widely used, imply unreasonable mechanical properties for the crust and upper mantle (Banks *et al.*, 1977), because they predict that independent movement would take place even for very small loads. The lithosphere is demonstrably not as weak as this implies, as large gravity anomalies exist over igneous intrusions with ages in excess of 100 Ma. More realistic models of isostasy involve regional compensation. A common approach is to make the analogy between the lithosphere and the behaviour of an elastic sheet under load. Figure 1.2C illustrates the elastic response to loading; the region beneath the load subsides over a relatively large area by displacing asthenospheric material, and is complemented by the development of peripheral bulges. Over long periods of time, however, the lithosphere may act in a viscoelastic manner and undergo some permanent deformation by creep. Loads with a half-width of less than about 50 km are supported by the finite strength of the lithosphere. Loads with half-widths in excess of about 500 km are in approximate isostatic equilibrium (Kearey & Vine, 1996).

The principles of isostatic compensation are discussed with reference to the gravity anomaly field of Southeast Asia in Chapter 6 and conclusions are drawn about the geometry and strength of the crust in this region.

1.3 Project Data

The main data sets used in this study were land, ship and satellite gravity, bathymetry, sedimentary isopach and geoid anomaly data sets. These data sets are briefly discussed in this section.

1.3.1 Gravity Data

Two previous land gravity surveys of Sabah were made available for this project. A new gravity survey of Sabah was collected in 1995 by the author and John Milsom of University College London, and Dzazali bin Ayub of the Geological Survey of Malaysia. These data sets are discussed in Chapter 5.

Ship gravity data were kindly made available by Prof. K. Hinz (Bundesanstalt für Geowissenschaften und Rohstoffe, Hannover, Germany) and Gilles Balma (Bureau Gravimetrique International, Toulouse, France).

The quality of satellite gravity compilations has improved rapidly in the last decade due to the continual acquisition of altimetry data during this time. Within the term of this project (1994 - 1997) the minimum spatial resolution of the marine gravity anomaly field has improved from 50 km to 20 km (Chapter 4). Figure 1.3 shows three vintages of satellite free-air gravity anomaly maps of the South China Sea - the first from the 1985 Haxby compilation of recomputed Seasat measurements (NGDC, 1993), the second from the 1994 Sandwell & Smith compilation (Sandwell & Smith, 1994), and the final map from the 1995 Sandwell & Smith World Gravity Image V7.2 (WGI7.2) data set which was released mid 1995 (Smith & Sandwell, 1995; Sandwell & Smith, 1997).

WGI7.2 is a digital grid of marine satellite-derived free-air gravity anomalies between ± 72°. The grid was derived from all Geosat Geodetic Mission data, a stack of 62 repeat cycles of the Geosat Exact Repeat Mission, all the ERS-1 Geodetic Mission data, and the first 16 cycles of the ERS-1 35-day repeat orbit. The method to construct such a grid

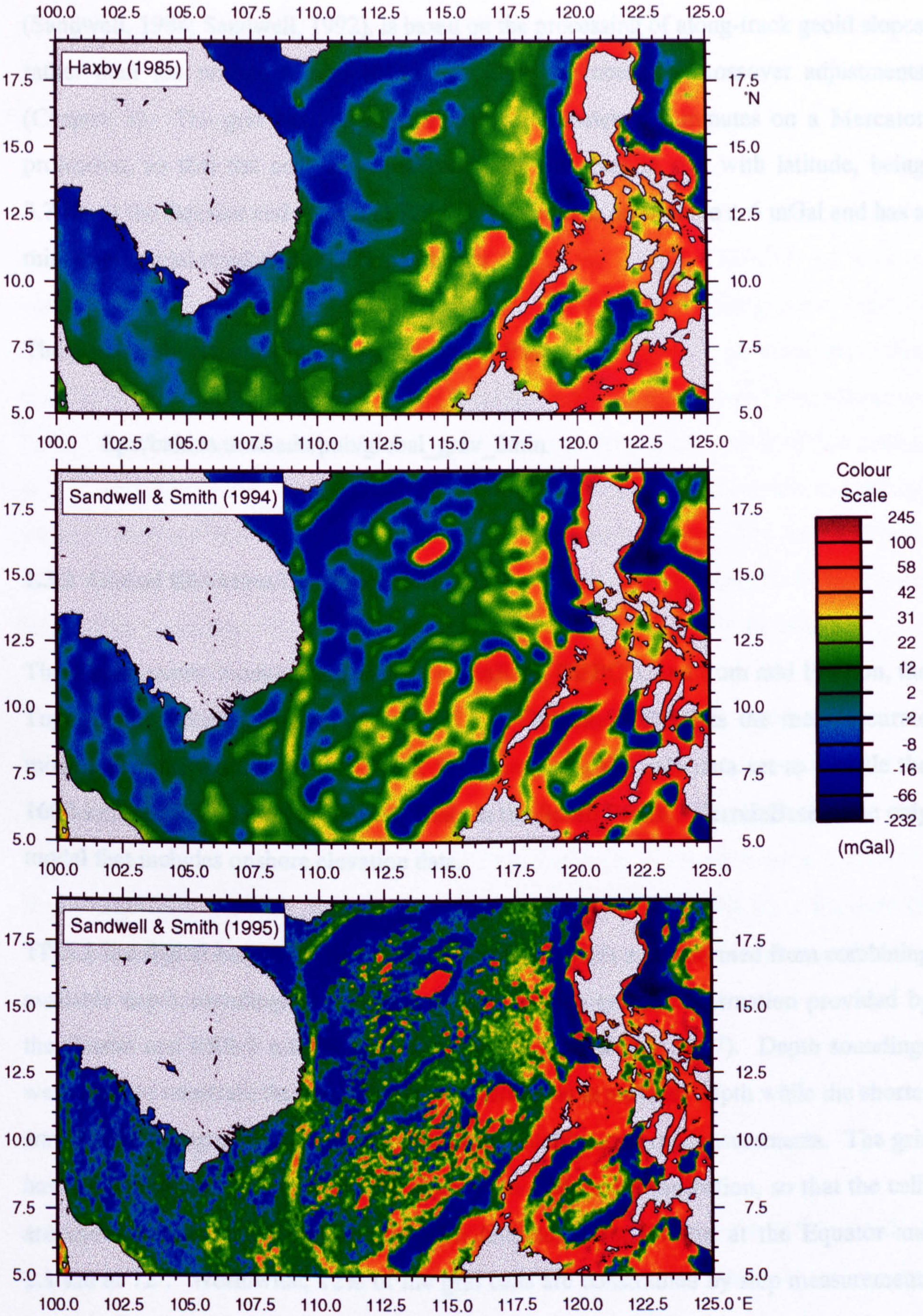

Figure 1.3. Improvement in the resolution of the Southeast Asian gravity field, 1985 - 1995.

(Sandwell, 1984; Sandwell, 1992), is based on the processing of along-track geoid slopes rather than sea surface heights thereby avoiding the need for crossover adjustments (Chapter 3). The grid has cell dimensions of 2 minutes × 2 minutes on a Mercator projection, so that the cells are equidimensional but vary in size with latitude, being 3.7 km at the Equator and 1.1 km at 72°. This data set is accurate to ± 6 mGal and has a minimum spatial resolution of 20 km (Chapter 4).

The grid is publicly available by anonymous FTP to:

ftp://baltica.ucsd.edu/pub/global_grav_2min

1.3.2 Global Elevation/Bathymetry Models

Three bathymetric models were used - TerrainBase, GEBCO, and from mid 1997 on, the Topographic Polished Image V5.2 (TPI5.2). Offshore, TPI5.2 is the most accurate model, TerrainBase the least. TPI5.2, for example, is the only data set to include the 1600-km long Foundation Seamounts chain in the South Pacific. TerrainBase is the only model that includes onshore elevation data.

TPI5.2 is a digital bathymetric map of the oceans between ± 72° formed from combining available depth soundings with high-resolution marine gravity information provided by the Geosat and ERS-1 satellite altimeters (Smith & Sandwell, 1997). Depth soundings were used to constrain the long wavelength variations in regional depth while the shorter wavelength topography was predicted from the satellite gravity measurements. The grid has cell dimensions of 2 minutes × 2 minutes on a Mercator projection, so that the cells are equidimensional but vary in size with latitude, being 3.7 km at the Equator and 1.1 km at 72°. Worldwide, 12% of the grid cells are constrained by ship measurements or coastlines while the remaining 88% are estimated. The map has an estimated minimum resolution of 1 to 12 km (Smith & Sandwell, 1997).

TPI5.2 is publicly available by anonymous FTP to:

ftp://topex.ucsd.edu/pub/global_topo_2min

Bathymetric data were extracted from the 1994 GEBCO Digital Atlas V1.06, which is a digitised edition of the General Bathymetric Chart of the Oceans (GEBCO) 5th edition which was published between 1978 and 1982 by the Canadian Hydrographic Service, Ottawa, Canada. It consists of 16 charts on Mercator Projection covering the world from 72°S to 72°N, on a scale of 1:10 million at the Equator; and two polar sheets on Polar Stereographic Projection to 64°S and 64°N respectively, on a scale of 1:6 million at 75° latitude. Each sheet depicts contoured bathymetry (in corrected metres) at standard depths of 200 m, 500 m and at 500 m intervals thereafter. For the most part, the bathymetry is based on a scientific interpretation of random tracklines of data from many different sources; the quality and coverage of these data is highly variable.

TerrainBase (NGDC, 1994) is a global 5-minute digital elevation model released by NGDC to succeed the earlier ETOPO5 global 5-minute digital elevation model (NGDC, 1988) which was known to contain major errors (Briggs, 1989; Smith, 1993). The TerrainBase model uses most of the same data that went in to developing ETOPO5. Major improvements were made in the parts of the model that cover the continents of North America, South America, Europe, Africa, Greenland, and Australia. Significantly, no improvements were made for Asia, Antarctica, and the oceans.

1.3.3 Sediment Isopach Maps

Two sediment isopach data sets were used during this project - the 1991 CCOP Offshore East Asia Total Sedimentary Isopach Maps, and the 1997 NGDC World's Oceans and Marginal Seas Sediment Isopach Database. Both of these data sets are likely to contain significant errors in Southeast Asia (R. Hall, *pers. comm.*). Visual inspection reveals that the CCOP data set shows more complex sedimentary bodies.

The Offshore East Asia Total Sedimentary Isopach Maps (CCOP, 1991) were compiled over the period 1986-90 on the basis of data contributed by the eight participating countries of the Working Group on Resource Assessment (WGRA): China, Indonesia, Japan, Korea, Malaysia, the Philippines, Thailand and Vietnam. The data set consists of six 1:4 million scale colour sedimentary isopach maps, contoured at 1000 m intervals.

The digital NGDC World's Oceans and Marginal Seas Sediment Isopach Database is gridded on a 5' × 5' grid. Sediment thickness data were compiled from three principle sources: previously published isopach maps including Ludwig & Houtz (1979), Matthias *et al.* (1988), Divins & Rabinowitz (1990), and Hayes & LaBrecque (1991); ocean drilling results, both ODP and DSDP; and seismic reflection profiles archived at NGDC as well as seismic data and isopach maps available as part of the IOC's Geological/Geophysical Atlas of the Pacific (GAPA) project (Divins & Eakins, 1997). The data values are in metres and represent the depth to acoustic basement, which may not actually represent the base of the sediments. These data are intended to provide a minimum value for the thickness of the sediment in a particular geographic region. The grid is available from the National Geophysical Data Center, Boulder, Colorado, U.S.A., or by anonymous FTP to:

ftp://ftp.ngdc.noaa.gov/MGG/sedthick

1.3.4 GEM-T3 Geopotential Model

The geopotential model used in this project is the GEM-T3 model which is complete to spherical harmonic degree and order 50 (Lerch *et al.*, 1992). The Goddard Earth Model (GEM)-T3 was developed by NASA/Goddard Space Flight Center in 1991 from a combination of satellite tracking, satellite altimeter, and surface gravimetric data. The minimum wavelength (λ_{min}) contained in this model is calculated from the formula:

$$\lambda_{min} = c_E / d \qquad (1.15)$$

where c_E is the circumference of the Earth (~ 40,000 km), and d is the degree of the model. Consequently the minimum wavelength contained in this model is 800 km. The global RMS geoid error is estimated at 59 cm through degree and order 50, but over the ocean areas mapped by altimetry, this number is less than 25 cm (Lerch *et al.*, 1994).

1.3.5 Coastline Database

The GSHHS digital coastline (Wessel & Smith, 1996) used in the project is a very high resolution coastline database that forms part of the GMT package (Section 1.5.1). The data set was compiled from two public domain data sets - the World Data Bank II (WDB; also known as CIA Data Bank) and the World Vector Shoreline (WVS). The precision of the GSHHS digital coastline is in the 50 - 500 m range.

1.4 Colour Display of Gravity Anomaly Data

The visualisation of gravity anomaly maps by geoscientists is performed by more or less sophisticated image processing tools and different kinds of enhancements (e.g. first/second derivatives, artificial sun-angle illuminations, 3D perspective images) in order to allow human analysts to better discriminate the geometrical features present in the data. The targets of this kind of analysis are mainly shallow geological lineaments such as faults, folds, geological contacts, and, more rarely, broad information about the extension and depth of the main causative bodies. This approach has the flavour of an art and requires specific training and expertise. As such, it has the disadvantage of being partly subjective, being influenced by the specific background and field of expertise of the analysing geoscientist (Boschetti *et al.*, 1997).

Examples of different colour images of the gravity anomaly field of the southwestern part of the South China Sea Oceanic Basin are given in Figures 1.4 to 1.8. The gravity field in this region is relatively smooth with localised gravity highs. Figures 1.4 and 1.5 show the most common type of colour display used for gravity anomaly data. The colour scales of these two images are divided into equal partitions with colours varying from red through blue to purple. Figure 1.5 is also illuminated from the northeast. More information can be seen qualitatively when a colour scale that apportions equal areas for each colour on the map is used (Figures 1.6 and 1.7). The colour scales for these two maps are not equally partitioned and the colours used vary from red to blue only. Purple is judged to be an inappropriate colour to use at either end of the colour scale as it is composed from both red and blue and may therefore be misleading. Figure 1.6 is illuminated from the northeast. Figure 1.7 demonstrates that overlaying contours spaced at regular intervals (here 10 mGal) onto a non-illuminated colour image imparts the maximum amount of quantitative information. Figure 1.8 shows a pseudo 3D perspective colour mesh image with the same colour scale as the map in Figure 1.7. Whilst this style of presentation can be very effective in showing features of interest, other information may be concealed behind more prominent features.

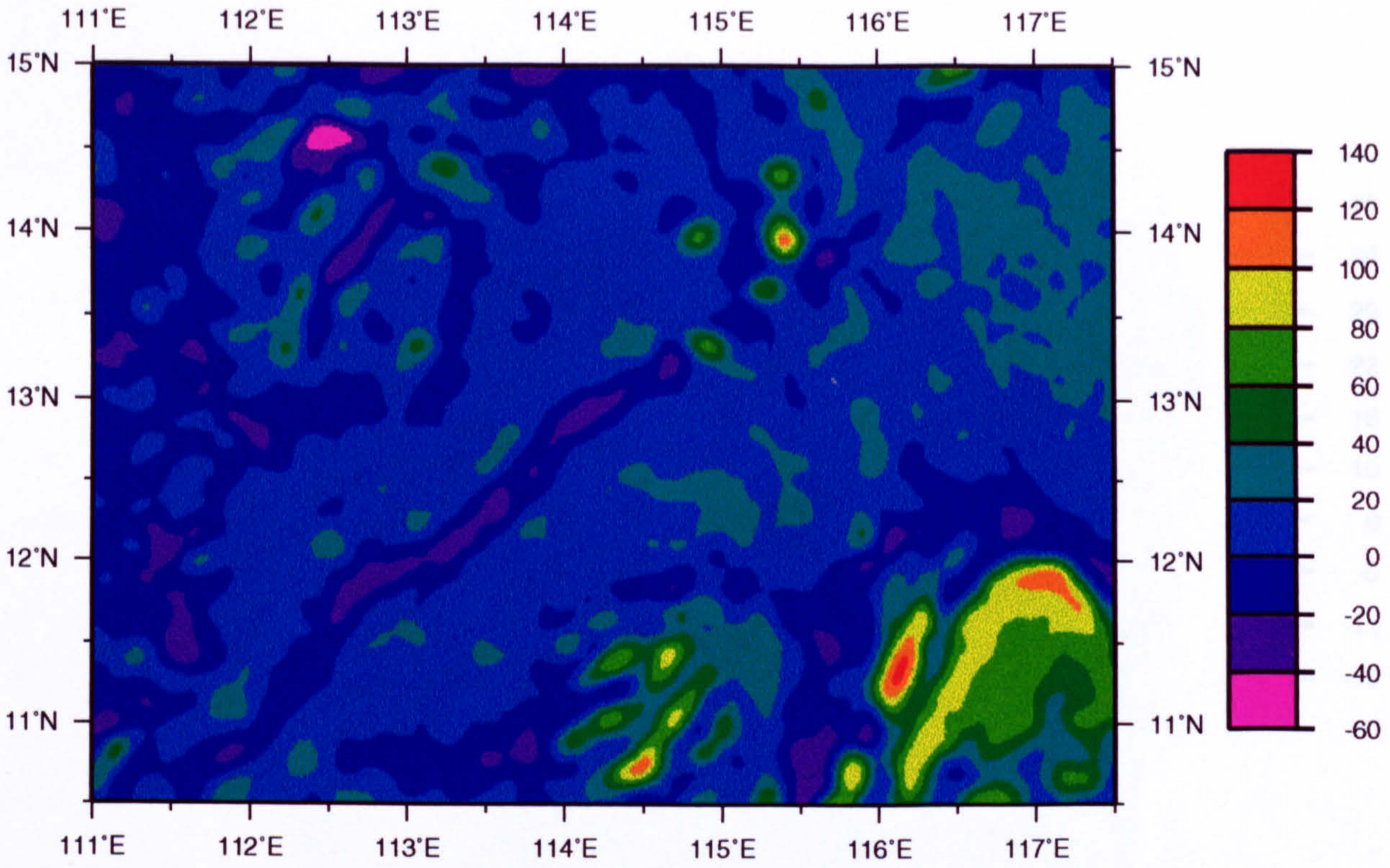

Figure 1.4. Basic colour gravity image. Colour scale in mGal.

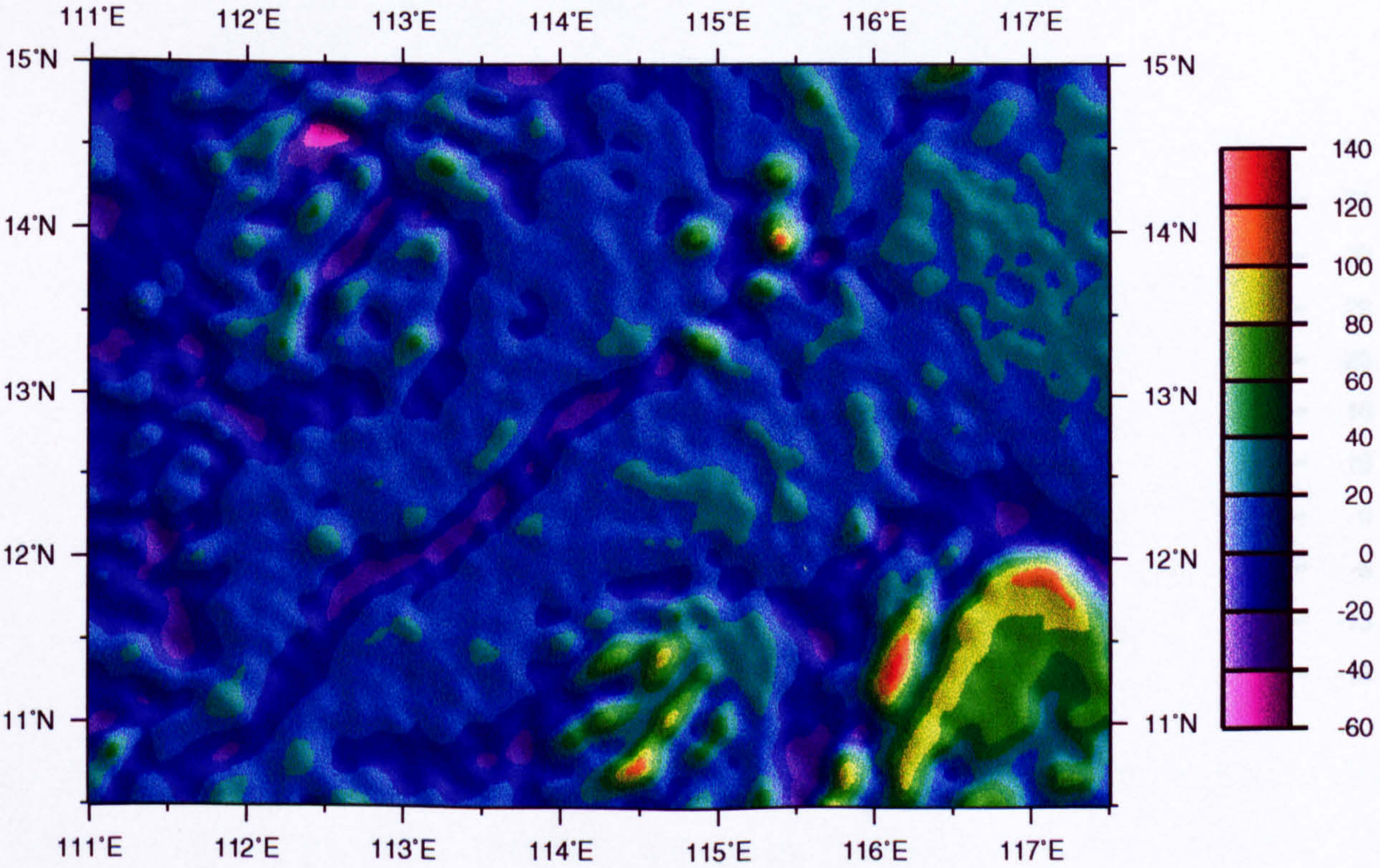

Figure 1.5. Basic colour gravity image illuminated from northeast.
Colour scale in mGal.

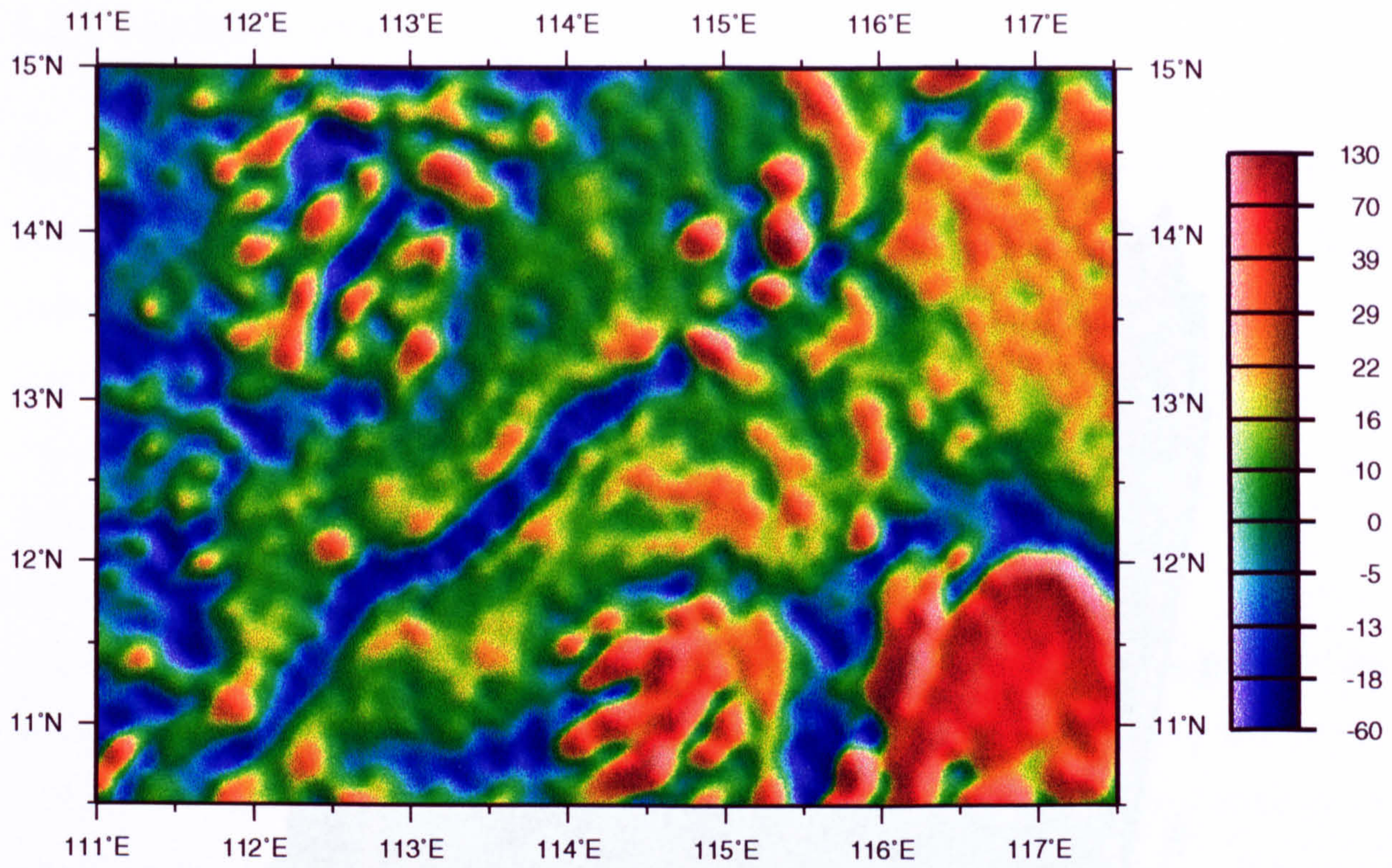

Figure 1.6. Colour gravity image that apportions equal areas of each colour, illuminated from northeast. Colour scale in mGal.

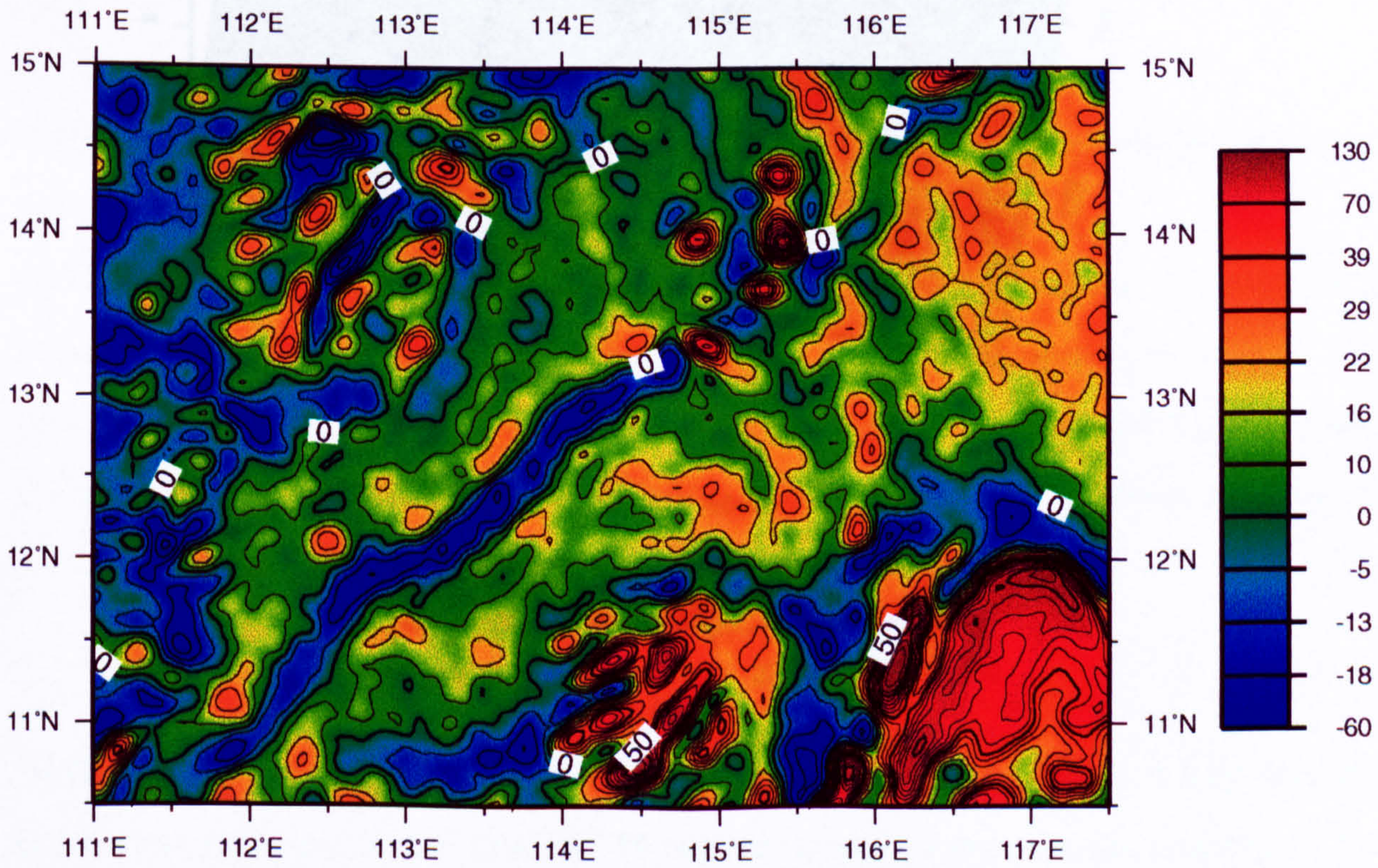

Figure 1.7. Colour gravity image that apportions equal areas of each colour. 10 mGal contour interval, bold contours every 50 mGal. Colour scale in mGal.

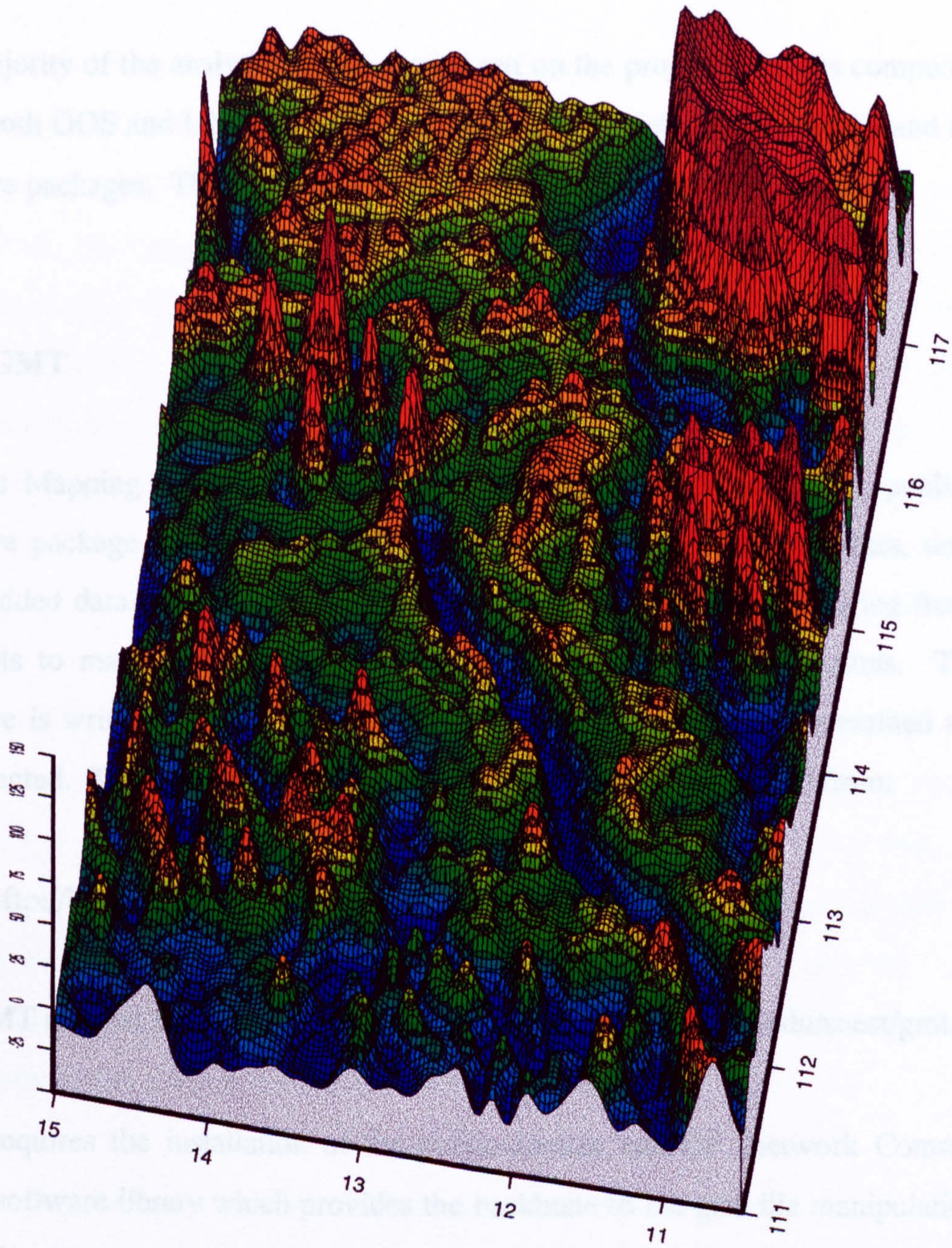

Figure 1.8. Pseudo 3D colour mesh gravity image viewed from W10°S.
Vertical Scale in mGal.

1.5 Computer Software

The majority of the analytical work carried out on the project data was computer-based, using both DOS and UNIX operating systems and a variety of commercial and academic software packages. These software packages are briefly described below.

1.5.1 GMT

Generic Mapping Tools or GMT (Wessel & Smith, 1995) is a free, public-domain software package that can be used to manipulate columns of tabular data, time-series, and gridded data sets, and display these data in a variety of forms ranging from simple *x*-*y* plots to maps and colour, perspective, and shaded-relief illustrations. The GMT software is written as a set of ~ 50 UNIX tools and is totally self-contained and fully-documented. The GMT package can be obtained by anonymous FTP from:

ftp://kiawe.soest.hawaii.edu/pub/gmt

The GMT internet home page address is http://www.soest.hawaii.edu/soest/gmt.html.

GMT requires the installation of the public-domain netCDF (network Common Data Form) software library which provides the backbone to the grid file manipulations. The netCDF software was developed at the Unidata Program Center in Boulder, Colorado, U.S.A. The freely available netCDF software can be obtained by anonymous FTP from:

ftp://unidata.ucar.edu/pub/netcdf

GMT and netCDF were installed onto a Sun computer and used to manipulate the gravity and bathymetry data sets. GMT was also used to produce the majority of the scientific illustrations in this thesis.

1.5.2 GM-SYS

The forward modelling gravity software package used during the project was a commercially available package called GM-SYS Version 1.75.

The 2D or 2½D modelling software calculates the theoretical gravity anomaly at an observation point resulting from a series of polygonal bodies of uniform densities. The gravity signature and end corrections are calculated for each polygon, simulating the effect of limited strike length. An output diagram shows the predicted gravity response of the depth modelled section and the observed gravity anomaly. The depth model is then refined subject to geologic controls (such as depth and density measurements) wherever possible until the predicted gravity response matches the observed gravity anomaly.

Values of -30000 and +30000 km (default values) were used as the *y* axis limits of the models, and the same values were also used for the limits of the *x* axis, although variations in the models ceased to have a significant effect on the gravity profile about 10 km beyond the end of the profile line. During modelling, it was assumed that bodies deeper than the Moho had no effect on the observed gravity profiles. The modelling philosophy of this study is described in detail in Section 6.2.

The models produced using GM-SYS are described in Section 6.4.

1.5.3 Other Software Packages

The other software packages used extensively throughout this project were CorelDRAW! Version 5.00.G1 (for graphical illustrations), Microsoft Word Version 6.0c (for word processing), and Microsoft Excel Version 5.0c (for spreadsheet data manipulation and production of graphs).

1.6 Data Retrieval from the Internet

The amount of material made publicly-available through internet pages has increased enormously since the start of this project in October 1994. Timely discoveries of data, pictures, text and software on the internet played a key role in the evolution of this project. However much time was wasted searching for the proverbial needle in the haystack. Therefore a couple of recommended starting points for web surfing are:

- http://www.seg.org/committees/grav_mag/gm_links.html (gravity home pages)
- http://www.cgrer.uiowa.edu/servers/servers_geodata.html (geoscience data sources)
- http://www.uh.edu/~jbutler/anon/anondata.html (more geoscience data sources)
- http://southport.jpl.nasa.gov/index.html (space science home pages)

This information is correct as of 24th October 1997 but could go out of date at any time owing to the ephemeral nature of internet pages.

CHAPTER 2

The Geology of Southeast Asia

CHAPTER 2. THE GEOLOGY OF SOUTHEAST ASIA

2.1 Overview

Southeast Asia is one of the most actively deforming regions in the world. This deformation is a consequence of the Cenozoic juxtaposition of the Indian, Eurasian, Pacific, Australian and Philippine Sea plates. These plate interactions culminated in the Paleogene to Present collision of India with Tibet and the Neogene to Present collision of Australia with Sundaland. Cenozoic reconstructions of Southeast Asia are often contradictory (e.g. Rangin *et al.*, 1990*b*; Daly *et al.*, 1991; Briais *et al.*, 1993; Lee & Lawver, 1994; Hall, 1996) especially when dealing with Borneo and the poorly constrained eastern boundary of the region. This chapter presents a regional geological overview and a discussion of the published tectonic reconstructions with emphasis on the work of Metcalfe (1996) and Hall (1996). For reference, the geological time scale and stratigraphic column are given in Table 2.1.

Era	Period	Sub-period	Epoch		Ma
Cenozoic	Quaternary		Holocene		0.01
			Pleistocene		1.64
	Tertiary	Neogene	Pliocene		5.2
			Miocene	Upper	10.4
				Middle	16.3
				Lower	23.3
		Paleogene	Oligocene		35.4
			Eocene		56.5
			Paleocene		65.0
Mesozoic	Cretaceous				146
	Jurassic				208
	Triassic				245
Paleozoic	Permian				290
	Carboniferous				363
	Devonian				409
	Silurian				439
	Ordovician				510
	Cambrian				570

Table 2.1. The Geological Timescale and Stratigraphic Column, modified from Harland *et al.* (1992).

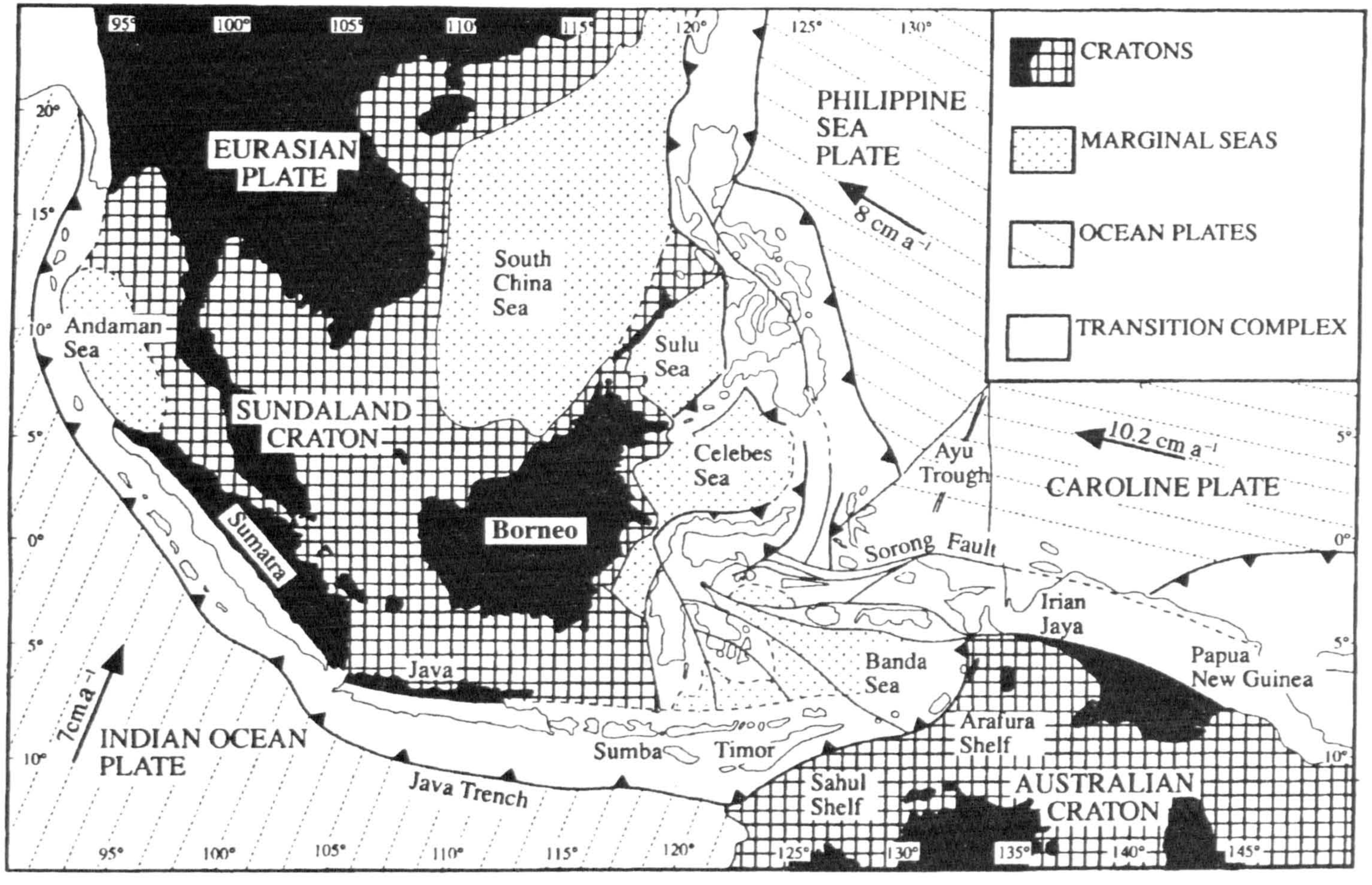

Figure 2.1. Tectonic setting of Southeast Asia, from Simandjuntak & Barber (1996).

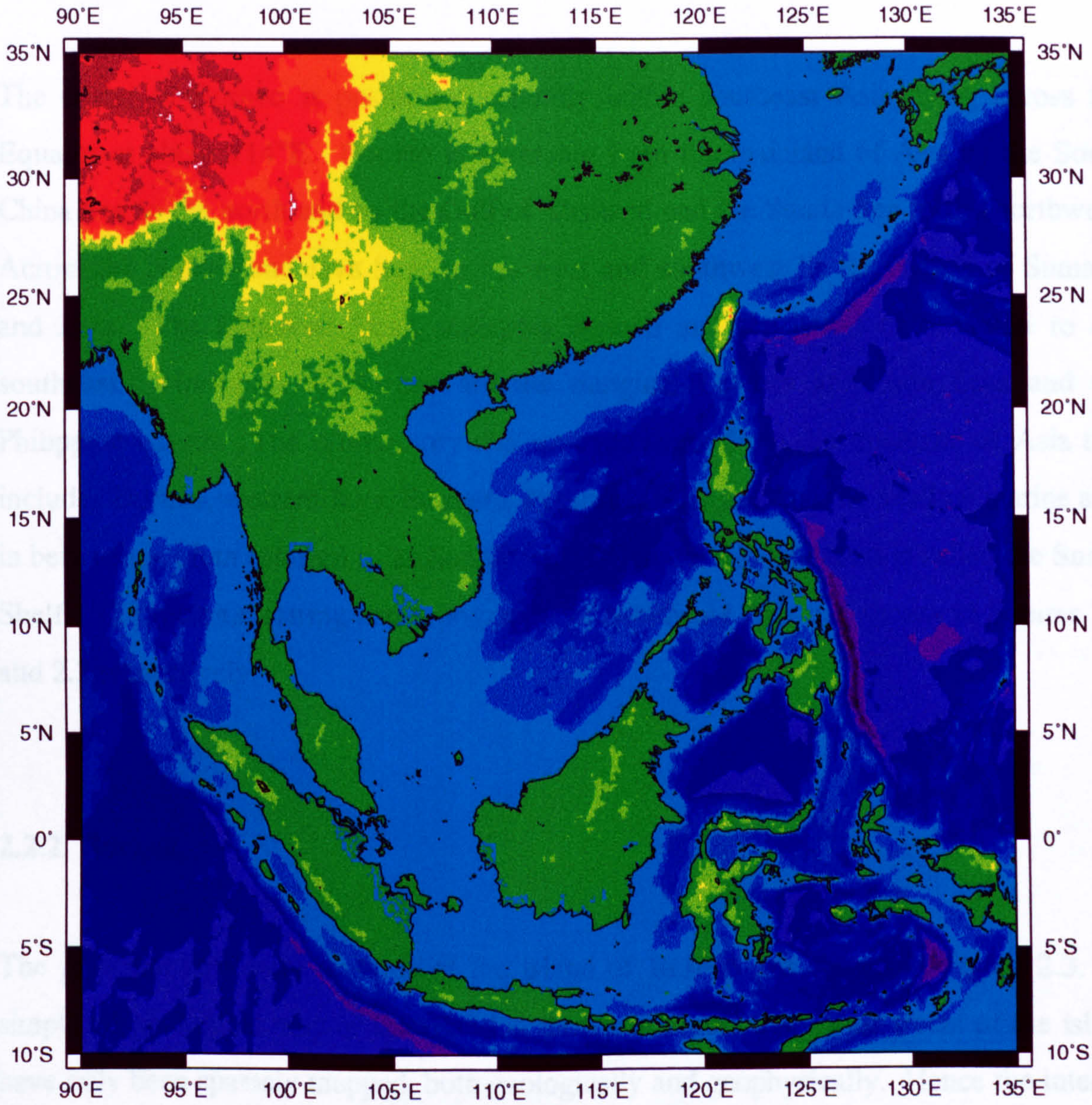

Figure 2.2. TerrainBase Elevation Model of Southeast Asia.

2.2 Physiography of Southeast Asia

2.2.1 Nomenclature

The island of Borneo is positioned centrally within southeast Asia, lying across the Equator at about 114°E. Borneo is separated from the mainland of Asia by the South China Sea to the north and by the Gulf of Thailand and the Sunda Sea to the northwest. Across the Natuna and Java Seas to the west and southwest lie the islands of Sumatra and Java. The Makassar Strait separates Borneo and the island of Sulawesi to the southeast. Northeast of Borneo are the marginal Celebes and Sulu Seas and the Philippine islands. The promontory that extends south from the mainland of Asia that includes Borneo, western Java, Sumatra, Peninsula Malaysia and the shallow marine area in between is often referred to as Sundaland. Offshore, this landmass is called the Sunda Shelf. The tectonic setting and topography of Southeast Asia are shown in Figures 2.1 and 2.2 respectively.

2.2.2 Borneo

The principal structural features of the island of Borneo are shown in Figure 2.3. A simplified geological map of the island is shown in Figure 2.4. Vast tracts of the island have only been sparsely mapped, both geologically and geophysically. Hence the interior of Borneo remains poorly known (Hutchison, 1996).

The Schwaner Mountains block which dominates the southwestern corner of Borneo constitutes the continental core of the island (Moss, 1994). This block contains abundant Cretaceous batholithic intrusions (Williams *et al.*, 1988; Pieters & Supriatna, 1990), intruded into a continental basement of slates, amphibolites, schists and gneisses of Silurian to Permian age. It has been suggested that this southwestern corner of Borneo was attached to the rest of Sundaland by the mid-Jurassic (Haile *et al.*, 1977; Hamilton, 1979; Williams *et al.*, 1988) and that the plutonic rocks within the Schwaner

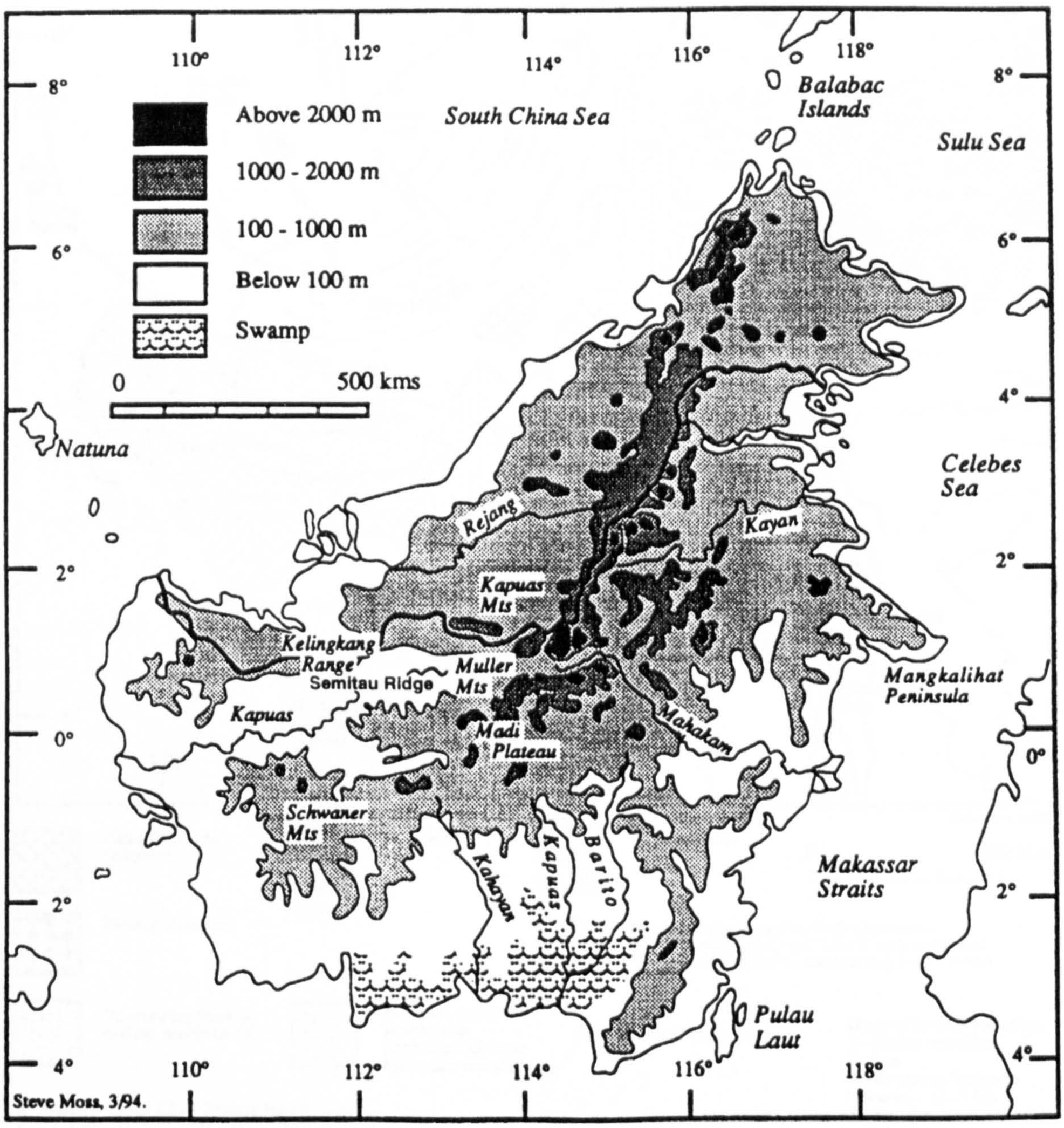

Figure 2.3. Physiography of Borneo (from Moss, 1994).

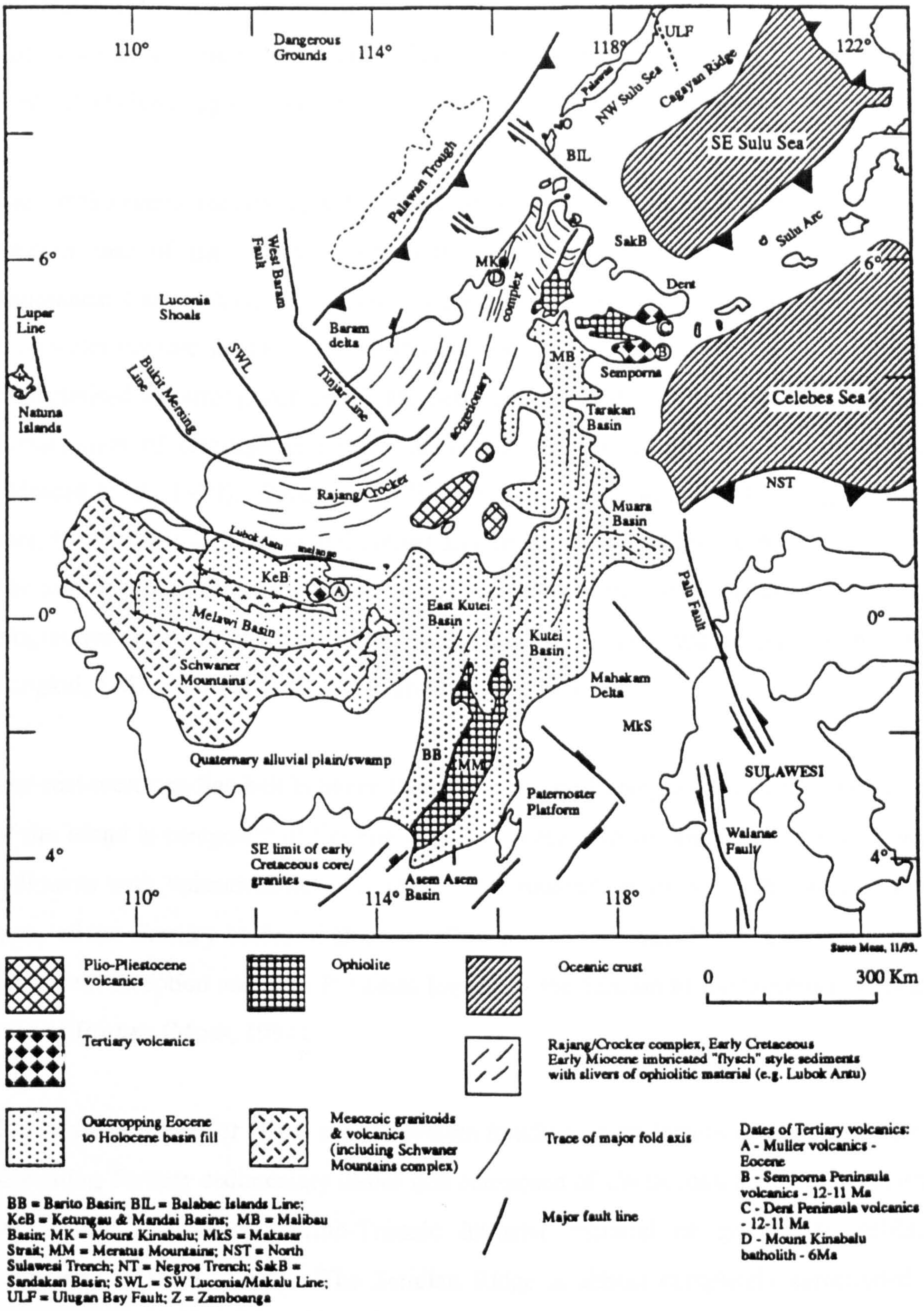

Figure 2.4. Simplified geological map of Borneo (from Moss, 1994).

Mountains represent a continuation of the Yenshanian magmatic arc of South China. Not all workers in the region support this hypothesis; both Gower (1990) and Lumadyo *et al.* (1993) have argued against Borneo being attached to Eurasia prior to the Eocene.

The northwestern (Sarawak) side of the island, the northern region (Sabah) and the western side of the central north-south highlands (sometimes referred to as the Kalimantan Central Range) form an S-shaped area underlain by Cretaceous to Tertiary deep water/oceanic sediments, in particular the Rajang Group. This orogenic complex is characterised by strong compressional deformation (folds and thrusts), and the local development of cleavage and many duplications of the stratigraphy due to faulting (Bérnard *et al.*, 1990). Several ophiolite slices occur within or on the margins of this area, for example at Telupid and Darvel Bay in Sabah and at Lubok Antu in Sarawak. The area has been interpreted as a large Cretaceous accretionary prism formed by the progressive accretion of material at the northwest Borneo margin (Hamilton, 1979; Tongkul, 1987; Bérnard *et al.*, 1990; Hutchison, 1996).

The east-west trending belt between the Schwaner and Rajang areas and the eastern side of the island is composed of Eocene (and Paleocene?) to Recent clastic and carbonate sediments with volcaniclastics and acid to intermediate intrusives. This area includes many of the Tertiary basins of Borneo. Two features of these basins are their roughly coincident inception and their locations bordering the Silurian to Cretaceous continental core of Borneo (Moss, 1994).

The Semitau Ridge (or High) is an east-west trending linear feature in west Kalimantan, separating Tertiary sedimentary basins and composed of Cretaceous deep marine clastics and volcaniclastics and Permo-Triassic intrusive material of granitic to gabbroic composition (Moss, 1994). The Semitau Ridge is almost completely surrounded by Tertiary sediments.

The Meratus Mountains in the southeastern corner of the island consist of ophiolitic, metamorphic, volcaniclastic, clastic and carbonate rocks of Early Cretaceous to Paleocene age (Sikumbang, 1990). The ophiolitic material is believed to have been

formed as ocean floor by the Early Cretaceous, but has been emplaced on Borneo by subsequent deformation which has juxtaposed it against Lower Cretaceous shelf sediments (Moss, 1994). Exposures of similar Cretaceous sediments and ophiolitic material occur on Sebuku and Laut islands offshore southeast Sulawesi and along the southwestern coastline of Kalimantan. The Meratus Mountains have a clear NNE-SSW trend which is commonly referred to as the Meratus trend (Wain & Berod, 1989).

2.2.3 Sabah

2.2.3.1 Introduction

Sabah, located at the northeastern tip of Borneo, has been the subject of a number of studies by members of the University of London Southeast Asia Research Group, including Tongkul (1987) - the Crocker Formation, Clennell (1992) - the East Sabah Melanges, and Omang (1993) - the Darvel Bay Ophiolite. Currently J. Noad (1994 -) is studying the sedimentology of the onshore Tertiary sedimentary basins.

In order to understand the geology and structure of Sabah, three areas have been selected for a brief discussion - geomorphology, chronostratigraphic units and structure. The tectonic evolution of Sabah is discussed in Chapter 6. A geological map of Sabah is given in Figure 2.5.

2.2.3.2 Geomorphology

Sabah is divisible into a number of distinct geomorphological provinces, Figure 2.6. To the west a narrow coastal plain gives way to the Crocker Ranges, a mountain belt some 100 km wide which rises up to about 2000 m above sea level. The Crocker Ranges drain in a trellis pattern, mostly discharging into the South China Sea. To the north of the Crocker Ranges, Mount Kinabalu, a granitoid massif, reaches 4093 m, making it the highest mountain in Southeast Asia. To the north lie the twin peninsulas of Kudat and Bengkoka, which are characterised by rocky inlets and undulating topography. The central part of Sabah is quite mountainous, and dissected by deep river valleys, which

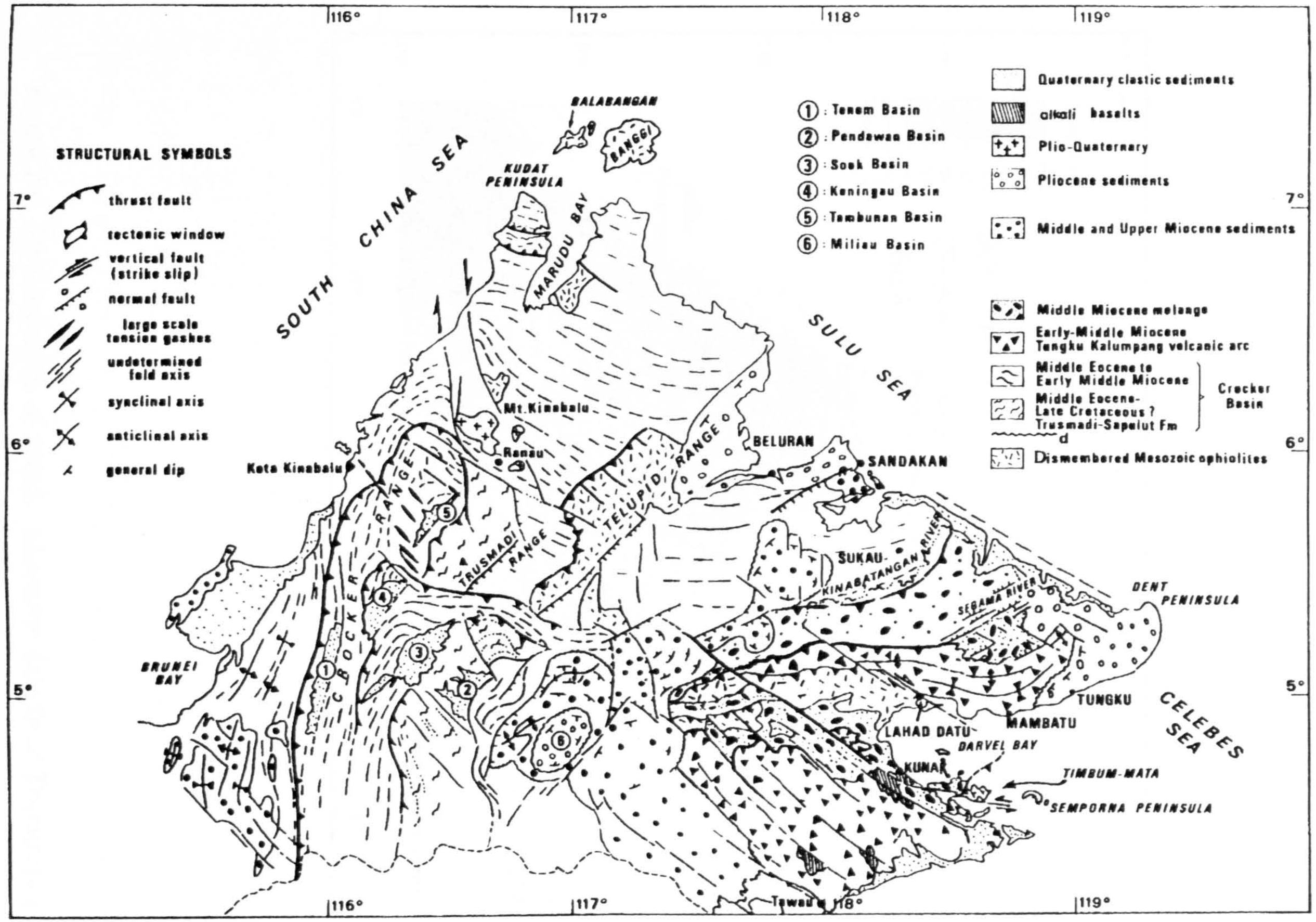

Figure 2.5. Geological Map of Sabah, from Rangin *et al.* (1990*a*).

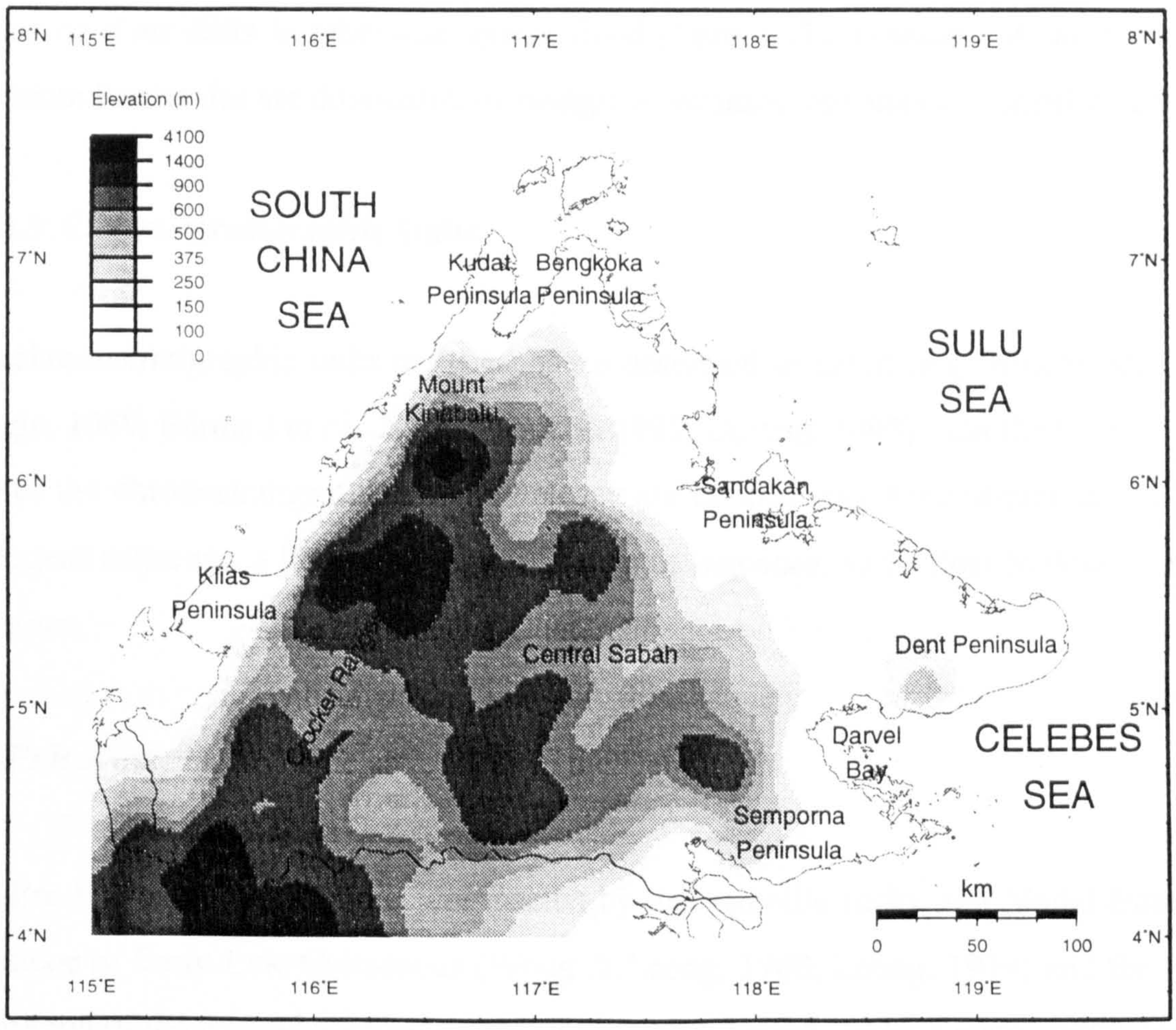

Figure 2.6. Physiography of Sabah. Elevation data from TerrainBase.

generally flow to the east. The mountains reach to the coast in the southeast, around Darvel Bay, where the shores and islands are rocky. The southeast of Sabah, the Semporna Peninsula, is mountainous to hilly, and drained by small, low-sinuosity rivers. The remainder of the east of Sabah comprises the flat to undulating terrain of the Sandakan and Dent Peninsulas, drained by the large Labuk, Kinabatangan and Segama river systems. These have switched courses many times in the recent geological past, and in several areas such upheavals are marked by sudden changes in direction, steep gorges or river cliffs in otherwise gentle flood plains. The coastline of the Dent and Sandakan Peninsulas are dominated by mangrove swamps, estuaries and small deltas.

2.2.3.3 Chronostratigraphic Units

The chronostratigraphic units of Sabah were described in detail (e.g. Hutchison, 1988; Rangin, 1989; Bérnard *et al.*, 1990; Tongkul, 1991; Omang, 1993). On the basis of their studies the chronostratigraphic units of Sabah are divided into three sequences - a Pre-Paleogene sequence, a Paleogene-Middle Miocene sequence, and a Post Middle Miocene sequence.

Pre-Paleogene Sequence

The Pre-Paleogene sequence is represented by the ophiolite rocks, the Madai-Baturong limestone of Early-Late Cretaceous (Wong & Leong, 1968; Leong, 1974) and the Chert Formation of the Early-Late Cretaceous (Kirk, 1968; Leong, 1974; Leong, 1977; Jasin *et al.*, 1985; Jasin & Tahir, 1988).

Ophiolite outcrops are distributed throughout Sabah, and are found in a belt running from Banggi Island in the north to Ranau and Telupid in central Sabah, and also outcrop in the Lahad Datu area in the east. Leong (1974) suggested that the age of the formation of the ophiolite is as old as Early Jurassic (210 ± 3 Ma), based on an isotopic age obtained from tonalite intruded into metagabbros. The Darvel Bay ophiolite complex+ is the most extensive outcrop, extending 100 km westward from Darvel Bay. This complex was subject to a detailed geochemical analysis by Omang (1993) who concluded

+ (of late Early Cretaceous to middle Jurassic age, Omang (1993))

that the complex represents a segment of oceanic crust and upper mantle which has had several kilometres removed by erosion since its emplacement on Sabah (Omang & Barber, 1996). The complex has been interpreted as being of either proto-South China Sea (Holloway, 1981; Rangin *et al.*, 1990*a*) or Celebes Sea (Hutchison, 1988) origin. The ophiolitic complex was obducted onto Sabah either in the latest Cretaceous or earliest Paleogene (Rangin *et al.*, 1990*a*).

Cherts and spilites/basalts of the ophiolite complex are always associated with one another and have been called the Chert-Spilite Formation of Late Cretaceous age (Reinhard & Wenk, 1951). Leong (1974) considered the Madai-Baturong as probably an older sedimentary formation preceeding the deposition of the Chert-Spilite Formation and deposited in shallow marine warm water. The occurrence of unmetamorphosed limestones of Late Cretaceous age in the Segama Valley (Wong & Leong, 1968; Leong, 1974) probably represent lateral facies equivalent of the Early-Late Cretaceous Madai-Baturong limestone Formation and contain shallow and deep foraminifera and algae (Tongkul, 1991).

Paleocene to Eocene shallow water limestones are found resting unconformably on the ophiolite in central, western, eastern and northern Sabah (Collenette, 1958; Collenette, 1965; Fitch, 1958; Wilson & Wong, 1964; Leong, 1974; Jasin *et al.*, 1988; Tongkul, 1990).

Paleogene-Middle Miocene Sequence

This sequence can be divided into a sedimentary rock unit, a volcanic rock unit, and a melange unit. The sedimentary rock unit comprises flysch sediments which were deposited in a deep to shallow marine environment in the huge Crocker basin (Tongkul, 1987). This sedimentary unit is represented by the Trusmadi, Sapulut, Temburong, Crocker, Tanjung, South Banggi, Setap Shale, Kalabakan and Kapilit Formations (Tongkul, 1991; Hutchison, 1988). They show numerous lateral facies changes and consist predominantly of quartz sandstones with varying amounts of silt and clay (Bérnard *et al.*, 1990). In central Sabah, Oligocene to Lower Miocene sedimentation

produced two units known as the Labang and Kulapis Formations which are primarily distinguished on the basis of colour.

The volcanic rock unit is represented by Late Oligocene to Middle Miocene pyroclastics and lavas, forming the Dent Peninsula volcanic arc (Rangin *et al.*, 1990*a*; Tongkul, 1991; Clennell, 1991). Volcaniclastic rocks form the Silabukan-Tungku Formation (Tahir, 1989). Andesite lavas form the Tungku Arc (Leong, 1974; Rangin, 1989; Rangin *et al.*, 1990*a*). Some authors (e.g. Taylor & Hayes, 1983; Hinz *et al.*, 1991) have suggested that the Dent Peninsula volcanic arc was formed due to the southeastward subduction of the proto-South China Sea oceanic lithosphere beneath the Borneo microcontinental plate. Mitchell *et al.* (1986) and Rangin (1989) favour a northwestward subduction of the Celebes Sea as the cause of this volcanism.

Melange units (chaotic deposits) are found in many parts of western Sabah. In the east of the state melanges outcrop over some 12,000 km^2 of terrain (Clennell, 1992). These chaotic units are represented by Crocker Melange, Wairu, Garinono, Ayer and Kuamut Formations. These formations were formed respectively during Early Miocene-early Middle Miocene (Letouzey *et al.*, 1988), Middle Miocene (Tongkul, 1990) and late Early Miocene-early Middle Miocene (Clennell, 1990; Clennell, 1991). The formation of these melanges can be related to tectonism (tectonic faulting), mud diapirism and olistostrome (sedimentary mass-transport) processes (Barber *et al.*, 1986; Barber & Brown, 1988; Clennell, 1991; Clennell, 1992). In eastern Sabah the source of the melange matrix and most of the sandstone blocks is disaggregated Labang Formation sediments (Clennell, 1996). Subordinate volumes of melange and broken formation are derived from slumping of Kulapis Formation sediments. There is a small amount of ophiolitic material within the melanges, and in the south of Sabah, both the matrix and the blocks are sourced increasingly by volcaniclastics. The melanges were mostly produced by submarine slope failures that were triggered by tectonic rearrangement of central Sabah at the end of the Early Miocene. A relatively small volume of melange emplaced into Middle Miocene and younger sediments are of diapiric origin, associated with the effusive mud volcanism which continues to the present day in eastern Sabah and in the Sandakan Basin (Clennell, 1996).

Post Middle Miocene Sequence

This sequence may be divided into a sedimentary unit, a volcanic unit, and a plutonic unit. The sedimentary unit is represented by Late Miocene-Pleistocene fluvio-deltaic sediments which were deposited in a shallow water environment (Tongkul, 1991). Among formations included in this unit are the Bongaya, Sandakan, Belait, Umas-Umas, Liang and Timohing Formations.

The volcanic unit consists of pyroclastic rocks, lavas and volcaniclastic rocks. Pyroclastic rocks and lavas are represented by the Tawau-Semporna volcanic arc of Late Miocene to Quaternary age (Hutchison, 1988). This volcanic arc represents the southwestward extension of the Sulu volcanic arc resulting from the southeastward subduction of the southeast Sulu Sea basin along the Sulu Trench (Hamilton, 1979, Hutchison, 1978; Hutchison, 1988; Hinz *et al.*, 1991; Rangin, 1989; Rangin *et al.*, 1990*a*; Rangin & Silver, 1991). The volcaniclastic rocks are represented by the Dent Group (Sebahat, Ganduman and Togopi Formations) of Upper Miocene to Pliocene age, whereas the lava flows are of Pliocene-Quaternary age with basaltic, andesitic and dacitic compositions. The volcaniclastic unit of this sequence conformably overlies the Oligocene-Miocene volcaniclastic rocks in the Dent Peninsula area (Tahir, 1989).

The plutonic or intrusive bodies are mainly exposed in the Ranau area (western Sabah) and are represented by Mount Kinabalu and its satellite granitic plutons. The whole rock K/Ar dates are commonly as old as 10 Ma (Jacobson, 1970). The occurrence of these bodies is related to the Sabah Orogeny (Hutchison, 1996).

2.2.3.4 Structure

A structural map of Sabah and the surrounding area is given in Figure 2.7. Table 2.2 summarises the structures observed on Sabah. Figure 2.8 shows a representative section across Sabah.

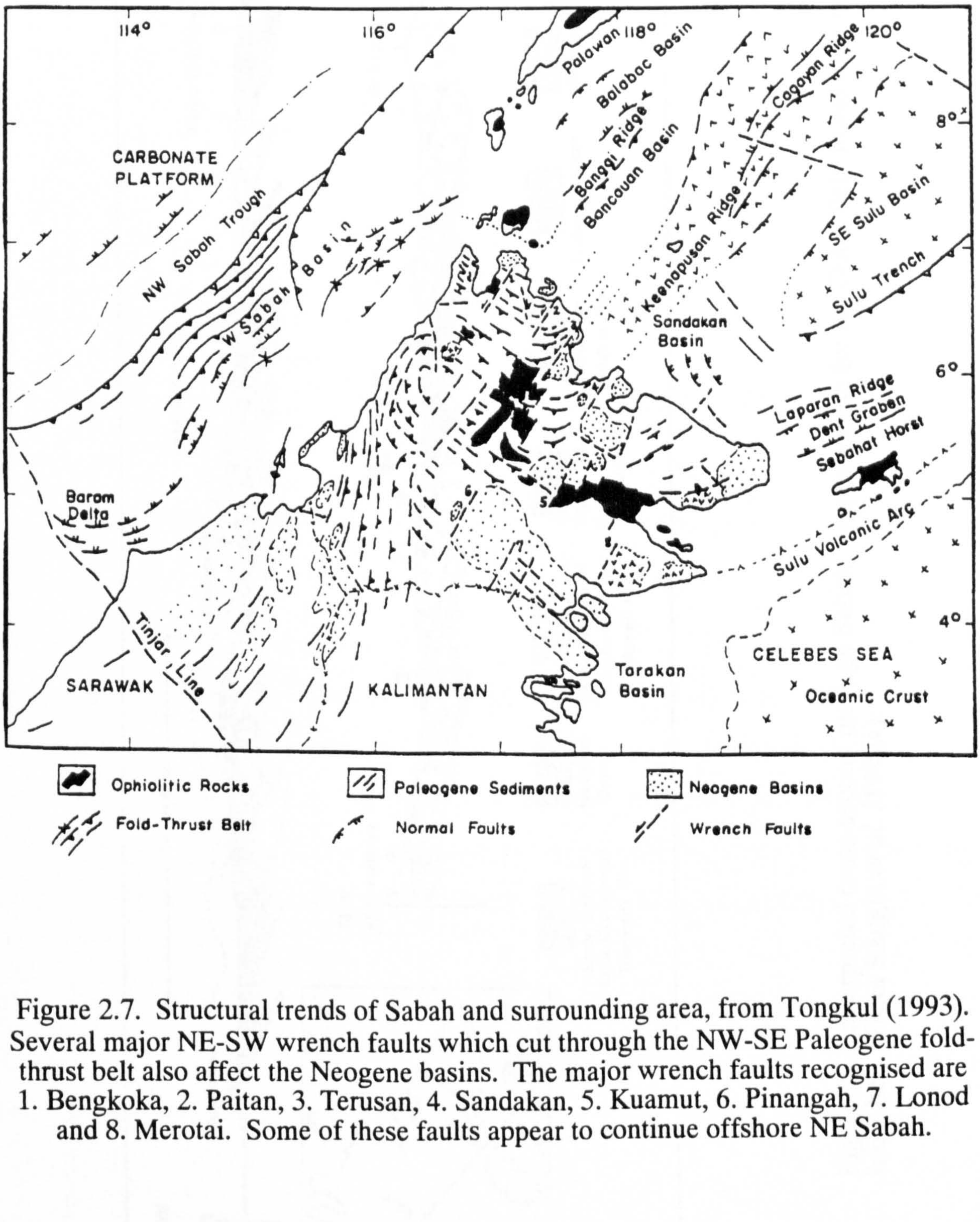

Figure 2.7. Structural trends of Sabah and surrounding area, from Tongkul (1993). Several major NE-SW wrench faults which cut through the NW-SE Paleogene fold-thrust belt also affect the Neogene basins. The major wrench faults recognised are 1. Bengkoka, 2. Paitan, 3. Terusan, 4. Sandakan, 5. Kuamut, 6. Pinangah, 7. Lonod and 8. Merotai. Some of these faults appear to continue offshore NE Sabah.

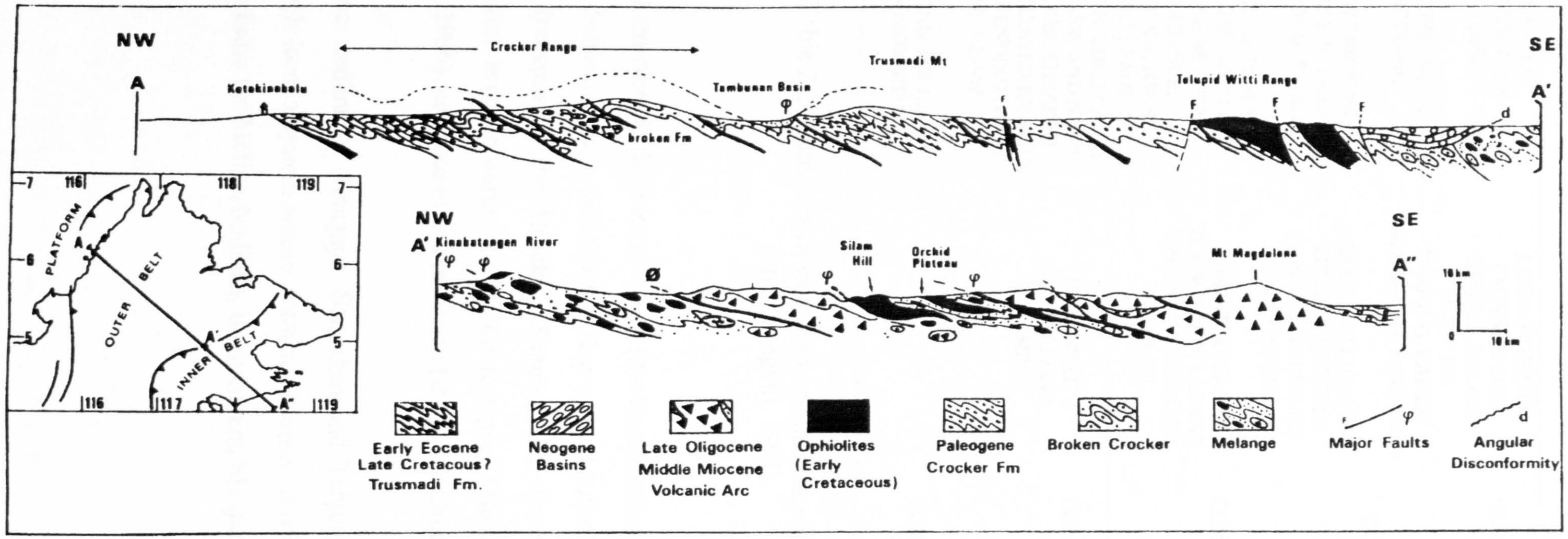

Figure 2.8. Interpreted cross-section through Sabah. Upper section for the Outer Belt, lower section for the Inner belt. From Rangin *et al.* (1990*a*).

STRUCTURE	FORMATION	DEFORMATION DIRECTION	EPISODE OF DEFORMATION
GENTLE NE-SW FOLD AXES	LIBONG TUFFITE, TABANAK CGL., TUNGKU, BELAIT, SETAP SH.	COMPRESSION NW-SE	LATE MIOCENE
STEEPENING OF BEDDING NE-SW TRENDING SLUMP FOLD AXES & NORMAL FAULTS	TANJONG, KAPILIT KALABAKAN, SANDAKAN LABANG, KALUMPANG KULAPIS, CROCKER SAPULUT, TRUSMADI CHERT-SPILITE	EXTENSION NW-SE	MIDDLE MIOCENE
FOLDED & THRUST FAULTED WITH A NW, NE, SE & SW VERGENCE; N-S, NE-SW, NW-SE WRENCH FAULTS	KUDAT, KULAPIS TEMBURONG, LABANG CROCKER, TRUSMADI SAPULUT	COMPRESSION N-S & NW-SE	EARLY MIOCENE LATE OLIGOCENE
TIGHTLY FOLDED CHERT WITH NE-SW AND N-S(?) FOLD AXES; SHEARED AND BRECCIATED IGNEOUS ROCKS TRENDING NW-SE AND NE-SW	CHERT-SPILITE CRYSTALLINE BASEMENT	COMPRESSION NW-SE & N-S	EARLY EOCENE
FAULTING, FOLDING METAMORPHISM		COMPRESSION NW-SE ?	? EARLY CRETACEOUS

Table 2.2. Summary of structures and their interpretations in Sabah (after Tongkul, 1991).

The onland structure in the west of Sabah (the Crocker Accretionary Complex / Crocker Ranges) is dominated by an NE-SW trending uplifted belt of folded and faulted turbiditic sediments (comprising the Crocker, Sapulut and Trusmadi Formations). These sediments were inverted during the Middle to Upper Miocene inversion. According to Hutchison (1996) the cause of this inversion (the Sabah Orogeny) remains obscure.

The Miocene sediments (Bongaya, Sandakan and Tanjong Formations) deposited in central Sabah form a system whose northeast-southwest trend parallels that of the Sulu Sea, and includes the Meliau, Malibau, Bukit Garam, Manjang and Sandakan Basins.

2.2.4 South China Sea

North and west of Borneo, the South China Sea and basins contiguous to it cover a surface area of 2.32×10^6 km^2. They are the result of a large amount of extension at the south China margin. According to Taylor & Hayes (1983), seismic and well data show that the onset of rifting along the south China margin most likely occurred during latest Cretaceous or Paleocene (65 ± 10 Ma). This predates the India-Asia collision which occurred at approximately 50 Ma (Besse *et al.*, 1984). Extension ceased in the Middle Miocene. A significant amount of shortening is believed to have followed, mostly along the eastern and southern margins of the sea, from the Middle Miocene to the present (Holloway, 1982; Fricaut, 1984). Within the South China Sea, there are a number of fault-bounded micro-continental fragments, including Macclesfield and Reed Banks and the Spratley (Dangerous Grounds) and Paracel Islands, which rifted from the Chinese mainland (Taylor & Hayes, 1980).

The South China Sea is floored by continental, attenuated continental and oceanic crust. Throughout this thesis the part of the South China Sea floored by oceanic crust is referred to as the South China Sea oceanic basin (SCSOB). The transition from continental to attenuated continental crust within the South China Sea is roughly coincident with the 1000 m bathymetry contour (Figure 2.9). The southern margin of the South China Sea is marked by the northeast-southwest trending Borneo-Palawan trough, which is a southeast-facing half-graben at the edge of the northwest Sabah platform. The Borneo-Palawan trough is interpreted either as a relict subduction zone, implying that the southern margin of the South China Sea was formerly active (e.g. Taylor & Hayes, 1980; Taylor & Hayes, 1983), or as a deep sedimentary graben in a passive margin (Fricaut, 1984; Hinz & Schluter, 1985). The eastern margin of the South China Sea terminates at the roughly north-south trending Manila Trench, where the oceanic basin is presently subducting beneath the Philippines Island arc. The northern margin abuts against the South China/Hainan margin.

The SCSOB has been extensively surveyed over the last thirty years (e.g. Taylor & Hayes, 1980; Taylor & Hayes, 1983; Briais *et al.*, 1989; Pautot & Rangin, 1989; Pautot *et al.*, 1990; Briais *et al.*, 1993; Coulon *et al.*, 1995). SeaBeam bathymetry, single

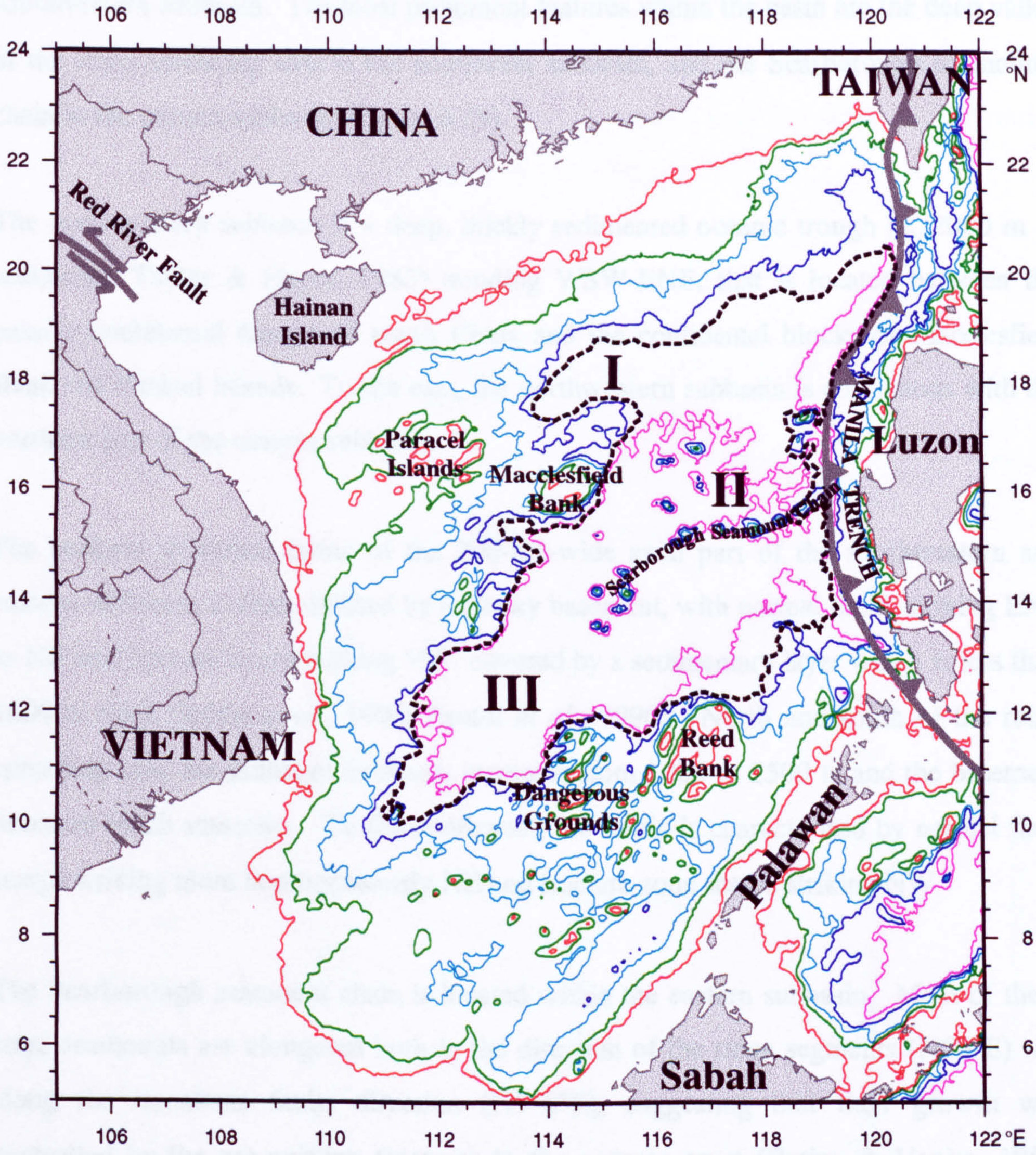

Figure 2.9. Location map for South China Sea Oceanic Basin. Dotted line is the approximate limit of the oceanic crust. Areas I, II and III are the northwestern, eastern and southwestern subbasins, respectively, as referred to in the text. Coloured lines are bathymetry: red - 200 m; green - 1000 m; light blue - 2000 m; blue - 3000 m; and purple - 4000 m. Bathymetric data from TPI 5.2.

channel seismic profiles, heat flow, magnetic and gravity data were collected, giving a clear picture of the physical structure and evolution of the basin. The oceanic basin may be divided into three subbasins - the northwestern subbasin, eastern subbasin and southwestern subbasin. The most prominent features within the basin are the deep valley of the relict spreading axis in the southwest subbasin, and the Scarborough seamounts chain in the eastern subbasin (Figure 6.29).

The northwestern subbasin is a deep, thickly sedimented oceanic trough (*c.* 2000 m of sediments, Taylor & Hayes, 1983) trending WSW-ENE, that is located between the passive continental margin of south China and the continental blocks of Macclesfield Bank and Paracel Islands. To the east, the northwestern subbasin is continuous with the northern part of the eastern subbasin.

The uniform structural fabric of the 200-km-wide axial part of the southwestern and eastern subbasins is characterised by a blocky basement, with normal faults striking ENE to NE and fracture zones striking NW, covered by a sedimentary layer which is less than 1000 m thick (Briais *et al.*, 1993; Pautot *et al.*, 1990). North and south of the relict spreading axis, the sediment thickness increases from 1000 to 2500 m and the basement becomes much smoother. To the southwest, the fabric is characterised by normal fault scarps striking more homogeneously NE and fracture zone scarps striking NW.

The Scarborough seamount chain is located within the eastern subbasin. Most of these large seamounts are elongated both in the direction of the ridge segments (N50°E) and along the transform faults direction (N140°E), suggesting that their growth was controlled by the pre-existing fractures in the oceanic crust (Batiza & Vanko, 1983; Pautot *et al.*, 1990). The alkalic lavas that form the Scarborough Seamount chain are dated 11-6 Ma (Pautot *et al.*, 1990).

The location of the relict spreading axis within the southwestern and eastern subbasins may be deduced from bathymetry, the geometry of inward-facing normal faults and gravity data. Sediments are irregularly distributed along this extinct spreading centre. The average sediment thickness increases from 500 m in the northeast, near the ridge, to

1000 - 1500 m towards the southwest abyssal plain (Pautot *et al.*, 1990). The southwestern tip of the fossil propagating ridge is located at 9° N, 110°15' E (Coulon *et al.*, 1995).

The oldest southeastern part of the oceanic crust in the basin appears to be partially concealed under a recent compressional thrust wedge and the thick sedimentation derived from it (Pautot *et al.*, 1990; Briais *et al.*, 1993).

Table 2.3. Seafloor spreading in southwestern (A) and eastern subbasins (B) of South China Sea Oceanic Basin, from Briais *et al.* (1993). Location of Points A and B shown in Figure 2.11.

Anomalies	Age end, Ma	Full rate, mm/yr Point A	Full rate, mm/yr Point B
		Patriat's [1987] Method	
End - 5c	15.64	49	56
5c - 5d	16.56	35	52
5d - 5e	17.81	43	34
5e - 6	19.00	34	36
6 - 6a	20.45	41	44
6a - 6b	21.73	36	36
6b - jump	23.44	36	45
jump - 8	25.91		60
8 - 9	27.74		44
9 - 10	29.32		62
10 - 11	30.32		93 (?)
		Hellinger's [1981] Method	
End - 5d	15.64	40	55
5d - 5e	17.81	39	30
5e - 6	19.00	36	32
6 - 6a	20.45	37	42
6a - 6b	21.73	36	44
6b - 8	23.44		52
8 - 9	27.74		52
9 - 10	29.32		55
10 - 11	30.32		92 (?)
8 - 10	27.74		50

A model of seafloor spreading within the SCSOB (Figure 2.10) has been inferred from magnetic lineation data (Figure 2.11) by Briais *et al.* (1993) which superseded the earlier interpretations of Taylor & Hayes (1980) and Pautot *et al.* (1986). According to Briais *et al.* (1993) spreading first occurred in the northwestern subbasin (from 32 to 27 Ma), then jumped south in one or possibly two steps, creating the much larger eastern and

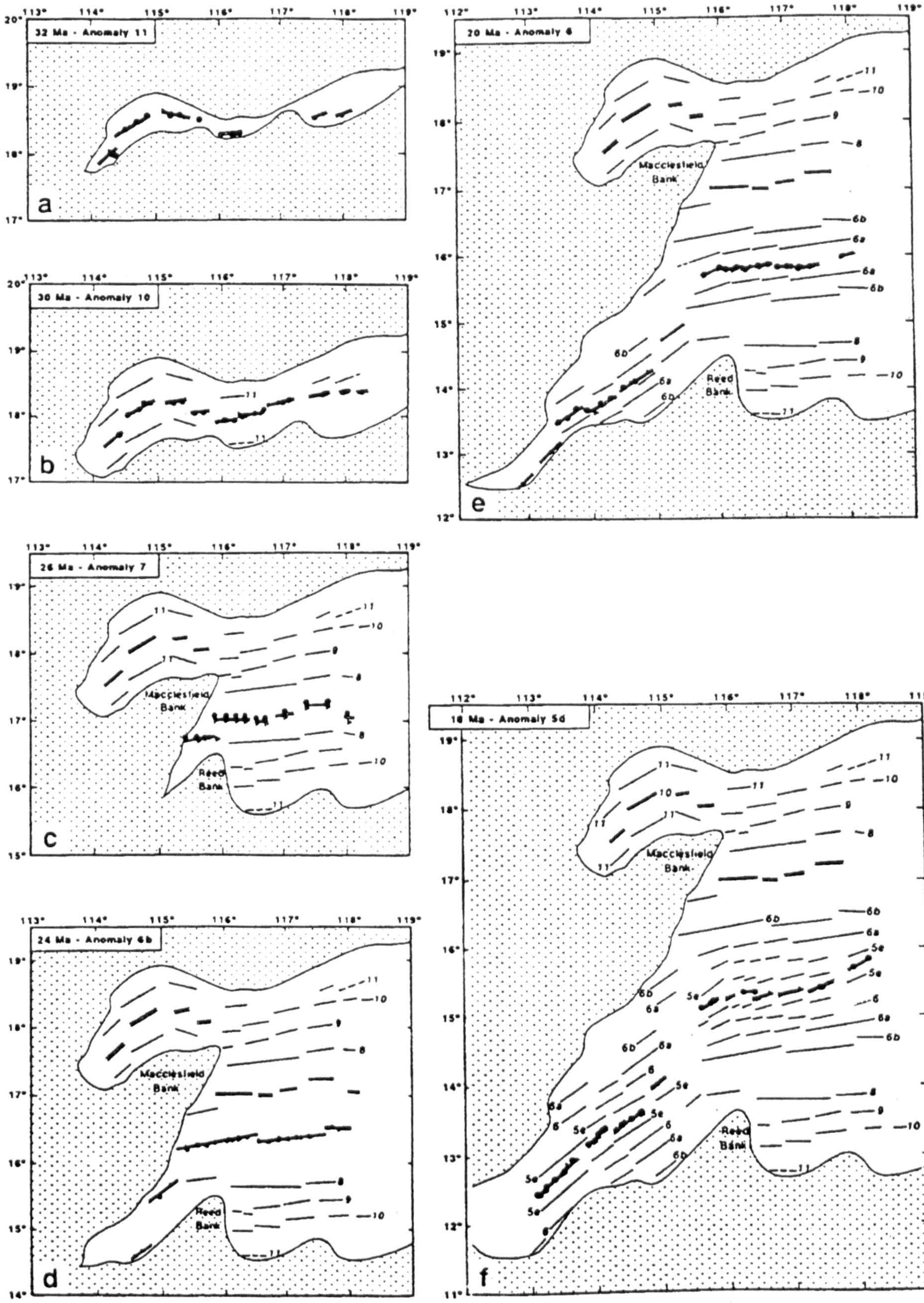

Figure 2.10. Sequential reconstruction of the opening of the South China Sea Oceanic Basin, from Briais *et al.* (1993).

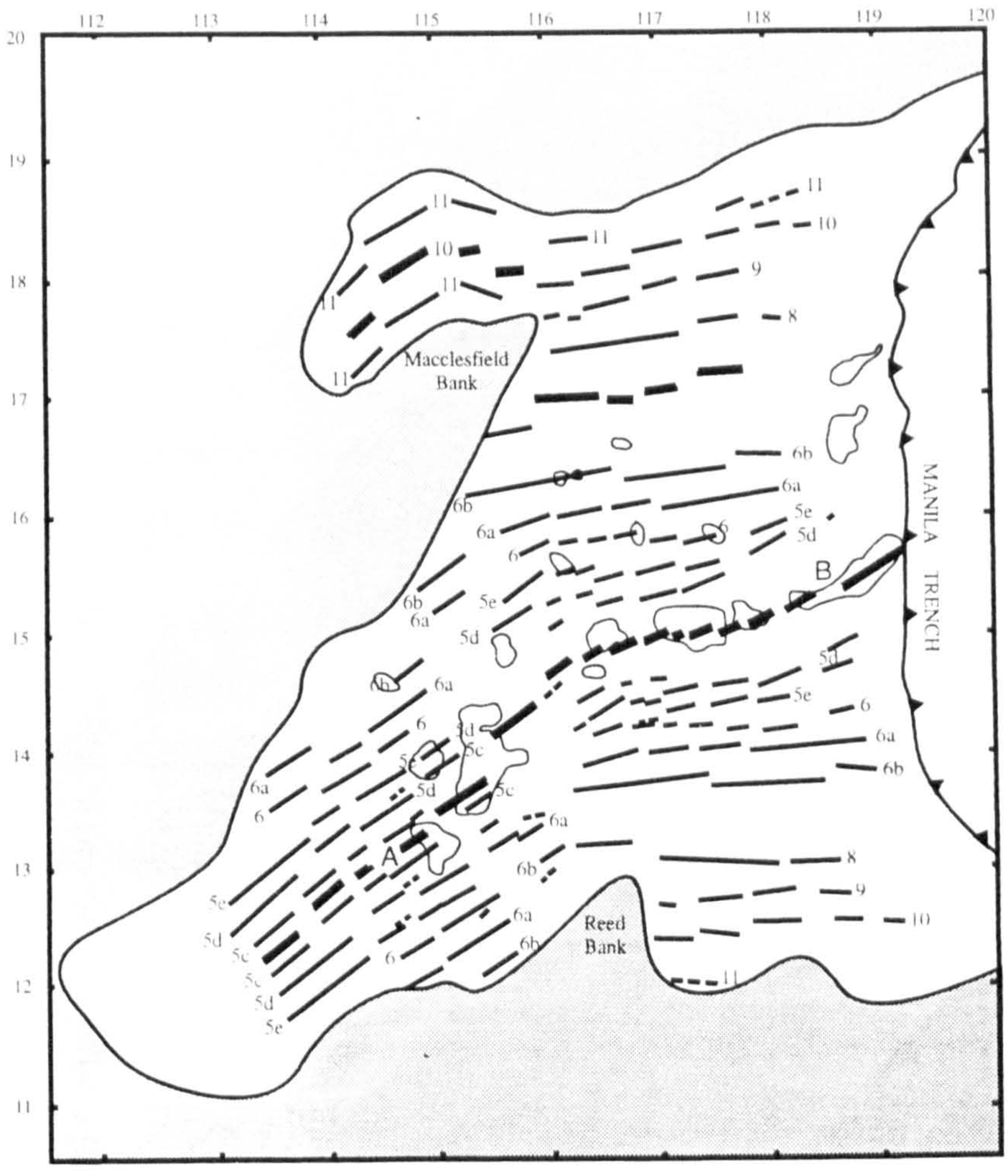

Figure 2.11. Magnetic lineations in South China Sea Oceanic Basin from Briais *et al.* (1993). Grey shaded areas within the basin indicate the locations of major seamounts.

Figure 2.12. South China Sea Oceanic Basin Spreading Rates from Briais *et al.* (1993).

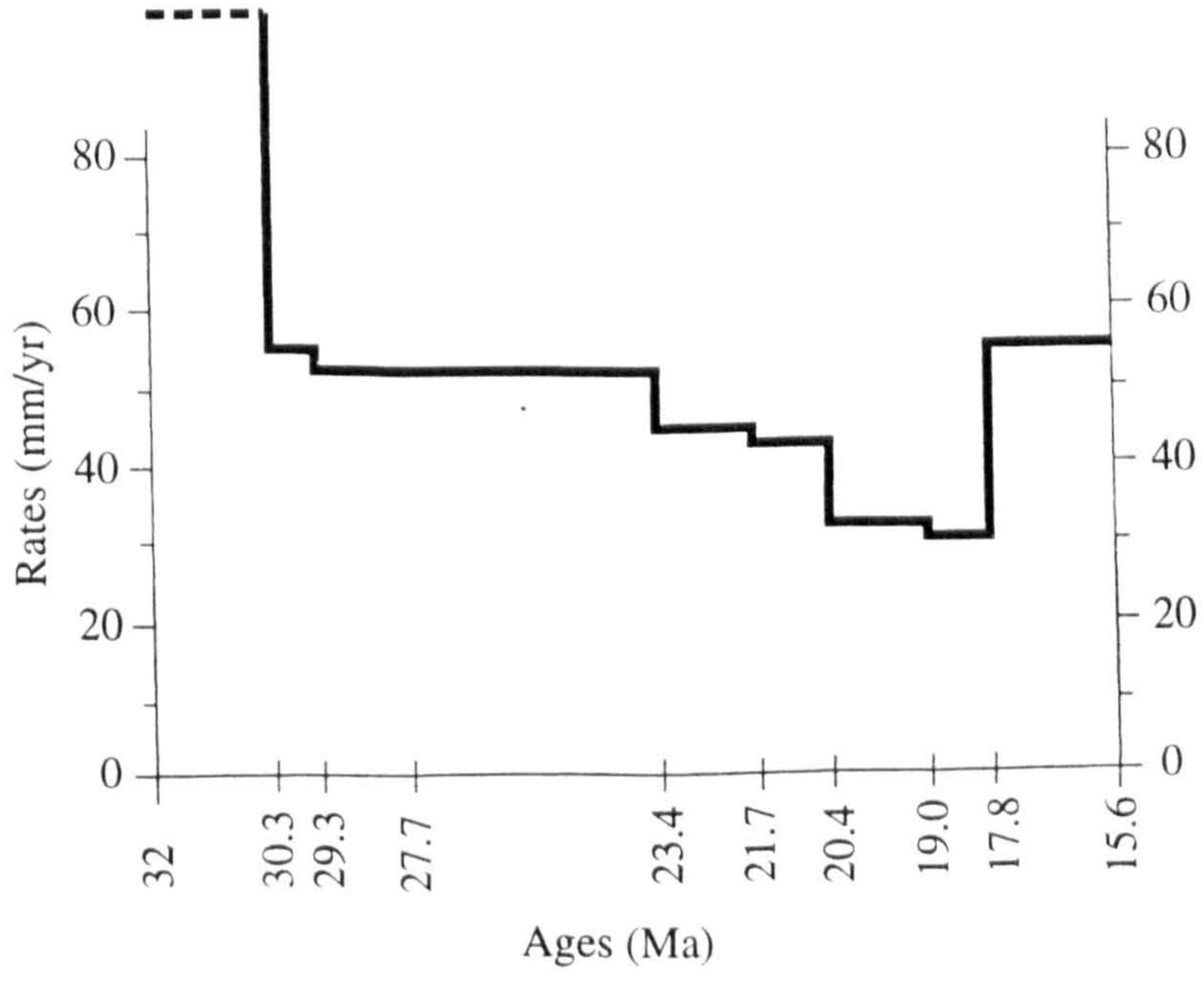

southwestern subbasins (from 27 to 15.5 Ma). Spreading occurred at different rates in the southwestern and eastern subbasins. The average full spreading rate in the eastern subbasin is predicted at ~50 mm/yr, and in the southwestern subbasin at ~35 mm/yr (Figure 2.12, Table 2.3). These estimates have an uncertainty of about 5 mm/yr caused by an uncertainty in the spreading direction of 20°. Seafloor spreading probably stopped after anomaly 5c (15.5 Ma) throughout the entire basin.

2.2.5 Mainland Asia and the Sunda Shelf

The basement of mainland Asia is made up of a number of sutured continental fragments which were progressively accreted to the Eurasia landmass from the Late Devonian to the Cretaceous (Section 2.4.1). Paleomagnetic data indicates that Sundaland has undergone clockwise rotation during the last 40 Ma, following the collision of India. (Tapponnier *et al.*, 1982).

The shallow Java Sea separates Borneo from Java to the southwest and Sumatra to the WSW. Oblique subduction of the Indian plate beneath Sumatra has been accommodated by a large displacement right lateral strike-slip fault that coincides with the volcanic line.

Sulawesi is separated from eastern Borneo by the Makassar Strait. The left lateral Adang and Sangkulurang faults offset the deep basins of the North and South Makassar Strait. The island of Sulawesi appears to be a major suture zone along which a large oceanic basin (probably the Neotethys) was subducted (Hamilton, 1979; Silver *et al.*, 1983*a*; Silver *et al.*, 1983*b*). The Banda and Celebes-Sulu blocks were welded together along this suture zone in Middle Miocene time (Kundig, 1956).

2.2.6 Celebes and Sulu Seas Region

The northeastern margin of Borneo is bounded by the Sulu and Celebes Seas. The Sulu and Celebes Seas are located at the convergent triple junction of three major plates - the Eurasian, Philippine Sea, and Australian plates. Thus the sources of potential intraplate stress are diverse (Rangin *et al.*, 1995). This complex geodynamic environment is marked by active arc-arc or arc-continent collision zones, subduction zones, and long strike-slip fault zones (Rangin & Silver, 1990). In the east, these basins are currently being overridden by the Philippine Mobile Belt, which is colliding against the Palawan, Cagayan, and Sulu Ridges (Rangin *et al.*, 1990*b*). In the south, a block that originated in Australia (the Sula platform) is colliding with Sulawesi forming the southern margin of the Molucca and Celebes Sea (Silver *et al.*, 1983*a*; Silver *et al.*, 1983*b*).

The Celebes and Sulu seas are deep (4000 - 5000 m) restricted basins located between the island of Borneo to the west and the north-south elongated Philippine Archipelago to the east. They are part of a succession of subparallel oceanic basins trending roughly northeast. Separating the basins from south China to Banda are narrow, elongated ridges such as the Cagayan Ridge, the Palawan and Sulu Archipelagos, the arms of Sulawesi, and the Sulu platform, Figure 2.13. Cross-sections from Reed Bank to Central Sulawesi and Halmahera, shown in Figure 2.14, reveal the Neogene internal deformation of the Celebes-Sulu block (Rangin & Silver, 1990; Rangin & Silver, 1991). These transects are based on published refraction, multichannel seismic and dredging data, as well as land geology observations.

The Celebes Sea contains middle Eocene oceanic crust (Packham, 1996). Weissel (1980) mapped magnetic anomalies 20 to 18 (46-52 Ma) which parallel the Sulu ridge and young to the south, into the North Sulawesi Trench. Evidence suggests a possible (although controversial) anticlockwise rotation of the Celebes Sea (Weissel, 1980; Shibuya *et al.*, 1989). Silver & Rangin (1991) concluded that the Celebes Sea is either a marginal basin formed behind an arc or a trapped fragment of a larger entity, including the Molucca Sea now separated from it by the narrow Sangihe Arc. Assuming that the arc is not allochthonous the Celebes Sea has a backarc relationship to the Palaeogene

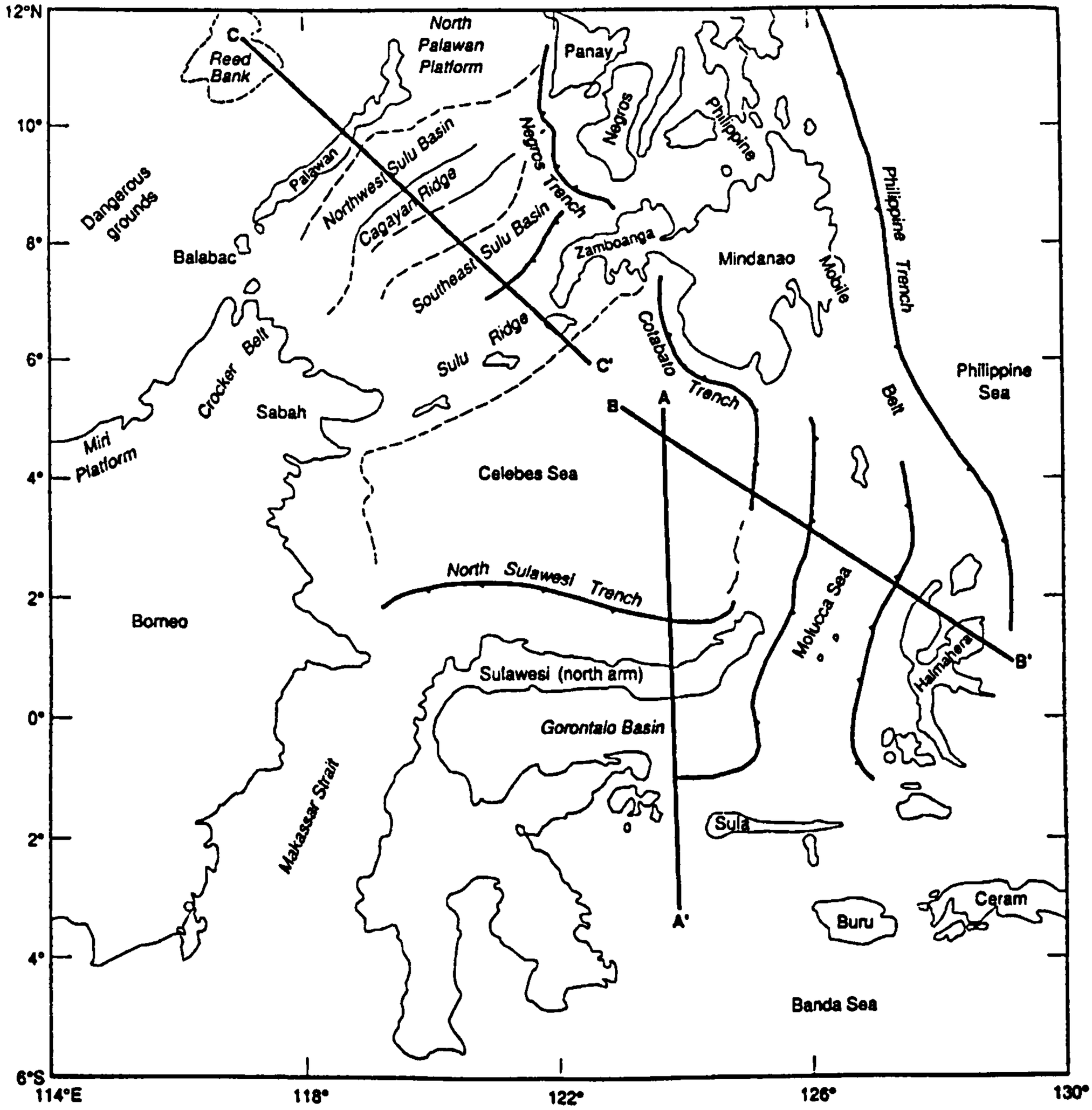

Figure 2.13. Structural sketch map of the Sulu-Celebes Seas area, from Rangin & Silver (1990), showing the location of transects AA′, BB′, and CC′ (Figure 2.14).

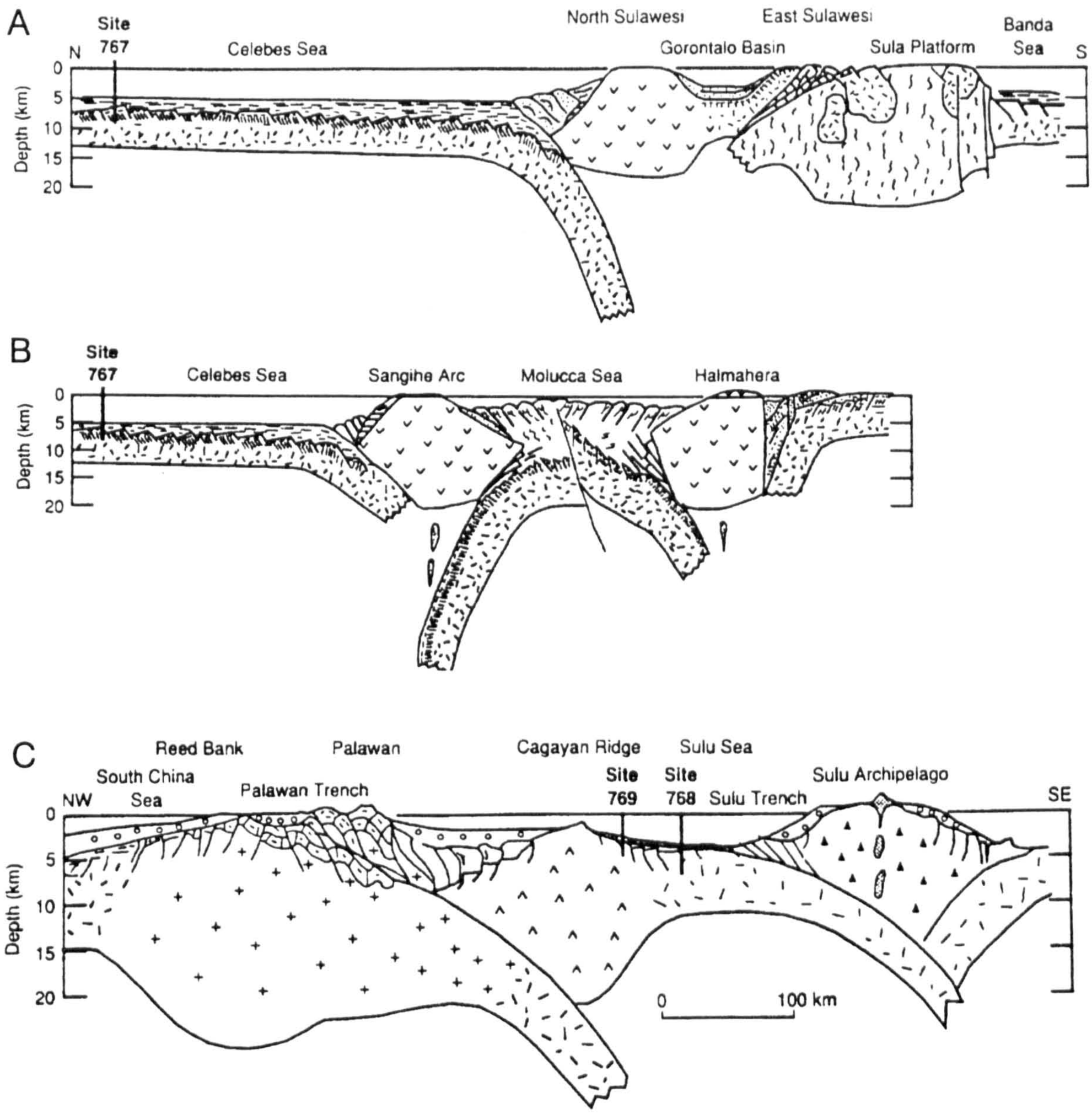

Figure 2.14. Interpreted cross-sections of the Celebes and Sulu Seas, located on Figure 2.13. A: transect AA´. B: transect BB´. C: transect CC´. From Rangin & Silver (1990).

volcanic rocks in the north arm of Sulawesi (Ratman, 1976) and the eastern part of the southwest arm (Sukamto, 1982) where they have been broadly dated as lower Eocene to upper Oligocene. Marginal basin formation was probably enhanced at anomaly 20 time when Australia increased its velocity away from Antarctica from *c.* 10 mm/yr prior to anomaly 20, to about 30 mm/yr between anomalies 18 and 20 (Royer & Sandwell, 1989). Subduction of the Celebes Sea is taking place at the present day at the Cotabato Trench to the east and at the North Sulawesi Trench to the south, Figure 2.13.

On its northwestern side, the Sulu Sea is bounded by the northeast-southwest trending island of Palawan and on its southwestern side by the northeast-southwest trending Sulu volcanic arc (or Sulu Ridge) which separates the Sulu and Celebes Seas. The Miocene Cagayan volcanic ridge also has a northeast-southwest trend and divides the Sulu Sea into two distinct subbasins - the southeast Sulu Sea Basin, floored by oceanic crust at water depths of as much as 5000 m (McCabe *et al.*, 1985), and the northern Sulu Sea Basin which is floored by island arc or continental crust and where maximum water depths are less than 2000 m. This northern basin contains a thick sedimentary cover, amounting to more than 7500 m in places (Mascle & Biscarret, 1979). The southeast basin is characterised by a thin cover of sediments. Within this basin, poor quality magnetic anomalies are observed which are tentatively identified as being 30 to 10 Ma (Roesar, 1991) with an asymmetrical pattern. Caution is urged on the interpretation of these anomalies by Rangin & Silver (1991) as the smoothness of the oceanic crust implies a much faster spreading rate than that suggested by the observed magnetic lineaments (6 mm/yr). Scientific drilling results (Rangin & Silver, 1990) suggest that the southeast Sulu Sea Basin was initiated in latest Oligocene or earliest Miocene time. The oceanic crust of this basin is presently subducting along the Sulu Trench, Figure 2.14.

The Cagayan Ridge appears to have formed by two successive episodes of volcanism (Rangin & Silver, 1991). The first was an episode of latest Oligocene-early Miocene age marked by eruptions of andesites and basalts. The second episode was marked by emplacement of large volumes of pyroclastics, from 19 to 16 Ma.

The accretionary wedge of the Palawan Ridge is composed of a complex pile of thrust slices with evident polyphase deformation (Rangin & Silver, 1991). Ophiolites are imbricated with a clastic sequence of late Paleocene to early Middle Miocene age (Raschka *et al.*, 1985; Mitchell *et al.*, 1986; Wolfart *et al.*, 1986; Letouzey *et al.*, 1988). Harzburgite bodies sliced with lower to possibly middle Eocene pelagic sediments and pillow basalts are thrust northwestward onto the limestone and clastic sequences (Rangin & Silver, 1991). These ophiolites may have originated in the northwest Sulu Sea Basin where a relict fragment of oceanic crust was suspected (Hinz & Block, 1990). Alternatively, they might represent remnant pieces of the proto-South China Sea (Rangin & Silver, 1991). Obduction of these ophiolites occurred before collision ceased in early-middle Miocene time.

The tectonic boundary between the rifted continental material of the south China margin and the Cagayan Ridge is difficult to trace because it is blanketed by Neogene sediments on both sides of Palawan Island. This suture zone was thought by Holloway (1982) to be represented by the Palawan Trench. Hinz *et al.* (1985) suggested the presence of a southward-dipping slab of continental crust below Palawan, reaching far into the Sulu Sea. According to this interpretation, based on analysis of multichannel seismic data, the Palawan accretionary prism represents the deformed and imbricated continental-slope sediments of the rifted south China margin. Hinz *et al.* (1985) interpret the Palawan Trough as a foreland thrust zone for the Cagayan-Reed Bank collision (Figure 2.14). Deformation has been inactive in Palawan and the northwest Sulu Sea Basin area since early-middle Miocene time, and a thick undisturbed package of Neogene sediments covers the folded sequences unconformably (Rangin & Silver, 1991).

The Celebes and Sulu Seas are separated by the shallow, partly emerged Sulu Archipelago (or Sulu Ridge), which is 150 to 200 km wide (Figure 2.13), and extends from western Mindanao (Zamboanga Peninsula) to northeast Borneo (Semporna and Dent Peninsulas, Sabah). Arc volcanic activity along the Sulu archipelago is Plio-Pliestocene in age. Basilan and Jolo islands are active volcanoes. Older volcanic-arc sequences are known at both ends of the archipelago (Rangin & Silver, 1991). Tawi-Tawi Island to the west is formed by dismembered ophiolites, probably similar to the

ones exposed in Sabah (Rangin & Silver, 1990). A Paleogene volcanic sequence is reported by Antonio (1972) in the Zamboanga Peninsula, where it is imbricated with ophiolites and metamorphic rocks (crystalline schists, marbles, and amphibolites). The Sulu Archipelago is fringed on the northwest by a trench shallowing progressively to the southwest and deepening eastwards towards its junction with the Negros Trench. No focal mechanism has been determined for this south-dipping subduction zone and the related volcanoes are in the fumarolic stage (Rangin & Silver, 1990). The southern flank of the Sulu Archipelago is a relatively steep slope which is interpreted either as a normal-faulted passive margin or as a starved subduction zone (Rangin & Silver, 1991). Single-channel seismic lines published by Hamilton (1979) do not clarify this ambiguity.

Towards the east, the Sulu and Celebes seas are bounded by the Negros and Cotabato Trenches, Figure 2.13, separating these basins from the central and southern part of the Philippine Mobile Belt (PMB) (Gervaiso, 1971). These short subduction zones are the southern extension of the Manila Trench (Lewis & Hayes, 1984). This trench enters the North Palawan Platform offshore Mindoro (Rangin *et al.*, 1988) and connects southward with the northern Negros Trench through complex strike-slip and wrench faults (Marchadier & Rangin, 1989). To the west of this active and recent plate boundary, the PMB is a mosaic of allochthonous terranes extending from Luzon to Mindanao (Karig, 1983; McCabe *et al.*, 1985; Mitchell *et al.*, 1986). To the east, the PMB is again composed of a mosaic of terranes, bounded to the east by the Philippine Trench and the East Luzon Trough (Lewis & Hayes, 1983) and dissected by the complex left lateral Philippine fault zone (Allen, 1962).

The eastern part of the Philippine islands is substantially composed of rocks built up by island arc processes from the Cretaceous onwards, on oceanic basement dating back to Late Jurassic (Geary *et al.*, 1988). Continental basement of at least Jurassic age is present in the west around Mindoro and western Panay. This basement is an extension of the North Palawan Block on the South China Sea drifted margin (Packham, 1996). Pubellier *et al.* (1991) have identified a terrane in western Mindanao, including Zamboanga and the Daguma Range, which may also be continental. These continental blocks, part of the Asia margin, were incorporated into the Philippines as the Philippine

Sea plate rotated clockwise and an essentially transform boundary brought the south to southwest facing Philippine arc northward to collide obliquely with the Asian margin (Packham, 1996).

2.2.7 Sedimentary Basins

A total of 135 basins delineated at the 1 km isopach contour have been identified in the offshore and nearshore areas of East Asia (CCOP, 1991). Examination of this data reveals that the East Asia region is still a relatively underdeveloped and unexplored region, as 80 % of the basins are very sparsely investigated or totally unexplored. Production of oil or gas is established in 27 of the basins. However, a large proportion of the sparsely to unexplored basins are found at great water depths or in very remote areas (CCOP, 1991).

The South China Sea is rapidly developing into the most important hydrocarbon producing province of Southeast Asia, with significant production in Thailand, Malaysia, Indonesia, Brunei, the Philippines and China and with the beginnings of exploration offshore Cambodia. The producing basins have developed by simple rifting, by complex rifting associated with major strike-slip faults, and in collision environments. The three major deltaic complexes, at the mouths of the Red River, the Mekong and the Baram, are all proven sources of oil or gas but the majority of production to date has come from the Baram Delta which, although the smallest of the three, has been the most intensively explored. A peculiarity of the area is the preponderance of lacustrine source rocks, major marine incursions having occurred only during the Neogene. A second factor in the petroleum geology of the area has been the relatively high heat flow and elevated geothermal gradient, as a consequence of which sediments as young as Pliocene have in places entered the oil window (Milsom & Moss, 1993).

A number of sedimentary basins are identified offshore northwest of Borneo, around the edge of the South China Sea and on the Sunda shelf, as shown in Figure 2.15. Following

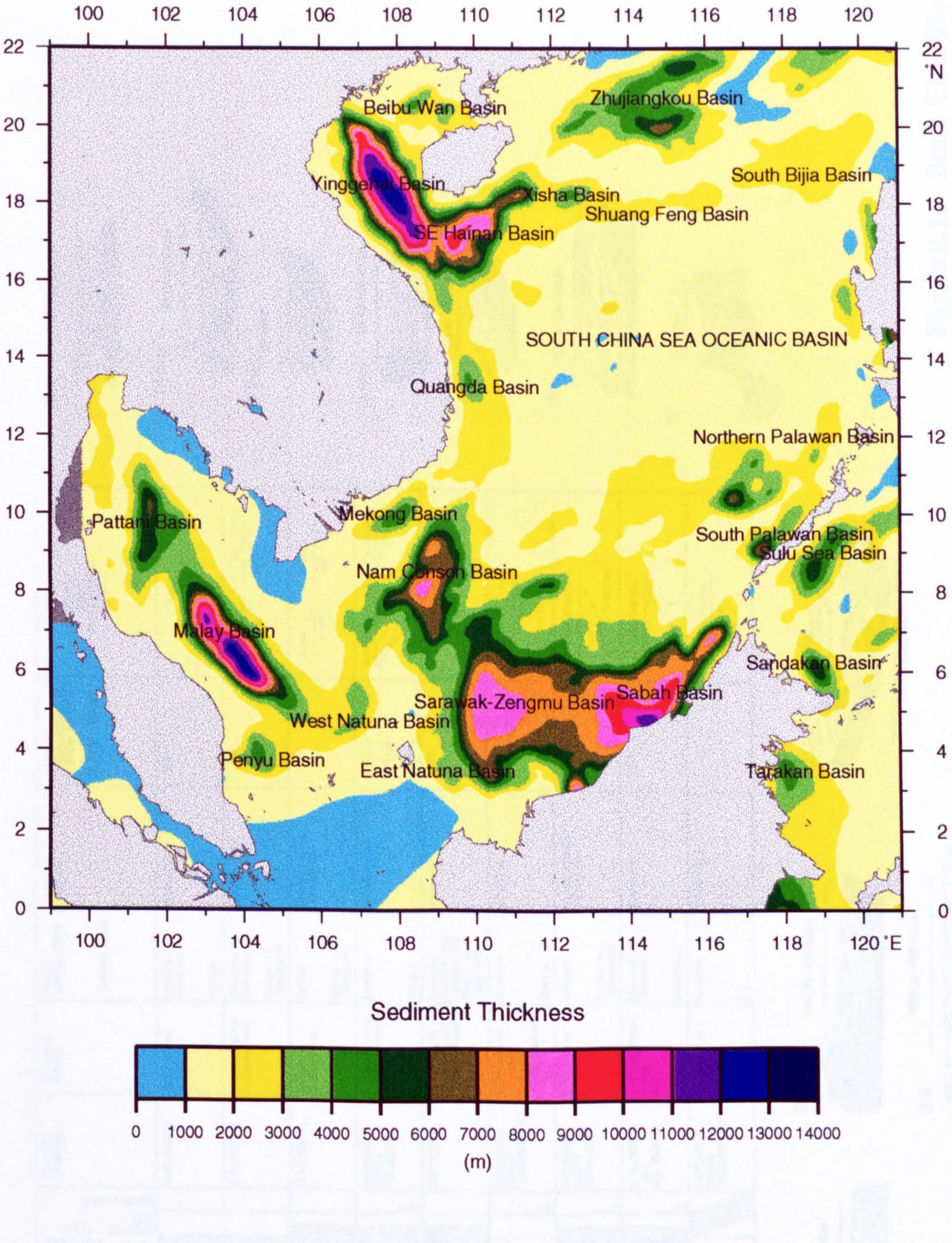

Figure 2.15. Total Sedimentary Isopach Map, Offshore Southeast Asia. Data from 1997 NGDC World's Oceans and Marginal Seas Sediment Isopach Database.

PETROLEUM BASIN TYPES	CRATON / Continental Crust / ACCRETED ZONE / OCEANIC CRUST	TECTONIC LOCATION	REGIONAL STRESS	BASIN AERIAL SHAPE (Aerial Size)	BASEMENT PROFILE	RATIO Basin Volume M³ / Basin Area M² 65 Prod. Basins	SEQUENTIAL BASIN ARCHITECTURAL FORM
I. CRATON INTERIOR BASINS		CONTINENTAL	Extensional Sag	Circular to Elongate (Large)	Symmetrical	85%	Sag
II. CONTINENTAL MULTICYCLE BASINS IIA. CRATONIC MARGIN -Composite		CONTINENTAL	2. Compression 1. Extension?	Elongate to Circular (Large to Moderate)	Asymmetrical	195%	2. Foredeep 1. Platform or Sag
IIB. CRATON/ACCRETED MARGIN -Complex		CONTINENTAL	2. Sag 1. Extension	Random (Large to Moderate)	Symmetrically Irregular	160%	2. Sag 1. Rift
IIC. CRUSTAL COLLISION ZONE -Convergent Plate Margin -downwarp into small ocean basin		CONVERGENT MARGIN "COLLISION"	2. Compression 1. Extension?	Elongate (Large)	Asymmetrical	a)250% b)High c)250%	2. Foredeep 1. Platform or Sag
III. CONTINENTAL RIFTED BASINS IIIA. CRATON and ACCRETED ZONE RIFT		CONTINENTAL	1. Extension (Local wrench compression)	Elongate (Narrow Fault controlled) (Small to Moderate)	Irregular	235%	Rift/ Sag
IIIB. RIFTED CONVERGENT MARGIN -Oceanic consumption a)Back Arc b)Transform c)Median		CONVERGENT MARGIN "CONSUMPTION"	1. Extension plus 2. Wrench compression	Elongate (Small)	Irregular	180% (Variable)	1. "Rift / Wrench" Rift/ Sag
IIIC. RIFTED PASSIVE MARGIN -Divergence		DIVERGENT MARGIN "PULL-APART"	1. Extension	Elongate (Small to Moderate)	Asymmetrically Irregular	200%	1. "Rift / Drift" Rift/Sag
IV. DELTA BASINS -Tertiary to Recent		CONTINENTAL and ALL MARGINS	A. Extensional Sag B. ?	Circular to Elongate (Moderate)	Depocenter	350%	1. "Modified Sag" ?
V. FOREARC BASINS		CONVERGENT MARGIN "CONSUMPTION"	Compression and Extension	Elongate (?)	Asymmetrical	?	Subduction

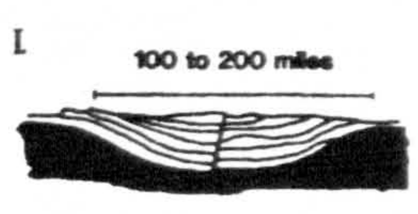

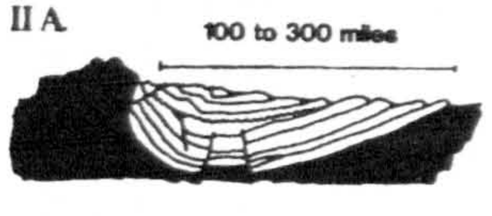

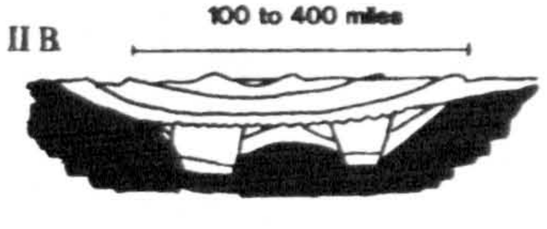

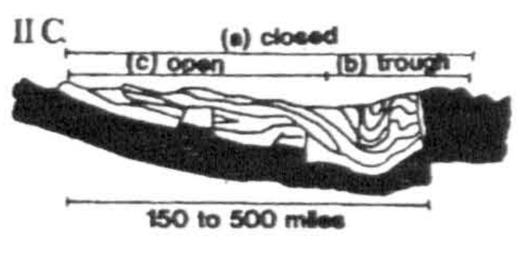

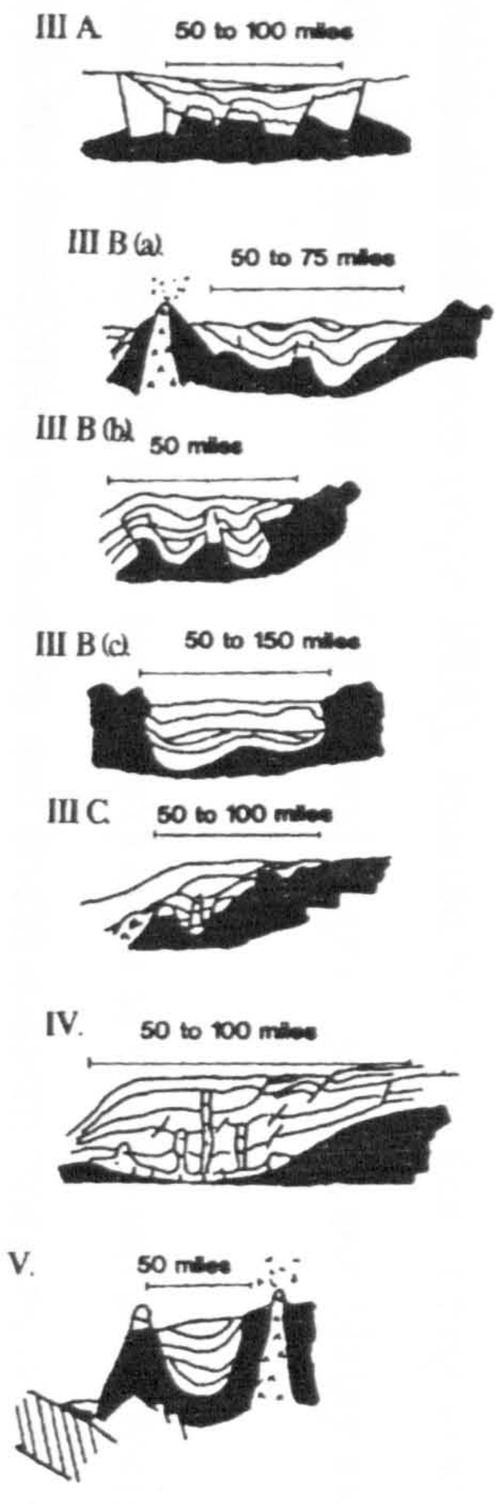

Figure 2.16. Basin Classification Table (modified from Klemme, 1983)

the basin classification system of Klemme (1983), Figure 2.16, three types of basin are identified:

- Rifted passive margin basins (type IIIC), found along the southern margin of Eurasia, including the Mekong, Nam Conson, Southeast Hainan and Zhujiangkou (Pearl River Mouth) Basins.

- Continental rift basins (type IIIA), formed by complex rifting associated with major strike-slip faults in the Gulf of Thailand region, such as the Malay and Pattani Basins.

- Crustal collision zone basins (type IIA) such as the Sabah and North Palawan Basins, which are found along the eastern and south-eastern margins of the South China Sea.

2.3 Tectonic Reconstructions of Southeast Asia

Southeast Asia has been an area of diverse and rapidly changing tectonic and sedimentary environments throughout the last 100 Ma or so. It is generally agreed that large-scale plate motions provided the ultimate driving force of the main periods of basin formation in Southeast Asia (e.g. Hamilton, 1979; Hutchison, 1989). There are three main schools of thought regarding the Cenozoic tectonic evolution of Southeast Asia and specifically the Sunda Shelf - South China Sea region, which are discussed below.

The first attributes all the tectonic movements in the region to the collision and northward movement of the Indian plate into the Eurasian margin. The effect of this indentation propagated eastward in time, causing the block rotation of Southeast Asia (Figure 2.17). This rotation led to fracturing of the crust within the South China Sea and the opening of the South China Sea oceanic basin. The northwestern margin of Borneo is believed to be a simple continent-continent collision zone. This school of thought is based on the results of plasticine collision models which assume (unrealistic) free-boundaries at their eastern and southeastern edges. Proponents of this scheme include Peltzer & Tapponnier (1988) and Fournier (1994).

Briais *et al.* (1993) attribute the tectonic evolution of the South China Sea to extrusion tectonics. They propose that the India-Eurasia collision resulted in large (500 - 600 km) left-lateral displacement along the Red-River-Ailao Shan shear zone, which drove extension and the formation of oceanic crust within the South China Sea (Figure 2.18). As with the indentor tectonic models, the northwestern margin of Borneo is believed to be a simple continent-continent collision zone. One problem with this model lies in the fact that extension started at the south China margin some 10 to 15 Ma before the collision of India and Eurasia (Section 2.2.4).

The third school of thought believe that extension and rifting of material from the south China margin was caused by slab pull from the southwards subduction of the 'proto-South China Sea' which has since been totally consumed. This model was first proposed

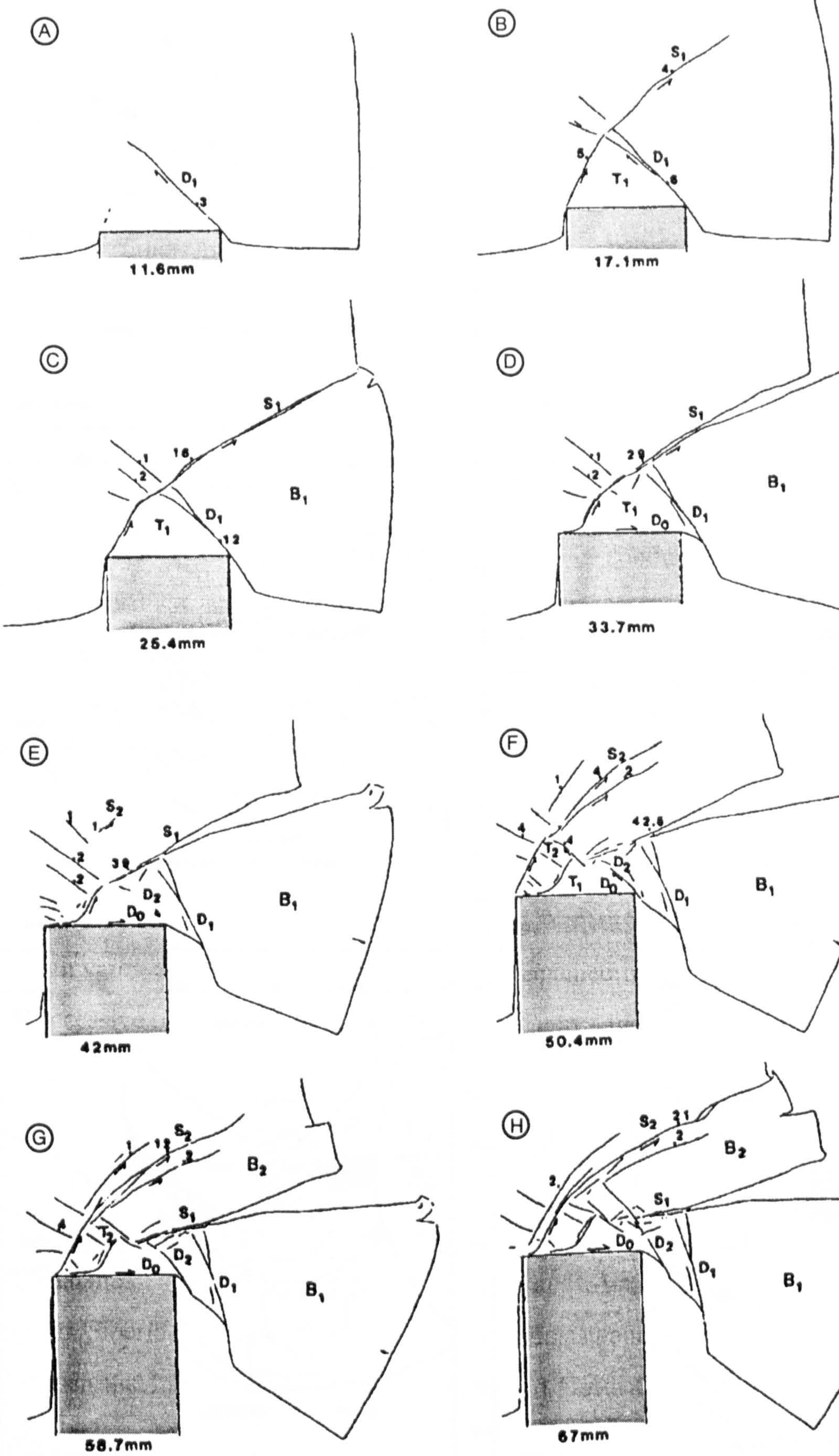

Figure 2.17. Indentor tectonics model explaining the evolution of SE Asia (block B_1) as the result of the India/Eurasia collision, from Peltzer & Tapponnier (1988).

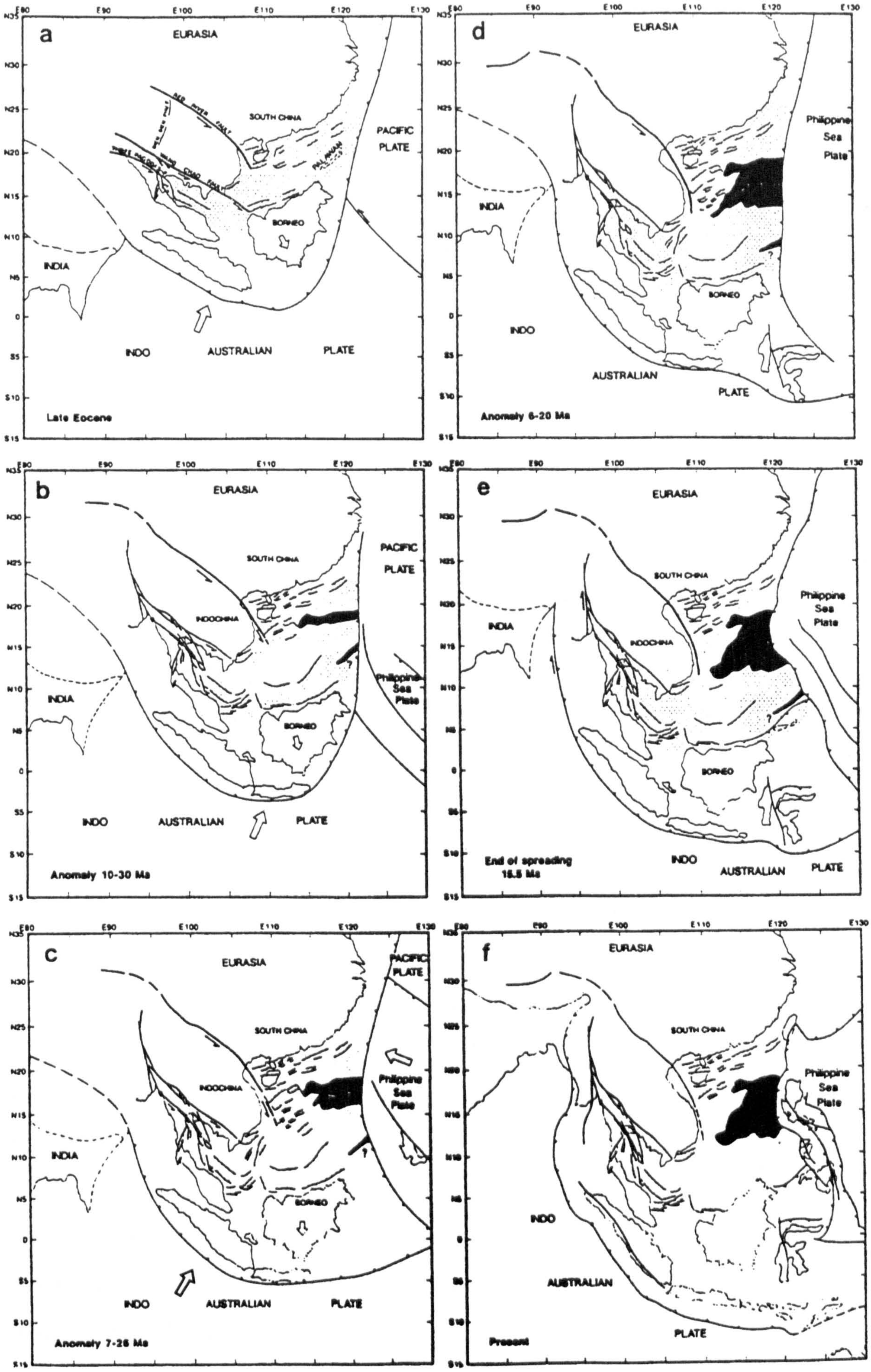

Figure 2.18. Tectonic reconstruction of SE Asia, from Briais *et al.* (1993).

by Taylor & Hayes (Figure 18, 1983) and has been subsequently refined, the most recent model being that of Hall (1996) which is discussed in Section 2.4.2.

The models proposed for the tectonic evolution of the region also vary in terms of detail due to different interpretations of the rather scant (in places) and occasionally contentious geological data. One obvious example concerns the rotation(?) of Borneo:

The results from paleomagnetic studies of Borneo have been reported from Kalimantan and Sarawak (Haile *et al.*, 1977; Haile, 1979) and from Sabah (Schmidtke *et al.*, 1990). Haile *et al.* (1977) reported paleomagnetic data from the Late Cretaceous basement rock of western Kalimantan. Their study suggested a 50° anticlockwise rotation with no latitudinal change for the western portion of Kalimantan since the Cretaceous. Paleomagnetic data from Oligocene/Miocene red beds on Sarawak were reported by Haile (1979). These results are not distinguishable from the present magnetic field suggesting that any anticlockwise rotation of Kalimantan was complete by the late Tertiary. The data of Schmidtke *et al.* (1990) imply up to 108° of anticlockwise rotation of Kalimantan with respect to Eurasia sometime during the Cretaceous or Cenozoic.

Current views of the rotational history of Borneo divide into two opposing groups, one favouring a significant anticlockwise rotation of Borneo in the Tertiary and the other favouring an essentially stationary Borneo. However, both hypotheses are based on limited data sets which have often used samples from locations near major tectonic lineaments and/or allochthonous areas, so their validity is questionable (Moss, 1994).

More fundamental problems also limit the validity of plate tectonic reconstructions which currently describe the interactions between slowly moving, large plates with relatively simple geometries. These reconstructions ignore the fact that convergence of continent-continent collision zones continues for a long time after the initial collision, and that much deformation of continents may be distributed rather than concentrated at plate margins (Hall, 1997).

Finally all of the tectonic reconstructions have a large degree of uncertainty in the vicinity of the numerous old and active subduction zones where there is little constraint on the amount of subducted crust.

2.4 Tectonic Evolution of Southeast Asia

This section summarises the geological history of Southeast Asia in the context provided by the reconstructions of Metcalfe (1996) and Hall (1996). The reconstruction of Metcalfe (1996) covers the interval from the Early Carboniferous to the Late Cretaceous, and the reconstruction of Hall (1996) runs from 50 Ma to the present day. A number of other sources have been used, including Briais *et al.* (1993), Daly *et al.* (1991), Lee & Lawver (1993), Milsom & Moss (1993) and Richter & Fuller (1996).

2.4.1 Pre-Cretaceous Tectonic Evolution

During the last decade, a number of pre-Cretaceous continental terranes have been recognised in East and Southeast Asia. These terranes are bounded by sutures (representing former oceans), narrow mobile belts or major fault zones (Figure 2.19). It is probable that all these terranes were derived from Gondwanaland (Metcalfe, 1996).

The evolution of Gondwanaland and Tethys during the Paleozoic and Mesozoic involved the rifting of continental slivers/fragments from northern Gondwanaland, and their northwards drift and amalgamation/accretion to form proto-East and Southeast Asia. The northwards drift of these terranes was accompanied by the opening and closing of three successive oceans, the Paleo-Tethys, Meso-Tethys and Ceno-Tethys.

According to Metcalfe (1996), assembly of Gondwanaland-derived Asian terranes (Figure 2.20) began with the amalgamation of South China and Indochina/East Malaya along the Song Ma/Song Da zone during the Late Devonian/Early Carboniferous to form 'Cathaysialand'. The Tarim, Kunlun, Qaidan and Ala Shan terranes accreted to Kazakstan/Siberia in the Permian. Suturing of Sibumasu and Qiangtang to Cathaysialand occurred in the Late-Permian-Triassic. South and North China amalgamated and then accreted to Laurasia by Late Triassic-Early Jurassic times. The highly disrupted Kurosegawa terrane of Japan accreted to Japanese Eurasia in the Late Jurassic. The northwest and southeast Hainan terranes, reached their current positions, relative to

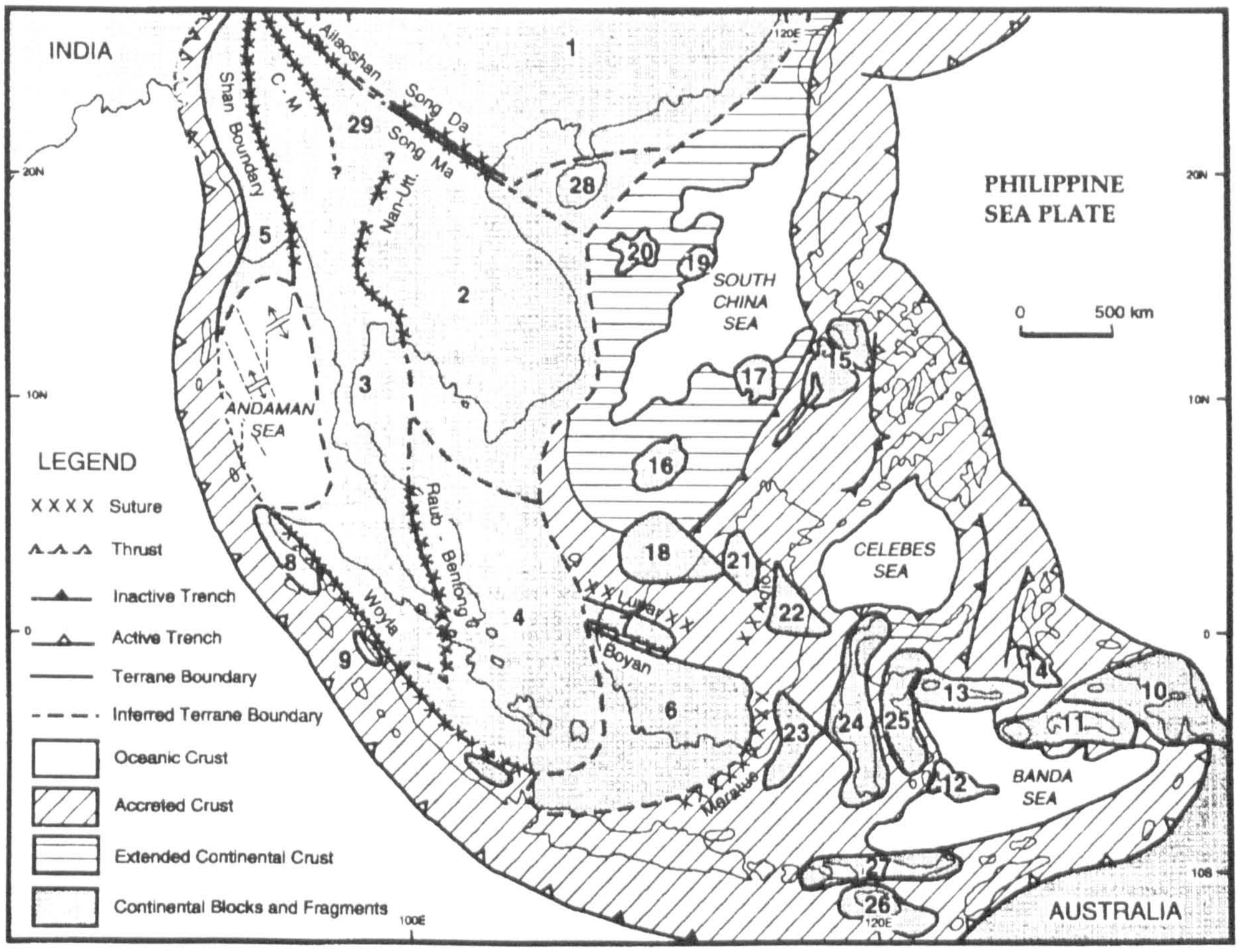

Figure 2.19. Distribution of continental blocks and fragments (terranes) and principle sutures of SE Asia (from Metcalfe, 1996). 1. South China; 2. Indochina; 3. Sibumasu; 4. East Malaya; 5. West Burma; 6. SW Borneo; 7. Semitau; 8. Sikeluh; 9. Natal; 10. West Irian Jaya; 11. Buru-Seram; 12. Buton; 13. Bangai-Sula; 14. Obi-bacan; 15. North Palawan; 16. Spratley Islands-Dangerous Ground; 17. Reed Bank; 18. Luconia; 19. Macclesfield Bank; 20. Paracel Islands; 21. Kelabit-Longbowan; 22. Mangkalihat; 23. Paternoster; 24. West Sulawesi; 25. East Sulawesi; 26. Sumba; 27. Banda Allochthon; 28. Qiongzhong and Yaxian terranes of Hainan; 29. Simao terrane.

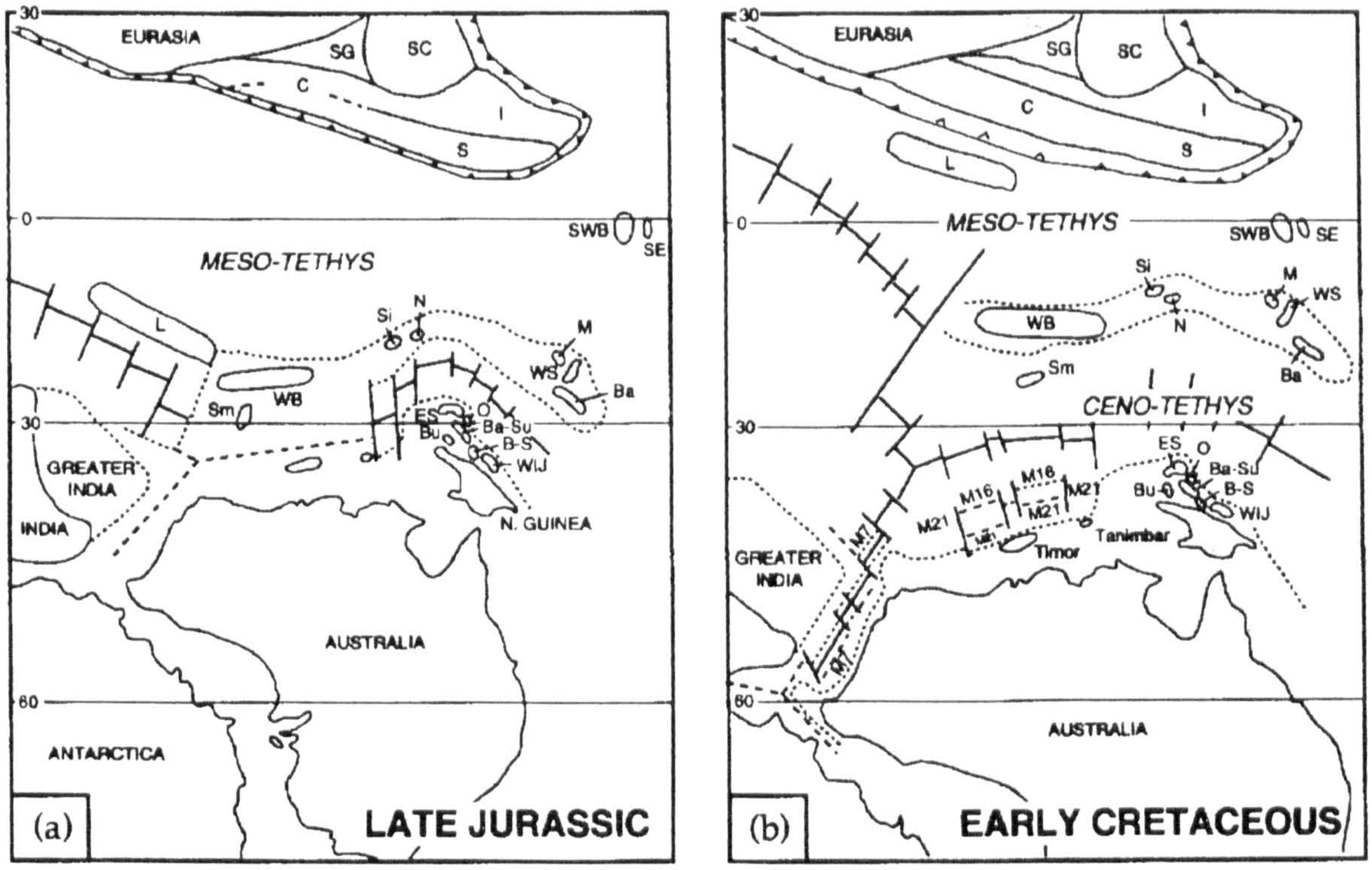

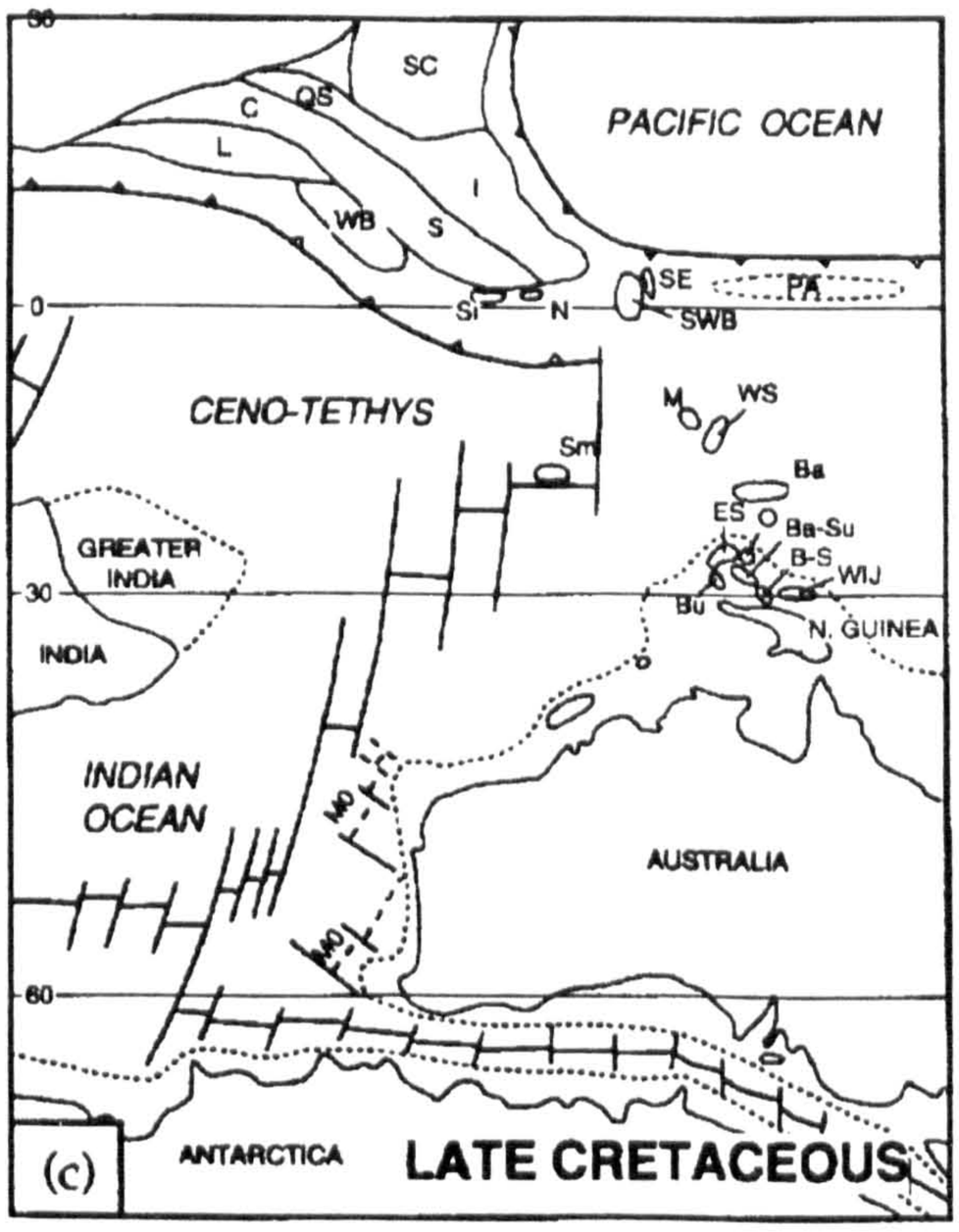

Palaeogeographic reconstructions for Eastern Tethys in (**a**) Late Jurassic, (**b**) Early Cretaceous and (**c**) Late Cretaceous times. SG, Songpan Gangzi accretionary complex; SWB, South West Borneo; SE, Semitau; Si, Sikule ı; N, Natal; M, Mangkalihat; WS, West Sulawesi; Ba, Banda Allochthon; ES, East Sulawesi; O, Obi–Bacan; Ba-Su, Bangai–Sula; Bu, Buton; B-S, Buru–Seram; WIJ, West Irian Jaya; Sm, Sumba; PA, Philippine Arc. M numbers represent Indian Ocean magnetic anomalies.

Figure 2.20. Late Mesozoic reconstructions for Eastern Tethys (from Metcalfe, 1996).

South China, sometime in the Jurassic-Cretaceous. The Lhasa, West Burma and Woyla terranes drifted northwards during the Jurassic and Early Cretaceous as the Meso-Tethys was destroyed by subduction below Eurasia. Accretion of these terranes to proto-Southeast Asia occurred in the Cretaceous.

2.4.2 Cenozoic Tectonic Evolution

The Cenozoic evolution of Southeast Asia was the result of four major tectonic events, namely the collision of India with Eurasia, extension at the southern margin of South China, rotation of the Philippine Sea plate, and the ongoing collision of Australia with eastern Indonesia (Packham, 1996).

The Cenozoic model of Hall (1996) is quite well constrained on a regional scale as the motion of the Indian-Australian and Eurasian plates are reasonably well known. Their positions provide limits to the zone within which the Southeast Asian collage of microplates and sub-plate fragments can be moved during the tectonic reconstruction. The sequential reconstruction of the evolution of Southeast Asia of Hall (1996) is shown in Figure 2.21.

During the Eocene, the region which now forms Southeast Asia was attached at the north and west to the Eurasian plate, and bounded to the south by the Indian-Australian plate.

In an attempt to simplify the highly complex regional tectonic evolution, the effects of the different tectonic events are discussed separately. However, it should be born in mind that none of these events took place in isolation.

The India-Asia Collision

Southeast Asia moved with respect to Eurasia during the Cenozoic (Hall, 1996). The India-Asia collision, initiated in the Paleogene, indented the margin of Eurasia, with the

A

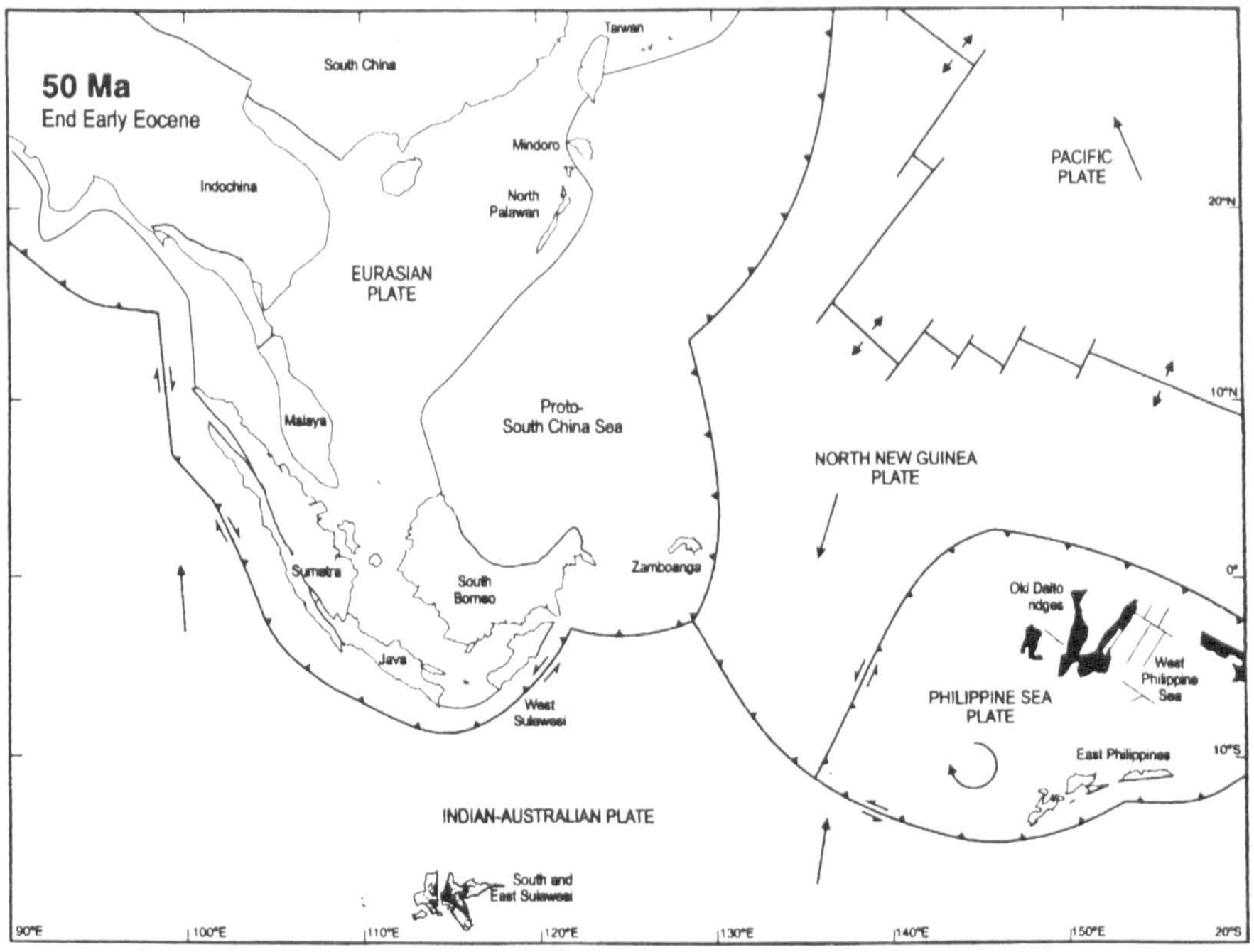

B

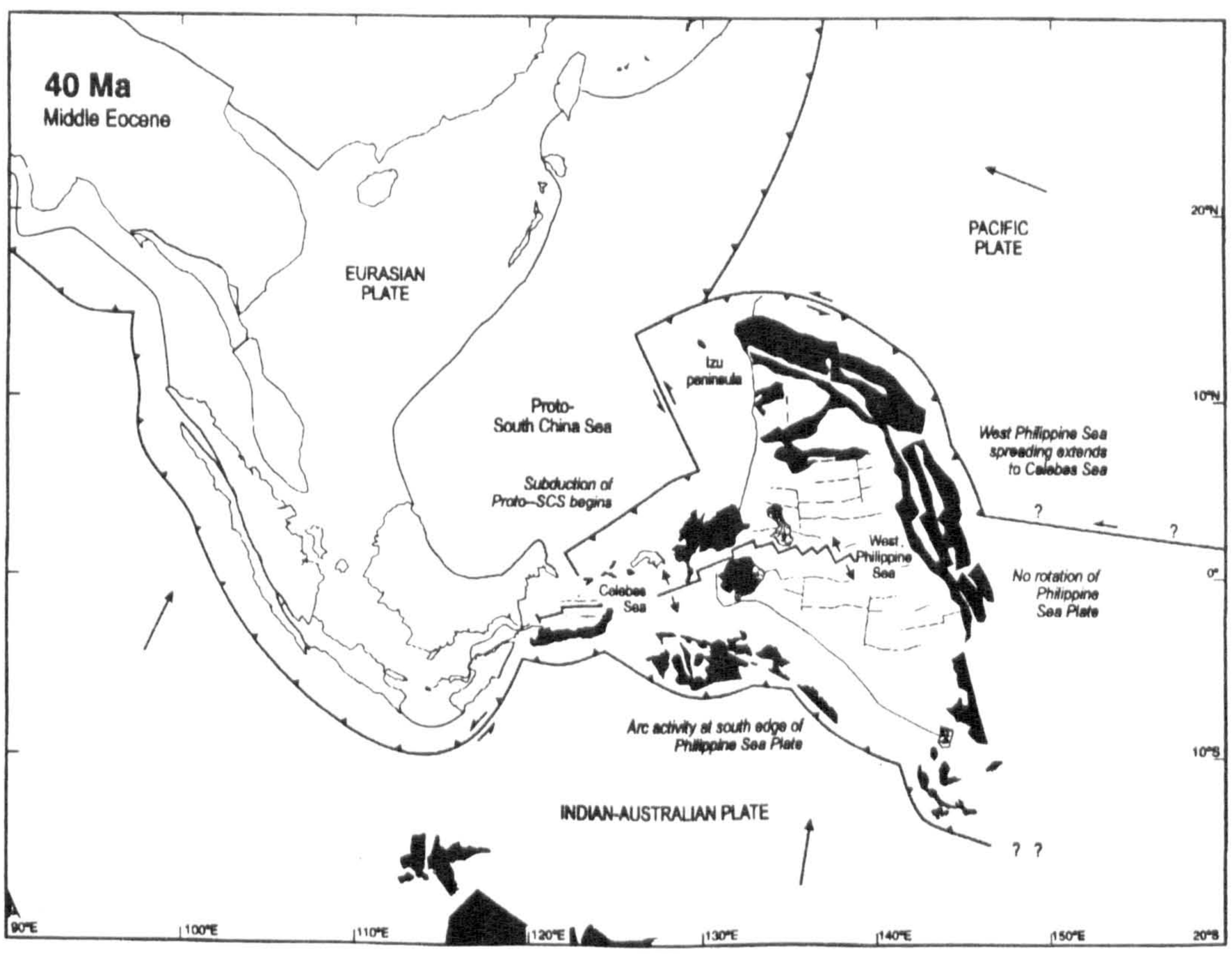

Figure 2.21. Model of tectonic evolution of SE Asia, from Hall (1996). A: 50 Ma, B: 40 Ma, C: 30 Ma, D: 20 Ma, E: 10 Ma, F: Present Day.

C

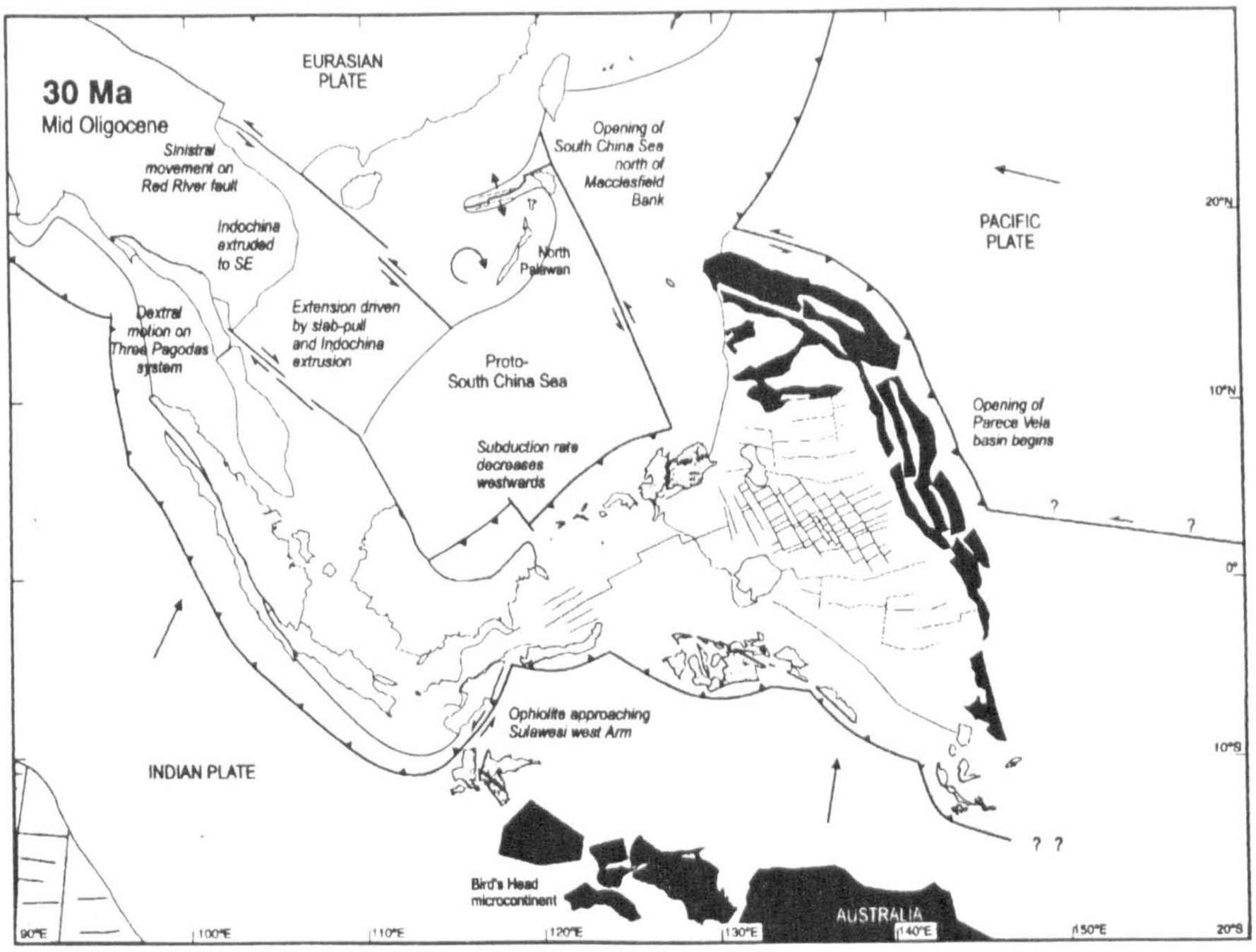

D

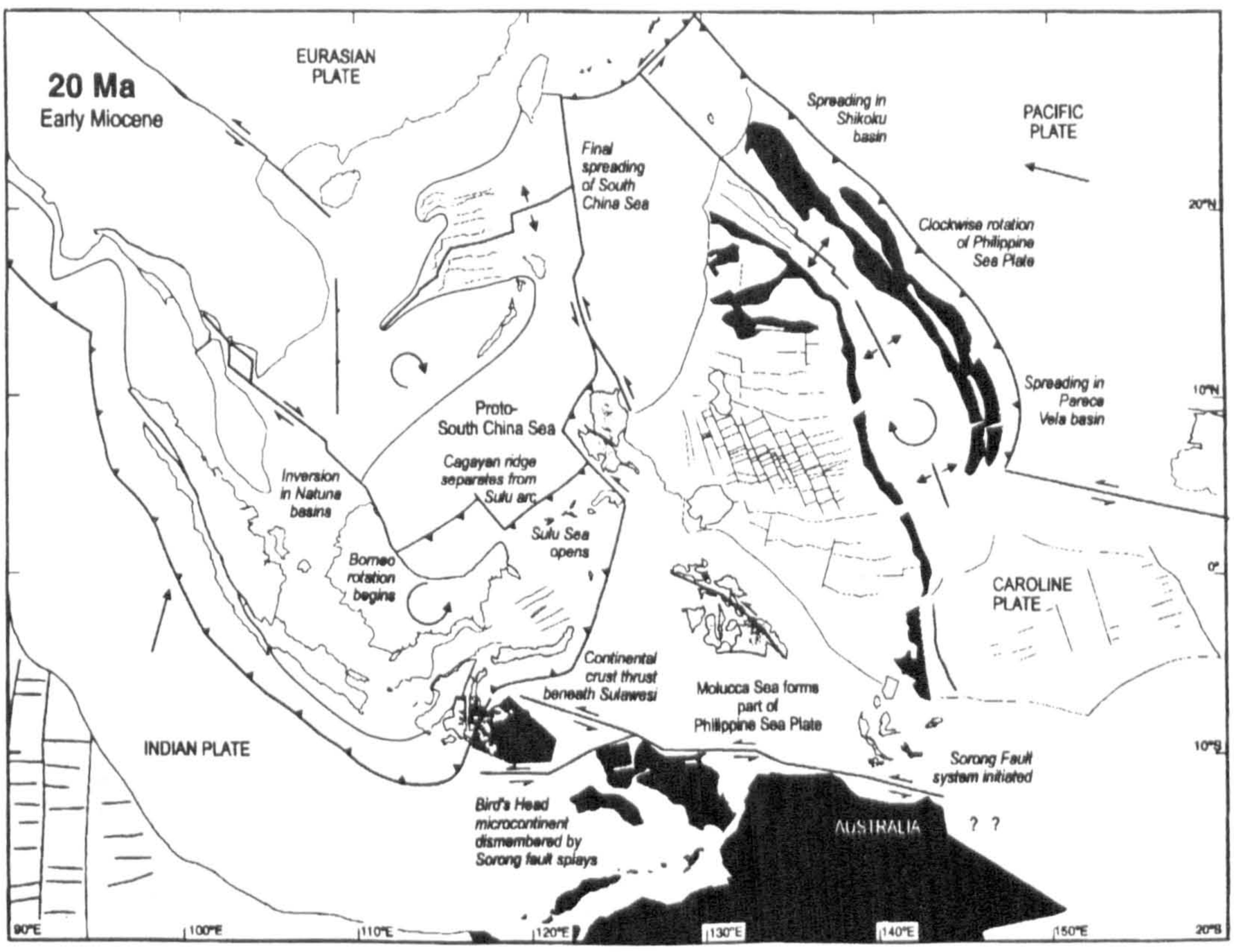

Figure 2.21. continued.

E

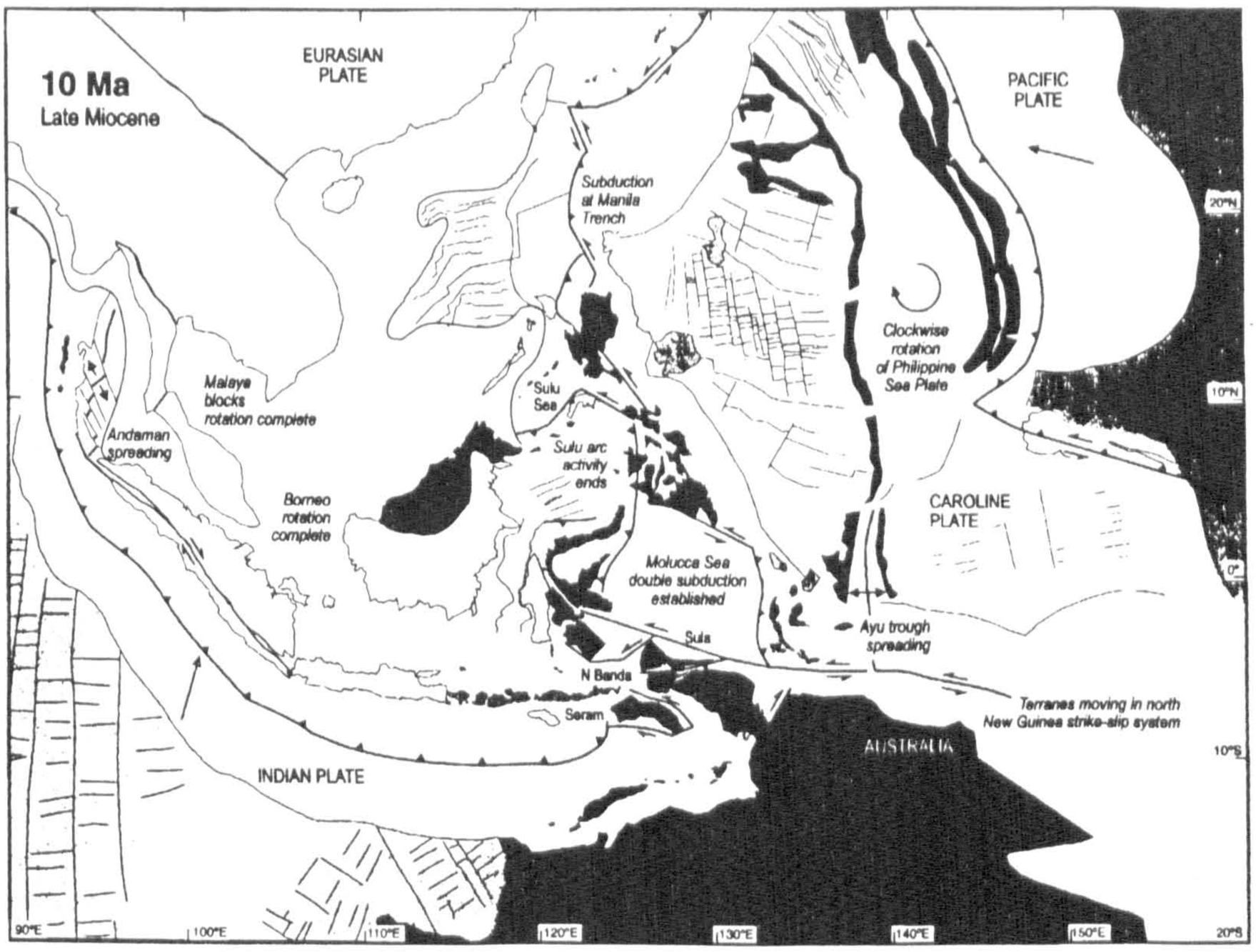

F

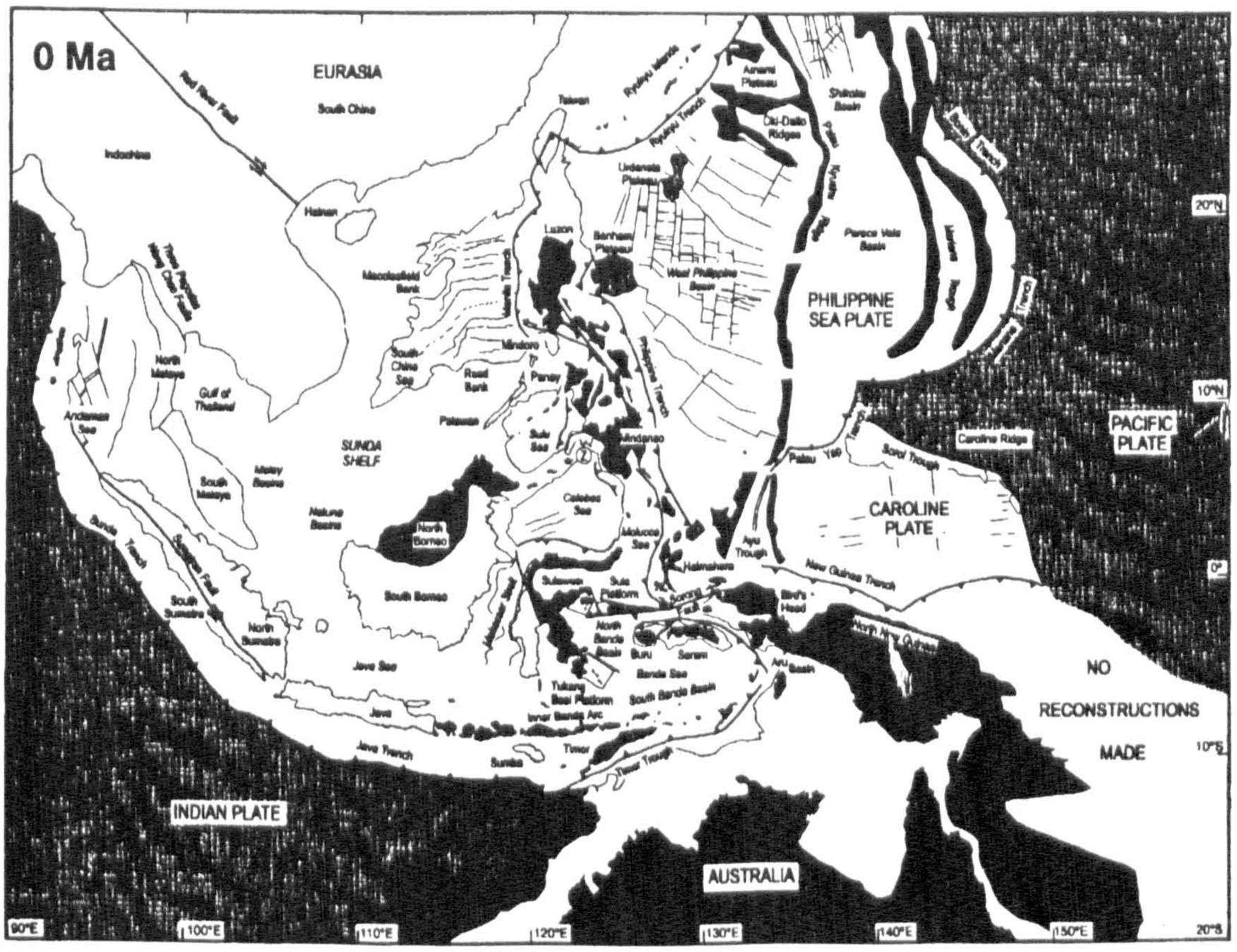

Figure 2.21. continued.

strain of the collision being absorbed by substantial crustal thickening. Models (e.g. Tapponnier *et al.*, 1986) suggest that much of the deformation associated with the India-Eurasia collision was accommodated by rigid clockwise rotation of fragments of the Eurasian plate and southeastward translation and deformation of the Indochina and Sibumasu blocks out of the collision zone (Richter & Fuller, 1996). Active subduction of the Indian plate at the Sunda and Java Trenches continues to this day.

Extension at the south China margin

The southwest Borneo and Semitau terranes, derived from the South China/Indochina southern margin, were emplaced in the Late Cretaceous to Eocene.

Subduction of the proto-South China Sea began in the Middle Eocene at its southern margin when a trench north of Zamboanga-Luzon became active due to the rapid opening of the Celebes Sea-West Philippine Sea Basin (active spreading in the Celebes Sea-West Philippine Sea Basin ended at 34 Ma). By the Early Oligocene, extension in the Sunda Shelf and in the Eurasian continental margin was being driven by the pull of the subducting proto-South China Sea slab.

The subduction of the proto-South China Sea rifted the Reed Bank-Dangerous Grounds terrane from south China and produced the NE-SW trending South China Sea and a series of basins along the south China margin, including the Southeast Hainan and Pearl River Mouth Basins. The South China Sea oceanic basin first opened north of Macclesfield Bank at 32 Ma (Briais *et al.*, 1993). The active spreading ridge later jumped south of Macclesfield Bank at 27 Ma. The final spreading phase in the South China Sea was the southwest propagation of the oceanic basin spreading ridge into the Sunda Shelf, which stopped at the end of Early Miocene when the Dangerous Grounds block collided with northern Borneo (Noad & Harbury, 1996).

Collision of Australian and Philippine Sea Plates with Eurasia

Around 50 Ma, the Indian-Australian plate was converging northwards on the Sunda Shelf, and the early rotation of the Philippine Sea plate began. Significant arc activity, including arc magmatism and arc splitting occurred over the next *c.* 25 Ma at the active subduction zones.

The Late Oligocene collision of the Australian continental margin in New Guinea, and the Bird's Head microcontinent block with the arc from north Sulawesi to Halmahera, caused a major reorganisation of plate boundaries and major effects which propagated westwards through the region. By the Early Miocene this had prompted the anticlockwise rotation of Borneo and parts of Malaya, Sumatra and Java, and caused inversion in the Natuna basins (Hall, 1996).

The Philippine Sea plate began to rotate clockwise in the Early Miocene initiating new subduction systems at its western edge. This ultimately led to the assembly of the Philippines Archipelago, initiated new arc systems from north Sulawesi through to the Philippines, and led to the growth and partial destruction of marginal basins such as the Sulu Sea. The continued rotation of the Philippines Sea plate had, by 15 Ma, resulted in the elimination of the Molucca Sea plate and the westward accretion of fragments torn from the northern Australian margin (including the Bird's Head microcontinent) into the Southeast Asian plate boundary zone. The controversial anticlockwise rotation of Borneo and the related rotations of Sundaland are believed to have terminated in the Late Miocene (Hall, 1996).

The collision of the Philippine arc and the Eurasian continental margin occurred in Taiwan at *c.* 5 Ma. The Philippine Sea plate motion then changed, initiating new subduction systems, such as those currently active on the east and west sides of the Philippines.

2.4.3 Current Tectonic Activity

Today, the terranes of Southeast Asia form a broad orogenic belt between the converging Eurasian and Indo-Australian plates.

The active tectonics can be characterised by the interactions of large, rigid plates separated by broad zones of deformation. The active tectonics of Sumatra, the Himalayan thrust, the Philippines, the New Guinea fold-and-thrust belt, the Huon-Finisterre collision, and the San Cristobal Trench can be understood in terms of upper plate deformation associated with oblique convergence. Western Java may also exhibit partitioning of oblique subduction (McCaffrey, 1996).

CHAPTER 3

The Marine Gravity Field

CHAPTER 3. THE MARINE GRAVITY FIELD

3.1 Introduction

Until recently, the Earth's offshore gravity field was less densely sampled than the onshore gravity field, and it was consequently less well mapped and understood. Although the marine gravity field has been measured for many years using shipborne gravity meters, these measurements have been distributed very unevenly. Older ship gravity data also suffer from large datum and reduction errors. Satellite altimetry has been used to measure the marine gravity field since the 1970's, and provides a more even global coverage of gravity measurements, as illustrated in Figure 3.1.

Maps of marine free-air gravity anomalies are usually obtained:

- with regional gravity data sets obtained from the inversion of satellite derived geoid heights
- by a process like least squares collocation, which combines all of the available marine gravity data
- with predictions made using distant data and/or topo-isostatic models

Results from a number of radar satellite missions have greatly increased the resolution of the marine gravity field in the last ten years. However the success with which the marine gravity field is determined still relies on the distribution and quality of the available data.

This chapter discusses the factors that limit the accuracy and resolution of both ship and satellite gravity (Sections 3.2 and 3.3), and also the techniques used to merge these data sets (Section 3.4). This information may be used when examining a marine gravity map in order to determine areas where the gravity field remains poorly resolved, as discussed in Section 3.5.

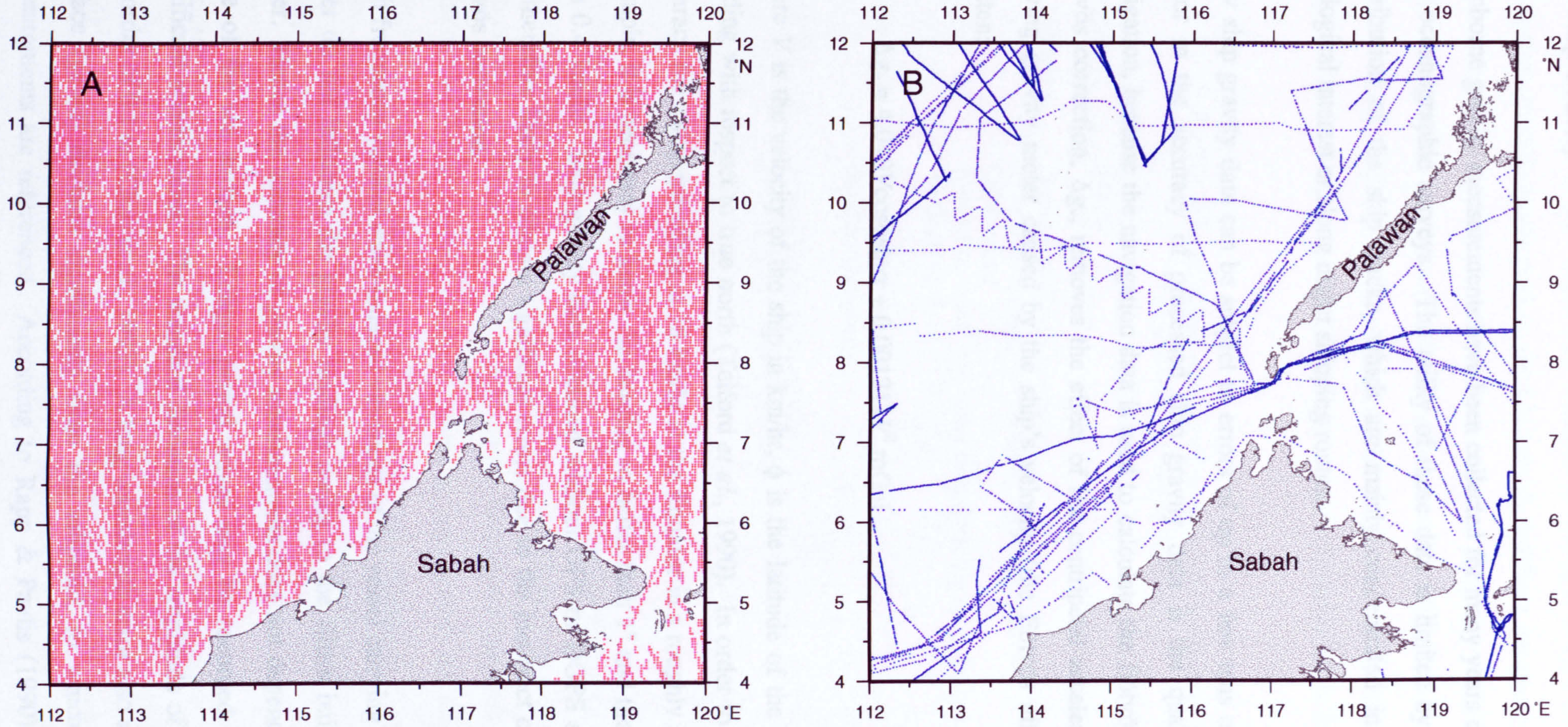

Figure 3.1. Comparison of satellite and ship gravity coverage north of Sabah.
A: WGI7.2 Satellite Altimeter Coverage, B: BGI Shiptrack Coverage.

3.2 Ship Gravity

Shipborne gravity measurements have been collected for many years during geophysical and oceanographic surveys. The utility of these data is limited by the semi-random distribution of the ship tracks, which are mainly concentrated in areas of known geological interest or along major shipping routes.

Raw ship gravity data can be subject to errors of up to a few tens of mGal. A major factor in the accuracy of processed ship gravity data is the quality of the ship's navigation, because the navigation data is used to calculate the Eötvös correction. The Eötvös correction, Δg_v, removes the effect of the centripetal acceleration acting on a moving gravity meter caused by the ship's velocity (the Eötvös effect), and may be written:

$$\Delta g_v = 4.040 V \cos\phi \sin\alpha + 0.001211 V^2 \text{ mGal} \qquad (3.1)$$

where V is the velocity of the ship in km/hr, ϕ is the latitude of the ship, and α is the heading with respect to true north (Telford *et al.*, 1990). In order to achieve a 1 mGal accuracy for a ship travelling at 18 km/hr at the Equator in a roughly E-W direction, for example, it is necessary to know the heading to better than 1° and the velocity to better than 0.4 km/hr. Ship gravity data obtained without GPS or DGPS satellite navigation are therefore likely to contain significant errors due to the incorrect computation of the Eötvös correction.

High frequency vertical wave-induced vibrations of the vessel carrying the marine gravity meter do not influence the gravity readings owing to the filters built into the gravity meter. Hence the accuracy of gravity measurements does not depend too much on the state of the sea surface. Longer period waves may be recorded and may produce significant accelerations. The standard deviation of the amplitude of these waves is of the order of 0.1 m (Chao *et al.*, 1993). A long wavelength error also arises when the sea surface (geoid) deviates significantly from the ellipsoid, to which the ship gravity measurements are referenced. According to Rapp & Pavlis (1990), the global mean

value of this error is 0.27 mGal (the standard deviation is ± 1.54 mGal). Asymmetric spring-type gravity meters such as the LaCoste & Romberg are prone to cross-coupling errors when the horizontal accelerations of the ship are translated into vertical accelerations of the gravity meter during data acquisition, Figure 3.2. Other sources of error include gravity meter off-leveling, nonlinear drift and mechanical 'tares' or 'jars' of the gravity measuring system. These errors are summarised in Table 3.1.

Table 3.1. The principal sources of error in marine gravity surveys. From Wessel & Watts (1988).

Source	Errors
Instrument	Dynamic sensitivity of sensor
	Cross-coupling (asymmetric spring-type gravity meters)
	Off-levelling
	Mechanical 'tares' of suspension constraining mass displacement
	Nonlinear drift
Navigation	Incorrect Eötvös correction
	Incorrect positioning
Other	Incorrect tie-in to base station
	Inconsistent use of reference field

It is difficult to quantify the accuracy of ship gravity data because the types of navigation, measuring system response and sea conditions vary widely. The principal method used to estimate the accuracy of gravity data at sea has been the analysis of the difference in free-air gravity anomaly values at intersections of ship tracks (Talwani, 1971). This is called crossover error (COE) analysis. Wessel & Watts (1988) analysed marine gravity data worldwide and their map of the standard deviation of COE is shown in Figure 3.3.

Long wavelength and datum errors in ship gravity survey data may be reduced by either: (1) application of a simple datum shift (Heiskanen & Moritz, 1967; Mainville *et al.*, 1992); (2) processing using the along-track gravity gradient (Kirby & Hipkin, 1994); or (3) adjustment to the satellite-only gravity field using a quadratic polynomial in time (Hwang *et al.*, 1994).

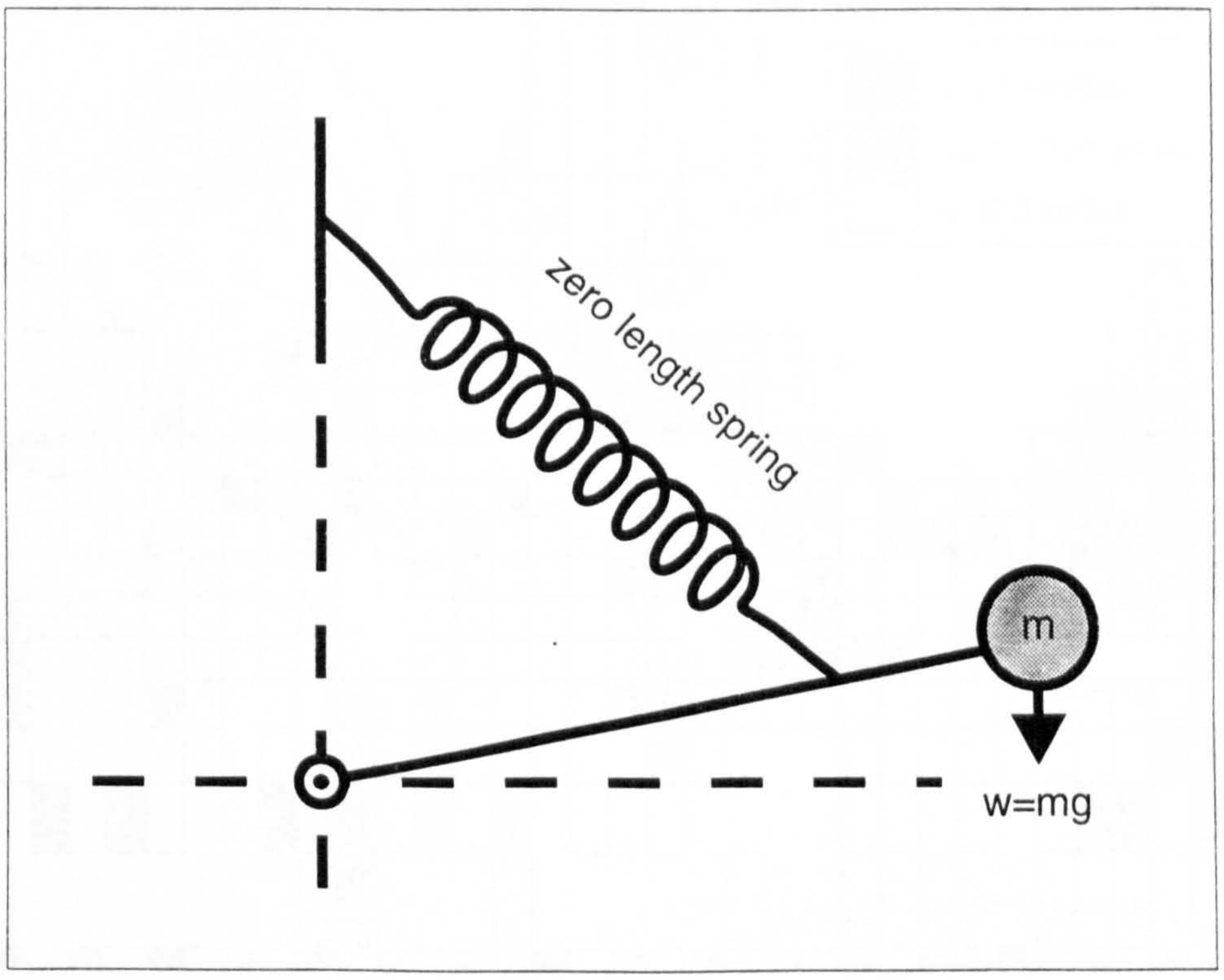

Figure 3.2. LaCoste & Romberg gravity meter suspension. Horizontal accelerations of the gravity meter cause the pivoted weight to move in the vertical plane and result in cross-coupling errors during gravity measurement.

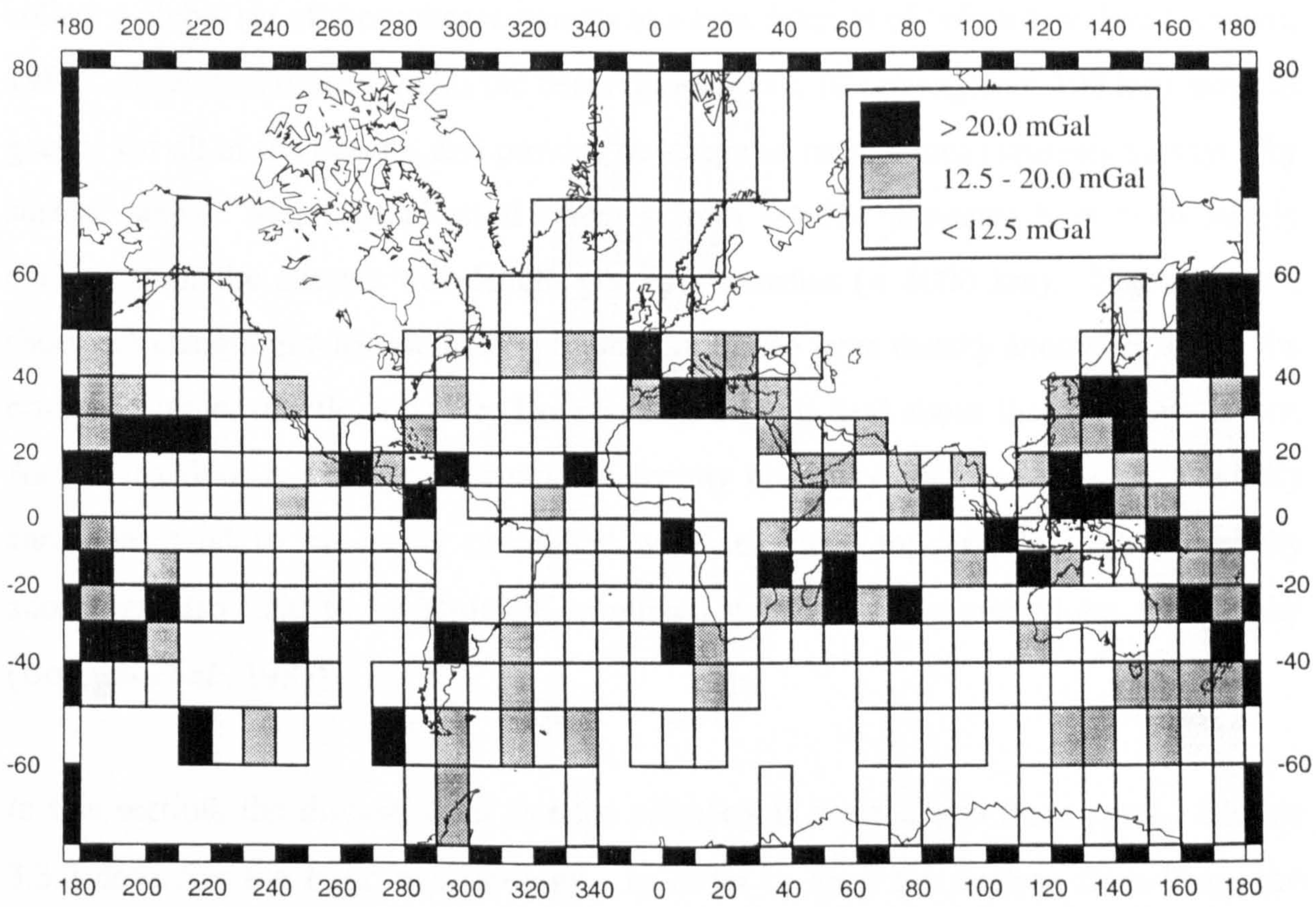

Figure 3.3. Map showing the standard deviation of ship gravity crossover errors (COEs) within 10° × 10° blocks. High COE values seem to correlate with regions of rapidly varying high-amplitude gravity field, whereas low values are generally found over the abyssal plains. Intermediate COEs are found along continental margins. The white regions have no COEs. From Wessel & Watts (1988).

3.3 Satellite Gravity

3.3.1 Introduction

The Earth's marine gravity field may be measured using satellite altimetry. Characteristics unique to satellite altimetry are: (1) the high accuracy with which the sea surface topography, wave height and wind speed can be measured, and (2) the ability to collect a global set of these measurements in a time interval of only a few days (Stewart, 1985). Satellite altimetry yields the best regional-scale (wavelengths > 100 km) maps of gravity for all of the oceans, and provide coverage of remote areas sparsely surveyed by surface ships. Major geophysical findings from satellite altimetry have been largely derived from the shorter wavelength gravity anomalies (< 1000 km). Because these short-wavelength gravity anomalies primarily originate from density anomalies within the crust and upper mantle, altimetry has revealed a great deal about these shallow layers. As the sea floor is a shallow, prominent density boundary, shorter wavelength gravity anomalies tend to be highly correlated with sea floor topography. These gravity anomalies also tend to be strongly correlated with basement and Moho topography (Douglas *et al.*, 1987).

In this section, the discussion of satellite altimetry is divided into three parts. Section 3.3.2 describes the basic methodology. In order to keep this section from being too long, the main sources of error are discussed in Section 3.3.3. Finally, the satellite altimeters which acquired the gravity data used in this study are discussed in Section 3.3.4.

3.3.2 Satellite Altimetry

3.3.2.1 Overview

Four processing stages are followed when the Earth's gravity field is determined from satellite altimetry. First, the instantaneous sea surface height is determined, and the non-gravitational components of the sea surface topography are removed. The data are then edited to remove outliers (erroneous data points), and finally converted to gravity values, ready for compilation into maps and data sets. For reference, Figure 3.4 shows the magnitude of various quantities related to the Earth's gravity perturbations at different resolutions.

3.3.2.2 Measurement of Sea Surface Height

A pulse-limited satellite altimeter directs a short pulse (3.1 ns) of microwave radiation towards the Earth, which fans out in the atmosphere to illuminate a 'footprint' on the ocean surface. The size of this footprint depends on the frequency of the radar and on the sea state, and varies between 2 and 20 km in diameter (Jolly, 1996). The altimeter infers the height of the satellite above the ocean surface from the two-way travel time of the reflected pulse. Corrections are made to this height measurement for instrumental, atmospherical, sea state and tidal effects. Using precise orbit data calculations, the height of the sea surface relative to the reference ellipsoid is then determined. The geometry of this measurement is shown in Figure 3.5.

The satellite altimeter derived observation of sea surface height, h, may be described by

$$h^o = h + \varepsilon + h_B \tag{3.2}$$

where h^o is the observed height, h_B is a bias that is the sum of the invariant bias in the altimeter and the error in the knowledge of the semi-major axis of the Earth's reference ellipsoid (Marsh *et al.*, 1990), and ε is the error of the observation:

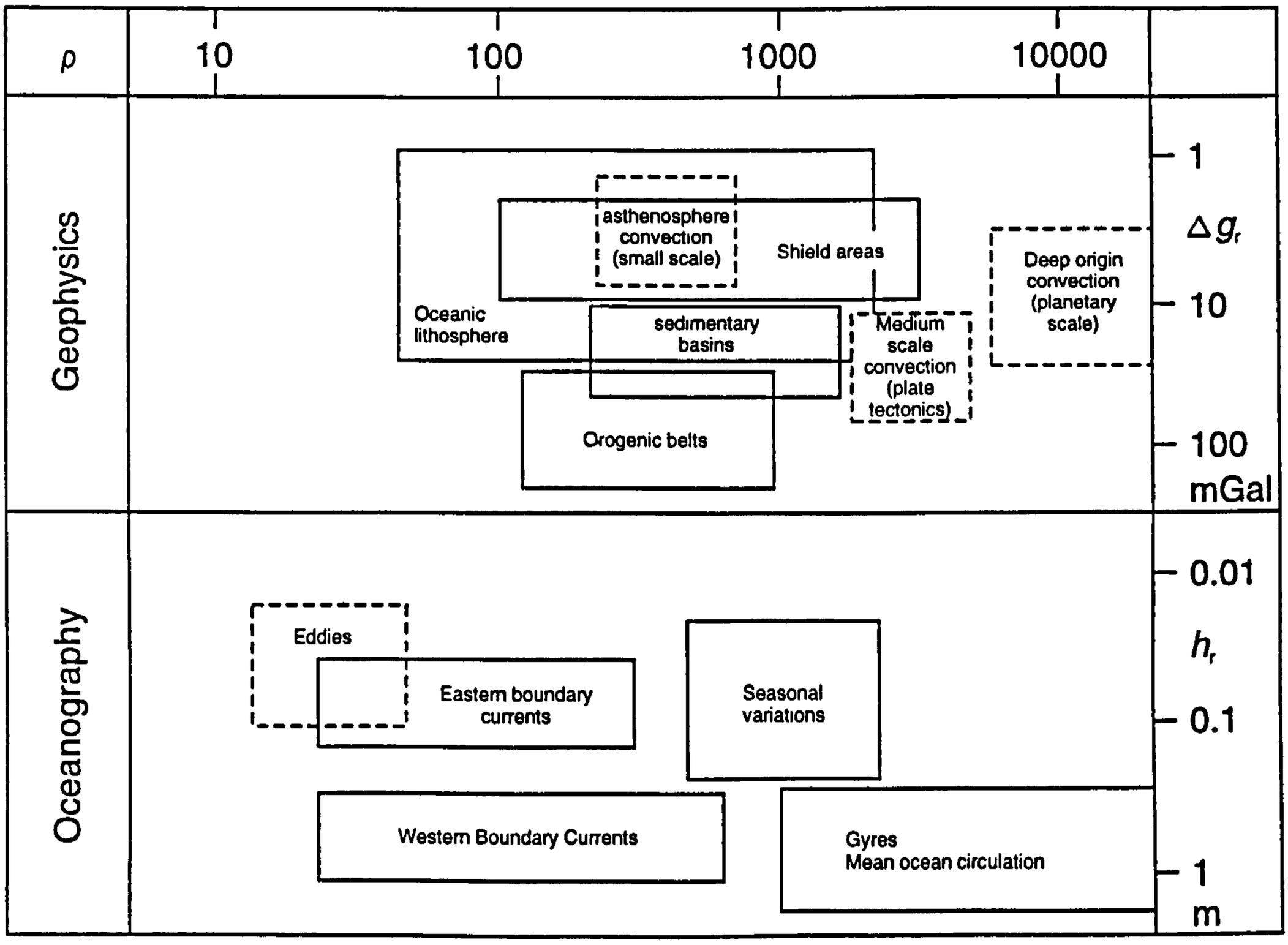

Figure 3.4. Magnitude of various quantities related to Earth gravity perturbations at different resolutions. ρ: resolution, or half wavelength of phenomenon (km); Δg_r, relative variation of gravity anomaly (mGal); and h_r, relative variation of sea surface height (m). From Anderson & Cazenave (1986).

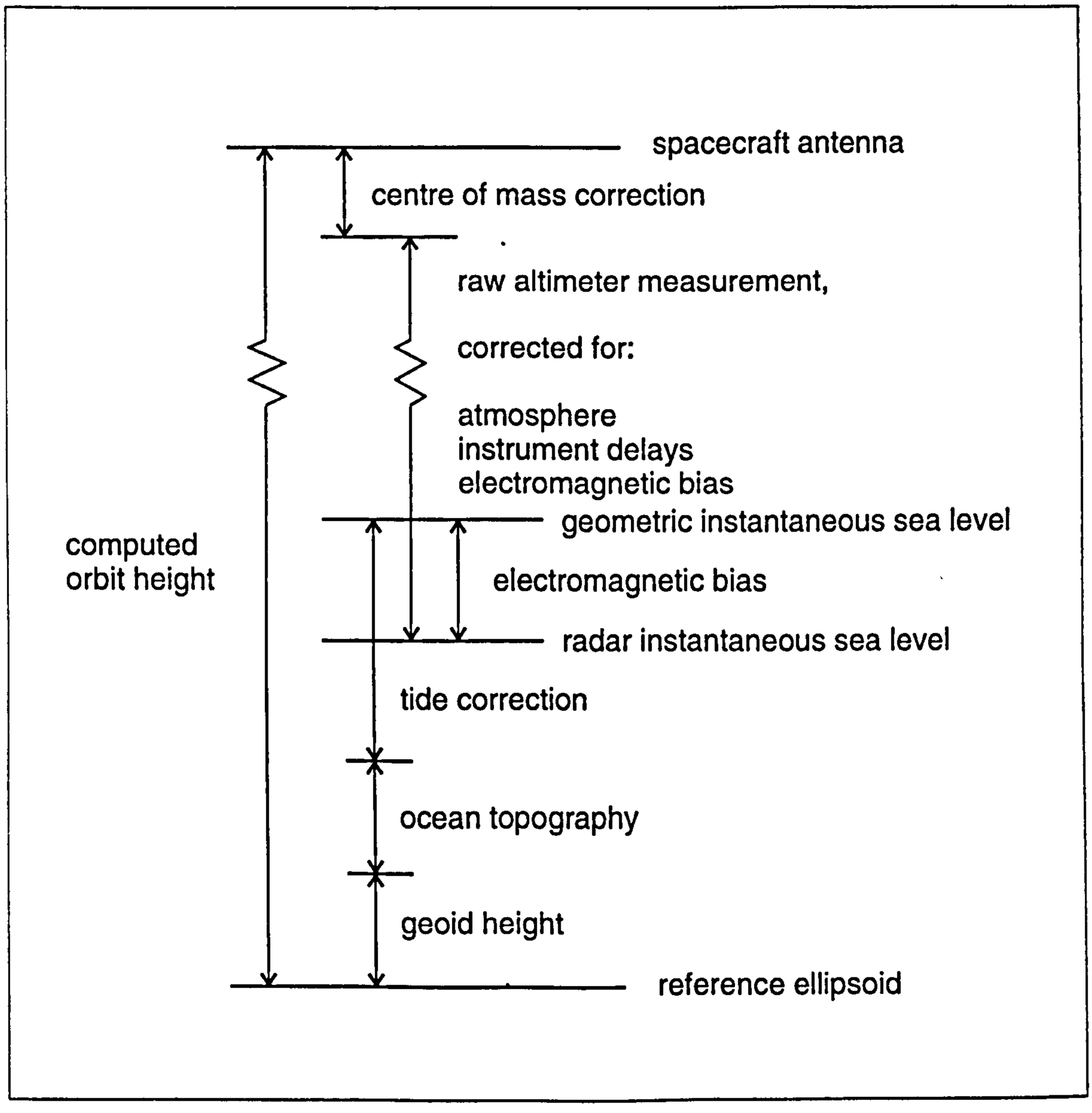

Figure 3.5. Altimeter measurement geometry, from Visser *et al.* (1993).

$$\varepsilon = \varepsilon^{o} + \varepsilon^{i} + \varepsilon^{wt} - \varepsilon^{dt} + \varepsilon^{io} + \varepsilon^{lw} + \varepsilon^{swh} + \varepsilon^{b} + \varepsilon^{o\tau} + \varepsilon^{e\tau} + n \qquad (3.3)$$

where ε^{o} is the orbit error, ε^{i} is the instrument error, ε^{wt} and ε^{dt} are the errors in correction for delay caused by water vapour and other gases in the wet and dry troposphere respectively, ε^{io} is the error in correction for delay caused by free electrons in the ionosphere, ε^{lw} is the error due to liquid water in rain and clouds, ε^{swh} is the error in correction for sea state related bias, ε^{b} is the error in correction for barometer effects, $\varepsilon^{o\tau}$ is the error in correction for ocean tides, $\varepsilon^{e\tau}$ is the error in correction for Earth tides (deformation of elastic Earth), and n is the measurement noise.

3.3.2.3 Removal of Sea Surface Topography

If the sea surface was only influenced by gravitational forces, it would coincide with the geoid, which is the equipotential surface of gravity coinciding with the mean sea level. However, superimposed on the geoid undulations are the generally much weaker and often short lived undulations of the sea surface topography. Phenomena which influence the sea surface topography include meandering currents, western boundary currents, gyre circulations, zonal equatorial flows, tropical circulation, mesoscale eddies ($\lambda < 1000$ km), tides, storm surges, winds, variations of atmospheric pressure, rings of anomalous water temperature, seasonal variations of temperature and salinity, possible long-term climatic changes, and eustatic changes of sea level (Apel, 1980; Tschernia, 1980; Fu & Cheney, 1995). Maximum variabilities correspond to seasonal (30%) and interannual fluctuations. Seasonal fluctuations are caused by local changes of wind curl (Chao *et al.*, 1993).

Relative to the GRS80 reference ellipsoid, the RMS spatial variability of the geoid is about 25 m (Wunsch & Zlotnicki, 1984). The time-varying changes of sea surface topography, although small compared to the permanent undulations created by the geopotential, are large compared to the precision (a few cm) of the modern satellite altimeters (Section 3.3.4). Other fluctuations of the same magnitude as ocean tides and

currents result from the inverse barometer effect and wind effects (Cartwright & Ray, 1990).

As the geoid height (N) is required for gravity field determination, ocean dynamic topography and tides are considered to be error sources. The geoid height may be described by:

$$N = h^o - \xi - \Delta\xi + \varepsilon^N \tag{3.4}$$

where h^o is the observed height, ξ is the permanent sea surface topography, $\Delta\xi$ is the time-varying sea surface topography, and ε^N is the error in the observed geoid height. ε^N may be described by:

$$\varepsilon^N = \varepsilon + \varepsilon^{\xi} + \varepsilon^{\Delta\xi} \tag{3.5}$$

where ε is the error of the observation (Equation (3.3)), ε^{ξ} is the error in the correction for permanent sea surface topography, and $\varepsilon^{\Delta\xi}$ is the error in the correction for the time-varying sea surface topography.

Sea surface topography is eliminated as much as possible from the altimetric measurements by first removing the permanent (quasi-stationary) effects caused by tidal and meteorological forcing using, for example, the M_2 Schwiderski (1980) $1° \times 1°$ global ocean tide model (Merriam, 1983; Melchior, 1983). The remaining time-varying sea surface topography cannot be removed or modelled, and remains in the altimeter data.

In many studies, especially at a local scale, sea surface height measurements are converted to geoid slopes rather than geoid heights before further processing and stacking (e.g. Sandwell, 1992). This avoids sea surface datum problems. In this case,

the long wavelength component of the gravity field is dealt with separately using a long wavelength model such as JGM-3 (Nerem *et al.*, 1994).

3.3.2.4 Data Editing

Satellite altimeter data need to be edited to remove outliers and data over land or ice. High values of altimeter Automatic Gain Control (AGC > 36 dB), and/or low values of significant wave height (SWH = 0), might indicate the presence of sea ice in the altimeter footprint (Marsh & Martin, 1982). A value of AGC > 36 dB may also indicate the presence of land. Thus Shum *et al.* (1990) edited their altimeter data when: (1) spacecraft attitude > 1.2° from nadir; (2) significant wave height = 0 m or > 16 m; (3) standard deviation of significant wave height > 1 m; (4) measurement standard deviation > 20 cm; (5) AGC > 36 dB; (6) standard deviation of AGC > 0.15 dB; (7) ocean tide height > 10 m; and (8) data were obtained over known areas of land or ice.

3.3.2.5 Conversion from Geoid to Gravity Anomaly Data

Altimeter measurements of the geoid can be easily converted to gravity data (e.g. Rapp, 1983; Rummel & Haagmans, 1991). The anomalous gravity potential (T) is obtained to a first approximation from the geoidal height (N) using Brun's formula:

$$N \cong T/\gamma \tag{3.6}$$

where γ is the normal value of gravity on the reference ellipsoid (Phinney & Nerem, 1997). The anomalous gravity field is the vertical derivative of the gravitational potential:

$$\Delta g = -\delta T/\delta z \tag{3.7}$$

The gravity anomaly field has more detail than the geoid anomaly field, as a consequence of the fact that gravity is proportional to the differential of the geoid. This is illustrated in Figure 3.6, which shows the geoid and gravity anomalies over Reed Bank in the South China Sea.

The gravity data are usually stacked since the major error sources, such as short wavelength dynamic topography and broad-band altimeter noise, are reduced by averaging many repeats, provided that these errors are uncorrelated in time (Brenner *et al.*, 1990). Stacking reduces the random error proportionally to the square root of the number of repeats used in the stack (Yale *et al.*, 1995).

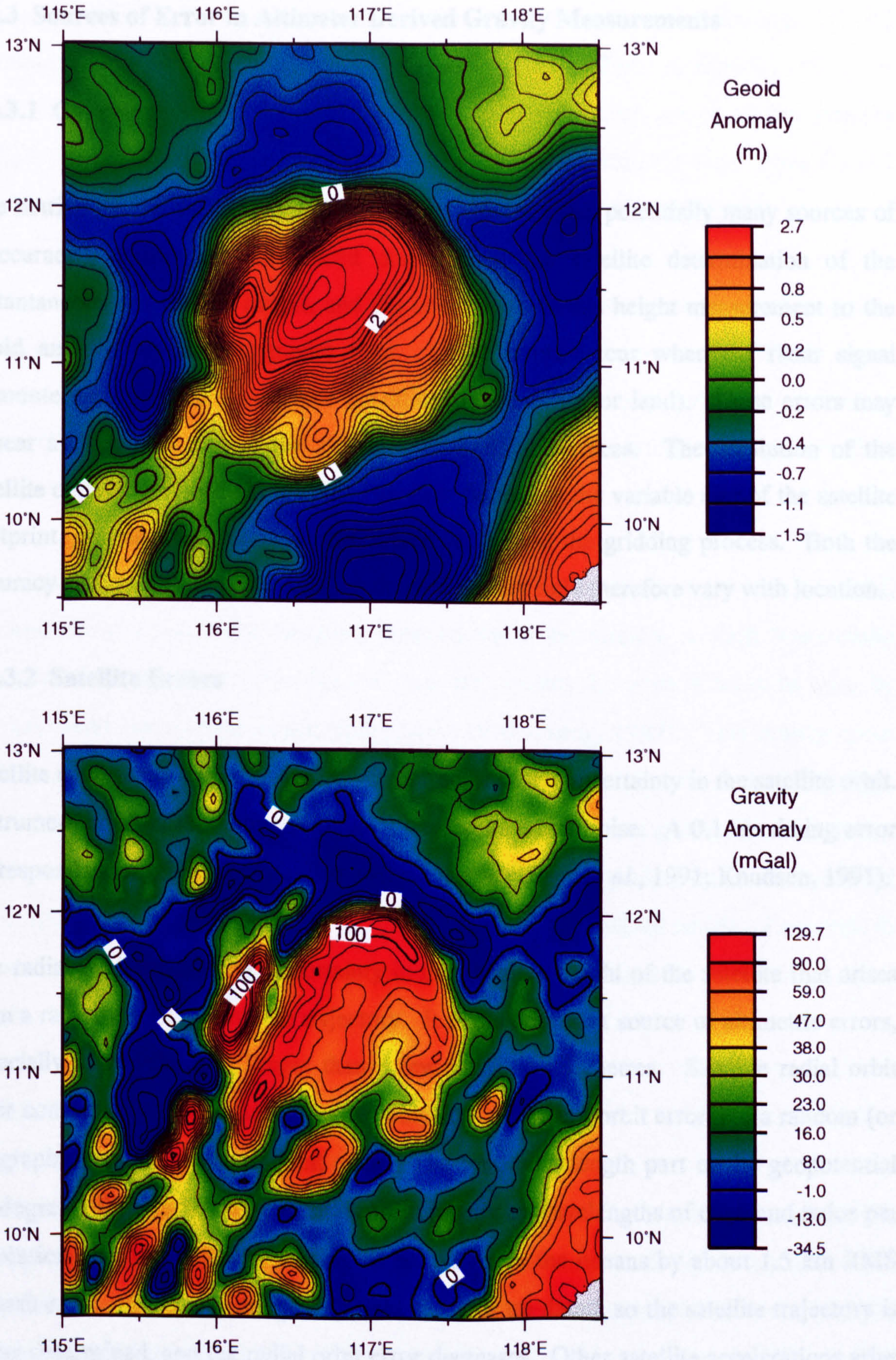

Figure 3.6. WGI7.2 geoid anomaly (top) and gravity anomaly (bottom) over Reed Bank, South China Sea.

3.3.3 Sources of Error in Altimeter Derived Gravity Measurements

3.3.3.1 Overview

The marine gravity field measured by satellite altimetry has potentially many sources of inaccuracy. Errors are introduced during both the satellite determination of the instantaneous sea surface height, and the conversion of this height measurement to the geoid and the anomalous gravity field. Other errors occur when the radar signal encounters unexpected sea surface conditions (such as ice or land). These errors may appear as biases or tilts of the altimetric or geoidal surfaces. The resolution of the satellite derived gravity field is limited by such factors as the variable size of the satellite footprint, ground-track misalignment, water depth, and the gridding process. Both the accuracy and resolution of the satellite derived gravity field therefore vary with location.

3.3.3.2 Satellite Errors

Satellite errors arise due to either instrument noise or the uncertainty in the satellite orbit. Instrument error of the altimeter radar is treated as white noise. A 0.1 ns timing error corresponds to a 1.5 cm error in sea surface height (Blanc *et al.*, 1991; Knudsen, 1991).

The radial orbit error is the uncertainty in the absolute height of the satellite that arises from a rather uncertain satellite trajectory. It is the dominant source of altimetric errors, especially at wavelengths longer than a few hundred kilometres. Satellite radial orbit error consists of a systematic (or geographically correlated) orbit error and a random (or geographically uncorrelated) orbit error. The long wavelength part of the geopotential (to degree 10) perturbs the spacecraft orbit, mostly at wavelengths of once and twice per revolution around the globe, varying its height above the oceans by about 1.5 km RMS (Marsh *et al.*, 1990). As the gravity field model is up-dated, so the satellite trajectory is better determined, and the radial orbit error decreases. Other satellite accelerations arise from numerous forcing effects, including tides, drag force, solar radiation pressure, and the point mass effects of the Earth, Moon, Sun and planets (Marsh *et al.*, 1988). The magnitude of the effect of atmospheric drag on a satellite is extremely difficult to model,

and is fast becoming the dominant component in radial orbit error, contributing a 30 - 40 cm radial error to the current Topex/Poseidon orbit data (Berry & Blewitt, 1994). A result of the uncertainty in satellite trajectories is that repeat orbits of the satellite altimeter may differ from each other radially by several metres. In some cases Geosat repeat orbits differed by as much as 15 m radially (Wyrtki & Mitchum, 1990).

Orbit errors are determined by the analysis of crossing arcs (Arent *et al.*, 1992) and may be minimised with the constrained sinusoidal crossover adjustment (Tai, 1988) or by least squares detrending (Marsh *et al.*, 1992). A geographically-correlated orbit error may still be present in the solution, but is relatively small when modern gravity field models are used (Mazzega, 1986; Visser *et al.*, 1993).

When altimeter satellites are maintained in a repeating orbit, such as the Geosat ERM, atmospheric drag and solar radiation pressure cause the satellite to drift horizontally about its orbit trajectory. For Geosat, this drift causes the ground track to vary by ± 1 km about the nominal repeat path (Sandwell & Zhang, 1989). This misalignment leads to an error in the estimate of the sea surface height that increases as the local slope in the geoid increases. Brenner *et al.* (1990) estimated this error globally for the Geosat ERM and found that over most of the ocean where the geoid gradient is small, the repeat track misalignment leads to errors of only 1 - 2 cm in sea surface height. However, in the vicinity of trenches, continental shelves, islands, and seamounts, errors can exceed 20 cm.

3.3.3.3 Radar Measurement Errors

Errors arise during the calculation of the effects of the Earth's atmosphere on the propagation of the altimeter's radar signal. Significant errors arise from the lack of an onboard radiometer to provide an accurate estimate of tropospheric water vapour (Geosat), errors due to the liquid water in rain and clouds, and the significant wave height bias. Effects due to the ionosphere may be important, if, for example, altimeter data collected in a period of increased solar activity are used. Errors due to wet

troposphere, atmospheric pressure, and Earth tides are negligible (Knudsen, 1991; Chao *et al.*, 1993).

The correction necessary to compensate for the retarding influence of the water vapour in rain and clouds on the propagation speed of the radar signal produces a path length correction of 10 - 50 cm as the signal goes from a very dry to a very wet atmosphere. For the Seasat altimeter, this correction was obtained from the onboard Scanning Multifrequency Microwave Radar (SMMR) instrument which was accurate to a few centimetres, and had a spatial resolution of 40 km. Along test tracks, Bernstein *et al.* (1982) found that this SMMR correction varied between 15 and 25 cm. When Knudsen (1991) analysed Seasat data, he found that the short wavelength part of the error was mainly correlated with errors due to liquid water in rain and clouds. Knudsen (1991) also noted that whilst this water vapour 'appears to absorb parts of the short wavelength gravity field' and may have a 'considerable effect', errors can be detected as spikes during pre-processing.

The inverse barometric correction is based on the direct proportionality between changes in sea surface height and changes in the surface atmospheric pressure. An increase (or decrease) of 1 mbar in atmospheric pressure brings about a decrease (or increase) of about 1 cm in sea surface height (Bernard *et al.*, 1983; Dickman, 1988; Shum *et al.*, 1990). Inverse barometric corrections was not applied to the Geosat altimeter data.

Sea state related bias is caused by the height and form of the ocean surface waves. On average, the significant wave height (SWH) will be below 4 m, but in extreme conditions may be as large as 20 m (Visser *et al.*, 1993). Sea state bias occurs because more energy is returned from the wave trough than from the crest, thus causing the altimeter-determined mean sea level to shift toward the wave troughs. Furthermore, the ocean waves have a skewed distribution and the receiver pulse is not exactly Gaussian. The satellite footprint also grows with increasing sea state (Stewart, 1985). The superposition of the reflections from this area stabilizes the shape of the echo but it also smoothes the echo so that the timing of its leading edge is more uncertain. The accuracy

of a correction for these effects is 1 - 2 per cent of SWH (Born *et al.*, 1982; Tapley *et al.*, 1982; Knudsen, 1991).

As the satellite footprint increases with increasing sea surface roughness, so the resolution of the gravity field decreases. Sea surface roughness also seems to be correlated with the ocean bottom topography (Colton & Chase, 1983). According to Sandwell & Zhang (1989), higher than average variability occurs at mid latitude in deep water (> 3 km) adjacent to continental shelves, spreading ridges, and oceanic plateaus. Variability is low in shallower areas (< 3 km). The variability does not appear to be higher downstream of topographic protrusions. Instead, the areas of highest variability occur in the deep basins (> 4 km). No parameters of sufficient quality have been found, however, that would allow this dependency to be taken into account (Knudsen, 1991).

On a continental shelf, gusts of wind may produce upwelling phenomena and piling up of water against the coast (Bernard *et al.*, 1983). According to the study of Elliot (1979), a wind speed of 20 knots may induce a maximum variation in sea level of about 15 cm.

3.3.3.4 Oceanographic Contamination

Oceanographic contamination of satellite gravity data arises from the incorrect calculation of the ocean tide correction and from the failure to remove the remaining variable (non-gravitational) component of sea surface topography. The oceanographic component of sea surface topography consists of a semi-permanent and a variable part. The semi-permanent part, often referred to as the dynamic sea surface topography, has a global RMS value of about 65 cm. The variable part of the ocean surface, the variable sea surface topography, has a global RMS value of approximately 20 cm (Knudsen, 1991; Visser *et al.*, 1993).

Ocean Tide Correction

Ideally, altimeter measurements are adequately corrected for the tidal and meteorological forcing effects of the sun and the moon using a global marine tide model. In the open

ocean, tidal variations of the sea surface are of the order of 0.5 m (Cartwright & Ray, 1990). The accuracy of the correction for ocean tides is of the order of 10 - 20 cm, but is not well determined in areas without tide gauges (Caldwell *et al.*, 1989; Shum *et al.*, 1990; Knudsen, 1991). The global marine tide models loose much of their validity in the shallow waters of continental shelves and (semi-)enclosed seas where non-linear bottom friction and irregular shaped coastlines produce large variations in tidal water elevations (Oskam, 1990; Knudsen, 1991; Imawaki *et al.*, 1992). Both the variation in tidal water elevation and the non-linearities induced by bottom friction decrease as the water depth increases. When the global Schwiderski model is used in the North Sea, for example, the computed variability reaches up to 20 - 50 cm towards the shores. Dedicated regional hydrodynamic models reduce this variability to about 10 cm (Oskam, 1990).

Dynamic Sea Surface Topography

The dynamic sea surface topography consists of the mean time-averaged currents which are produced by the general circulation of the oceans. The ocean circulation signal has a magnitude of the order of 10 cm to 2 m at most. These currents produce variations in sea level with wavelengths ranging from 40 km to the dimensions of the ocean basins, and with periods ranging from weeks to centuries or longer (Bernstein *et al.*, 1982; Stewart, 1984; Blanc *et al.*, 1991; Marsh *et al.*, 1992). The dynamic topography may be estimated with an average accuracy of ± 16 cm, although this accuracy ranges from ± 14 cm to ± 48 cm depending on the area (Rapp & Wang, 1994). Errors due to the unknown permanent dynamic topography of the sea cannot be reduced and therefore one must be especially careful when interpreting satellite altimeter profiles near areas associated with intense western boundary currents which have typical sea surface dynamic topography gradients of the order of 10^{-5} rad (Imawaki *et al.*, 1992; Gille, 1994; Hogg & Johns, 1995).

A good example of the effect of currents on the dynamic sea surface topography is given by the Gulf Stream. The Gulf Stream is a narrow ribbon of high velocity water that flows along a boundary between cooler, denser slope water to the shoreward side and warmer, lighter water in the Sargasso Sea. The sea surface topography shows 1 m

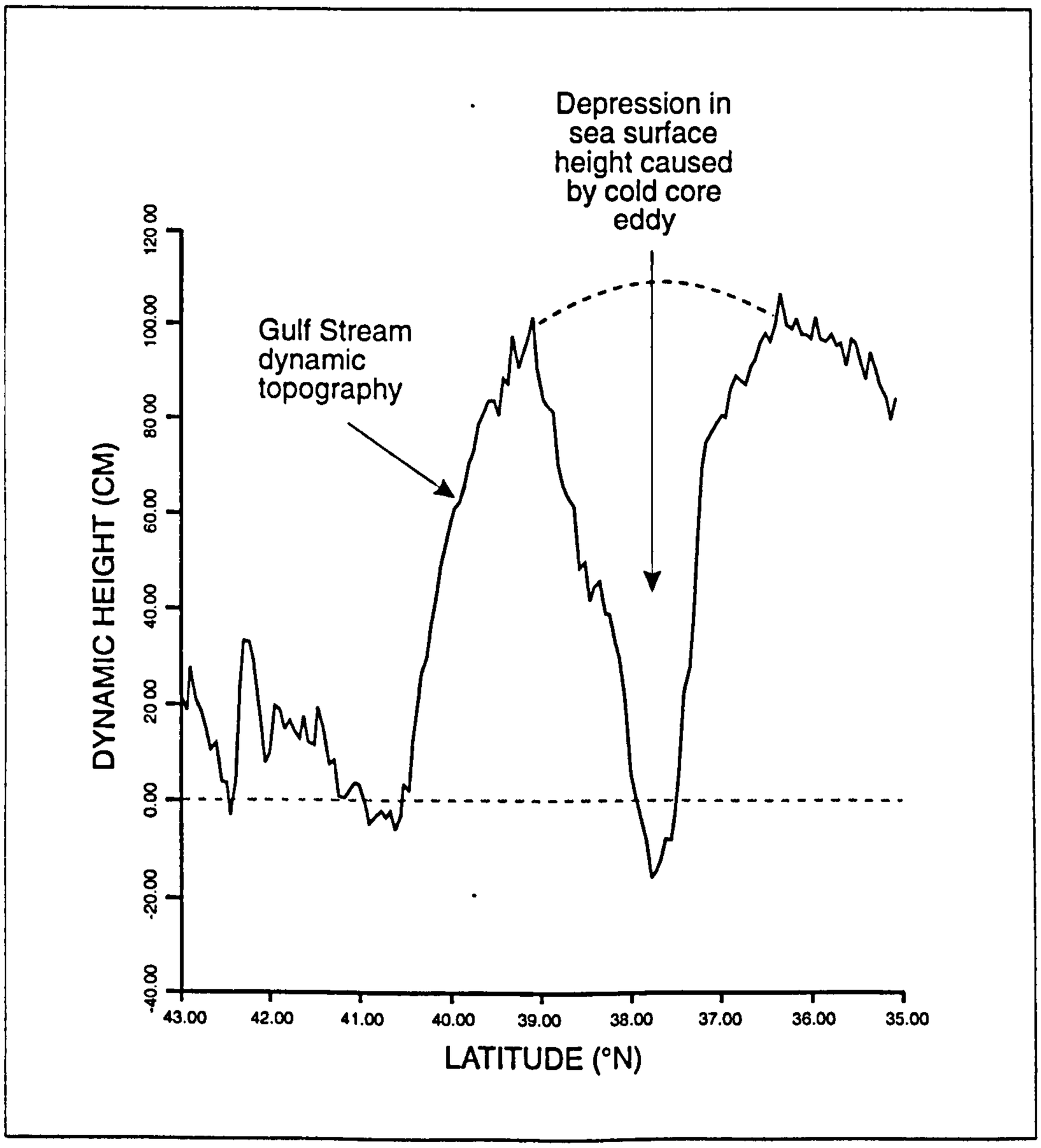

Figure 3.7. The dynamic sea surface topography caused by the Gulf Stream on May 7, 1987. The depression near 38°N is caused by a cold core eddy. Modified from Rapp & Wang (1994).

height differences across the Gulf Stream (Leitao *et al.*, 1979). Patches of anomalous water temperature such as cold core eddies and warm rings result in sea surface variability. In Figure 3.7, the dynamic sea surface topography along Geosat track A12 of 7 May 1987 is shown. The Gulf Stream elevates the sea surface by about 1.1 m. The depression near 37.8°N represents a cold core eddy (Rapp & Wang, 1994).

Similar currents circulate through the South China Sea, as illustrated in Figure 3.8. According to Tschernia (1980), the February winds are northeast in the South China Sea. Part of the north branch of the North Equatorial Current penetrates into the China Sea between Luzon and Taiwan to join a current coming from the Yellow Sea by the Formosa Strait. A huge eddy then turns within the South China Sea, along its western side, passes between Sumatra and Borneo, and by way of the eddy-rich (Semtner & Chervin, 1992) Java, Banda and Ceram Seas combines with the Equatorial Counter Current. In the summer monsoon (August) the current of the South China Sea reverses itself, and its waters, which are then provided mostly by the Southern Equatorial Current, join north of the Philippines with the northern branch of the North Equatorial Current.

Other dynamic topography is generated by internal waves, gyres and eddy currents. Internal waves generated, for example, at spreading ridges and continental shelves, modulate the amplitude of the surface tide by ~ 5 cm (Ray & Mitchum, 1996). They are often spatially coherent over great distances (> 1000 km), and have wavelengths of ~ 150 km. Gyres are circular or spiral motions of water, generated mainly by surface winds, displaced towards the western side of oceans. A major gyre exists in each of the main ocean basins. The Northern Atlantic Subtropic Gyre has a dynamic sea surface topographic height of ~ 0.25 m (diameter 1500 km), whilst the Southern Atlantic Subtropic Gyre has a height of ~ 0.5 m (Marsh *et al.*, 1990). It is likely that gyres exist in all partially-enclosed shelf seas, including the South China Sea and the Gulf of Thailand. Eddy currents cause changes in sea surface height of the order of 20 cm (Bernstein *et al.*, 1982; Menard, 1983), and are typically 100 - 300 km in width (Douglas *et al.*, 1987).

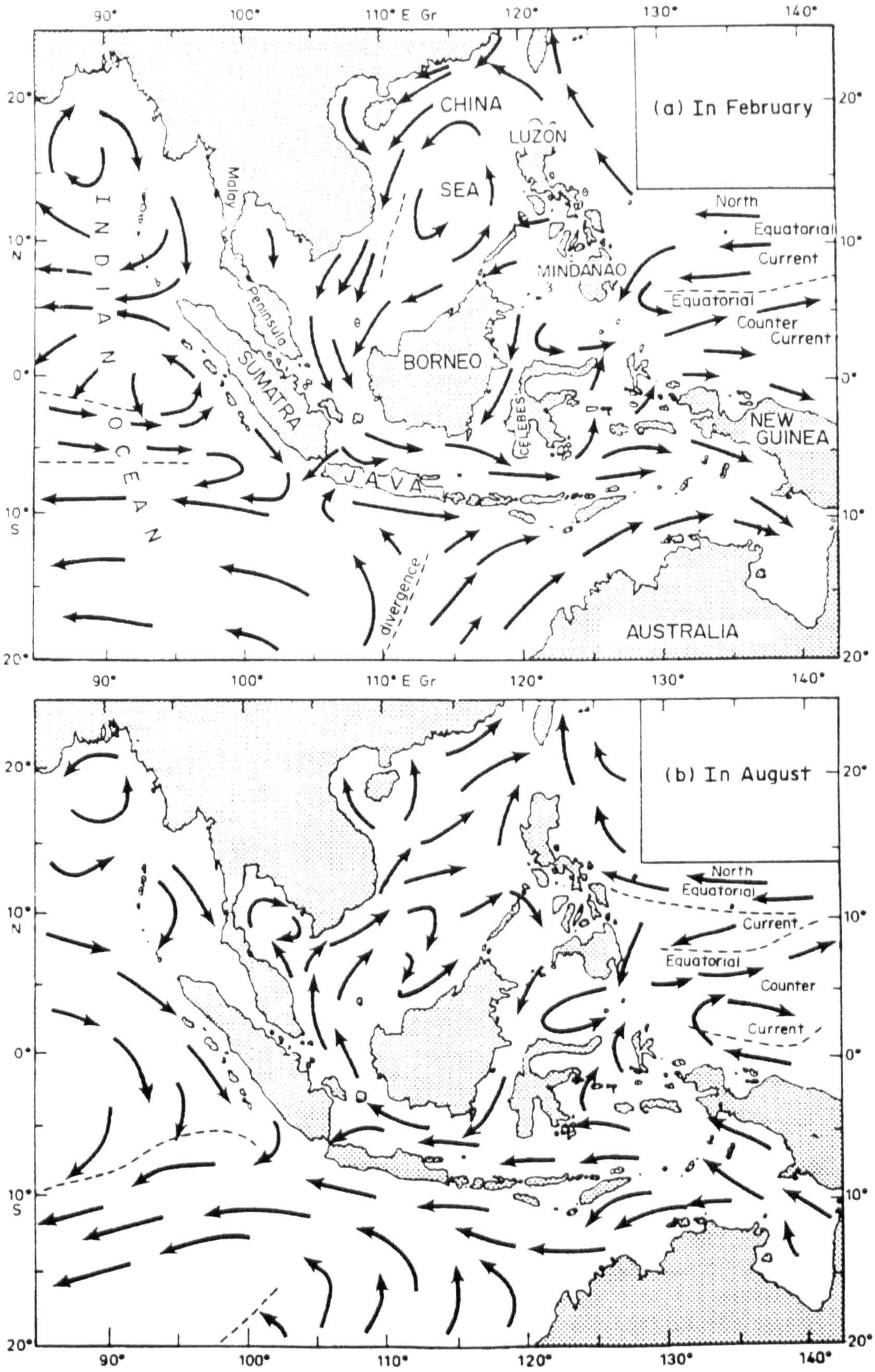

Figure 3.8. Outline of the circulation of the western Pacific, from Tschernia (1980).

Variable Sea Surface Topography

The random time-varying component of sea surface topography cannot be completely removed from the satellite altimeter data. The amount of sea height variability can be observed independently of geoid topography either at intersections (crossovers) of the satellite ground-tracks, or along repeating (collinear) tracks (Douglas *et al.*, 1987). High sea surface variability (10 - 40 cm RMS) is observed for some small high-energetic western boundary systems such as the Gulf Stream, Kuroshio, Agulhas and Brazil-Falkland systems and the Antarctic-circumpolar system. The sea surface has a 20 cm RMS variability in SE Pacific, and a 55 cm RMS variability in the vicinity of Drake's Passage between South America and Antarctica in the Southern Ocean (Marsh *et al.*, 1992). Results obtained by Douglas *et al.* (1983) from the repeated Geos-3 profiles show peaks of variability created by the Loop Current in the Gulf of Mexico and by the Gulf Stream east of Cape Hatteras. Medium sea surface variability (5 - 10 cm RMS) is found in the slower, larger systems such as the equatorial currents in the Pacific and Atlantic (Chao *et al.*, 1993), and in the tropical Pacific. Low variability (3 - 5 cm RMS) is found in the larger eastern ocean basins at mid-latitude (Oskam, 1990). Near the Equator, where currents are very small, sea surface variability is of the order of 3 - 6 cm. Figure 3.9 shows a map of sea surface variability observed for ERS-1 cycles 6 to 18.

Sea level energetics at wavelengths longer than the mesoscale are no less important. The El Niño Southern Oscillation (ENSO), one of the most dramatic air-sea interaction phenomena, is a ready example. During an El Niño there is a collapse of the trade winds which results in sea level changes of several decimetres over vast regions of the equatorial Pacific. In recent years, these sea level changes have been well documented in the western Pacific using tidal gauge data. This network has provided clear evidence of the very large scales of sea level response during an El Niño, particularly the pronounced 1982-83 event when 40 cm monthly mean anomalies were observed. In contrast, the El Niño signal is poorly observed in the eastern half of the Pacific where few islands (and tidal gauges) are found (Douglas *et al.*, 1987).

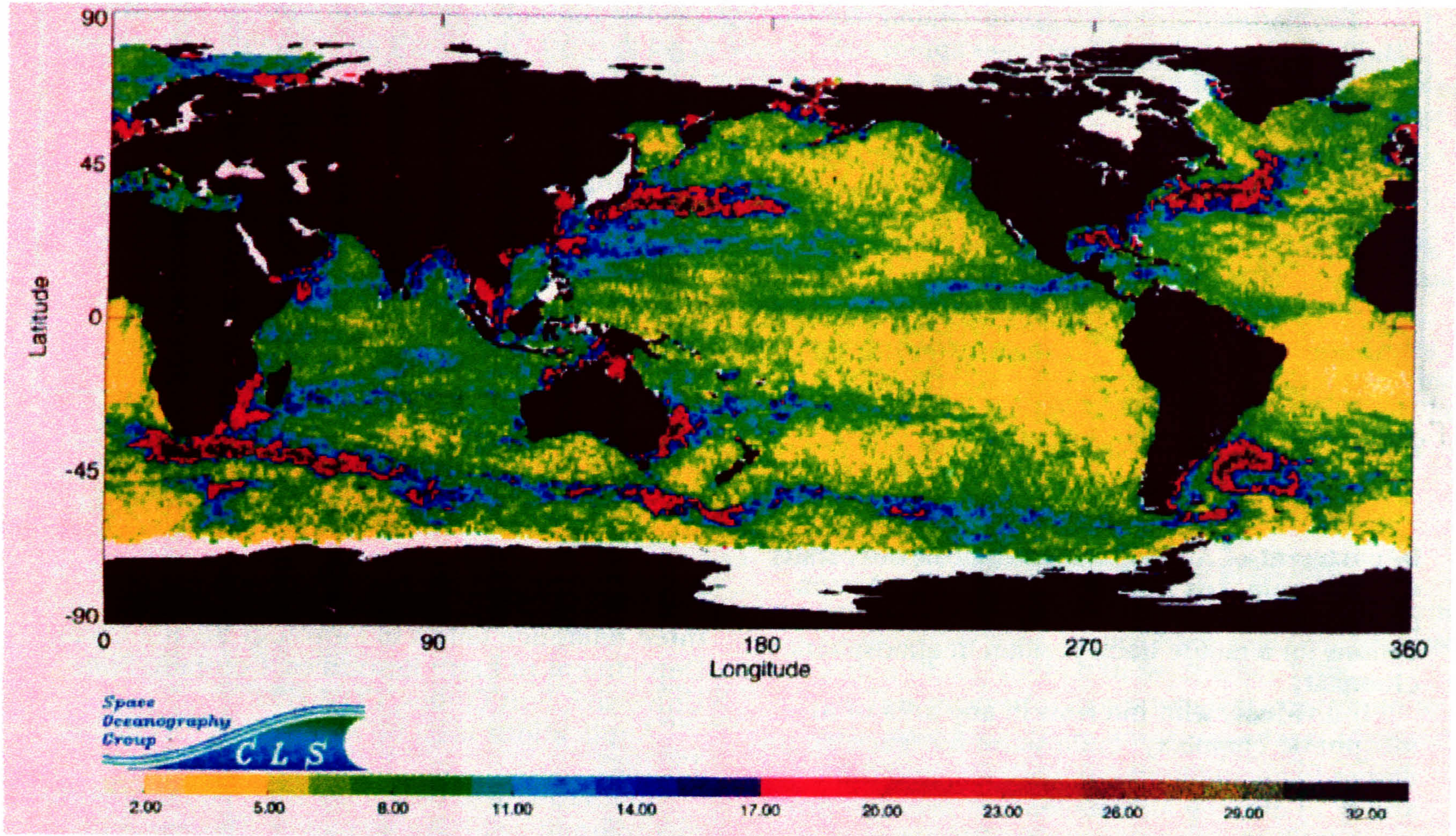

Figure 3.9. RMS of sea level variability in cm for ERS-1 cycles 6 to 18 after correction with Topex/Poseidon data. The RMS is 4-5 cm in low-eddy energy areas, ~ 10 cm in the South China Sea and ~ 20 cm in the Gulf of Thailand. Poor quality original. From LeTraon *et al.* (1995).

A component of the variable sea surface topography may be caused by sea surface temperature variations because sea water density, the physical characteristic which rules the ocean structure, is a function of temperature, salinity, and pressure. In polar and equatorial regions, seasonal temperature variations are of the order of 2 °C. These temperature variations attenuate rapidly with depth, and are not detectable below a maximum of 200 - 300 m. In the open sea, diurnal variations are very small - at the most of the order of 0.3 - 0.5 °C. They are stronger in shallow, sheltered coastal areas, where they reach 2 - 3 °C. They do not penetrate more than 10 or 20 m below the surface in temperate or tropical regions. In contrast, the seasonal variations of surface salinity are generally weak, not exceeding 0.5 ‰ (Tschernia, 1980). It is not possible to quantify the significance of sea surface temperature variations on sea surface variability. However, it seems likely that this would be more significant in shallow sheltered coastal waters which experience a large diurnal temperature variation.

3.3.3.5 Near-Shore Errors

Altimetry errors increase close to land, islands and ice. When the altimeter footprint intersects land or ice a rapid change in elevation occurs which is unrelated to the geoid. According to Sandwell (1992), this elevation change is typically of the order of 4 m and occurs over a distance of a few Geosat footprints (~10 km), corresponding to a 'very large' slope error of 400 μrad. These contaminated data points may be removed with a very precise land-sea mask. In practice however, only data points that actually lie over large land masses are removed. Smith *et al.* (1995) similarly observed that satellite data within 20 km of the coast are 'not reliable', owing to gaps in the data as the satellite tracks leave the land and to tidal effects in the shallower water. The presence of islands or land interrupting a sequence of measurements may also cause problems as the ocean tide models may be inaccurate with different errors on each side of the land (Knudsen, 1991).

3.3.3.6 Typical Satellite Altimeter Error Budget

Sandwell (1992) analysed the errors for Geosat Geodetic Mission data, and the error budget of this analysis is shown in Table 3.2. One microradian (μrad) of sea surface slope corresponds to 0.98 mGal of along-track gravity disturbance. By far the most significant error arises when the altimeter footprint crosses land or ice. Other significant errors are caused by the dynamic sea surface topography, water vapour in rain and clouds, and altimeter noise.

Table 3.2. Errors in Sea Surface Slope for Geosat Geodetic Mission Data, modified from Sandwell (1992) and Stewart (1984).

Error Source	*Height (m)*	*Length Scale (km)*	*Slope (μrad)*
Land, Ice	< 4.0	10	< 400
Dynamic Topography	1.0	> 100	< 10
Water Vapour	< 0.3	50	< 6
Altimeter Noise	0.05	> 10	< 5
Wet Troposphere	< 0.1	> 100	< 1.0
E/M Bias	0.1	> 200	< 0.5
Height Acceleration	< 0.02	> 70	< 0.5
Orbit	3.0	10000	0.30
Ocean Tide	0.10	> 1000	< 0.10
Ionosphere	0.10	> 1000	< 0.10
Geoid	0.85	10000	0.085

3.3.4 The Satellite Altimeters

The requirements for NASA's satellite altimetry program were formulated at the 1969 Williamstown Conference on Solid Earth and Ocean Physics (Kuala *et al.*, 1970). Since this conference, satellite altimeters have flown on Skylab (McGoogan *et al.*, 1974), Geos-3 (Stanley, 1979), Seasat (Tapley & Born, 1980), Geosat (Mitchell & Hallock, 1984; Douglas & Cheney, 1990), Topex/Poseidon (Fu *et al.*, 1994) and ERS-1 (Cheney & Lillibridge, 1992). Satellite altimeters launched after 1992 (e.g. ERS-2 in 1996) have not contributed data to this project and are not discussed further in this thesis.

In 1973, a radar altimeter made the first range measurement to the sea surface from space. Flown on board NASA's Skylab, the experiment demonstrated the feasibility of using satellite-borne radar altimetry for oceanography. With an instrument accuracy of 1 m and a radial orbit accuracy of tens of metres, the measurements were of little practical use. The launch three years later of Geos-3 brought routine altimetry one step closer, but with radial accuracies still measured in metres, the data were capable of resolving only the largest of features (Jolly, 1996).

Seasat collected 70 days of data over the 100-day period from 5 July to 10 October 1978. Whilst only 45 days represented independent ground tracks (Dixon & Parke, 1983), the altimeter achieved a fivefold improvement in height measurement over the altimeter aboard Geos-3 (Bernstein *et al.*, 1982).

The United States Navy launched Geosat on 12 March 1985 into an 800-km altitude, 108° inclination geodetic drifting orbit, in order to map the marine geoid with a resolution of a few kilometres. Designed for military objectives, this mission lasted 18 months. Geosat was then moved to a 17.0505-day repeat orbit to study the ocean circulation. The Exact Repeat Mission (ERM) ground-tracks followed the ground-tracks previously covered by Seasat to within 1 km (Shum *et al.*, 1990). The Geosat ERM became operational on 6 November 1986 (McConathy & Kilgus, 1987), and collected global altimeter data for more than 3 years until the tape recording mechanism failed on 5 January 1990. After mid 1988, the orbits for Geosat began to deteriorate

steadily because of sparser tracking and excessive drag caused by increased solar activity, and the data quality decreased accordingly (Fu & Cheney, 1995). Data from the Geosat Geodetic Mission remained classified until June 22, 1995, except for data south of 30°S which were released earlier. The total Geosat error budget is approximately 15 cm (Fu & Cheney, 1995).

The remote-sensing ERS-1 satellite was launched in July 1991 by the European Space Agency to study the Earth's environment, and was initially placed on 3-day and 35-day repeat orbits. In early April 1994 the satellite was moved to a 168-day repeat orbit to realise a global mapping between 82°N and 82°S of the mean sea surface with its onboard altimeter to a resolution everywhere of better than 8 km.

The joint U.S./France Topex/Poseidon altimeter satellite was launched in August 1992 to study the ocean circulation and its variability (Fu *et al.*, 1994). Its inclination is 66° and its altitude is 1330 km. The satellite ground-tracks repeat every 9.916 days. The Topex/Poseidon orbit is very accurately determined, the RMS accuracy being currently of the order of 2 - 3 cm radially (Nouel *et al.*, 1994; Tapley *et al.*, 1994). Hence these data are more accurate than the data from the previous satellite missions (Arabelos & Tziavos, 1996).

The precision of the satellite altimeter data depend on the satellite, the year of processing, and the gravity field model used for the reduction of the orbit error. As the gravity field has become better resolved in time, so these errors have been reduced. Thus the current generation of satellites (Topex/Poseidon and ERS-1) produce generally more precise sea surface height measurements than the older generation of satellites, although re-evaluation of old satellite data using improved orbit calculations has, for example, improved the precision of Seasat altimetry to 3 - 5 cm (Marsh *et al.*, 1992). A precision of 10 - 20 mm can be achieved with stacked data from the Topex/Poseidon and ERS-1 satellites (Sandwell & Smith, 1997). Over a distance of 4 km (i.e. 1/4 wavelength) this corresponds to a sea surface slope error of 4 - 8 μrad and a gravity error of about 6 mGal.

The resolutions of the altimeter missions have also improved in time. Altimeter resolution is limited by the sea state, atmospheric effects, and the noise level in the return signal which require that the signal be edited and smoothed before processing. This smoothing is probably the primary limitation on the along-track resolution of the satellite data (Small & Sandwell, 1992). The along-track resolution of the different satellite missions may be determined from coherency analysis of repeated measurements, and is defined at 50% coherence (Yale *et al.*, 1995), as shown in Figure 3.10. Across-track, the resolution depends on the satellite orbit and the latitude. To recover all the wavelengths down to 15 km requires a very dense coverage, which is only achieved with a non-repeat orbit such as that of the Geosat Geodetic Mission (Blanc *et al.*, 1991).

The properties of the different satellite missions are summarised in Table 3.3.

Table 3.3. Comparative resolution and accuracy of satellite altimeter data. Modified from Long & Spurling (1993) and Yale *et al.* (1995).

Satellite	Precision (1 μrad ≈ 1 mGal)	Along-Track Resolution	Cross-Track Resolution*	Date
Geos-3	30 μrad	75 km	20-400 km	1975
Seasat	10 μrad	50 km	80-120 km	1978
Geosat GM	6 μrad	24 km	10 km	1985
Geosat ERM	<1 μrad	20 km	160 km	1987
ERS-1 (35-day repeat)	<1 μrad	30 km	80 km	1991
ERS-1 (168-day repeat)	6 μrad	30 km	16 km	1994
Topex/Poseidon	<1 μrad	22 km	314 km	1992

*Cross-track resolution is twice the track spacing at the Equator

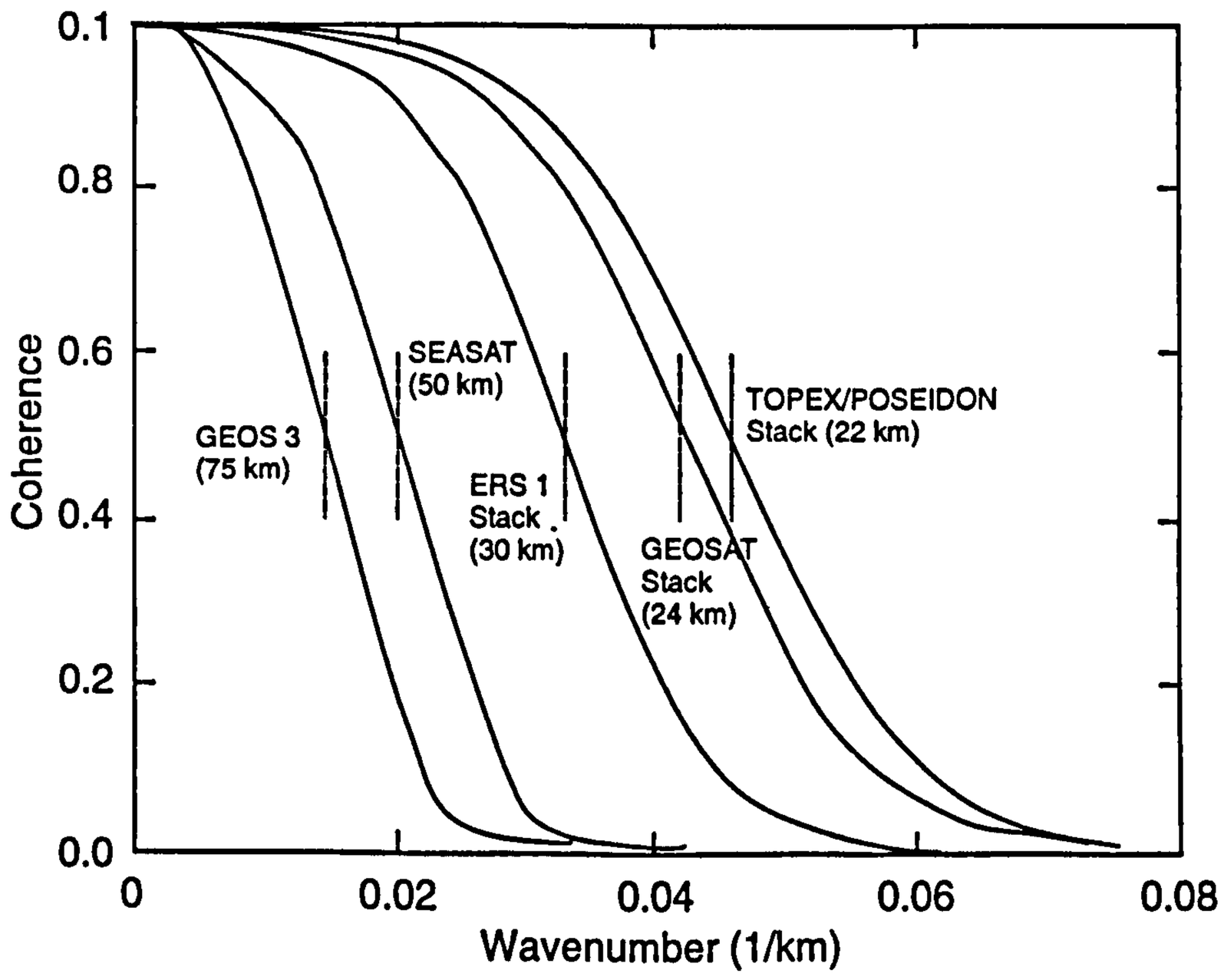

Figure 3.10. Comparison of coherences for single profiles of Geos-3 and Seasat, along with stacked ERS-1, Geosat and Topex/Poseidon profiles. From Yale *et al.* (1995).

3.4 Merging Satellite and Ship Gravity Data

3.4.1 Introduction

This section contains the abridged findings of background work undertaken during the first six months of this study. At this time it was desirable to merge the available ship and satellite gravity data because this merger would significantly increase the resolution of the regional gravity field. The declassification of the Geosat GM data on June 22, 1995, and the public release of WGI7.2 later that year increased the resolution of the Southeast Asian gravity field to such a level that further work on this topic was unwarranted. The merger of ship and satellite data is now only beneficial in smaller-scale studies.

3.4.2 Available Methods

The combination of satellite and ship gravity data for mapping purposes is a complex problem, owing to the different frequency contents and accuracies of the two data sets, and often also due to the random distribution of the data points. Three techniques are commonly used to merge satellite and ship gravity data, namely, the least squares collocation method (used by Ohio State University, Oxford University, and the University of Copenhagen); the fast Fourier transform technique (used by the University of Edinburgh and the University of Texas); and the 'cut-and-paste' technique (used by AMAROK A.S., GETECH and LCT Inc.).

3.4.2.1 Least Squares Collocation

Least squares collocation (LSC) is a technique for combining observational data of different types for an optimal determination of the Earth's figure and gravitational field. LSC has been widely used to derive free-air gravity anomaly values from the combination of satellite data of different vintages and different observational accuracies (e.g. Marsh *et al.*, 1988; Lerch, 1991; Knudsen, 1991; Sneeuw, 1994) and from the

combination of satellite and ship gravity data (e.g. Tscherning *et al.*, 1990; Strange, 1991; Xu, 1992; Hwang *et al.*, 1994; Arabelos & Tziavos, 1996). A modification of the LSC method allows for the inclusion of bathymetric data to boost the high frequency content of the derived gravity anomaly field (Rapp & Bašic, 1992). LSC is also used to derive geoidal models (e.g. Rapp & Pavlis, 1990; Lerch *et al.*, 1993; Rapp & Wang, 1994). In other fields of research LSC is called objective analysis, the inverse method and optimal interpolation (Imawaki *et al.*, 1992).

LSC works best when the data which are to be merged do not have a long-wavelength trend and when the expected values of both the observations and the predictions are equal to zero (Moritz, 1978; Moritz, 1980*b*; Tscherning, 1986; Herzfeld, 1992). Thus the standard LSC method is the remove/restore procedure. In this method, the Earth's gravity field is considered to be a linear combination of two components - a long wavelength component, called N_{GM} (modelled by potential coefficient models such as OSU91 (Rapp *et al.*, 1991) or GEM-T1 (Marsh *et al.*, 1988)), and a short wavelength component, y, which is predicted by the LSC process. N refers to the geoid height.

i.e. $$N = N_{GM} + y \tag{3.8}$$

$$y = C_{yx}(C_{xx} + C_{nn})^{-1}x \tag{3.9}$$

where C_{xx} and C_{yx} are the auto- and cross-covariance matrices between the observations x and predictions y according to some selected analytic model approximating the empirical covariance function. The x is here a vector of reduced anomalies (Δg - Δg_{GM}) and y represents the reduced undulations (N - N_{GM}). C_{nn} is the error covariance matrix of the gravity anomalies (Mainville *et al.*, 1992).

Values predicted by LSC are linear combinations of the samples in the vicinity of the prediction point, with weighting coefficients calculated from the correlation between the prediction and sampling places. This correlation is determined through the covariance function. The weighting coefficients are determined so that the differences between the observations and predictions are minimised in a least squares sense. Covariance

functions may be derived empirically, from the data, or through models. Models are usually developed from an *a priori* knowledge of the data types involved or from their mathematical relationships (Strange, 1991).

3.4.2.2 Fast Fourier Transform

The fast Fourier transform (FFT) method provides a relatively simple method for deriving gravity anomalies from the geoid and vice versa (McAdoo & Marks, 1992*a*; Kirby & Hipkin, 1994). Fast Fourier transforms can process very large data sets quickly, but generally require the data to be available on a complete and regular grid. Multiple data sets are combined into one output for a specified area by Fourier transforming the input data sets, multiplying each by its appropriate filter and combining the results in the frequency domain. An inverse transformation then produces the output field (Schwarz *et al.*, 1990). The flat Earth assumption that each block of data has a regular size when the discrete Fourier transform is taken is not strictly true, and has the effect of reducing the accuracy of medium to long wavelength features. This problem is ameliorated when the long wavelength part of the gravity field is independently dealt with using a geopotential model (Rummel & Haagmans, 1991). Sandwell (1992) used a 'Projection onto Convex Sets' method which is similar to the FFT method, although not as straightforward (McAdoo & Marks, 1992*a*).

3.4.2.3 'Cut-and-Paste'

Variations on the 'cut-and-paste' technique to merge satellite and ship gravity data are commonly used by gravity contractors to the oil industry. This technique is not well documented. The basis of the technique is to use ship gravity in preference to satellite gravity when the ship survey line spacing is closer than the satellite track spacing (R. Stanley, LCT Inc., 1995, *pers. comm.*). It is often necessary to correct the ship data for datum and long wavelength errors, which GETECH does by 'draping the ship gravity data over the satellite gravity data' (C. Green, GETECH, 1995, *pers. comm.*).

3.4.2.4 Other Merger Techniques

According to Tscherning (1986), other suitable methods for gravity field approximation include series expansion in orthogonal functions; linear combinations of potentials of point masses, multipoles or mass lines; linear combinations of harmonic splines, kernel functions or finite elements; and minimum norm collocation. In these methods, the gravity potential is approximated by a linear combination of a number of base functions. Their differences lie in the choice of base functions and in the methods used to determine the coefficients of the linear combination. However, when these methods are compared in terms of the mean square differences between the observed and computed quantities, it is concluded that none are as good as LSC, because LSC minimizes exactly this difference.

3.4.3 Comparison of the Merger Techniques

It is concluded that the LSC method is the best method for combining different gravity data, since the accuracy of the input data (which may be randomly spaced) may be used as weights in the prediction of the gravity anomaly field. Thus the output is biased towards input values with high accuracies. It is possible to assess the error of each predicted gravity anomaly. Bathymetric information may be used to increase the resolution of the satellite gravity field. The main disadvantage with LSC is that it is computationally intensive (Strange, 1991) which has historically prevented the use of all of the available data, and led to a loss of resolution in the final solution (Belikov & Groten, 1993).

The FFT method is computationally more efficient than LSC. The technique requires gridded data sets and gives excellent results when these are available. However the resolution and covariance of the gravity field are decreased as a result of the gridding process (Knudsen, 1987). Discontinuities will arise at the edges of the merger area, although these can be reduced by applying a tapering filter. Finally, it is not possible to directly evaluate the errors of the gravity anomaly field obtained using the FFT method.

The 'cut-and-paste' method is mainly used by gravity contractors as it is easy and quick to implement, gives fast results, and does not require much software development. The results are however less accurate than those obtained using both the LSC and FFT methods because not all of the available data are used. A quantitative assessment of the accuracy of the final map is often not given.

3.5 Conclusions

This review has shown that individual satellite gravity measurements are prone to significant oceanographic noise which increases close to land or strong currents. This noise is reduced by stacking. If only a few satellite measurements are available in a particular area, it is unlikely that the gravity field will be well resolved. This conclusion is confirmed by the study of Wright (1997) who significantly improved the resolution of the marine gravity field in eastern Indonesia by reducing the number of satellite gravity measurements rejected during the processing sequence. Data acquired in areas where the global tidal model is poorly constrained are also likely to be inaccurate.

Modern ship gravity data collected with GPS or DGPS navigation are likely to be more accurate than satellite gravity data and have a significantly better along-track resolution. The optimum method for combining ship and satellite gravity data is the least squares collocation method. However the resolution of the regional satellite derived gravity field is now at such a level that the merger of ship and satellite data is only likely to be useful for basin or sub-basin scale studies.

It is clear that the accuracy of marine gravity data and maps will vary with both the vintage of the data and the processing sequence that has been followed, and that the maps will not be of uniform accuracy. The accuracy of a new satellite gravity data set should be evaluated before quantitative interpretation is carried out. Satellite gravity maps can be easily assessed by comparison with ground-truth data - which in practice means with ship gravity data. In Chapter 4, the WGI7.2 satellite gravity data set is compared with a high quality ship gravity survey in Southeast Asia.

CHAPTER 4

Assessment of the WGI7.2 Marine Gravity Field

CHAPTER 4. ASSESSMENT OF THE WGI7.2 MARINE GRAVITY FIELD.

4.1 Introduction

WGI7.2 is the highest resolution global grid of marine gravity data available in the public domain. Compiled from Geosat and ERS-1 satellite data, WGI7.2 resolves clearly many of the significant features in the offshore gravity field. Although this data set was released towards the end of 1995 (Smith & Sandwell, 1995), little information has since been published regarding either the accuracy or the spatial resolution of the data set. This information is necessary for both the qualitative and quantitative interpretation of maps extracted from this data set.

An example highlighting the need for a quantitative evaluation of the accuracy of the satellite gravity data set follows. Within the Gulf of Thailand, the satellite gravity field is generally found to be poorly resolved (J. Milsom, *pers. comm.*). Close examination of the gravity field in this region reveals a subtle line of anomalous gravity highs that runs NNW-SSE for a distance of approximately 900 km, as illustrated in Figure 4.1. Because all satellite ground-tracks run NNW-SSE (and NNE-SSW) near the Equator, it is judged more likely that this feature has arisen from contamination of the data set by a poor quality (noisy) satellite track than from a geological lineament. A qualitative assessment of the WGI7.2 satellite gravity grid is therefore required to determine the level of tolerance that should be attached to data extracted from this data set.

In this chapter, the accuracy and resolution of WGI7.2 are evaluated by comparison with a 'ground truth' high resolution ship gravity survey. This comparison is confined to an area north of Sabah, Malaysia, between 5°N and 9°N, 113°E and 120°E, shown in Figure 4.2. Since the satellite gravity grid is most poorly resolved near the Equator, this study evaluates the satellite gravity resolution under the least favourable conditions. Preliminary results of this work were presented by Holt (1997).

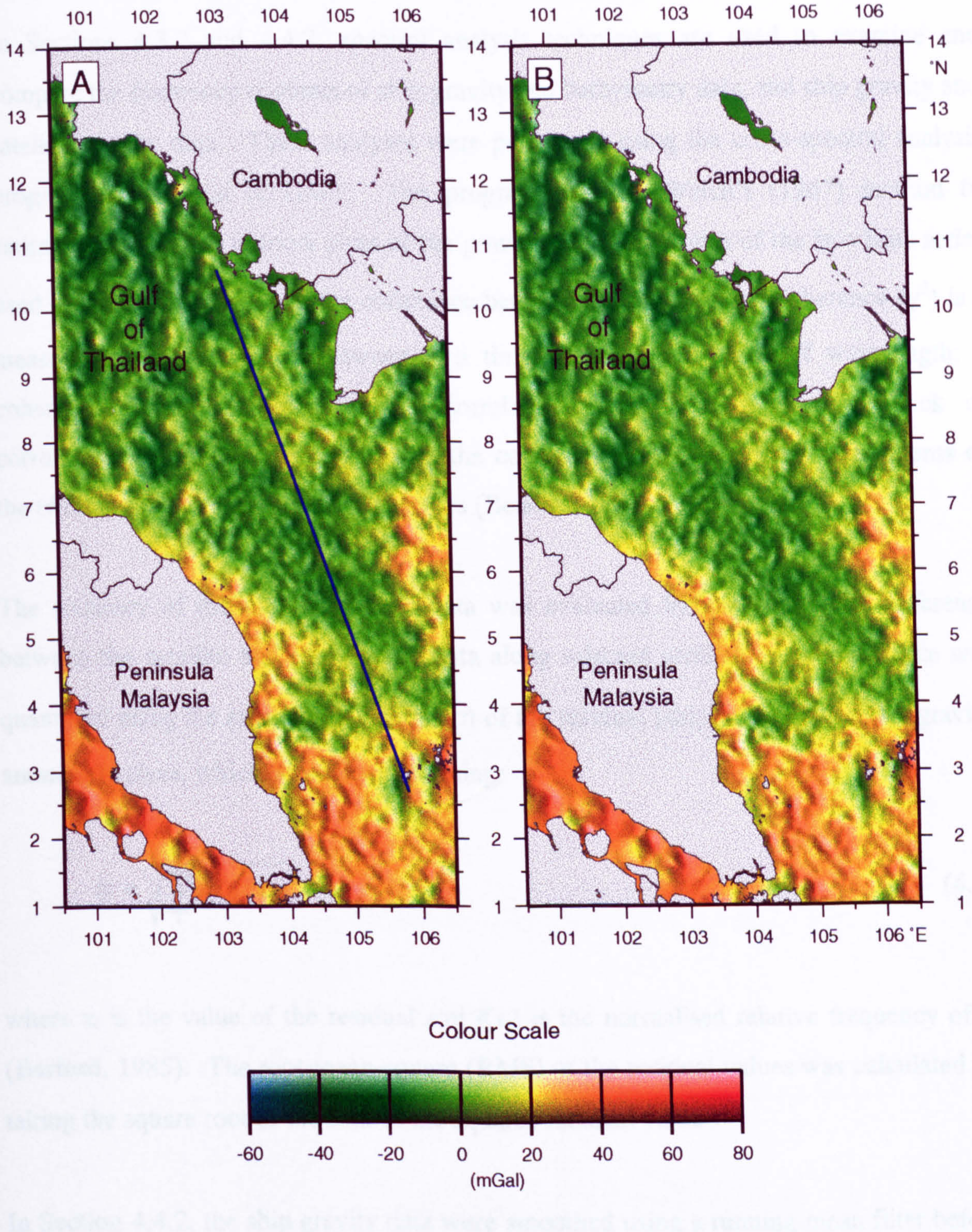

Figure 4.1. Two identical satellite free-air gravity anomaly maps of the Gulf of Thailand, illuminated from N70°E. A subtle line of gravity anomaly highs runs from 103°E, 10.6°N to 105.7°E, 2.7°N as indicated by the blue line on map A. Land areas are shaded grey.

4.2 Analytical Techniques

In Sections 4.3.2 and 4.4.2, spectral analysis techniques are used to examine and compare the frequency contents of ship gravity and bathymetry data, and ship gravity and satellite gravity data. These analyses were performed using the cross-spectral analysis program *spectrum1d* of GMT. The program employs Welch's (1967) method to estimate spectra, and outputs plots of the power spectral densities of the two time series used in the study and also of the coherence between the time series. Coherence (γ^2) is a measure of the correlation between two time series as a function of wavelength; a coherency of one indicates perfect correlation, zero indicates complete lack of correlation, and one-half indicates that the correlated and uncorrelated components of the two time series have equal magnitudes (Bendat & Piersol, 1986).

The accuracy of the satellite gravity data was evaluated by analysis of the difference between the satellite and ship gravity data along selected profiles. This difference was quantified using the standard deviation (σ) of the residual (ship - satellite free-air gravity anomaly) values, which was calculated using:

$$\sigma = \sqrt{\sum_i x_i^2 f(x_i)} \qquad (4.1)$$

where x_i is the value of the residual and $f(x_i)$ is the normalised relative frequency of x_i (Barford, 1985). The root-mean-square (RMS) of the residual values was calculated by taking the square root of the ~~sum of the~~ average squared residual value.

In Section 4.4.2, the ship gravity data were smoothed using a running-mean filter before comparison with the satellite data in an attempt to separate the loss of accuracy of the satellite data caused by the smoothing of the gravity field from the noise content of the data. The running-mean filtering of the ship gravity, applied effectively along track, was performed at each data point by averaging all of the data points within a specified distance (half the filter length) of the data point, using the Excel computer spreadsheet.

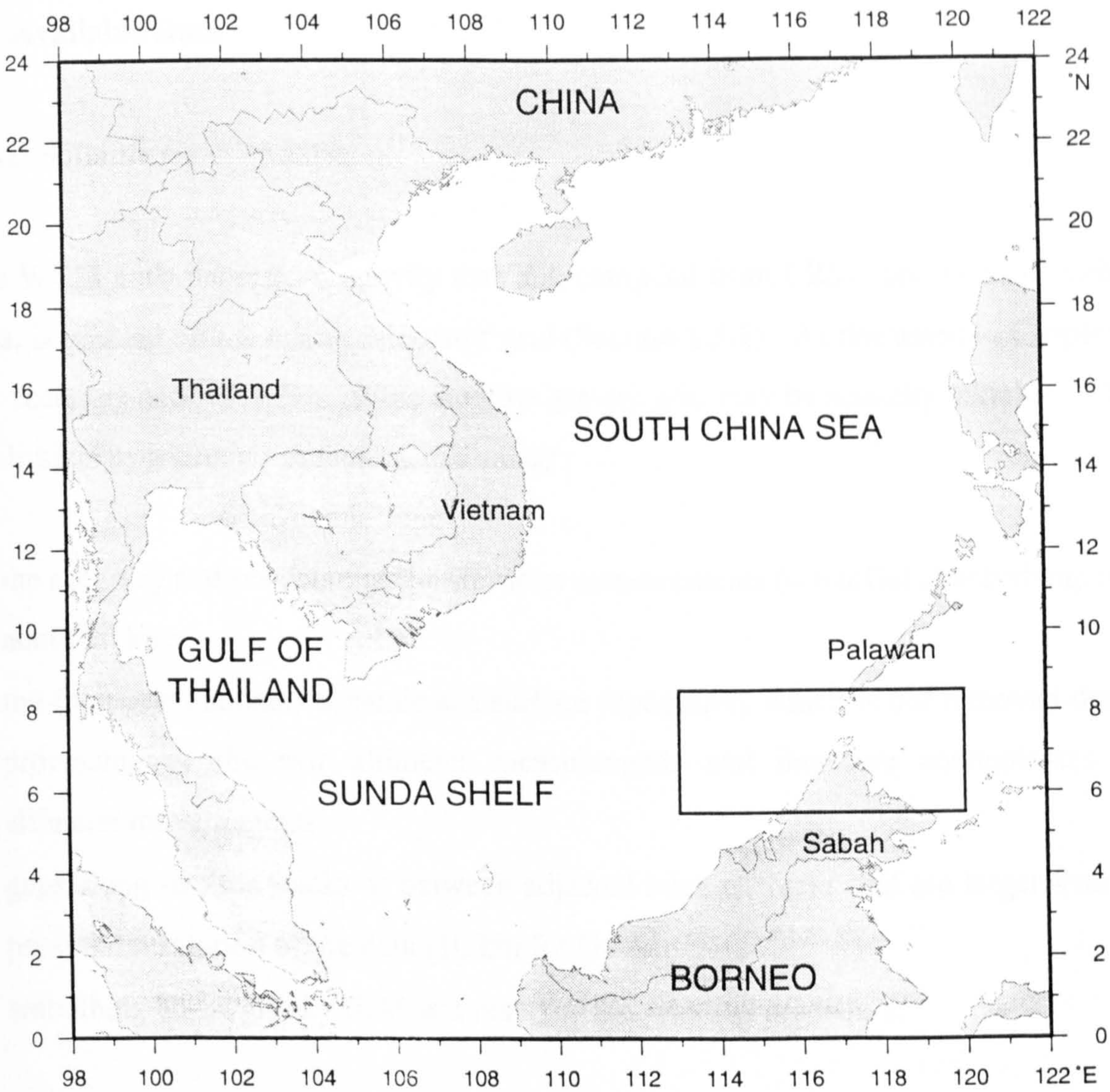

Figure 4.2. Location map for comparison of satellite and ship gravity anomalies. The black rectangle encloses the study area.

Figure 4.3. Ship track location map.

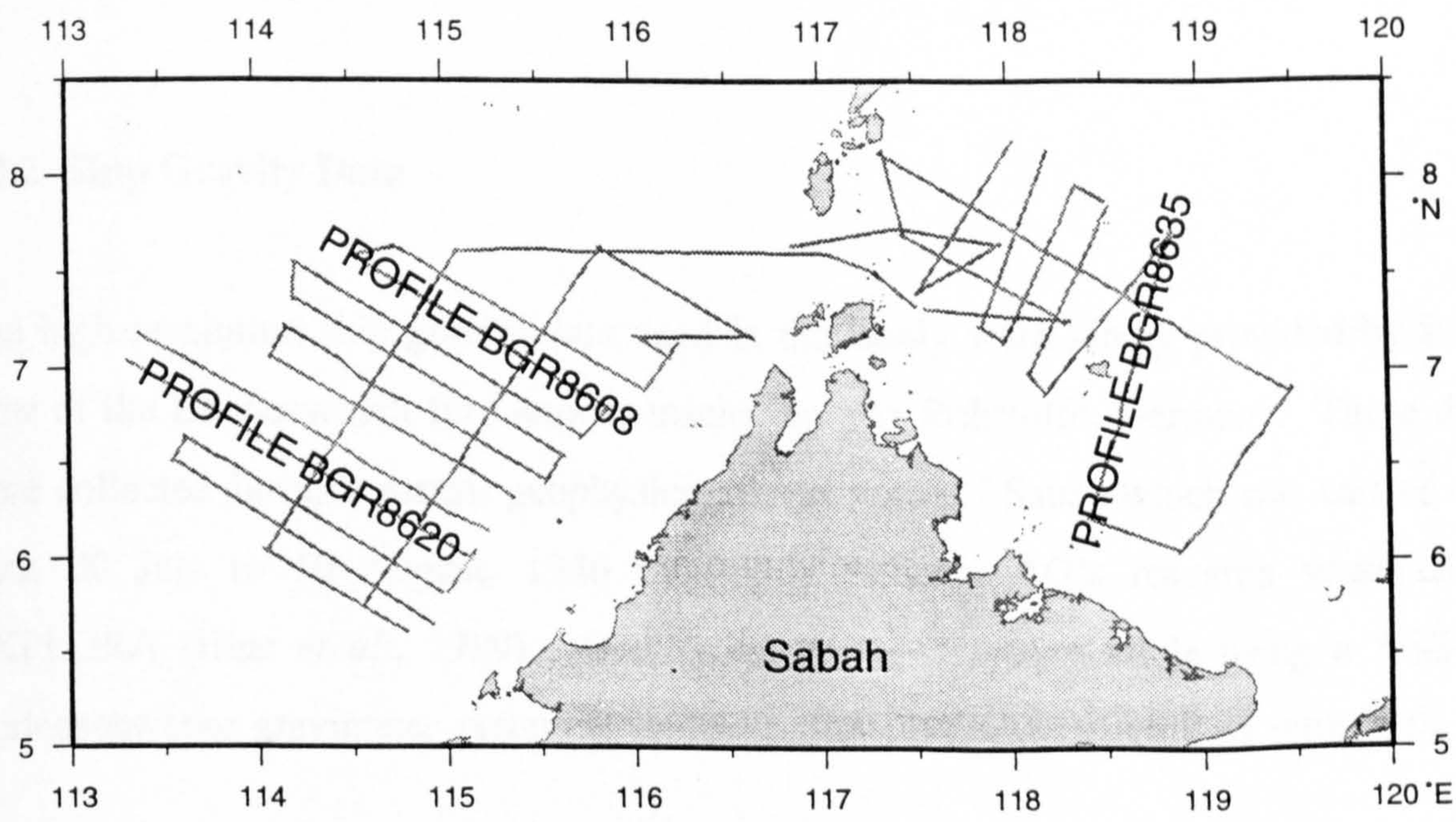

4.3 Available Data

4.3.1 Satellite Gravity Data

The WGI7.2 marine satellite gravity data set, compiled from ERS-1 and Geosat satellite data, is gridded on a 2 minute Mercator grid (Section 1.3.1). As discussed in Chapter 3, the accuracy and resolution of the satellite gravity grid may be spatially variable. They are limited by a number of factors, including:

- the accuracy and precision of the altimeter measurements (~ 6 mGal at wavelengths of about 20 km)
- the (non-gravitational) dynamic sea surface topography which is not removed during processing of the raw altimeter measurements and therefore contaminates the altimeter measurements
- gaps along satellite tracks or between adjacent satellite tracks that are larger than the potential resolution of the data (10 km for Geosat GM)
- smoothing of the gravity field as a result of the gridding procedure.

The shortest wavelength resolved in the satellite gravity field is fixed by the grid spacing of the data set. The grid spacing is greatest at the Equator (approximately 3.67 km) and decreases towards the poles. The minimum wavelength present in the gravity field at the Equator is therefore 7.3 km.

4.3.2 Ship Gravity Data

The high resolution ship gravity data used in this study were kindly provided by Prof. Hinz of the Bundesanstalt für Geowissenschaften und Rohstoffe, Germany. These data were collected during a marine geophysical survey north of Sabah which was carried out from 20 July to 10 August, 1986 by Prakla Seismos AG's research vessel S.V. EXPLORA (Hinz *et al.*, 1989). Gravity measurements were made using a KSS-30 Bodenseewerke gravimeter system. Station positioning was determined with both the

Global Positioning System (GPS) and the Transit Satellite System (NNS) using a Magnavox receiver MX 1107 GPS integrated with a Doppler Sonar (Alpha Logger of Krupp-Atlas). The coverage of the ship survey is shown in Figure 4.3.

The average value determined for the internal consistency at crossovers of the ship free-air gravity measurements is 1.1 mGal (0.7 mGal standard deviation). A plot of the ship free-air gravity and bathymetry data along ship track BGR8635 is shown in Figure 4.4A. The resolution of the bathymetry is limited by the spacing between measurements, which is ~ 50 m.

At short wavelengths (< 200 km), the free-air gravity anomaly field is dominated by the attraction of the rock/water interface, and therefore mimics the seafloor topography (Neuman *et al.*, 1993). The degree to which the free-air gravity and bathymetry match at short wavelengths may be quantified by analysis of the coherence between them. The coherence between the ship free-air gravity and the bathymetry data along ship track BGR8635 is plotted in Figure 4.5B. There is a high coherence (> 0.75) between the ship and bathymetry data for wavelengths in the range 5 - 50 km. The coherence falls below 0.5 at a wavelengths less than ~ 4 km, and is less than 0.1 for wavelengths under 2 km. This decrease in coherence is largely due to the high-cut noise filtering applied to the raw ship gravity, but also partly due to the 'filtering' effect caused by the (variable) separation of gravity meter from the source interface.

It is therefore concluded that these ship gravity data are accurate to ± 1 mGal, and have a minimum spatial resolution of 4 km ($\gamma^2 = 0.5$).

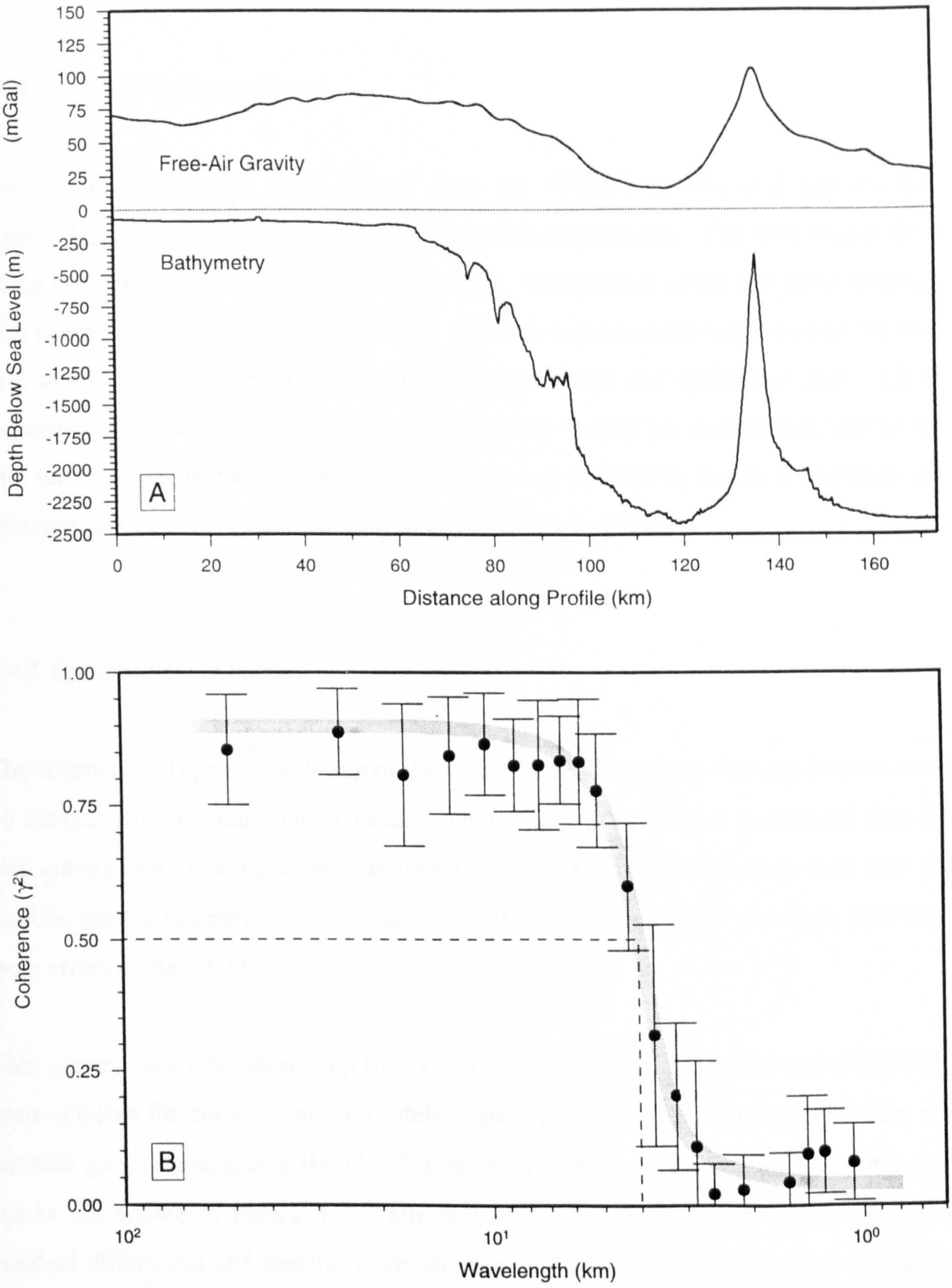

Figure 4.4. Comparison of ship free-air gravity and bathymetry measurements along Profile BGR8635. A: Ship free-air gravity exhibits high visual correlation with bathymetry. B: Spectral coherence of gravity and bathymetry measurements shows very high agreement ($\gamma^2 > 0.5$) for anomalies with wavelengths longer than ~ 4 km.

4.4 Comparison of Satellite and Ship Gravity Data North of Sabah

4.4.1 Qualitative Comparison

Free-air gravity anomaly maps derived from the WGI7.2 satellite grid and the ship gravity data are shown in Figures 4.5A and 4.5B respectively. The data points from which the maps were derived are shown in white. Comparison of the two maps reveals a high degree of visual correlation, and this indicates a good agreement between the two data sets in terms of dynamic range, wavelength content and spatial accuracy. Close inspection, however, shows that the regional gravity field is not as well resolved by the ship survey as it is by the satellite grid, especially east of 118.5°E, due to the variable and relatively large between-track spacing of the ship measurements.

4.4.2 Quantitative Analysis

The accuracy and spatial resolution of the WGI7.2 satellite gravity data are here assessed by comparison with ship gravity measurements. In this analysis, it is assumed that the ship gravity data are a more accurate representation of the gravity anomaly field than the satellite gravity anomaly field, and that the differences between the two data sets arise from errors in the satellite data.

Ship gravity data from three ship tracks (Profiles BGR8608, BGR8620 and BGR8635) were selected for comparison with satellite gravity measurements interpolated from the satellite gravity grid (using the GMT program *grdtrack*). The locations of these ship tracks are shown in Figure 4.3. The ship and satellite gravity measurements, their residual differences and spectral coherence are plotted for each of the three profiles in Figures 4.6 to 4.8.

Visual comparison of the satellite and ship gravity data along each profile reveals that whilst the satellite data accurately resolves the salient features seen in the ship data, the shorter wavelength, low amplitude features are not present in the satellite gravity data.

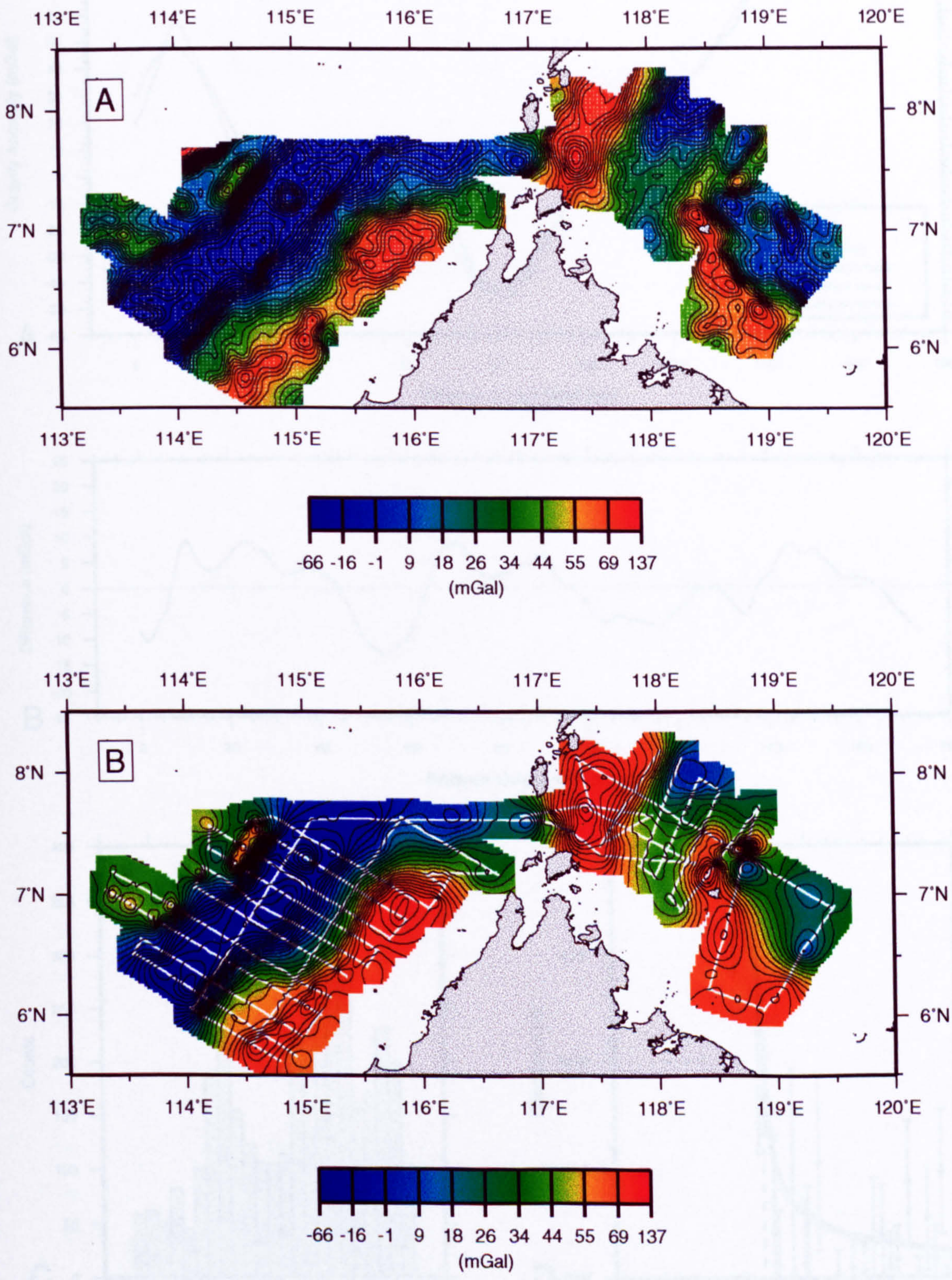

Figure 4.5. Maps of free-air gravity anomalies from WGI7.2 satellite data (A) and ship data (B) north of Sabah. Data points are overlain in white. 5 mGal contour intervals.

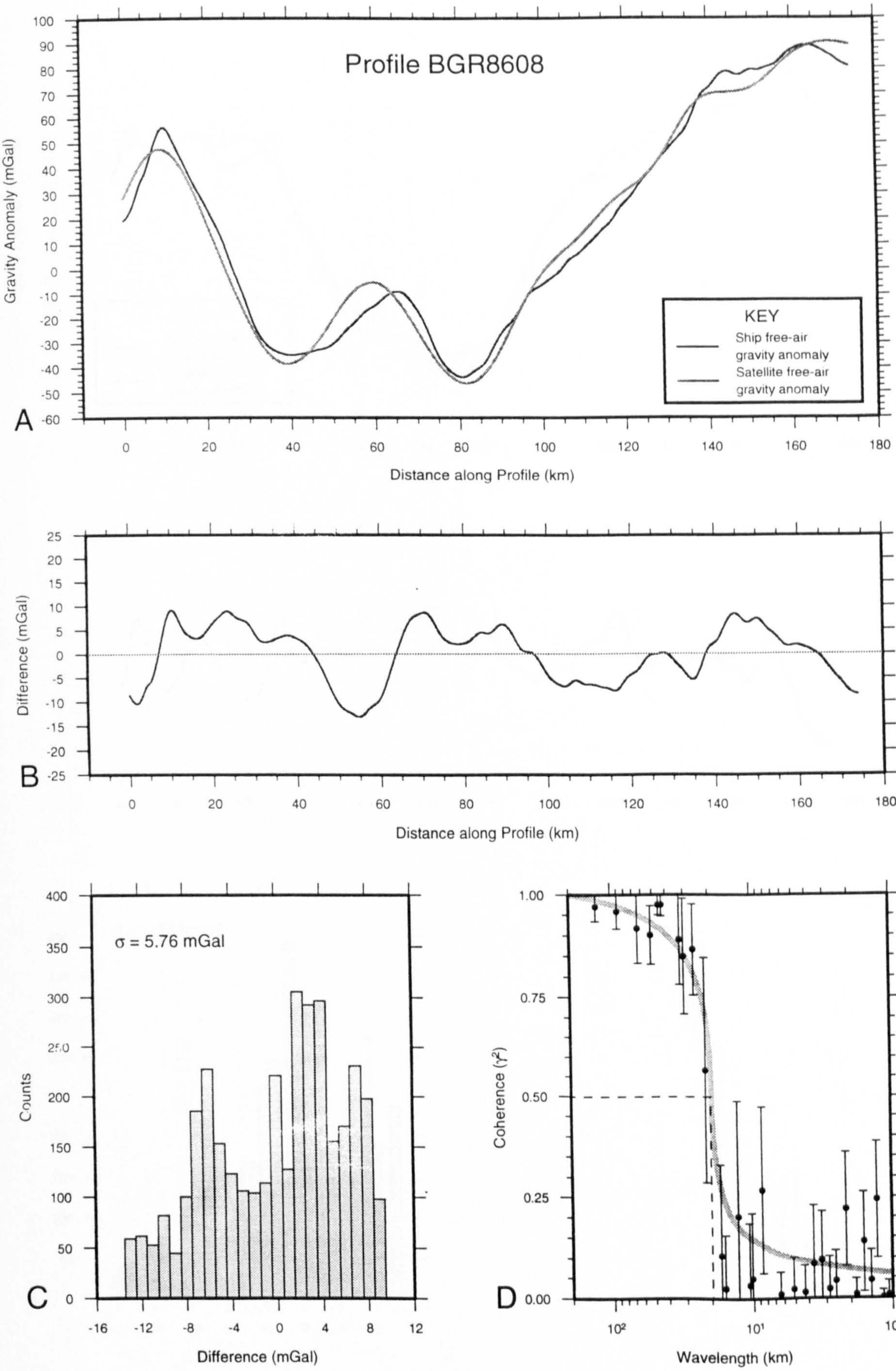

Figure 4.6. Comparison of ship and satellite free-air gravity anomalies along Profile BGR8608. A: Plot of ship and satellite gravity anomalies. B: Plot of difference between ship and satellite gravity anomalies. C: Histogram of the difference between ship and satellite gravity anomalies (bin width = 1 mGal). D: Spectral coherence between satellite and ship gravity anomalies.

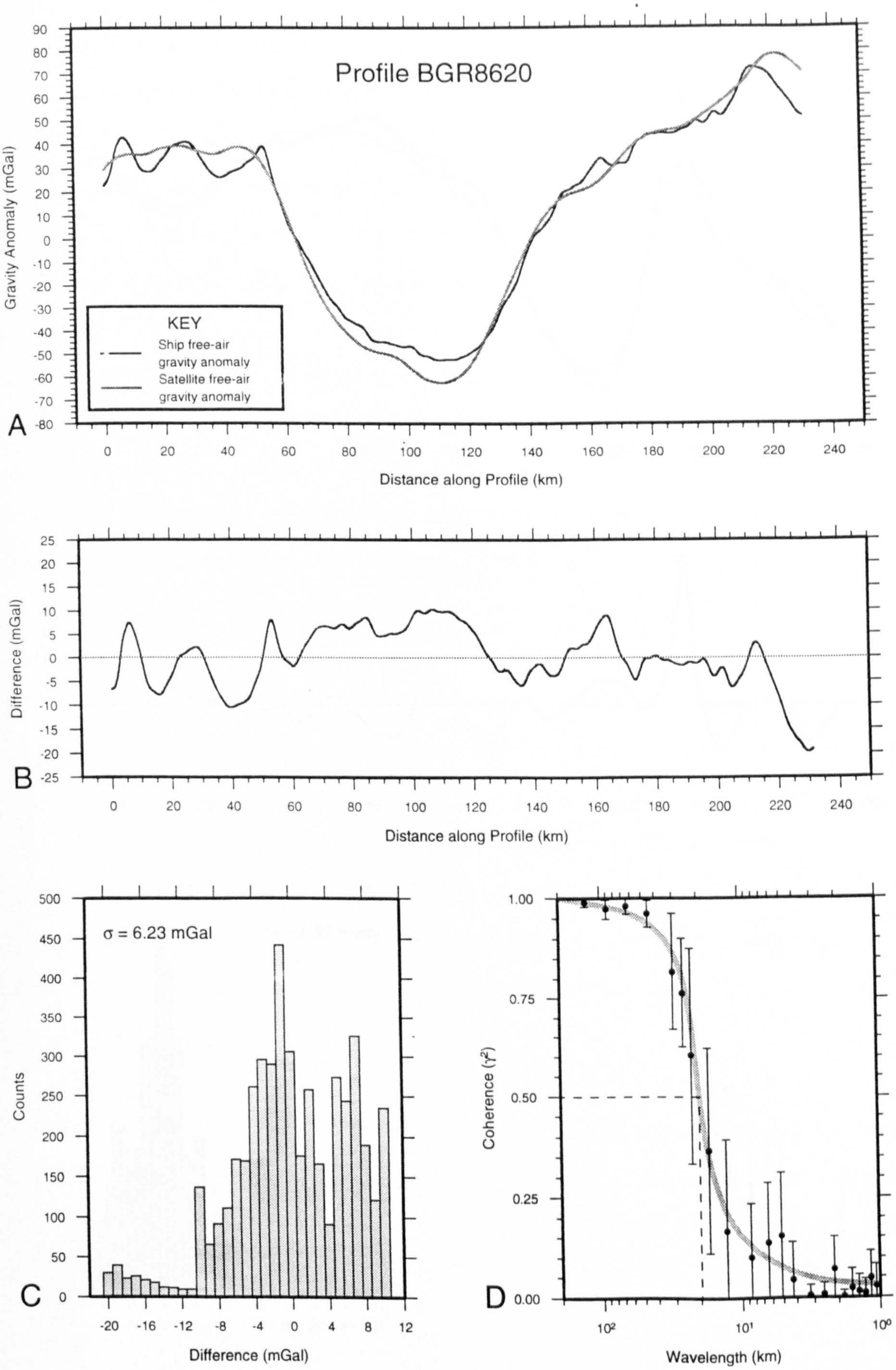

Figure 4.7. Comparison of ship and satellite free-air gravity anomalies along Profile BGR8620. A: Plot of ship and satellite gravity anomalies. B: Plot of difference between ship and satellite gravity anomalies. C: Histogram of the difference between ship and satellite gravity anomalies (bin width = 1 mGal). D: Spectral coherence between satellite and ship gravity anomalies.

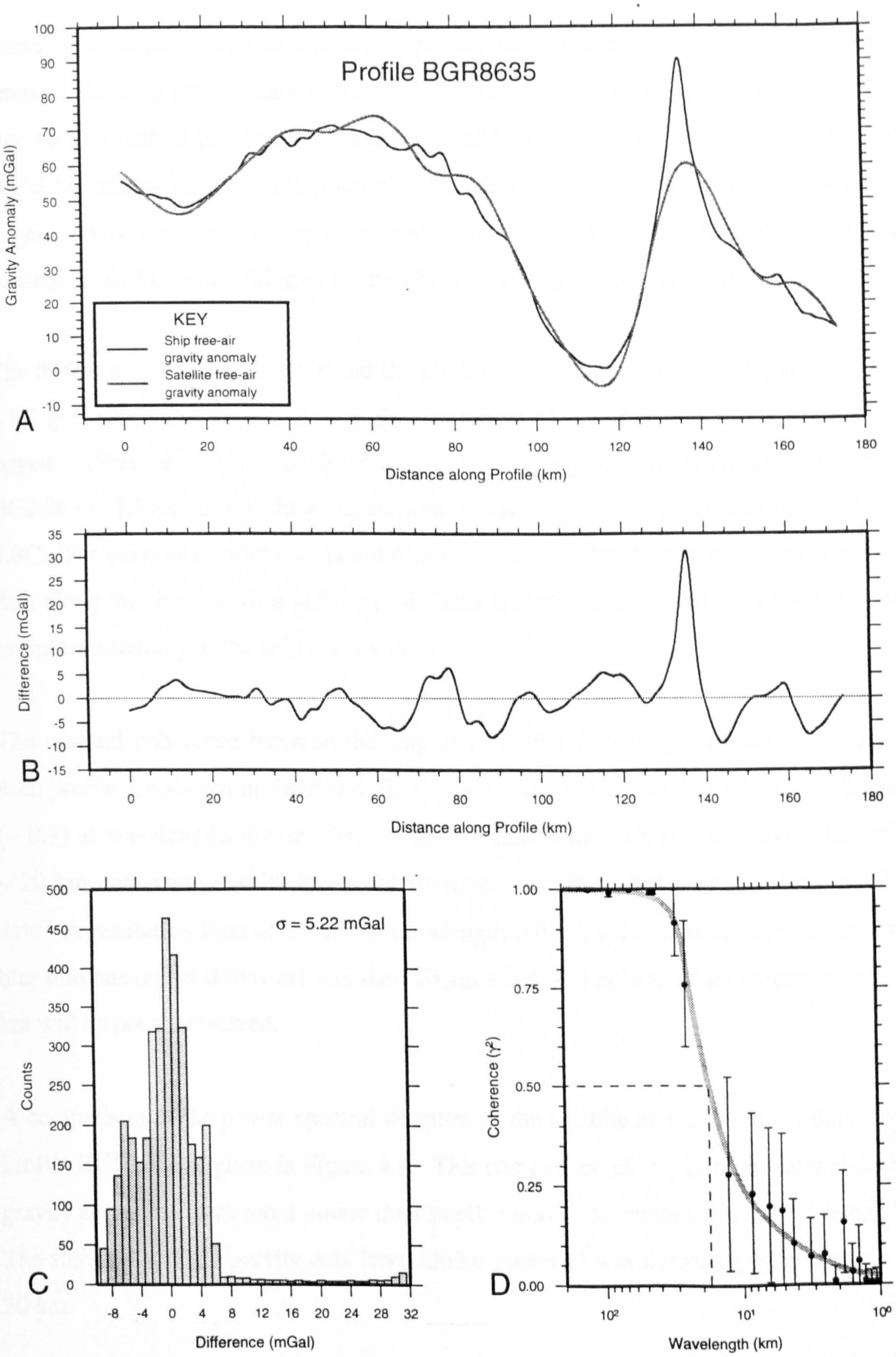

Figure 4.8. Comparison of ship and satellite free-air gravity anomalies along Profile BGR8635. A: Plot of ship and satellite gravity anomalies. B: Plot of difference between ship and satellite gravity anomalies. C: Histogram of the difference between ship and satellite gravity anomalies (bin width = 1 mGal). D: Spectral coherence between satellite and ship gravity anomalies.

These short wavelength, low amplitude features fall within the accuracy and resolution limits of the ship gravity data (Section 4.3.2) and are consequently judged to be real. One notable feature poorly resolved in the satellite gravity data is the seamount located at 135 km on Profile BGR8635 (Figure 4.8A). This seamount has a significantly sharper, larger gravity signature in the ship gravity data than in the satellite gravity data, a consequence of the smoothing of the gravity field during satellite altimetry.

The differences between the ship and the satellite gravity data plotted in Figures 4.6B to 4.8B generally vary between ± 10 mGal in a region of ~ 200 mGal total variation. The largest difference (31 mGal) is found in the vicinity of the seamount on Profile BGR8635. Histograms of these differences for each profile are given in Figures 4.6C to 4.8C. The average standard deviation of the difference between ship and satellite gravity data along the three profiles is 5.7 mGal. This is significantly higher than the ± 1 mGal estimated accuracy of the ship gravity data.

The spectral coherence between the ship and satellite free-air gravity anomalies along each profile are shown in Figures 4.6D to 4.8D. The coherence in each case is highest (~ 0.9) at wavelengths greater than 40 km but falls below 0.5 at wavelengths less than ~ 20 km, indicating that 20 km is the short wavelength resolution limit of the satellite data. A resolution limit of 20 km in wavelength indicates that two narrow objects may blur into one object if they are less than 10 km apart, and objects much narrower than 10 km will be poorly resolved.

A comparison of the power spectral densities of the satellite and ship gravity data along Profile BGR8635 is given in Figure 4.9. This comparison clearly demonstrates that ship gravity anomalies have more power than satellite gravity anomalies at short wavelengths. The ship and satellite gravity data have similar power at wavelengths greater than about 30 km.

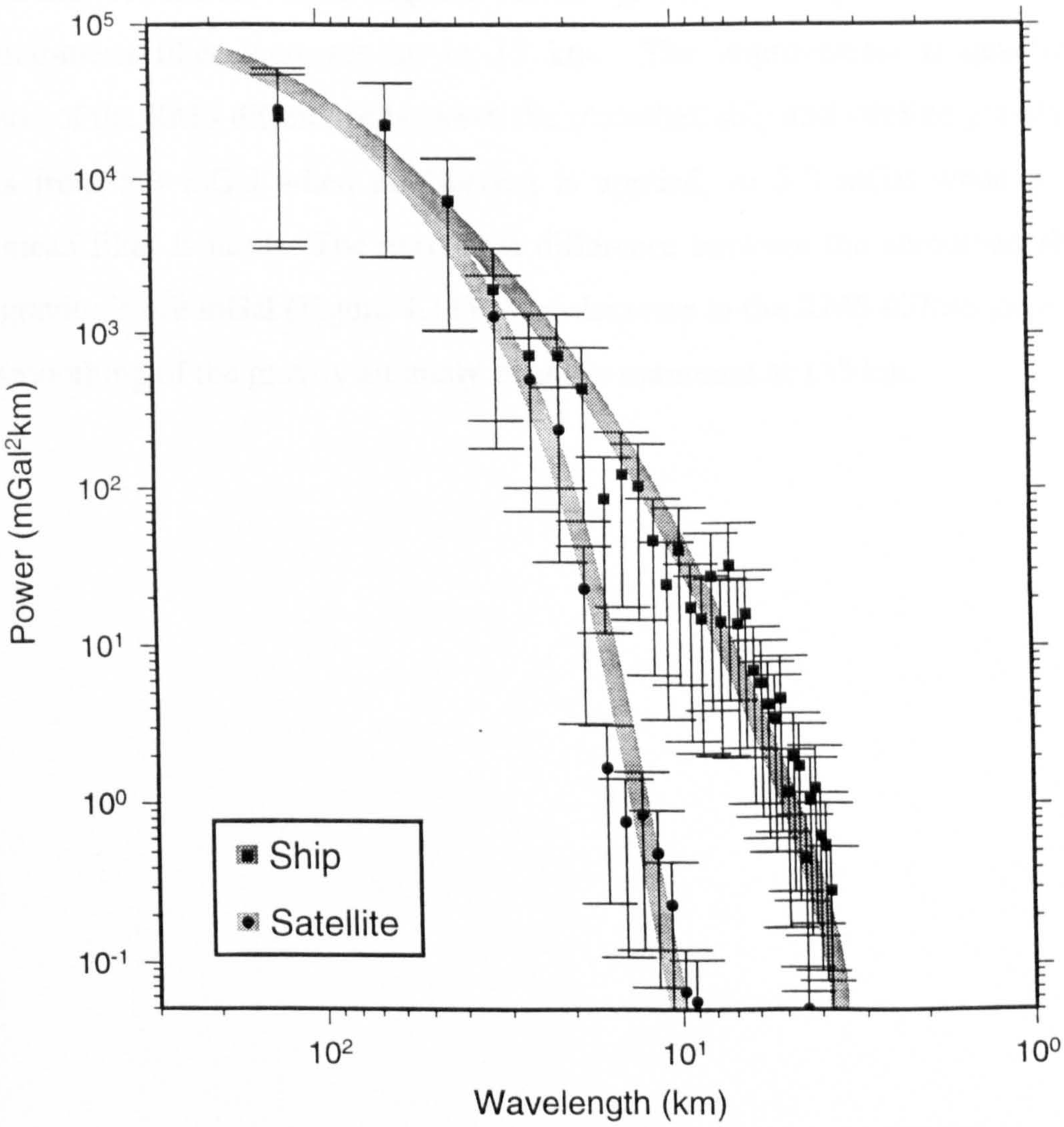

Figure 4.9. Graph showing typical power spectra of ship and satellite free-air gravity profiles, from Profile BGR8635. The ship free-air gravity profile has more power at wavelengths < 30 km than the satellite profile.

The effect of the smoothing of the satellite gravity field (e.g. by the measurement noise, satellite radar footprint, oceanographic contamination and gridding) can be assessed by comparing the satellite data with ship data smoothed using a running-mean filter, as illustrated in Figure 4.10. This comparison was performed along ship track BGR8635 since the largest differences between the two data sets were observed along this track. The match between the smoothed ship and satellite gravity data improves as the length of the running-mean filter increases up to 15 km. The improvement is quantified by comparison of the RMS difference between the smoothed ship and satellite gravity which decreases from 5.3 mGal when no filtering is applied, to 3.3 mGal when a 15 km running-mean filter is used. The maximum difference between the smoothed ship and satellite gravity is 6.9 mGal (Figure 4.11). The decrease in the RMS difference is largely due the smoothing of the gravity anomaly over the seamount at 135 km.

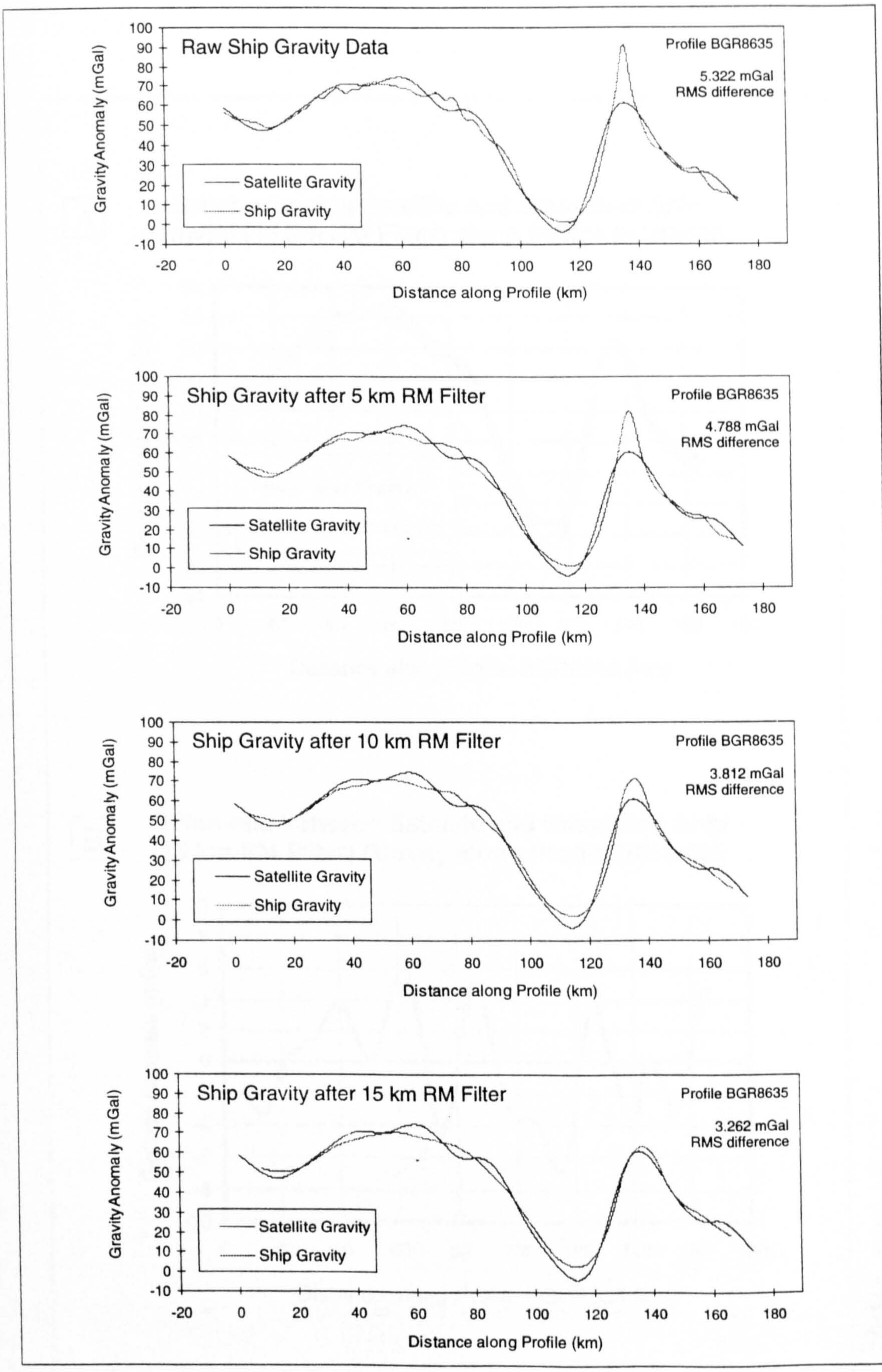

Figure 4.10. A comparison of smoothed ship gravity and satellite gravity along Profile BGR8635. The RMS difference between the two data sets decreases as the degree of smoothing applied to the ship gravity increases. A good match between the data sets is observed when the ship gravity is smoothed with a 15 km running-mean (RM) filter.

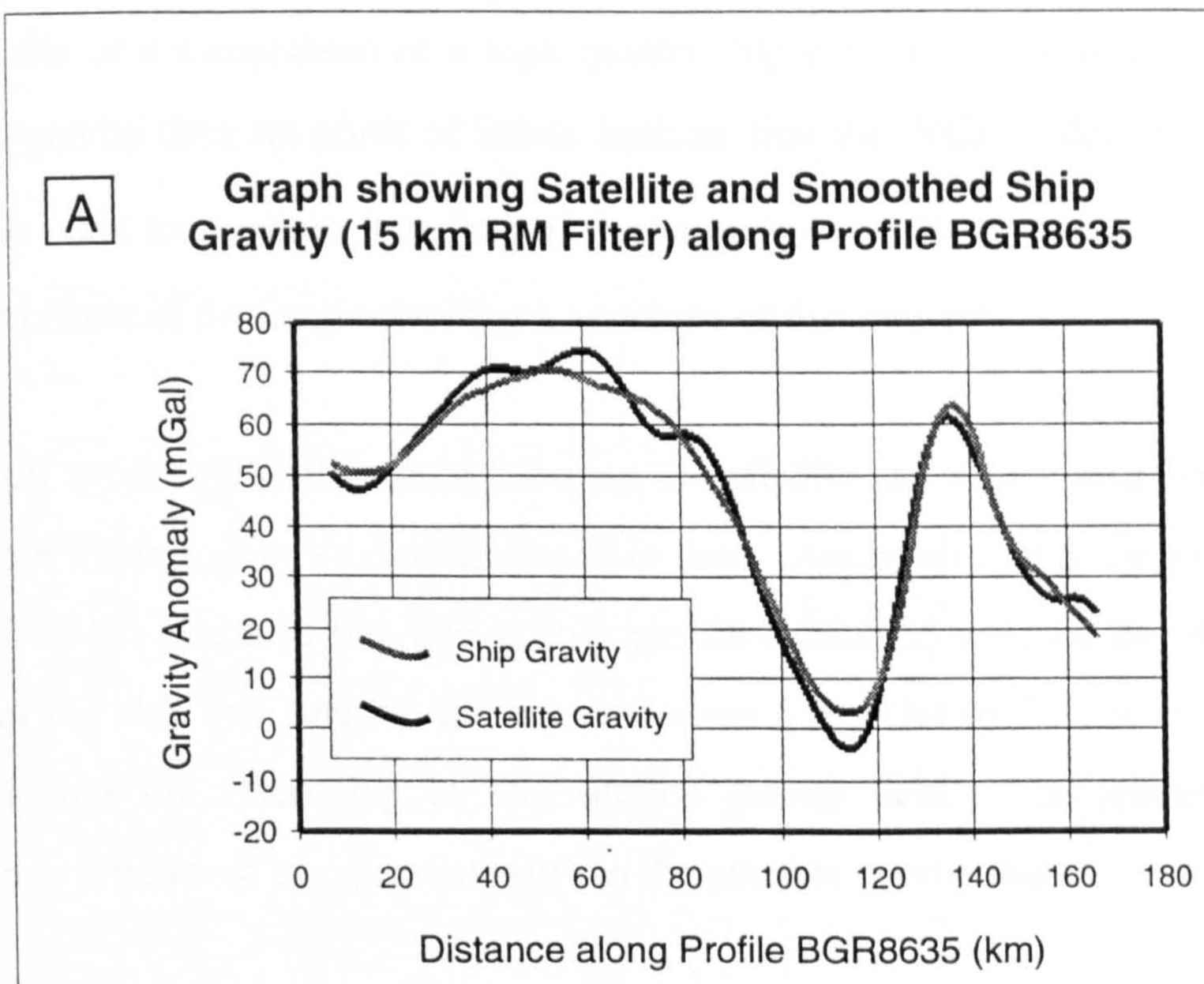

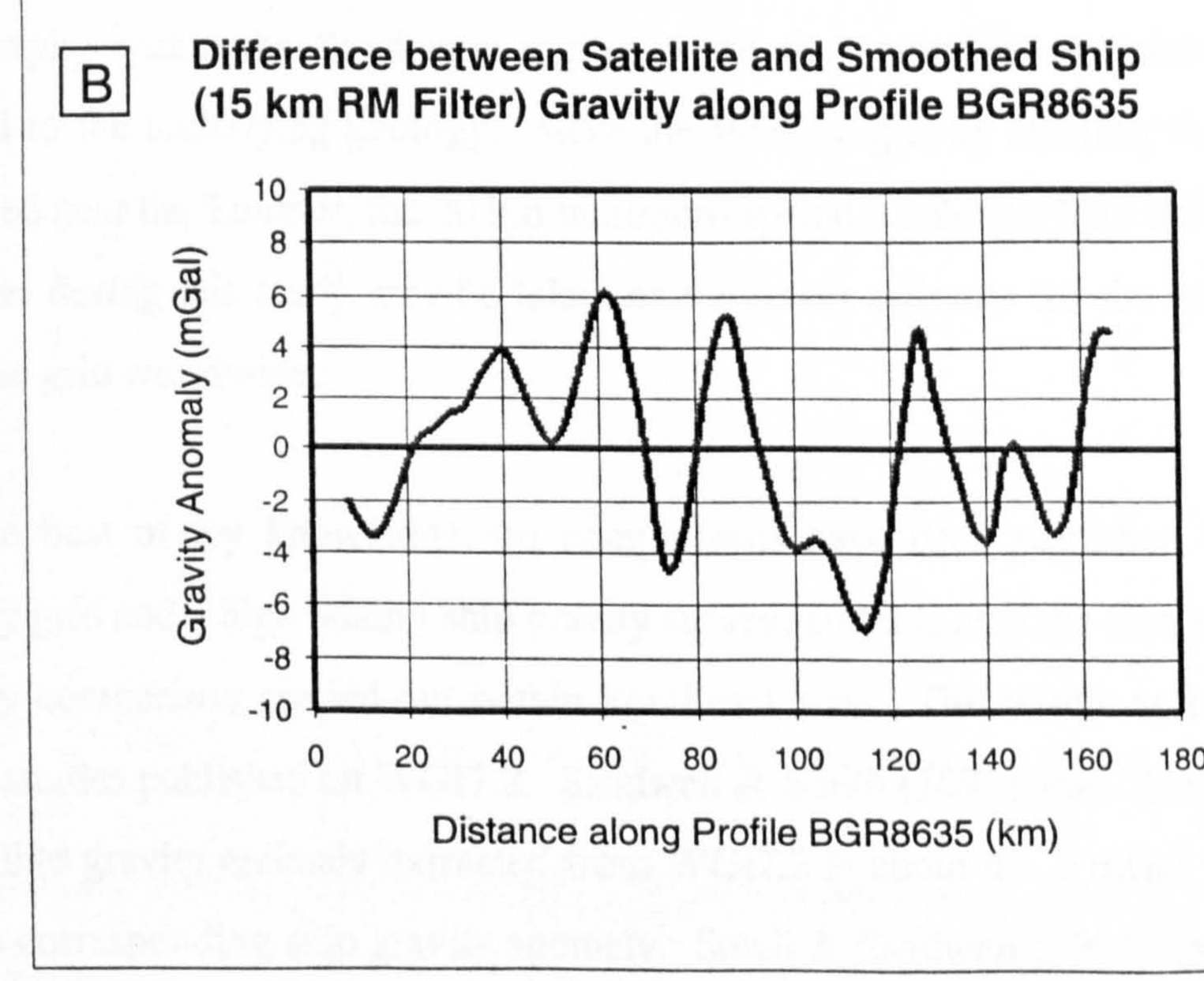

Figure 4.11. The difference between satellite gravity and ship gravity smoothed with a 15 km running-mean (RM) filter, Profile BGR8635.

4.4.3 Discussion

The results of a comparison of a high quality ship gravity survey and the new WGI7.2 satellite gravity data set north of Sabah indicate that the WGI7.2 data set is accurate to ± 6 mGal, and has a short wavelength resolution limit of 20 km ($\gamma^2 = 0.5$). No analysis has been made of the long wavelength accuracy of this data set.

The short wavelength differences between the satellite and ship free-air gravity anomaly data were minimised by smoothing the ship data. Application of a simple running-mean filter of 15 km length to the ship gravity profile BGR8635 reduced the RMS difference between the ship and satellite gravity data from 5.3 mGal to 3.3 mGal. This filtering approximates the smoothing of the satellite gravity field. The remaining 3.3 mGal difference is believed to represent noise in the satellite gravity data.

These results may be extrapolated outside of the comparison area. No evidence has been found during this study for false gravity anomalies arising from dynamic sea surface topography within the Sundaland region, as all the anomalies examined appear to be related to the underlying geology. Since the WGI7.2 gravity anomaly field is least well resolved near the Equator, the 20 km minimum spatial resolution limit determined for the data set during this study may be taken as the lower estimate for the resolution of this satellite grid worldwide.

To the best of my knowledge, no comparisons have been published of the WGI7.2 gravity grid and a high quality ship gravity survey, and this also the first ship and satellite gravity comparison carried out within Southeast Asia. The results agree well with the other studies published on WGI7.2. Sandwell & Smith (1997) state that the accuracy of a satellite gravity anomaly extracted from WGI7.2 is about 4 - 7 mGal when compared to the corresponding ship gravity anomaly. Small & Sandwell (1994) and Marks (1996) found from coherence analyses carried out between ship and satellite gravity profiles that the WGI7.2 satellite gravity field is coherent with ship gravity down to ~≥ 23 - 30 km. Both studies however used old (pre-satellite navigation), less accurate ship gravity data.

4.5 Conclusions

The accuracy and resolution of the satellite derived gravity field can be determined by analysing the differences between ship and satellite gravity profiles, assuming that the ship profile is more accurate. The standard deviation of the differences between gravity profiles interpolated from the WGI7.2 gravity grid and a high resolution ship gravity survey was found to be 5.7 mGal. This difference is significantly larger than the accuracy of the ship gravity data which was assessed to be of the order of ± 1 mGal, and matches exactly the quoted measurement precision of modern satellite altimeters (± 6 mGal, Section 3.3.4). The accuracy of the WGI7.2 satellite gravity grid is therefore judged to be ± 6 mGal. Spectral analysis has revealed that the WGI7.2 grid can resolve features with half-wavelengths greater than ~ 10 km. These values compare well with the few previously published results, and determine the level of tolerance that should be attached to geological models derived from the satellite gravity data.

The implications of this study are:

1) The resolution and accuracy of the WGI7.2 satellite gravity data set appears to be fairly uniform worldwide from the general level of agreement between the results of this study and those of previous studies.

2) Modern ship gravity surveys still provide significantly higher along-track resolution and accuracy measurements of the Earth's gravity anomaly field than the current generation of satellite radar altimeters.

CHAPTER 5

The Sabah Gravity Surveys

CHAPTER 5. THE SABAH GRAVITY SURVEYS

5.1 Introduction

Sabah, formerly known as British North Borneo and also, because it lies to the south of the South China Sea typhoon belt, as the 'Land Below The Wind', occupies the north-eastern tip of Borneo (Figure 5.1). In the west it is dominated by the rugged Crocker Ranges, culminating in Mt. Kinabalu which, at 4093 m, is the highest mountain in Southeast Asia. Further east the terrain is hilly rather than mountainous and tropical rainforest is being rapidly replaced by widespread oil palm plantations. The population is approximately 4 million, mainly concentrated near the coast. In addition to the capital, Kota Kinabalu, there are centres of population at Beaufort, Ranau, Sandakan, Lahad Datu, Sepulu and Tawau. Sabah joined the Malaysian Federation as a state in 1963.

A gravity survey carried out by the USAMS(FE), the Far East section of the US Army Map Service, in the 1960s covered the north and west of Sabah. The results are lodged with the US Defence Mapping Agency (DMA). A smaller survey was later carried out in the Darvel Bay area by Dalhousie University (Beattie, 1986) but was not tied to any gravity network. Other surveys are believed to have been completed by various oil companies but the results are not generally available.

The 1995 gravity survey had two aims. The primary objective was to extend the regional gravity coverage over as much of the previously unmapped scutheastern half of Sabah as was possible in the limited time available. The secondary aim was to link together the previous surveys, with the 1995 survey acting in part as a quality control on the earlier work, into a uniform data set tied to the IGSN71 base network. Figure 5.2 shows the area of Sabah covered by the USAMS(FE) survey and the area initially targeted for the 1995 survey. In the event, the survey was more successful than anticipated, with new gravity coverage extending farther west than shown in Figure 5.2 and with additional

Figure 5.1. Sabah location map.

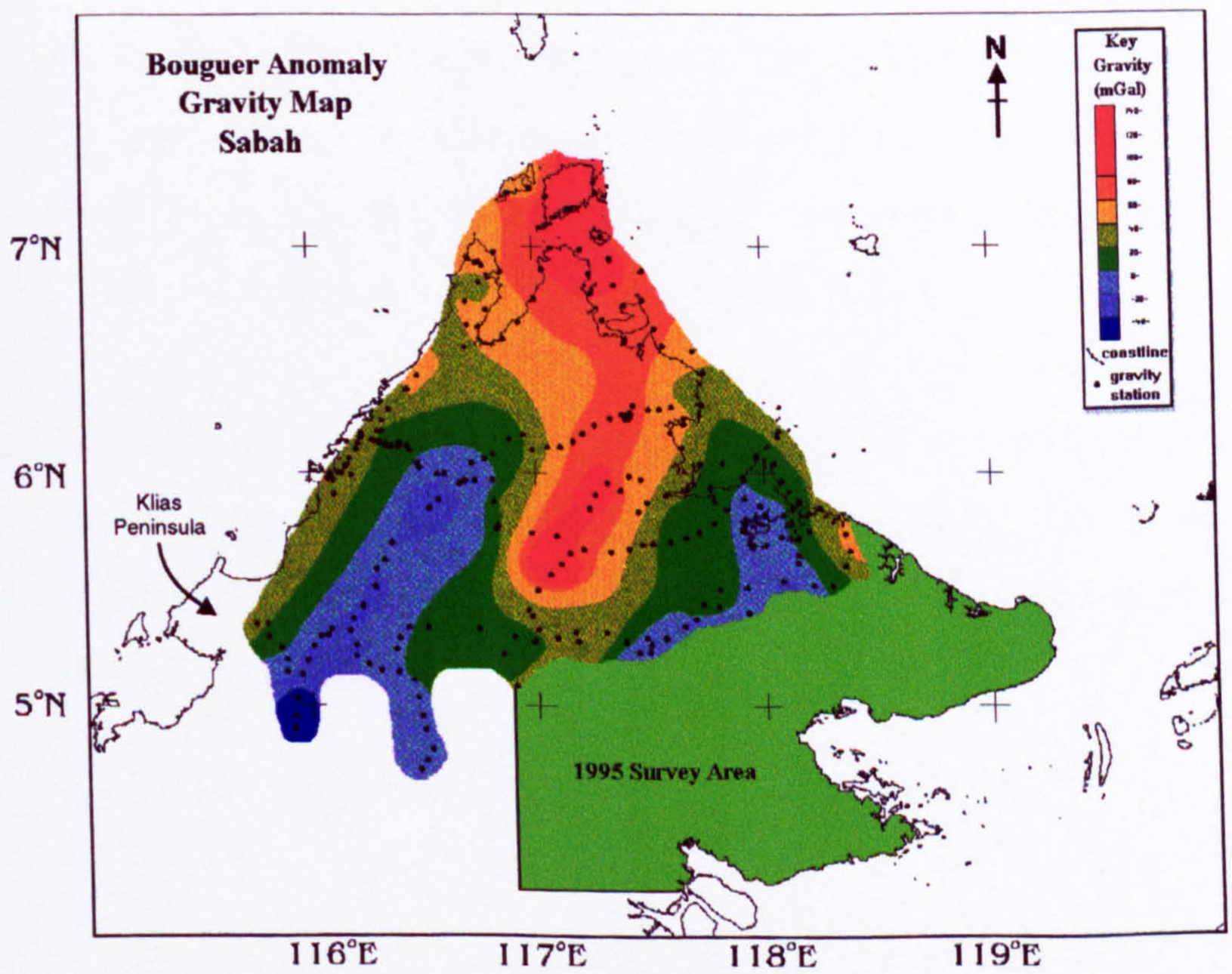

Figure 5.2. Map showing the USAMS(FE) gravity coverage of Sabah, and the area targeted for the 1995 Sabah gravity survey.

traverses on the Klias Peninsula in the extreme southwest. Approximate reoccupations of previously established stations and comparisons of contour patterns allowed the integration of all the Sabah gravity surveys into a regional data set. The USAMS(FE) data, based on a non-IGSN71 base station value, and the Darvel Bay survey, based on a local datum, were adjusted to the international IGSN71 network.

5.2 1995 Sabah Gravity Survey

5.2.1 Introduction

The 1995 Sabah gravity survey took place between 5 July and 7 August 1995. In this thesis day 1 corresponds to 8 July, and day 27 to 3 August. The survey was carried out by Rob Holt and John Milsom of University College London and Dzazali bin Ayub of the Geological Survey of Malaysia (Sabah), and was assisted by Anthony Lee, also of the Geological Survey of Malaysia (Sabah) (Plate 5.1). In addition to driving the vehicle, Mr Lee provided invaluable assistance with the actual measurements.

Three hundred new gravity stations and ten base stations were established in Sabah during the 1995 survey. The success of the survey was in part due to the new public roads which have been built in recent years. Even more important was the network of plantation tracks and logging roads. Access to these is normally restricted but the official GSM vehicle was granted immediate entry in almost all cases.

A LaCoste & Romberg Model G geodetic gravity meter on loan from Imperial College of Science, Technology and Medicine of the University of London was used to measure the gravity field (Plates 5.2 and 5.3). Station heights were determined barometrically and stations were located using a single GPS receiver (Plate 5.4).

A preliminary report on the 1995 Sabah gravity survey was written by Holt & Milsom (1996). A paper describing the new gravity base stations established in Sabah has been accepted for publication in Warta Geologi, the newsletter of the Geological Society of Malaysia (Holt *et al.*, in press).

Plate 5.1. The 1995 Sabah gravity survey team. Left to right: Dzazali bin Ayub, Rob Holt, John Milsom and Anthony Lee.

Plate 5.2. Rob Holt reading gravity meter.

Plate 5.3. John Milsom reading gravity meter.

Plate 5.4. Magellan Nav Pro 1000 GPS (left) and
Wallace & Tiernan Type 6 barometric altimeter (right).

5.2.2 Field Conditions

The wet season in Sabah includes both July and August. Whilst the mornings were generally dry, the afternoons were often wet, with thunderstorms on average every four days. The temperature each day was in the range 25 - 35 °C, and the humidity in the range 80 - 90 %. Fewer measurements were taken in the afternoons than in the mornings as the wet conditions made the going slow on the dirt roads in the plantations and on logging tracks. Also, in many cases, much of the afternoon period was occupied by returning along routes already surveyed earlier in the day. Occasional repeat gravity readings were made in these circumstances, and stations were reoccupied to improve barometric control whenever the opportunity arose.

Accommodation was plentiful and of a relatively good standard in the towns and cities. In more remote areas, clean accommodation was found in logging company rest-houses and at the Danum Valley Field Centre. Food was less easily obtained in the more remote regions.

5.2.3 Station Positioning

Station locations were established using GPS. The main GPS instrument used was a Magellan Nav Pro 1000 belonging to the University of London Southeast Asia Research Group but a problem with the battery connection necessitated the additional use of a Trimble Ensign borrowed from the Geological Survey of Malaysia. The two GPS instruments were used together on 20 occasions, so that the positional error of the GPS fixes could be estimated. Table 5.1 lists the differences, in minutes of arc, between the two readings for each of these fixes. The values were obtained by adding and then square-rooting the squares of the individual latitude and longitude differences. The average difference, in minutes of arc, between the pairs of simultaneous position estimates is 0.103 ± 0.074. This corresponds to an average difference of 0.188 ± 0.136 km. Because the root mean square error of two measurements each having an accuracy

of ± 0.133 km equals ± 0.188 km, the positional error of the stations located by a single GPS fix during the 1995 survey is estimated to be ± 133 metres.

Table 5.1. Arc differences in position (in minutes) between simultaneous positional fixes obtained with a Magellan and an Ensign GPS during 1995 Sabah gravity survey.

Difference (minutes)	Difference (minutes)
0.022	0.192
0.095	0.125
0.012	0.063
0.073	0.051
0.199	0.125
0.020	0.141
0.141	0.073
0.275	0.036
0.190	0.022
0.180	0.022

5.2.4 Barometric Levelling

The single base barometric levelling technique used during the 1995 Sabah gravity survey has been used for many years on gravity surveys in Southeast Asia (e.g. St. John, 1967; Milsom, 1970; Milsom, 1988; Harrison, 1991). The basis for this technique is as follows. It is assumed that atmospheric pressure variations occur uniformly across the survey area, and that temperature and humidity remain constant throughout the survey. By continually recording atmospheric pressure at a fixed location (the base station), the background pressure variation may be removed from pressure measurements taken at field stations leaving the pressure difference between the field station and the base station. As an approximately linear inverse relationship exists between pressure and altitude, the observed pressure difference between the base station and the field station can be directly converted into a height difference. By determining the height of the base station above mean sea level, the elevations of the field stations may finally be deduced.

The technique was used in Sabah to determine gravity station heights in preference to a GPS system since the estimated accuracy of ± 2.5 m is considerably better than the ± 100 m obtainable from a single GPS. Greater accuracy is obtainable using differential-mode GPS but this requires a second instrument at base and extensive processing, and is also very time consuming. The ± 2.5 m accuracy of the single base barometric levelling technique is equivalent to an error of ± 0.5 mGal in Bouguer anomaly and is adequate for a regional survey which is unlikely to be contoured at intervals of less than 10 mGal.

A detailed report on the levelling survey is given separately in Appendix 1.

5.2.5 Gravity Survey Field Procedure

One problem encountered early in the survey work was the absence of any reoccupiable IGSN71 base stations in Sabah.. An approximate reoccupation was made of the site of the original international station at the old "Jesselton" airport, which is now used for general aviation only, but the main link to IGSN71 was based on readings at the Malaysian national base station at the Universiti Malaya in Kuala Lumpur (accepted value 978034.450 ± 0.043 mGal). The link to Sabah therefore relies on a single loop which was begun on 6 July and was finally closed on 4 August.

A network of 10 new gravity base stations on Sabah was established during the 1995 survey. These bases and a temporary base in Kuala Lumpur are described in Appendix 2. The most important of the Sabah bases is the station at the Geological Survey building in Kota Kinabalu (Station 0002), and it is recommended that this be adopted as the primary gravity base for the state. Other described and reoccupiable bases were established in Telupid, Lahad Datu, the Danum Valley Field Centre, Tawau, Luasong and Tambunan. The network, illustrated in Figure 5.3, was established using a system of forward looping. Thus, a new station was established at Telupid en route from Kota Kinabalu to Lahad Datu, where a second new station served as a base for a number of days. Side loops from Lahad Datu allowed bases to be established at the Danum Valley Field

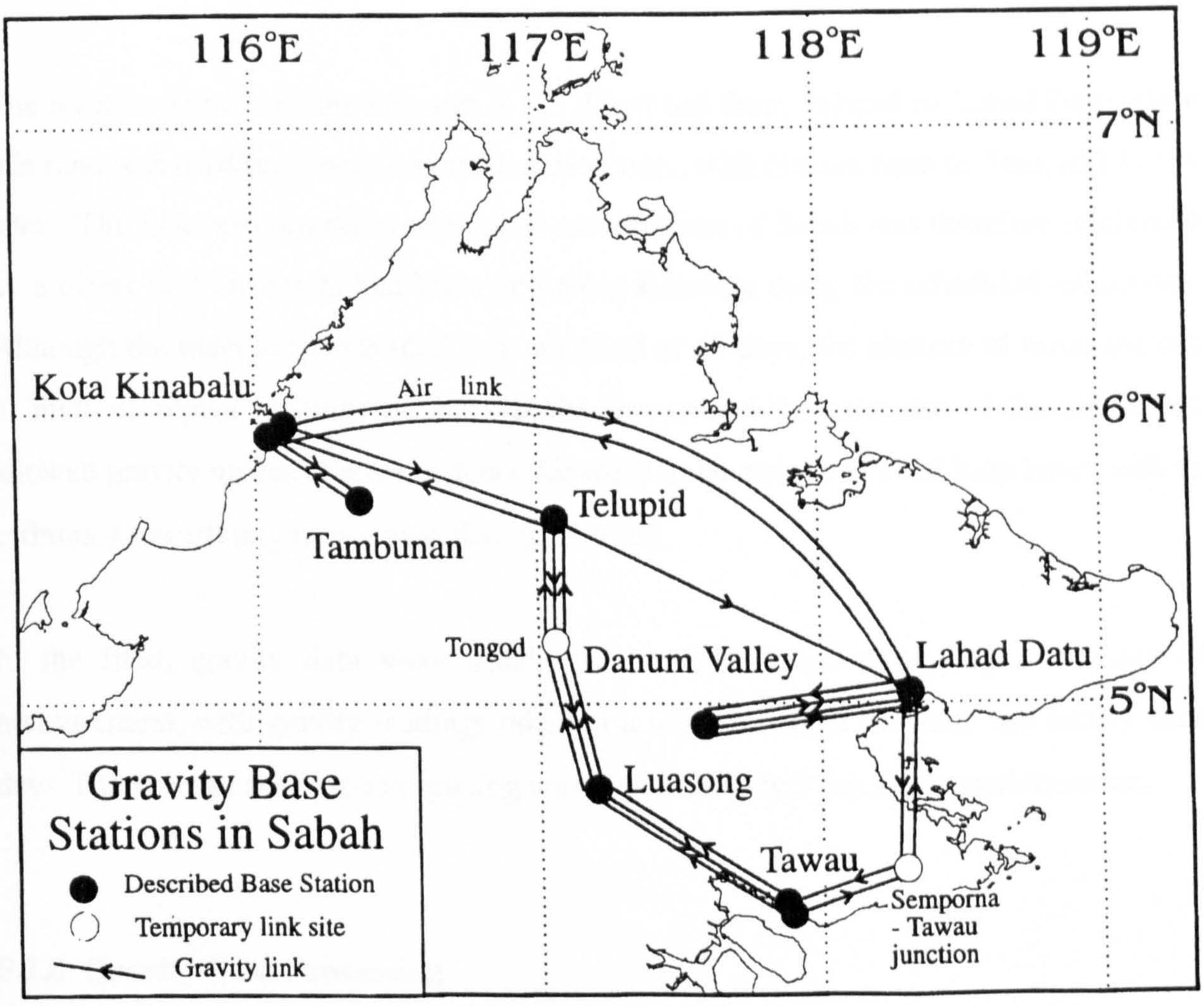

Figure 5.3. Gravity base station network established on Sabah during the 1995 survey.

Centre. From Lahad Datu a loop included a temporary site at the Semporna-Tawau road junction which was reoccupiable from Tawau after the base had been moved there. A loop from Tawau then reached the forestry base at Luasong, which was in turn used as a base for three loops, one of which included a temporary site at the forestry centre at Tongood. From Tongood the survey was tied back to Telupid and thence to Kota Kinabalu. An additional loop from Kota Kinabalu allowed a base to be established at Tambunan.

The weakest section of the network is the direct link from Telupid to Lahad Datu, since this road was used once only, in one direction only, with closure back to Telupid 17 days later. The link between the western and eastern sides of Sabah was therefore reinforced by a direct tie between Lahad Datu and Kota Kinabalu using the scheduled air service. Although the main loop extended over a period of 19 days, the absence of tares, the use of multiple repeat readings throughout the survey and the existence of the air tie has allowed gravity values relative to Kota Kinabalu to be estimated at all loop bases with an estimated uncertainty of no more than 0.05 mGal.

In the field, gravity data were usually acquired in loops occupying a full day of measurement, with gravity readings taken at a base station at the start and end of each day. The average field station spacing was approximately 5 km along road traverses.

5.2.6 Gravity Data Processing

Gravity data can be processed to Bouguer anomalies only when station heights and locations have been determined. A flow chart of the processing methodology is given in Figure 5.4.

The initial processing stages convert meter readings to gravity units and correct for time-variant changes within the meter caused by the small increases in the length of the gravity meter spring during the survey (drift), and also changes outside the meter (tidal gravity variations). Ideally, gravity meters should be calibrated periodically under laboratory

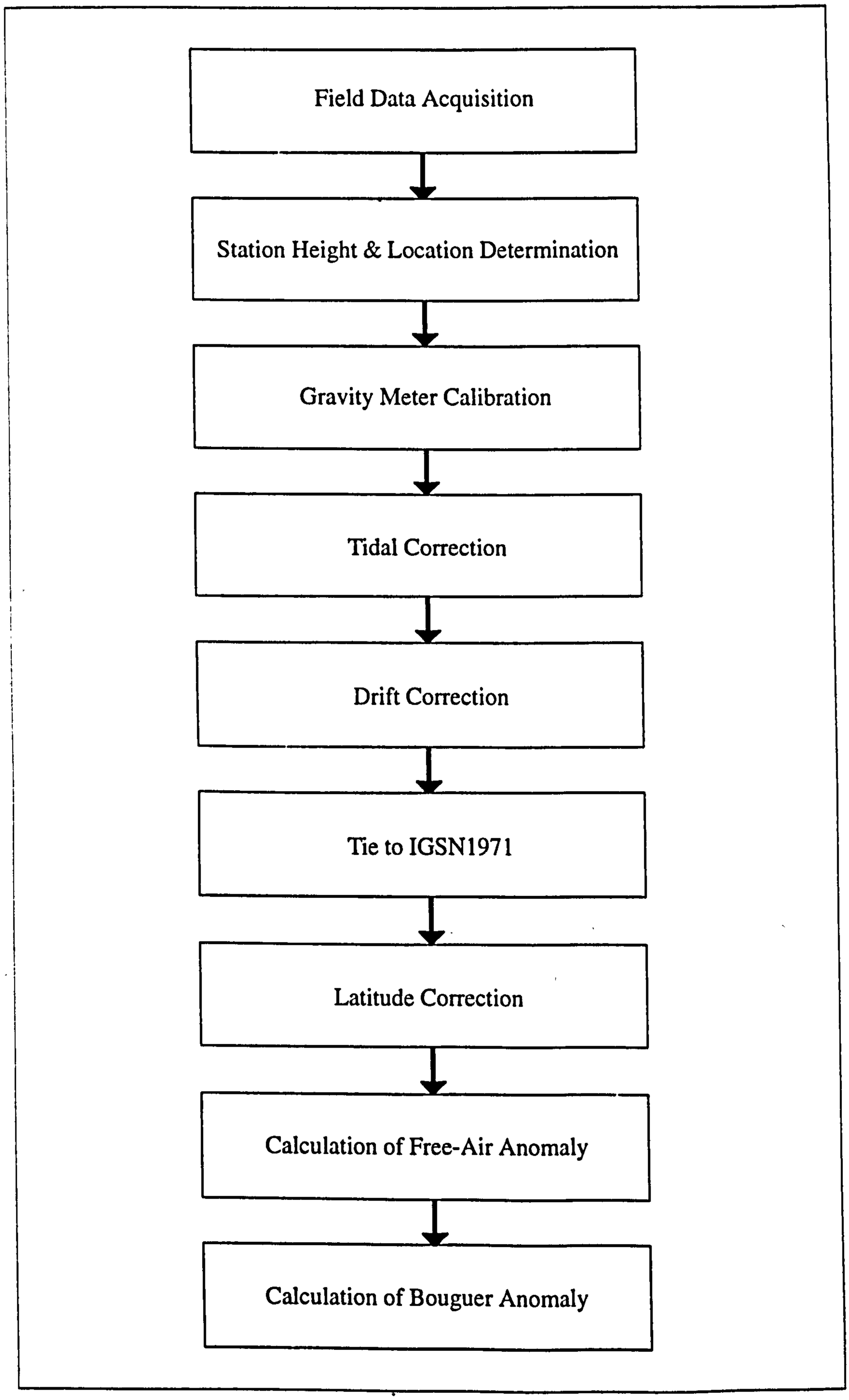

Figure 5.4. Flow chart of gravity processing methodology.

conditions to monitor any changes in length of the spring, although the manufacturers of the LaCoste & Romberg meter used on the survey claim that the calibration does not vary with time. The calibration table used with the 1995 survey data is given in Appendix 3.

Following conversion to milligals, the gravity measurements were corrected for tidal effects calculated using the computer program *et.com* written in 1986 by R. Almond for the Geological Survey of Indonesia (Almond, 1986).

Gravity meter drift was determined by plotting all of the tide-corrected values obtained at repeatedly read gravity stations within the survey area. A graph of these measurements is shown in Figure 5.5, which also shows the simplified drift curve used for the correction (represented by the solid black line) and the residual drift after correction. The variation of the drift-corrected repeated station measurements is of the order of ± 0.05 mGal. Using this simple although not rigorously accurate correction procedure considerably reduced the time taken in processing. The results obtained are not considered to be significantly worse than those which would have been obtained using the more accurate day by day correction process.

Gravity anomaly values were derived by subtracting the theoretical gravity value (g_ϕ) from the measured value (g_{obs}) at each station. The theoretical gravity for a point on the sea level reference surface vertically below (or above) the point of observation was calculated using the equation:

$$g_\phi = 978031.8(1 + 0.0053024\sin^2\phi - 0.000005\sin^4(2\phi)) \qquad (5.1)$$

where ϕ is the geographic latitude of the point of observation.

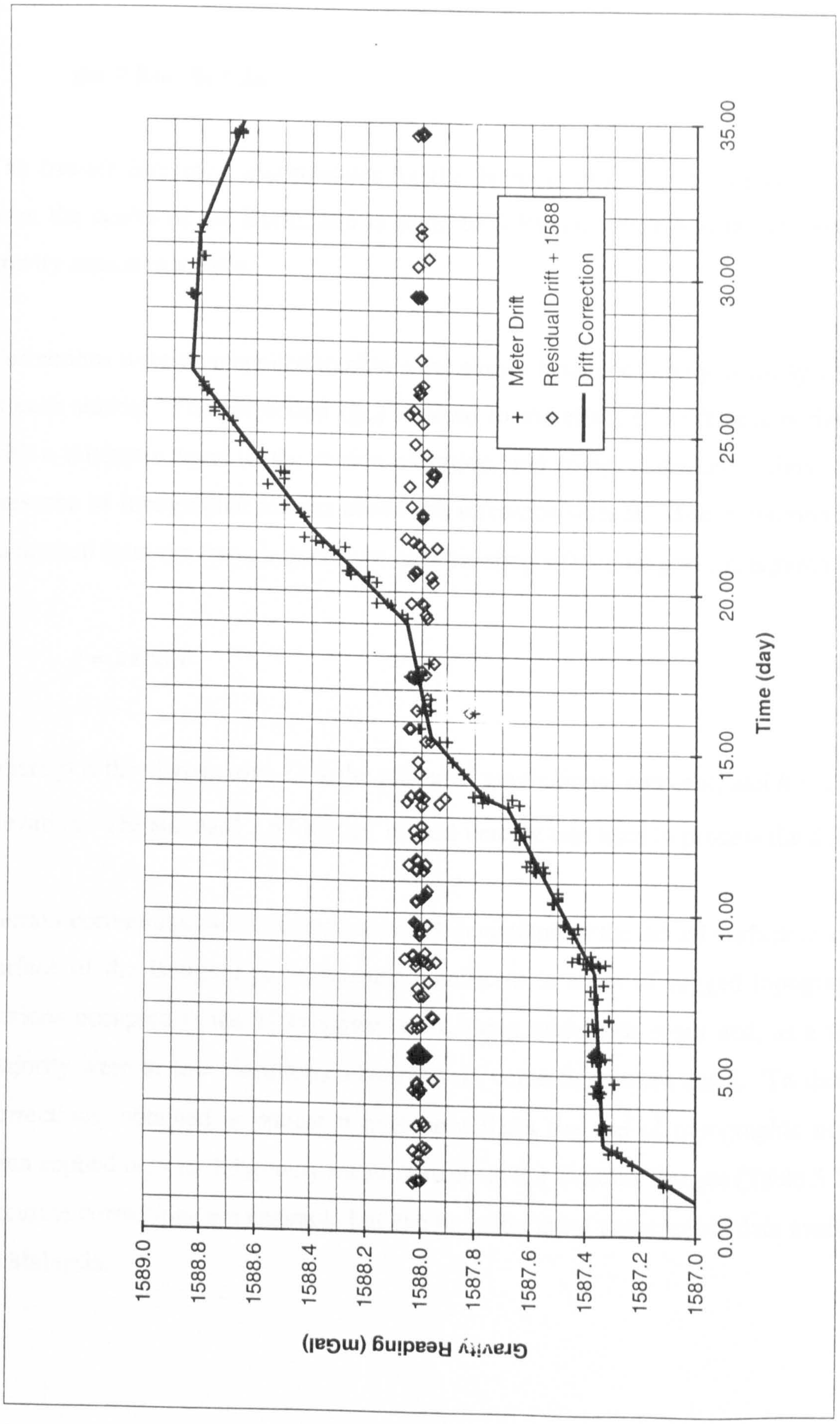

Figure 5.5. Gravity meter drift during the 1995 survey and residual drift after drift correction.

Free-air gravity anomaly values (g_{faa}) were obtained by applying the free-air correction (g_{fac}):

$$g_{faa} = g_{obs} - g_{\phi} + g_{fac} \tag{5.2}$$

The free-air correction compensates for the decrease in gravity with increased distance from the centre of the Earth, and is equal to $0.3086h$, where h is the elevation of the gravity station in metres.

Corrections were then applied to obtain the simple Bouguer gravity anomaly values (g_{ba}) at each station. The correction (g_{bc}) is equal to the effect of an infinite horizontal slab with a thickness equal to the station elevation, and compensates approximately for the presence of topographic masses above the reference surface. The correction, which is subtracted from the free-air gravity to give the simple Bouguer gravity, is given by

$$g = 2\pi\rho G h \tag{5.3}$$

where ρ is the slab density, G is the universal gravitational constant, and h is the station elevation. The standard 2.67 $Mg.m^{-3}$ crustal density was used to process the data.

Terrain corrections, which compensate for deviations of the actual surface from the flat surface of the Bouguer plate, become significant in areas of rugged topography. All stations occupied in the 1995 survey were along motorable roads and, as a result, the majority were at low elevations where terrain corrections were small. To date, terrain corrections, obtained as educated guesses without the use of topographic maps, have been applied only to the gravity measurements in the Crocker Ranges (Table 5.2). More accurate corrections are desirable but can be made using topographic data available only in Malaysia.

Table 5.2. Terrain corrections (TC) applied over the Crocker Ranges.

Station	Altitude (m)	Simple Bouguer Anomaly (mGal)	TC (mGal)	Bouguer Anomaly (mGal)
0292	164.4	-14.79	10	-4.79
0293	435.0	-41.98	20	-21.98
0294	840.0	-80.41	30	-50.41
0295	1262.8	-122.36	40	-82.36
0296	1547.9	-150.76	50	-100.76
0297	1696.9	-167.18	50	-117.18
0298	1142.4	-121.42	40	-81.42
0299	799.6	-94.56	30	-64.56
0300	634.2	-86.44	25	-61.44
0301	566.7	-78.05	20	-58.05

5.2.7 Gravity Survey Errors

Errors in the 1995 survey Bouguer gravity anomaly values arise from the following sources:

- gravity meter reading uncertainty
- drift correction
- IGSN base value uncertainty
- station height uncertainty
- missing terrain correction

On day 5 of the survey, a series of gravity measurements were taken at a fixed location over a period of about six hours with two aims - the first being to familiarise the author with the gravity meter, and the second being to determine the repeatability of the gravity measurements. Figure 5.6 shows the variation in these gravity measurements, after conversion from scale divisions to milligals. The standard deviation about the observed trend is 0.012 mGal. This ± 0.012 mGal error is a combination of meter error, meter reading error and the error in the tidal corrections.

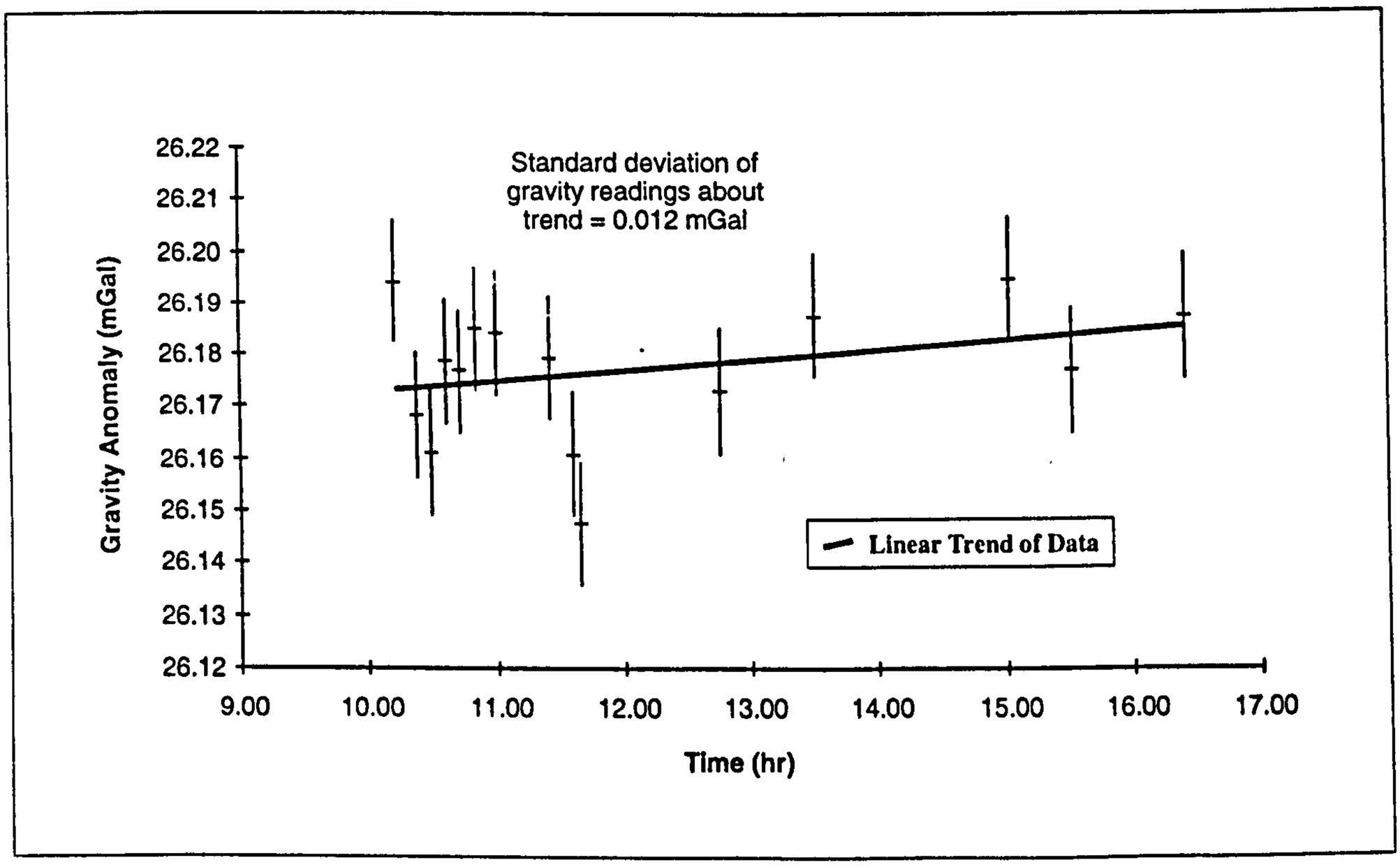

Figure 5.6. Day 5 Gravity Measurements, Hotel Asia, Kota Kinabalu.

As discussed above, drift corrections were made to an accuracy of about ± 0.05 mGal. The error in absolute gravity due to the quoted uncertainty in the value of the Malaysian national IGSN71 base in Kuala Lumpur is ± 0.043 mGal. There is an additional error involved in the tie between Kuala Lumpur and Kota Kinabalu which is very hard to quantify because only a single ABA loop was completed. The difference between the two measurements of the gravity interval (i.e. between the AB and BA uncontrolled links) is less than 0.1 mGal and this level of error is therefore currently assumed. Combining these two errors suggests an overall uncertainty in the absolute value of the Kota Kinabalu base of ± 0.11 mGal. This error will not affect the validity of the relative gravity contouring within Sabah. The average station height uncertainty of ± 2.5 m corresponds to an error of ± 0.5 mGal in Bouguer gravity (Section A1.9, Appendix 1). The error caused by the lack of a terrain correction is more variable. A value of +0.5 mGal is a realistic average but the actual errors will range from a few hundredths of a milligal in low lying areas to possibly tens of milligals in the Crocker Ranges.

The total error of the gravity stations in the 1995 survey, excluding the stations in the Crocker Ranges (Stations 0292-0301), is therefore estimated to be approximately ± 0.7 mGal. The uncertainty in the gravity values of the stations in the Crocker Ranges is likely to be of the order of ± 10 mGal.

5.2.8 Results

The area covered by the 1995 Sabah gravity survey is shown in Figure 5.7. The main work was done in southeastern Sabah, in an area approximately between geographic latitudes 4°00' N and 5°30' N and between longitudes 117°00' E and 119°00' E. Other data were collected on the Klias Peninsula in southwestern Sabah and on a single traverse across the Crocker Ranges due east of Kota Kinabalu. In all, three hundred stations were occupied. The gravity data collected during the survey are listed in full in Appendix 4, and are summarised in Appendix 5.

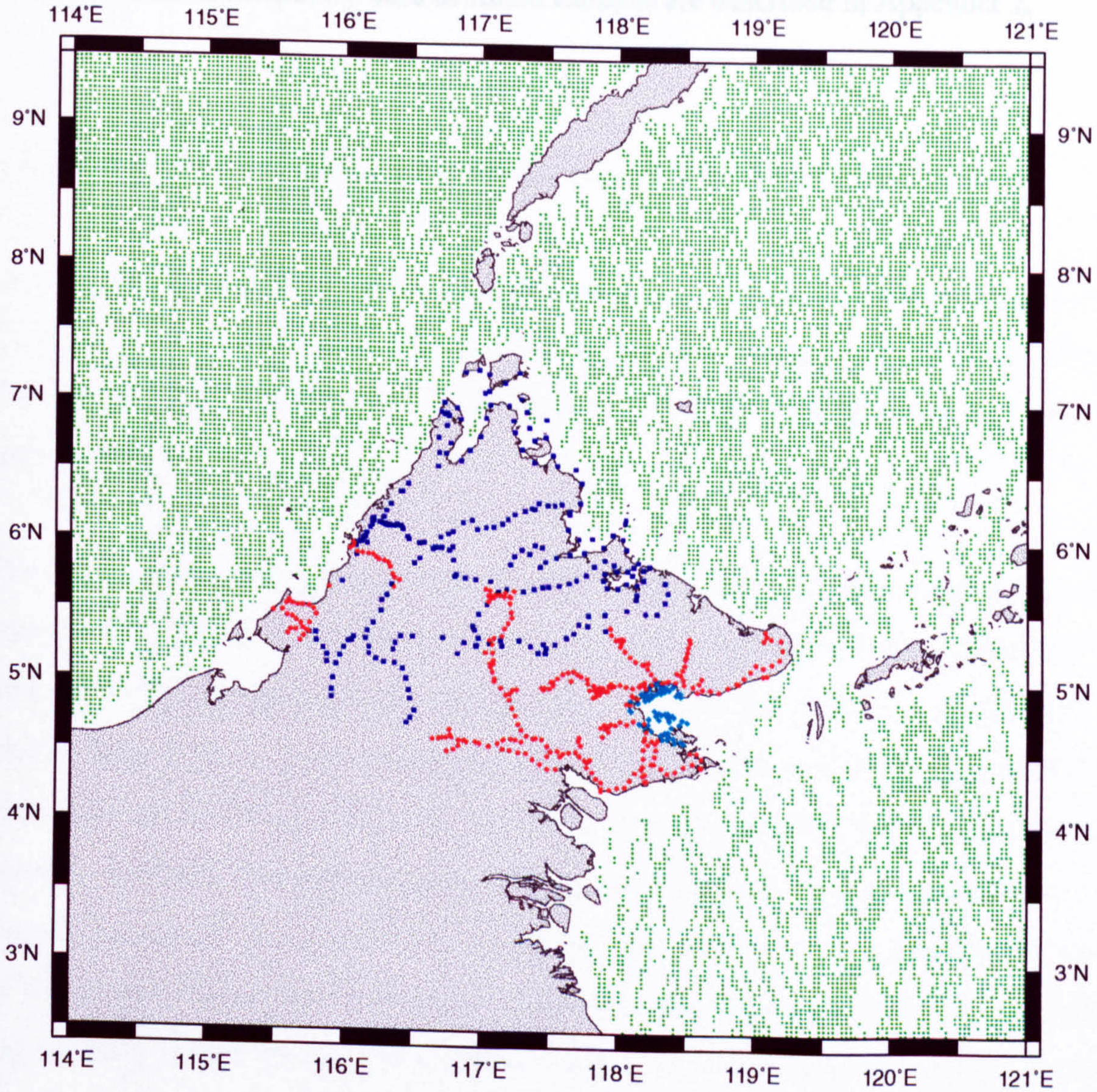

Figure 5.7. Gravity coverage, Sabah. Key: 1995 survey (red); USAMS(FE) survey (blue); Darvel Bay survey (turquoise); WGI7.2 satellite measurements (green).

Ten new gravity base stations were established during the course of the survey. Every effort was made to select sites which were describable, reoccupiable and had reasonable prospects of permanency. The station at the Geological Survey Offices in Kota Kinabalu will be protected in the future and should be regarded as the main gravity base for Sabah. These bases and a temporary base in Kuala Lumpur are described in Appendix 2.

5.3 Merger of the Sabah Gravity Data Sets

There have been three land gravity surveys of different vintages in Sabah (as well as an unknown but possibly large number of commercial surveys). This section describes the methods used to integrate these surveys into a single consistent data set.

5.3.1 Merger of the 1995 survey with the Darvel Bay survey

Data in the Darvel Bay region were acquired by P. Ryall of Dalhousie University, Canada, in 1975 and were used in a B.Sc. honours thesis prepared by D. Beattie (Beattie, 1986) and published in a joint report, 'A Gravity High in Darvel Bay' (Ryall & Beattie, 1989).

The Darvel Bay survey was not originally tied to any datum. The first stage in its merger with the 1995 Sabah survey was to compare the map provided by Ryall & Beattie (1989) with the 1995 Bouguer gravity contour map (Figures 5.8 and 5.9 respectively). In general form the two contour maps are very similar, but the values from the Darvel Bay survey are approximately 40 to 50 mGal less than the IGSN71 values from the 1995 survey. Detailed comparisons were then made, based on six gravity stations of the Darvel Bay survey which lay within 3.5 km of 1995 survey stations (the seventh station of the Darvel Bay survey satisfying this criterion was apparently read within a building and so has not been used). Differences between the two surveys at these six locations are shown in Figure 5.10; they increase systematically southwards by approximately 10 mGal over 0.4 degrees of latitude. There are two possible explanations for this trend. Either latitude corrections were not applied to the Darvel Bay survey, or corrections were applied but in the wrong sense.

The differences between the two surveys at the common locations are plotted in Figure 5.10, together with the differences between the 1995 survey and values generated by adjusting the Darvel Bay data with both single latitude corrections and double latitude corrections. When the single latitude corrections are applied to the Darvel Bay data, the

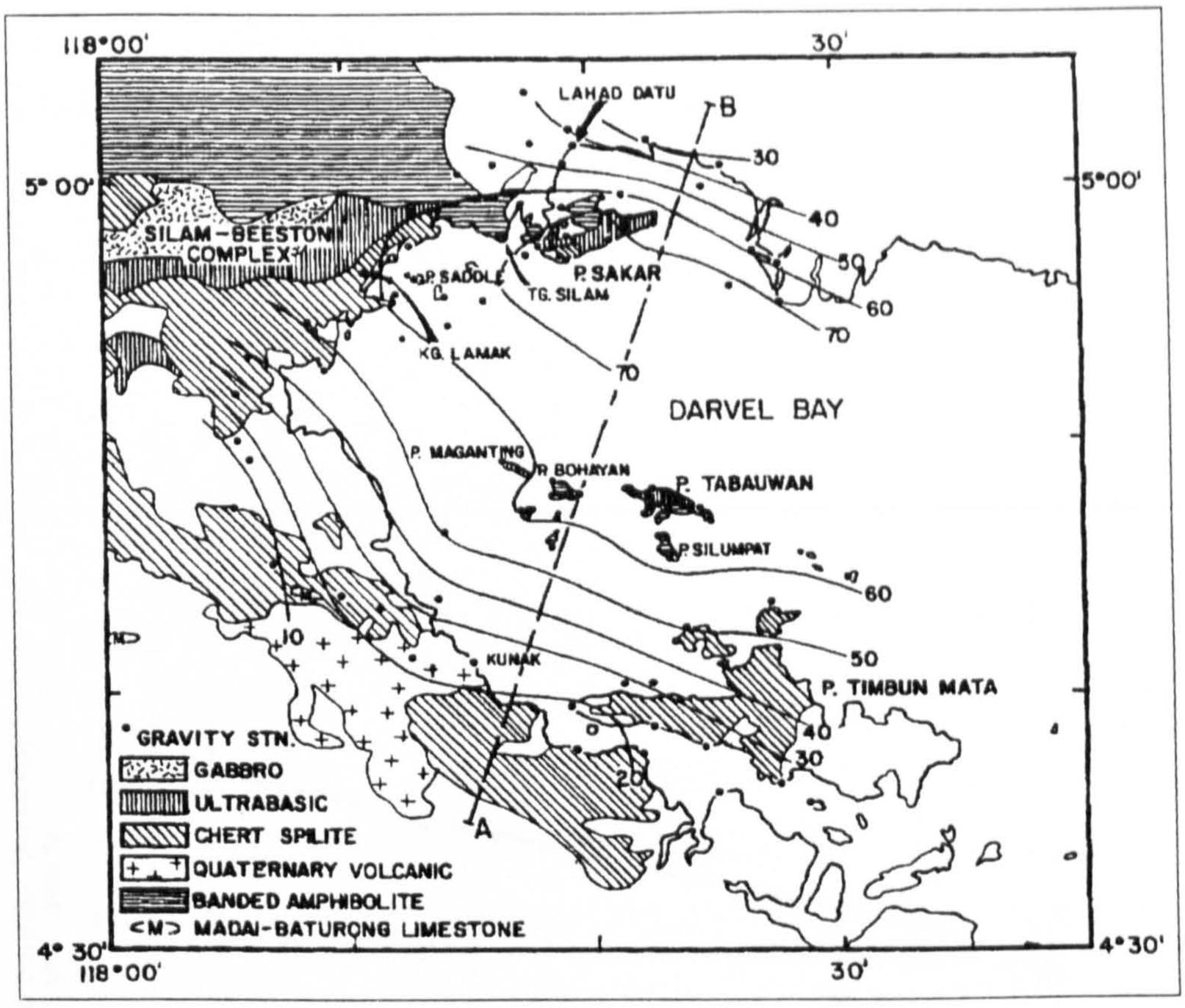

Figure 5.8. Darvel Bay gravity map from Ryall & Beattie (1989).

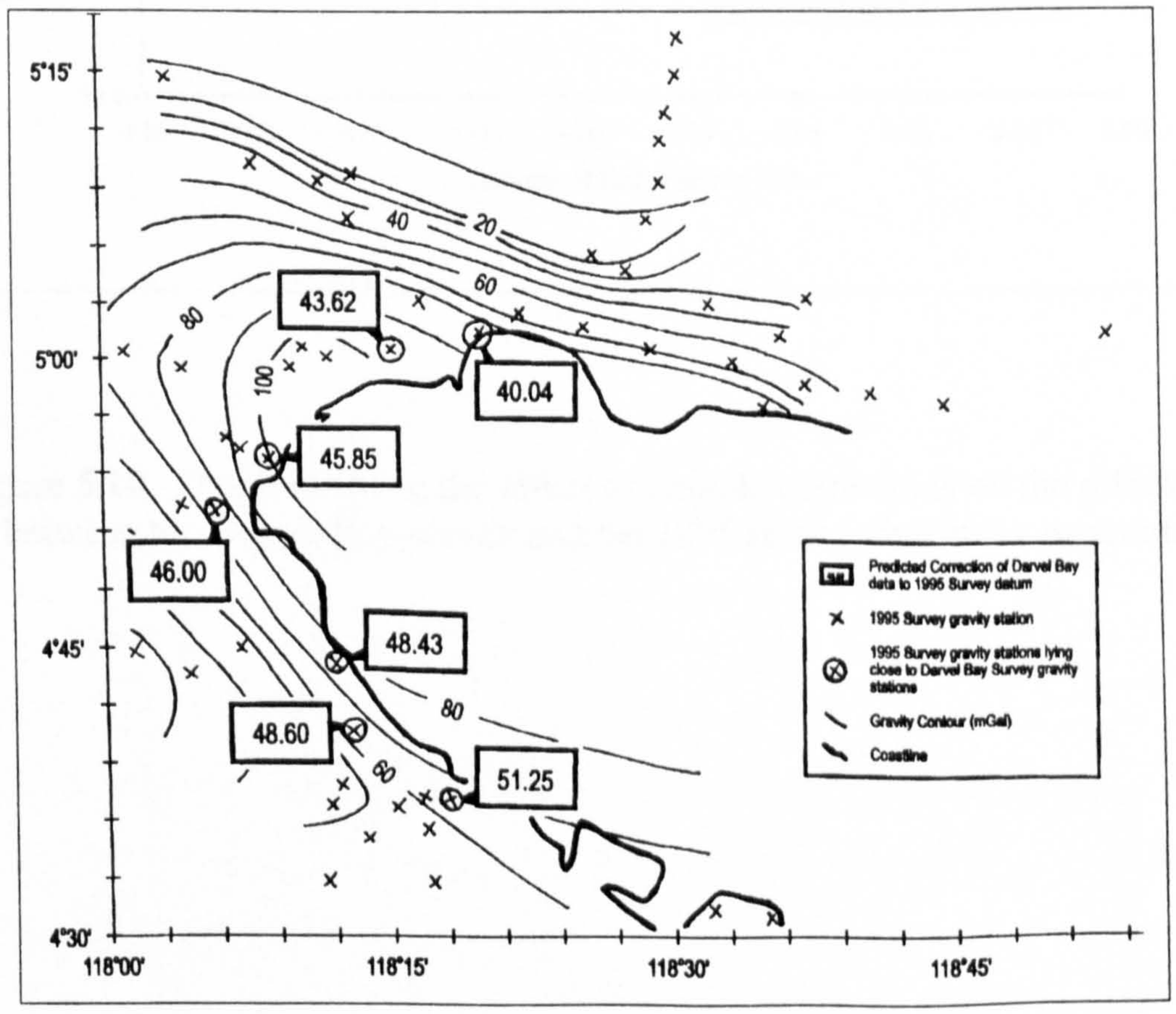

Figure 5.9. Darvel Bay gravity map from 1995 survey data.

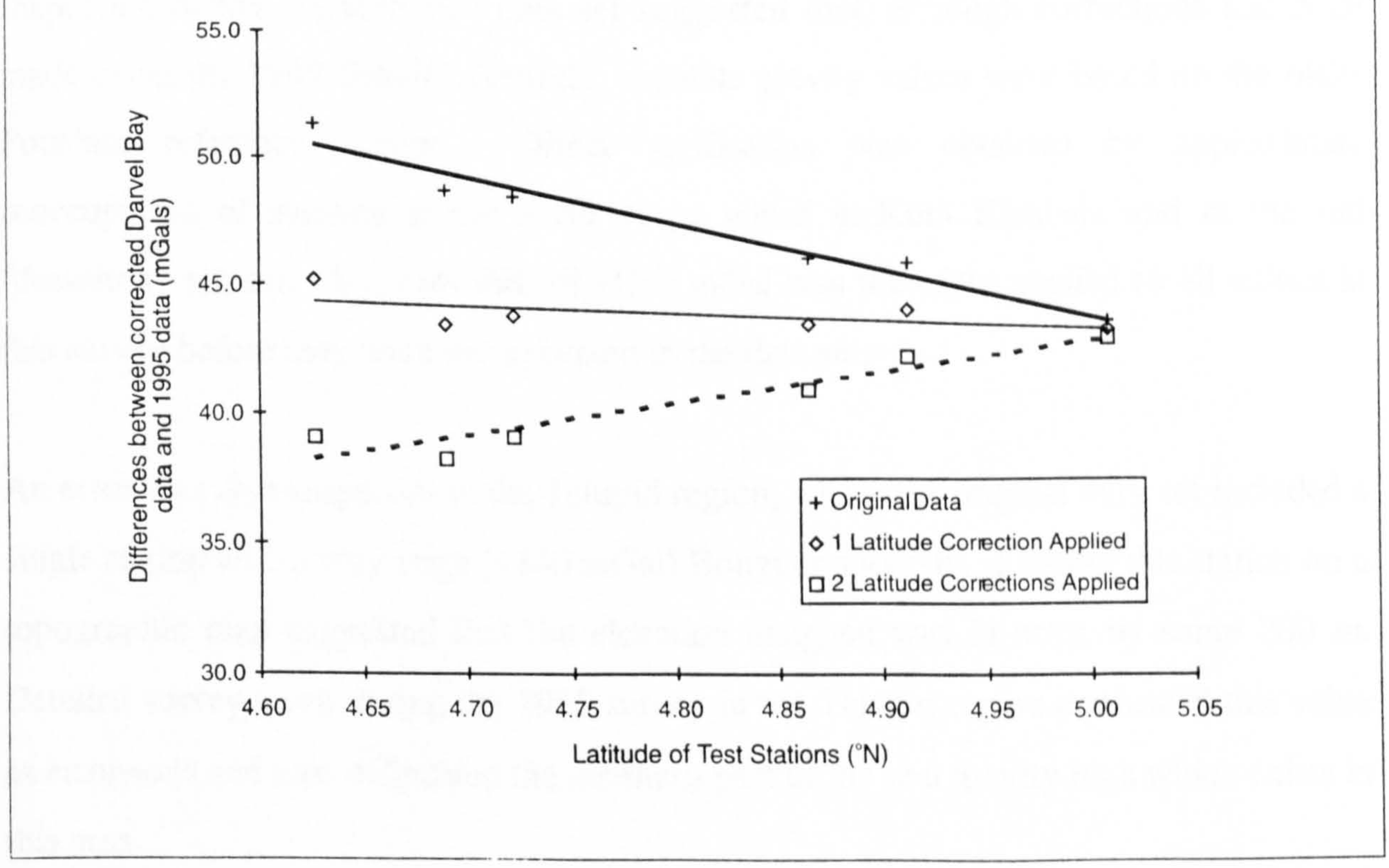

Figure 5.10. Graph showing the effect of latitude corrections on the difference between the Darvel Bay survey and the 1995 survey data at six locations.

differences from the 1995 data are approximately independent of latitude. This suggests that the original Darvel Bay data were not corrected for latitude and these were therefore merged with the 1995 survey data set by applying a latitude correction and a suitable datum shift. The corrected Darvel Bay gravity data are listed in Appendix 6.

5.3.2 USAMS(FE) Data Set Correction

Inspection of the USAMS(FE) data set suggested that, although corrections had been made using the 1967 Gravity Formula, absolute gravity values were based on the older Potsdam reference system. Direct verification was obtained by approximate reoccupation of stations at the small cargo wharf in Kota Kinabalu and at the old "Jesselton" airport. A datum shift of -13.7 mGal was therefore applied to all values in this survey before they were incorporated in the data set.

An error was also suspected in the Telupid region, where the original data set included a single station with a very large (+140 mGal) Bouguer anomaly. Plotting this station on a topographic map suggested that the elevation assigned was in error by some 200 m. Detailed survey work during the 1995 survey in the Telupid region confirmed this value as erroneous and also delineated the southern part of the real gravity high which exists in this area.

The corrected USAMS(FE) data set is listed in Appendix 7.

5.3.3 New Gravity Map of Sabah

The Sabah gravity data set, made up of the 1995, corrected USAMS(FE) and corrected Darvel Bay surveys, has been plotted on a map which also includes satellite marine gravity data (Figure 5.11). This map is interpreted in Chapter 6.

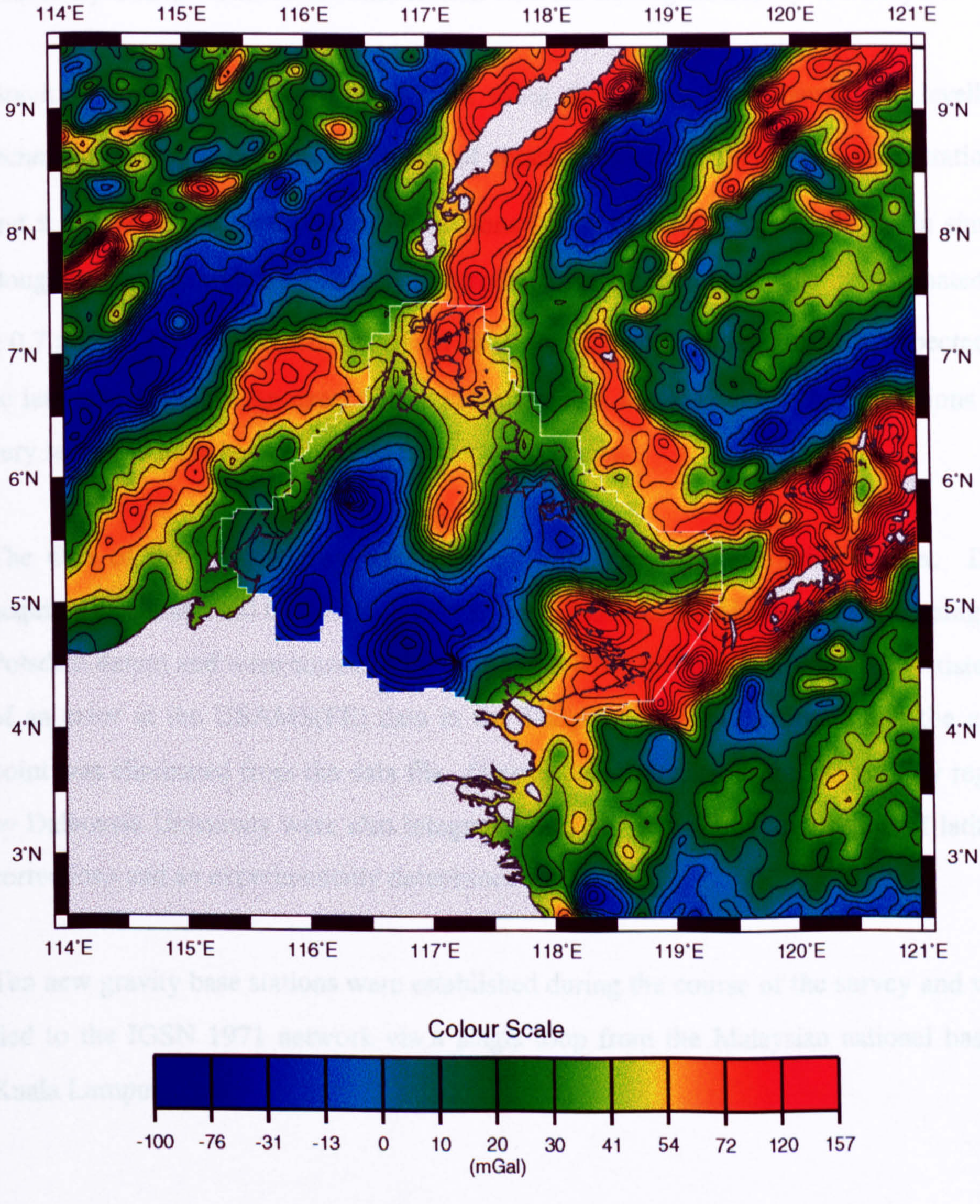

Figure 5.11. Sabah Gravity Anomaly Map. Free-air anomalies offshore, Bouguer anomalies onshore. 10 mGal contour interval.
White line delineates boundary.

5.4 Conclusions

Three hundred new gravity stations were established during a gravity survey of Sabah, East Malaysia, carried out during July and August 1995 by Rob Holt and John Milsom of University College London in collaboration with the Geological Survey of Malaysia.

Gravity station heights were established using the 'single base' barometric levelling technique, giving an estimated accuracy of about ± 2.5 metres for the low-lying stations, and ± 1.2 % of station elevation for stations in the Crocker Ranges. Errors in simple Bouguer gravity, which are largely controlled by elevation accuracy, are estimated at ± 0.7 mGal. Terrain corrections, which have not been applied, are generally expected to be less than 1 mGal. An exception is in the Crocker Ranges, where the corrections are very large and have been estimated very approximately.

The data of the 1995 survey were merged with the previously existing data. Data acquired in about 1960 by the USAMS(FE) were found to have been processed using the Potsdam datum and were corrected by applying a -13.7 mGal datum shift. The existence of an error in the USAMS(FE) data in the Telupid area was confirmed and the error point was eliminated from the data file. Gravity data collected in the Darvel Bay region by Dalhousie University were also integrated into the data set by application of latitude corrections and an experimentally determined datum shift.

Ten new gravity base stations were established during the course of the survey and were tied to the IGSN 1971 network via a single loop from the Malaysian national base in Kuala Lumpur.

CHAPTER 6

Interpretation of the Southeast Asian Gravity Field

CHAPTER 6. INTERPRETATION OF THE SOUTHEAST ASIAN GRAVITY FIELD

6.1 Introduction

Gravity measurements contain the basic data for investigations of the shape of the Earth and the structure and composition of its outer layers. The gravity anomaly data over Sundaland and its adjacent areas constitute a fundamental data set for systematic geological mapping and interpretation, mineral and petroleum exploration and resource assessment.

The two previously published regional interpretations of the gravity field of Sundaland (Angelich, 1986; Harder *et al.*, 1993) concluded that quantitative interpretation was at best unreliable owing to the poor quality of their data.

This chapter presents both qualitative and quantitative regional interpretations based on new high resolution gravity and bathymetry data. Section 6.2 discusses the modelling philosophy of this study. In Section 6.3, new free-air and Bouguer gravity maps are presented and discussed qualitatively. Section 6.4 presents a quantitative interpretation of the main features within the study area. Included in this section are models of the shelf edge anomaly, the gravity Moho, the South China Sea Oceanic Basin and Sabah. The principle conclusions drawn from this study and suggestions for future work are discussed in Section 6.5.

A map showing the locations of the major features discussed in this chapter is given in Figure 6.1.

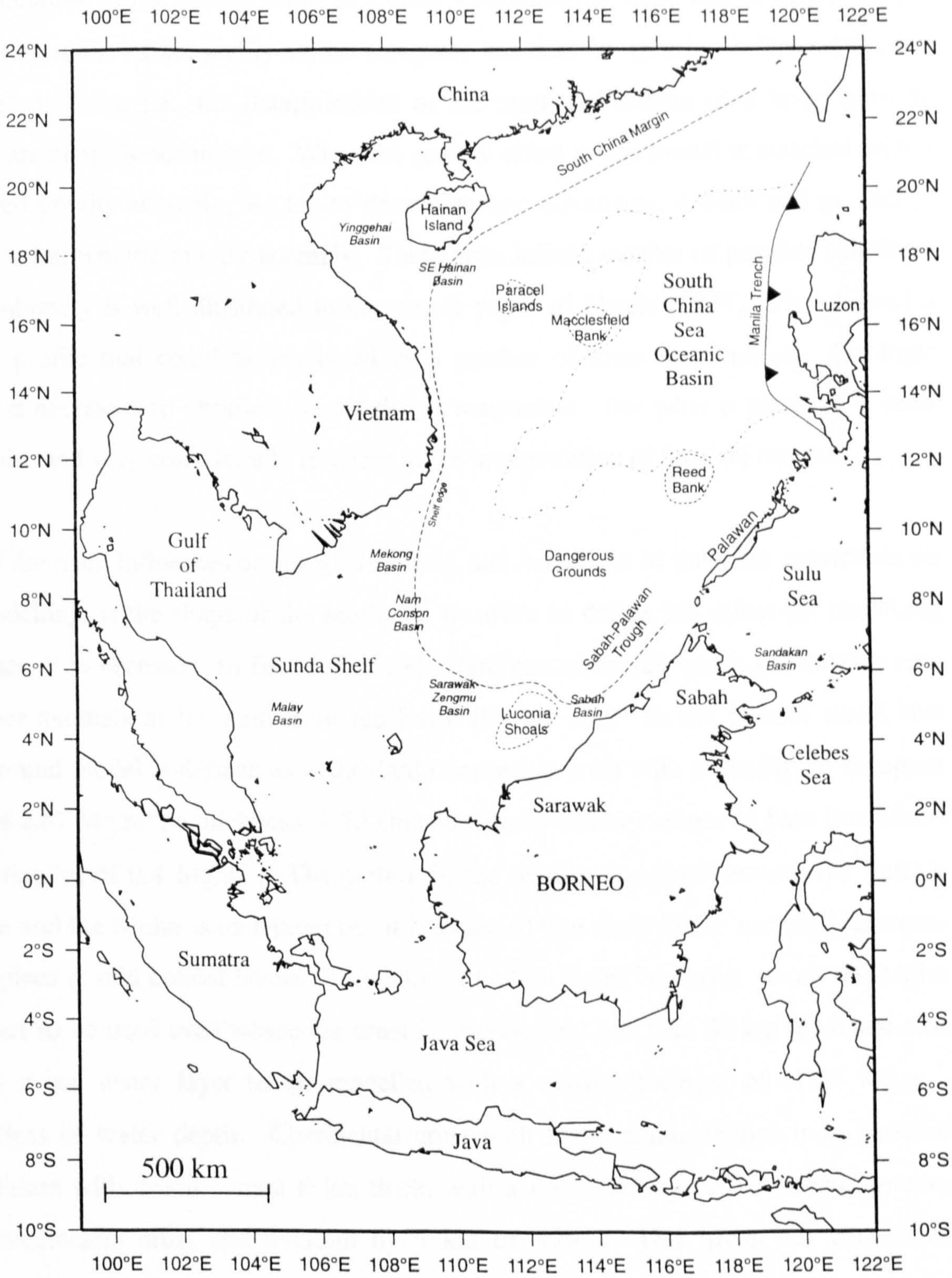

Figure 6.1. Map showing the locations of the principal features discussed in this chapter.

6.2 Gravity Interpretation

The calculation of the gravity effect of a body with a known shape and density is unique and can be made as accurately as the computer has time to spend. Unfortunately, the 'inverse' problem, i.e., the determination of the mass distribution of a body from its gravity anomaly, is not unique. When the gravity effect of the model is matched with a measured gravity anomaly, we try to determine two unknowns, density and geometry, from one known, the gravity anomaly. There is an infinite number of possible solutions. This ambiguity is well illustrated in the classic paper of Skeels (1947), who showed a gravity profile that could be produced by a number of mass distributions. Geologic insight is necessary to choose a model that is reasonable. But what is plausible is itself uncertain, and very considerable freedom in the interpretation of the data remains.

One of the main influences on the gravity field, and hence one of the main constraints on the modelling, is the shape of the seafloor. In order to define this effect for modelling purposes, it is necessary to first define a standard crustal model which produces a zero Bouguer anomaly at the surface of the Earth (Figure 6.2). In the present study, this background model is defined as a standard continental crust with a density, in its upper part, of 2.67 $Mg.m^{-3}$, a thickness of 30 km and density contrast across its base (the Moho discontinuity) of 0.4 $Mg.m^{-3}$. The pattern of the density variation between the Earth's surface and the Moho is undefined but it is assumed that most of the necessary increase takes place at mid crustal levels. This allows the 0.4 $Mg.m^{-3}$ contrast across the Moho interface to be used even where the crust is considerably less than 30 km thick and also allows a sea water layer to be modelled with a density contrast of -1.64 $Mg.m^{-3}$, regardless of water depth. Continental crust with these characteristics is in isostatic equilibrium with oceanic crust 6 km thick, with a mean density of 0.1 $Mg.m^{-3}$ greater than continental crust and overlain by 5 km of water. This gross but convenient oversimplification places some limits on the reliability of the deductions which can be drawn from the model studies but these are not usually of critical geological importance.

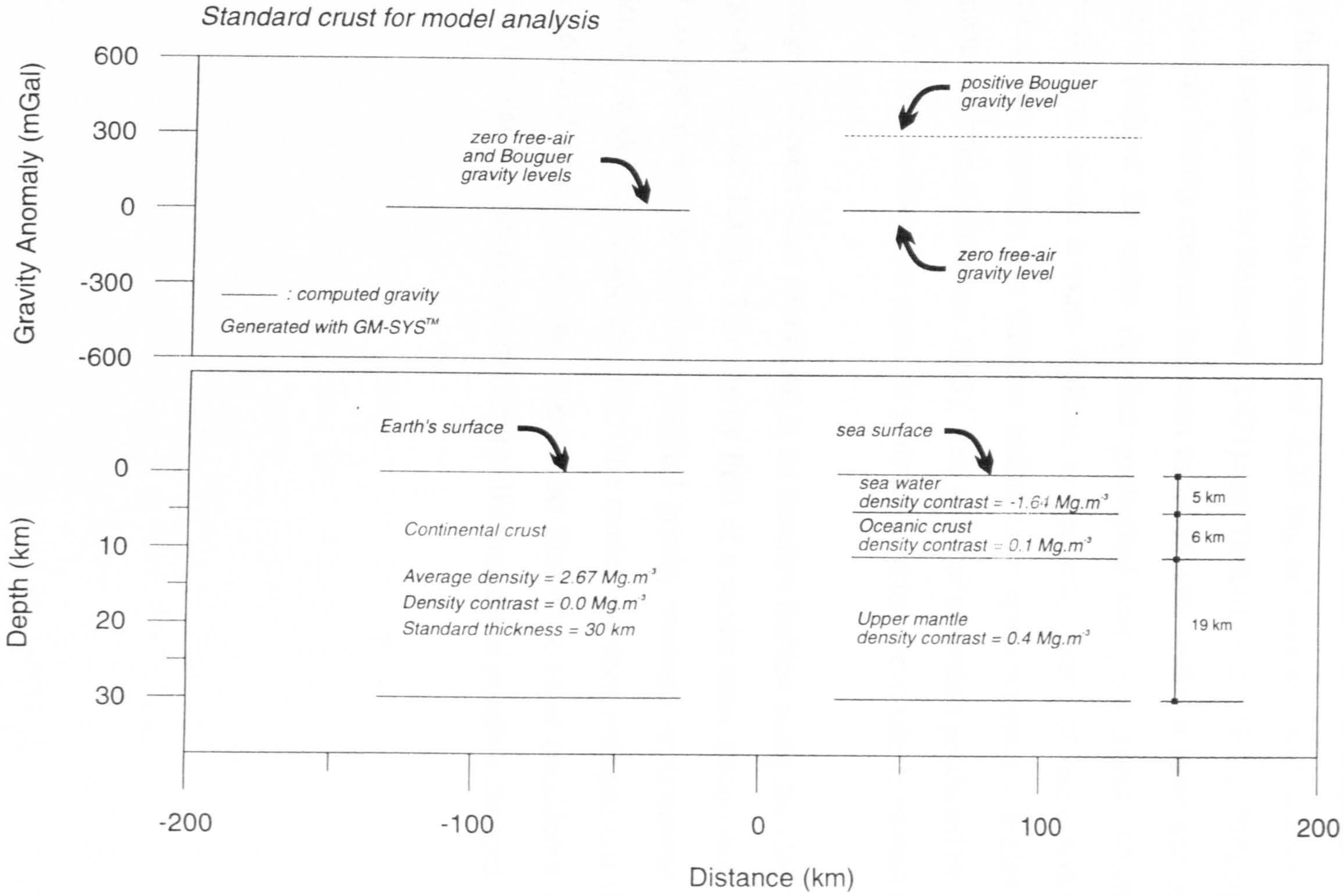

Figure 6.2. Standard crustal section used as the basis for analysing the gravity models in this study, after Sardjono (1996).

The geological control data available for constraining the models of this study were limited to published sections (CCOP, 1991), the 5 minute × 5 minute NGDC sediment isopach map (Section 1.3.3) and the TPI5.2 bathymetric data set (Section 1.3.2). No borehole data or seismic reflection sections were available. Thus the geological and geometrical information available for the sedimentary basins within the study area was very limited. A density contrast of -0.25 $Mg.m^{-3}$ was assumed between sediments and crust, as suggested by Nettleton (1971) and Telford *et al.* (1990). This figure represents the average density contrast between the sediments within a basin and the surrounding crust. Without far more detailed geological and geometrical information, it was impossible to create a more realistic or accurate model of these sedimentary basins because, for example, the different sedimentary types within the basins have different compaction rates (Lankester, 1993). The geological models produced by this study were therefore kept as simple as possible whilst honouring the available control data.

Geological models were developed in an iterative fashion using the GM-SYS computer program (Section 1.5.2). The gravity field of a model mass distribution was calculated and compared with the observed residual gravity anomaly to determine the effects for which the model could not account. The model was then changed and the calculations repeated until the differences became smaller than some value considered 'close enough'. Use of the standard density model limited the number of possible changes.

6.3 Southeast Asia Gravity Maps

The five gravity maps of Sundaland presented in this section cover an area of approximately 9.5×10^6 km^2 (99°E - 121°E, 10°S - 24°N). The maps were produced from the WGI7.2 and Sabah gravity data sets, ~~and~~ the TPI5.2 bathymetry data set.† Whilst many other gravity surveys have been collected in the region, none of these data were used in this study. The maps presented here are (1) regional marine free-air gravity anomaly map;× (2) regional Bouguer gravity anomaly map; (3) long wavelength gravity anomaly map; (4) residual marine free-air gravity anomaly map;× and (5) residual Bouguer gravity anomaly map - Figures ~~6.3 to 6.7~~ 6.3 to 6.5 and 6.7 to 6.8 respectively. On each of these maps, the coastline is marked by a black line, and areas with no data are coloured light grey.

† and the GEM-T3 long wavelength gravity model

× includes Bouguer anomalies over Sabah

6.3.1 Regional Free-Air Gravity Anomaly Map

Figure 6.3 shows the regional free-air gravity anomaly field compiled from the free-air marine gravity anomalies of WGI7.2, and the Sabah Bouguer gravity data. As discussed in Chapters 4 and 5, the maximum half-wavelength resolution and accuracy of the marine gravity anomalies are of the order of 10 km and 6 mGal respectively, and the accuracy of the Sabah gravity anomalies are better than 5 mGal.

The regional free-air gravity anomaly field is composed of gravity anomalies that arise from the water/crust interface, intra-crustal sources and deeper sources. The gravity field varies from -250 to +285 mGal. In general the map reflects the known tectonic trends of the area (Figure 2.1). Regions of low free-air gravity such as those southwest of Sumatra and Java, west of Luzon, and northwest of Sabah correspond to known bathymetric troughs. With the possible exception of the contentious Sabah-Palawan Trough, these troughs are generally accepted to correspond to former or active subduction zones. Other negative gravity anomalies are found over deep sedimentary basins, for example, the Southeast Hainan Basin and Maliau Basin (Figure 2.15). Other basins such as the Nam Conson Basin and the offshore Sandakan Basin show negligible gravity anomalies when anomalies in excess of -50 mGal would be expected, indicating

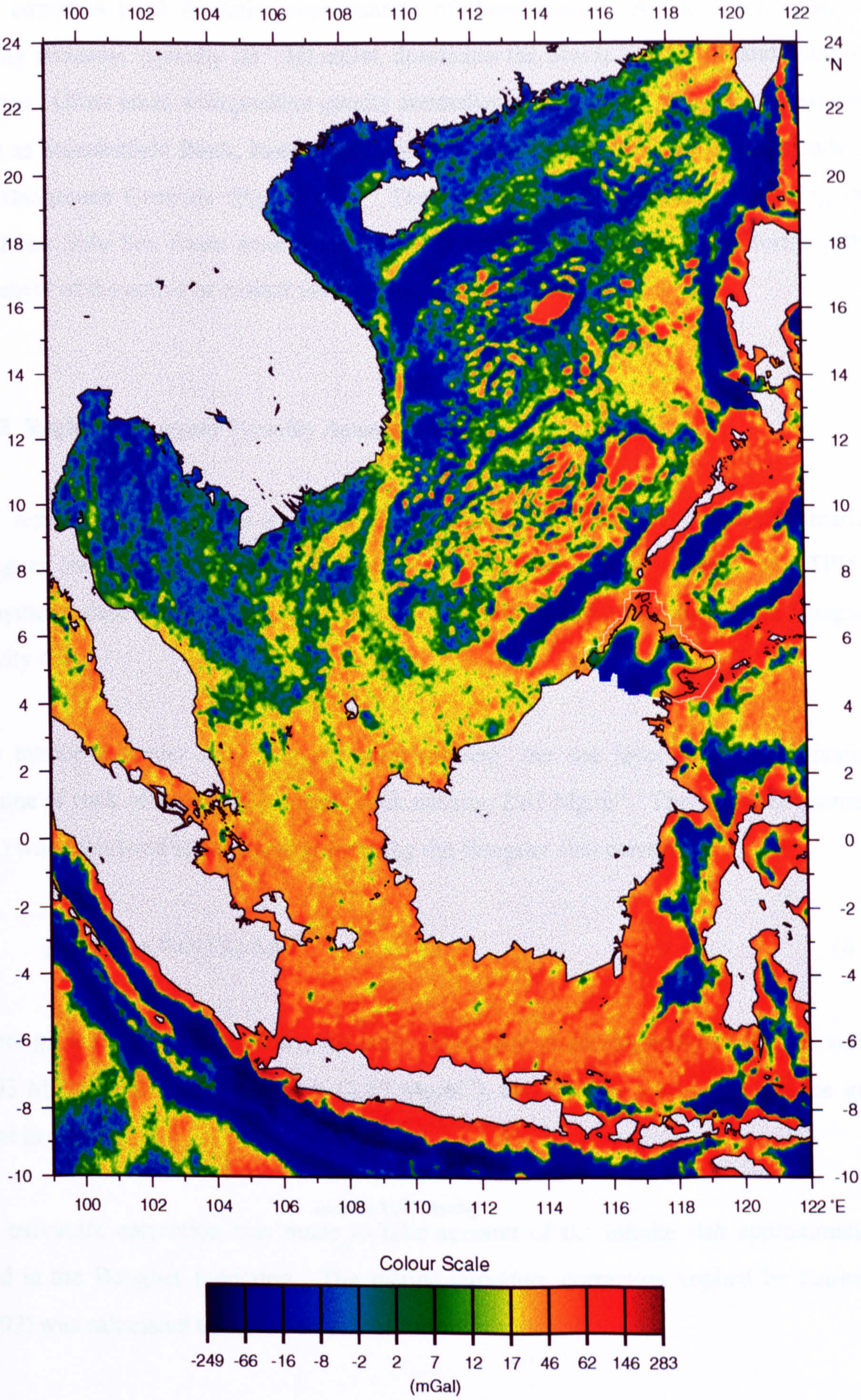

Figure 6.3. Regional Gravity Anomaly Map of Southeast Asia. Offshore: free-air gravity from WGI7.2. Onshore: Bouguer gravity. White line delineates boundary.

near complete local isostatic compensation of these basins. A widespread positive gravity anomaly, typically 20 - 60 mGal, dominates the Sunda Shelf west and south of Borneo. Other areas with positive gravity anomalies correlate with bathymetric features, such as Macclesfield Bank, Reed Bank, Palawan and the numerous reefs and islands of the Dangerous Grounds (Figure 6.1). The positive gravity anomalies enclosing the southeast Sulu Sea Basin arise from the dense material of oceanic origin forming the basement of the active or extinct volcanic arcs in these areas.

6.3.2 Regional Bouguer Gravity Anomaly Map

The regional Bouguer gravity anomaly map shown in Figure 6.4 includes marine Bouguer anomalies calculated from the WGI7.2 free-air gravity anomaly and TPI5.2 bathymetry data sets (which are collocated on 2-minute grids), and the Sabah Bouguer gravity data.

The marine Bouguer reduction involved 'infilling' the sea layer with an equivalent volume of rock of mean upper crustal rock density, 2.67 $Mg.m^{-3}$. The Bouguer anomaly (g_{Ba}) was calculated at each grid point using the Bouguer slab correction:

$$g_{Ba} = g_{fa} + 0.04192.\Delta\rho.h \qquad (6.1)$$

where g_{fa} is the free-air anomaly, $\Delta\rho$ is the difference in density between the sea water (1.03 $Mg.m^{-3}$) and the upper crust (2.67 $Mg.m^{-3}$), and h is the water depth at the grid point in metres.

No curvature correction was made during this study to take account of the infinite slab approximation used in the Bouguer reduction. The marine curvature correction applied by Fairhead (1992) was calculated using the empirical formula:

$$-6.40427 \times 10^{-4}\, h - 1.54751 \times 10^{-7}\, h^2 - 4.06303 \times 10^{-14}\, h^3 \text{ mGal} \qquad (6.2)$$

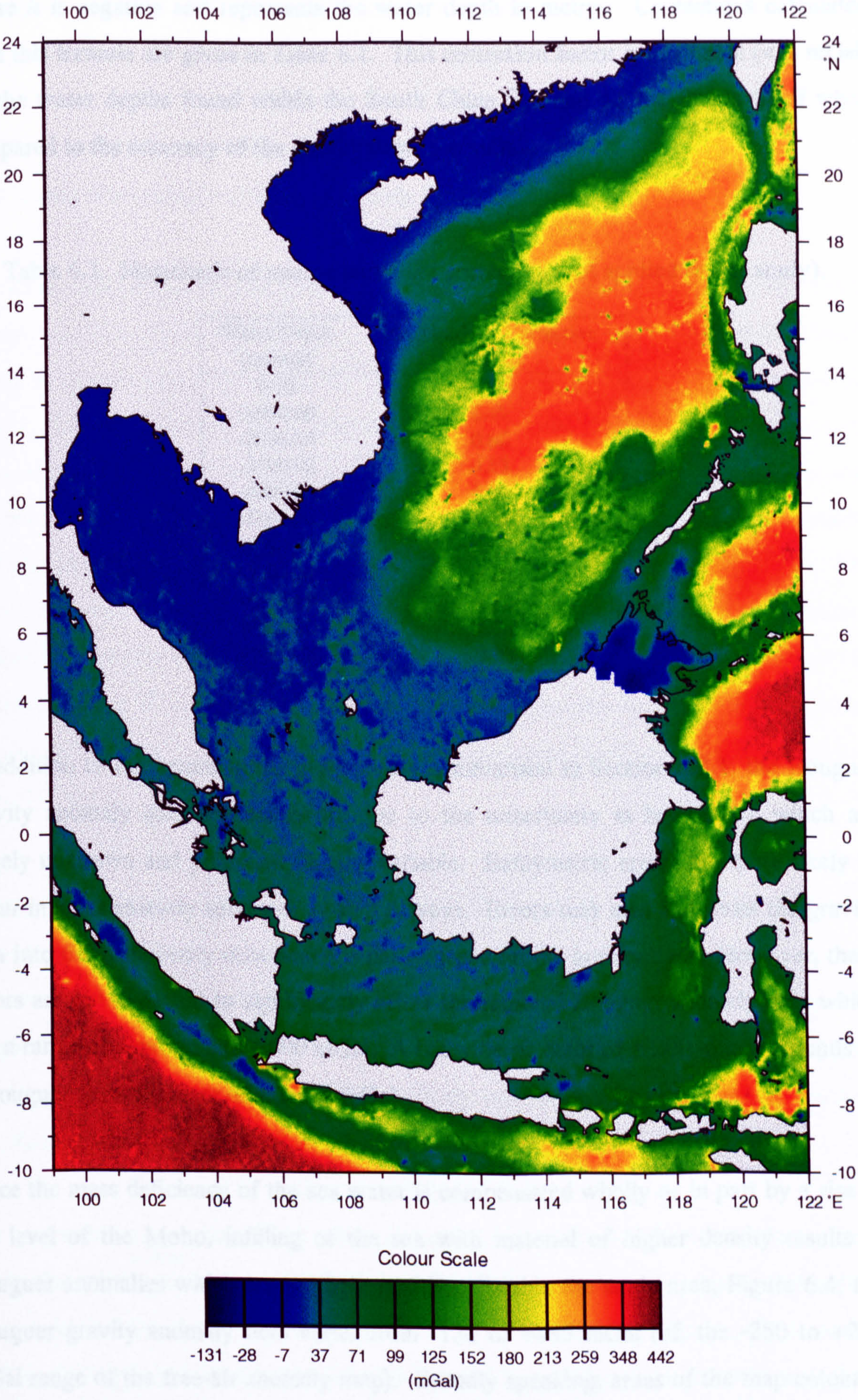

Figure 6.4. Regional Bouguer Gravity Anomaly Map of Southeast Asia.

where h is negative and represents the water depth in metres. Corrections calculated from this formula are given in Table 6.1. This correction factor is negligible (< 1 mGal) for the water depths found within the South China Sea and on the Sunda Shelf when compared to the accuracy of the gravity data (± 6 mGal).

Table 6.1. Magnitude of marine curvature correction (not applied in this study).

Water Depth (metres)	Magnitude of Correction (mGal)
0.00	0.00
-1000.00	0.49
-2000.00	0.66
-3000.00	0.53
-4000.00	0.09
-5000.00	-0.66
-6000.00	-1.72
-7000.00	-3.09
-8000.00	-4.76
-9000.00	-6.74
-10000.00	-9.03

In addition to the errors in the gravity data summarised in Section 6.3.1, the Bouguer gravity anomaly data contain errors due to the uncertainty in bathymetry which are largely unknown and potentially highly variable. Bathymetric errors are more likely to occur in areas sparsely surveyed by ship surveys. Errors may also leak from the gravity data into the bathymetry data which is partly based on the gravity data. However, these errors are not expected to significantly affect the regional Bouguer anomaly map which has a range of approximately 600 mGal. A bathymetric error of ± 200 m corresponds to a Bouguer anomaly error of ± 13.75 mGal.

Since the mass deficiency of the sea water is compensated wholly or in part by a rise in the level of the Moho, infilling of the sea with material of higher density results in Bouguer anomalies which are strongly positive. Within the study area, Figure 6.4, the Bouguer gravity anomaly field varies from -130 to +445 mGal (cf. the -250 to +285 mGal range of the free-air anomaly map). Broadly speaking, areas of the map coloured dark blue to turquoise are interpreted as areas of thick, relatively unstretched continental crust. Areas coloured green to yellow are interpreted as areas of highly attenuated and

stretched continental crust. Areas coloured red correlate with areas underlain by oceanic crust.

6.3.3 Long Wavelength Gravity Anomaly Map

In general, the longest wavelengths of the gravity anomaly field are dominated by density distributions that are an aspect of the very large-scale convective processes not closely linked to present day plate tectonics. These density anomalies are both deep and old (Chase, 1985). Global comparisons of tectonic features with gravity anomalies for harmonics $6 \leq n \leq 16$ show that positive anomalies mark trench and island arcs, as well as oceanic rises, while negative gravity is typical of both oceanic and continental basins. Oceanic spreading centers do not have a very conspicuous signature (Kaula, 1972). The gravity or geoidal anomaly that results from plate subduction will depend on a delicate balance between the driving density contrasts and the warping of density interfaces. The anomaly occurs in a wide strip surrounding the subduction zone and can be either positive or negative depending on the boundary conditions (McKenzie, 1977; Parsons & Daly, 1983).

A long wavelength gravity anomaly map of Southeast Asia (λ_{min} = 800 km), derived from the GEM-T3 model (Section 1.3.4), is shown in Figure 6.5. Within the study area (enclosed by the purple box on Figure 6.5), the long wavelength gravity anomaly field ranges from -22 to +50 mGal. The Sunda craton is characterised by a slightly negative to zero gravity anomaly. A large positive gravity anomaly lies beneath Borneo, the Java Sea, Sulawesi and the Celebes Sea. Elsewhere the gravity field is slightly positive.

The long wavelength gravity field within the study area is dominated by the effects of the subduction of the Indian, Australian and Philippine Sea Plates and the proto-South China Sea. Clear evidence for these subduction events can be seen in the tomographic inversion results of Widiyantoro & Van der Hilst (1996) for Indonesia, which are shown at three depth slices (the upper mantle, transition zone and lower mantle) in Figure 6.6. In Figure 6.6, areas found to have anomalously high velocities are coloured blue. These areas are

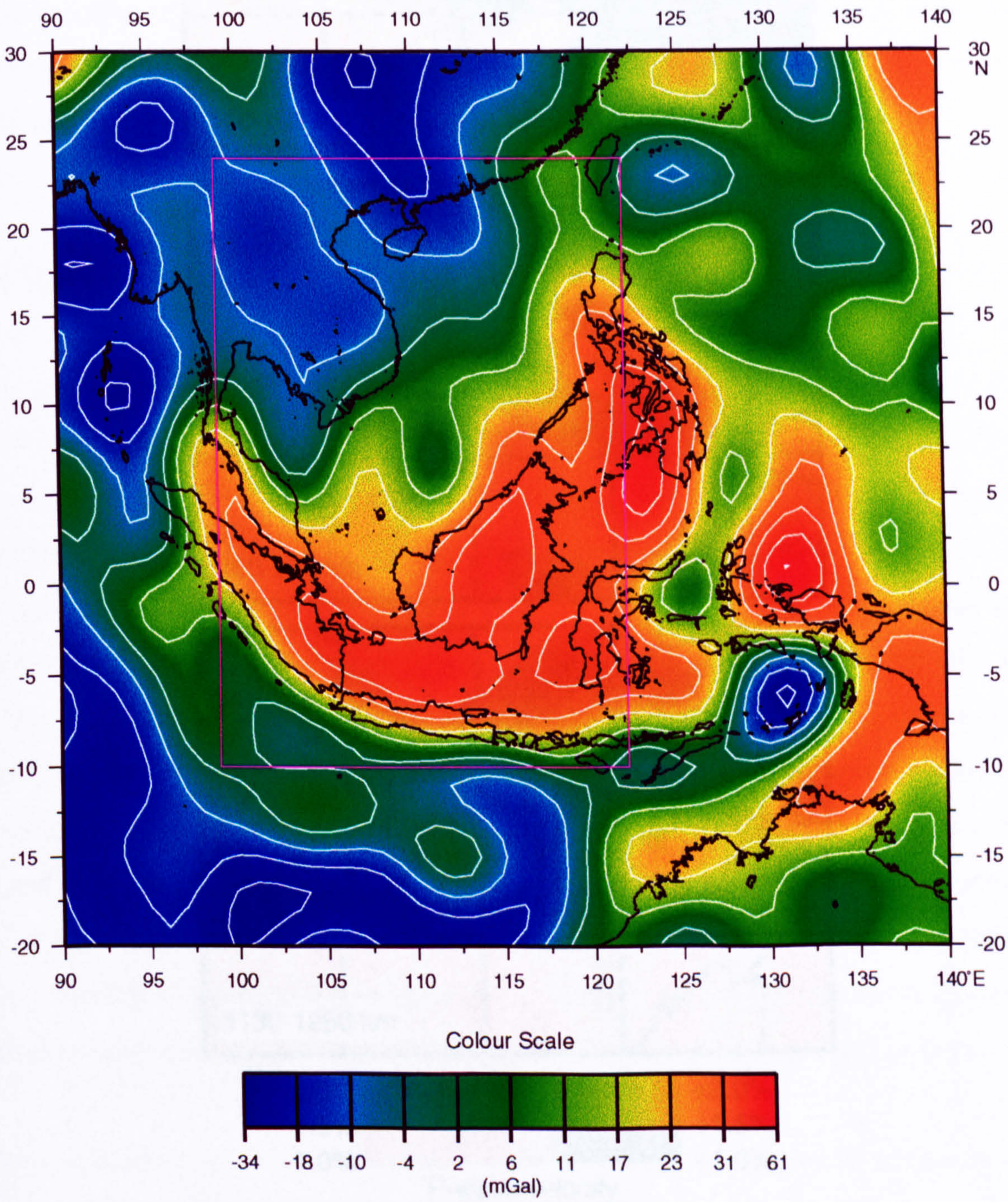

Figure 6.5. The long wavelength gravity anomaly field of SE Asia from the GEM-T3 model. Purple box delineates study area. 10 mGal contour interval.

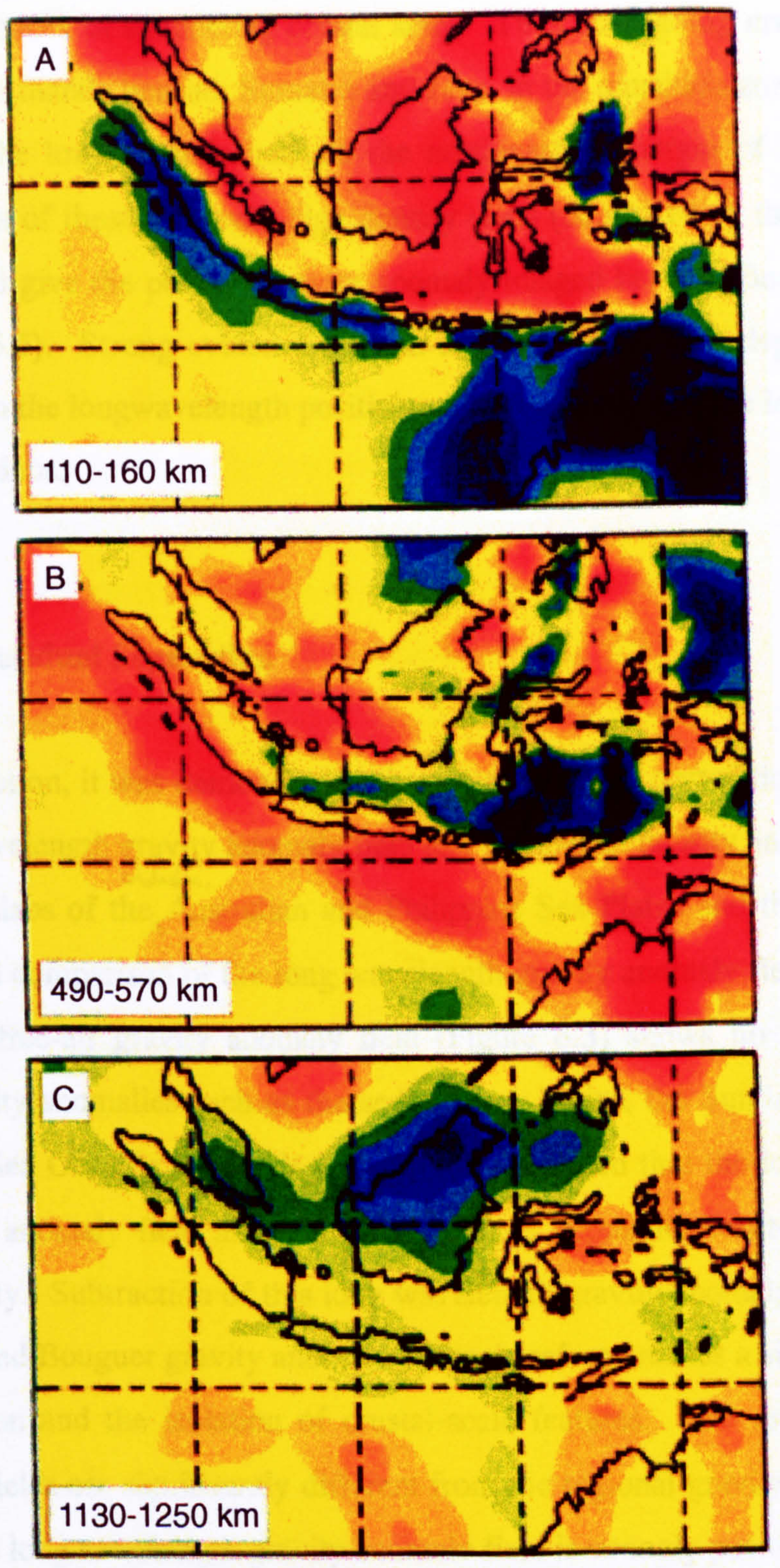

Figure 6.6. Layer anomaly maps depicting results of tomographic inversion for SE Asia. Blue (red) depicts high (low) P-wave velocity. (A) Upper mantle. (B) Transition zone. (C) Lower mantle. Blue areas interpreted as traces of subducting slabs. From Widiyantoro & Van der Hilst (1996).

interpreted as the traces of subducting crustal slabs. Thus downgoing crustal slabs are imaged in the upper mantle beneath Sumatra and Java, in the transition zone beneath the Java Sea, and in the lower mantle beneath the northwestern margin of Borneo. The gravitational effects of these relatively high density slabs (compared to the surrounding mantle) combine to give the positive gravity anomaly imaged beneath Borneo, Sumatra and Java (Figure 6.5). Strong evidence for this is given by the high degree of spatial correlation between the longwavelength positive gravity anomaly and the locations of the subducted crustal slabs.

6.3.4 Regional-Residual Separation

In the previous section, it was demonstrated that there is a high correlation between the GMT-T3 long wavelength gravity anomaly field and the mantle density anomalies arising from the sunken slabs of the Indian, Australian and Philippine Sea Plates and the proto-South China Sea. Visual comparison of the long wavelength gravity anomaly field (Figure 6.5) and the regional free-air gravity anomaly field (Figure 6.3) shows no correlation for crustal scale density anomalies such as the sedimentary basins, the Sunda Shelf edge or the South China Sea Oceanic Basin. It is therefore concluded that the long wavelength GEM-T3 gravity anomaly field arises fully from mass anomalies located beneath the Moho discontinuity. Subtraction of this long wavelength gravity anomaly field from the regional free-air and Bouguer gravity anomaly fields therefore enables a simple 'regional-residual' separation and the isolation of crustal-scale features. The resulting residual gravity anomaly fields are significantly different from the regional gravity anomaly fields in areas where the long wavelength gravity anomaly field is strongly positive or negative. Failure to subtract this regional component of the gravity field prior to interpretation would result in significantly different geological models in areas where the regional field is strong, for example, Sabah. The quantitative interpretations of this study (Section 6.4) are therefore based on the interpretation of the residual gravity anomaly field.

6.3.5 Residual Gravity Anomaly Maps

The residual free-air gravity anomaly field, Figure 6.7, was obtained simply by subtracting the GEM-T3 long wavelength gravity anomaly field from the regional free-air gravity anomaly field. The residual free-air gravity anomaly map may be directly compared with the regional free-air gravity anomaly map (Figure 6.3) as both maps have the same colour scale. As with all colour gravity maps, the amount of detail visible in a particular area depends on the colour scale. Less detail over Sabah is discernible on Figure 6.7 than on Figure 6.3 purely as a result of the reduction in values of the Sabah gravity anomalies and their consequent saturation on the blue side of the spectrum. The residual gravity anomaly map is however significantly different from the regional free-air gravity anomaly map at the southern end of the Sunda Shelf, because the residual field is significantly lower there (by ~ 30 mGal). The South China Sea Oceanic Basin is also more clearly resolved and has a more uniform, smooth gravity signature.

The residual Bouguer gravity anomaly field, Figure 6.8, was obtained simply by subtracting the GEM-T3 long wavelength gravity anomaly field from the regional Bouguer gravity anomaly field. Again the residual map may be directly compared with the regional map (Figure 6.4) as both maps have the same colour scale. The maps only significantly differ at the southern end of the Sunda shelf. The residual Bouguer anomaly map indicates that the entire Sunda Shelf is underlain by continental crust of a broadly uniform thickness.

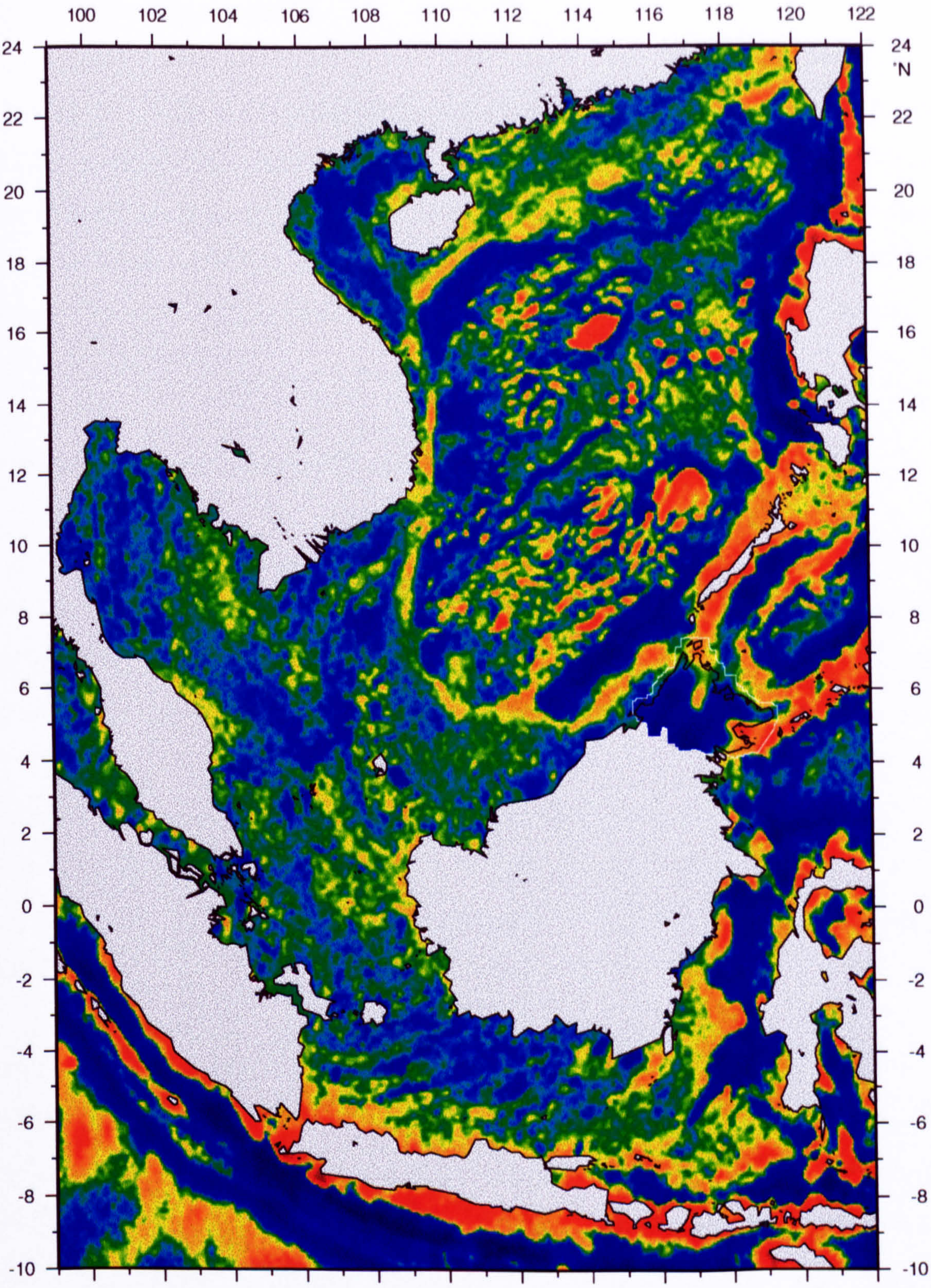

Figure 6.7. Residual Gravity Anomaly Map of Southeast Asia. Offshore: free-air gravity from WGI7.2. Onshore: Bouguer gravity. White line delineates boundary.

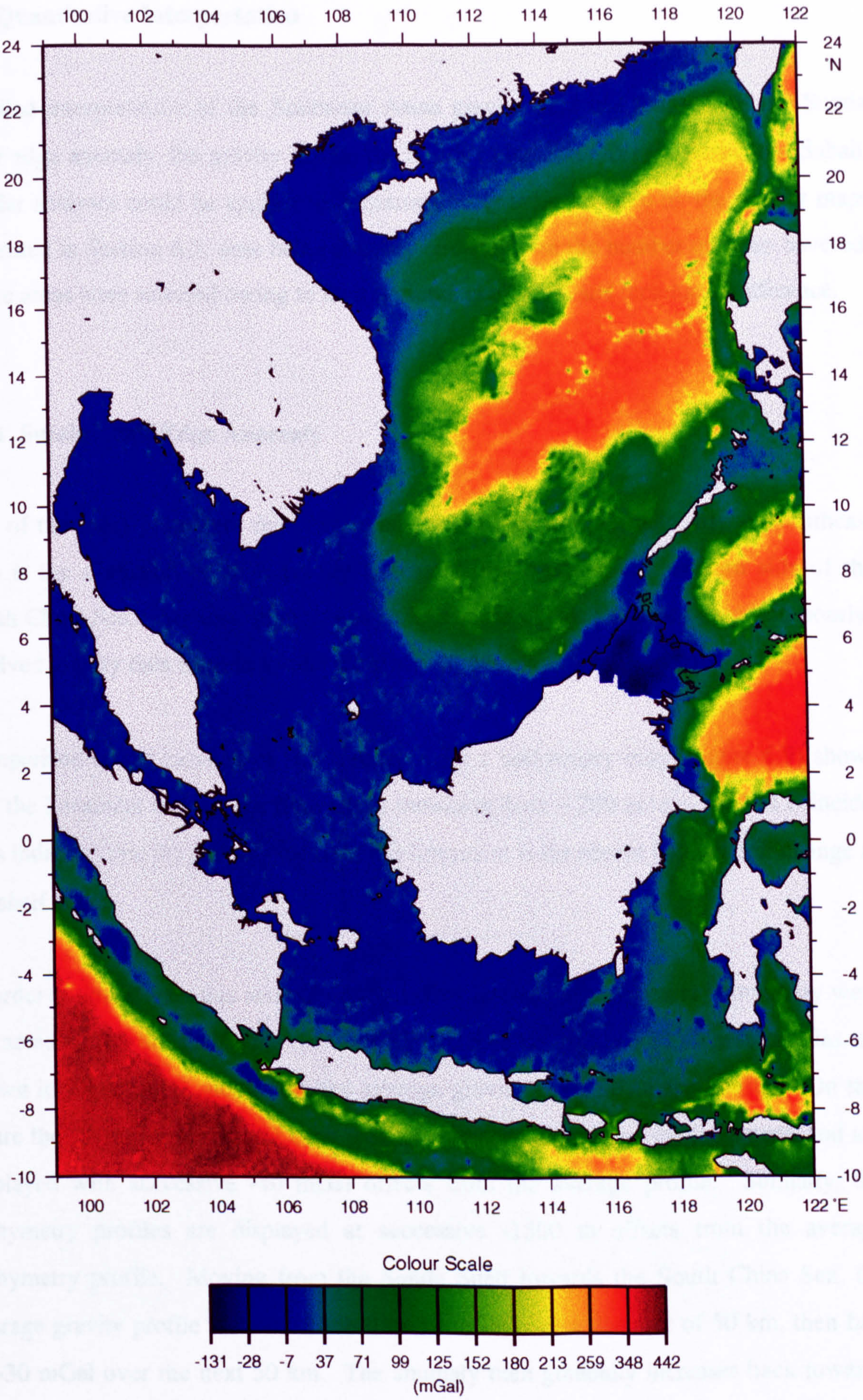

Figure 6.8. Residual Bouguer Gravity Anomaly Map of Southeast Asia.

6.4 Quantitative Interpretation

Detailed interpretation of the Southeast Asian gravity field has focused on the Sunda Shelf edge anomaly, the gravity Moho, the South China Sea Oceanic Basin, and Sabah. Similar analyses could be applied to numerous other areas covered by the gravity maps presented in Section 6.3, time being the only constraint on the number of areas covered. These areas were selected owing to their regional geological and tectonic significance.

6.4.1 Sunda Shelf Edge Anomaly

One of the most prominent features on any free-air gravity anomaly map of Southeast Asia is the *C*-shaped positive gravity lineament that encircles the western side of the South China Sea. Previous suggestions for the cause of this lineament based on poorly-resolved gravity data include a volcanic chain (R. Murphy, *pers. comm.*).

Comparison of the location of this anomaly with a bathymetry map (Figure 6.9) shows that the lineament and the sea floor depth transition from ~ 200 m to ~ 1000 m coincide. This indicates that the primary cause of the lineament is the abrupt bathymetric change at the shelf edge.

In order to investigate this anomaly further, five profiles of gravity and bathymetry were extracted across the shelf edge (Profiles SE1 to SE5 on Figure 6.9). These profiles are shown in Figure 6.10, along with the average gravity and bathymetry profiles. On this figure the gravity anomalies of each profile have been aligned on the lineament, and are displayed with successive -40 mGal offsets from the average profile. Similarly, the bathymetry profiles are displayed at successive -1500 m offsets from the average bathymetry profile. Moving from the Sunda Shelf towards the South China Sea, the average gravity profile increases from 0 to 30 mGal over a distance of 50 km, then falls to -30 mGal over the next 50 km. The anomaly then gradually increases back towards

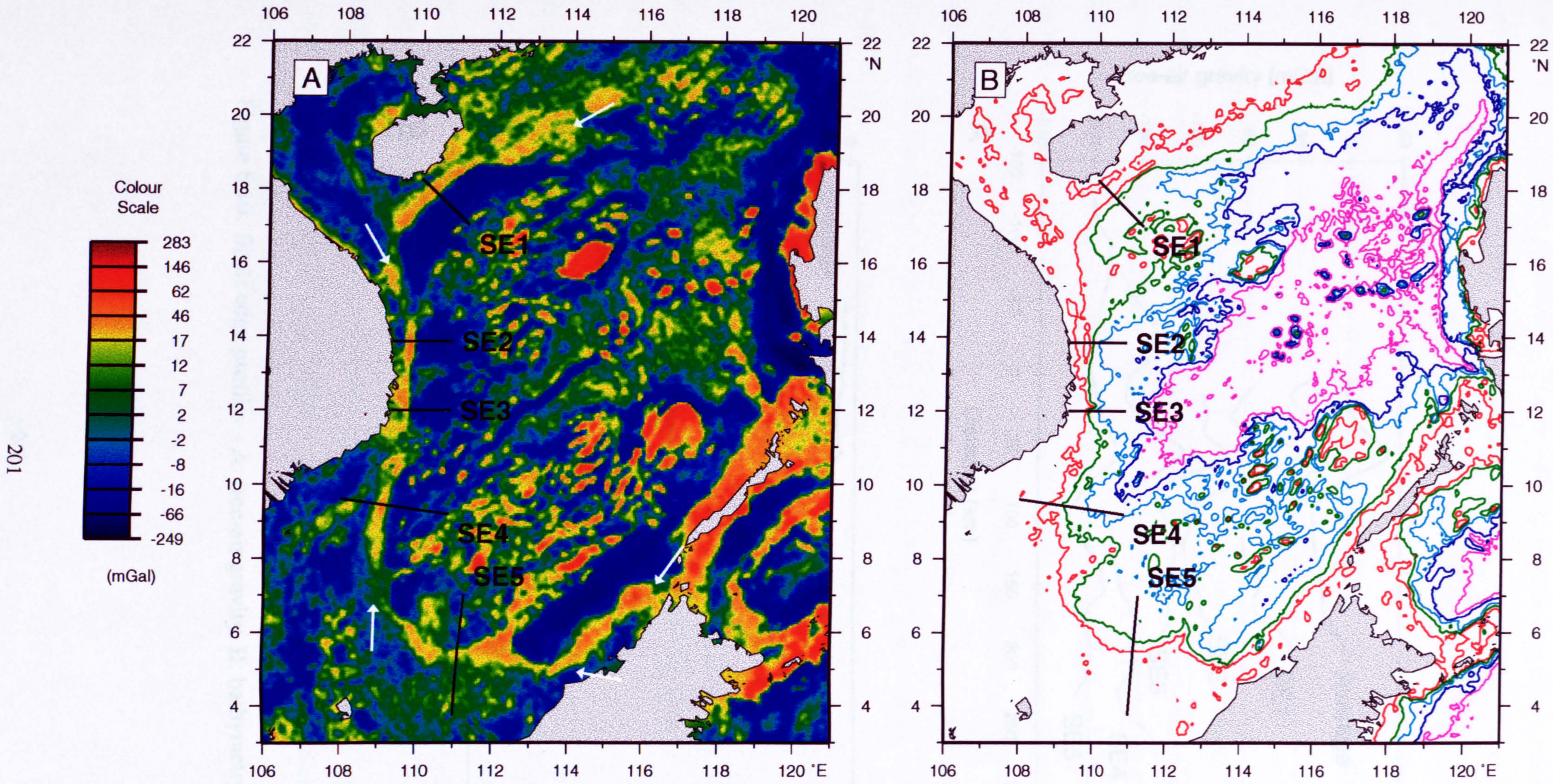

Figure 6.9. Gravity anomaly at Sunda Shelf edge (position indicated by white arrows). A: Residual free-air gravity anomaly map. B: TPI5.2 bathymetry map, contours: 200m, red; 1000m, green; 2000m, light blue; 3000m, dark blue; 4000m, purple.

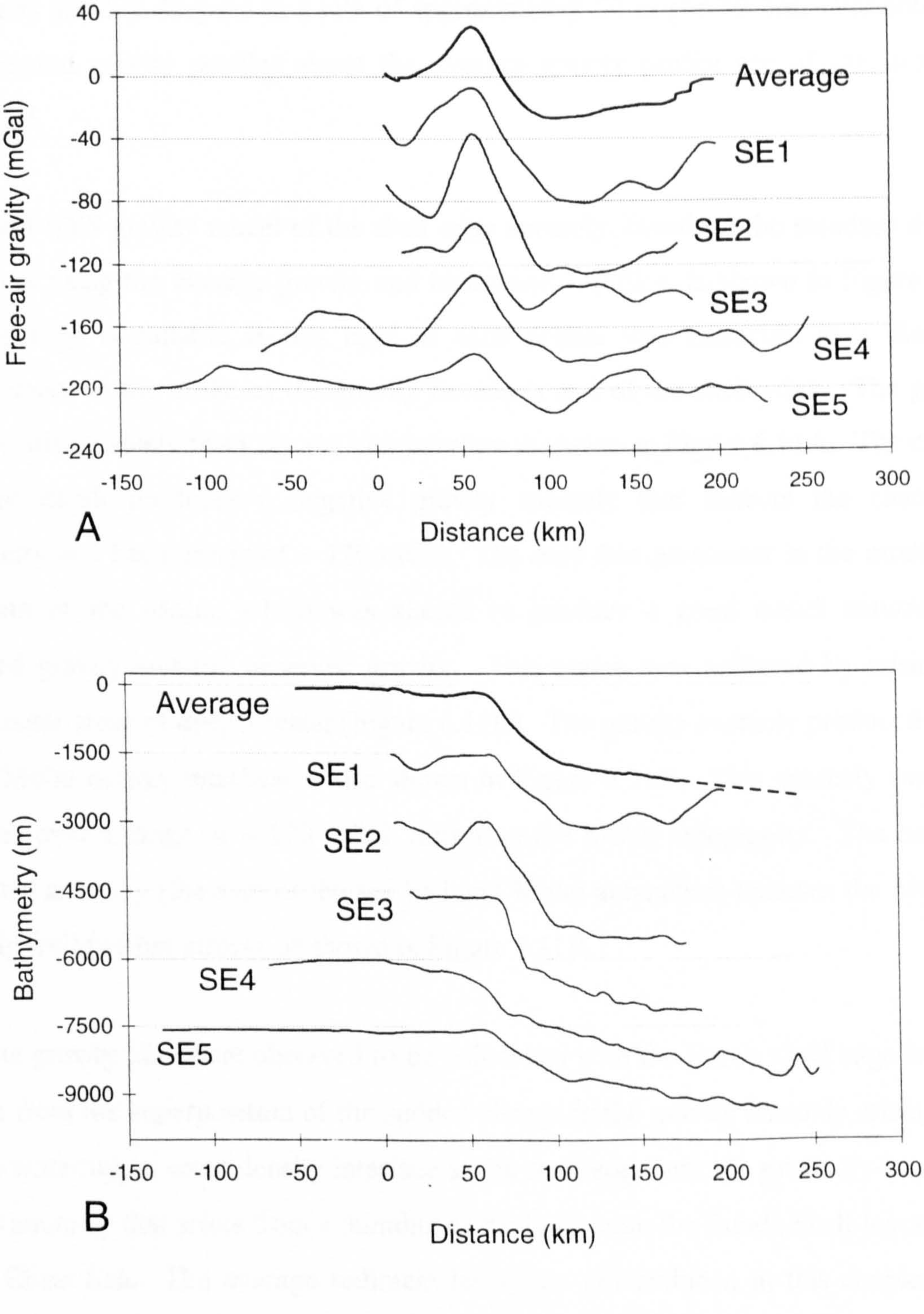

Figure 6.10. Shelf edge profiles - A: free-air gravity, B: bathymetry.

0 mGal over a distance of 100 km. The bathymetry approaching the South China Sea gradually deepens to ~ 200 m below the peak of the gravity anomaly, then sharply deepens to ~ 1700 m over the next 50 km. Moving further into the South China Sea, the bathymetry steadily deepens at a rate of approximately 50 m per 10 km. Variations of the measured gravity profiles about the average gravity profile are of the order of ± 15 mGal.

A 2D GM-SYS gravity model of the shelf edge anomaly, based on the standard density model and using the average gravity and bathymetry profiles, is shown in Figure 6.11. 2D modelling is suitable in this case as each profile was extracted in a direction perpendicular to the strike of the gravity lineament and of the shelf edge. The gravity anomaly arising solely from the sea bed interface is shown in Figure 6.11A. The change in water depth produces a negative gravity anomaly that mirrors the change in bathymetry and has a range of ~ 120 mGal. The only free parameter in the model was the depth of the Moho, which was altered to produce a good match between the modelled gravity and the observed gravity. This match was achieved by raising the Moho under areas of deeper water (Figure 6.11C). The gravity anomaly produced solely by the Moho density interface is also shown in Figure 6.11A. This anomaly smoothly increases over a range of ~ 120 mGal, mirroring the Moho topography. The resultant calculated anomaly (the sum of the sea bed and Moho anomalies) matches the observed anomaly well (within errors), as shown in Figure 6.11B.

Thus the gravity lineament observed to be coincident with the Sunda shelf edge is found to arise from the superposition of the sudden change in the gravity anomaly arising from the sea water/upper crust density interface at the shelf edge and the gradually-increasing gravity anomaly that arises from a thinning of the crust from the Sunda Shelf towards the South China Sea. The average sediment layer was not included in this simple model since it represents a relatively minor density anomaly that, to a first approximation, has a constant thickness along the average profile.

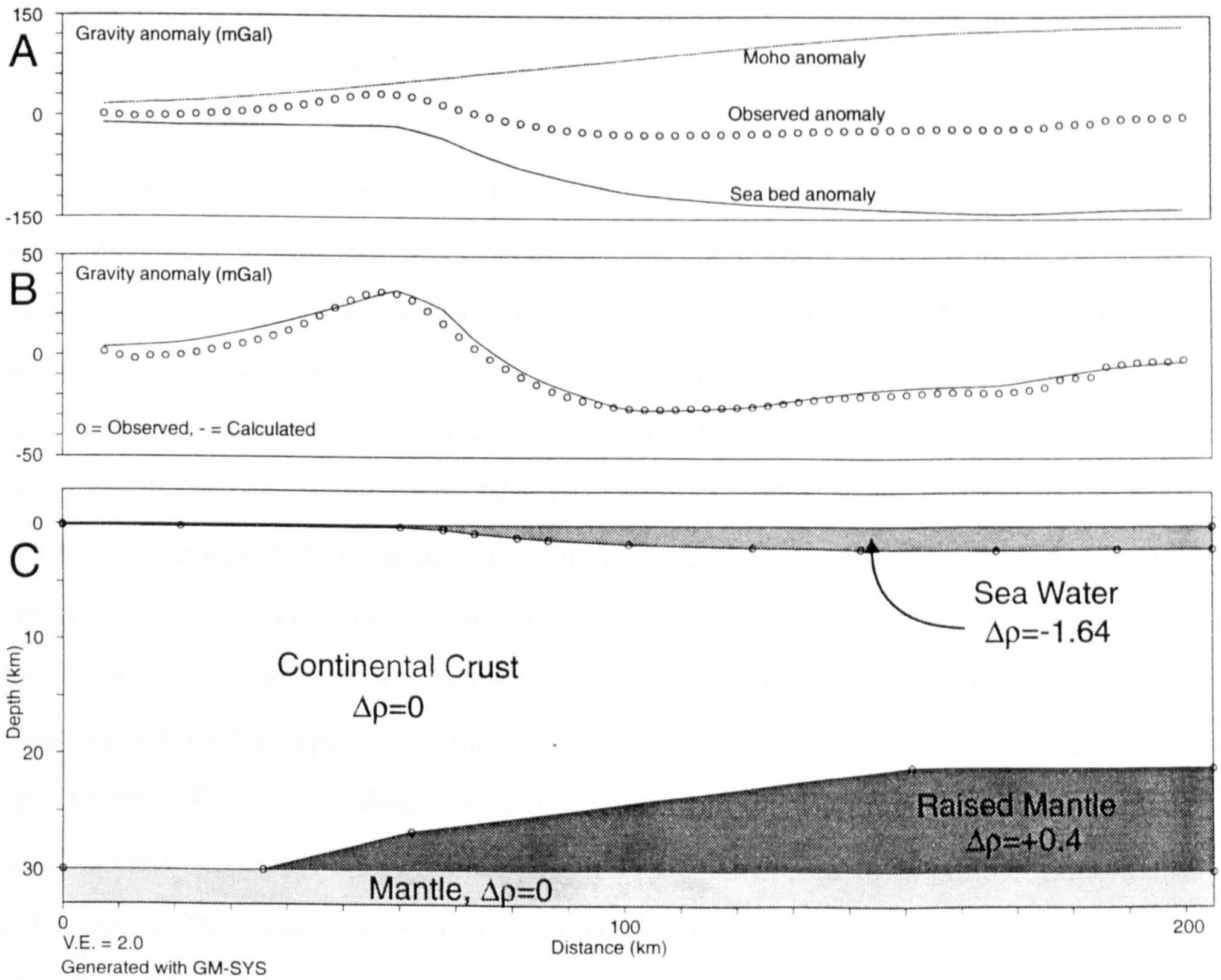

Figure 6.11. Gravity model of shelf edge anomaly using observed free-air gravity and bathymetry from average of Profiles SE1 to SE5. A: the gravity anomaly contribution of the Moho interface and the sea bed interface. B: the observed and calculated anomalies agree well. C: the geological model.

This model, based on the average of five profiles spread over a distance of 1500 km at the western edge of the South China Sea, shows a gradual thinning of the continental crust at the shelf edge, rather than a sudden change. This indicates a certain degree of regional compensation and thus crustal strength across the shelf edge.

It is likely that a similar anomaly exists within the Sulu Sea, obscuring, for example, the gravity low associated with the offshore extension of the Sandakan Basin (Figure 6.37).

It should be noted that analysis of an averaged gravity profile over the South China Sea shelf edge yields results lacking in the geological detail that one would expect to derive from well-constrained interpretations of individual gravity profiles. Elsewhere, detailed analyses have been carried out over the Hatton Bank, South Africa, Nova Scotia, Gabon, East Coast, USA, Brazil (Campos basin), Goban Spur, Carolina and Valencia Trough (Western Mediterranean) margins (Watts & Fairhead, 1997). These analyses were based on gravity modelling, flexural backstripping and crustal balancing studies, and show that rifted margins can be divided into two main groups: wide (> 250 km) and narrow (< 75 km) rifts. Narrow margins are represented by Hatton Bank, Valencia Trough, Carolina and Goban Spur; wide margins by the East Coast, USA, Gabon, South Africa and Brazil. There is evidence from both the narrow (e.g. Carolina) and wide rifts (e.g. Gabon, Brazil and Nova Scotia) that the locus of crustal thinning is not necessarily confined to the continental/ocean boundary region but may occur some distance landward of the boundary.

The reason why the pattern of crustal thinning varies so much along the strike of rifted margins is not well understood. According to the model of Buck (1991), narrow rifts form when the lithosphere is initially cold; wide rifts form when it is warm. Bassi *et al.* (1993) have shown, however, that in the case of large amounts of extension the patterns of rifting are a complex function of continental geotherm, lithospheric composition and strain rate. Other factors such as the presence of significant amounts of magmatism may serve to focus rifting (Watts & Fairhead, 1997). If good control data (such as seismic sections) were to become available, then detailed modelling of the significant crustal variation observed along the South China Sea shelf edge may potentially help clarify this uncertainty.

6.4.2 Crustal Variations on the Northern Sunda Shelf and Within the South China Sea

6.4.2.1 Overview

Inversion of the WGI7.2 satellite gravity data set has resulted in maps of the depth to Moho, crustal thickness and β (crustal extension) factor covering the northern Sunda Shelf and South China Sea (99°E - 124°E, 0° - 25°N). Prior to inversion, the effect of long-wavelength deep-sourced gravity anomalies (mainly sunken slabs) was removed from the gravity field by subtraction of the GEM-T3 long wavelength gravity anomaly field. Sediment isopach and bathymetry data provide the control data. The modelling was mainly concerned with the position of the Moho which was located by one-dimensional inversion of the gravity data assuming a 30 km thick reference crust and Airy isostasy. A comparison with seismic refraction depth to Moho estimates along the south China margin shows excellent agreement. Comparison of β values with independent unpublished β values from basin subsidence analyses also showed good agreement. The Moho rises from an average depth of approximately 29 km under the Sunda Shelf to a minimum of ~ 16 km below the South China Sea oceanic basin. An estimate has been made of the lateral extent of the proto-South China Sea which has since been destroyed by subduction.

6.4.2.2 Introduction

The northern Sunda Shelf and the South China Sea lie at the heart of the collision zone between the Indian, Australian, Philippine Sea and Eurasian Plates. As described in Chapter 2, the region has experienced extensive deformation throughout the Cenozoic by compressional, extensional and rotational forces. Extensional and strike-slip sedimentary basins are found on the northern Sunda Shelf and margins of the South China Sea. The extensional South China Sea Oceanic Basin occupies the central part of the South China Sea. A subduction zone is located at the eastern margin of the South China Sea. It is postulated that subduction also occurred at the southern margin of the South China Sea (e.g. Milsom *et al.*, 1997).

This study is based on one dimensional gravity modelling of the observed gravity anomaly field, where attention is focused on the topography of the Moho. The model is based on data extracted from the WGI7.2 gravity data set (Section 1.3.1), the GEM-T3 long wavelength gravity model (Section 1.3.4), the NGDC sediment isopach map (Section 1.3.3) and the TPI5.2 bathymetry data set (Section 1.3.2). The study is confined to the offshore area (99°E - 124°E, 0° - 25°N).

Previous regional gravity modelling within this area has been very limited, owing to the poor quality of the gravity data available at the time. A map of the gravity Moho produced by the Chinese in 1987 will be discussed later. The accuracy of the depth to Moho estimates of this study was analysed quantitatively by comparison with expanding spread profile (ESP) seismic refraction data from the south China margin (Section 6.4.2.9).

6.4.2.3 Gravity Data

The gravity interpretation presented here is based on the residual free-air gravity anomaly map discussed in Section 6.3.5. The residual free-air gravity anomaly field is generally observed to be near zero indicating a state of near-isostatic equilibrium. Because there are considerable near surface density variations which require compensation, this provides evidence that significant Moho topographic variations should be found.

6.4.2.4 Densities

With no density data available, the standard density model discussed in Section 6.2 was used in this analysis. This is the simplest possible density model expected to yield sensible results, and assigns uniform density contrasts for the sea water (-1.64 $Mg.m^{-3}$), sediments (-0.25 $Mg.m^{-3}$), crystalline crust (0.00 $Mg.m^{-3}$), raised upper mantle (+0.40 $Mg.m^{-3}$), upper mantle (0.00 $Mg.m^{-3}$) and crustal root (-0.40 $Mg.m^{-3}$). The adopted density values are regarded as average values, and represent useful approximations, even in the case of density changes with depth. A deviation from the real average density will lead to an upward or downward shift of the whole Moho

topography, whereas the structural characteristics will be preserved. All densities were held constant throughout the area discussed in this study.

6.4.2.5 Modelling Philosophy

The main purpose of this study was to try to match the calculated with the observed gravity data, while keeping constant the sedimentary section as defined by the sediment isopach map (Figure 6.12), and using the Moho depth as the only free parameter.

The actual 1D gravity modelling was carried out as follows. Water and sedimentary layers, with their appropriate densities, were imagined to be replaced by crustal material (density 2.67 $Mg.m^{-3}$) using the infinite Bouguer slab correction (Equation 6.1). The corresponding gravity effect was calculated and used as a correction to the observed residual free-air gravity anomalies. This yields the 'sediment-reduced residual Bouguer anomaly field' shown in Figure 6.13. These gravity anomalies were assumed to arise from the density contrast at the Moho and were modelled in terms of variations in Moho depth with respect to a 30 km thick reference crust.

A comparison of a Moho depth profile extracted from the 1D gravity inversion is made with a 2D modelled GM-SYS profile in Figure 6.14. The two Moho estimates are highly correlated, giving confidence in the fidelity of the 1D modelling philosophy.

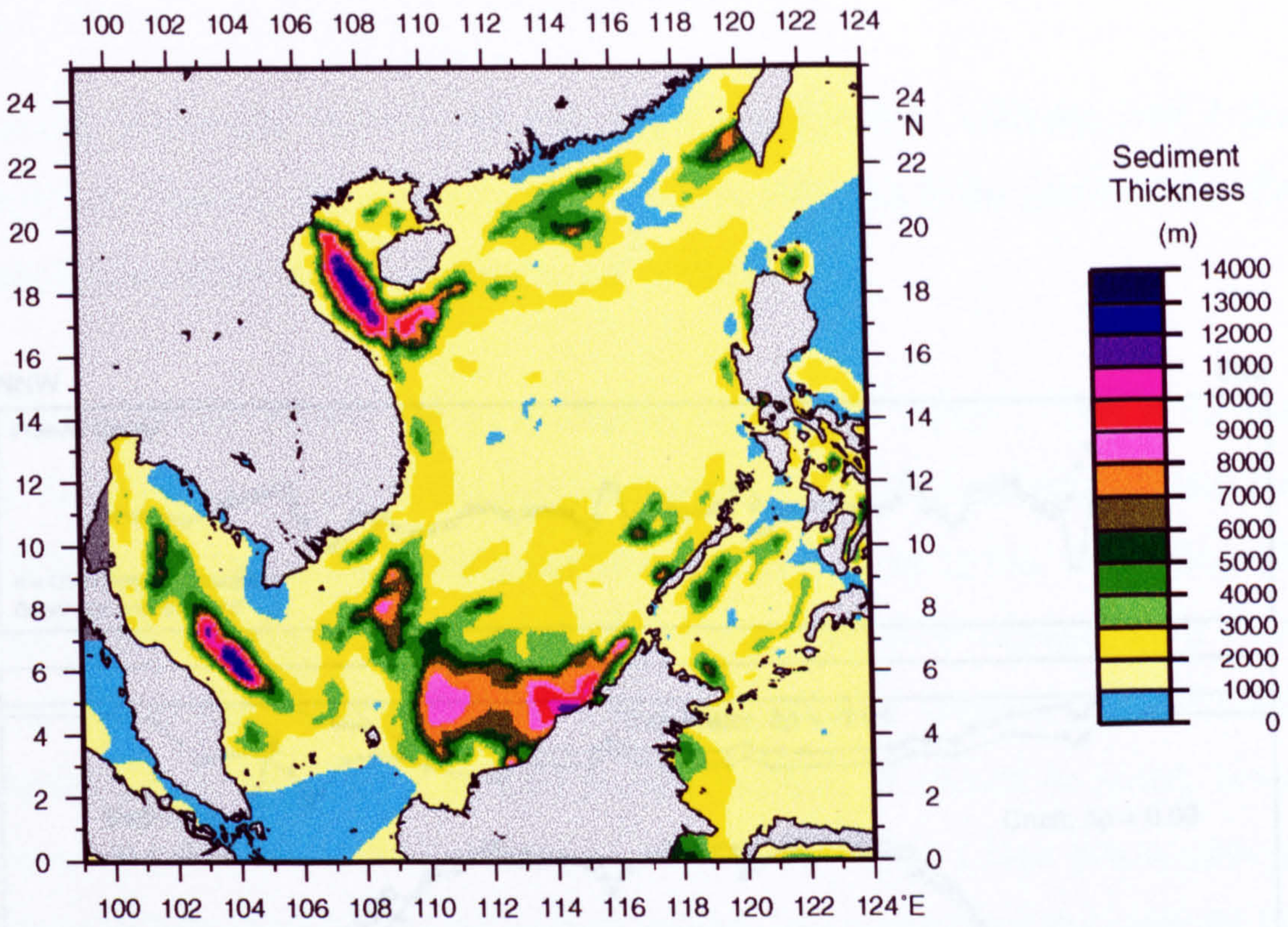

Figure 6.12. NGDC Sediment Isopach Map, SE Asia.

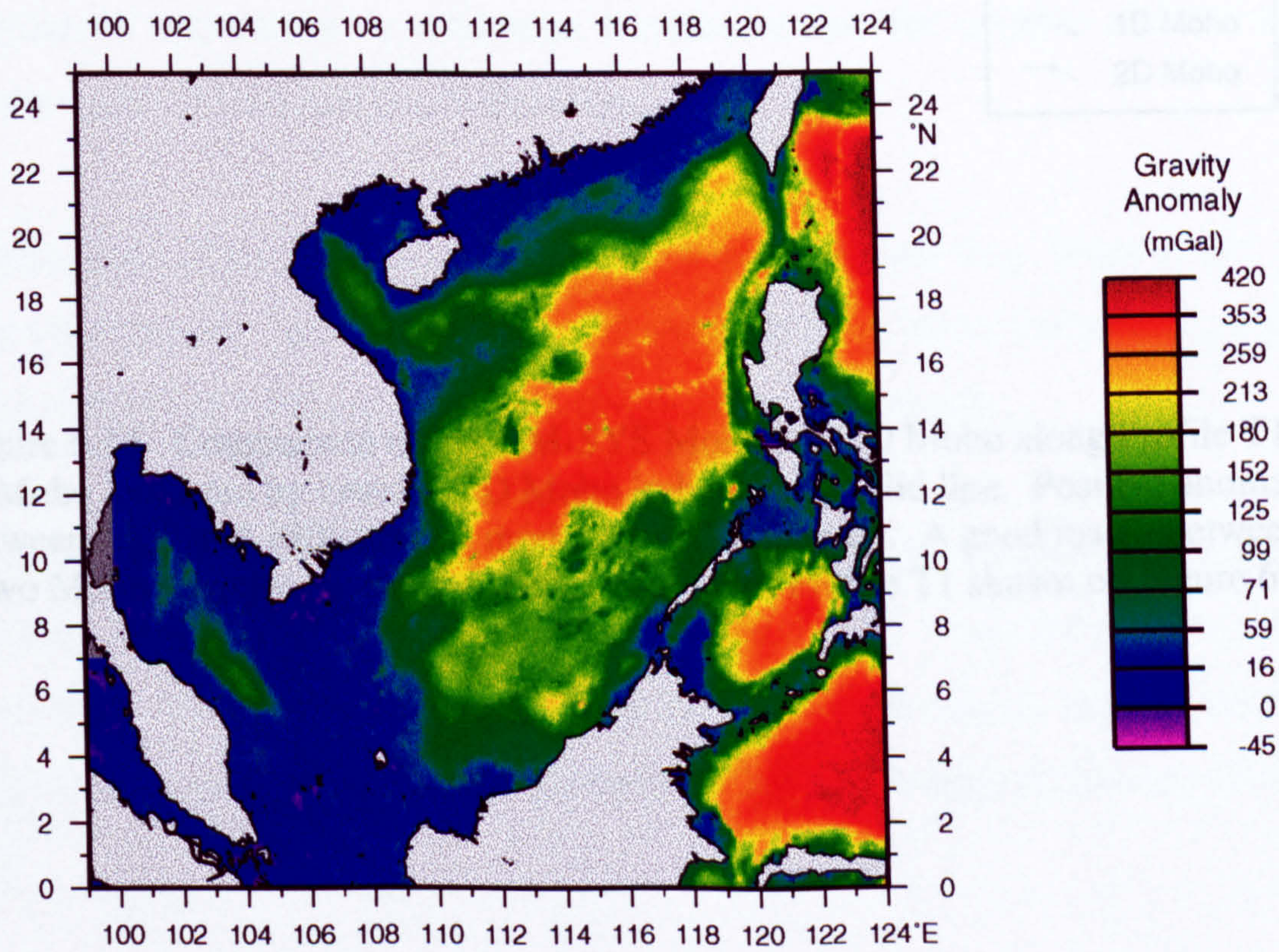

Figure 6.13. Sediment-Reduced Residual Bouguer Gravity Anomaly Map.

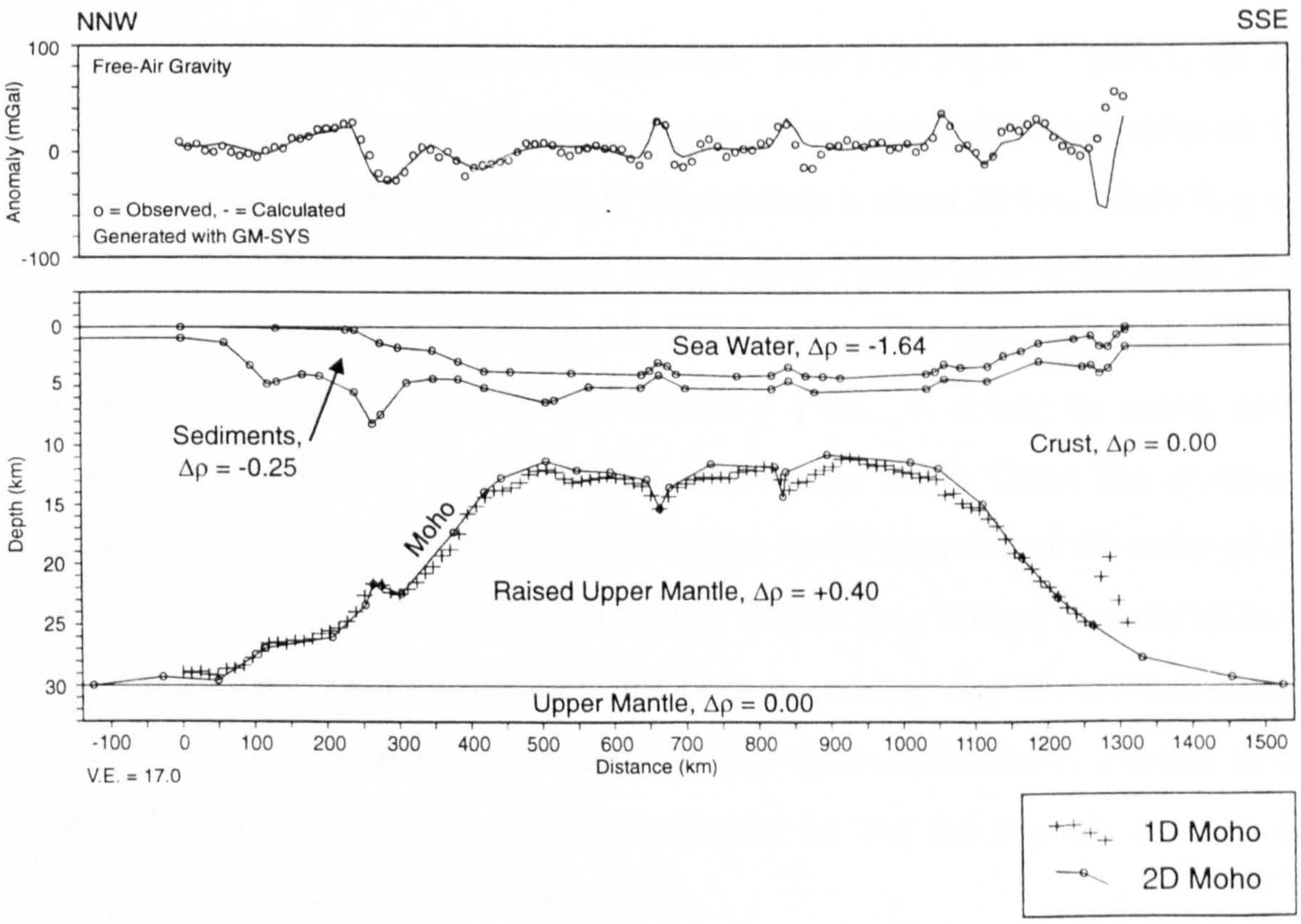

Figure 6.14. Comparison of 2D GM-SYS Moho and 1D Moho along Profile T1. 1D Moho indicated by crosses, 2D Moho indicated by solid line. Positive anomaly between 1200 and 1300 km not modelled in 2D solution. A good match between the two Moho estimates is clearly seen. Location of Profile T1 shown on Figure 6.21.

6.4.2.6 Accuracy

The gravity Moho was derived with two major assumptions - constant crustal density and local Airy isostatic compensation of all features observed in the gravity field. Errors arise when these assumptions are invalid, for example:

- When the crustal density differs significantly from 2.67 $Mg.m^{-3}$. This is the case in the vicinity of the South China Sea oceanic basin, where the depth estimate for the Moho obtained using the initial set of assumptions is about 12 km. Modelling using a more realistic higher crustal density (+0.1 $Mg.m^{-3}$) gives an average depth to Moho of about 16 km. Thus depth to Moho estimates over areas of oceanic crust are consistently underestimated by approximately 4 km. It should be noted, however, that a 16 km depth to Moho estimate beneath the South China Sea oceanic basin implies that the thickness of the oceanic crust in this region is of the order of 10 km, which is remarkable since it is significantly thicker than normal oceanic crust. Only by reducing the density assigned to the oceanic crust to that of standard continental crust would one get a 'normal' oceanic crustal thickness estimate. Further modelling should be undertaken to determine whether or not the oceanic crust is indeed anomalously thick in the South China Sea.

- When regionally-compensated features such as seamounts (e.g. Watts *et al.*, 1975) are encountered. Inaccurate (too thick) sediment cover above the seamounts yield a larger-than-realistic crustal root with this modelling philosophy.

Errors also arise because the 1D calculation of the Moho depth assumes infinite extent of the modelled anomalies. Thus gravity effects in the vicinity of narrow features are over compensated. This 'edge effect' depends on the depth of the source, and is generally not significant at distances beyond approximately 10 km of the edge of features (Harrison, 1991).

Quantifiable errors in the estimates for the depth to the gravity Moho arise from errors in the bathymetry, sedimentary thickness, gravity measurements and density estimates. The effects of these errors are given in Table 6.2.

Table 6.2. Likely magnitude of errors in gravity Moho estimation.

Error Source	Potential Error	Effect on Moho estimate
Bathymetry	± 100 m	± 410 m
Sediment Isopach	± 1000 m	± 625 m
Sediment Density	± 0.15 $Mg.m^{-3}$	± 1875 m•
Gravity Data	± 6 mGal	± 360 m

•Assuming 5 km of sediments

Less quantifiable errors arise from factors such as the omission from the model of lateral and vertical density changes within the sedimentary rocks. These uncertainties combine (by taking the square-root of the sum of the squared uncertainties) to give a probable error of ± 2 km in the estimates for the depths to the gravity Moho.

6.4.2.7 The β (stretching) Factor

The amount of crustal extension is often quantified by the β factor, which corresponds to the ratio of crustal thickness before and after extension in uniform stretching models (McKenzie, 1978). In this study the β factor is calculated as the ratio of the thickness of the reference crust (30 km) to the basement thickness inferred from the gravity modelling. These calculated β factors represent the combined effects of all phases of stretching. As discussed in Section 6.4.2.6, errors in basement thickness are of the order of ± 2 km, which lead to uncertainties of +0.3 and -0.2 for a typical β factor of 2.0.

According to Le Pichon & Sibuet (1981) oceanic crust begins to form at β values above 3.0. A β value of 3.0 is therefore used in this study to define the limits of the South China Sea oceanic crust.

6.4.2.8 Results

Maps showing the depth to the gravity Moho, crustal thickness, and β factor covering the area 99°E - 124°E, 0° - 25°N are shown in Figures 6.15 to 6.17 respectively. The resolution of these maps, limited by the resolution of the NGDC sedimentary isopach data set, is 5 minutes × 5 minutes.

6.4.2.9 Comparison of Moho Depth Predictions with Previous Estimates

The depths to Moho derived in this study can be quantitatively compared to the two-ship expanding spread profile (ESP) seismic refraction data of Nissen *et al.* (1995) and the gravity Moho of Chen & Lei (1987) along the northern margin of the South China Sea (110°E - 120°E, 16°N - 23°N). No other published data were available for comparison within the project area. Figure 6.18 gives a location map for the points at which the present study was compared with the earlier studies, the results of which are given in Table 6.3. ESP data considered unreliable by Nissen *et al.* (1995) were omitted from this analysis (ESPs 7/7A, 22, 23 and 24).

Table 6.3. Depths to Moho from Sea Level (in km).

Longitude °E	Latitude °N	ESP	[A] Nissen *et al.* (1995)	[B] This Study	[C] Chen & Lei (1987)	Δ(A-B)	Δ(A-C)	Δ(B-C)
118.4450	19.0100	1	11.11	11.97	9.00	-0.86	2.11	2.97
118.2300	19.4880	2	15.56	14.18	11.50	1.38	4.06	2.68
117.9575	19.8810	3	15.98	16.99	14.50	-1.01	1.48	2.49
117.8525	20.2305	4A	17.13	18.94	15.50	-1.81	1.63	3.44
117.8345	20.7290	5	22.46	22.21	17.50	0.25	4.96	4.71
117.6765	21.0600	6	24.63	24.43	20.50	0.20	4.13	3.93
117.2000	21.8900	8	30.55	28.02	24.50	2.53	6.05	3.52
116.9760	22.2700	9	28.04	28.68	25.50	-0.64	2.54	3.18
111.9675	20.7170	11	32.54	28.41	27.00	4.13	5.54	1.41
112.4265	19.8785	12	23.70	25.74	25.50	-2.04	-1.80	0.24
112.699	19.3635	13	27.80	27.23	24.00	0.57	3.80	3.23
112.8715	19.0205	14	26.50	25.80	22.50	0.70	4.00	3.30
113.0400	18.7400	15	25.53	24.07	21.00	1.46	4.53	3.07
113.2580	18.3315	16	16.58	20.86	18.50	-4.28	-1.92	2.36
113.3930	17.7170	17	23.80	21.35	16.00	2.45	7.80	5.35

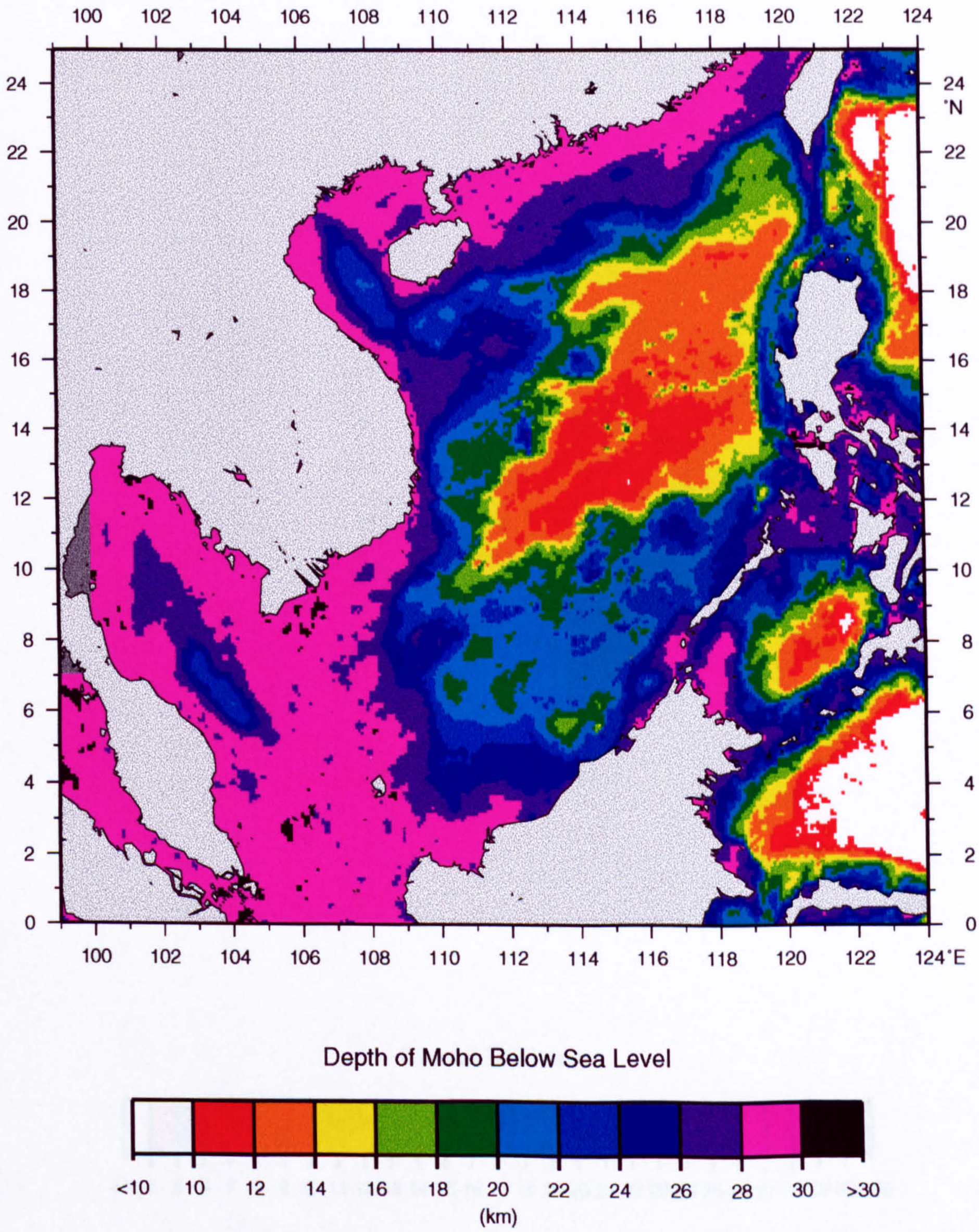

Figure 6.15. Gravity Moho Map, South China Sea.

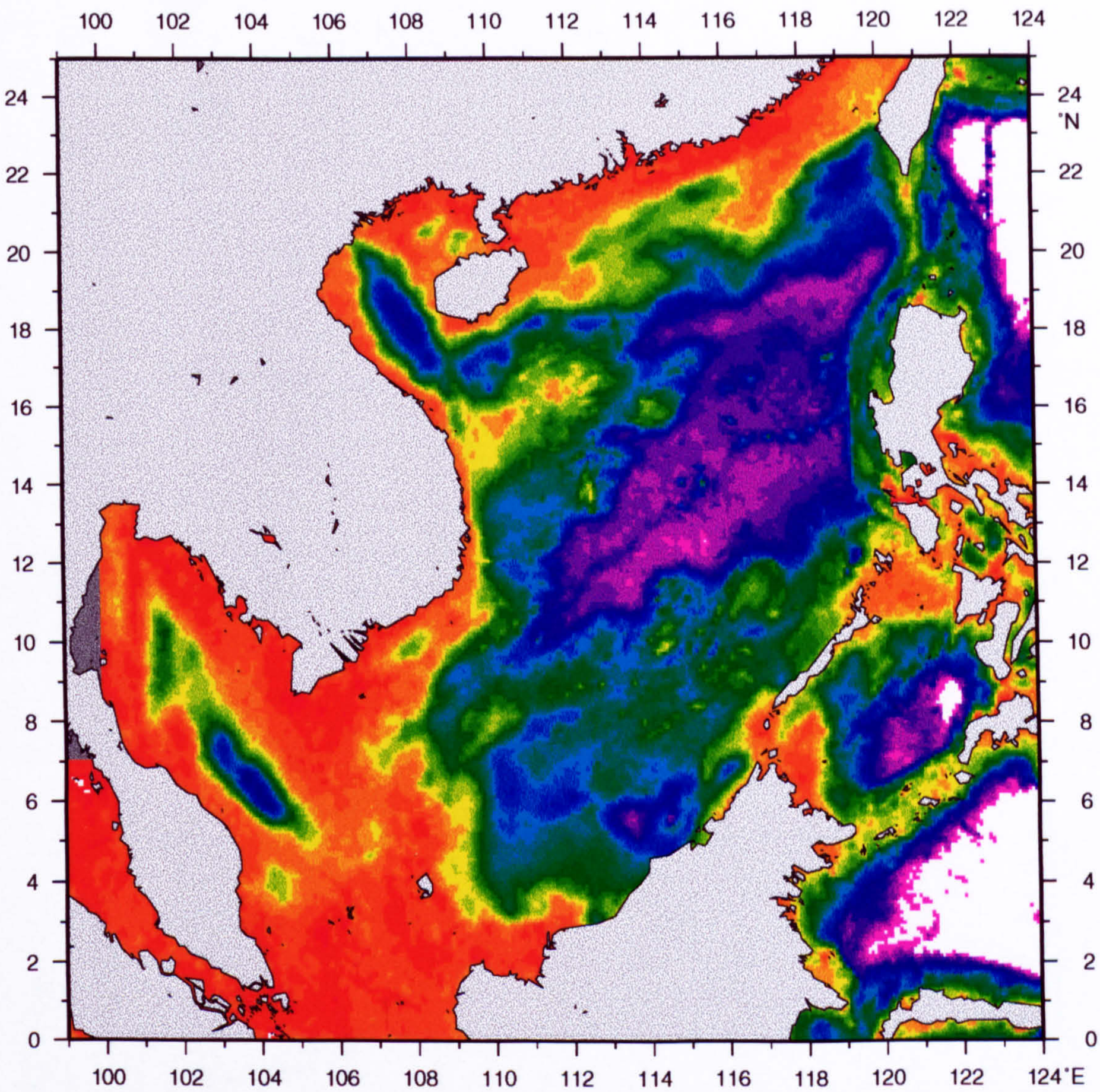

Figure 6.16. Crustal Thickness Map, South China Sea.

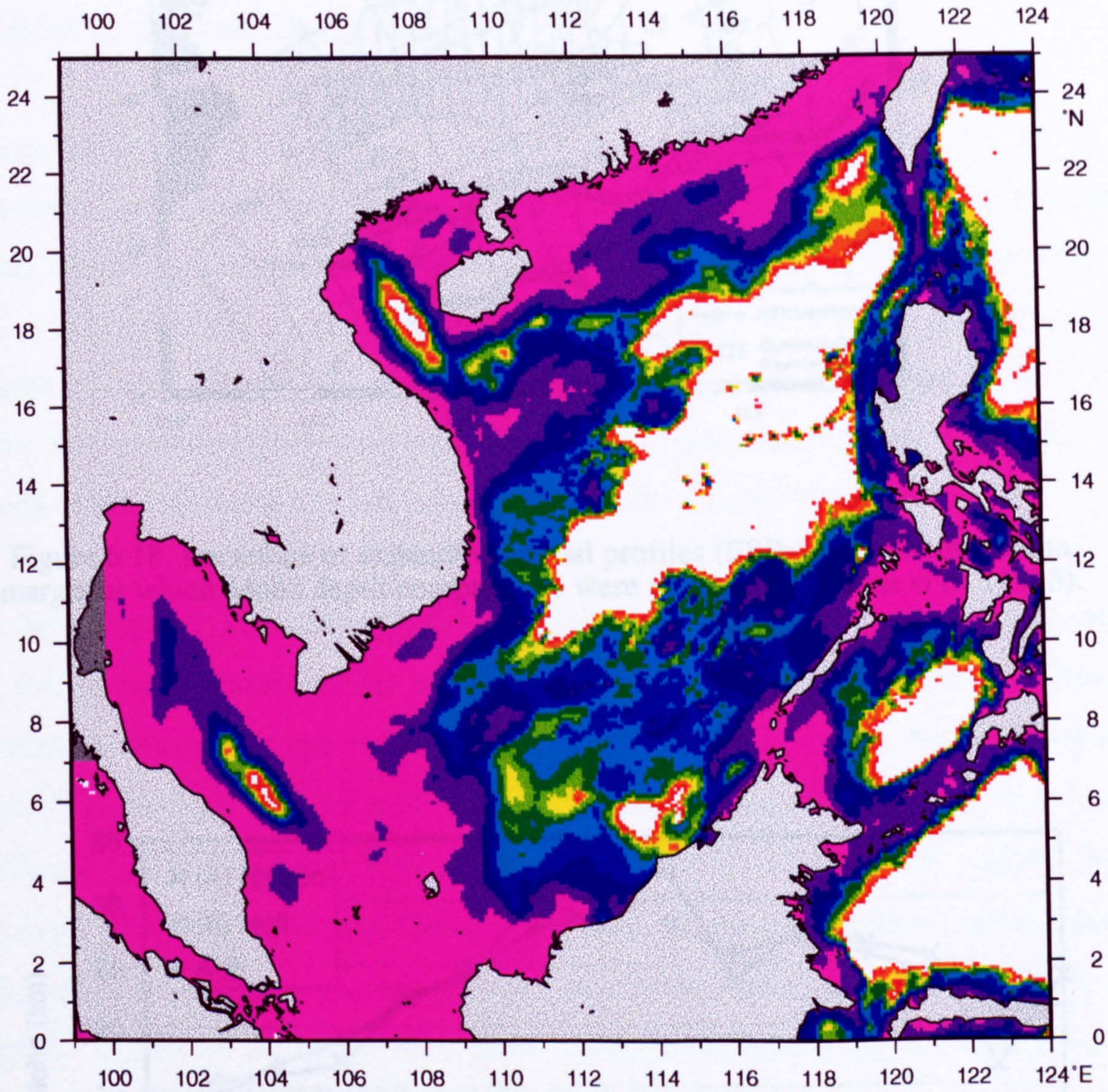

Figure 6.17. β (stretching) factor map, South China Sea.
Initial 30 km thick crust assumed.

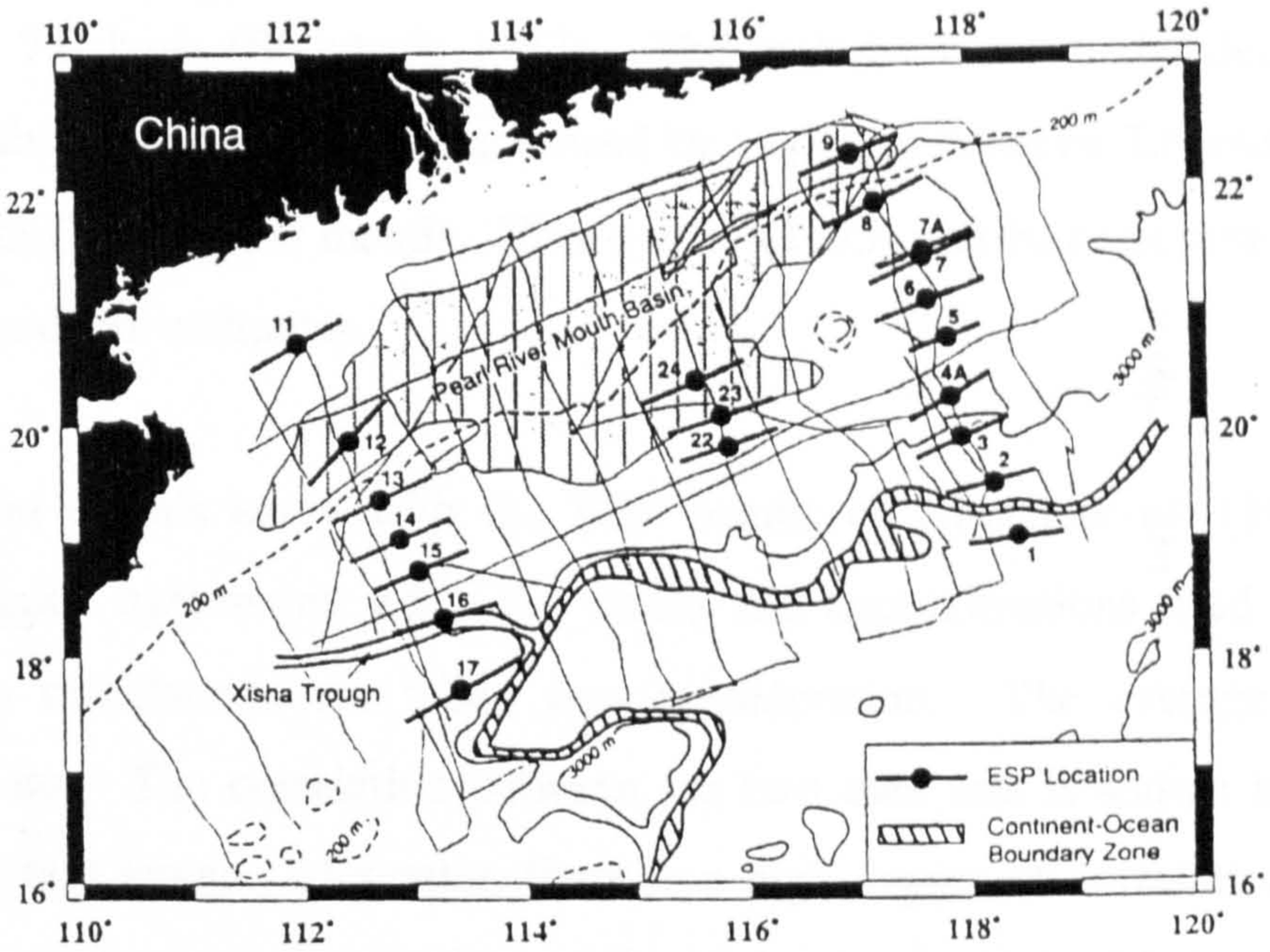

Figure 6.18. Locations of expanding spread profiles (ESPs) on the south China margin at which Moho depth comparisons were made, after Nissen *et al.* (1995).

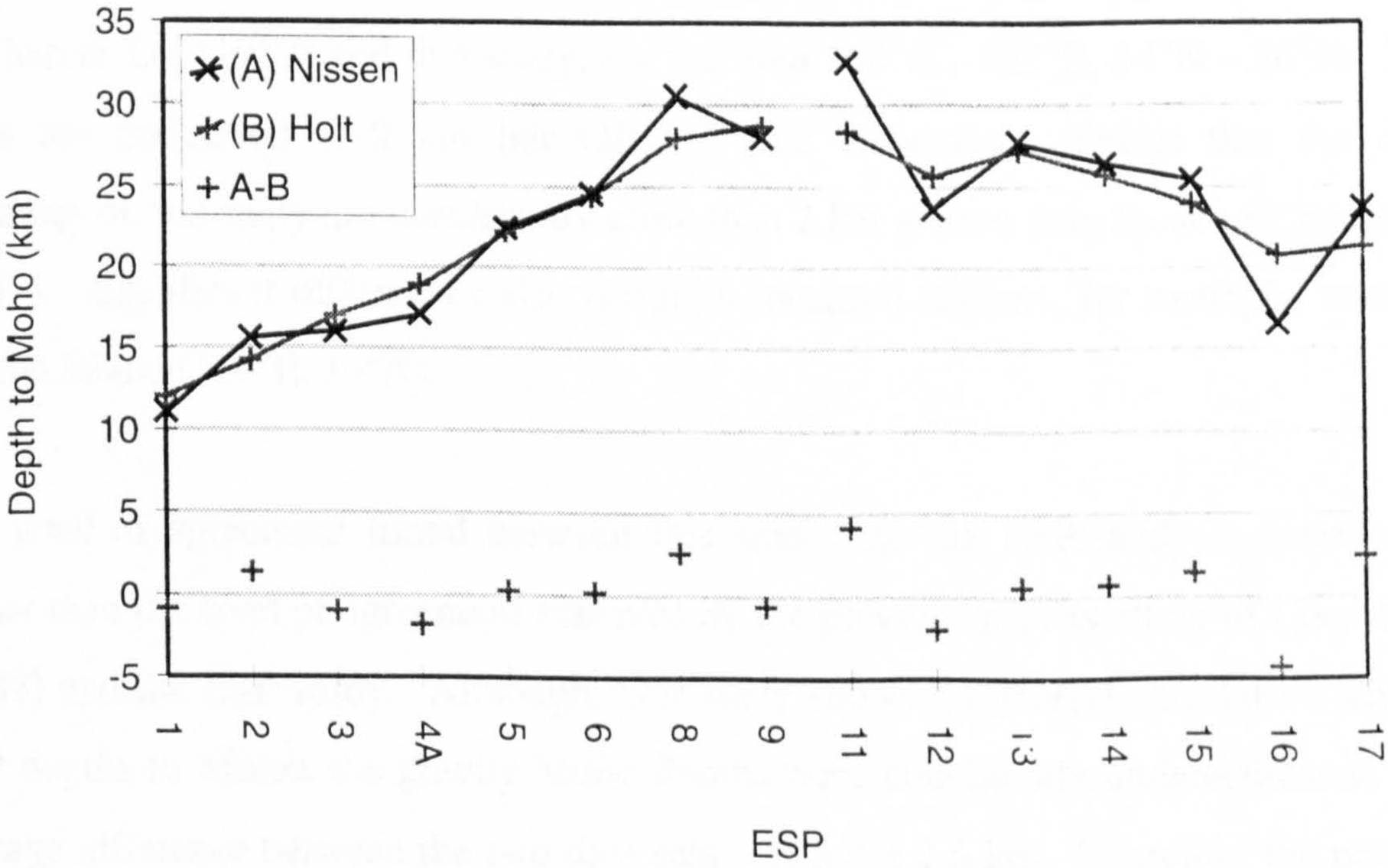

Figure 6.19. Graph showing comparison of Moho depth estimates of (B) this study and (A) Nissen *et al.* (1995). A high degree of correlation is observed between the two data sets.

The seismic Moho is typically defined as the horizon below which P wave velocities are greater than 7.6 km/s (Steinhart, 1967). The material beneath the deepest reflector detected on the ESP data was characterised by velocities between 7.6 and 9.0 km/s and was thus identified as upper mantle. Nissen *et al.* (1995) ascribe an accuracy of ± 1.5 km to their Moho depth estimates.

A comparison of this study with the ESP results of Nissen *et al.* (1995) shows a remarkably good agreement, when the errors and approximations used in the gravity Moho depth calculations are taken into consideration. The average difference is 0.20 ± 2.03 km. The correlation between the two data sets is shown in Figure 6.19. Despite a certain amount of scatter, there is a high degree of correlation between the Moho depths derived gravimetrically and the Moho depths derived from the ESPs. The gravity Moho appears to be a smoothed version of the seismic Moho.

The Moho map of Chen & Lei (1987) was derived primarily from gravity data, although the depths were constrained by seismic evidence at five points, one on the Chinese mainland at Guangzhou and four in the deep ocean (Liu *et al.*, 1985). No information is available regarding the accuracy of this map. Figure 6.20 shows the gravity Moho maps of Chen & Lei (1987) and this study, for the area 104°E - 122°E, 14°N - 26°N. Both maps are contoured at 2 km intervals. Visual comparison reveals that the depth estimates of this study are consistently more than 2 km greater than those of Chen & Lei (1987). Significant differences also occur in localised regions, for example, south of Hainan Island (110°E, 19°N).

The level of agreement found between this study and the ESP study is considerably higher than the level of agreement achieved by the previous gravity study of Chen & Lei (1987) and the ESP study. Although their study showed a general correlation with the ESP depths to Moho, the gravity Moho depths were consistently underestimated. The average difference between the two data sets was 3.3 ± 2.6 km. Therefore the previous gravity Moho also has a greater scatter about the ESP results than the current study (average difference 0.20 ± 2.03 km), indicating a less well determined Moho.

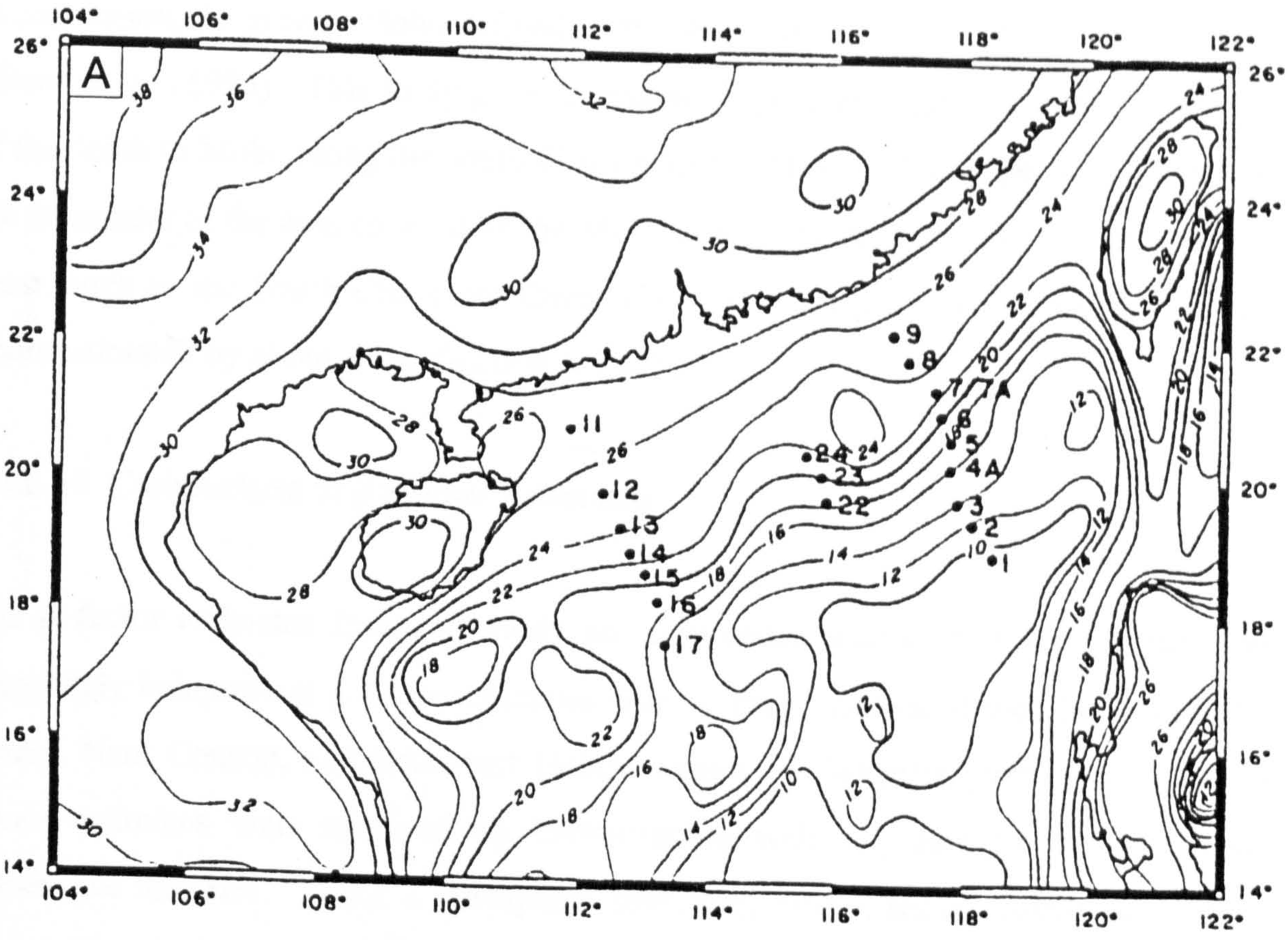

Figure 6.20. Maps of depth to the gravity Moho - A: from Chen & Lei (1987), overlain by ESP locations; B: results of this study. 2 km contour intervals.

In conclusion, the gravity Moho defined in this study coincides with the seismic Moho of Nissen *et al.* (1995). This study gives a reliable (if perhaps slightly smoothed) estimate of the depth to Moho along the south China margin. This result is expected to hold over the remainder of the area covered by the Moho map, excluding areas underlain by denser crust, such as the South China Sea Oceanic Basin, where the depths to the Moho are underestimated by about 4 km (Section 6.4.2.6).

6.4.2.10 Comparison of β Factor Estimates

The β factor estimates from this study are compatible within error with unpublished completely independent β factor estimates derived from analysis of well log data in the Malay, Nam Conson, and Southeast Hainan Basins (P. Wheeler, *pers. comm.*, 1997). These estimates were obtained by backstripping well log data to the give basin subsidence histories. Using a lithosphere stretching model, these subsidence data are inverted to give the temporal strain rate variation history for each basin (White, 1993). The β estimate is simply the cumulative strain rate variation of the basin, which is derived with an estimated error of ± 0.2.

6.4.2.11 Interpretation of Results

There are four distinct crustal areas that can be identified on the northern Sunda Shelf and within the South China Sea, as characterised by crustal thickness - the Sunda Shelf, south China margin, South China Sea and South China Sea Oceanic Basin. Five crustal cross-sections (T1 to T5, Figures 6.22 to 6.26 respectively) were produced to illustrate the different characteristics of these regions. A location map for these cross-sections is given in Figure 6.21. The cross-sections are interpreted in terms of continental crust, highly attenuated continental crust and oceanic crust. As the cross-sections were produced using the 1D modelling technique discussed in Section 6.4.2.5, Moho depths beneath the South China Sea Oceanic Basin are underestimated by about 4 km (Section 6.4.2.6).

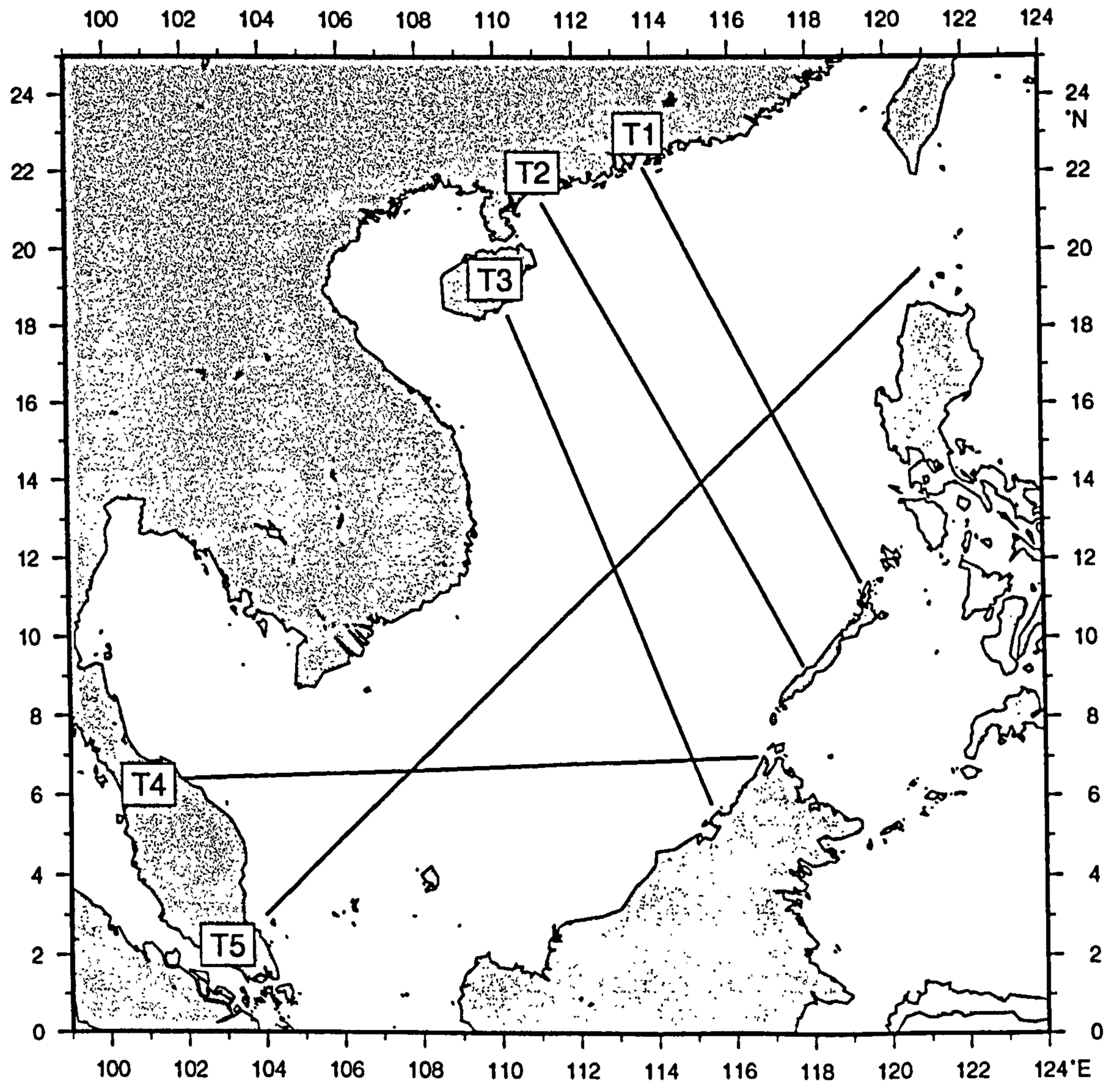

Figure 6.21. Crustal sections location map.

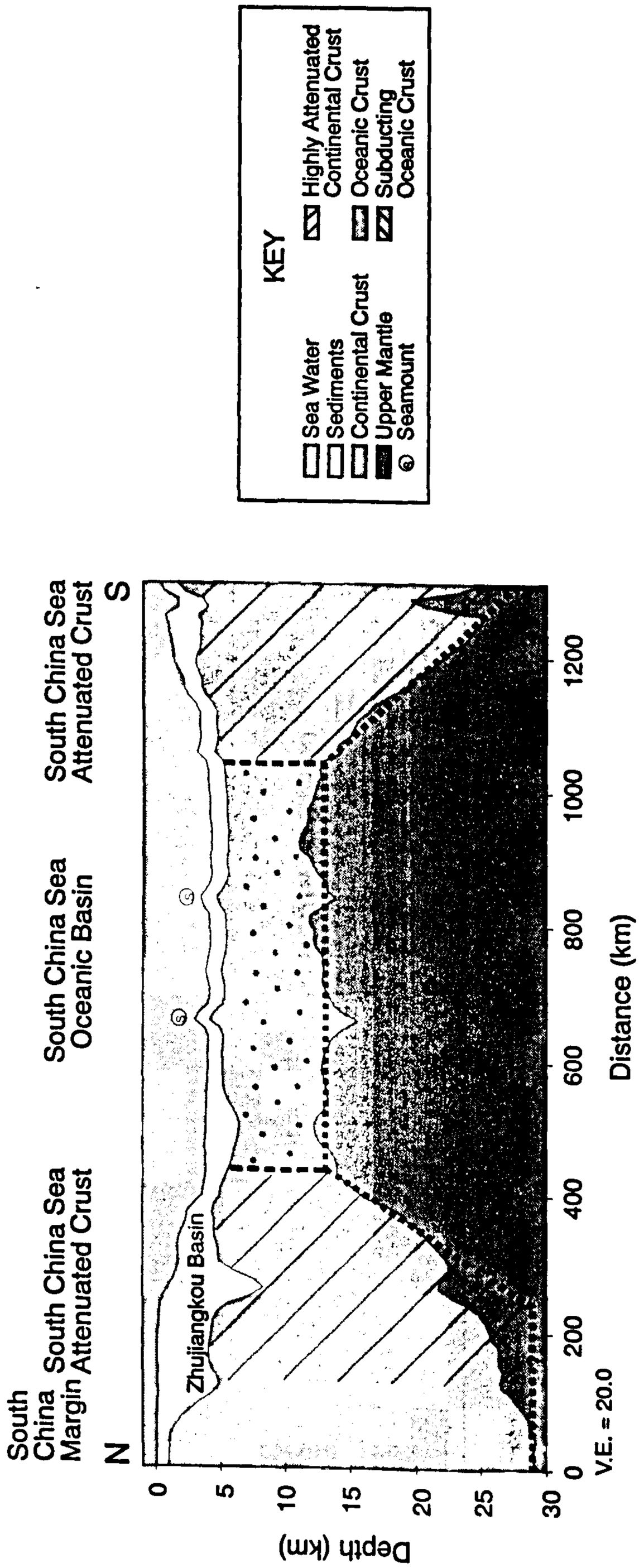

Figure 6.22. Interpreted cross-section T1.

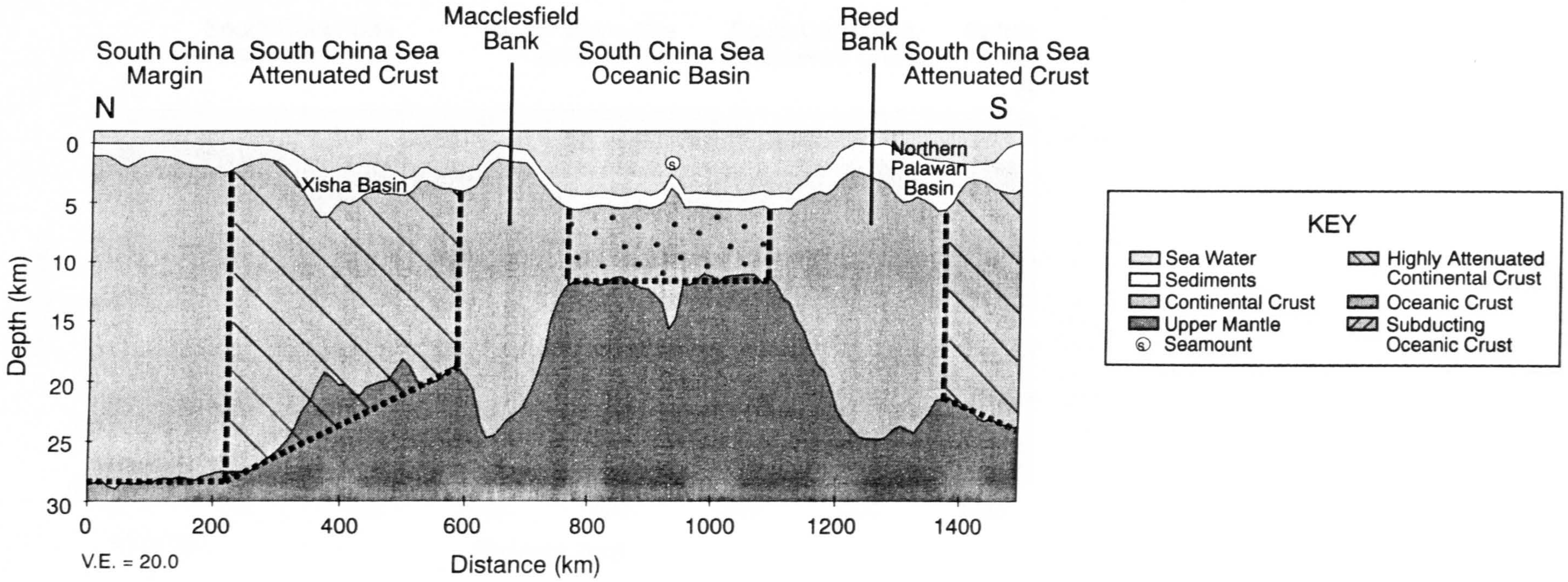

Figure 6.23. Interpreted cross-section T2.

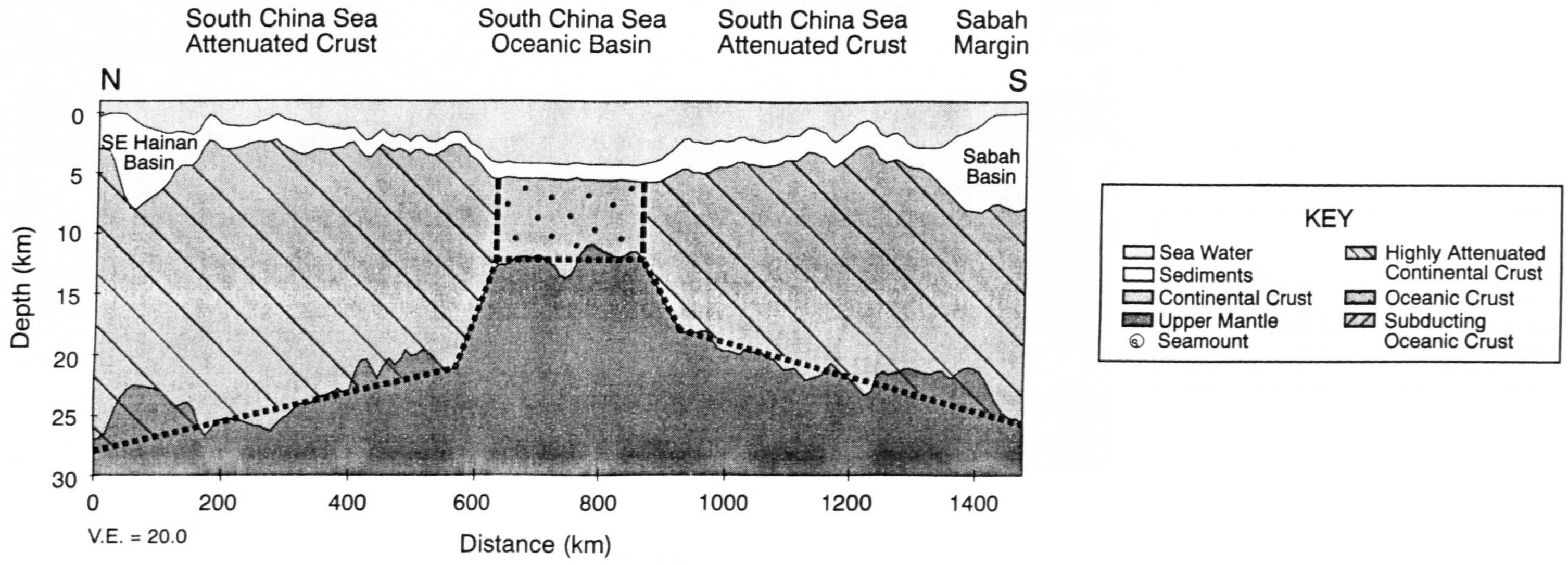

Figure 6.24. Interpreted cross-section T3.

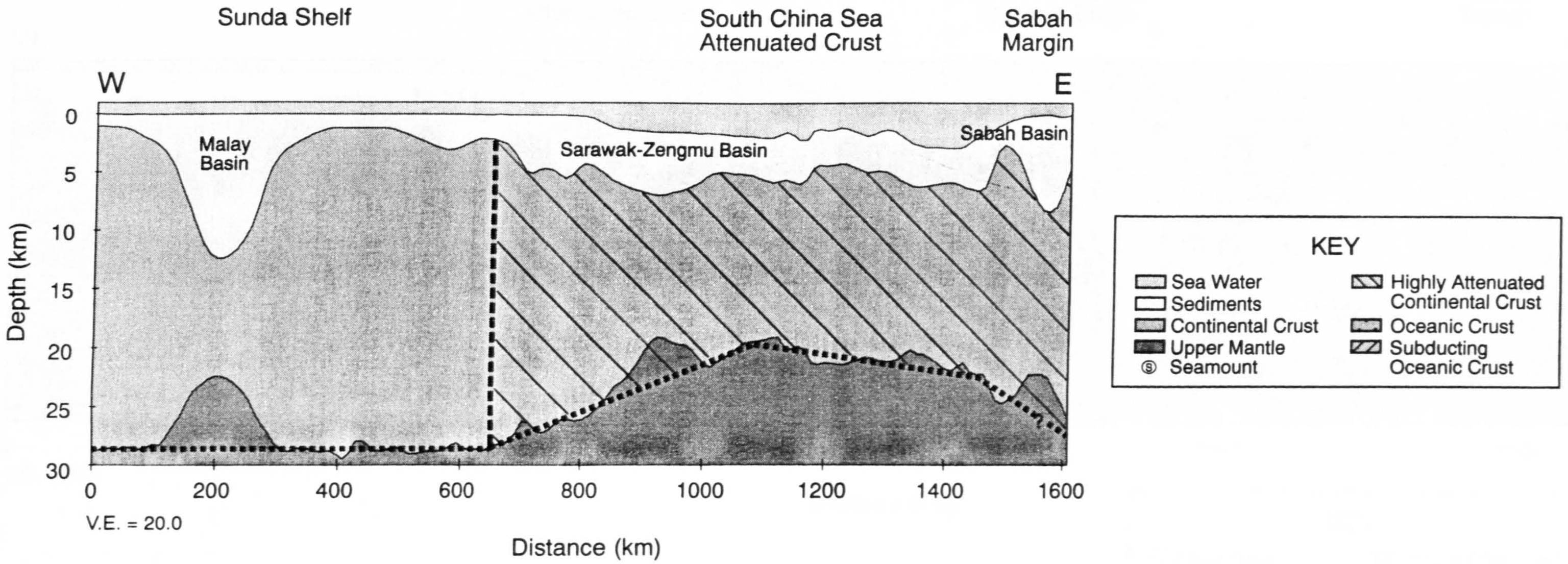

Figure 6.25. Interpreted cross-section T4.

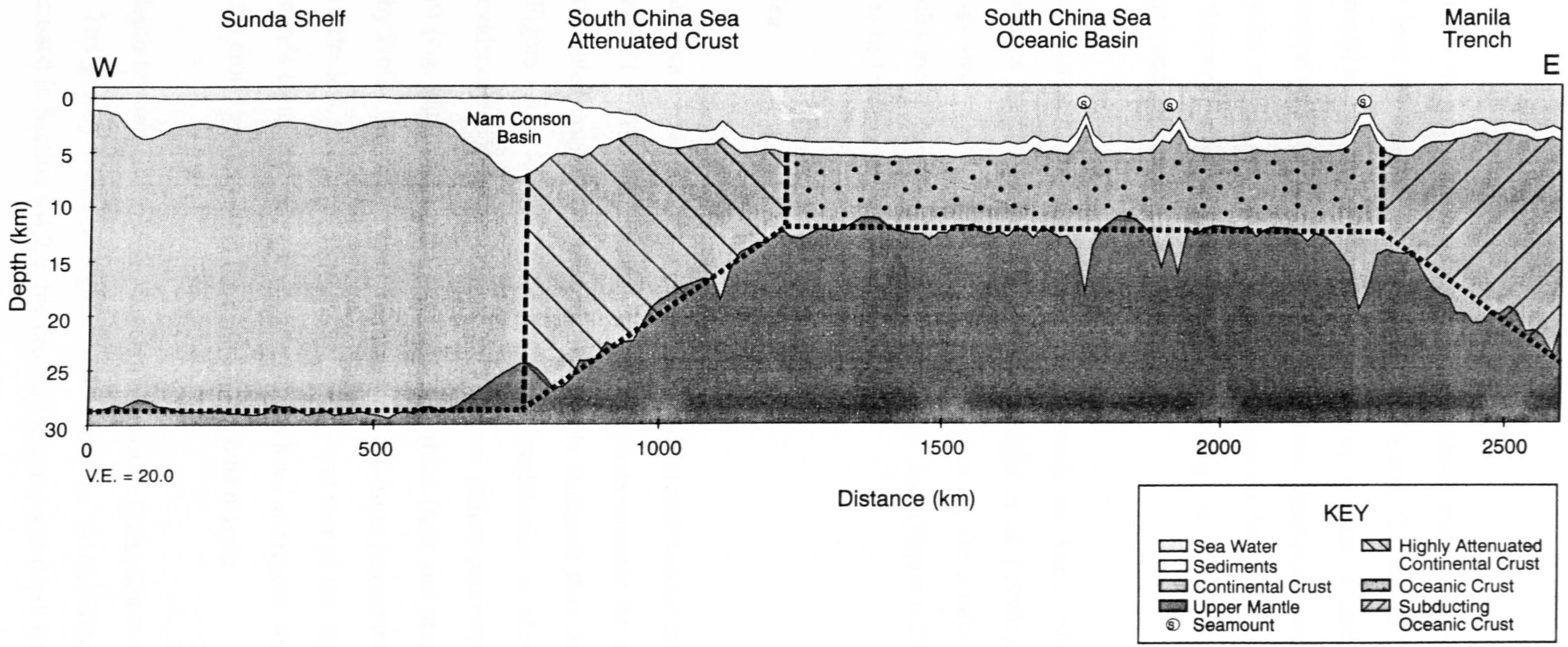

Figure 6.26. Interpreted cross-section T5.

Sunda Shelf

The Sunda Shelf is characterised by a relatively deep Moho that lies between 28 and 30 km below sea level (Figure 6.15). Cross-sections T4 and T5 show that the Moho is generally horizontal and smooth in this area, although up to 6 km of crustal thinning has occurred in a limited area beneath the Malay Basin. Other significant crustal thinning has occurred along the margin between the Sunda Shelf and the South China Sea, between Vietnam and Sarawak, along the line now occupied by the Mekong, Nam Conson, Sarawak-Zengmu and Sabah Basins.

The result that a smooth, horizontal Moho lies beneath the Sunda Shelf contradicts previous predictions for the Moho in this area. Rangin *et al.* (1990*c*), for example, predicted a large degree of variation in crustal thickness on the Sunda Shelf from an indentor tectonics model for the evolution of Southeast Asia (Figure 6.27). This model is now shown to be incorrect.

South China Sea

The South China Sea is underlain by attenuated continental and oceanic crust. As shown on cross-sections T1 to T3, the crustal thickness decreases towards the central oceanic basin. This attenuated crust has a much more variable thickness than the crust on the Sunda Shelf (Figure 6.16), indicating the differential exploitation of pre-rift structures. There is also evidence for localised rafts of thicker crust (micro-continents?) within the attenuated crust (e.g. Figure 6.16). Examples include Reed Bank and Macclesfield Bank which are cut by Profile T2. The crustal thickness in these areas lies somewhere between the thickness of the less attenuated continental margin and that of the highly attenuated crust that surrounds them, indicating that these blocks have undergone some attenuation and/or significant erosion since rifting from the south China margin.

The average depth to the gravity Moho beneath the South China Sea is of the order of 20 - 22 km. The gravity Moho is highest underneath the South China Sea Oceanic Basin. As discussed in Section 6.4.2.6, the crustal thickness and depth to gravity Moho

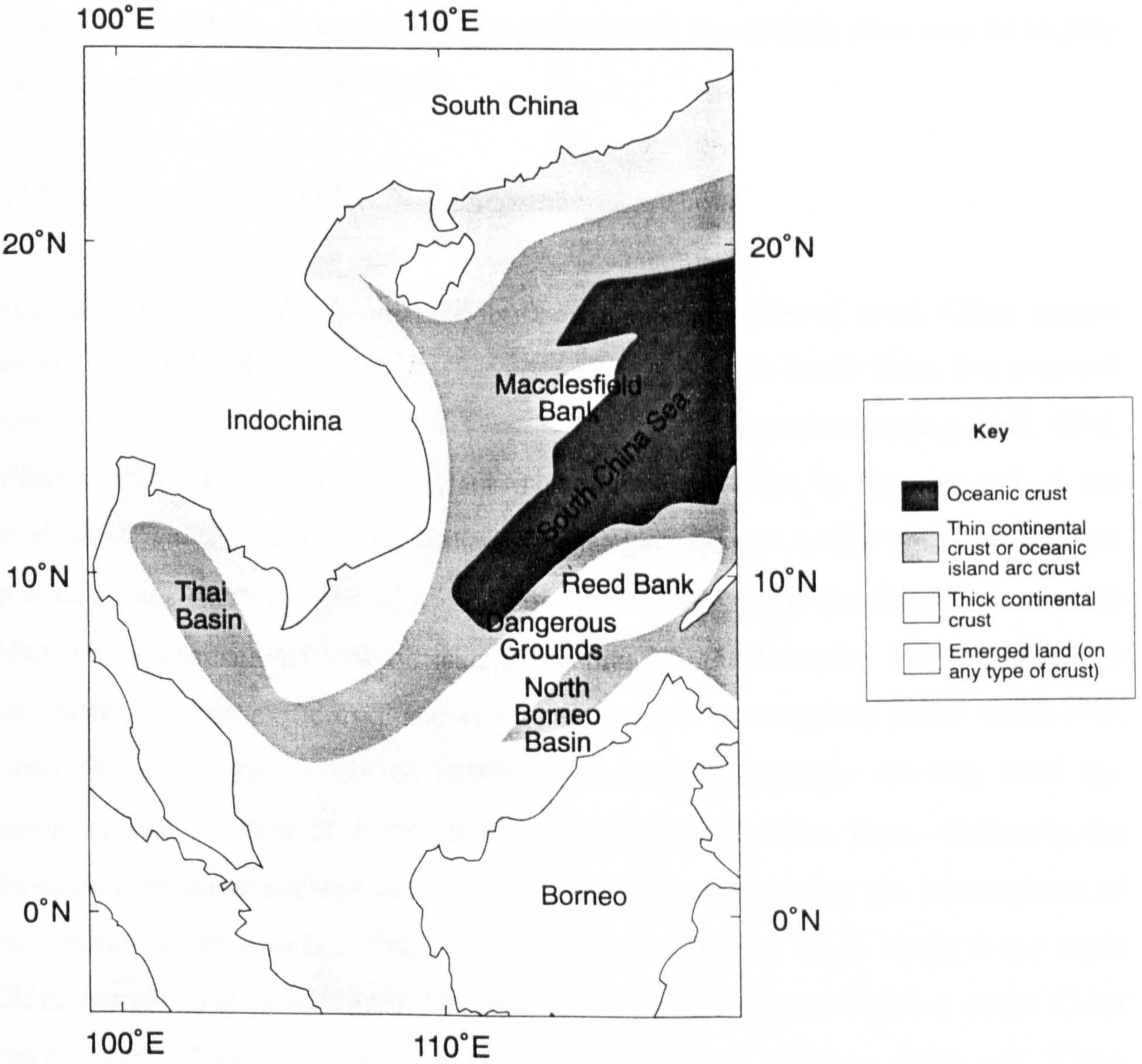

Figure 6.27. Present day crustal thickness variation within South China Sea and on the northern Sunda Shelf, according to Rangin *et al.* (1990*c*).

is underestimated in this area with the 1D modelling technique, and false variations in crustal thickness are produced by the axial valley and seamounts. 2D GM-SYS modelling (Section 6.4.3.4) indicates that the gravity Moho lies approximately 16 km below sea level beneath the oceanic basin. The cross-sections (T1, T2, T3 and T5) show that the crust has a relatively even thickness as one would expect from relatively recent oceanic crust. These cross-sections also indicate that the oceanic crust may be slightly thicker in the southwestern subbasin.

6.4.2.12 Implications for Tectonic Reconstructions

According to Taylor & Hayes (1983), southwards extension of south China margin started at 65 ± 10 Ma. Formation of oceanic crust within the South China Sea occurred between *c.* 32 Ma and c. 15.5 Ma (Briais *et al.*, 1993). Some authors (e.g. Hall, 1996; Milsom *et al.*, 1997) believe that this extension was driven by the slab-pull of the subducting 'proto-South China Sea' (which has since been totally consumed) at the southern and eastern margins of this sea (at or near the present day Sabah-Palawan and Manila Troughs). Other authors (e.g. Briais *et al.*, 1993; Fournier, 1994) believe that this extension occurred for other reasons, and that the 'accretionary prism' which runs along the northwest margin of Borneo is a collisional feature resulting from the northwestward collision of the Australian Plate with the Eurasian Plate. Critical to the divergence of these tectonic syntheses are assumptions regarding the paleolatitude of Borneo during the Eocene. Briais *et al.* (1993) put 'Borneo' much closer to the south China margin than Hall (1996) who leaves the N-S separation between south China margin and 'Borneo' virtually at its present distance (Figures 2.18 and 2.21A respectively). By 'rewinding' the South China Sea crust to its pre-rift thickness (30 km), it is possible to quantify the maximum separation between 'Borneo' and the south China margin before space balancing makes the existence of the proto-South China Sea mandatory.

Figure 6.28 shows a map of the South China Sea 'rewound' northwards towards the south China coastline to a constant crustal thickness of 30 km. This 'rewinding' was performed at 40 points within the South China Sea. The northward distance that each

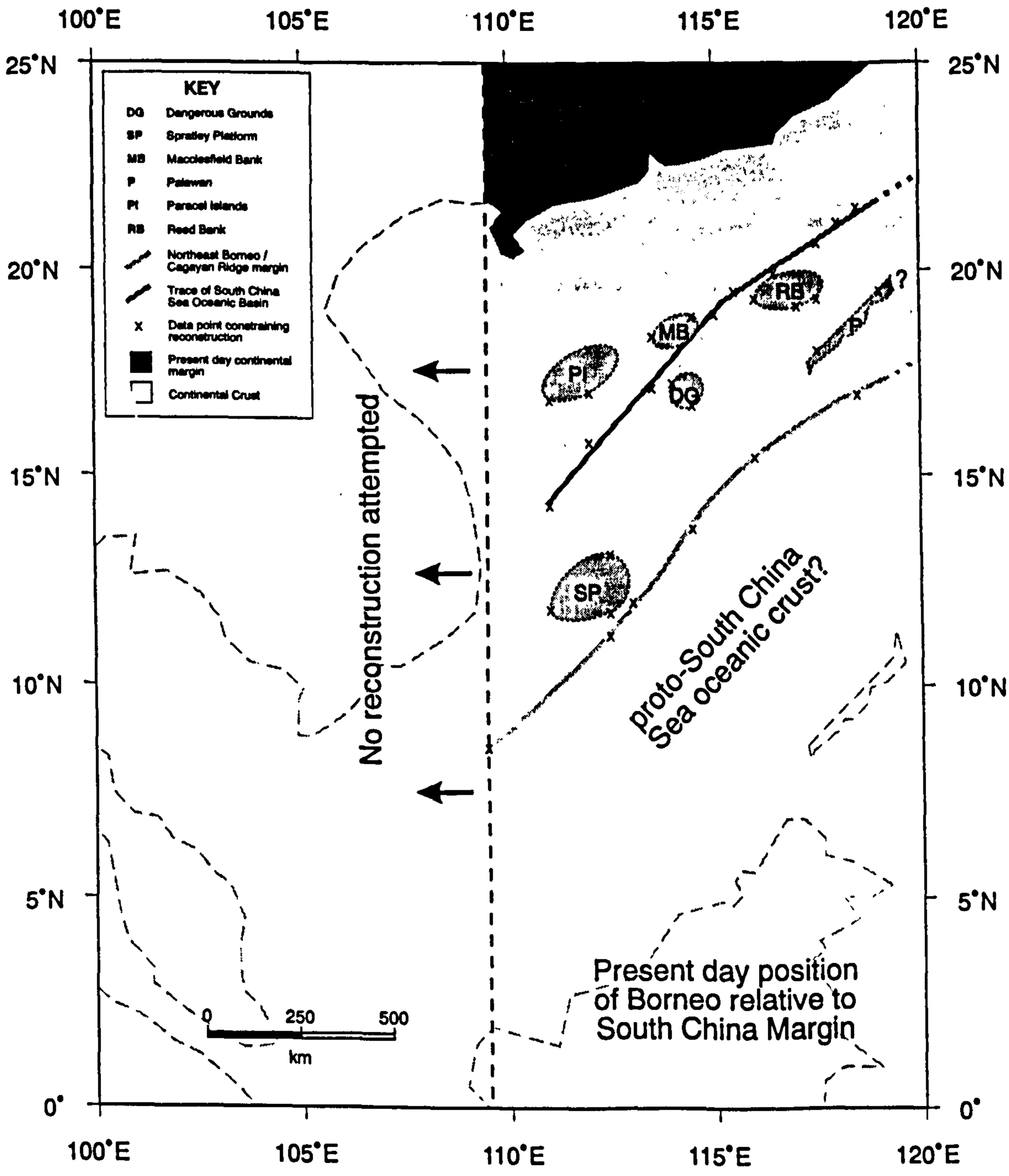

Figure 6.28. Hypothetical Configuration of the South China Margin *c.* 50 Ma. Present day geographic coordinates shown.

reconstruction point had to move relative to the south China coastline was calculated from β factor map (Figure 6.17). The oceanic crust was not included in this calculation. Furthermore, the south China coastline was fixed and no 'rewinding' was performed north of this line. One critical assumption of this reconstruction was that all the extension of the South China Sea took place in the N-S direction, which is justified by the W-E orientation of the magnetic lineations in the northwestern and eastern subbasins of the South China Sea Oceanic Basin (Figure 2.11).

The reconstruction of the south China margin (Figure 6.28) shows that the maximum N-S separation between the continental core of 'Borneo' and the south China margin during the Eocene before a proto-South China Sea is required for space balancing is of the order of 8 - 11 degrees, depending on longitude. If 'Borneo' had the same separation from China during the Eocene as it does presently, then approximately 1100 km of oceanic crust has been subducted beneath the northwest margin of Borneo during this period.

6.4.2.13 Summary

New maps of the gravity Moho, crustal thickness and β factor have been produced for the South China Sea and northern Sunda Shelf. These maps are in excellent agreement with the previous sparsely-distributed Moho and β factor data, and therefore represent an important new source of regional geological information.

6.4.3 South China Sea Oceanic Basin

6.4.3.1 Introduction

The South China Sea Oceanic Basin is located equidistant between Sabah to the south, China to the north, Vietnam to the west and Luzon to the east (Figure 2.9). The basin covers an area of approximately 410,000 km^2, and is presently subducting at the Manila trench (Pautot & Rangin, 1989). The basin may be divided into three subbasins - the northwestern, eastern and southwestern subbasins. The most prominent features within the basin are the deep valley of the relict spreading axis in the southwest, and the chain of seamounts (the Scarborough Seamounts) that runs along the relict spreading axis in the east.

Analysis of the satellite gravity data over the South China Sea Oceanic Basin is somewhat limited owing to the intrinsic uncertainties associated with gravity data interpretation. In the absence of good control data (e.g. seismic depth constraints and ocean drilling results), it is difficult to distinguish the effects of crustal thickness variations from those of crustal and upper mantle density variations (e.g. Minshull *et al.*, 1995; Pariso *et al.*, 1995; Minshull, 1996).

The WGI7.2 gravity data set is used in this section to map features within the oceanic basin, and also to analyse the relict spreading axis of the southwestern subbasin. Comparison of the free-air gravity anomaly at this fossil spreading ridge with present day spreading ridge gravity anomalies enabled an estimate of the spreading rate of the ridge to be made.

6.4.3.2 Oceanic Basin Spreading Ridges

The world's mid-ocean ridges can be divided into two classes, namely 'slow-spreading' and 'fast-spreading' (Wang & Cochran, 1995). Slow-spreading ridges are characterised by a rift valley (typically 1 - 2 km deep and 30 - 50 km wide) at the crest and rugged topography along the flanks. The depth of a slow-spreading axial valley frequently varies

along axis by 1000 m or more (Lin & Phipps-Morgan, 1992) and decreases rapidly with increasing spreading rate (Malinverno, 1993; Small, 1994), whilst the width reduces only slowly (Owens & Parsons, 1994). In contrast, fast-spreading ridges are marked by a triangular-shaped axial peak (several hundred metres high and ~ 20 km wide) and have more subdued topographic relief along their flanks (Hu & Rabinowitz, 1996). Fast-spreading ridges are much less variable than slow-spreading ridges (Wang & Cochran, 1993). The transition from slow- to fast-spreading is an abrupt one with respect to spreading rate (Small & Sandwell, 1989; Chen & Morgan, 1990; Owens & Parsons, 1994), occurring at rates of approximately 60 - 65 mm/yr. The exact spreading rate at which this transition occurs is affected by the crustal thickness (Chen & Morgan, 1990; Phipps-Morgan & Chen, 1993; Detrick *et al.*, 1995; Cannat, 1996).

A recent high resolution study of slow-spreading mid-ocean ridges by Smith *et al.* (1997) found that the ridges are composed of individual accretionary segments that are tens of kilometres long. The overall shape of the axial zone is that of a major graben composed of an inner valley floor and bordered by valley walls in which large normal faults displace the crust upwards to form the crestal mountains. The inner valley floor is the primary site of crustal construction, and most, but not all, segments contain large axial volcanic ridges within their valley floors that are the principal sites of lava extrusion.

The South China Sea Oceanic Basin relict spreading ridge is an example of an abandoned slow-spreading centre. Abandoned centres can be found in many locations, including the Labrador, Coral and Scotia seas, the Pacific Ocean, the Indian Ocean and on the African Plate east of the Mid-Atlantic Ridge near latitudes 40°S - 50°S (Freed *et al.*, 1995).

Modelling of mid-ocean ridges by Freed *et al.* (1995) suggests that the axial valley topography created at active slow-spreading centres may be preserved for tens of millions of years after cessation of spreading. The axial valley associated with an active spreading centre could potentially be removed by either of two mechanisms: (1) ductile relaxation of the lithosphere itself; or (2) reversal of motion on rift-bounding faults. The temperature distribution that would be required to allow significant ductile flow of the crust may only be found near a fast-spreading centre, where low viscosities prevent the

formation of an axial valley (Chen & Morgan, 1990). Extinction of a spreading centre could lead to additional normal faulting either during the relaxation process or due to an increase in the regional extensional strain rate if the extinction process is gradual. The only way that the faults could be reversed would be to introduce a compressional strain rate to the region immediately upon cessation of active spreading. Because conductive cooling increases lithospheric strength with time after extinction, a high level of compressional stress would be required to reverse the existing normal faults or to create new thrust faults. These results therefore suggest that the topography of the axial valley of the South China Sea Oceanic Basin has been 'frozen' since spreading ceased *c.* 15.5 Ma.

6.4.3.3 The Gravity Signature of the South China Sea Oceanic Basin

Figure 6.29 shows the interpreted residual free-air gravity anomaly field over the South China Sea Oceanic Basin. The continental-oceanic boundary is delineated by the 3.0 β factor contour (Le Pichon & Sibuet, 1981).

In general, the South China Sea Oceanic Basin has a near zero gravity signature indicating isostatic equilibrium. A prominent gravity low runs along the relict spreading axis of the southwestern subbasin, indicating the presence of a bathymetric depression at the spreading ridge. The relict spreading axis is modelled in Section 6.4.3.4. The southwestern extension of this axis mapped to 110°15'E, 9°N by Coulon *et al.* (1995) is not clearly visible on the residual free-air gravity map beyond about 111°30'E, 10°45'N.

In the east, the Scarborough Seamounts are located by their 50 - 100 mGal positive gravity anomalies. These seamounts run along the relict spreading axis (Pautot *et al.*, 1990). It is not possible, however, to say whether there is an axial trough in the eastern subbasin from the gravity data alone. Without detailed modelling not undertaken during this study, it was not possible to differentiate between the cause of the negative anomalies surrounding the seamounts as being due to an axial trough or to flexural downbending of the crust under the load of the seamounts (Watts *et al.*, 1975).

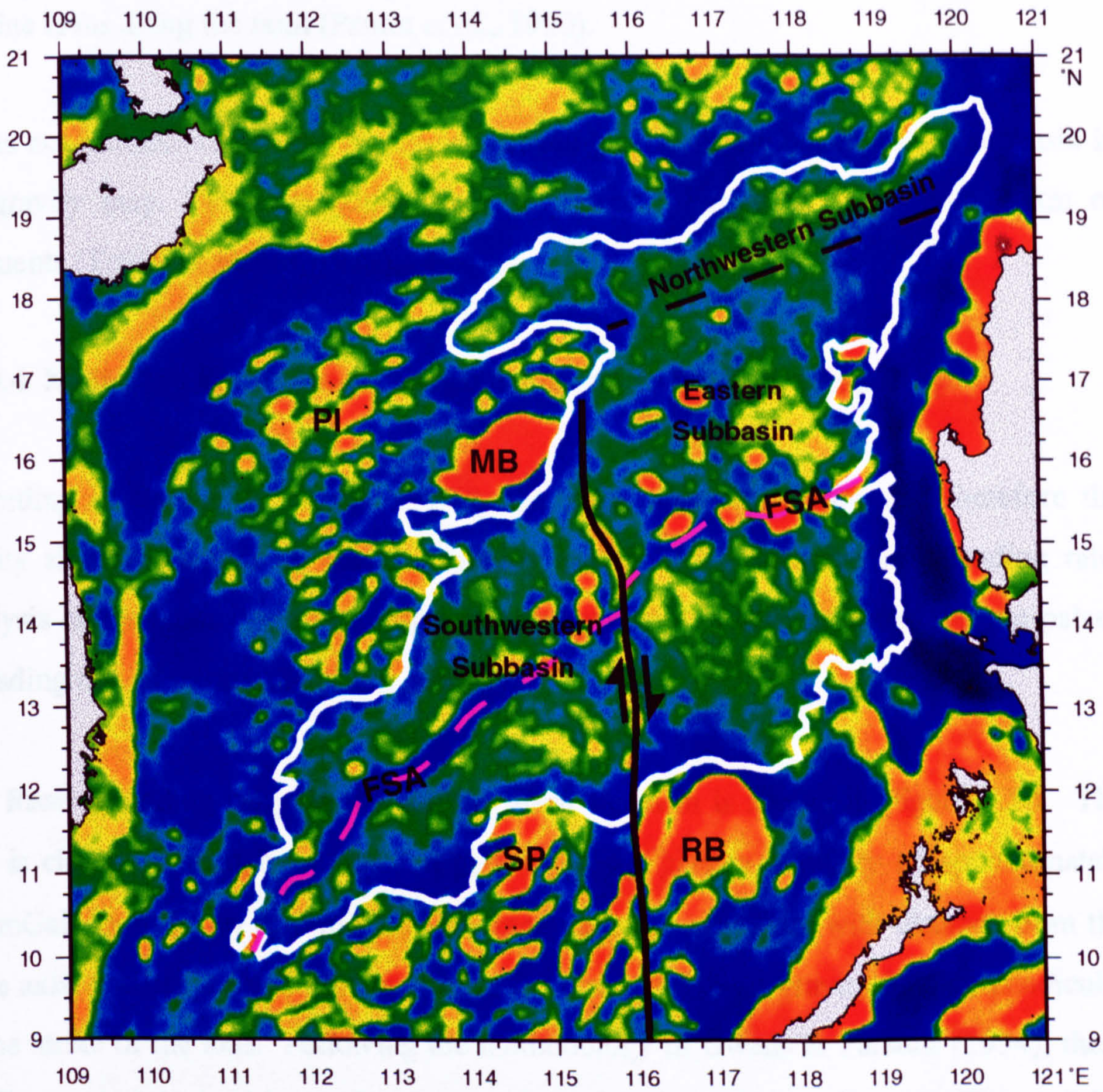

Figure 6.29. Interpreted free-air residual gravity map of South China Sea Oceanic Basin. White line delineates 3.0 β contour. SP = Spratley Platform; FSA = Fossil Spreading Axis; MB = Macclesfield Bank; PI = Paracel Islands; RB = Reed Bank.

Elsewhere in the oceanic basin, there is a prominent NNW-SSE lineament at approximately 116°E, which is interpreted as the trace of the transform fault between the faster-spreading eastern subbasin and the slower-spreading southwestern subbasin (Table 2.3). The positive gravity anomaly marking this fault results from the injection of alkaline lavas along the fault (Pautot *et al.*, 1990).

It was not possible to identify the fossil spreading ridge of the northwestern subbasin in the gravity map. This spreading ridge is presently buried by more than 2 km of sediments (Taylor & Hayes, 1983).

6.4.3.4 Modelling of the Southwestern Subbasin Relict Spreading Ridge

According to Owens & Parsons (1994), the axial ridge topography and therefore the gravity signature across an ocean spreading axis is highly sensitive to spreading rate. Analysis of the fossil spreading ridge gravity anomalies is here used to infer the paleo-spreading rate of the southwestern subbasin.

The fossil spreading ridge in the southwestern subbasin is shown in Figure 6.30. The axis is clearly defined by a linear negative free-air gravity anomaly of approximately -30 mGal. In order to determine the average variation of gravity with distance from the ridge axis, profiles were constructed from the residual free-air gravity field perpendicular to the strike of the axis. Following the methodology of Owens & Parsons (1994), these profiles were taken at intervals of approximately 10 km along the axis, Figure 6.31. Seventeen such profiles and the average profile are shown in Figure 6.32. The average profile was reflected about the axis and the two sides averaged, to give an effective average over 34 half-profiles; this significantly reduces the variability about the mean.

A 2D GM-SYS computer model of the axial ridge was constructed to fit the average free-air gravity profile over the fossil spreading axis (Figure 6.33), using the standard density model. The axial ridge is modelled to have a median valley, approximately 1100 m deep, bounded by steep valley walls. 500 m of post-spreading sediments (< 15.5 Ma) half-fill this valley (Pautot *et al.*, 1990). Crestal mountains on either side of

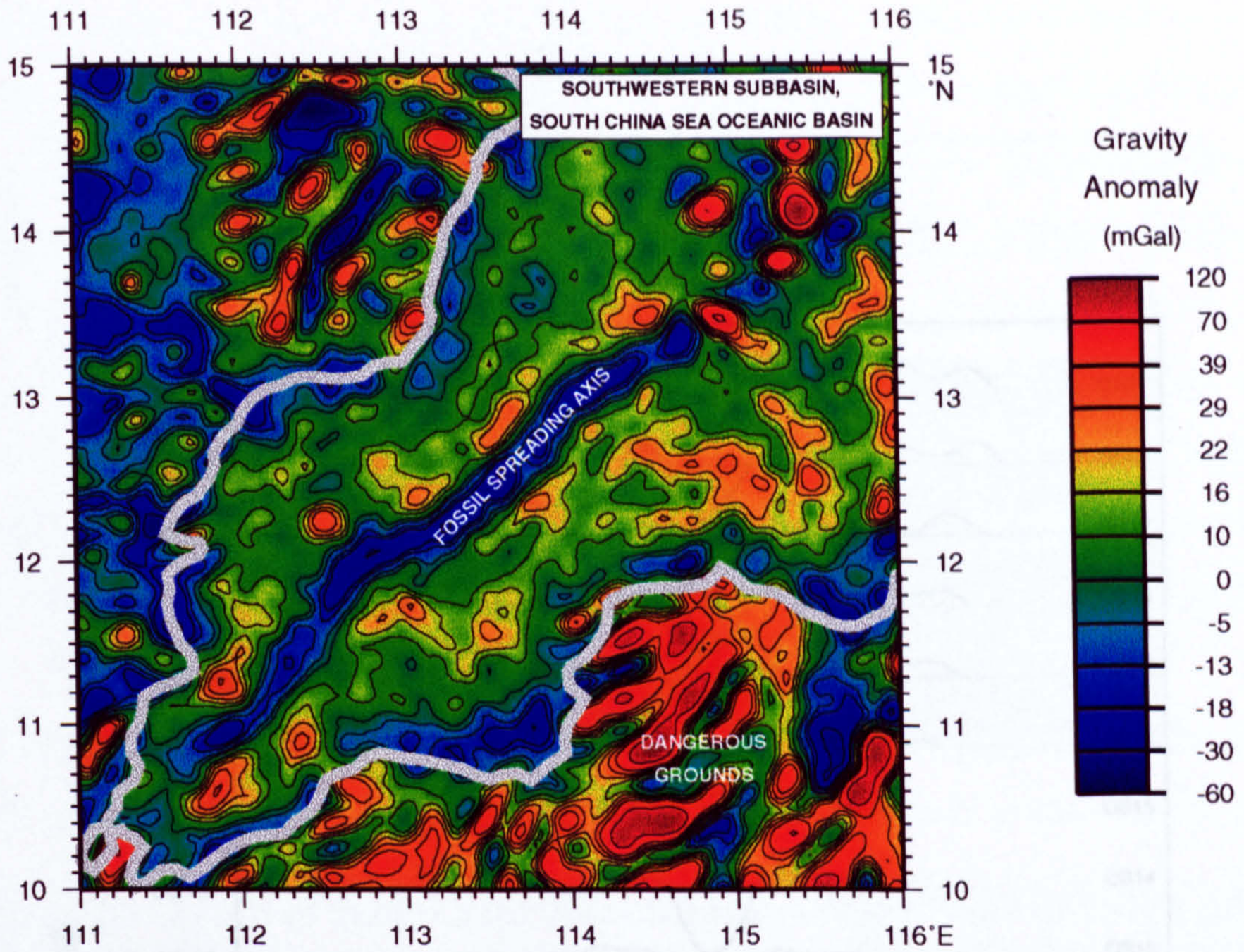

Figure 6.30. Free-air residual gravity anomaly map of the southwestern subbasin of the South China Sea Oceanic Basin. Grey line delineates 3.0 β contour.

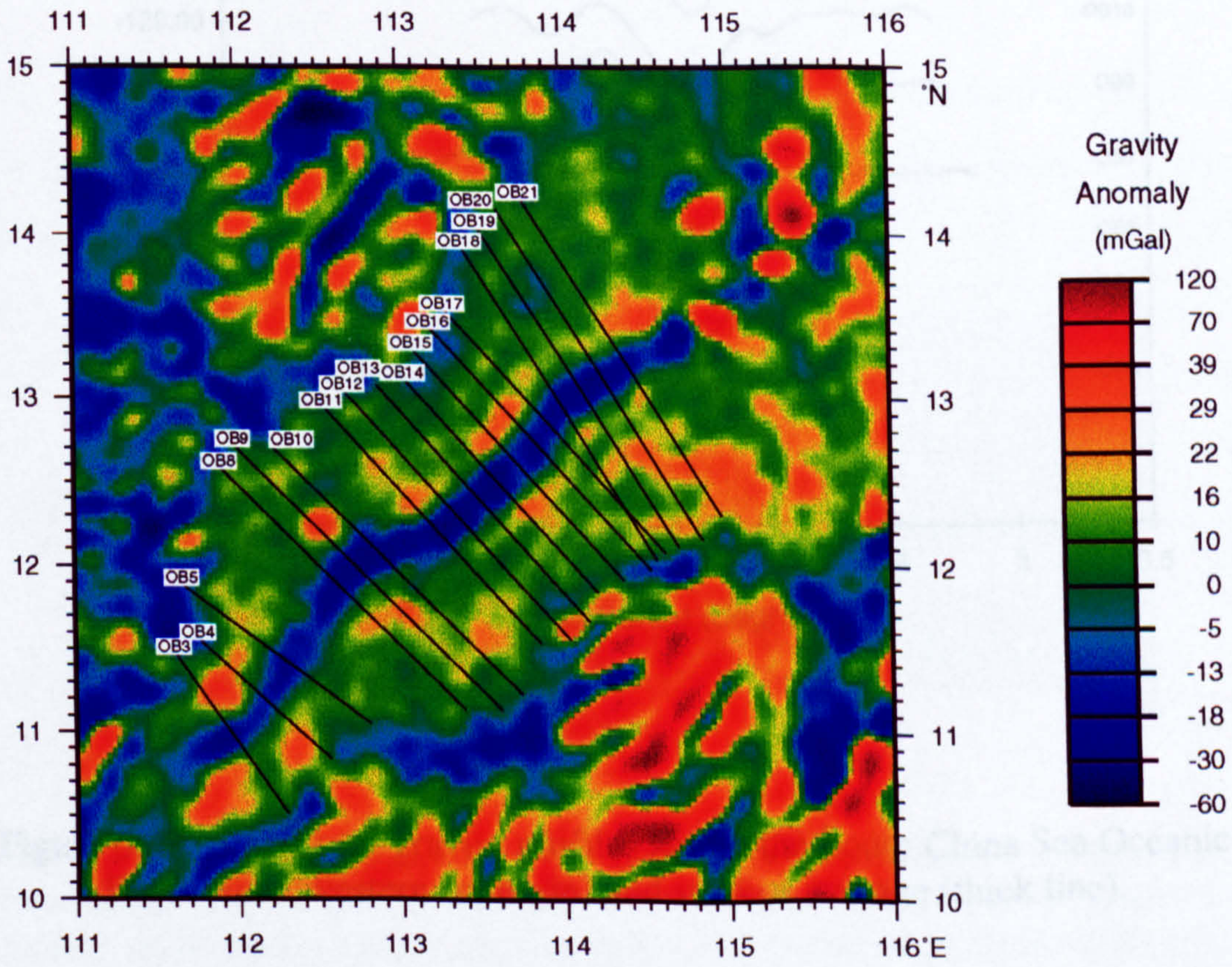

Figure 6.31. Map showing locations of gravity profiles in southwestern subbasin.

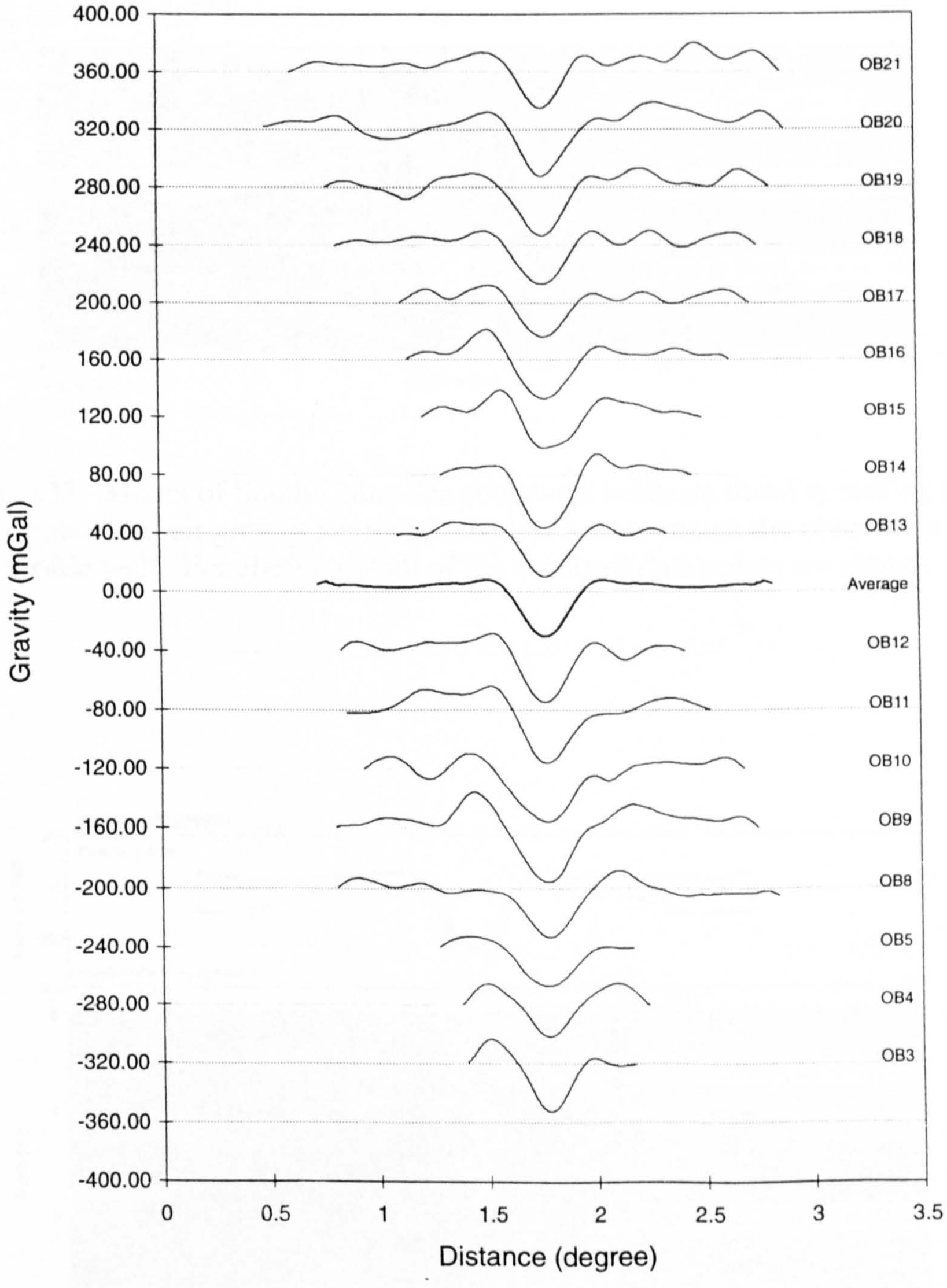

Figure 6.32. 17 free-air gravity profiles across the South China Sea Oceanic Basin (southwestern subbasin) and stacked average (thick line).

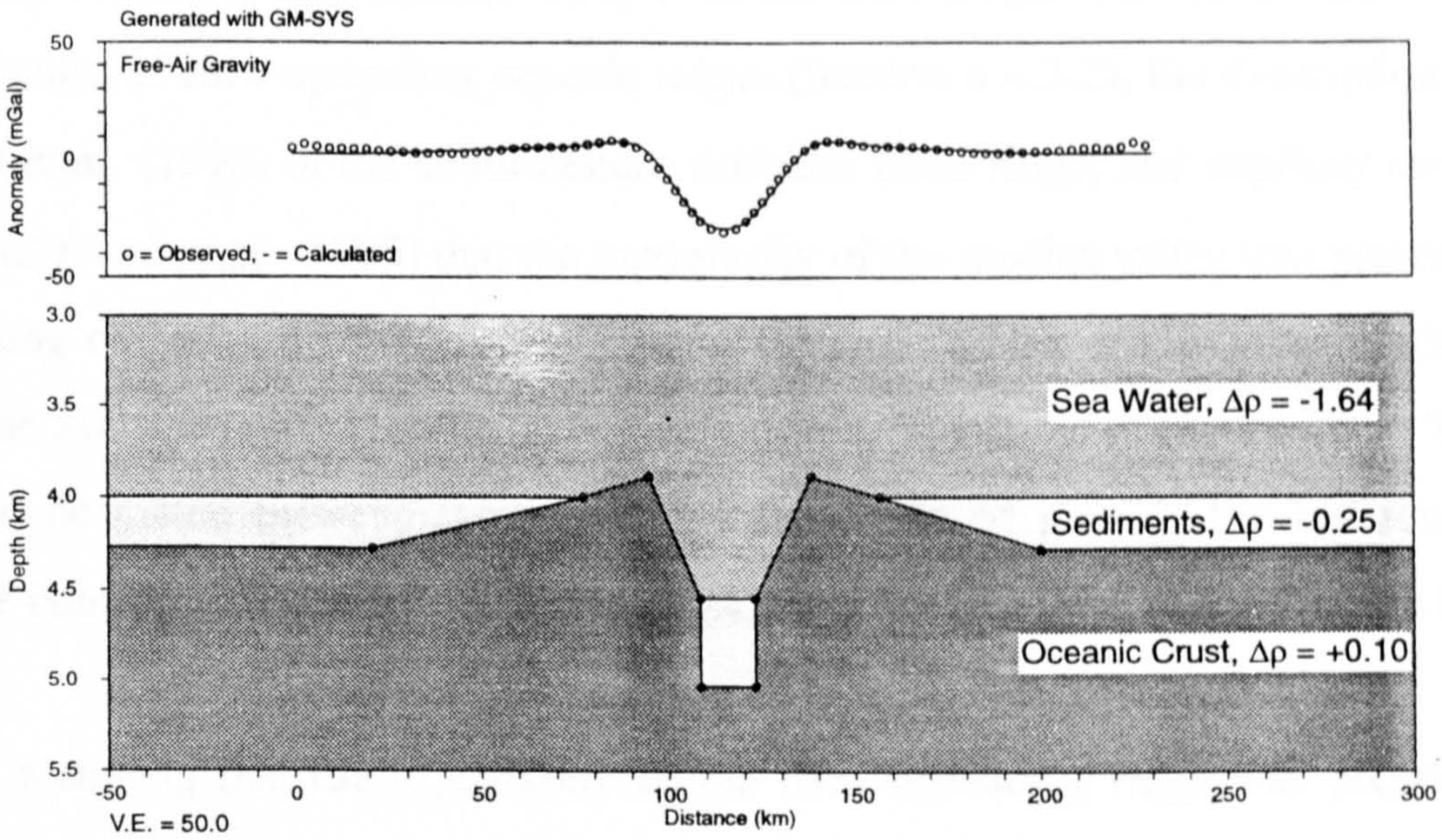

Figure 6.33. Model of South China Sea southwest subbasin fossil spreading ridge and associated free-air gravity anomaly, which is seen to match the observed average profile well. For clarity, not all of the observed data points are shown.

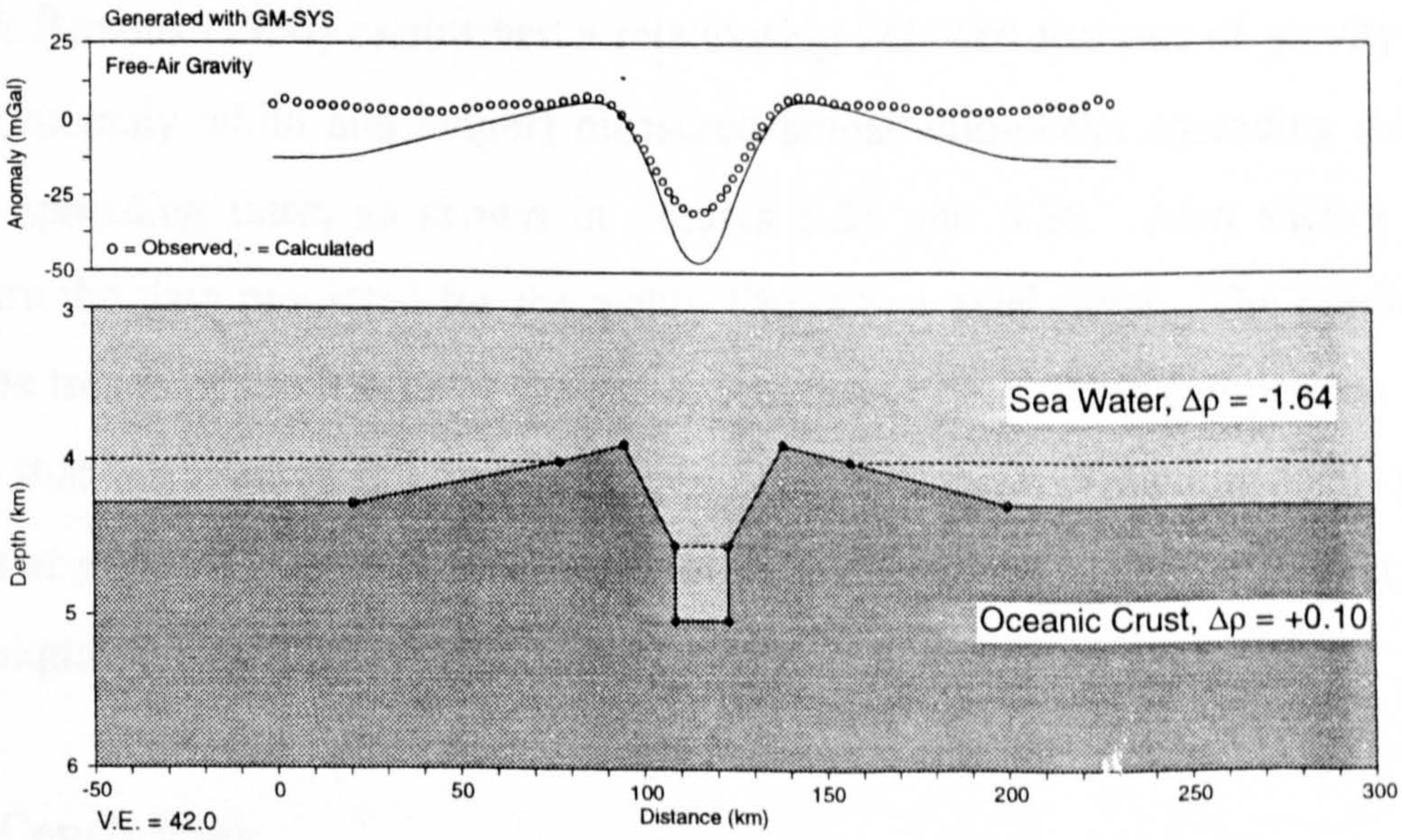

Figure 6.34. Model of South China Sea southwest subbasin fossil spreading ridge and associated free-air gravity anomaly after removal of post-spreading sediments. The gravity signature both at the median valley and on the ridge flanks is significantly lower in this model than in the model with post-spreading sediments.

the median valley are raised above the surrounding seafloor, which is covered by a layer of recent sediments that thickens away from the axial ridge. This model fits with recent descriptions of slow-spreading oceanic ridges (Section 6.4.3.2), the description given by Pautot *et al.* (1990) of the southwestern subbasin fossil ridge, and implicity assumes the result of Freed *et al.* (1995) that the topography of the median valley was preserved after spreading ceased *c.* 15.5 Ma. The gravity signature of the model gives a good match with the average gravity profile across the ridge, as illustrated in Figure 6.33. To ensure a good dc match between the model and the observed gravity, the horizontal crust-mantle boundary was set at a depth of 16.24 km below sea level (not shown on figure).

Again assuming that the topography of the fossil spreading ridge was preserved after spreading stopped, it was possible to remove the gravity effect of the post-spreading sediments, and therefore to predict the gravity signature across the ridge at the time of final spreading. No account was taken for possible changes in crustal or mantle densities. This predicted gravity anomaly was thus simply obtained by replacing the sediment layers in the first model of the axial ridge (Figure 6.33) by water, as illustrated in Figure 6.34.

Owens & Parsons (1994) established a relationship between features of gravity anomaly profiles (anomaly width and height) measured across mid-ocean spreading ridges with different spreading rates, as shown in Figures 6.35 and 6.36. Also shown on these figures are the data predicted for the South China Sea axial ridge. The predicted data lies on the trends of the results of Owens & Parsons (1994). This comparison therefore suggests that the average full spreading rate of 35 ± 5 mm/yr (Section 2.2.4) predicted by Briais *et al.* (1993) from interpretation of magnetic lineation data is correct, and that the technique used by Owens & Parsons (1994) is, in fact, widely applicable.

6.4.3.5 Conclusions

The South China Sea Oceanic Basin has been mapped to a higher resolution than previously possible using the new high resolution satellite gravity data. Analysis of the fossil spreading ridge in the southwestern subbasin has proved fruitful. An average

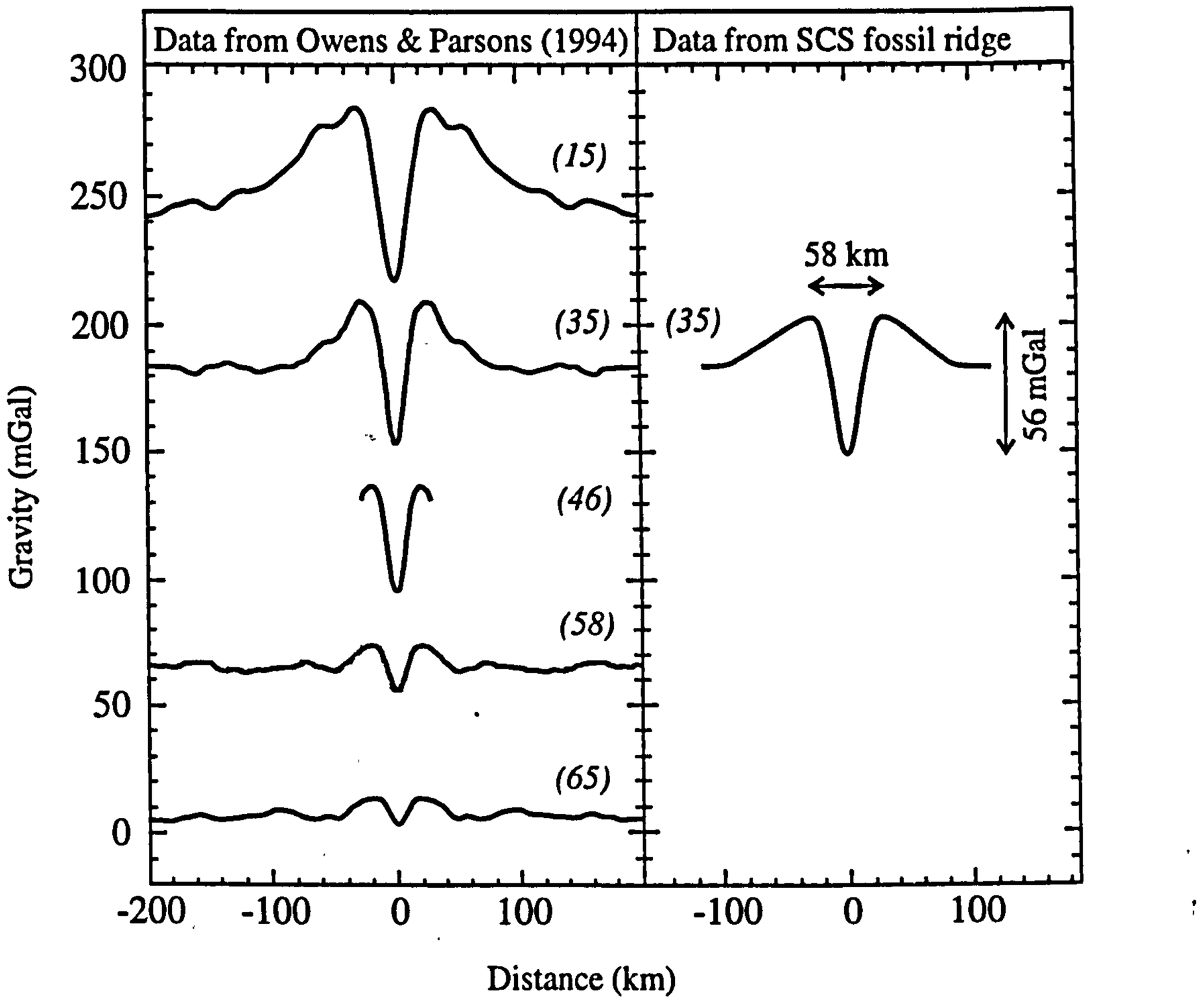

Figure 6.35. The average of stacked free-air gravity profiles for the slow-spreading mid-ocean ridges measured by Owens & Parsons (1994) and for the SCS relict spreading axis. Spreading rate is given in brackets.

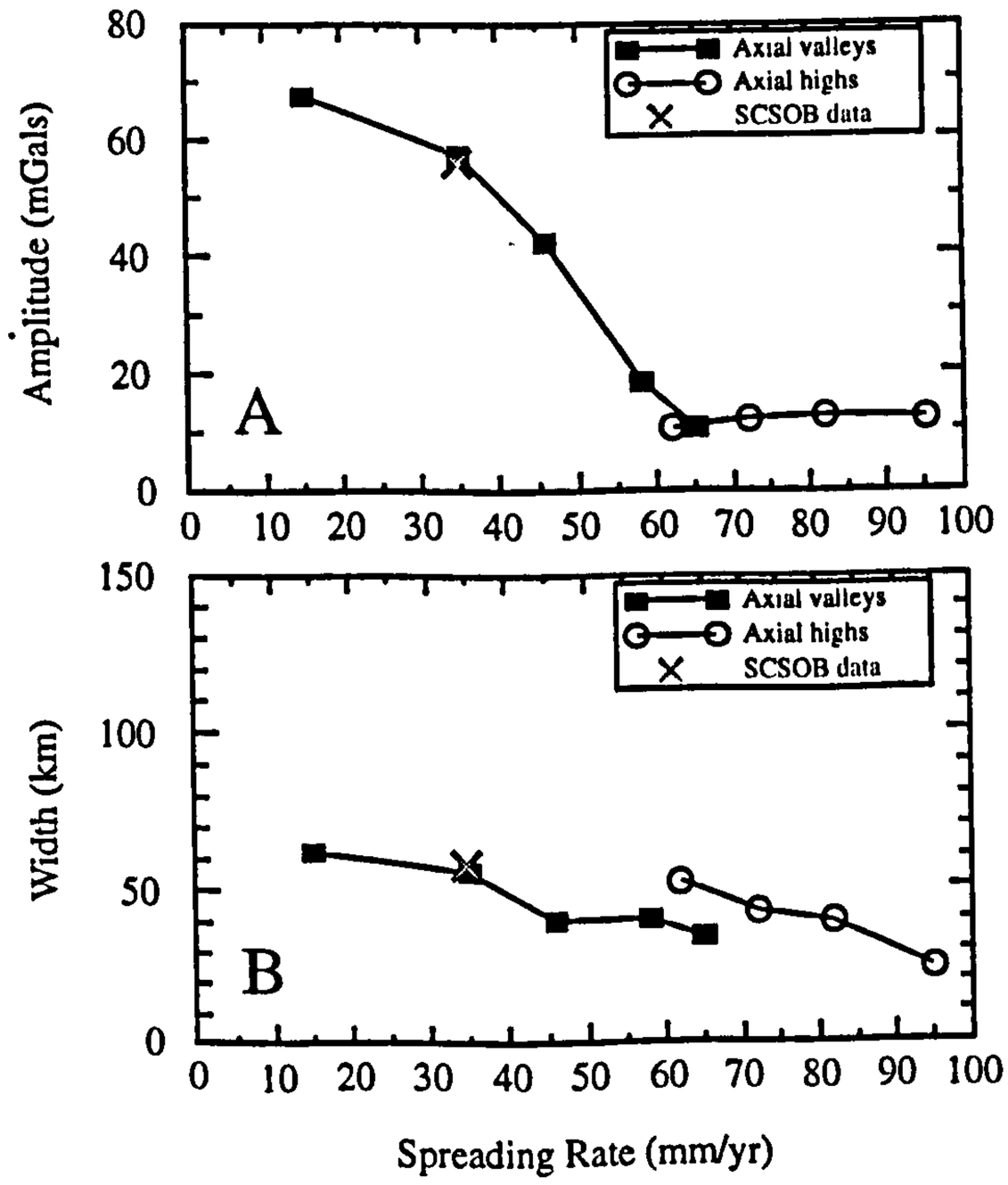

Figure 6.36. A: Peak-to-trough amplitudes of average free-air gravity profiles of Owens & Parsons (1994) and the SCSOB. B: Widths across axial free-air gravity lows and highs. The width across an axial low was measured between the peaks of the flanking highs.

gravity profile across the ridge in the direction of paleo-spreading was obtained by averaging 17 profiles and modelled. The model was then altered by the removal of the post-spreading sediments, and the corresponding gravity anomaly was calculated. This anomaly is believed to represent the ridge gravity anomaly at the time when spreading stopped in the South China Sea owing to the stability of axial valleys for tens of millions of years after cessation of extension. A comparison of this gravity anomaly with average gravity anomalies measured over a series of modern spreading ridges of different spreading rates yields a good match for a spreading rate of ~ 34 mm/yr. This predicted value of spreading rate is in excellent agreement with the average full spreading rate of 35 ± 5 mm/yr given by Briais *et al.* (1993) on the basis of interpretation of magnetic lineaments, and therefore independently confirms the accuracy of the magnetic lineation interpretation.

The gravity anomaly measured over the fossil spreading axis in the southwestern subbasin of the South China Sea oceanic basin may also be compared with gravity anomalies measured at other extinct spreading centres. Comparison of the free-air gravity lows over the extinct spreading centres of the Coral, Labrador and South China Seas reveal a similar spreading rate dependency to that observed at active spreading ridges, Table 6.4. In each case, however, the free-air gravity anomalies measured at the extinct spreading centres are ~ 15 mGal less negative than those found at active spreading centres, possibly as a result of post-extinction sedimentary infill (Figure 6.34). Since the gravity anomalies in the Coral and Labrador Seas were derived from single ship gravity profiles, there is considerable scope for additional research using the average satellite-derived gravity profiles over these extinct spreading centres and detailed comparison with the results of this study.

Table 6.4. Free-air gravity anomalies measured at extinct spreading centres.

Location	Spreading Rate (mm/yr)	Time of Extinction (Ma B.P.)	Amplitude of Free-air anomaly (mGal) [A]	Amplitude of Free-Air Anomaly at Active Spreading Centres with Equivalent Spreading Rates[2] (mGal) [B]	Difference [B]-[A] (mGal)
Coral Sea[1]	48	56	20*	35*	15
Labrador Sea[1]	7	40	55*	70*	15
SCSOB	35	15.5	40*	55*	15

[1] From Jonas *et al.* (1991) [2] From Owens & Parsons (1994) * Accurate to ± 5 mGal

6.4.4 Sabah

6.4.4.1 Introduction

Sabah lies at the geological junction between the cratonic core of Sundaland, the Sulu, Celebes and South China Sea marginal basins, and the volcanic arc systems of the Philippines (Chapter 2). Several regional tectonic events have occurred in this area since the Early Tertiary, producing well-developed compressional and extensional structures of considerable geological complexity. Although the number of field geological measurements has increased significantly in the last few years, there are still major geological questions to be answered, such as:

- Is Sabah underlain by continental or oceanic crust?
- Do the Darvel Bay and Telupid ophiolites form part of a NW-SE trending suture zone?
- What is the depth of the crustal root beneath the Crocker Ranges?
- What is the thickness of sediment within the Maliau Basin?

This study has produced a new gravity anomaly map of Sabah which is complete at a regional reconaissance level and is a major improvement on the previous gravity map which only covered western Sabah (Chapter 5). The qualitative and quantitative interpretations of this new map presented in this section have specifically addressed the geological questions outlined above.

6.4.4.2 Qualitative Interpretation of the Sabah Gravity Field

An interpreted residual gravity anomaly map of Sabah is shown in Figure 6.37. The map was formed by the subtraction of the long wavelength GEM-T3 gravity anomaly field from the onshore Bouguer and offshore free-air gravity anomaly fields, as discussed in Section 6.3. This regional-residual separation has the effect of reducing the gravity anomaly field of Sabah by approximately 35 mGal and is therefore a very significant correction. Offshore, the residual free-air anomalies tend to follow bathymetry, while the

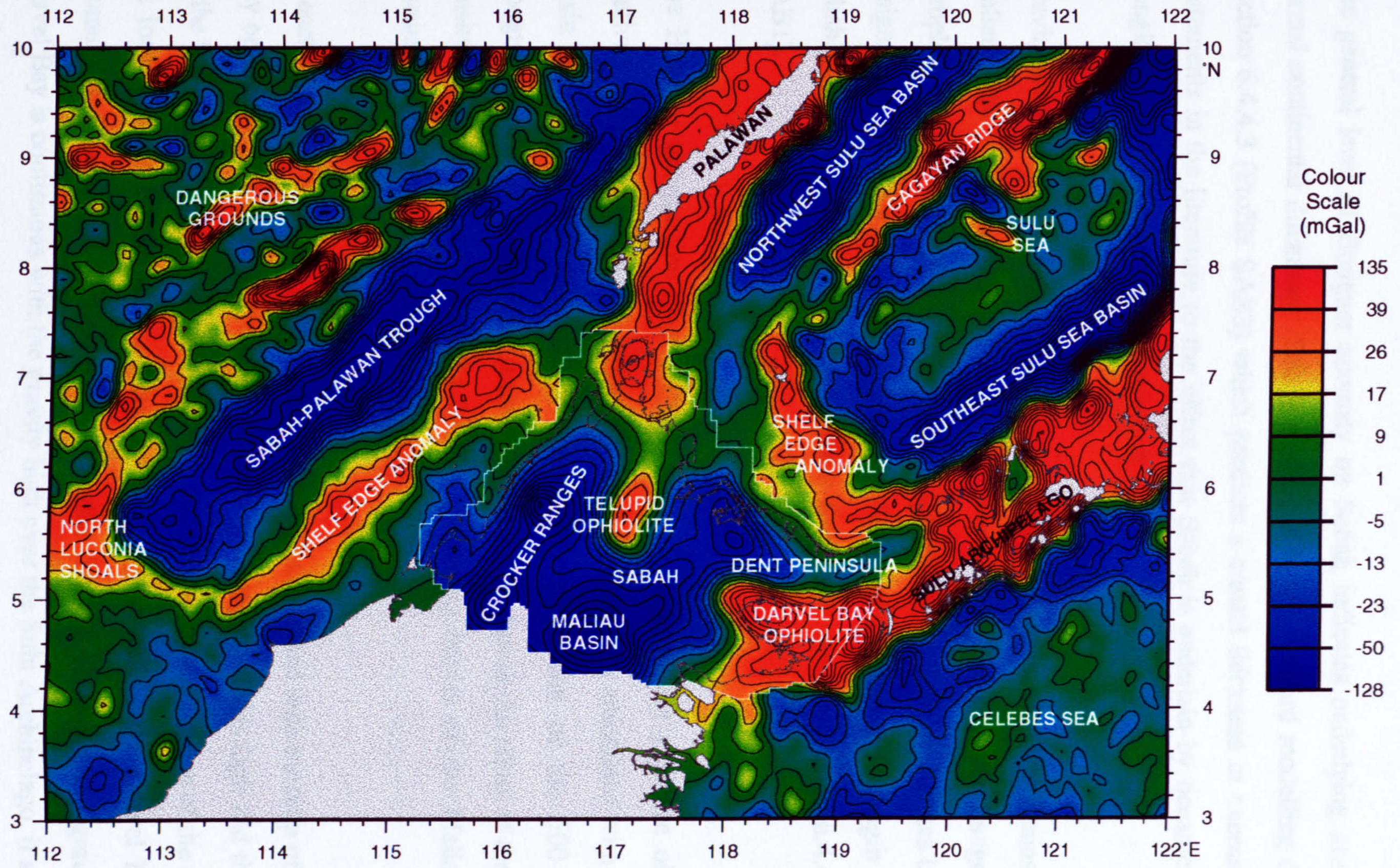

Figure 6.37. Interpreted gravity anomaly map of Sabah. Onshore: residual Bouguer anomalies. Offshore: residual free-air anomalies. White line delineates boundary. 10 mGal contour interval.

Bouguer anomalies onshore bear an inverse relationship to topography. Over low lying areas, such as those found near the coastline, the free-air and Bouguer anomalies are approximately equal.

The general level of Bouguer anomaly on Sabah indicates underlying crust of near-normal continental thickness. This is confirmed by the forward modelling discussed in Section 6.4.4.3 (Profile SAB3) which predicts a crustal thickness in excess of 30 km. Statements in the literature to the effect that Sabah is underlain by oceanic crust (e.g. Tongkul, 1991) must therefore be rejected.

Gravity lows are found in the vicinity of the Crocker Ranges, the Dent Peninsula and the Maliau Basin. The deep Bouguer gravity low beneath the Crocker Ranges indicates complete or almost complete local isostatic support for the Crocker Ranges by means of a significant crustal root, and suggests low levels of lithospheric strength in western Sabah. A gravity model across the Crocker Ranges is given in Section 6.4.4.3 (Profile SAB1).

The Bouguer gravity low on the Dent peninsula suggests the presence of thick and relatively light crust. The very strong Bouguer anomaly low associated with the Maliau Basin can in part be attributed to isostatic compensation of the 500 metres of topographic relief in the area, but a major part must be due to the effect of the thick, low density sediments deposited in the basin. A gravity model of the Maliau Basin is discussed in Section 6.4.4.3 (Profile SAB2).

In eastern Sabah, there is a prominent gravity high associated with outcrop of the Darvel Bay ophiolite. The direct correlation between the margins of this high and the coastline of the bay strongly suggest that the bay has been formed by subsidence of the crust under the load imposed by the mass of the ophiolite. A model of the Darvel Bay gravity anomaly is discussed in Section 6.4.4.3 (Profile SAB3). Because the gravity high in Darvel Bay is continuous with the gravity high over the Sulu Archipelago, it seems likely that these areas are part of the same geological feature.

The gravity high in the Telupid region of central Sabah is associated with the outcrops of mafic and ultramafic rocks. Several authors (e.g. Tjia, 1988; Ryall & Beattie, 1989) have been tempted to link the ophiolite outcrops in Darvel Bay to those in Telupid and to those running north from Telupid to Banggi Island, forming the 'Kinabalu Suture zone', as illustrated in Figure 6.38. However the new gravity anomaly map shows that the gravity highs in Darvel Bay and Telupid are divided by a deep gravity low, which is interpreted as a NE-SW trending belt of thick continental crust (Section 6.4.4.3, Profile SAB3). There is no evidence for a link between the Darvel Bay and Telupid ophiolites in the gravity data, and therefore the existence of the 'Kinabalu Suture zone' is rejected.

It is the author's opinion that there are two plausible theories for the origin of the Telupid ophiolite - either the ophiolite was obducted onto Sabah during the subduction of the proto-South China Sea, or it represents a fragment of Sulu Sea oceanic crust which became trapped during the Sabah Orogeny. The new gravity map does not however provide any clues favouring either theory.

Offshore, prominent positive gravity lineaments caused by the shelf-edge effect (Section 6.4.1) dominate the nearshore gravity fields of both the South China Sea and the Sulu Sea. Other gravity highs are associated with the Cagayan Volcanic Ridge and the bathymetric variations (mainly reefs) on the highly attenuated continental crust of the Dangerous Grounds (microcontinental?) block. The deep gravity low associated with the Sabah-Palawan Trough is largely caused by the bathymetry of the trough (Milsom *et al.*, 1997). Other deep gravity lows are found over the thick sedimentary sequences of the northwest and southeast Sulu Sea Basins (Section 2.2.6).

DESCRIPTION

The Kinabalu Suture zone contains most of the mafic-ultramafics, Chert-Spilite ophiolite and melange, and olistostromes of the Wairu (W), Trusmadi-Crocker (in the Ranau area), Kuamat (Ku) and Kalumpang (Ka) formations. Other diamictites/ olistrostromes of the Kalabakan (Kb), Ayer (A) and Garinono (G) formations occur in the vicinity of the suture zone.

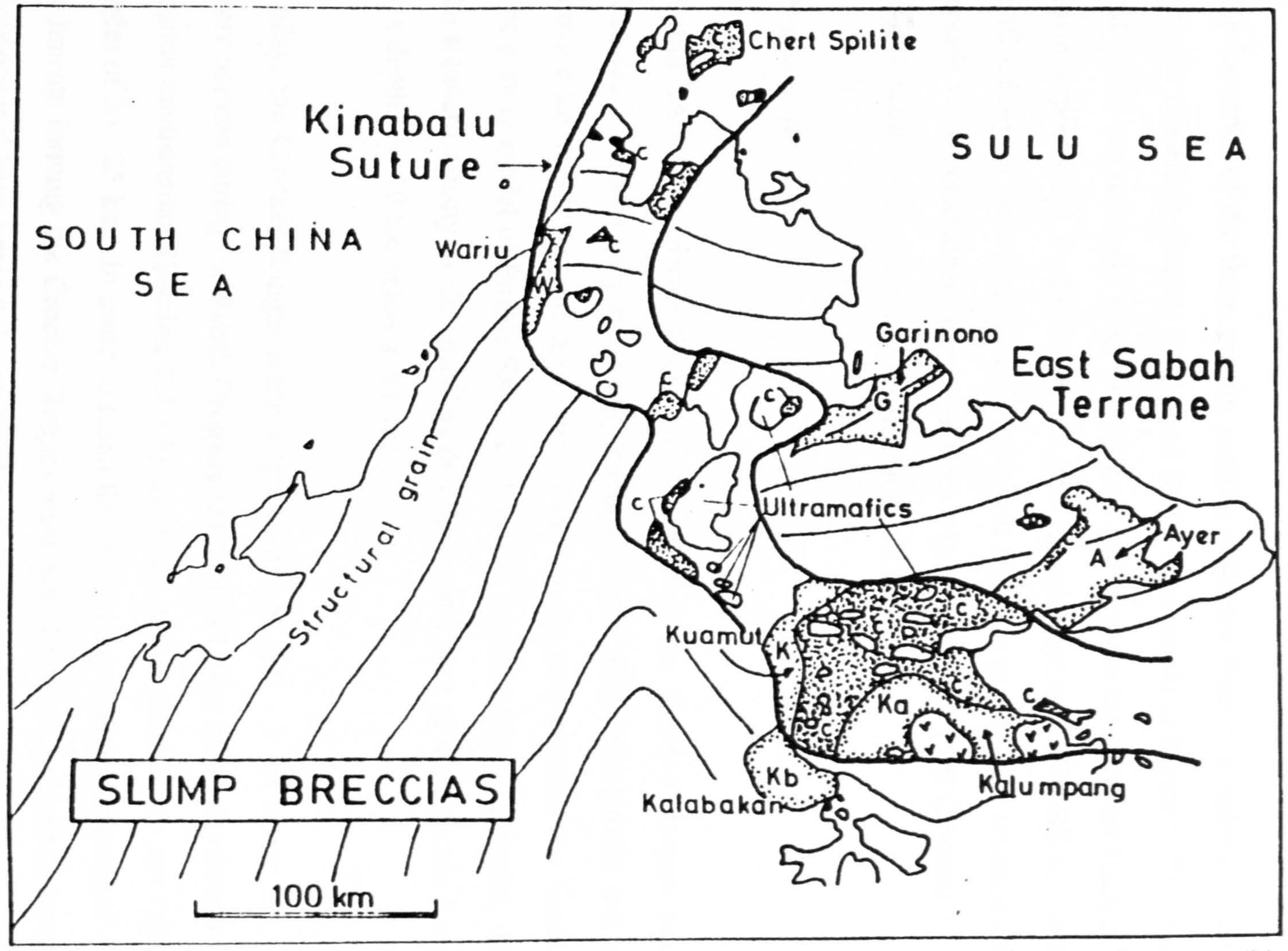

Figure 6.38. Qualitative interpretation of the Sabah gravity anomaly field rejects the existence of the 'Kinabalu Suture zone' as shown here. From Tjia (1988).

6.4.4.3 Quantitative Interpretation of the Sabah Gravity Field

The locations of the three gravity profiles extracted from the residual gravity anomaly map for modelling (SAB1, SAB2 and SAB3) are shown in Figure 6.39. Profiles SAB1 and SAB2 are relatively short (~ 150 km) and traverse the Crocker Ranges and Maliau Basin respectively. Profile SAB3 is ~ 850 km long and runs NW-SE across Sabah. The 2½D GM-SYS geological models produced from the profiles are discussed below. The models were constrained using the TPI5.2 bathymetry data set (Section 1.3.2) and the NGDC sediment isopach data set (Section 1.3.3).

Profile SAB1

Profile SAB1 runs perpendicular to the strike of the Crocker Ranges south of Kota Kinabalu in an area of good gravity control (Figure 5.7). This profile was modelled to provide information about the depth of the crustal root beneath the Crocker Ranges. The gravity model of Profile SAB1 is shown in Figure 6.40. The model, derived using the standard density model, predicts that the crustal root of the Crocker Ranges extends to a depth of ~ 49 km below sea level.

Today, the Crocker Ranges reach a typical height of 1 - 2 km above sea level. They were uplifted during the Sabah Orogeny (Middle to Upper Miocene) from a marine/deep marine environment (Section 2.2.3.3) in which crustal thicknesses are typically of the order of 20 - 25 km. In order to reach the present day crustal thickness of ~ 50 km, the sediments forming the Crocker Ranges must have been compressed to less than half of their original lateral extent during the Sabah Orogeny.

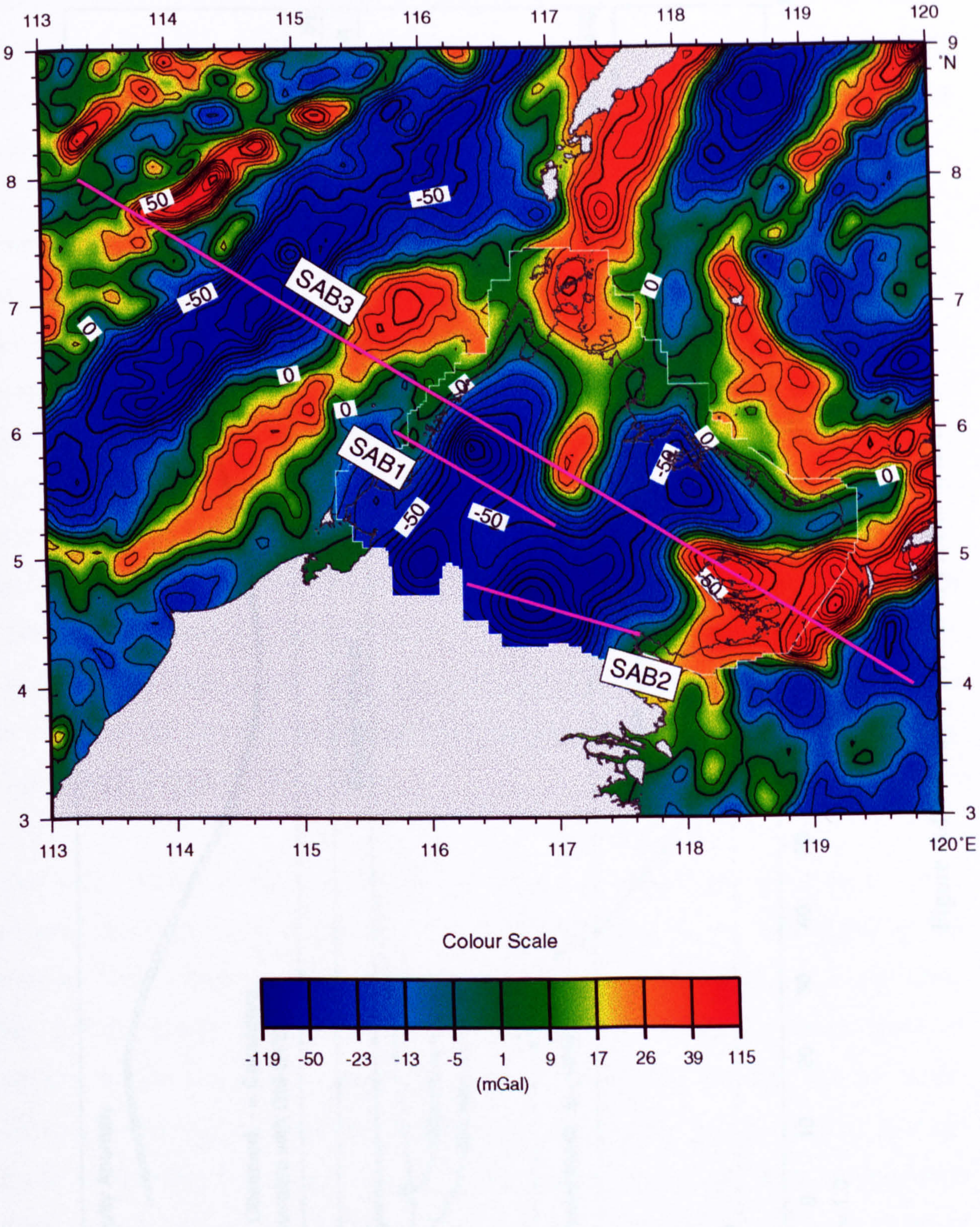

Figure 6.39. Residual Gravity Anomaly Map of Sabah.
Free-Air Offshore, Bouguer Onshore, GEM-T3 Subtracted.
White line delineates boundary. 10 mGal contour interval.
Gravity profile lines shown in purple.

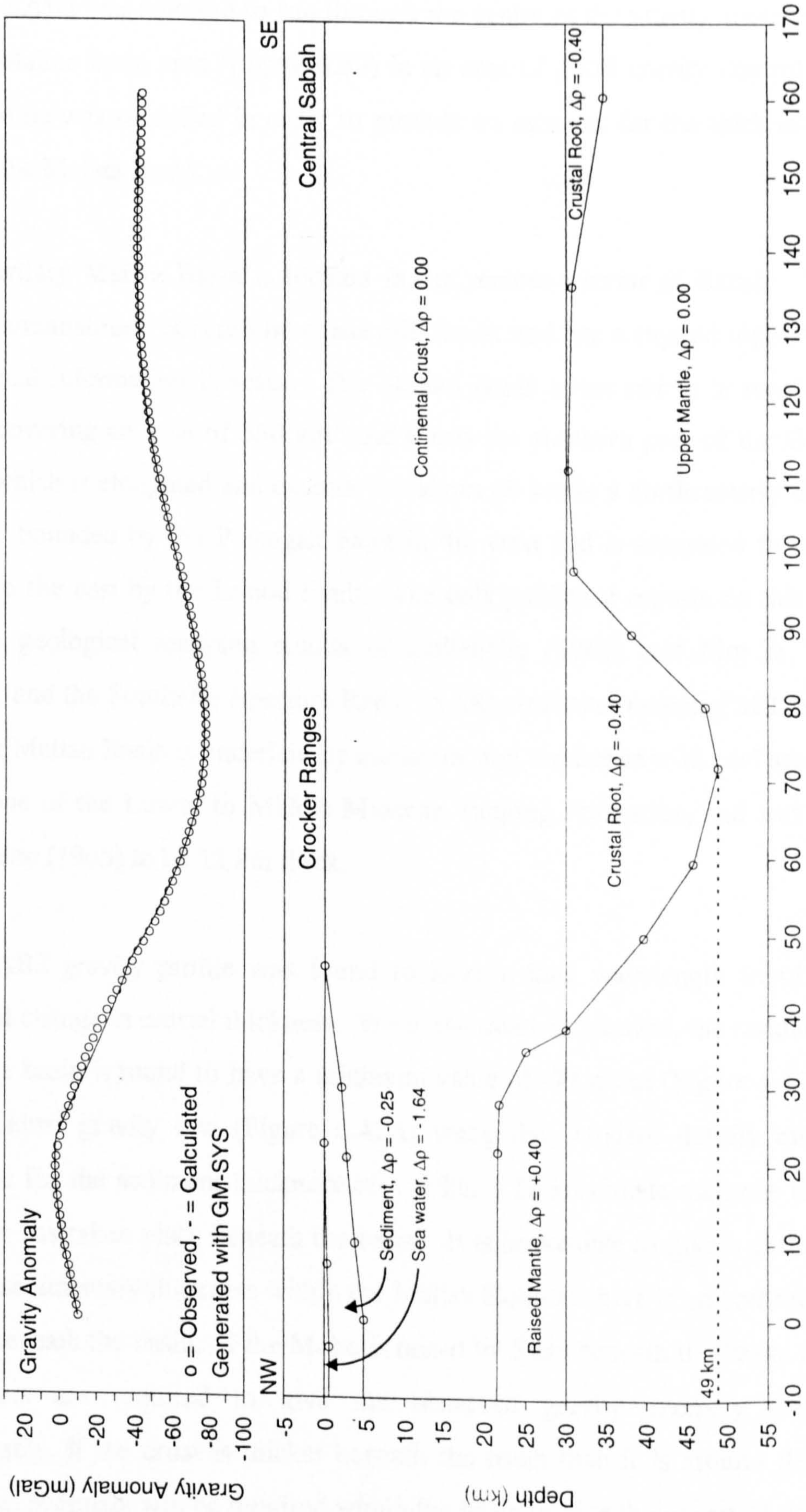

Figure 6.40. Gravity Model of Profile SAB1.

Profile SAB2

Profile SAB2 was selected to run through the centre of the gravity anomaly low defined in the Maliau basin area (Figure 6.39) in an area of good gravity control (Figure 5.7). The profile was modelled in order to provide an estimate for the thickness of sediment within the Maliau Basin.

The Tertiary Maliau Basin is located in the remote interior of Sabah. The region is largely uninhabited, covered by dense rain forest and has a rugged topography. Hence geological information is scant. The Maliau Basin *sensu stricto* is roughly circular in shape covering an area of 550 km^2 and forms the southern part of the Greater Maliau Basin which is elongated and extends for about 60 km in a northeasterly direction. The basin is bounded by the Pinangah Fault in the west and is separated from the Malibau Basin to the east by the Lonod Fault. The only published reports on this basin are the surface geological mapping results of Collenette (1965) and Lim & Tungah-Surat (1989), and the Synthetic Aperture Radar (SAR) structural mapping of Lai (1990). The Greater Maliau Basin is underlain by mudstone and sandstone with coal seams and minor limestone of the Lower to Middle Miocene Tanjong Formation, and was estimated by Collenette (1965) to be 12 km thick.

The SAB2 gravity profile was found to have a long wavelength trend caused by a regional change in crustal thickness. When the trend is removed, the residual gravity low over the basin is found to have a minimum value of -72 mGal (Figure 6.41). Modelling this residual gravity low (Figure 6.42A) using the standard density model gives an estimate for the sediment thickness of ~ 8 km. This estimate assumes that no crustal thinning has taken place beneath the basin. It is impossible to give a definitive estimate for the sedimentary thickness within the Maliau Basin as there is no control on the Moho depth beneath the basin. If the Moho is raised by 5 km beneath the basin, then 12 km of sediments are required to give the observed gravity anomaly (Figure 6.42C). Conversely, if the crust is thicker beneath the basin than it is around the surrounding area, less sediment will be required within the basin to give the observed gravity anomaly

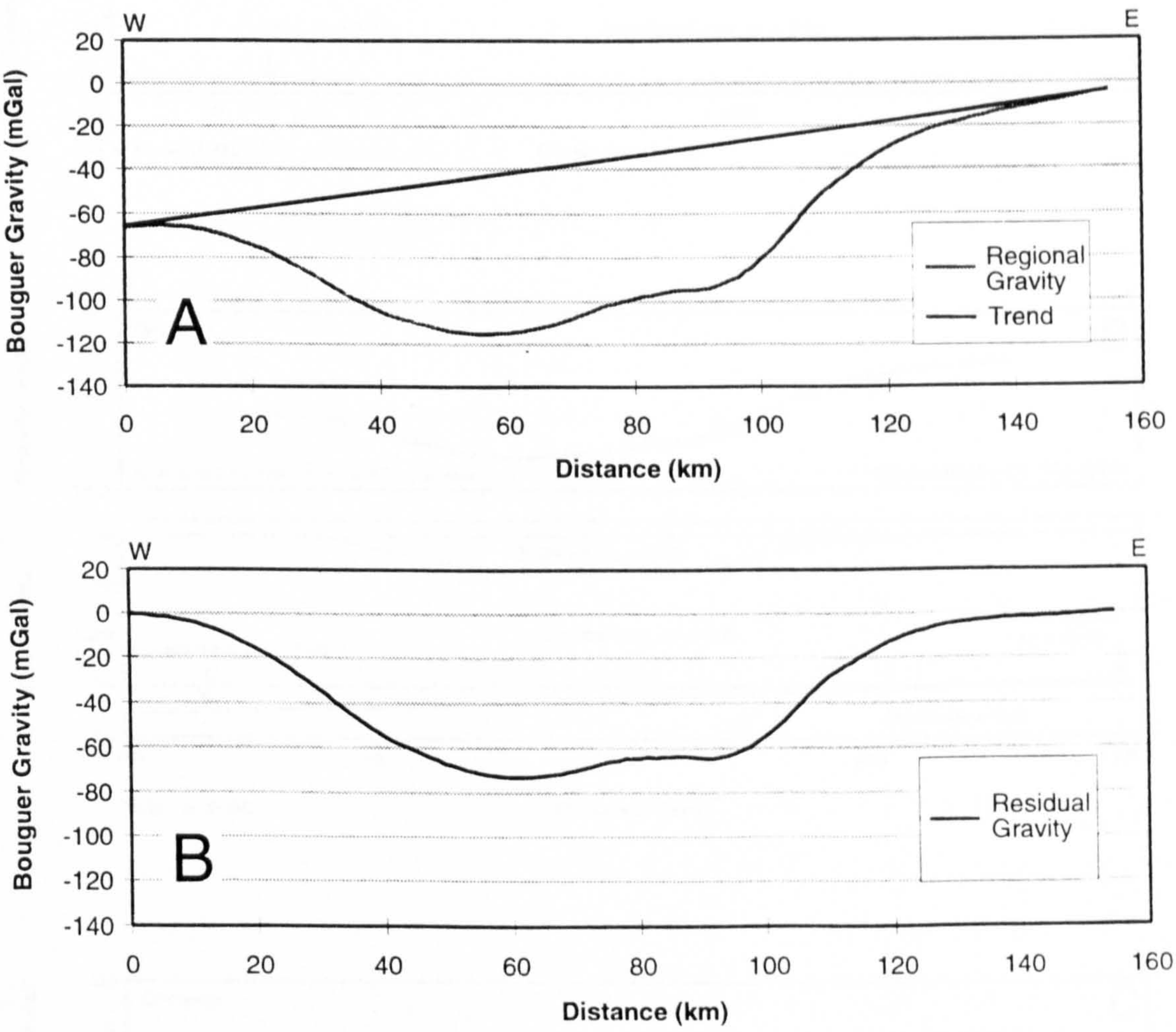

Figure 6.41. A: Regional gravity and trend along Profile SAB2 across Maliau Basin, Sabah. B: Residual gravity anomaly.

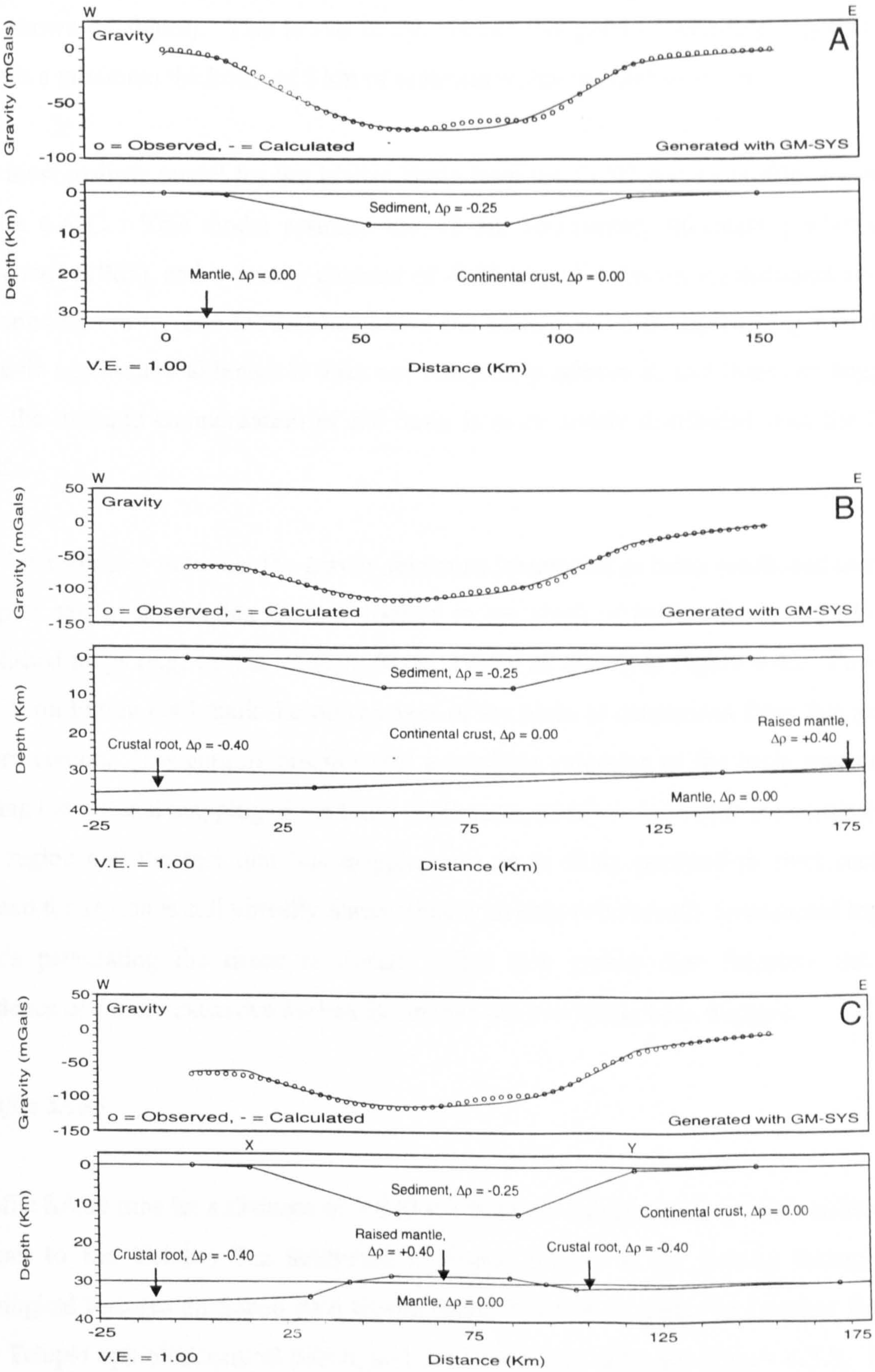

Figure 6.42. Three 2.5D GM-SYS gravity models of the Maliau Basin. A: Residual anomaly model. B: Regional anomaly model, no crustal thinning. C: Regional model with 5 km of crustal thinning beneath basin.

(not shown on figure). This is less likely. Hence this gravity modelling suggests that there is a minimum thickness of 8 km of sediment within the Maliau Basin.

The most realistic model for the Maliau Basin from the SAB2 gravity profile is given in Figure 6.42C. This model assumes the 12 km sedimentary thickness predicted by Collenette (1965), and a density contrast of -0.25 $Mg.m^{-3}$ between the sediment and the surrounding crust. The model shows that the Maliau Basin is approaching a state of isostatic equilibrium although it does not completely achieve it, and therefore suggests that the isostatic compensation of the basin is more widely distributed than the basin itself.

It is interesting to note that the gravity minimum interpreted as being positioned over the deepest part of the Maliau Basin is located to the south of Maliau Basin according to published maps (e.g. Lim & Tungah-Surat, 1989), as shown in Figure 6.43. Points X and Y on Figure 6.43 mark the outer edges of the basin as determined from this gravity interpretation. It is entirely possible that a southern extension of the basin was missed during the original mapping of the basin (Collenette, 1965) owing to the inaccessibility of the region and the fact that this mapping was most likely confined to river sections. Indeed the region is still virtually inaccessible with only two recently constructed logging roads penetrating the dense rainforest. This new gravity data therefore provides evidence of a more extensive Maliau Basin than has previously been mapped.

Profile SAB3

Profile SAB3 runs for a distance of ~ 850 km from the Dangerous Grounds northwest of Sabah to the Celebes Sea southeast of Sabah (Figure 6.39), cutting through key geological features on Sabah such as the Sabah-Palawan Trough, the Crocker Ranges, the Telupid ophiolite, central Sabah, and the Darvel Bay ophiolite (Figure 6.37). SAB3 was selected to run in the same directions as published geological sections (e.g. Figure 2.8) and hypothetical geological interpretations (e.g. Figure 6.44E). Figure 6.44 shows a previous hypothetical tectonic reconstruction of Sabah based on the geological interpretation of surface outcrop data (Tongkul, 1991) unconstrained by either seismic

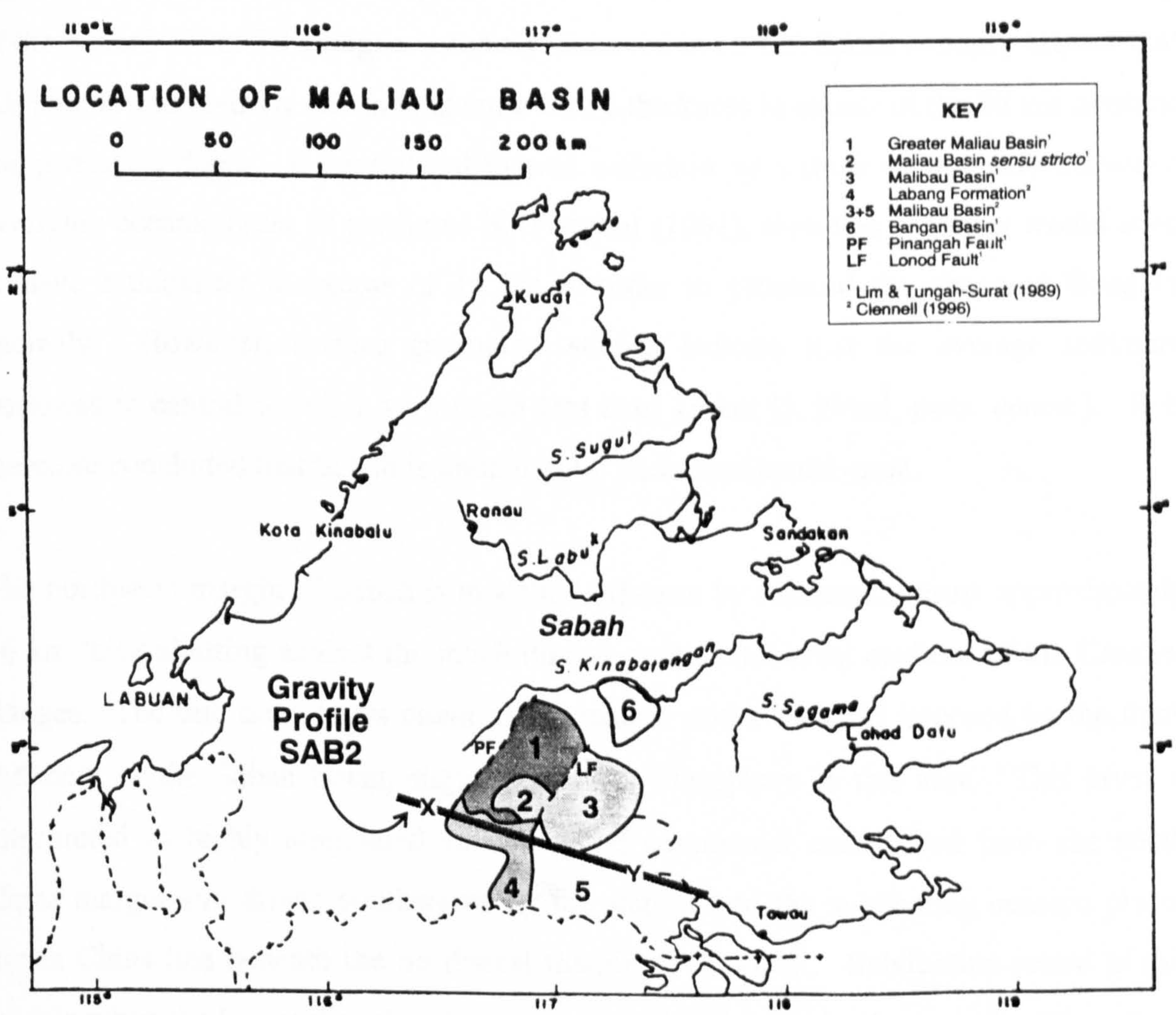

Figure 6.43. Locations of the Maliau Basin and Gravity Profile SAB2.

sections or gravity data. A new geological cross-section of Sabah, obtained by GM-SYS forward modelling of the SAB3 residual gravity anomaly profile, is presented in Figure 6.45.

Visual comparison of the model of SAB3 (Figure 6.45) and the model of Tongkul (Figure 6.44E) shows that these models of Sabah are quite different. Perhaps the most significant difference is the interpretation of the basement of Sabah. Gravity modelling of the typical -50 mGal Bouguer anomaly observed in central Sabah strongly implies that this area is underlain by continental crust with a thickness in excess of the 30 km isostatic compensation depth. If central Sabah was underlain by a thick sedimentary sequence overlying oceanic crust as predicted by Tongkul (1991), then this sediment would need to have a thickness in excess of 15 km in order to produced the observed Bouguer anomaly. However, surface geological studies indicate that the average sediment thickness in central Sabah is very much less than 15 km (J. Noad, *pers. comm.*). It is therefore concluded that Sabah is underlain by thick continental crust.

The northwest margin of Sabah is modelled offshore by continental crust approximately 16 km thick abutting against the much thicker continental crust onshore of the Crocker Ranges. The thin crust bows down at the margin under the load imposed by the thick sediment of the Sabah Basin, suggesting weak lithosphere in this area. This crust is interpreted as highly attenuated and stretched continental crust rifted from the south China margin and driven southwards by the slab-pull of the subducting oceanic proto-South China Sea beneath the northwest margin of 'Borneo'. Subduction ended at this margin when the buoyant continental crust arrived at the subduction trench. There is no evidence in the gravity data for any remaining fragments of oceanic crust at this margin.

The crust underlying the Crocker Ranges is modelled as extending to a depth of ~ 46 km, which is in close agreement with the more detailed model of the Crocker Ranges obtained from Profile SAB1 which shows this crustal root extending to a depth of 49 km (Figure 6.40).

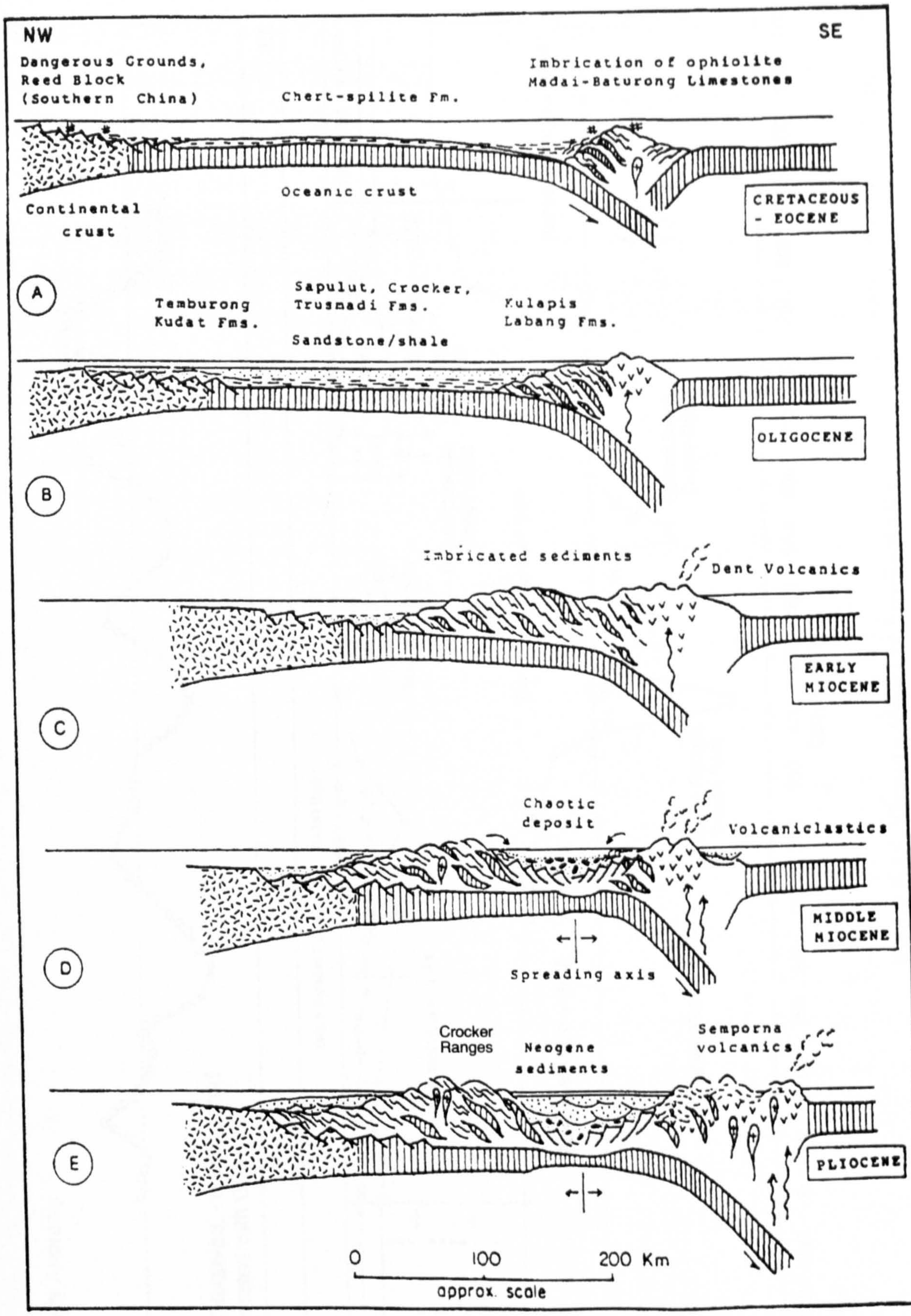

Figure 6.44. Model for the tectonic evolution of Sabah proposed by Tongkul (1991). Figure shows schematic NW-SE sequential cross-sections across Sabah.

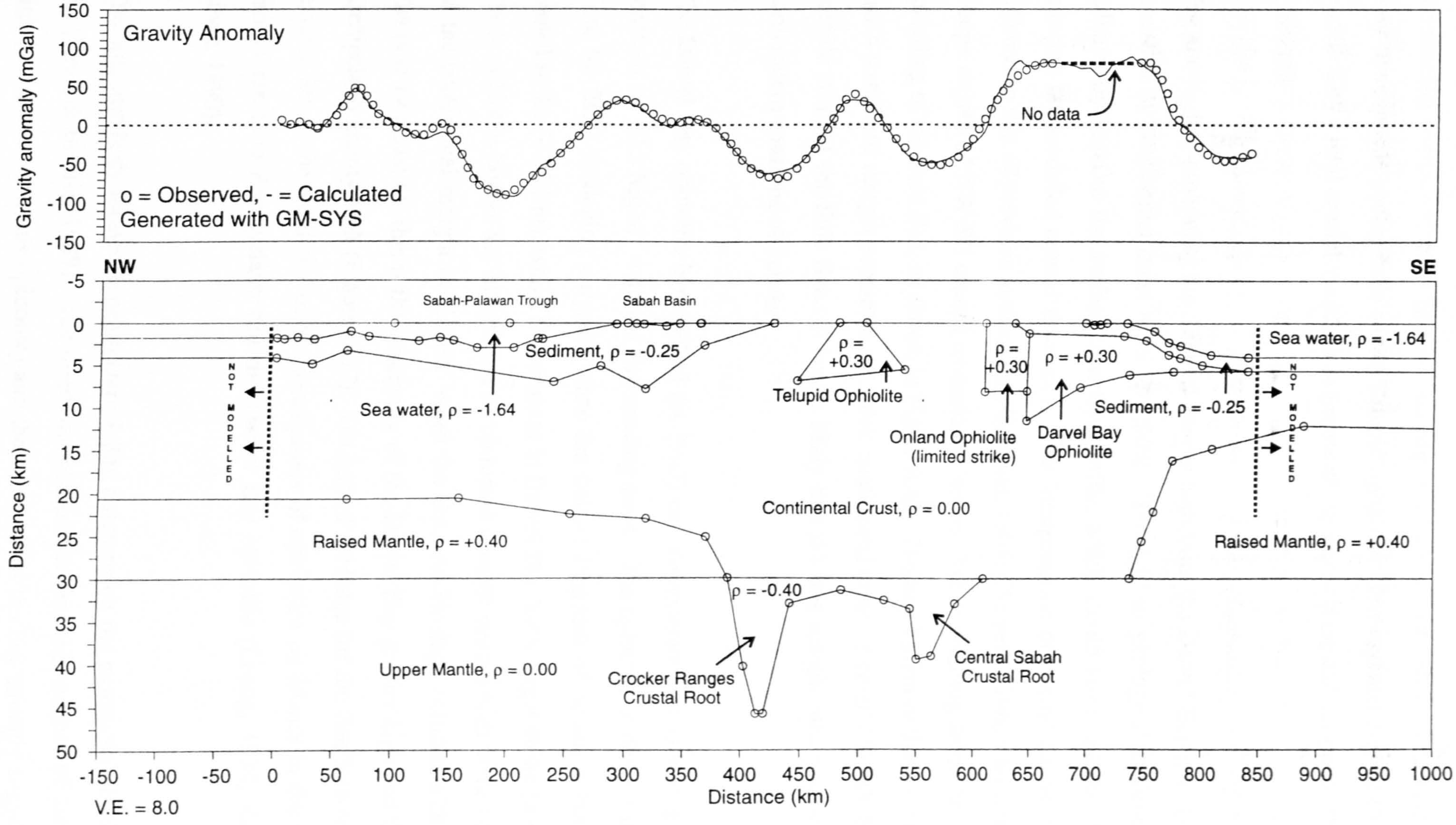

Figure 6.45. Gravity Model of Profile SAB3.

The gravity high at Telupid is modelled by a block of material of higher density than the surrounding continental crust ($\Delta\rho$ = +0.3 $Mg.m^{-3}$) located just below the surface. This body corresponds geologically to the Telupid ophiolite. The regional gravity trend was modelled by a total crustal thickness in excess of the standard crustal thickness (thickness ~ 32 km).

The gravity low separating the Telupid gravity high from the Darvel Bay gravity high is modelled by continental crust ~ 39 km thick. There is no geological evidence for a sedimentary basin at the surface near this profile, which would have had the effect of reducing the modelled crustal thickness. This interpretation of central Sabah is totally different to that of previous authors (e.g Tongkul, 1991; Clennell, 1996) who interpreted a large degree of NW-SE crustal extension in central Sabah resulting from the NW-SE spreading of the Sulu Sea, as shown in Figure 6.43. The implication of this new result is that a transform margin separates the thick continental crust of central Sabah from the oceanic crust of the Sulu Sea. It seems likely that ~~the~~ this margin runs parallel to the northeastern coastline of Sabah.

The Darvel Bay ophiolite is modelled (in 2½D) by two separate bodies having density contrasts of +0.3 $Mg.m^{-3}$ with the surrounding crust. The ophiolite is divided into two parts for 2½D modelling purposes since the onland fragment of ophiolite has a very limited strike (~ 20 km), whilst the remnant in Darvel Bay has a larger strike (≥ 40 km). These ophiolite bodies are interpreted as obducted oceanic crust which were emplaced on the continental margin of 'Sabah' when the Sulu Archipelago collided with Sabah. The new evidence for this is the continuity of the Darvel Bay gravity high and the Sulu Archipelago gravity high (Figure 6.37). Geological evidence for the link between these features lies in the similarity of the descriptions of ophiolites on islands in the western part of the Sulu Archipelago and the Darvel Bay ophiolite (Leong, 1974; Rangin & Silver, 1990).

The ophiolite body located beneath Darvel Bay outcrops on the numerous islands in the bay (Ryall & Beattie, 1989). The direct correlation between the margins of the gravity high (associated with this ophiolite) and the coastline of the bay strongly suggests that

the bay was formed by the subsidence of the crust under the load imposed by the mass of the ophiolite. The smaller onshore ophiolite body appears to be supported by the strength of the crust.

Southeast of Darvel Bay the gravity field decreases rapidly as the continental crust underlying the ophiolite body thins towards its (unmodelled) boundary with the Celebes Sea oceanic crust.

6.4.4.4 Conclusions

The new results given by this study show that Sabah is underlain by crust of continental density of thickness in excess of 30 km. This contradicts previous theories (e.g. Tongkul, 1991) which suggested that Sabah is underlain by oceanic crust, and has significant implications for regional tectonic syntheses. The crustal root of the Crocker Ranges reaches a maximum depth of about 49 km below sea level. Assuming that the original thickness of this crust was 20 - 25 km, this present day depth estimate indicates that the compression that occurred during the Sabah Orogeny at least doubled the crustal thickness.

The Telupid and Darvel Bay gravity highs appear to have different geological origins. The Darvel Bay ophiolite is interpreted as the landward extension of the Sulu Archipelago which was obducted onto Sabah. The Telupid ophiolite either represents an obducted fragment of the proto-South China Sea or a trapped fragment of the Sulu Sea oceanic crust. There is no evidence that the Darvel Bay ophiolite and the Telupid ophiolite form a continuous suture zone. These ophiolitic bodies are separated by thick continental crust which runs NE-SW along a trend previously known at the Central Sabah Basin (Clennell, 1996). A transform fault is postulated to separate the thick compressed crust of central Sabah and the nearby extensional Sulu Sea oceanic basin.

A minimum estimate of 8 km is obtained for sediments within the Maliau Basin. This study suggests that this basin extends for a significant distance south of the previously

mapped southern limit. This is perhaps unsurprising given the logistical mapping difficulties experienced during the 1960s in this very remote and rugged region.

6.5 Interpretation Summary

This chapter has presented a detailed qualitative and quantitative interpretation of the gravity field of Sundaland, the South China Sea and Sabah. The principal results of this study are new maps of residual free-air and Bouguer gravity anomaly, β (stretching) factor, crustal thickness and depth to the gravity Moho. Quantitative interpretation focussed on the the Sunda Shelf edge, the fossil spreading ridge of the South China Sea Oceanic Basin and Sabah.

The task of unravelling the complexities of the tectonic evolution of the northwest Borneo margin are largely beyond the scope of this project. A lively geological debate rages within even a relatively small area such as that occupied by present-day Sabah (e.g. Hutchison, 1991; Rangin, 1991). Highly contentious issues are the existence of the proto-South China Sea and the amount (and even direction) of rotation undergone by Borneo. Major problems arise due to factors such as limited and even erroneous published formation ages, confusing formation nomeclature, paucity of accessible outcrops, not to mention the highly complex local and regional geology. Offshore, numerous different, often contradictory and even erroneous maps have been published, caused by the extrapolation of known features away from ship tracks.

Despite the fundamental limitations of the gravity anomaly data such as low resolution of surficial geological bodies, this study has yielded a number of results that will contribute to a better understanding of the tectonic evolution of Southeast Asia, namely:

1. It is estimated that approximately 1100 km of oceanic crust of the proto-South China Sea was subducted at the northwest Borneo margin. Strong evidence for the existence of the proto-South China Sea is found in the tomographic inversion results of Widiyantoro & Van der Hilst (1996), Figure 6.6C. The slab imaged between 1130 and 1250 km is interpreted as sunken proto-South China Sea oceanic crust.

2. Gravity modelling independently confirms the full spreading rate prediction of ~ 35 mm/yr for the southwestern subbasin of the South China Sea Oceanic Basin made by Briais *et al.* (1993) on the basis of intepretation of magnetic lineation data.

3. Interpretation of the gravity anomaly field of Sabah shows that Sabah is underlain by thick continental crust. This contradicts previous interpretations which show Sabah underlain by oceanic crust.

REFERENCES

REFERENCES

Airy, G.B., 1855. On the computation of the effect of the attraction of the mountain masses as disturbing the apparent astronomical latitude of stations in geodetic surfaces. *Trans. Roy. Soc. (London)*, ser.B., v.145.

Allen, C.R., 1962. Circum-Pacific faulting in the Philipines-Taiwan region. J. Geophys. Res., v.67(12), p.4795-4812.

Almond, R., 1986. *Earth Tide Computer Program*, Technical Worknote, Indonesian-Australian Geological Mapping Project (IAGMP), Geological Research and Development Centre 1986, Indonesia, Unpublished Report.

Anderson, A.J., & Cazenave, A., 1986. *Space Geodesy and Geodynamics*, Academic Press, Harcourt Brace Jovanovich Publ., London.

Angelich, M.T., 1986. Use of Seasat-derived free-air gravity to interpret the crustal structure of Southeast Asia. *Proceedings Indonesian Petroleum Association 15th Annual Convention.*

Antonio, L.R., 1972. *Geology and Mineral Resources of East Central Zamboanga Peninsula, Mindanao, Philippines*. Philippines Bureau of Mines, Manila.

Apel, J.R., 1980. Satellite sensing of ocean surface dynamics. *Ann. Rev. Earth Planet. Sci.*, v.8.

Arabelos, D., & Tziavos, I.N., 1996. Combination of ERS-1 and TOPEX altimetry for precise geoid and gravity recovery in the Mediterranean Sea. *Geophys. J. Int.*, v.125, p.285-302.

Arent, N., Hückelheim, G., & Koch, K.R., 1992. Method for obtaining geoid undulations from satellite altimetry data by a quasi-geostrophic model of the sea surface topography. *man. geod.*, v.17, p.174-185.

Banks, R.J., Parker, R.L., & Huestis, S.P., 1977. Isostatic compensation on a continental scale: Local versus regional mechanisms. *Geophys. J. Roy. astr. Soc.*, v.51, p.431-452.

Barber, A.J., & Brown, F., 1988. Mud diapirism: the origin of melanges in accretionary complexes? *Geology Today*, May-Jun, p.89-94.

Barber, A.J., Tjokrosapoetro, S., & Charlton, T.R., 1986. Mud volcanoes, shale diapirs, wrench faults and melanges in accretionary complexes, Eastern Indonesia. *AAPG Bull.*, v.70(11), p.1729-1741.

Barford, N.C., 1985. *Experimental measurements: precision, error and truth (second edition)*, John Wiley & Sons Ltd., Chichester.

Batiza, R., & Vanko, D., 1983. Volcanic development of small oceanic central volcanoes on the flank of the East Pacific rise inferred from narrow beam echo sounder survey. *Mar. Geol.*, v.54, p.53-90.

Beattie, D. 1986. *Gravity modelling of a mafic-ultramafic association, Darvel Bay, Sabah*. B.Sc. Thesis, Dalhousie University (unpub.), 56pp.

Belikov, M.V., & Groten, E., 1993. An Inverse Problem Related to a Finite Part of a Compact Surface: Potential Deduced From Gravity Gradients in Space. *J. Geophys. Res.*, v.98(B10), p.17,773-17,785.

Bendat, J.S., & Piersol, A.G., 1986. *Random data, analysis and measurement procedures (second edition)*, John Wiley & Sons Ltd., New York.

Bérnard, F., Muller, C., Letouzey, J., Rangin, C., & Tahir, S., 1990. Evidence of multistage deformation in the Rajang-Crocker Range (northern Borneo) from Landsat imagery interpretation: geodynamical implications. *Tectonophysics*, v.183, p.321-339.

Bernard, J., Barlier, F., Bethowe, J.P., & Souriau, M., 1983. First Seasat altimeter data analysis on the western Mediterranean Sea. *J. Geophys. Res.*, v.88(C3), p.1581-1588.

Bernstein, R.L., Born, G.H., & Whritner, R.H., 1982. SEASAT altimeter determination of ocean current variability. *J. Geophys. Res.*, v.87(C5), p.3261-3268.

Berry, P.A.M., & Blewitt, G., 1994. Geodesy from Space. *Geoscientist*, v.4(4), p.14-15.

Besse, J., Courtillot, V., Pozzi, J.P., & Zhoou, Y.X., 1984. Paleomagnetic estimate of Cenozoic convergence in the Himalayan thrusts and Zangbo suture. *Nature*, v.311, p.621-626.

Blanc, F., Houry, S., Mazzega, P., & Minster, J.F., 1991. High-Resolution, High-Accuracy Altimeter Derived Mean Sea Surface in the Norwegian Sea. *Marine Geodesy*, v.14, p.57-76.

Born, G.H., Richards, M.A., & Rosborough, G.W., 1982. An Empirical Determination of the Effects of Sea State Bias on SEASAT Altimetry. *J. Geophys. Res.*, v.87(C5), p.3221-3226.

Boschetti, F., Hornby, P., & Horowitz, F., 1997. Wavelet based inversion of potential field data. *59th EAGE Meeting Extended Abstracts*, Geneva, F035.

Brenner, A.C., Koblinsky, C.J., & Beckley, B.D., 1990. A preliminary estimate of geoid-induced variations in repeat orbit satellite altimeter observations. *J. Geophys. Res.*, v.95, p.3033-3040.

Briais, A., Patriat, P., & Tapponnier, P., 1993. Updated Interpretations of Magnetic Anomalies and Seafloor Spreading Stages in the South China Sea: Implications for the Tertiary Tectonics of Southeast Asia. *J. Geophys. Res.*, v.98(B4), p.6299-6328.

Briais, A., Tapponnier, P., & Pautot, G., 1989. Constraints of Sea Beam data on crustal fabrics and seafloor spreading in the South China Sea. *Earth Planet. Sci. Letts.*, v.95, p.307-320.

Briggs, P., 1989. *What's wrong with this picture?* M.S. Thesis, Trent University, Petersborough, Ontario.

Caldwell, P., Wyrtki, K., & Nakahara, S., 1989. TOGA Sea Level Center: Data from the Pacific, *JIMAR 89-202*, University of Hawaii, 34 pp.

Cannat, M., 1996. How thick is the magmatic crust at slow spreading oceanic ridges? *J. Geophys. Res.*, v.101(B2), p.2847-2857.

Cartwright, D.E., & Ray, R.D., 1990. Oceanic tides from Geosat altimetry. *J. Geophys. Res.*, v.95(C3), p.3069-3090.

CCOP, 1991. The Total Sedimentary Isopach Maps Offshore East Asia. *CCOP Tech. Bull. v.23*, Geological Survey of Japan, Ibaraki-ken, Japan.

Chao, Y., Halpern, D., & Perigaud, C., 1993. Sea surface height variability during 1986-1988 in the tropical Pacific Ocean. *J. Geophys. Res.*, v.98(C4), p.6947-6959.

Chase, C.G., 1985. The Geological Significance of the Geoid. *Ann. Rev. Earth Planet. Sci.*, v.13, p.97-117.

Chen, B., & Lei, S., 1987. Map of crustal structures. In: *Atlas of Geology and Geophysics of South China Sea* (Eds. He, L., & Chen, B.), sheet no. 10, Map Publishing House of Guangdong Province, China.

Chen, Y., & Morgan, W.J., 1990. A nonlinear rheology model for mid-ocean ridge axis topography. *J. Geophys. Res.*, v.95, p.17583-17604.

Cheney, R.E., & Lillibridge, J.L., 1992. ERS-1 fast delivery altimeter data for tropical ocean monitoring. *EOS Trans. Amer. Geophy. U.*, v.74(14) p.84.

Clairaut, A. C., 1743. *Théorie de la figure de la terre*, Paris.

Clennell, M.B., 1990. A comparison of small-scale structures in melanges with those from recent landslides: examples from Sabah, Malaysia and North Island, New Zealand. In: *Geological Society of New Zealand Annual Conference 1990, Napier, Programme with Abstracts*, p.42-43.

Clennell, M.B., 1991. The origin and tectonic significance of the melanges in Eastern Sabah. *J. SE Asian Earth Sci.*, v.6(3), p.407-429.

Clennell, M.B., 1992. *The Mélanges of Sabah.* Unpublished Ph.D. Thesis, University of London.

Clennell, B., 1996. Far-field and gravity tectonics in Miocene basins of Sabah, Malaysia. In: *Tectonic Evolution of Southeast Asia* (Eds. Hall, R., & Blundell, D.), Geological Society Special Publication No. 106, Geological Society, London, p.307-320.

Collenette, P., 1958. *The geology and mineral resources of the Jesselton-Kinabalu area, North Borneo.* British Borneo Geological Survey Memoir, No.6, 194pp.

Collenette, P., 1965. *The Geology and Mineral Resources of the Pensidangan and Upper Kinabatangan area, Sabah, Malaysia.* Geological Survey of Malaysia Borneo Region, Memoir 12, pp.150.

Colton, M.T., & Chase, R.R.P., 1983. Interaction of the Antarctic circumpolar current with bottom topography: an investigation using satellite altimetry. *J. Geophys. Res.*, v.88, p.1825-1843.

Coulon, O., Huchon, P., Nguyen Thi Ngoc, H., Marquis, G., Chamot-Rooke, N., Le Pichon, X., Phan Truong, T., & Rangin, C., 1995. Tectonic structure and age of the South China Sea fossil propagating ridge. In: *Program and Abstracts - Symposium on the Cenozoic Evolution of the Indochina Peninsula: Tectonics and Sedimentary Basins* (Eds. Le Pichon, X., & Thanh, T-D.), Ha Noi, Vietnam, p.51-52.

Crone, D.R., 1948. Heights by Aneroid Barometer. *Empire Survey Review*, v.69, p.311-316.

Crone, D.R., 1960. Note on Terrestrial Altimetry. *Empire Survey Review*, v.122, p.160-168.

Dalloubeix, C., Fleitout, L., & Diament, M., 1988. A new analysis of gravity and topography data over the Mid-Atlantic Ridge: non-compensation of the axial valley. *Earth Planet. Sci. Letts.*, v.88, p.308-320.

Daly, M.C., Cooper, M.A., Wilson, I., Smith, D.G., & Hooper, B.D.G., 1991. Cenozoic plate tectonics and basin evolution in Indonesia. *Marine and Petroleum Geology*, v.8, p.2-21.

Detrick, R.S., Needham, H.D., & Renard, V., 1995. Gravity anomalies and crustal thickness variations along the Mid-Atlantic Ridge between 33°N and 40°N. *J. Geophys. Res.*, v.100(B3), p.3767-3787.

Dickman, S.R., 1988. Theoretical Investigation of the Ocean Inverted Barometer Response. *J. Geophys. Res.*, v.93(B12), p.14941-14946.

Divins, D.L., & Eakins, B., in preparation 1997. Total Sediment Thickness Map for the Southeast Pacific Ocean. In: *International Geological-Geophysical Atlas of the Pacific Ocean* (Ed. Udintsev, G.B.), Intergovernmental Oceanographic Commission.

Divins, D.L., & Rabinowitz, P.D., 1990. Total sediment thickness map for the South Atlantic Ocean. In: *International Geological and Geophysical Atlas of the Atlantic and Pacific Oceans (GAPA)* (Ed. Udintsev, G.B.), Intergovernmental Oceanographic Commission, p.147-148.

Dixon, T.H., & Parke, M.E., 1983. Bathymetry estimates in the southern oceans from Seasat altimetry. *Nature*, v.304, p.406-411.

Douglas, B.C., & Cheney, R.E., 1990. GEOSAT - Beginnings of a new era in satellite oceanography. *J. Geophys. Res.*, v.95(C3), p.2833-2836.

Douglas, B.C., Cheney, R.E., & Agreen, R.W., 1983. Eddy energy of the northwest Atlantic and Gulf of Mexico determined from Geos 3 altimetry. *J. Geophys. Res.*, v.88(C14), p.9595-9603.

Douglas, B.C., McAdoo, D.C., & Cheney, R.E., 1987. Oceanographic and Geophysical Applications of Satellite Altimetry. *Revs. Geophys.*, v.25(5), p.875-880.

Elliot, A.J., 1979. The effect of low frequency winds on sea level and currents in the gulf of Genova. *Oceanol. Acta*, v.2(4), p.429-433.

Fairhead, J.D., 1992. *Southeast Asia Gravity Project - Progress Report 1.* Unpublished Report, GETECH, University of Leeds, Leeds.

Fitch, F.H., 1958. *The geology and mineral resources of part of the Segama Valley and Darvel Bay area, colony of North Borneo.* Geological Survey Department of British Territories in Borneo, Memoir, No.4, 142pp.

Fournier, M., 1994. *Ouverture de bassins marginaux et déformation continentale: l'exemple de la Mer du Japon.* Université Paris VI, Thèse du Doctorat.

Freed, A.M., Lin, J., Shaw, P.R., & Melosh, H.J., 1995. Long-term survival of the axial valley morphology at abandoned slow-spreading centers. *Geology*, v.23(11), p.971-974.

Fricaut, L., 1984. *Etude géologique et structurale de la marge nord-Palawan*, Thèse de 3ème cycle, Univ. Paris XI.

Fu, L.-L., & Cheney, R.E., 1995. Application of satellite altimetry to ocean circulation studies. *1995 Revs. Geophys. Supplement, AGU*, p.213-223.

Fu, L.-L., Christensen, E.J., Yamarone, C.A., Lefebvre, M., Menard, Y., Dorrer, M., & Escudier, P., 1994. Topex-Poseidon mission overview. *J. Geophys. Res.*, v.99, p.24369-24382.

Geary, E.E., Harrison, M.T., & Hiertzler, M., 1988. Diverse ages and origins of basement complexes, Luzon, Philippines. Geology, v.16, p.341-344.

Gervaiso, F.C., 1971. Geotectonic developments of the Philippines. J. Geol. Soc. Philipp., v.25(1), p.18-38.

Gille, S.T., 1994. Mean sea surface height of the Antarctic circumpolar current from Geosat data: Method and application. *J. Geophys. Res.*, v.99, p.18255-18273.

Gower, R.J.W., 1990. Early Tertiary plate reconstructions for the South China Sea region: constraints from northwest Borneo. *J. SE Asian Earth Sci.*, v.4(1), p.29-35.

Haalck, H., 1953. *Lehrbuch der Angewandten Geophysik, Abschnitt 1*, Bornträger, Berlin, p.27-155.

Haile, N.S., McElhinny, M.W., & McDougall, I., 1977. Paleomagnetic data and radiometric ages from the Cretaceous of west Kalimantan (Borneo) and their significance in interpreting regional structure. *J. Geol. Soc. London*, v.133, p.133-144.

Haile, N.S., 1979. Rotation of Borneo microplate completed by Miocene: Paleomagnetic evidence. *Warta Geologi*, v.5, p.19-22.

Hall, R., 1996. Reconstructing Cenozoic SE Asia. In: *Tectonic Evolution of Southeast Asia* (Eds. Hall, R., & Blundell, D.), Geological Society Special Publication No. 106, Geological Society, London, p.153-184.

Hall, R., 1997. Cenozoic Tectonics of SE Asia and Australia. *Proceedings of the Petroleum Systems of SE Asia and Australasia Conference, May 1997*, Indonesian Petroleum Association, p.47-62.

Hamilton, W., 1979. *Tectonics of the Indonesia Region.* United States Geological Survey Professional Paper 1078.

Hammer, S., 1939. Terrain corrections for gravimeter stations. *Geophysics*, v.4, p.184-209.

Harder, S.H., Mauri, S.J., & Marshall-Arrazola, S., 1993. Gravity modelling of extensional basins in Southeast Asia. *Geol. Soc. Malaysia Bulletin*, v.33, p.153-162.

Harland, W.B., Armstrong, R.L., Craig, L.E., Smith, A.G., & Smith, D.G., 1992. *A Geologic Time Scale*. Cambridge University Press, Cambridge.

Harrison, D., 1991. *The Gravity Field of the Papuan Fold Belt and its Geological Implications.* Unpublished Ph.D. Thesis, University of London, London.

Haurwitz, B., 1955. The thermal influence on the daily pressure wave. *Bull. Am. Met. Soc.*, v.36, p.311-317.

Hayes, D.E., & LaBrecque, J.L., 1991. Sediment Isopachs: Circum-Antarctic to 30°S. In: *Marine Geological and Geophysical Atlas of the Circum-Antarctic to 30°S* (Ed. Hayes, D.E.), Amer. Geophys. U., Washington, D.C., p.29-33.

Heiskanen, W., & Moritz, H., 1967. *Physical Geodesy*, W.H. Freeman, New York.

Heiskanen, W.A., & Vening Meinesz, F.A., 1958. *The Earth and Its Gravity Field.* McGraw-Hill Book Co., London, p.51.

Hellinger, S.J., 1981. The uncertainties of finite rotations in plate tectonics. *J. Geophys. Res.*, v.93, p.2803-2811.

Herzfeld, U.C., 1992. Least-squares collocation, geophysical inverse theory and geostatistics: a bird's eye view. *Geophys. J. Int.*, v.111, p.237-249.

Hinz, K., & Block, M., 1990. Summary of geophysical data from the Sulu and Celebes Seas. *Proc. ODP, Init. Repts.*, v.124, College Station, Texas (Ocean Drilling Program), p.87-92.

Hinz, K., & Schluter, H.U., 1985. Geology of the Dangerous Grounds, South China Sea, and the continental margin off Southwest Palawan: Results of Sonne cruises SO-23 and SO-27. *Energy*, v.10, p.297-315.

Hinz, K., Block, M., Kudrass, H.R., & Meyer, H., 1991. Structural elements of the Sulu Sea, Philippines. *Geologische Rundschau*, v.127(A), p.483-506.

Hinz, K., Fritsch, J., Kempter, E.H.K., Manaf Mohammad, A., Meyer, J., Mohamad, D., Vosberg, H., Weber, J., & Benavidez, J., 1989. Thrust tectonics along the north-western continental margin of Sabah/Borneo. *Geologische Rundschau*, v.78(3), p.705-730.

Hinz, K., Kemper, E.H.K., & Schluter, H.U., 1985. The Southern Palawan-Balabac area: an accreted or non-accreted terrane?. *Proc. 3rd Asian Council on Petrol. (ASCOPE), Conf. Exhib., Kuala Lumpur, Malaysia, v.2*, p.48-60.

Hogg, N.G., & Johns, W.E., 1995. Western boundary currents. *Revs. Geophys., Supplement, U.S. National Report to International Union of Geodesy and Geophysics 1991-1994*, AGU, p.1311-1334.

Holloway, N.H., 1981. The North Palawan Block, Philippines; its relation to the Asian mainland and its role in the evolution of the South China Sea. *Geological Society of Malaysia Bulletin*, v.14, p.19-58.

Holloway, N.H., 1982. North Palawan Block, Philippines, Its relation to Asian mainland and role in evolution of the South China Sea. *Am. Assoc. Pet. Geol. Bull.*, v.66, p.1355-1383.

Holt, R., 1997. Accuracy of satellite compilation maps - a comparison with ship gravity in Southeast Asia. *59th EAGE Meeting, Geneva, Extended Abstracts*, P184.

Holt, R., & Milsom, J., 1996. *The 1995 Sabah Gravity Survey.* University of London Consortium for Research in Southeast Asia, Unpublished Report No. 153.

Holt, R., Milsom, J., & bin Ayub, D., in press. Gravity base stations in Sabah, East Malaysia. *Warta Geologi, Geol. Soc. Malaysia.*

Hotine, M., 1969. *Mathematical Geodesy, ESSA Monograph 2*, U.S. Dept. Commer., Washington.

Hu, Y., & Rabinowitz, P.D., 1996. Spreading Rate Dependence of the Axial Topography and Gravity of the Mid-Atlantic Ridge between 22°N and 38°N. *Marine Geodesy*, v.19, p.215-233.

Hutchison, C.S., 1978. Ophiolite metamorphism in northeast Borneo. *Lithos*, v.11, p.195-208.

Hutchison, C.S., 1988. Stratigraphic-tectonic model for Eastern Borneo. *Geological Society of Malaysia Bulletin*, v.22, p.135-151.

Hutchison, C.S., 1989. *The Geological Evolution of SE Asia*. Oxford University Press, Oxford.

Hutchison, C.S., 1991. Neogene arc-continental collision in Sabah, Northern Borneo (Malaysia) - Comment. *Tectonophysics*, v.200, p.325-329.

Hutchison, C.S., 1996. The 'Rajang accretionary prism' and the 'Lupar Line' problem of Borneo. In: *Tectonic Evolution of Southeast Asia* (Eds. Hall, R., & Blundell, D.), Geological Society Special Publication No. 106, Geological Society, London, p.247-261.

Hwang, C., Parsons, B., Strange, T., & Bingham, A., 1994. A detailed gravity field over the Reykjanes Ridge from Seasat, Geosat, ERS-1 and TOPEX/Poseidon altimetry and shipborne gravity. *Geophys. Res. Letts.*, v.21(25), p.2841-2844.

IAG, 1967. *Geodetic Reference system 1967*. IAG Special Publication, No.3.

Imawaki, S., Ichikawa, K., & Nishigaki, H., 1992. Mapping the Mean Sea Surface Elevation Field from Satellite Altimetry Data Using Optimal Interpolation. *Mar. Geod.*, v.15, p.31-46.

IUGG, 1967. *International Union of Geodesy and Geophysics General Assembly*, held in Switzerland.

Jacobson, G., 1970. *Gunung Kinabalu area, Sabah, Malaysia*. Geological Society of Malaysia Report 8.

Jasin, B., & Tahir, S., 1988. Barremian radiolaria from Chert-Spilite Formation, Sabah. *Sains Malaysianna*, v.16, p.1-5.

Jasin, B., Tahir, S., & Samsudin, A.R., 1985. Lower Cretaceous age of radiolarian from the Chert-Spilite Formation, Kudat, Sabah. *Warta Geologi*, v.11(4), p.161-162.

Jasin, B., Tahir, S., & Selvarajah, M., 1988. Paleogene planktonic foraminifera from Pulau Kalampunian Kecil, Sabah. *Sains Malaysiana*, v.17, p.99-113.

Jolly, G., 1996. *Satellite Radar Altimetry*, Unpub. Rep., Satellite Observing Systems Ltd., England.

Kahn, M.A., 1983. Satellite contributions to geophysical exploration at sea. In: *CRC Handbook of Geophysical Exploration at Sea* (Ed. Geyer, R.A.), CRC Press, Boca Raton, p.3-68.

Karig, D.E., 1983. Accreted terranes in the northern part of the Philippines Archipelago. *Tectonics*, v.2(2), p.211-236.

Kaula, W.M., 1972. Global gravity and tectonics. In: *The Nature of the Solid Earth* (Ed. Robertson, E.C.), McGraw-Hill, New York, p.385-405.

Kearey, P., & Vine, F.J., 1996. *Global Tectonics Second Edition*, Blackwell Science, Oxford.

Kirby, S.J., & Hipkin, R.G., 1994. Combination of Heterogeneous Gravity Datasets: a Study Over the North Atlantic. Abstract of Paper GGY8, *UKGA-18*.

Kirk, H.J.C., 1968. The Igneous of Sabah and Sarawak. *Geol. Soc. Malaysia Bull.*, v.5.

Klemme, H.D., 1983. Field Size Distribution Related to Basin Characteristics. *Oil and Gas Journal*, v.83(52).

Knudsen, P., 1987. Simultaneous use of gravity and satellite altimeter data for geoid determination. *Boll. di Geod. e Sci. Aff.*, v.46(1), p.1-20.

Knudsen, P., 1991. Simultaneous estimation of the gravity field and sea surface topography from satellite altimeter data by least-squares collocation. *Geophys. J. Int.*, v.104, p.307-317.

Kuala, K.M., *et al.*, 1970. The terrestrial environment: Solid Earth and ocean physics. *NASA CR-1599*, Mass. Inst. of Tech., Cambridge, Mass.

Kundig, E., 1956. Geology and ophiolite problems of east Celebes. *Verh. K. Ned. Geol. Mijnbouwkd. Genoot.*, v.16, p.210-235.

Lai, K.H., 1990. Structural Mapping of the Maliau Basin, Sabah, by Synthetic Aperture Radar (SAR). *Warta Geologi*, v.16(5), p.239-243.

Lankester, T.H.G., 1993. *Computer modelling of carbonate platform stratigraphies.* Unpub. Ph.D. Thesis, University of London, London.

Lee, T-Y., & Lawver, L.A., 1994. Cenozoic plate tectonic reconstruction of the South China Sea region. *Tectonophysics*, v.235, p.149-180.

Leitao, C.D., Huang, N.E., & Parra, C.G., 1979. A note on the comparison of radar altimetry with IR and in situ data for the detection of the Gulf Stream surface boundaries. *J. Geophys. Res.*, v.84, p.3969-3973.

Leong, K.M., 1974. *The geology and mineral resources of the Upper Segama Valley and Darvel Bay area, Sabah, Malaysia*. Geol. Soc. Malaysia, Mem. 4 (Revised), pp.354.

Leong, K.M., 1977. New ages from radiolarian cherts of the Chert-Spilite Formation, Sabah. *Bull. Geol. Soc. Malaysia*, v.8, p.109-111.

Le Pichon, X., & Sibuet, J.C., 1981. Passive margins: a model of formation. *J. Geophys. Res.*, v.86(B5), p.3708-3720.

Lerch, F.J., 1991. Optimum data weighting and error calibration for estimation of gravitational parameters. *Bull. Geod.*, v.65, p.44-52.

Lerch, F.J., Nerem, R.S., Putney, B.H., Felsentreger, T.L., Sanchez, B.V., Klosko, S.M., Patel, G.B., Williamson, R.G., Chinn, D.S., Chan, J.C., Rachlin, K.E., Chandler, N.L., McCarthy, J.J., Marshall, J.A., Luthcke, S.B., Pavlis, D.E., & Pavlis, E.C., 1992. Geopotential models of the Earth from satellite tracking, altimeter and surface gravity observations: GEM-T3 and GEM-T3S. *NASA Tech. Memo 10455*, NASA, U.S.A.

Lerch, F.J., Nerem, R.S., Chinn, D.S., Chan, J.C., Patel, G.B., & Klosko, S.M., 1993. New error calibration tests for gravity models using subset solutions and independent data: Applied to GEM-T3. *Geophys. Res. Letts.*, v.20(2), p.249-252.

Lerch, F.J., Nerem, R.S., Putney, B.H., Felsentreger, T.L., Sanchez, B.V., Marshall, J.A., Klosko, S.M., Patel, G.B., Williamson, R.G., Chinn, D.S., Chan, J.C., Rachlin, K.E., Chandler, N.L., McCarthy, J.J., Luthcke, S.B., Pavlis, N.K., Pavlis, D.E., Robbins, J.W., & Kapoor, S.,1994. A geopotential model from satellite tracking, altimeter, and surface gravity data: GEM-T3. *J. Geophys. Res.*, v.99(B2), p.2815-2839.

Letouzey, J., Sage, L., & Muller, C., 1988. *Geological and Structural Maps of Eastern Asia. Introductory Notes.* AAPG.

LeTraon, P.Y., Gaspar, P., Bouyssel, F., & Dorandeu, J., 1995. Satellites Work in Tandem to Improve Accuracy of Data. *EOS Trans.*, v.76(39), p.385-389.

Lewis, S.D., & Hayes, D.E., 1983. The tectonics of northward propagating subduction along eastern Luzon, Philippine Islands. In: *The Tectonic and Geologic Evolution of the Southeast Asian Seas and Islands, Part 2, Geophys. Monogr. Ser., Vol. 27* (Ed. Hayes, D.E.), AGU, Washington, D.C., p.57-78.

Lewis, S.D., & Hayes, D.E., 1984. A geophysical study of the Manila Trench, Luzon, Philippines. 2. Fore-arc basin structural and stratigraphic evolution. *J. Geophys. Res.*, v.89(B1), p.9196-9214.

Lim, P.S., & Tungah-Surat, 1989. Geology and Coal Potential of the Northeast Maliau Basin. *Proceedings of the Geological Survey of Malaysia 20th Geological Conference*, p.108-118.

Lin, J., Phipps-Morgan, J., 1992. The spreading rate dependence of three dimensional mid-ocean ridge gravity structure. *Geophys. Res. Letts.*, v.19, p.13-16.

Liu, Z., Wang, Q., Yuan, H., & Su, D., 1985. The Bouguer anomalies and depths of the Mohorovicic discontinuity in the South China Sea region. *Acta Oceanol. Sin.*, v.4, p.579-590.

Long, A.S., & Spurling, T.A., 1993. Increased Resolution of Processed Satellite Altimeter Data: The Development of a Quality Global Gravity Database. *Exploration Geophysics*, v.24, p.663-670.

Ludwig, W.J., & Houtz, R.E., 1979. *Isopach Map of the Sediments in the Pacific Ocean Basin*, Am. Assoc. Pet. Geol., Tulsa, OK.

Lumadyo, E., McCabe, R., Harder, S., & Lee, T., 1993. Borneo: a stable portion of the Eurasian margin since the Eocene. *J. SE Asian Earth Sci.*, v.8, p.255-231.

Mainville, A., Forsberg, R., & Sideris, M.G., 1992. Global Positioning System Testing of Geoids Computed From Geopotential Models and Local Gravity Data: A Case Study. *J. Geophys. Res.*, v.97(B7), p.11,137-11,147.

Malinverno, A., 1993. Transition between a valley and a high at the axis of the mid-ocean ridges. *Geology*, v.21, p.639-642.

Marchadier, Y., & Rangin, C., 1989. Passage subduction-collision et téctoniques superposées à l'extremité méridonale de la fosse de Manille (Mindoro-Tablas: Philippines). *C. R. Acad. Sci. Ser. 2*, v.308, p.1715-1720.

Marks, K.M., 1996. Resolution of the Scripps/NOAA marine gravity field from satellite altimetry. *Geophys. Res. Letts.*, v.43(16), p.2069-2072.

Marsh, J.G., & Martin, T.V., 1982. The Seasat altimeter mean sea surface model. *J. Geophys. Res.*, v.87(C5), p.3269-3280.

Marsh, J.G., Lerch, F.J., Putney, B.H., Christodoulis, D.C., Smith, D.E., Felsentreger, T.L., & Sanchez, B.V., 1988. A new gravitational model for the Earth from satellite tracking data: GEM-T1. *J. Geophys. Res.*, v.93, p.6169-6215.

Marsh, J.G., Koblinsky, C.J., Lerch, F., Klosko, S.M., Robbins, J.W., Williamson, R.G., & Patel, G.B., 1990. Dynamic sea surface topography, gravity, and improved orbit accuracies from the direct evaluation of Seasat altimeter data. *J. Geophys. Res.*, v.95(C8), p.13129-13150.

Marsh, J.G., Koblinsky, C.J., Zwally, H.J., Brenner, A.C., & Beckley, B.D., 1992. A Global Mean Sea Surface Based Upon GEOS 3 and Seasat Altimeter Data. *J. Geophys. Res.*, v.97(B4), p.4915-4921.

Mascle, A., & Biscarret, P.A., 1979. The Sulu Sea: a marginal basin in Southeast Asia. In: *Geological and Geophysical Investigations of Continental Margins* (Eds. Watkins, J., *et al.*), AAPG Memoir No. 29, p.373-381.

Matthias, P.K., Rabinowitz, P.D., & Dipiazza, N., 1988. *Sediment Thickness map of the Indian Ocean, Map 505*, Am. Assoc. Pet. Geol., Tulsa, OK.

Mazzega, P., 1986. How radial orbit errors are mapped into altimetric surfaces. *J. Geophys. Res.*, v.91(C5), p.6609-6628.

McAdoo, D.C., & Marks, K.M., 1992*a*. Gravity fields of the Southern Ocean from Geosat data. *J. Geophys. Res.*, v.97, p.3247-3260.

McCabe, R., Almasco, J.N., & Yumul, G., 1985. Terranes of the Central Philippines. In: *Terrane Analysis of the Pacific Basin, Special Volume* (Ed. Howell, D.), AAPG, Tulsa, Oklahoma, p.421-432.

McCaffrey, R., 1996. Slip partitioning at convergent plate boundaries of SE Asia. In: *Tectonic Evolution of Southeast Asia* (Eds. Hall, R., & Blundell, D.), Geological Society Special Publication No. 106, Geological Society, London, p.3-18.

McConathy, D.R., & Kilgus, C.C., 1987. The Navy Geosat Mission: An overview. *John Hopkins APL Tech. Dig.*, v8(2), p.170-175.

McGoogan, J.T., Miller, L.S., Brown, G.S., & Hayne, G.S., 1974. The S-193 radar altimeter experiment. *IEEE Trans.*

McKenzie, D.P., 1977. Surface deformation, gravity anomalies, and convection. *Geophys. J. R. Astron. Soc.*, v.18, p.1-32.

McKenzie, D.P., 1978. Some remarks on the development of sedimentary basins. *Earth Planet. Sci. Letts.*, v.40, p.25-32.

Melchior, P., 1983. Effect of the ellipticity and inertial forces of the Earth on M_2 and O_1 tidal gravity measurements in the trans-World profiles. In: *Proc. 9th Int. Symp. on Earth Tides*, Schweizerbart, Stuttgart, p.155-165.

Menard, Y., 1983. Observations of eddy fields in the northwest Atlantic and northwest Pacific by SEASAT altimeter data. *J. Geophys. Res.*, v.96, p.259-272.

Merriam, J.B., 1983. Inertial and ellipsoidal Earth effects on gravity tide observations, in *Proc. 9th Int. Symp. on Earth Tides*, Schweizerbart, Stuttgart, p.137-144.

Metcalfe, I., 1996. Pre-Cretaceous Evolution of Southeast Asian terranes. In: *Tectonic Evolution of Southeast Asia* (Eds. Hall, R., & Blundell, D.), Geological Society Special Publication No. 106, Geological Society, London, p.97-122.

Milsom, J., 1970. *The Structure of Eastern Papua: an approach via Gravity and other Geophysical Methods*. Ph.D. Thesis, University of London (unpub.), 183 pp.

Milsom, J., 1988. Report on barometric levelling for gravity surveys in the Sumatra Forearc 1986-87. *Internal University College London Gravity Research Group Report 1988/7*, University of London (unpub.), 19 pp.

Milsom, J., & Moss, S., 1993. Evolution of the South China Sea and its Margins. *Unpublished report of the University of London Group for Research in Southeast Asia, Report 124.*

Milsom, J., Holt, R., bin Ayub, D., & Smail, R., 1997. Gravity anomalies and deep structural controls at the Sabah-Palawan margin, South China Sea. In: *Petroleum Geology of Southeast Asia* (Eds. Fraser, A.J., Matthews, S.J., & Murphy, R.W.), Geological Society Special Publication No. 126.

Minshull, T.A., 1996. Along-axis variations in oceanic crustal density and their contribution to gravity anomalies at slow-spreading ridges. *Geophys. Res. Letts.*, v.23(8), p.849-852.

Minshull, T.A., Morris, E., & Detrick, R.S., 1995. Gravity anomalies and crustal structure at the Mesozoic Blake Spur Fracture Zone. *J. Geophys. Res.*, v.100(B9), p.17771-17779.

Mitchell, A.H.G., Hernandez, F., & De la Cruz, A.P., 1986. Cenozoic evolution of the Philippine Archipelago. *J. SE Asian Earth Sci.*, v.1(1), p.3-22.

Mitchell, J.L., & Hallock, Z.R., 1984. Plans for Oceanography from the U.S. Navy Geosat. *Pacific Congress Marine Technol. (PACON '84)*, University of Hawaii.

Moritz, H., 1978. Least Squares Collocation. *Revs. Geophys. Space Phys.*, v.16(3), p.421-430.

Moritz, H., 1980*a*. Geodetic Reference System 1980. Geodesists Handbook 1980, *Bull. Geod.*, v.54(3), p.395-405.

Moritz, H. 1980*b*. *Advanced Physical Geodesy*, H. Springer Verlag, Berlin.

Moss, S., 1994. *Tertiary Basins of Kalimantan - A Pre-survey Report.* University of London SE Asia Research Group, Unpublished Report No. 127, London.

Nerem, R.S., *et al.*, 1994. Gravity model development for the Topex/Poseidon: Joint gravity models 1 and 2. *J. Geophys. Res.*, v.99, p.24421-24447.

Nettleton, L.L., 1971. *Elementary Gravity and Magnetics for Geologists and Seismologists.* Society of Exploration Geophysicists Monograph Series Number 1, Tulsa, Oklahoma, USA.

Neuman, G.A., Forsyth, D.W., & Sandwell, D., 1993. Comparison of marine gravity from shipboard and high-density satellite altimetry along the Mid-Atlantic Ridge, 30.5°S-35.5°S. *Geophys. Res. Letts.*, v.20(15), p.1639-1642.

Newton, I., 1687. *Philosophiae Naturalis Principia Mathematica*, Royal Society, London.

NGDC, 1988. ETOPO5 bathymetry/topography data, *Data Announcement 88-MGG-02*, Natl. Oceanic and Atmos. Admin., U.S. Dept. Commer., Boulder, Colo.

NGDC, 1993. SEASAT Haxby gravity database, *Data Announcement 93-MGG-01*, Natl. Oceanic and Atmos. Admin., U.S. Dept. Commer., Boulder, Colo.

NGDC, 1994. TerrainBase Worldwide Digital Terrain Data. On: *CD-ROM 1090-A27-001*, Natl. Oceanic and Atmos. Admin., U.S. Dept. Commer., Boulder, Colo.

Nissen, S.S., Hayes, D.E., Buhl, P., Diebold, J., Bochu, Y., Weijun, Z., & Yongqin, C., 1995. Deep penetration seismic soundings across the northern margin of the South China Sea. *J. Geophys. Res.*, v.100(B11), p.22407-22433.

Noad, J., & Harbury, N., 1996. The sedimentology of Miocene shallow marine clastics of the Sandakan Formation of Eastern Sabah. *Geol. Soc. Malaysia Annual Geological Conference 1996 Abstracts*, p.43.

Nouel, F. *et al.*, 1994. Precise CNES orbits for Topex-Poseidon: is reaching 2 cm still a challenge? *J. Geophys. Res.*, Topex-Poseidon special issue, v.99, p.24405-24420.

Omang, S.A.K.S., 1993. *Petrology, Geochemistry and Structural Geology of the Darvel Bay Ophiolite, Sabah, Malaysia.* Unpublished Ph.D. Thesis, University of London.

Omang, S.A.K., & Barber, A.J., 1996. Origin and tectonic significance of the metamorphic rocks associated with the Darvel Bay Ophiolite, Sabah, Malaysia. In: *Tectonic Evolution of Southeast Asia* (Eds. Hall, R., & Blundell, D.), Geological Society Special Publication No. 106, Geological Society, London, p.263-279.

Oskam, D., 1990. Sea surface variability in the North Sea as derived from Seasat altimetry. *Geophys. J. Int.*, v.100, p.1-7.

Owens, R., & Parsons, B., 1994. Gravity Fields over Mid-Ocean Ridges from GEOSAT GM data: Variations as a Function of Spreading Rate. *Geophys. Res. Letts.*, v.21(25), p.2837-2840.

Packham, G., 1996. Cenozoic SE Asia: reconstructing its aggregation and reorganization. In: *Tectonic evolution of Southeast Asia* (Eds. Hall, R., & Blundell, D.). Geological Society Special Publication No. 106, p.123-152. London.

Pariso, J.E., Sempere, J-C., & Rommevaux, C., 1995. Temporal and spatial variations in crustal accretion along the Mid-Atlantic Ridge (29° - 31°30' N) over the last 10 m.y.: Implications from a three-dimensional gravity study. *J. Geophys. Res.*, v.100(B9), p.17781-17794.

Parsons, B., & Daly, S., 1983. The relationship between surface topography, gravity anomalies, and temperature structure of convection. *J. Geophys. Res.*, v.88, p.1129-1144.

Patriat, P., 1987. *L'évolution du système de dorsales de l'Océan Indien, Terres Australes et Antartiques Françaises*, Paris, 310pp.

Pautot, G., & Rangin, C., 1989. Subduction of the South China Sea axial ridge below Luzon (Philippines). *Earth Planet. Sci. Letts.*, v.92, p.57-69.

Pautot, G., Rangin, C., Briais, A., Tapponnier, P., Beuzart, P., Lericolais, G., Mathieu, X., Wu, J., Han, S., Li, H., Lu, Y., & Zhao, J., 1986. Spreading direction in the Central South China Sea. *Nature*, v.321, p.150-154.

Pautot, G., Rangin, C., Briais, A., Wu, J., Han, S., Li, H., Lu, Y., & Zhao, J., 1990. The axial ridge of the South China Sea: a Seabeam and geophysical survey. *Oceanologica Acta*, v.13(2), p.129-143.

Peltzer, G., & Tapponnier, P., 1988. Formation and evolution of strike-slip faults, rifts, and basins during the India-Asia collision: an experimental approach. J. Geophys. Res., v.93, p.15085-15117.

Phinney, E., & Nerem, S., 1997. *An analysis of satellite altimeter derived gravity anomaly data.* Unpublished report, University of Texas at Austin, U.S.A.

Phipps-Morgan, J., & Chen, Y., 1993. Dependence of ridge-axis morphology on magma supply and spreading rate. *Nature*, v.364, p.706-708.

Pieters, P.E., & Supriatna, S., 1990. *Geological Map of the West, Central and East Kalimantan Area, 1:1,000,000*, GRCD, Bandung, Indonesia.

Pratt, J.H., 1855. On the attraction of the Himalaya Mountains and of the elevated regions beyond upon the plumb-line in India. *Trans. Roy. Soc. (London)*, ser. B, v.145.

Pubellier, M., Quebral, R., Rangin, C., Deffontaines, B., Muller, C., *et al.*, 1991. The Mindanao Collision Zone: a soft collision event with a continuous Neogene strike-slip setting. Journal of Southeast Asian Earth Sciences, v.6, p.239-248.

Rangin, C., 1989. The Sulu Sea, a back-arc basin within a Noogene collision zone. *Tectonophysics*, v.161, p.119-141.

Rangin, C., 1991. Neogene arc-continental collision in Sabah, Northern Borneo (Malaysia) - Reply. *Tectonophysics*, v.200, p.330-332.

Rangin, C., & Silver, E., 1990. Geological setting of the Celebes and Sulu Seas. In: P*roceedings of the ODP, Initial Reports* (Eds. Rangin, C., Silver, E.A., & von Breymann, M.T.), Ocean Drilling Program, v.124, p.35-42.

Rangin, C., & Silver, E., 1991. Neogene tectonic evolution of the Celebes-Sulu Basins: new insights from Leg 124 Drilling. *Proc. ODP, Sci Results*, v.124, College Station Texas, p.51-63.

Rangin, C., Stephan, J.F., Blanchet, R., Baladad, D., Bouysee, P., Pen Chen, M., Chotin, P., Collot, J., Daniel, J., Drouhot, J.M., Marchadier, Y., Marsset, B., Pelletier, B., Richard, M., & Tardy, M., 1988. SeaBeam survey at the southern end of the Manila Trench: transition between subduction and collision processes offshore Mindoro Island, Philippines. *Tectonophysics*, v.146, p.261-278.

Rangin, C., Bellon, H., Bernard, F., Letouzey, J., Muller, C., & Sanudin, T., 1990*a*. Noegene arc-continent collision in Sabah, Northern Borneo (Malaysia). *Tectonophysics*, v.183, p.305-319.

Rangin, C., Jolivet, L., Pubellier, M., & the Tethys Pacific working group, 1990*b*. A simple model for the tectonic evolution of southeast Asia and Indonesia region for the past 43 m.y. *Bulletin de la Societe geologique de France*, v.8(VI), p.889-905.

Rangin, C., *et al.*, 1990*c*. The quest for the Tethys in the western Pacific; 8 paleogeodynamic maps for Cenozoic time. *Bulletin de la Société Géologique de France*, Supplément 8e série, tome VI, no. 6 et dernier, p.907-913.

Rangin, C., Silver, E.A., & Tamaki, K., 1995. Closure of Western Pacific Marginal Basins: Rupture of the Oceanic Crust and the Emplacement of Ophiolites. In: *Active Margins and Marginal Basins of the Western Pacific*, Geophysical Monograph 88, American Geophysical Union, p.405-417.

Rapp, R.H., 1983. The Determination of Geoid Undulations and Gravity anomalies from Seasat Altimeter Data. *J. Geophys. Res.*, v.88(C3), p.1552-1562.

Rapp, R.H., & Bašic, T., 1992. Oceanwide gravity anomalies from GEOS-3, Seasat and Geosat Altimeter Data. *Geophys. Res. Letts.*, v.19, p.1979-1982.

Rapp, R.H., & Pavlis, N.K., 1990. The Development and Analysis of Geopotential Coefficient Models to Spherical Harmonic Degree 360. *J. Geophys. Res.*, v.95(B13), p.21,885-21,911.

Rapp, R.H., & Wang, Y.M., 1994. Dynamic topography estimates using Geosat data and a gravimetric geoid in the Gulf Stream region. *Geophys. J. Int.*, v.117, p.511-528.

Rapp, R.H., Wang, Y.M., & Pavlis, N., 1991. *The Ohio State 1991 geopotential and sea surface topography harmonic coefficient models*, Rep. 410, Dep. of Geod. Sci. and Surv., The Ohio State Univ., Columbus, U.S.A.

Raschka, H., Nacario, E., Rammimair, D., Samonte, C., & Steiner, L., 1985. Geology of the ophiolite of central Palawan Island, Philippines. *Offioliti*, v.10, p.375-390.

Ratman, N., 1976. *Geological map of the Tolitoli Quadrangle, North Sulawesi*, 1:250,000. Geological Survey of Indonesia.

Ray, R.D., & Mitchum, G.T., 1996. Surface manifestation of internal tides generated near Hawaii. *Geophys. Res. Letts.*, v.23(16), p.2101-2104.

Reinhard, M., & Wenk, E., 1951. *Geology of the colony of North Borneo.* Geological Survey Department of the British Territories in Borneo, Bulletin, No.1, 160pp.

Richter, B., & Fuller, M., 1996. Palaeomagnetism of the Sibumasu and Indochina blocks: implications for the extrusion tectonic model. In: *Tectonic Evolution of Southeast Asia* (Eds. Hall, R., & Blundell, D.), Geological Society Special Publication No. 106, Geological Society, London, p.203-224.

Roesar, H.A., 1991. Age of the crust of the southeast Sulu Basin based on magnetic anomalies and age determined at site 768. *Proc. ODP, Sci Results*, v.124, College Station Texas, p.339-344.

Royer, J-Y., & Sandwell, D.T., 1989. Evolution of the eastern Indian Ocean since the Late Cretaceous: constraints on Geosat altimetry. *J. Geophys. Res.*, v.94, p.13,755-13782.

Rummel, R., & Haagmans, R.H.N., 1991. Gravity Gradients from Satellite Altimetry. *Marine Geodesy*, v.14, p.1-12.

Ryall, P.J.C., & Beattie, D., 1989. *A gravity high in Darvel Bay.* Dalhousie University report (unpublished), pp.18. Also in: The 1995 Sabah Gravity Survey (Holt, R. & Milsom, J., 1995), University of London Southeast Asia Research Group Report No. 153 (Unpub.).

Sandwell, D.T., 1984. A detailed view of the South Pacific geoid from satellite altimetry. *J. Geophys. Res.*, v.89, p.1089-1104.

Sandwell, D.T., 1992. Antarctic marine gravity from high density satellite altimetry. *Geophys. J. Int.*, v.109, p.437-448.

Sandwell, D.T., & Smith, W.H.F., 1994. New global marine gravity map/grid based on stacked ERS-1, Geosat and Topex altimetry. *EOS Trans. Amer. Geophys. U. 1994 Spring Meeting Suppl.*, v.75(16), p.321.

Sandwell, D.T., & Smith, W.H.F., 1997. Marine gravity anomaly from Geosat and ERS-1 satellite altimetry. *J. Geophys. Res.*, in press.

Sandwell, D.T., & Zhang, B., 1989. Global Mesoscale Variability from the Geosat Exact Repeat Mission: Correlation with Ocean Depth. *J. Geophys. Res.*, v.94(C12), p.17971-17984.

Sardjono, 1996. *Gravity field and Structur of the Sorong Fault Zone Eastern Indonesia.* Unpublished Ph.D. Thesis, University of London, London.

Schmidtke, E., Fuller, M., & Haston, R., 1990. Paleomagnetic data from Sarawak, Malaysian Borneo, and the Late Mesozoic and Cenozoic tectonics of Sundaland. *Tectonics*, v.9, p.123-140.

Schwarz, K.P., Sideris, M.G., & Forsberg, R., 1990. Review paper: The use of FFT techniques in physical geodesy. *Geophys. J. Int.*, v.100, p.485-514.

Schwiderski, E.W., 1980. Ocean tides, Part I: global ocean tidal equations; Part II: a hydrodynamical interpolation model. *Mar. Geod.*, v.3, p.161-255.

Semtner, A.J. Jr., & Chervin, R.M., 1992. Ocean General Circulation From a Global Eddy-Resolving Model. *J. Geophys. Res.*, v.97(C4), p.5493-5550.

Sharma, P.V., 1986. *Geophysical Methods in Geology, Second Edition*, Elsevier, London, 442 pp.

Shibuya, H., Hsu, V., & Merrill, D., 1989. Paleomagnetic results of Leg 124: Celebes and Sulu Seas. *EOS*, v.70, p.1365.

Shum, C.K., Zhang, B.H., Schutz, B.E., & Tapley, B.D., 1990. Altimeter crossover methods for precision orbit determination. *J. Astron. Sci.*, v.38(3).

Sikumbang, N., 1990. The geology and tectonics of the Meratus mountains, south Kalimantan, Indonesia. *Geologi Indonesia*, Journal of the Indonesian Association of Geologists, v.13(2), p.1-31.

Silver, E.A., & Rangin, C., 1991. Development of the Celebes Sea in the context of Western Pacific marginal basin history. In: *Scientific Reports of the Ocean Drilling Program 124* (Eds. Silver, E.A., Rangin, C., & von Breymann, M.), College Station Texas, p.39-49.

Silver, E.A., McCaffrey, R., Joyodiwiriyo, Y., & Stevens, S., 1983*a*. Ophiolite emplacement by collision between the Sula Platform and the Sulawesi Island arc, Indonesia. *J. Geophys. Res.*, v.88, p.9419-9435.

Silver, E.A., McCaffrey, R., Smith, R.B., *et al.*, 1983*b*. Collision, rotation and the initiation of subduction in the evolution of Sulawesi, Indonesia. *J. Geophys. Res.*, v.88, p.9407-9418.

Simandjuntak, T.O., & Barber, A.J., 1996. Contrasting tectonic styles in the Neogene orogenic belts of Indonesia. In: *Tectonic Evolution of Southeast Asia* (Eds. Hall, R., & Blundell, D.), Geological Society Special Publication No. 106, Geological Society, London, p.185-201.

Skeels, D.C., 1947. Ambiguity in gravity interpretation. *Geophysics*, v.12, p.43-56.

Small, C., 1994. A global analysis of mid-ocean ridge axial topography. *Geophys. J. Int.*, v.116, p.64-84.

Small, C., & Sandwell, D.T., 1989. An abrupt change in ridge axis gravity with spreading rate. *J. Geophys. Res.*, v.94, p.17383-17392.

Small, C., & Sandwell, D.T., 1992. A comparison of satellite and shipboard gravity measurements in the Gulf of Mexico. *Geophysics*, v.57(7), p.885-893.

Small, C., & Sandwell, D.T., 1994. Imaging mid-ocean ridge transitions with satellite gravity. *Geology*, v.22, p.123-126.

Smith, D.K., Humphris, S.E., Tivey, M.A., & Cann, J.R., 1997. Viewing the Morphology of the Mid-Atlantic Ridge from a New Perspective. *EOS*, v.78(26), p.265-269.

Smith, I.F., Dabek, Z.K., & Jolly, G.W., 1995. A comparison between sea-surface and satellite-derived gravity anomalies on the UK continental shelf. *EAGE 57th Conference and Technical Exhibition Extended Abstracts*, Paper D023

Smith, W.H.F., 1993. On the accuracy of digital bathymetric data. *J. Geophys. Res.*, v.98(B6), p.9591-9603.

Smith, W.H.F., & Sandwell, D.T., 1995. Marine gravity field from declassified Geosat and ERS-1 altimetry (abstract). *EOS Trans. AGU*, v.76, p.156.

Smith, W.H.F., & Sandwell, D.T., 1997. Global Seafloor Topography from Satellite Altimetry and Ship Depth Soundings. *Science*, in press.

Sneeuw, N., 1994. Global spherical harmonic analysis by least-squares and numerical quadrature methods in historical perspective. *Geophys. J. Int.*, v.118, p.707-716.

Stanley, H.R., 1979. The Geos-3 Project. *J. Geophys. Res.*, v.84.

Steinhart, J.S., 1967. Mohorovicic discontinuity. In: *International Dictionary of Geophysics, Volume 2* (Ed. Runcorn, K.), Pergamon, Tarrytown, N.Y.

Stewart, R.H., 1984. Oceanography from Space. *Ann. Rev. Earth Planet. Sci.*, v.12, p.61-82.

Stewart, R.H, 1985. *Methods of Satellite Oceanography*, University of California Press, Berkeley, 360pp.

St. John, V.P., 1967. *The Gravity Field of Papua New Guinea*. Ph.D. Thesis, University of Tasmania (unpub.).

Strange, T., 1991. *The determination and geophysical applications of free-air gravity anomalies using satellite altimetry and ship gravity*, Ph.D. Thesis, Department of Earth Sciences, Oxford University.

Sukamto, R., 1982. *The geology of the Pangkajene and western part of Watampone, Sulawesi 1:250,000.* Geological Research and Development Centre, Indonesia.

Tahir, S., 1989. Geology of the Tabin area, Lahad Datu, Sabah. *Sabah Museum Monograph*, v.3, p.1-20.

Tai, C.-K., 1988. Geosat Crossover Analysis in the Tropical Pacific 1. Constrained sinusoidal crossover adjustment. *J. Geophys. Res.*, v.93(C9), p.10621-10629.

Talwani, M., 1971. Gravity. In: *The Sea, vol. 4, part 1*, (Ed. Maxwell, A.), John Wiley, New York, p.251-297.

Tapley, B.D., & Born, G.H., 1980. The Seasat precision orbit determination experiment, *J. Astron. Sci.*, v.28(4), p.315-326.

Tapley, B.D., Born, G.H., & Parke, M.E., 1982. The Seasat altimeter data and its accuracy assessment. *J. Geophys. Res.*, v.87, p.3179-3188.

Tapley, B.D., *et al.*, 1994. Precise orbit determination for Topex-Poseidon. *J. Geophys. Res.*, Topex-Poseidon special issue, v.99, p.24369-24382.

Tapponnier, P., Peltzer, G., LeDain, A.Y., Armijio, R., & Cobbold, P., 1982. Propagating extrusion tectonics in Asia: New insights from simple experiments with plasticine. *Geology*, v.10, p.611-616.

Tapponnier, P., Peltzer, G., & Armijo, R., 1986. On the mechanics of the collision between India and Asia. In: *Collision Tectonics* (Eds. Coward, M.P., & Ries, A.C.), Geological Society Special Publication No. 19, London, p.115-157.

Taylor, B., & Hayes, D.E., 1980. The tectonic evolution of the South China Basin. In: *The Tectonic and Geologic Evolution of the Southeast Asian Seas and Islands, Part 1, Geophys. Monogr. Ser., Vol. 23* (Ed. Hayes, D.E.), AGU, Washington, D.C., p.89-104.

Taylor, B., & Hayes, D.E., 1983. Origin and History of the South China Basin. In: *The Tectonic and Geologic Evolution of the Southeast Asian Seas and Islands, Part 2, Geophys. Monogr. Ser., Vol. 27* (Ed. Hayes, D.E.), AGU, Washington, D.C., p.23-56.

Telford, W.M., Geldart, L.P., & Sheriff, R.E., 1990. *Applied Geophysics Second Edition*, Cambridge University Press, Cambridge.

Tjia, H.D., 1988. Accretion tectonics in Sabah: Kinabalu Suture and East Sabah accreted terrane. Geol. Soc. Malaysia, Bull., v.22, p.237-251.

Tongkul, F., 1987. *Sedimentology and Structure of the Crocker Formation in the Kota Kinabalu area, Sabah, East Malaysia.* Unpublished Ph.D. Thesis, University of London.

Tongkul, F., 1990. Structural style and tectonics of western and northern Sabah. *Bull. Geol. Soc. Malaysia*, v.27, p.227-239.

Tongkul, F., 1991. Tectonic evolution of Sabah, Malaysia. *J. SE Asian Earth Sci.*, v.6(3/4), p.395-405.

Tongkul, F., 1993. Tectonic control on the development of the Neogene basins in Sabah, East Malaysia. *Bull. Geol. Soc. Malaysia*, v.33, p.95-103.

Torge, W., 1980. *Geodesy*, Walter de Gruyter, Berlin.

Tschernia, P., 1980. *Descriptive Regional Oceanography, Pergamon Marine Series Volume 3*, Pergamon Press, Oxford.

Tscherning, C.C., 1986. Functional methods for gravity field approximation. In: *Lecture Notes in Earth Sciences, 7: Mathematical and Numerical Techniques in Physical Geodesy* (Ed. Sünkel, H.), Springer-Verlag, Berlin.

Tscherning, C.C., Christoffersen, T., & Schultzen, J., 1990. *Combined use of conventional gravity and satellite altimetry.* Paper presented at the 52nd meeting of the European Association of Exploration Geophysicists, Copenhagen.

van Blaricom, R., 1992. *Practical Geophysics II for the Exploration Geologist.* Northwest Mining Association, Spokane, WA, USA.

Verma, R.K., 1985. *Gravity Field, Seismicity and Tectonics of the Indian Peninsula and the Himalayas*, D. Reidel Publishing Company, Dordrecht, Holland, 213 pp.

Visser, P.N.A.M., Wakker, K.F., & Ambrosius, B.A.C., 1993. Dynamic Sea Surface Topography from GEOSAT Altimetry. *Marine Geodesy*, v.16, p.215-239.

Wain, T., & Berod, B., 1989. The tectonic framework and paleogeographic evolution of the Upper Kutei Basin. *Indonesian Petroleum Association, Proceedings 18th Annual Convention, Jakarka, 1989*, v.1, p.55-78.

Wang, X., & Cochran, J.R., 1993. Gravity Anomalies, Isostacy and Mantle Flow at the East Pacific Rise Crest. *J. Geophys. Res.*, v.98, p.19505-19531.

Wang, X., & Cochran, J.R., 1995. Along-axis gravity gradients at mid-ocean ridges: Implications for mantle flow and axial morphology. *Geology*, v.23(1), p.29-32.

Watts, A.B., Cochran, J.R., & Selzer, G., 1975. Gravity anomalies and flexure of the lithosphere: a three-dimensional study of the Great Meteor seamount, northeast Atlantic. *J. Geophys. Res.*, v.80, p.1391-1398.

Weissel, J.K., 1980. Evidence for Eocene oceanic crust in the Celebes Sea. In: *The Tectonic and Geologic Evolution of the Southeast Asian Seas and Islands* (Ed. Hayes, D.E.), American Geophysical Union, Geophysical Monograph Series,v.23, p.37-48.

Welch, P.D., 1967. The use of the fast Fourier transform for the estimation of power spectra: A method based on time averaging over short, modified periodograms. *IEEE Trans. Audio Electroacoust.*, v.15(AU), p.70-73.

Wessel, P., & Smith, W.H.F., 1995. New version of the Generic Mapping Tools released. *EOS Trans. Amer. Geophys. U.*, v.76, p.329.

Wessel, P., & Smith, W.H.F., 1996. A global, self-consistent, hierarchical, high-resolution shoreline database. *J. Geophys. Res.*, v.101(B4), p.8741-8743.

Wessel, P., & Watts, A.B., 1988. On the Accuracy of Marine Gravity Measurements. *J. Geophys. Res.*, v.93(B1), p.393-413.

White, N., 1993. Recovery of strain rate variation from inversion of subsidence data. *Nature*, v.366, p.449-452.

Widiyantoro, S., & Van der Hilst, R., 1996. Structure and evolution of lithospheric slab beneath the Sunda arc, Indonesia. *Science*, v.271, p.1566-1570.

Williams, P.R., Johnston, C.R., Almond, R.A., & Simamora, W.H., 1988. Late Cretaceous to Early Tertiary structural elements of West Kalimantan. *Tectonophysics*, v.148, p.279-297.

Wilson, R.A.M., & Wong, N.P.Y., 1964. *The geology and mineral resources of the Labuan and Padas Valley area, Sabah, Malaysia*. Geological Survey of Malaysia Memoir, No.17.

Wolfart, R., Cepek, P., Gramann, F., & Porth, H., 1986. Stratigraphy of Palawan island, Philippines. *Newsl. Stratigr.*, v.15, p.19-48.

Wong, N.P.Y, & Leong, K.M., 1968. Unconformity between the Chert-Spilite Formation and Crystalline Basement around Sungai Agob and Sungai Dabalan. *Geol. Soc. Malaysia Bull., Borneo Region,* v.9, p.23-24.

Wright, T.J., 1997. *Improving marine gravity determination in eastern Indonesia by reprocessing ERS-1 altimeter waveform data*, Unpub. M.Sc. Dissertation, University of London, London.

Wunsch, C., & Zlotnicki, V., 1984. The accuracy of altimetric surfaces. *Geophys. J. Roy. astr. Soc.*, v.78, p.795-808.

Wyrtki, K., & Mitchum, G., 1990. Interannual differences of Geosat altimeter heights and sea level: The importance of a datum. *J. Geophys. Res.*, v.95(C3), p.2969-2975.

Xu, P., 1992. Determination of surface gravity anomalies. *Geophys. J. Int.*, v.110, p.321-332.

Yale, M.M., Sandwell, D.T., & Smith, W.H.F., 1995. Comparison of along-track resolution of stacked Geosat, ERS-1 and Topex satellite altimeters. *J. Geophys. Res.*, v.100, p.15117-15127.

ADDITIONAL REFERENCES

Bassi, G., Keen, C.E., & Porter, P., 1993. Contrasting styles of rifting: Models and examples from the eastern Canadian margins. *Tectonics*, v.12, p.639-655.

Buck, R., 1991. Modes of continental lithosphere extension. *J. Geophys. Res.*, v.96, p.20161-20178.

Jonas, J., Hall., S., & Casey, J.F., 1991. Gravity Anomalies Over Extinct Spreading Centers: A Test of Gravity Models of Active Centers. *J. Geophys. Res.*, v.96, p.11759-11777.

Luther, G.G., & Towler, W.R., 1982. Redetermination of the Newtonian Gravitational Constant G. *Phys. Rev. Letts.*, v.48(3), p.121-123.

Watts, A.B., & Fairhead, J.D., 1997. Gravity anomalies and magmatism along the western continental margin of the British Isles. *J. Geol. Soc. London*, v.154, p.523-529.

APPENDIX 1

Barometric Levelling of the 1995 Sabah Gravity Survey

BAROMETRIC LEVELLING OF THE 1995 SABAH GRAVITY SURVEY

A1.1 Introduction

The single base barometric levelling technique used during the 1995 Sabah gravity survey has been used for many years on gravity surveys in Southeast Asia (e.g. St. John, 1967; Milsom, 1970; Milsom, 1988; Harrison, 1991). The basis for this technique is as follows. It is assumed that atmospheric pressure variations occur uniformly across the survey area, and that temperature and humidity remain constant throughout the survey. By continually recording atmospheric pressure at a fixed location (base station), the background pressure variation may be removed from pressure measurements taken at field stations leaving the pressure difference between the field station and the base station. As an approximately linear inverse relationship exists between pressure and altitude, the observed pressure difference between the base station and the field station can be directly converted into a height difference. By determining the height of the base station above mean sea level, the elevations of the field stations may finally be deduced.

A1.2 Theory

When pressure is measured in a dry atmosphere in which temperature decreases with height at a uniform rate, it is possible to derive height estimates directly from pressure measurements using Equation (A1.1) -

$$H = r.\Theta(x - x^2/2 + x^3/3 - x^4/4) / g \qquad \text{(A1.1)}$$

where H is the height difference between two points having pressures p_0 and p_1, $x = (p_1-p_0)/p_0$, g is the acceleration due to gravity, Θ is the mean temperature of the air column between the two points, and r is the gas constant (per gram). The exact value of r for air varies somewhat, but the international standard value of 287.03 Joules.°K.gm^{-1} has been found generally satisfactory for levelling work (Milsom, 1970).

When Equation (A1.1) is used directly for height estimation, additional temperature and humidity measurements are required. Very humid conditions, such as prevailed on Sabah, have the effect of increasing the height difference predicted by Equation (A1.1) by between 0.6 and 1.2 % (Crone, 1948). A humidity of 80 - 90 % would account for a 1 % increase in estimated height. According to Crone (1960), "the temperature required is the temperature of the (fictitious) air column, the length of which represents the difference in height. The observer on the ground is unfavourably placed to determine this, and there is some evidence that temperature corrections may do more harm than good." This conclusion was drawn from the radiosonde and wireline balloon observations of Haurwitz (1955) and Crone (1948), which showed that diurnal temperature variations in the first 100 metres above ground level may be as much as three to four times greater than those in the air column as a whole.

A1.3 Instrumentation

Two Wallace & Tiernan Type 6 (Model FA-112) barometric altimeters, on loan from the Department of Photogrammetry and Remote Sensing, University College London, were used throughout the 1995 Sabah gravity survey. They were probably manufactured in the later stages of the Second World War for the US Corps of Engineers but, despite their considerable age, are still excellent instruments for regional gravity surveys. They proved extremely robust and reliable, and no instrument deterioration was detected during the survey. Figure A1.1 shows a typical Wallace & Tiernan Type 6 barometric altimeter.

Readings with the Type 6 altimeter are obtained directly from a circular scale backed by a mirror against which the pointer can be read with low parallax error. With the aid of the mirror (and good eyesight) it is possible to estimate readings to the nearest foot. The instrument is compensated for changes in temperature in so far as they affect the mechanical parts but not, of course, for the effect of the temperature of the air column. The scale is graduated directly in feet and may be corrected using a scale card for the standard atmosphere specified in the Smithsonian Meteorological Table 51, the most

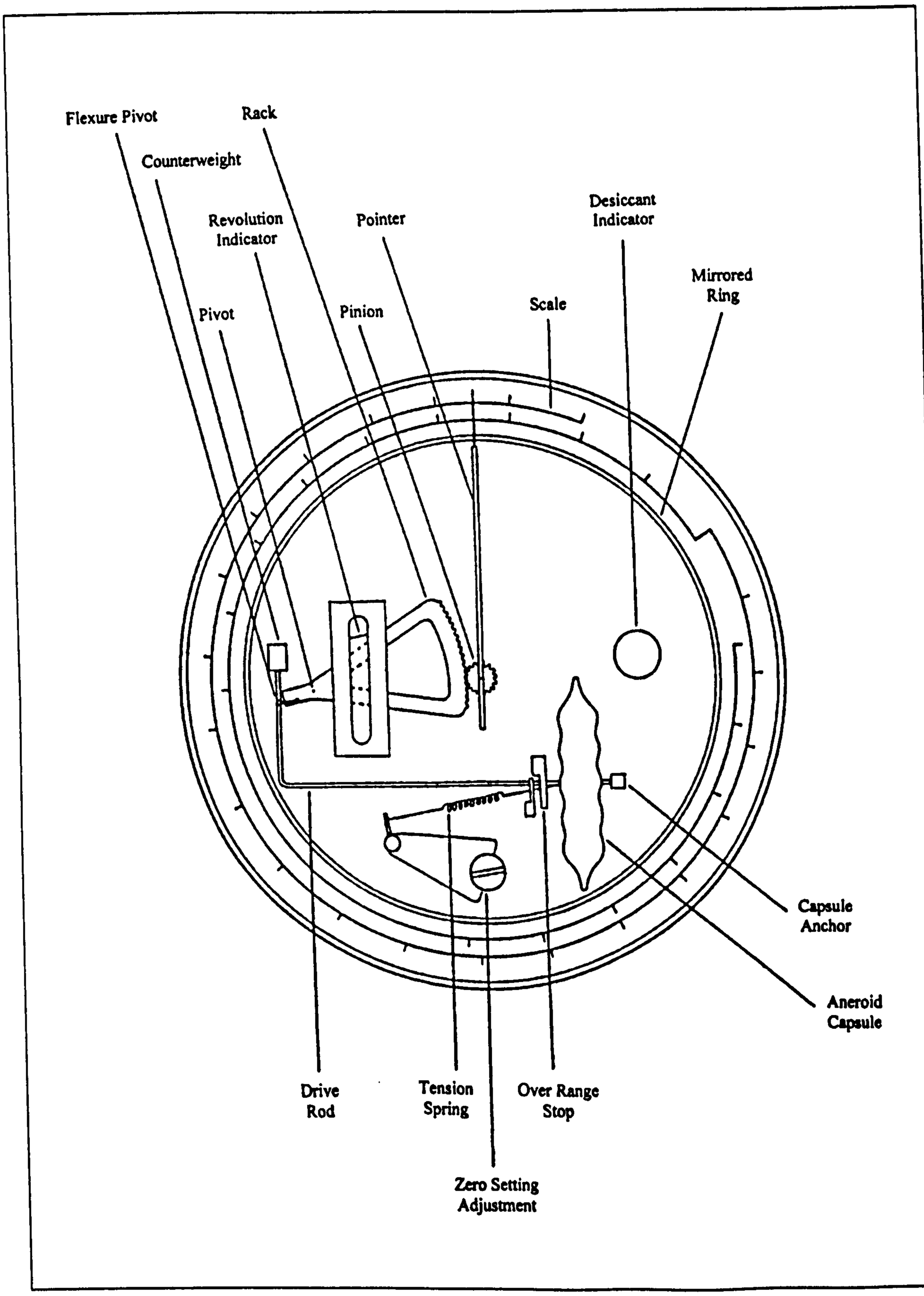

Figure A1.1. A Wallace & Tiernan Type 6 barometric levelling altimeter.

important characteristic of which is the constant temperature of 10 °C assumed for the air column. According to the makers' handbook, each scale card is printed individually and is adjusted at the time of printing to the instrument concerned. No comment is made as to the variation to be expected in this calibration over a period of years. The instrument dial is based on a false 'zero' to avoid the inconvenience of negative heights. Since in altimetry it is, to a first approximation, only differences in readings which are significant, this zero shift is not important.

In the discussion that follows, heights or height differences expressed in feet are values obtained directly from the altimeter readings, and may therefore appear anomalously large. For example, the 'zero' of Barometer 8 was set at ~ 1050 ft. Values in metres are final corrected height differences or absolute elevations. Direct calibration of the altimeters in terms of height implies that an increase in reading corresponds to a decrease in atmospheric pressure. An altimetric increase of 100 ft corresponds to a pressure decrease of about 3.6 millibars.

Recommendations for optimum instrument use include that whilst reading the altimeters, they should be level and should not be "tapped" to free the needle; forceful tapping can even be harmful. It would be clearly unwise to place the instruments in a pressure environment far outside their 7000 ft operating range, thus if transported by air they should be carried only in a pressurised compartment. Ideally, base and field instruments should be observed under similar conditions, i.e. outdoors but protected from harsh sunlight and strong wind. The instruments should be protected against sudden shock and should be well cushioned during transport. Finally, thunderstorm, whirlwind or storm conditions should be avoided as data acquired under these conditions are of poor to very poor quality. On two occasions, storms occurred whilst the background barometric variation was being measured. Graphs showing the effects of the storms on the background variation are given in Figure A1.2. The main feature is the sudden large pressure change that accompanies the onset of the storm. On day 3, for example, the pressure was observed to fall by the equivalent of 40 ft in about 15 minutes (approximately 1/3 of the total diurnal variation).

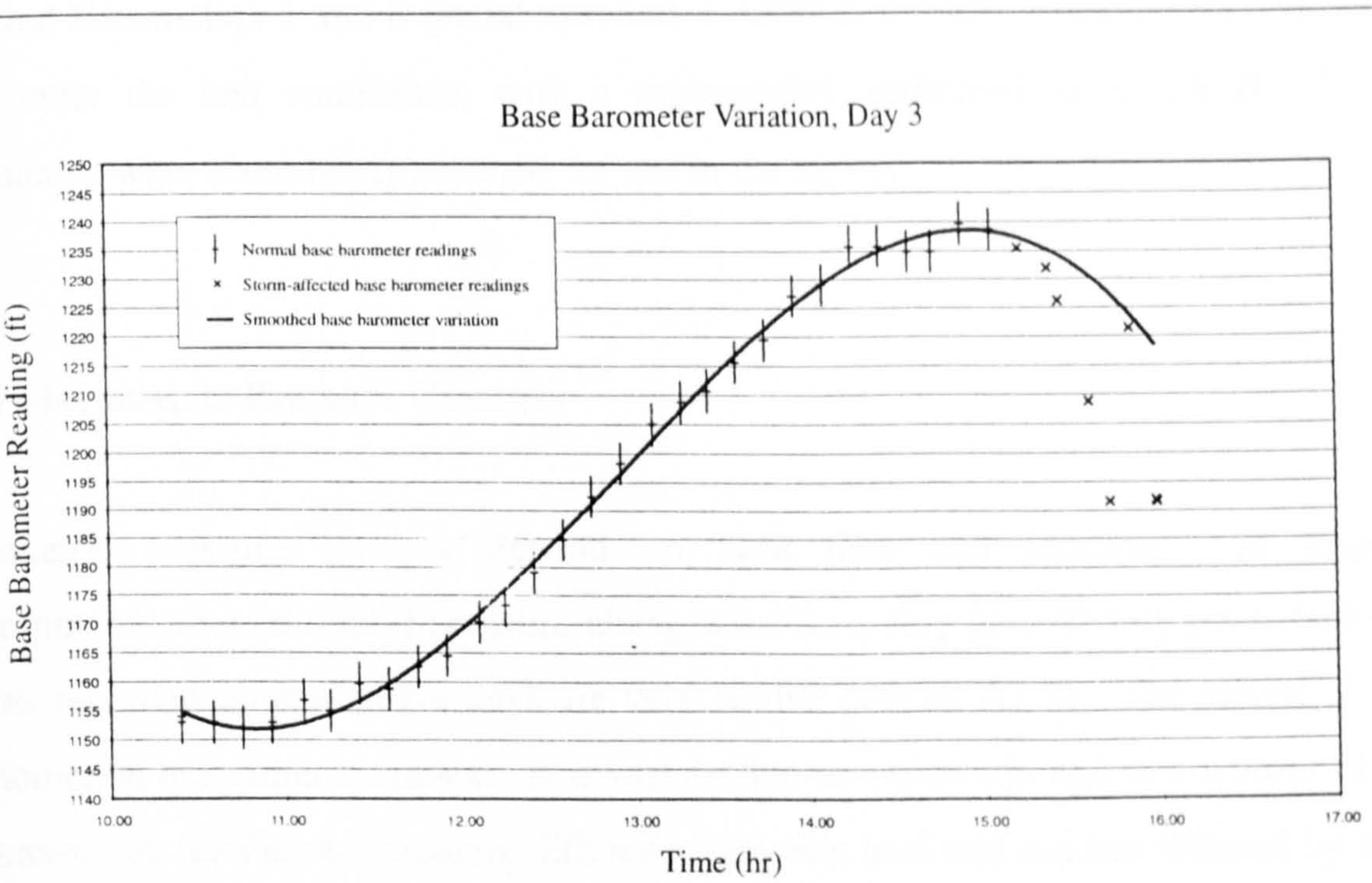

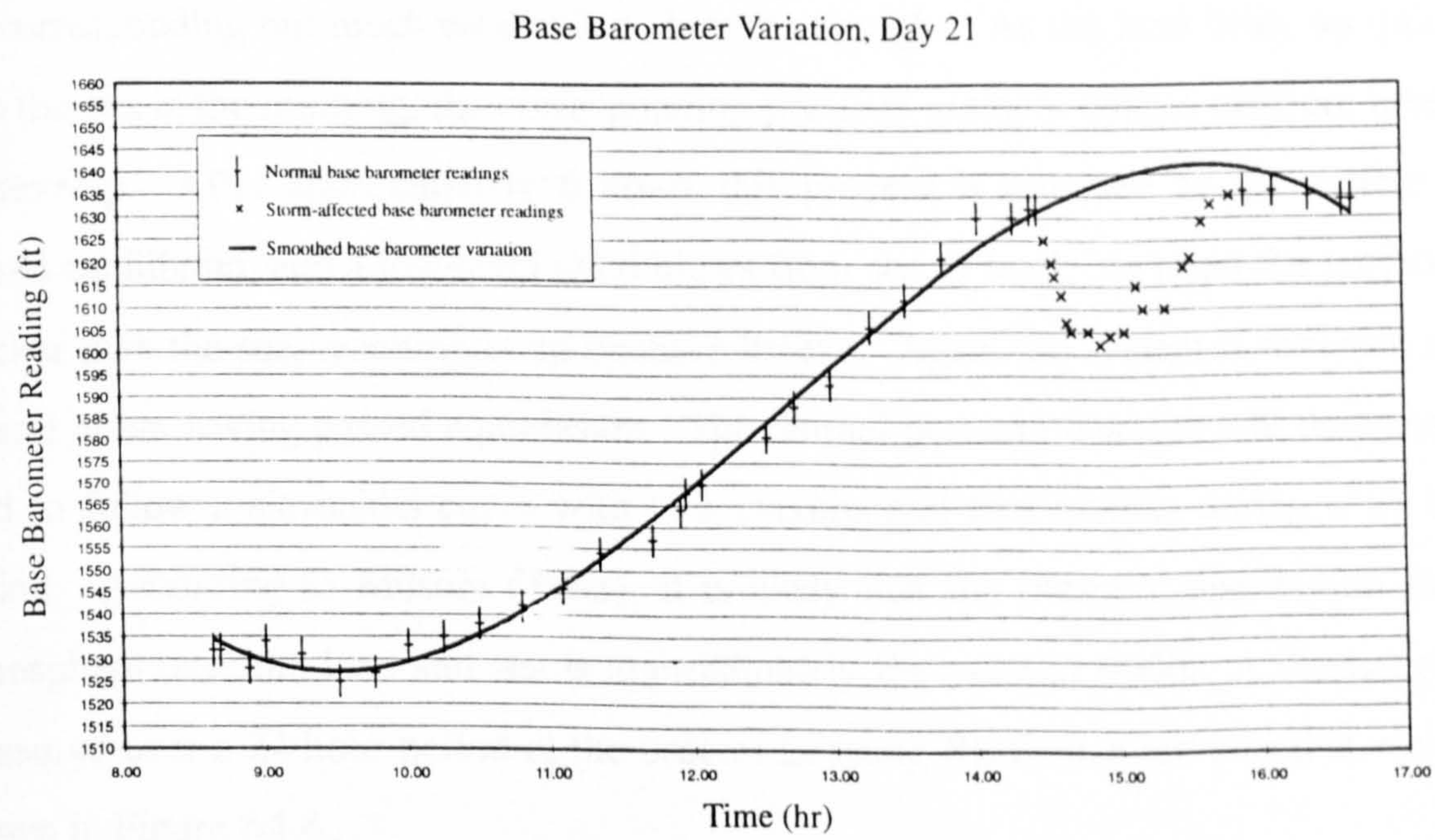

Figure A1.2. Graphs showing the effect of storms on base barometer readings.

Prior to the 1995 gravity survey, the four available barometers (Barometers 1, 8, 9 and 10) were tested in order to determine the optimum pair for the survey. The conclusion was that Barometers 1 and 8 (serial numbers 6-1570 & 6-1708 respectively) performed best under the test conditions, with a repeatability estimated as ± 1.6 ft. These barometers were accordingly selected for use in the survey.

A1.4 Barometric Pressure Changes

Barometric pressure changes depend on both time and location. In tropical environments, diurnal (daily) pressure changes are in a very general way predictable, as curves recorded on successive days are very similar (Figure A1.3). The causes of this phenomenon are rather complex. It is mainly due to expansion and contraction of the air, caused by the thermal capacity difference between land and sea and affected by solar radiation, and to the tides. This air movement leads to sea breezes during the day and the corresponding but much weaker land breezes at night. As the land heats up quicker than the sea in the morning, the corresponding pressure gradient causes offshore breezes to develop. After approximately 6 hours this process is reversed as the system has passed equilibrium and a low-level wind blows from sea to land. At night the land cools quicker than the sea, resulting in an onshore breeze. Again the system is reversed after several hours having passed equilibrium. The diurnal pressure changes will thus usually tend to follow a sinusoidal curve with two maxima and two minima during a 24 hour period. According to Milsom (1988), it is likely that the pressure distribution in the atmosphere over the land and sea is approximately the same at 0900. A diurnal curve measured over a 24 hour period at the base at Luasong Resthouse (an inland station), is shown in Figure A1.4.

In detail, the shape of the diurnal pressure variation curve will vary from day to day and from station to station. In particular, elevation above sea level will influence its amplitude, which decreases with increasing elevation. Given the uncertainties connected with the temperature and humidity of the air column, the magnitude of these changes is best determined experimentally at points within the survey area at the time of the survey.

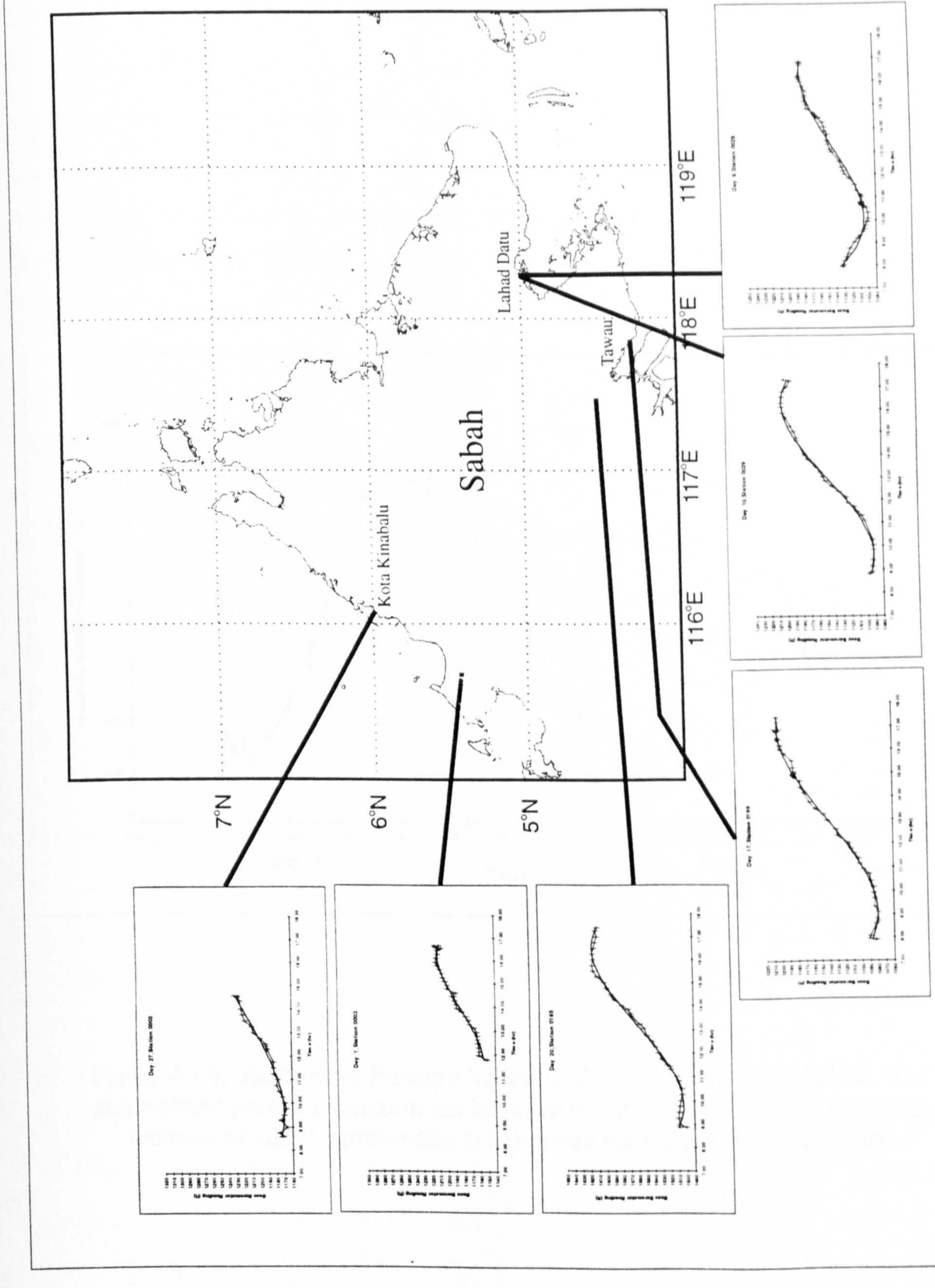

Figure A1.3. A selection of base barometer pressure variations as observed on Sabah at different locations, July 1995.

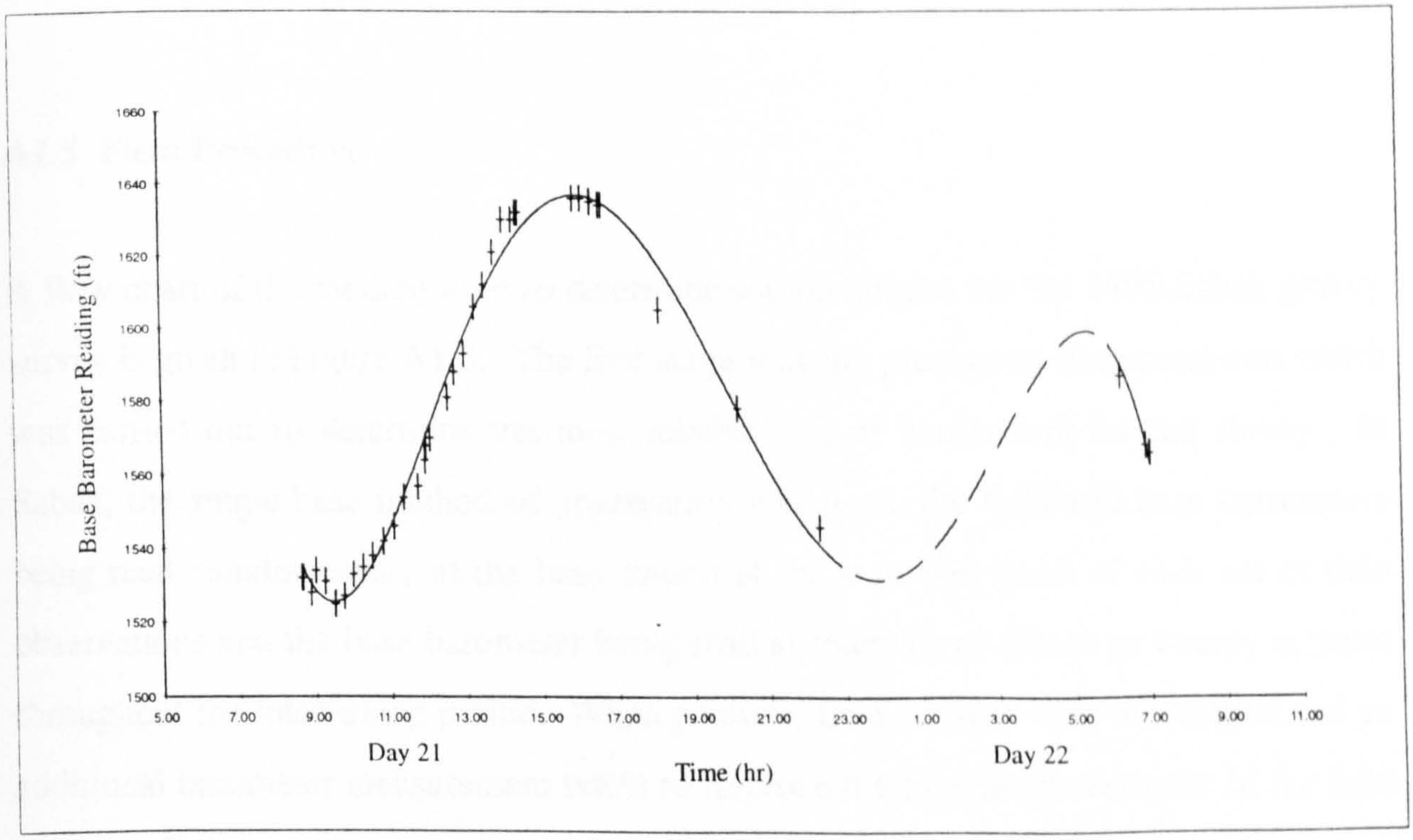

Figure A1.4. Barometric Pressure Variation, 21st - 22nd July 1995, Sabah. The atmospheric pressure variation has been recored in units of feet - an altimetric increase of 100 ft corresponds to a pressure decrease of ~ 3.6 millibars.

Local pressure changes arise because the air is in motion. There will often be a succession of gusts and lulls, sometimes with rapid and irregular alterations in direction. Even when wind is steady, natural or artificial obstructions may produce local pockets of air with high or low pressure. A sheltered barometer will tend to record a lower pressure, and pressure may therefore be anomalously low in a car or inside a building. In the evenings, cooler, denser air may collect in the bottom of a narrow valley, causing a high pressure pocket, but no readings were taken under these conditions during the 1995 survey.

A1.5 Field Procedure

A flow chart of the method used to determine station heights for the 1995 Sabah gravity survey is given in Figure A1.5. The first stage was the pre-survey barometer test which was carried out to determine the most reliable pair of barometers for the survey. In Sabah, the single base method of observation was used, the field and base barometers being read simultaneously at the base station at the start and finish of each set of field observations and the base barometer being read at intervals of fifteen or twenty minutes throughout the intervening period. When possible, field stations were reoccupied and an additional barometer measurement taken to improve the final height estimate of the field station. This was the case for 56% of the station height estimates made during the survey.

According to Milsom (1970), this method is normally satisfactory provided that field observations are not made at more than 30 kilometres from the base station, that there is not a significant pressure gradient between the field station and base, that a number of points of known height are occupied, and that not more than two hours elapse between repeat readings at base with the field barometer. Because of the difficulties associated with Sabah operations all these rules were broken, the most serious obstacle being the lack of usable known heights within the survey area. Only one such point could be occupied, a trig point just outside Lahad Datu. The inland heights are thus built up on height differences from 'sea-level' stations.

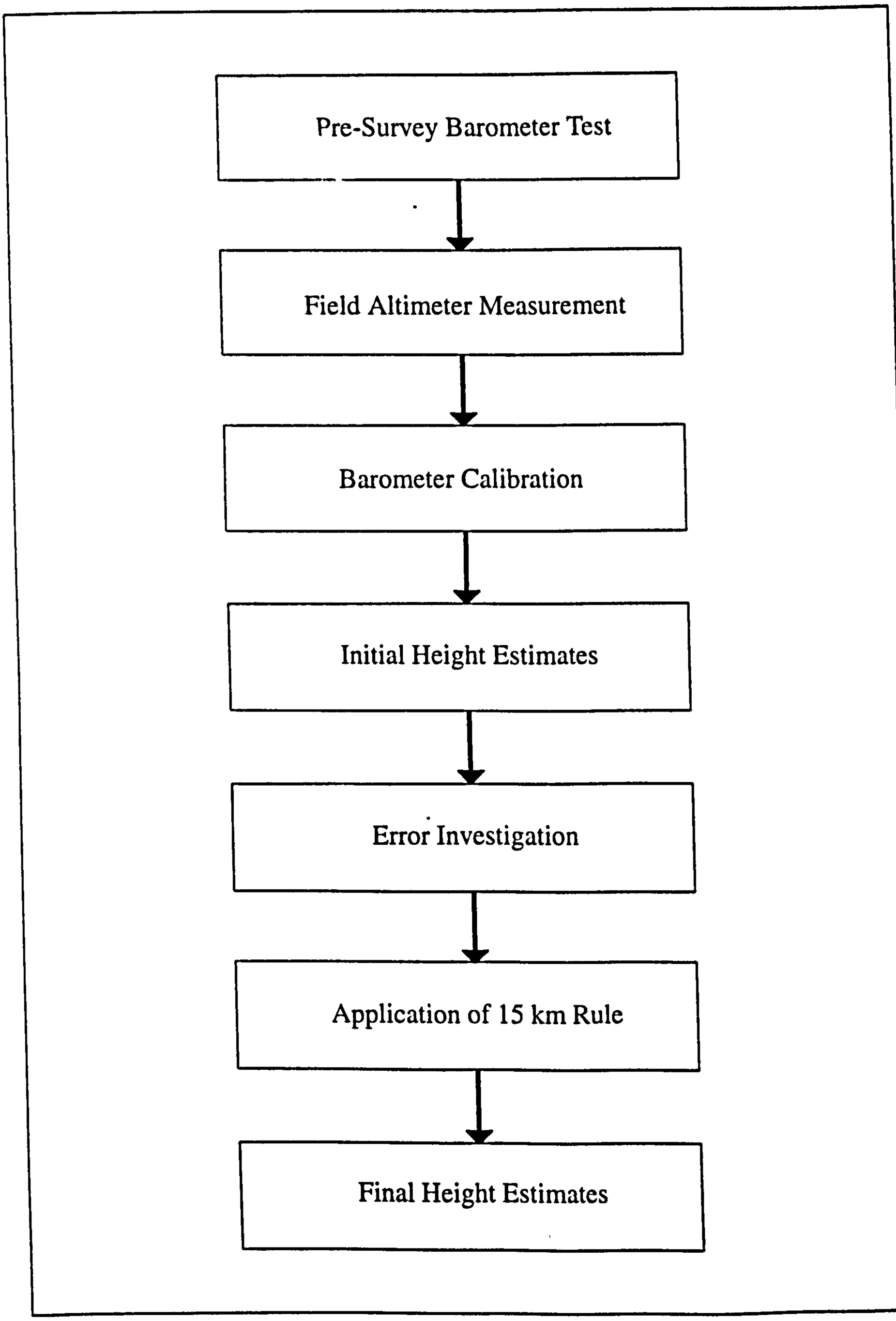

Figure A1.5. Barometric Levelling Flow Chart.

After returning to London, pressure variations were converted to height estimates using a number of processing stages. The two barometers were first calibrated, in so far as this was possible, on the basis of data extracted from the field readings. Then initial height estimates were obtained for all of the field stations. The height errors were assessed by comparing all the available repeated station height estimates. The final height estimates were obtained after an improvement in the method used to correct for the effect of the background barometric variation in the reduction of field barometric readings, here termed the '15 km rule'.

A1.6 Barometer Calibration

Barometer calibration was a two stage process, the first stage accounting for factors such as mechanical and material imperfections in the barometers, and the second stage accounting for the temperature and humidity conditions encountered in the field.

The first calibration stage was to determine the degree of linearity between the responses of the two barometers' readings to height changes. This was necessary because there was not a 1:1 relationship between these height responses, and because the false 'zero' of each barometer was different. To establish the relationship between the responses of the two barometers, all simultaneous barometer readings throughout the survey were plotted, with the results shown in Figure A1.6. A linear relationship was found to exist between the responses of Barometer 1 and Barometer 8 to elevation changes, of the form:

$$\text{(Barometer 8 reading)} = m \cdot \text{(Barometer 1 reading)} + c \qquad \text{(A1.2)}$$

where $m = 0.9630 \pm 0.0017$, and $c = 468.35 \pm 1.60$. The fact that m does not equal 1.00 indicates that at least one of the barometers' altitude calibrations is inaccurate. It is worth noting that the linear relationship between the responses of Barometer 1 and Barometer 8 has only been demonstrated over a range of 800 ft, and therefore some caution should be used when extrapolating the relationship outside this range. However,

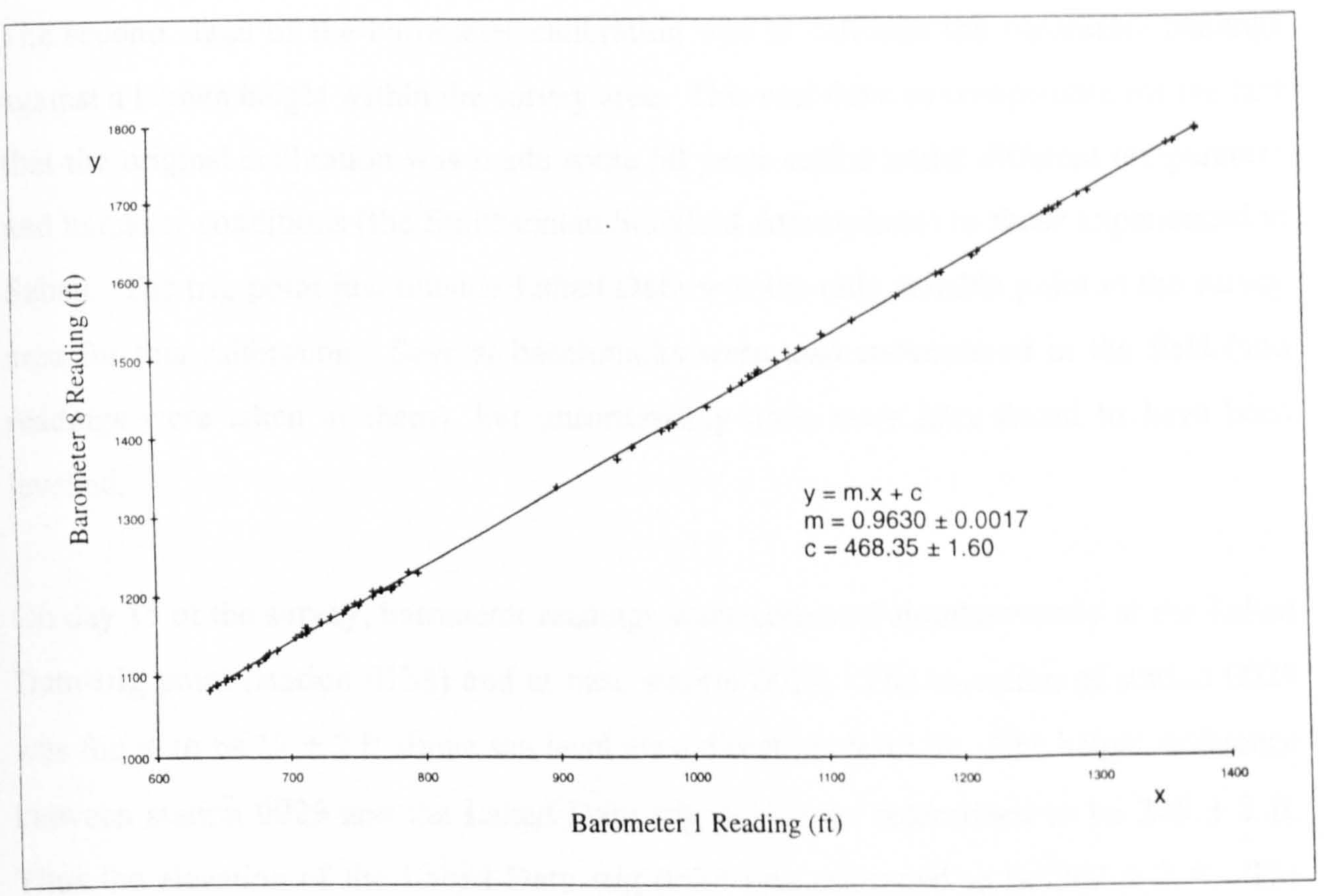

Figure A1.6. Graph showing the linear relationship between the readings of Barometers 1 and 8.

with no additional data available, it was assumed that this linear relationship held over the full 5700 ft range encountered during the survey.

Having developed this relationship between the height responses of the two barometers, all barometer height readings obtained with Barometer 1 were converted into their equivalent reading on Barometer 8 using Equation (A1.2).

The second stage of the barometer calibration was to calibrate the barometer readings against a known height within the survey area. This was done to compensate for the fact that the original calibration was made some 50 years earlier under different temperature and humidity conditions (the Smithsonian Standard Atmosphere) to those experienced in Sabah. The trig point just outside Lahad Datu was the only suitable point in the survey area for this calibration. Several benchmarks were also encountered in the field (and readings were taken at them), but unfortunately none were later found to have been levelled.

On day 15 of the survey, barometer readings were collected simultaneously at the Lahad Datu trig point (station 0133) and at base station 0029. The elevation of station 0029 was found to be 18 ± 2 ft above sea level via a direct sea level tie. The height difference between station 0029 and the Lahad Datu trig point was determined to be 245 ± 2 ft. Thus the elevation of the Lahad Datu trig point was estimated to be 263 ± 3 ft. The 1:50,000 scale map of Sabah gives an elevation of 291 ft for the Lahad Datu trig point. A correction factor of 1.106 was applied to height estimates made using Barometer 8 to account for this discrepancy.

A1.7 Height Estimation

Since the barometers gave readings directly in feet, the first stage in the data processing was to plot the diurnal curves measured at the base stations and the values obtained at the field stations, and to determine the height differences in feet by direct subtraction of the base diurnal curve. A smoothed background curve was obtained by fitting a third-

order polynomial to the base barometer variation (using the Microsoft Excel least-squares program), which, as demonstrated in Figure A1.7, gives a good fit to the data.

Two initial height estimates for each station were obtained by (1) subtracting the field barometer readings from the observed base barometer variation, and (2) subtracting the field barometer readings from the smoothed version of the base barometer variation. It is assumed that the high frequency deviations from the smoothed background variation result from localised pressure variations. Thus field station heights obtained from a smoothed background variation should not be affected by the effect of localised pressure changes only experienced in the vicinity of the base barometer.

By subtracting the base barometer variation from the field barometer reading, a height estimate was made for each station. Over the course of the survey, sixteen stations were reoccupied on different days. These stations were used to determine whether more repeatable height estimates were obtained using the observed base barometer variation or using the smoothed base barometer variation. A comparison of the results suggests that the observed base barometer variation gives more repeatable results when the distance between the base and field stations is small than when this distance is large, as shown in Figure A1.8. This result led to the development of the '15 km rule' which states that "the optimum height estimates for field stations within 15 km of the base station are obtained using the observed base station variation, whilst outside a 15 km radius of the base station the smoothed base barometer variation gives more repeatable height estimates". This result, based on sixteen data points, tentatively suggests that the range of the correlatable local pressure variations is of the order of 15 km.

Final height differences were calculated following the '15 km rule'. Final height estimates were obtained by correcting these height differences to sea level, and then scaling by a factor of 1.106 as determined from the Lahad Datu trig point calibration.

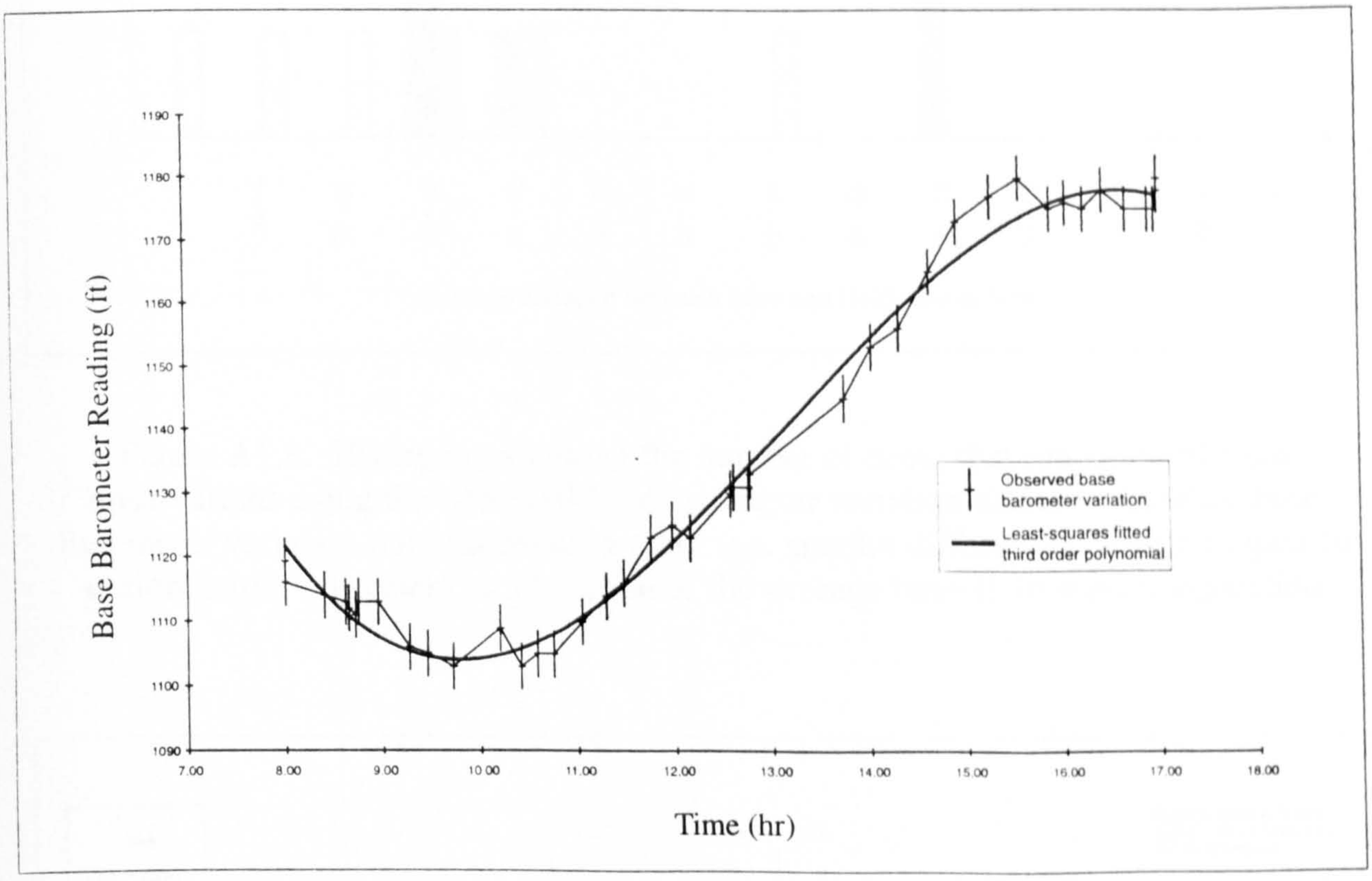

Figure A1.7. Graph showing the good match between the observed base barometer variation and a third-order polynomial on day 7 of the survey.

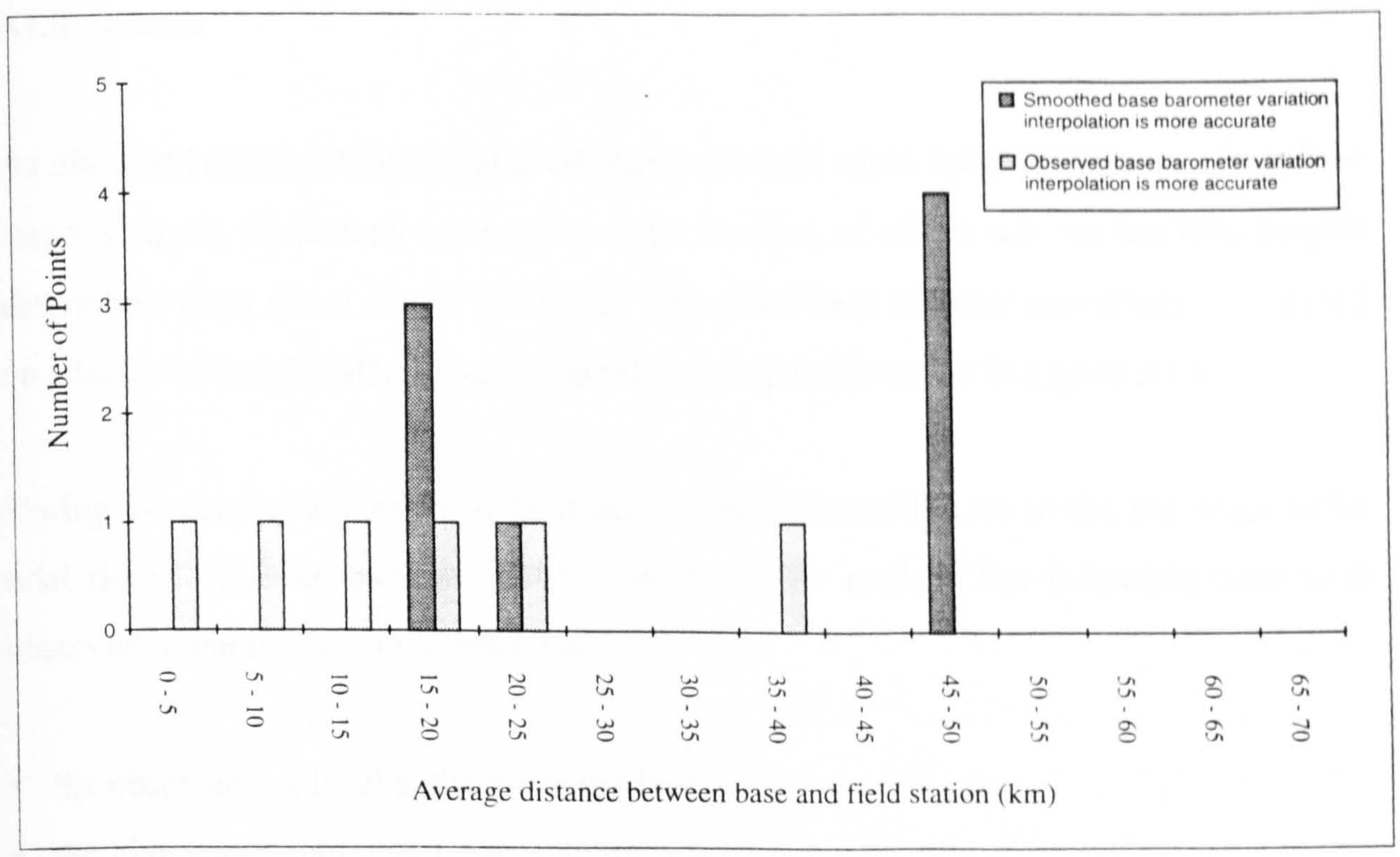

Figure A1.8. Histogram showing the number of times that reduction of field observations using the observed base barometer variation and the smoothed base barometer variation outperform each other (i.e. smaller differences between repeated station height estimates) as a function of the average base-field station separation.

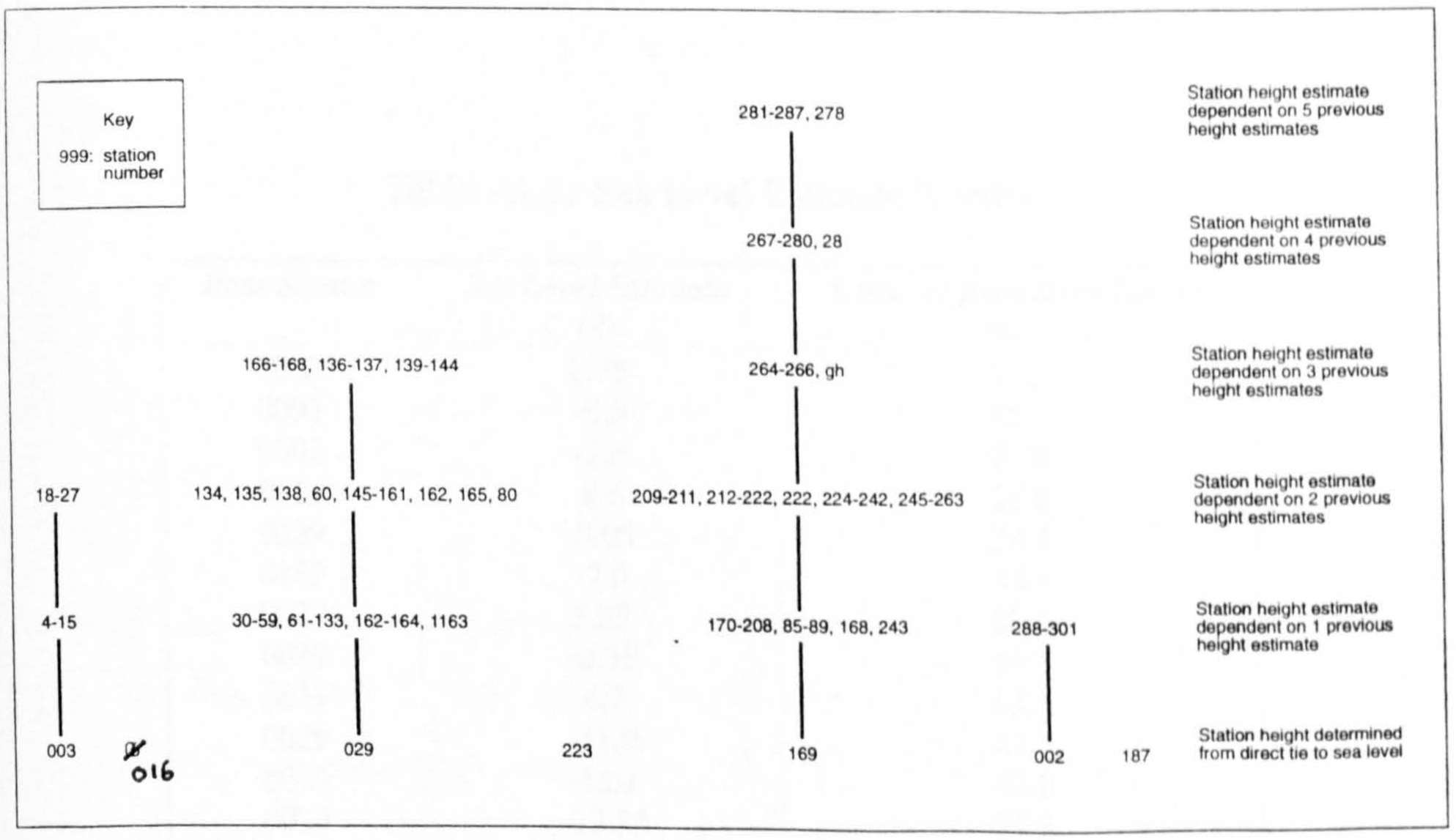

Figure A1.9. Diagram showing hierachical nature of station height determination.

A1.8 Results

As discussed earlier, station height estimates are built up as height differences from base stations. In all, 25 stations were used as base stations, of which only six had their heights determined from direct ties to sea level. The other base stations' elevations relied on addition of height differences. This relationship is illustrated in Figure A1.9.

During the survey, a number of field stations were located close to the sea shore or by tidal rivers. This enabled sea level estimates to be made. The following rules were observed in the estimation of sea level:

- the observed sea level is the mean sea level
- the high water mark lies 1 metre above mean sea level

Although these rules are coarse approximations, analysis of sea level estimates can give an indication of the accuracy of the height estimation results of the single base barometric levelling technique. The results of the sea level estimation are shown in Table A1.1. Ideally, this will average 0.0 ft.

Table A1.1. Sea Level Estimate Results

Base Station	*Sea Level Estimate (ft)*	*Distance from Base Station (km)*
0003	2.75	8.5
0003	-0.3	16.6
0003	-2.8	23.9
0014	-6.6	26.8
0029	-3.05	28.9
0169	-7.0	46.0
0029	1.25	59.4
0029	-0.35	59.7
0029	4.7	61.1
0029	-11.0	62.6
0029	-12.1	67.8
0029	-13.25	72.8
0029	-10.5	73.7
0029	-3.05	84.3

The average sea level estimate was -4.9 ± 5.4 ft. This was obtained at an average distance of 49 ± 23 km from the base station. This is a highly satisfactory result given the average estimation distance, and the crude nature of the initial approximations.

A1.9 Error Analysis and Assumptions

A1.9.1 Introduction

The two main error groups are (1) measurement and calibration errors, and (2) errors due to pressure variations. Measurement errors arise from the material and mechanical defects within the barometers which result in meter inaccuracies, and from barometer reading errors. Calibration errors are caused by temperature and humidity variations in the field. Errors also arise from the underlying assumption that the atmospheric variation is exactly the same in the field as it is at the base station, because this ignores:

- the effects of local pressure variations
- the pressure gradient created by the sea breeze effect, which causes the barometric pressure variation measured inland to have a different phase and amplitude to the barometric pressure variations measured at coastal sites
- the decrease in amplitude of the sea breeze effect with altitude

It is assumed that the background barometric variation was recorded faithfully by the base barometer at all times, even though on occasions the base barometer was housed inside a sheltered hotel room.

The validity of the extrapolation of the pressure variation measured at the base station out to the field station is expected to decrease as this distance increases. Thus the accuracy of height estimate obtained as a consequence of this extrapolation is also expected to decrease as the estimation distance increases.

A final error source is caused by the fact that the height estimates for many of the stations depend on height estimates obtained for other survey stations, as shown in Figure A1.9. Each station's height has an inherent inaccuracy. Thus as a station's height estimate becomes dependent on an increasing number of other height estimates, the estimate becomes less and less accurate.

A1.9.2 Measurement and Calibration Errors

The errors associated with the measurement of the atmospheric pressure have two causes, namely the barometer reading error (parallax error), and the error associated with the inaccuracy of the meter. The parallax error is judged to have a magnitude of ± 1.6 ft. This figure is the intercept error on the barometer calibration graph (Figure A1.6), and also matches exactly the error determined in the pre-survey barometer test. The meter accuracy can be assessed by examining the variation about the linear fit between responses of the two barometers to height changes. The standard deviation of this variation is 3.298. Therefore, the meter accuracy is assessed as being ± 3.3 ft. The total measurement error, a combination of the parallax error and the meter accuracy error, is estimated to be ± 3.7 ft.

The calibration error is the error associated with the calibration factor 1.106. This error is estimated to be ± 0.013 (i.e. ± 1.2 %), due to the ± 3 ft uncertainty in the measured height of the Lahad Datu trig point (263 ± 3 ft). It is assumed that no additional calibration errors arise outside the range over which the calibration has been proved.

Temperature and humidity changes in the field will alter the barometer calibration. A humidity change of ± 10 % will change height estimates by ± 0.1 % (Crone, 1948). Humidity variations of the order of ± 10 % were probably encountered during the survey. This will result in a ± 0.1 % height uncertainty. The effect of temperature changes is less well understood, and associated errors are assumed to be insignificant. It is assumed that the Lahad Datu trig point calibration took place under average temperature and humidity conditions.

A1.9.3 Amplitude and Phase Effects

Amplitude variations between the base and field pressure recordings arise from elevation differences between the base and field stations. During the Lahad Datu trig point calibration (day 15), barometric pressure variations were measured at two locations (Stations 0133 and 0029) at 15 minute intervals throughout the whole day. The observed pressure variations are plotted in Figure A1.10. Figure A1.11 shows the smoothed pressure variation at each station, after correction for the height difference between the two stations. Although the height difference between the two stations is 245 ft, the smoothed barometric variations are remarkably similar. It is clear from Figure A1.11 that the amplitude of the variation of the elevated station (0133) is slightly less than that of the lower station, by about 4.5 ft (~ 5 %). This supports the idea that the amplitude of the diurnal pressure variation falls with increasing elevation. However, this one result was not thought to be accurate enough to establish a correction factor for the amplitude effect. Errors arising from the failure to correct for the amplitude effect are expected to increase as the height difference between the base station and field station increases. This effect is only expected to be significant during the survey on day 27 over the Crocker Ranges, as on most other occasions the height difference between the base barometer and the field barometer was small.

Barometric levelling errors can be introduced when either the base station or the field station (but not both) is close to the sea, because of the pressure gradient that exists between land and sea. This would result in a phase difference between the base and field pressure recordings. The results of Lahad Datu trig point calibration of day 15 (Figures A1.10 and A1.11) could not provide evidence of a phase change caused by the difference between the distance of the two stations from the sea, as both stations were sited less than one kilometre from the sea. No other suitable measurements were available to analyse the effect of the pressure gradient, which is assumed to be negligible.

It is recommended that if amplitude and phase effects are thought likely to produce significant errors during a future survey, then some time should be spent in the field with

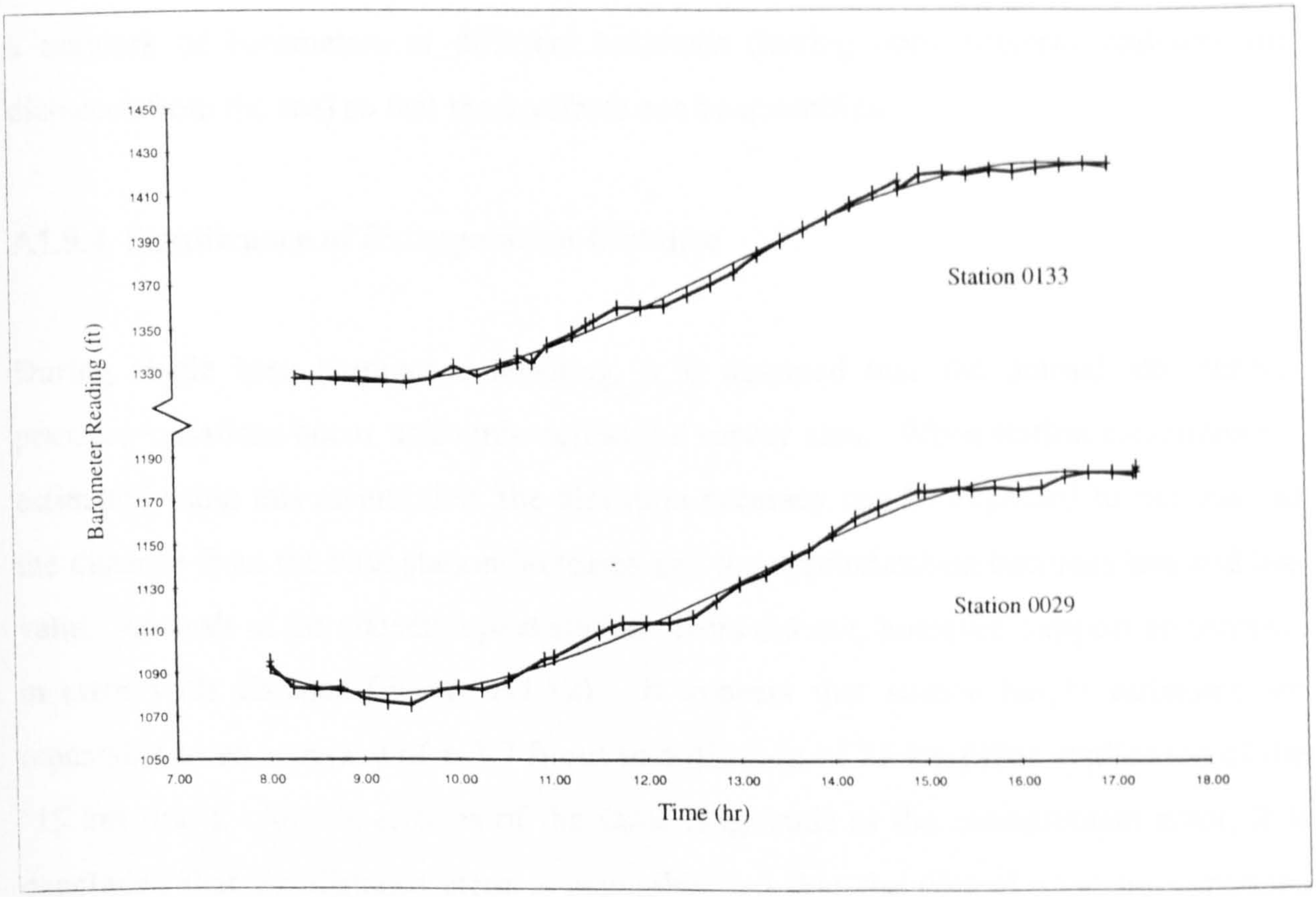

Figure A1.10. Graph showing the barometric variation at Stations 0133 and 0029 on day 15 of the survey.

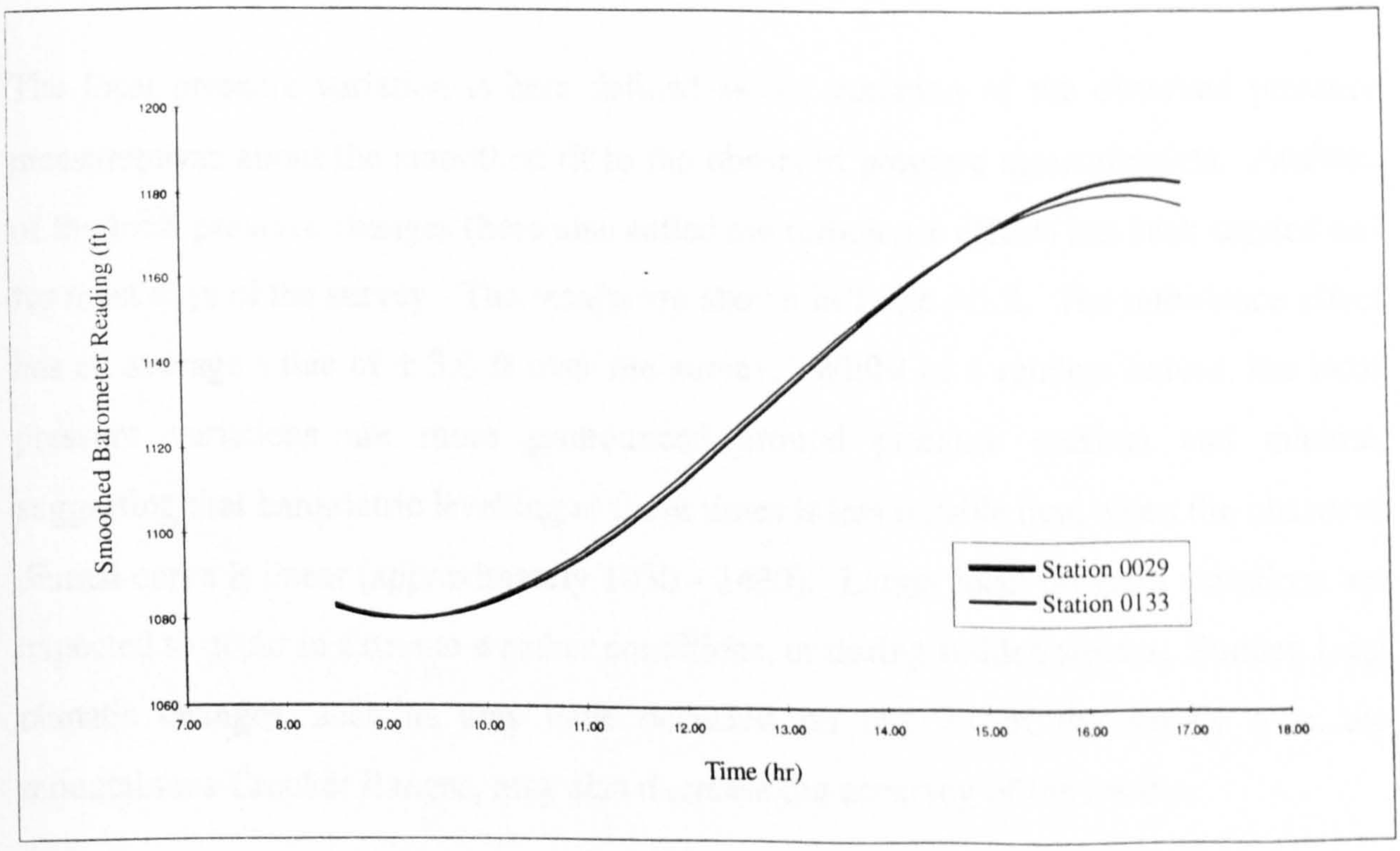

Figure A1.11. Graph showing the smoothed barometer readings at Stations 0029 and 0133, after a correction has been applied to account for the height difference between the two stations.

a network of barometers at different locations (having both different altitudes and distances from the sea) so that these effects can be quantified.

A1.9.4 Significance of Extrapolation Distance

During single base barometric levelling, it is assumed that the diurnal atmospheric pressure variations occur uniformly across the survey area. When station elevations are estimated using this assumption, the elevation accuracy can be expected to decrease as the distance from the base station increases and the approximation becomes less and less valid. Analysis of the sixteen repeat station errors did not, however, support an increase in error with distance (Figure A1.12). It appears that station height estimates are repeatable to an accuracy of ± 3.7 ft out to a distance of 75 km (after application of the '15 km rule'). As this error is of the same magnitude as the measurement error, it is concluded that the distance error is negligible and that the diurnal pressure variations were uniform over distances of at least 75 km.

A1.9.5 Effect of Local Pressure Changes

The local pressure variation is here defined as the variation of the observed pressure measurements about the smoothed fit to the observed pressure measurements. Analysis of the local pressure changes (here also called the turbulence effect) has been carried out for most days of the survey. The results are shown in Table A1.2. The turbulence effect has an average value of ± 3.0 ft over the survey. Whilst of a random nature, the local pressure variations are more pronounced around pressure maxima and minima, suggesting that barometric levelling at these times is less reliable than when the observed diurnal curve is linear (approximately 1030 - 1430). Larger local pressure variations are expected to occur in extreme weather conditions, or during sudden storms. Sudden local climatic changes, such as may have occurred on day 27 of the survey over the mountainous Crocker Ranges, may also decrease the accuracy of the results.

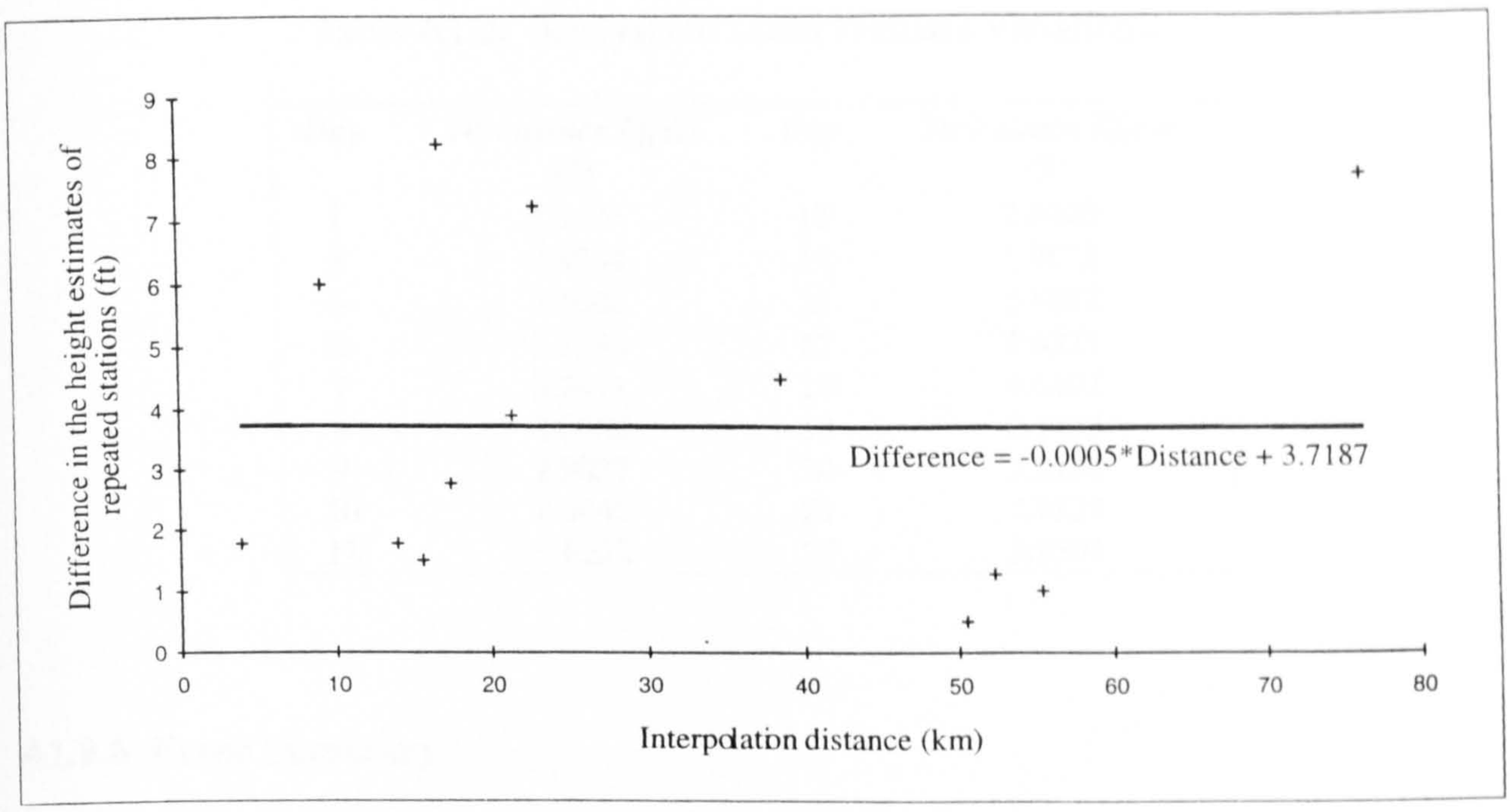

Figure A1.12. Graph of repeated station error vs. interpolation distance. The graph shows that the interpolation error is approximately independent of interpolation distance and of the order of the observed measurement error in the range 0 - 75 km.

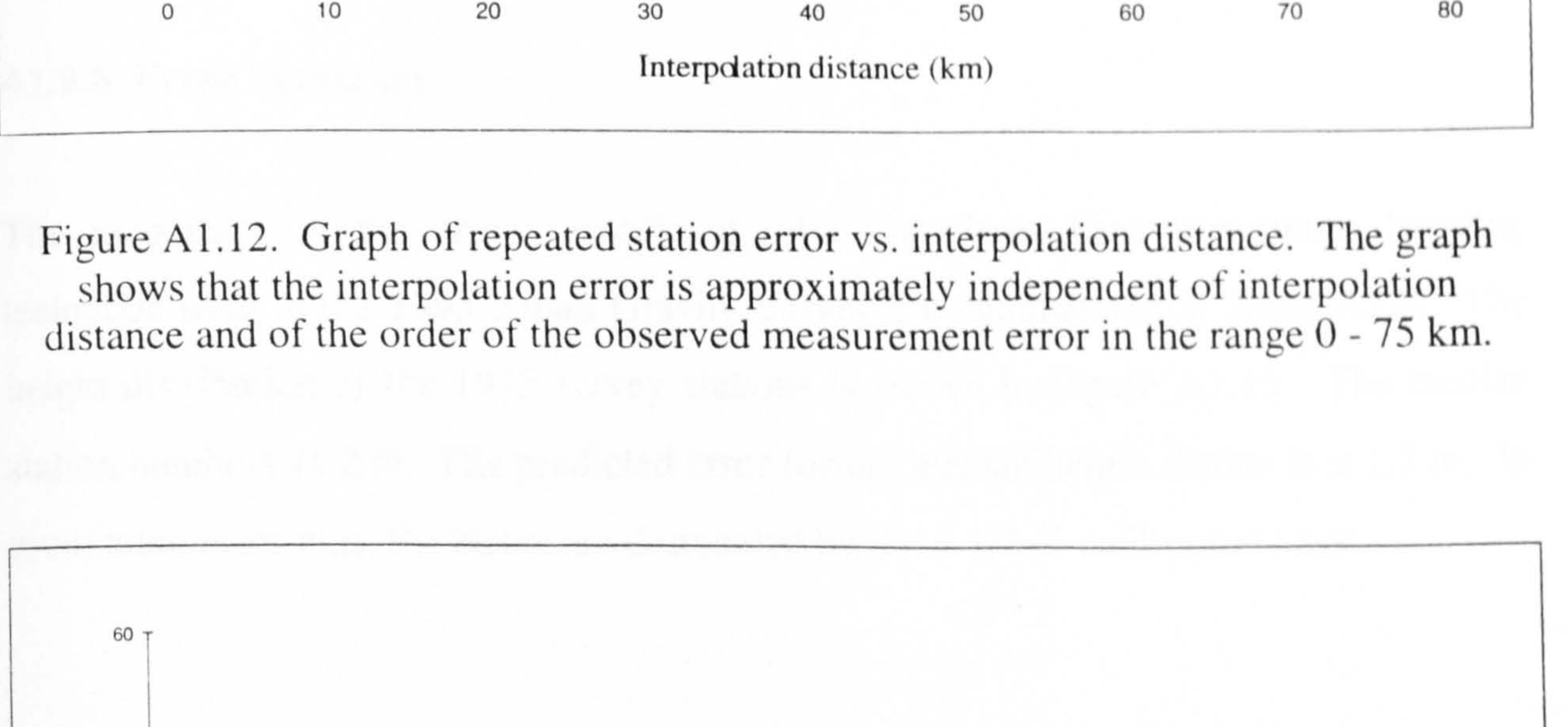

Figure A1.13. Histogram of 1995 Sabah gravity survey station heights.

Table A1.2. Analysis of Local Pressure Variations.

Day	*Turbulence Effect (ft)*	*Day*	*Turbulence Effect (ft)*
1	2.6476	13	2.8020
3	2.3264	14	1.9622
5	4.1604	15	3.5632
6	3.1184	17	2.6325
7	2.7491	18	4.6402
8	2.6082	19	2.7433
9	2.9037	20	3.2152
10	2.6442	21	2.9525
11	4.6252	27	2.9593

A1.9.6 Error Summary

The magnitude of the errors associated with the single base barometric levelling technique used in the 1995 Sabah Gravity Survey are summarised in Table A1.3. The height distribution of the 1995 survey stations is shown in Figure A1.13. The median station height is 74.2 m. The predicted error for the median height station is ± 1.7 m. In mountainous terrains, the errors are dominated by the ± 1.2 % calibration error.

Table A1.3. Significant Error Magnitudes.

Error	*Magnitude*
Measurement	± 3.7 ft
Calibration	± 1.2 %
Humidity	± 0.1 %
Turbulence	± 3.0 ft
Storm Effect	± 25 ft
Amplitude Effect	negligible*

*For all but the highest stations, where this error is uncertain

The hierarchical nature of station height determination (Figure A1.9) means that many of the station height estimates are dependent on one or more other station height estimates. As the length of this dependency chain increases, so the error associated with the height estimate increases (Table A1.4). The magnitude of this error is determined from an

estimated ± 0.6 m sea level tie error, and a ± 1.7 m barometric levelling error per single barometric height estimate (assuming normal weather conditions).

Table A1.4. Station Height Estimate Error*

Predicted Station Height Error (m)	Position in Hierarchy	Number of Stations Affected
±0.6	Station height determined from direct tie to sea level	7
±1.7	Station height estimate dependent on 1 previous height estimate	179
± 2.5	Station height estimate dependent on 2 previous height estimates	87
± 3.0	Station height estimate dependent on 3 previous height estimates	14
± 3.5	Station height estimate dependent on 4 previous height estimates	15
± 3.8	Station height estimate dependent on 5 previous height estimates	8

*See Figure A1.9 to determine individual station height errors

Confidence in the magnitude of the predicted errors is given by the sea level estimates (standard deviation ± 5.4 ft), and the sixteen repeated stations (standard deviation ± 3.7 ft).

A final error estimate of ± 2.5 m is judged to be reasonable for stations of the 1995 Sabah gravity survey, excluding the stations over the Crocker Ranges (Stations 0292 - 0301) where the error is given by ± 1.2 % of station elevation. This result can be compared favourably to those found by previous workers. St. John (1967) regarded ± 10 m as a reasonable level of accuracy, with a maximum error of ± 25 m. Milsom (1970) claimed a maximum error of ± 20 m, and a standard deviation between the true and measured values of ± 5 m. Both these earlier surveys however used helicopters to cover the much greater distances between stations.

A1.10 Conclusions

1995 Sabah gravity survey station heights were established using the single base barometric levelling technique, giving an estimated accuracy of about ± 2.5 metres for the low-lying stations, and ± 1.2 % of station elevation for stations in the Crocker Ranges. A station elevation accuracy of ± 5 m equates to an accuracy of ± 1 mGal in the Bouguer anomaly values. Unfortunately, none of the benchmarks found during the survey had been levelled, so the height errors could not be more accurately determined, and the heights better constrained (especially over the Crocker Ranges).

Barometric pressure variations observed in the coastal regions of Sabah followed similar patterns on successive days. The diurnal pressure variation has been shown to be roughly constant out to a distance of ~ 75 km from the base station under the conditions prevailing in Sabah in July - August 1995. Local turbulence effects could be expected to extend over areas less than about 30 km across, and beyond 15 km from a base station the best results are obtained by using a smoothed base pressure variation curve.

It is the author's opinion that the optimum time for data collection using the 'single base' barometric levelling technique is from about 1030 to 1430 when the atmospheric pressure variation is approximately linear and local pressure variations are not too significant.

A1.11 References

Crone, D.R., 1948. Heights by Aneroid Barometer. *Empire Survey Review*, v.69, p.311-316.

Crone, D.R., 1960. Note on Terrestrial Altimetry. *Empire Survey Review*, v.122, p.160-168.

Harrison, D., 1991. *The Gravity Field of the Papuan Fold Belt and its Geological Implications*. Ph.D. Thesis, University of London (unpub.).

Haurwitz, B., 1955. The thermal influence on the daily pressure wave. *Bull. Am. Met. Soc.*, v.36, p.311-317.

Milsom, J., 1970. *The Structure of Eastern Papua: an approach via Gravity and other Geophysical Methods*. Ph.D. Thesis, University of London (unpub.), 183 pp.

Milsom, J., 1988. Report on barometric levelling for gravity surveys in the Sumatra Forearc 1986-87. *Internal University College London Gravity Research Group Report 1988/7*, University of London (unpub.), 19 pp.

St. John, V.P., 1967. *The Gravity Field of Papua New Guinea*. Ph.D. Thesis, University of Tasmania (unpub.).

APPENDIX 2

Gravity base station descriptions

GRAVITY STATION DESCRIPTION

Station number and name
9502.9002 Geological Survey of Malaysia, Sabah

Nearest City	State / Province / County	Country
Kota Kinabalu	Sabah	Malaysia

Latitude	Longitude	Source
5° 57.53' N	116° 4.43' E	Magellan GPS Fix

Elevation	Source
3.4m	Barometer tie to sea level

Observed gravity (IGSN 71)	Free-air gravity	Bouguer gravity ($\rho = 2.67$ Mg.m^{-3})
978112.19 mGal ±0.11	25.55 mGal	24.89 mGal

DESCRIPTION

The station is at the top of the steps leading in to Block A of the offices in south Kota Kinabalu occupied by the Geological Survey of Malaysia. It can be located either by measuring from the walls a distance of 50 cm in both directions or on the basis of the pattern of floor tiles. Access to the station may not be possible outside normal office hours without prior arrangement.

Described by John Milsom **Date** 2 August 1995

GENERAL

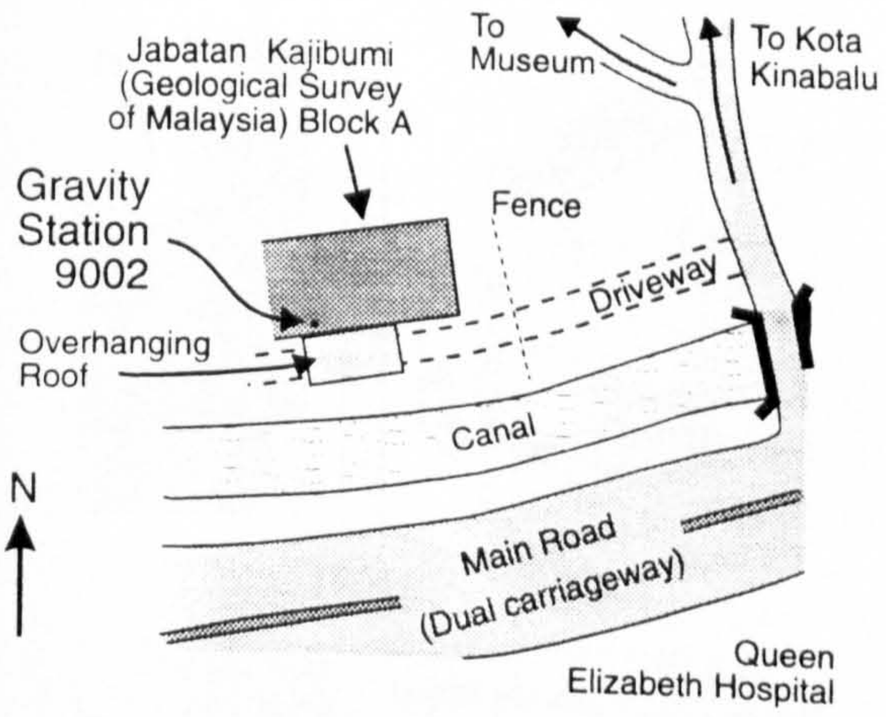

DETAIL

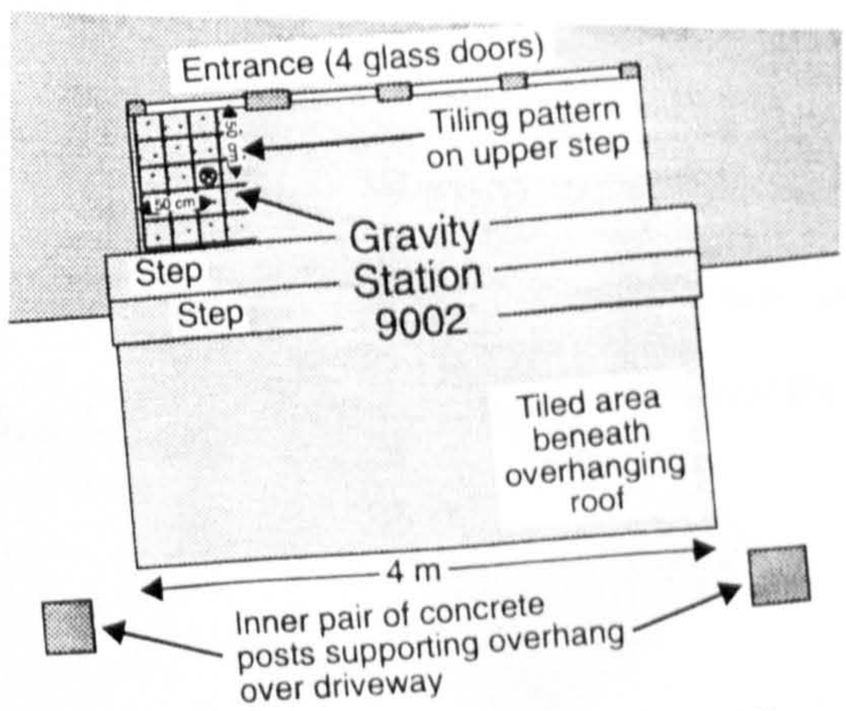

Diagram by John Milsom **Date** 8 May 1996

STATION HISTORY

The station was established in the course of the 1995 Geological Survey of Malaysia / University College London Sabah gravity survey. It is linked to the main Malaysian gravity base station in the Physics Department, University of Malaya in Kuala Lumpur by a single A-B-C-B-A tie through intermediate station 'B' at the Hotel Sungei Wang in KL. The reference value at the University base (G4/76) has been taken as 978034.45 mGal.

Source organisation(s) Geological Survey of Malaysia / University College London

GRAVITY STATION DESCRIPTION

Station number and name: 9502.9028 Telupid, Sabah

Nearest City	State / Province / County	Country
Ranau	Sabah	Malaysia

Latitude	Longitude	Source
5° 37.68' N	117° 07.86' E	Magellan GPS Fix

Elevation	Source
100.7m	Barometer tie to sea level

Observed gravity (IGSN 71)	Free-air gravity	Bouguer gravity ($\rho = 2.67$ Mg.m^{-3})
978151.66 mGal ±0.11	101.06 mGal	81.26 mGal

DESCRIPTION

In the shopping complex at the eastern end of Telupid Airstrip, between two mirror-image buildings housing shops, west of a large car park. The station is on the concrete floor, 0.5 m SE of the rear corner of the northernmost building, underneath the overhanging roof. A fire hydrant is located approximately 20 m south of this location, embedded in the concrete surround of the eastern of a pair of large decorative flower beds.

Described by Rob Holt **Date** 12 November 1996

DIAGRAM

GENERAL

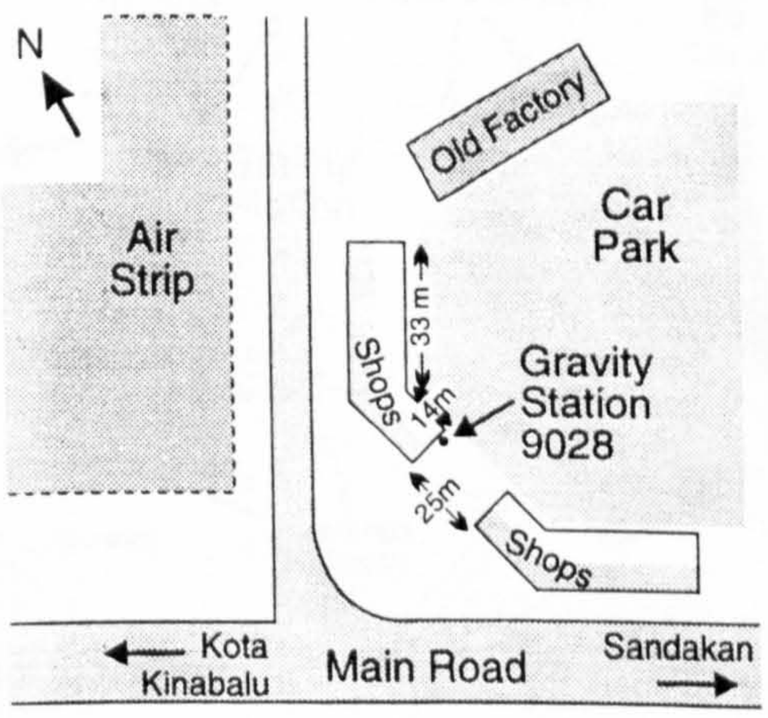

DETAIL

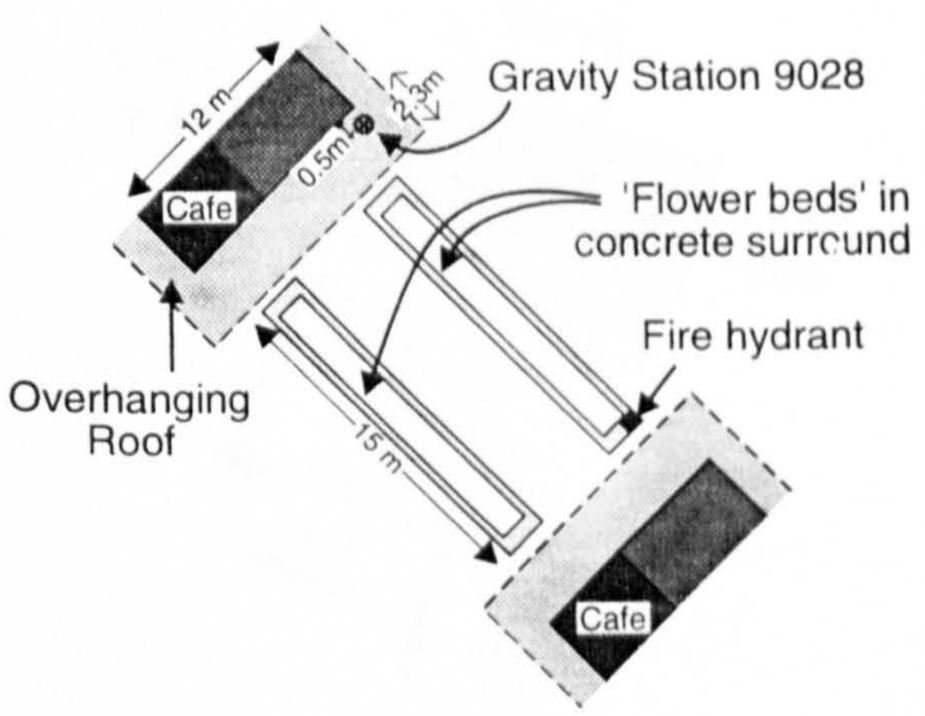

Diagram by Rob Holt **Date** 26 June 1996

STATION HISTORY

Established in the course of the 1995 Geological Survey of Malaysia / University College London Sabah gravity survey. Linked to the Geological Survey of Malaysia gravity base station in Kota Kinabalu (9502.9002), and to the Hotel Permaisaba gravity base station in Lahad Datu (9502.9029).

Source organisation(s) Geological Survey of Malaysia / University College London

GRAVITY STATION DESCRIPTION

Station number and name
9502.9029 Hotel Permaisaba, Sabah

Nearest City	State / Province / County	Country
Lahad Datu	Sabah	Malaysia

Latitude	Longitude	Source
5° 01.58' N	118° 20.01' E	Magellan GPS Fix

Elevation	Source
6.1m	Barometer tie to sea level

Observed gravity (IGSN 71)	Free-air gravity	Bouguer gravity ($\rho = 2.67$ Mg.m^{-3})
978156.53 mGal ±0.11	86.81 mGal	85.61 mGal

DESCRIPTION

The station lies on the broad covered walkway directly in front of the main entrance to the Hotel Permaisaba, Lahad Datu. The station is positioned in line with the northern edge of the reception doors, 50 cm out onto the walkway from the upper flight of steps leading to the reception area.

Described by	Rob Holt	Date	7 May 1997

DIAGRAM

GENERAL

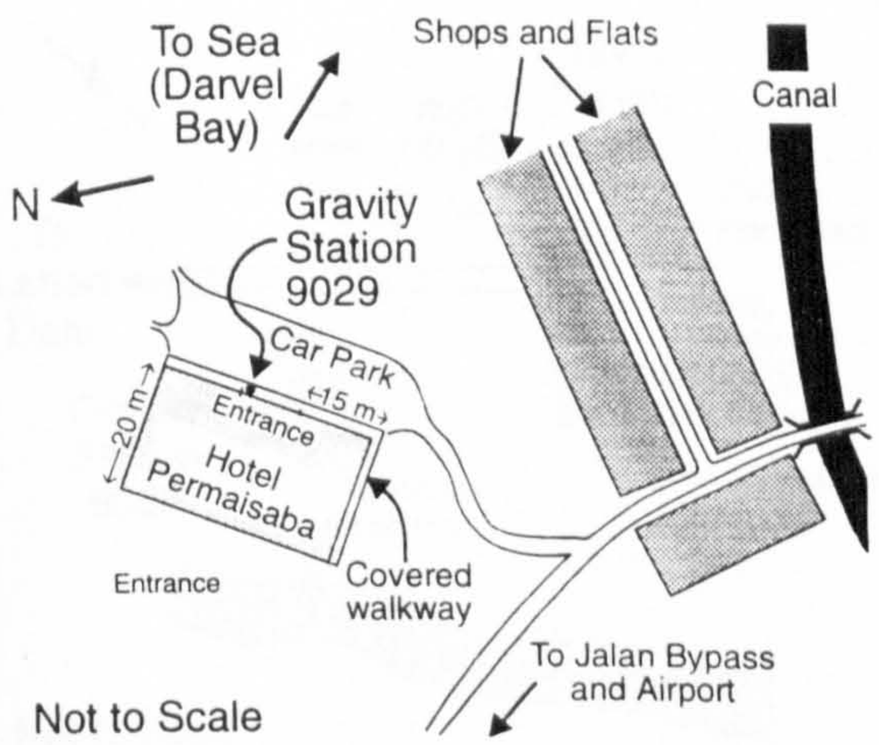

DETAIL

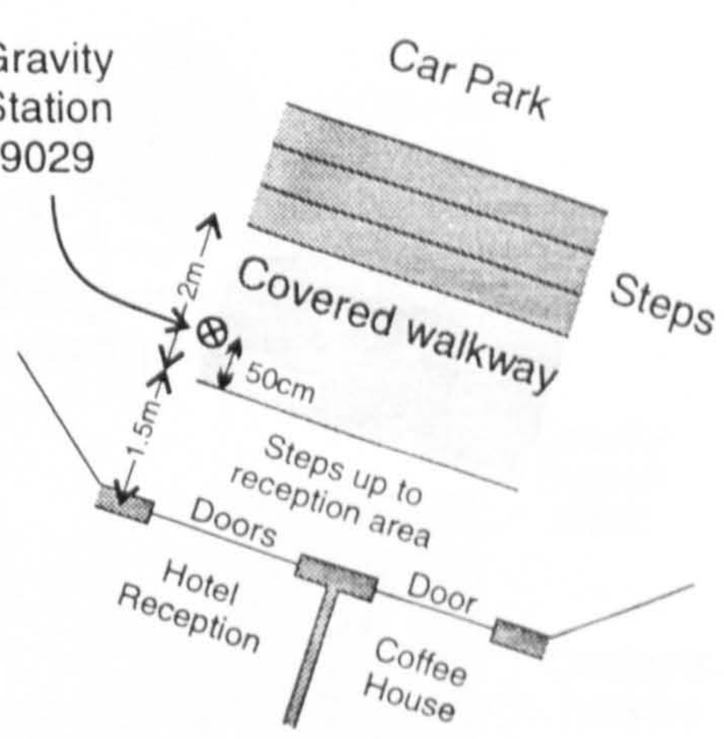

Diagram by	Rob Holt	Date	7 May 1997

STATION HISTORY

Established in the course of the 1995 Geological Survey of Malaysia / University College London Sabah gravity survey. It is tied by road and air links to the Geological Survey of Malaysia gravity base station in Kota Kinabalu (9502.9002).

Source organisation(s)	Geological Survey of Malaysia / University College London

GRAVITY STATION DESCRIPTION

Station number(s) and name(s)
9502.9059 & 9502.9060 Danum Valley, Sabah

Nearest City	State / Province / County	Country
Lahad Datu	Sabah	Malaysia

Latitude	Longitude	Source
4° 57.83' N (9059) 4° 57.83' N (9060)	117° 48.17' E (9059) 117° 48.16' E (9060)	Magellan GPS Fix

Elevation	Source
154.5 m (9059) 162.9 m (9060)	Barometer tie to sea level

Observed gravity (IGSN 71)	Free-air gravity	Bouguer gravity ($\rho = 2.67$ Mg.m^{-3})
978064.12 mGal (9059) ±0.12 978062.75 mGal (9060) ±0.14	41.16 mGal (9059) 42.40 mGal (9060)	10.78 mGal (9059) 10.35 mGal (9060)

DESCRIPTION

Gravity stations 9059 and 9060 are both located near the administrative centre of the Danum Valley Field Centre. Station 9059 is sited at the centre of the helipad. Station 9060 is located at the centre of the octagonal picnic hut.

Described by	Rob Holt	Date	8 May 1997

DIAGRAM

GENERAL

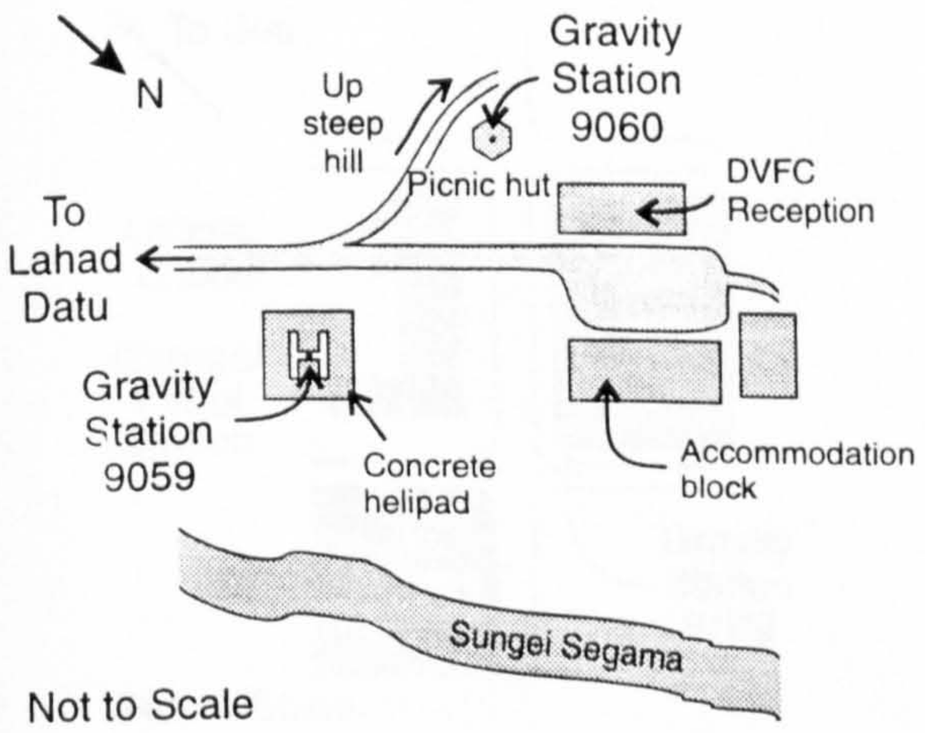

DETAIL

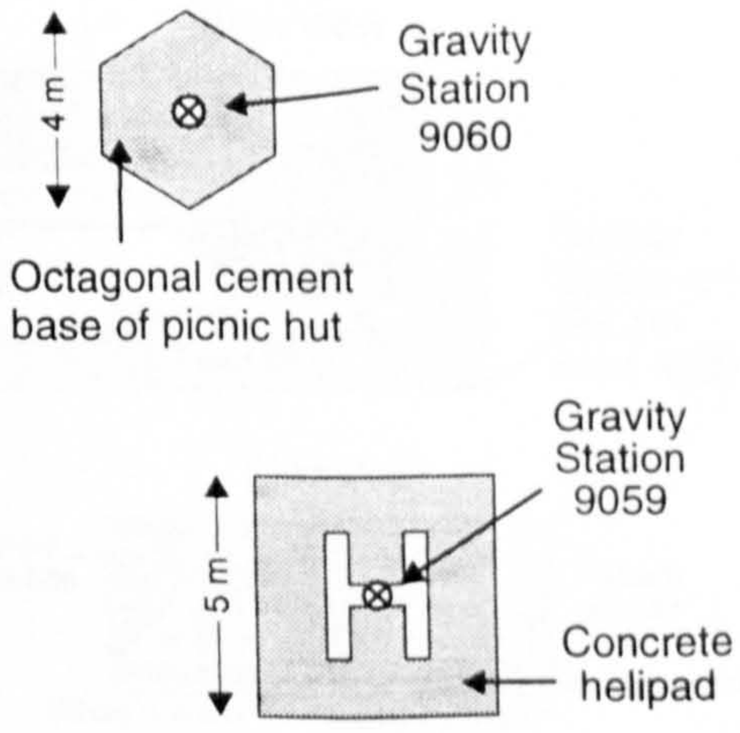

Diagram by	Rob Holt	Date	8 May 1997

STATION HISTORY

Both stations were established during the 1995 Geological Survey of Malaysia / University College London Sabah gravity survey. Stations linked to the Hotel Permaisaba gravity base station in Lahad Datu (9502.9029).

Source organisation(s)	Geological Survey of Malaysia / University College London

GRAVITY STATION DESCRIPTION

Station number and name
9502.9169 Hotel Emas, Sabah

Nearest City	State / Province / County	Country
Tawau	Sabah	Malaysia

Latitude	Longitude	Source
4° 14.80' N	117° 52.93' E	Magellan GPS Fix

Elevation	Source
1.9m	Barometer tie to sea level

Observed gravity (IGSN 71)	Free-air gravity	Bouguer gravity ($\rho = 2.67$ Mg.m^{-3})
978112.93 mGal ± 0.11	53.27 mGal	52.90 mGal

DESCRIPTION

The station lies to the right of the front entrance to Hotel Emas, Tawau, approximately 1 m from the corner of the building, 25 cm from the hotel wall. The station is positioned in relation to the pattern in the granite on the hotel wall.

Described by Rob Holt **Date** 11 November 1996

DIAGRAM

GENERAL

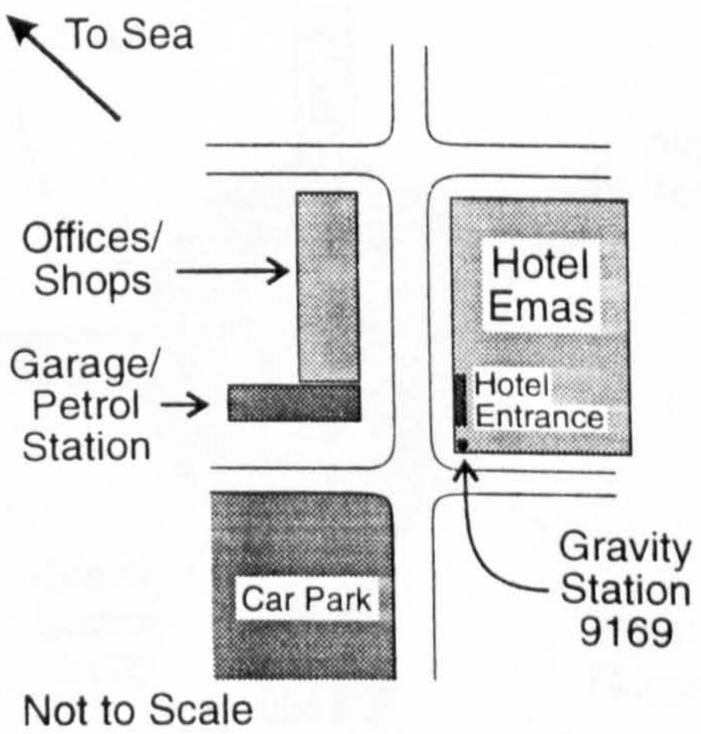

DETAIL

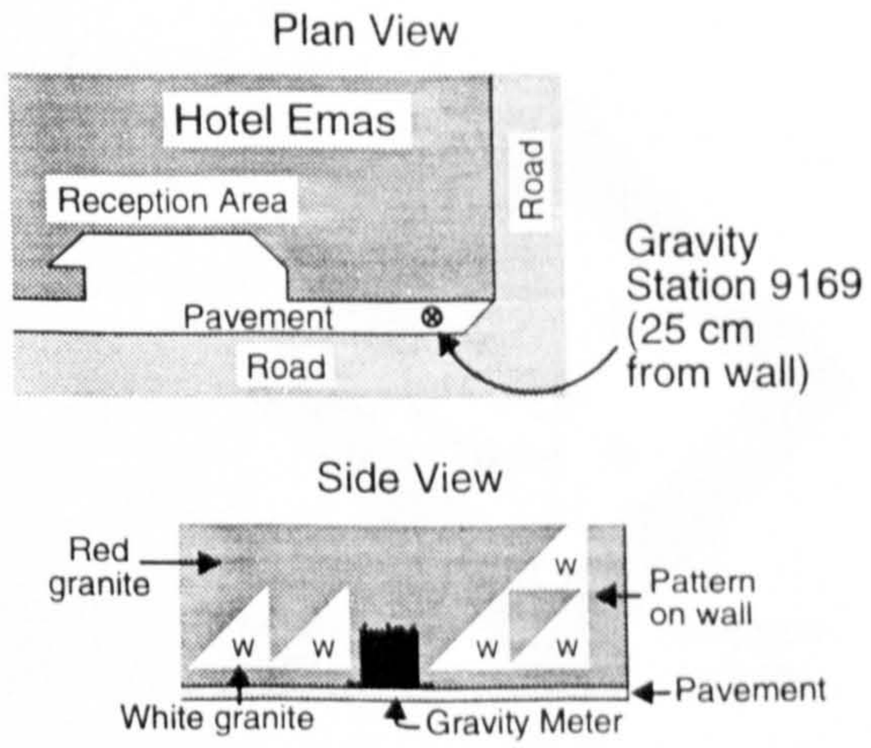

Diagram by Rob Holt **Date** 26 June 1996

STATION HISTORY

Established in the course of the 1995 Geological Survey of Malaysia / University College London Sabah gravity survey. Linked to the Hotel Parmaisaba gravity base station in Lahad Datu (9502.9029) and to the Luasong gravity base station (9502.9243).

Source organisation(s) Geological Survey of Malaysia / University College London

GRAVITY STATION DESCRIPTION

Station number and name
9502.9170 Tawau Airport, Sabah

Nearest City	State / Province / County	Country
Tawau	Sabah	Malaysia

Latitude	Longitude	Source
4° 15.72' N	117° 53.04' E	Magellan GPS Fix

Elevation	Source
14.3m	Barometer tie to sea level

Observed gravity (IGSN 71)	Free-air gravity	Bouguer gravity ($\rho = 2.67$ Mg.m^{-3})
978110.89 mGal ±0.11	54.87 mGal	52.05 mGal

DESCRIPTION

The station is sited outside Tawau Airport, Tawau, in the centre of a roundabout, beneath the "Selamat Datang ke Tawau" monument. The station lies in the centre of the plinth directly below the monument.

Described by	Rob Holt	Date	18 November 1996

DIAGRAM

GENERAL

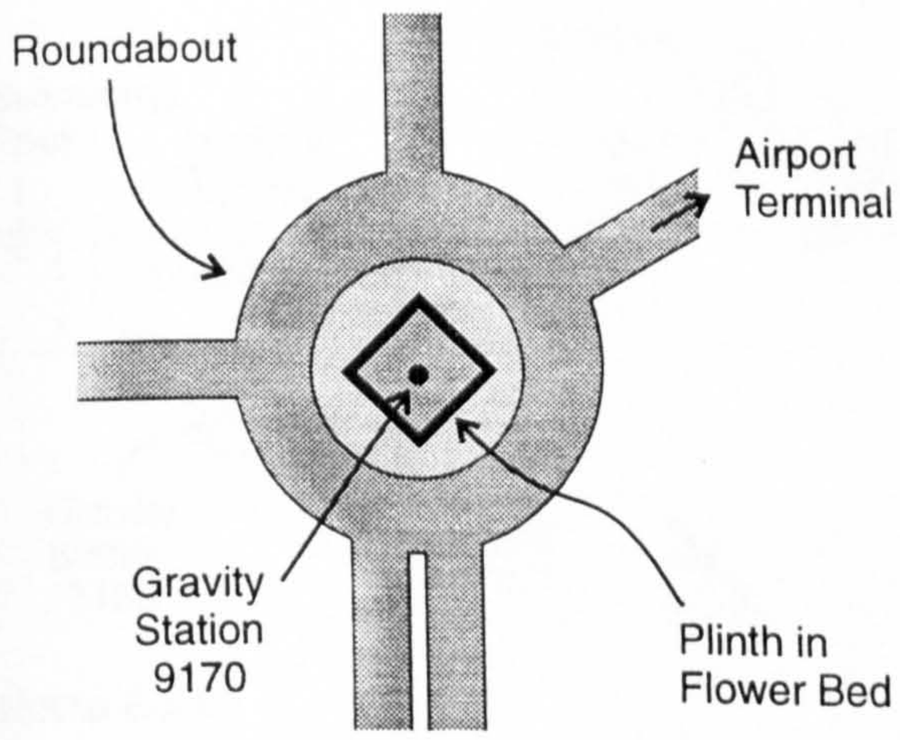

DETAIL

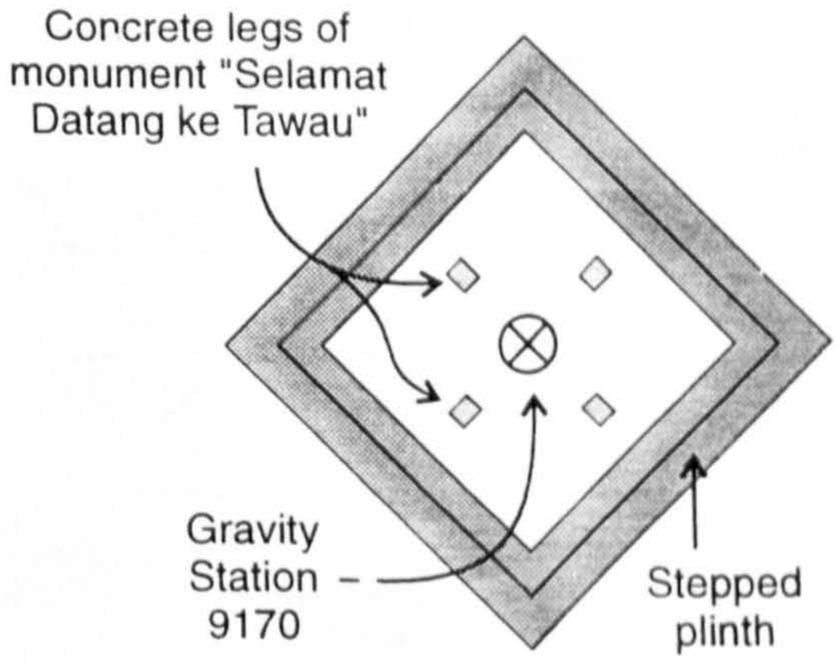

Diagram by	Rob Holt	Date	18 November 1996

STATION HISTORY

The station was established in the course of 1995 Geological Survey of Malaysia / University College London Sabah gravity survey. Linked to the Hotel Parmaisaba gravity base station in Lahad Datu (9502.9029) and to the Luasong gravity base station (9502.9243).

Source organisation(s)	Geological Survey of Malaysia / University College London

GRAVITY STATION DESCRIPTION

Station number(s) and name(s)
9502.9185 & 9502.9243 Luasong, Sabah

Nearest City	State / Province / County	Country
Tawau	Sabah	Malaysia

Latitude	Longitude	Source
4° 36.60' N (9185) 4° 36.60' N (9243)	117° 23.71' E (9185) 117° 23.68' E (9243)	Magellan GPS Fix

Elevation	Source
134.1 m (9185) 134.1 m (9243)	Barometer tie to sea level

Observed gravity (IGSN 71)	Free-air gravity	Bouguer gravity ($\rho = 2.67$ Mg.m^{-3})
978042.45 mGal (9185) ±0.12 978042.48 mGal (9243) ±0.11	18.52 mGal (9185) 18.55 mGal (9243)	-7.85 mGal (9185) -7.82 mGal (9243)

DESCRIPTION

The stations are located beneath the covered walkway and on the helipad at Luasong Rest House, Luasong. Station 9185 is at the base of the righthand post supporting the walkway roof leading to the Rest House nearest the covered car park, 9 m north of the front steps. Station 9243 is at the centre of the helipad which is 25 m west of the western corner of the Rest House.

Described by Rob Holt **Date** 12 November 1996

DIAGRAM

GENERAL

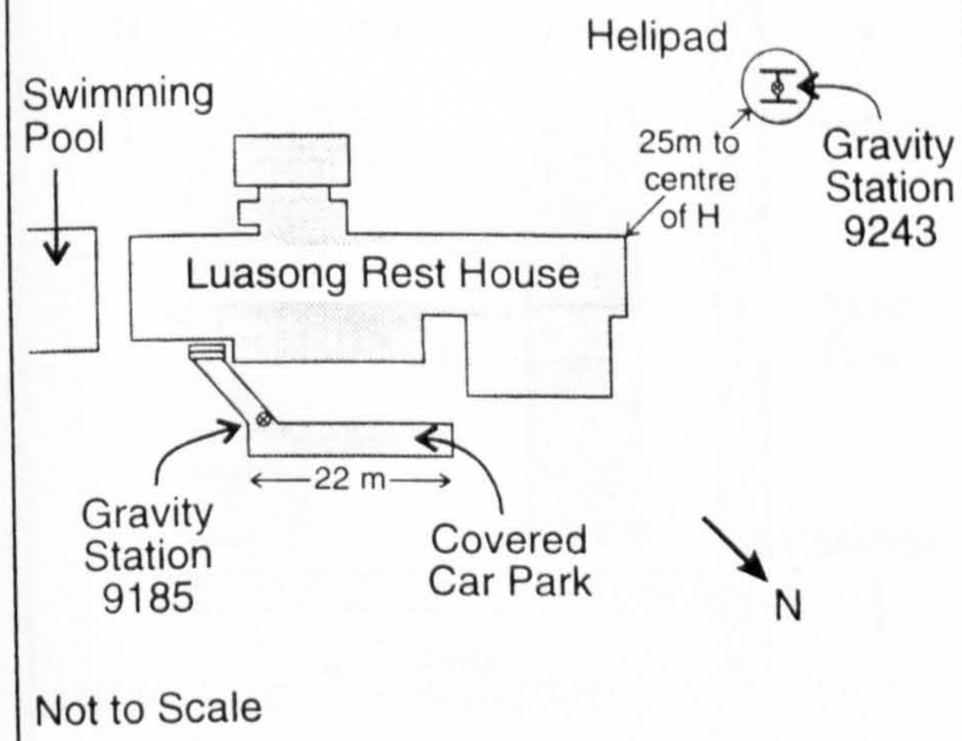

DETAIL

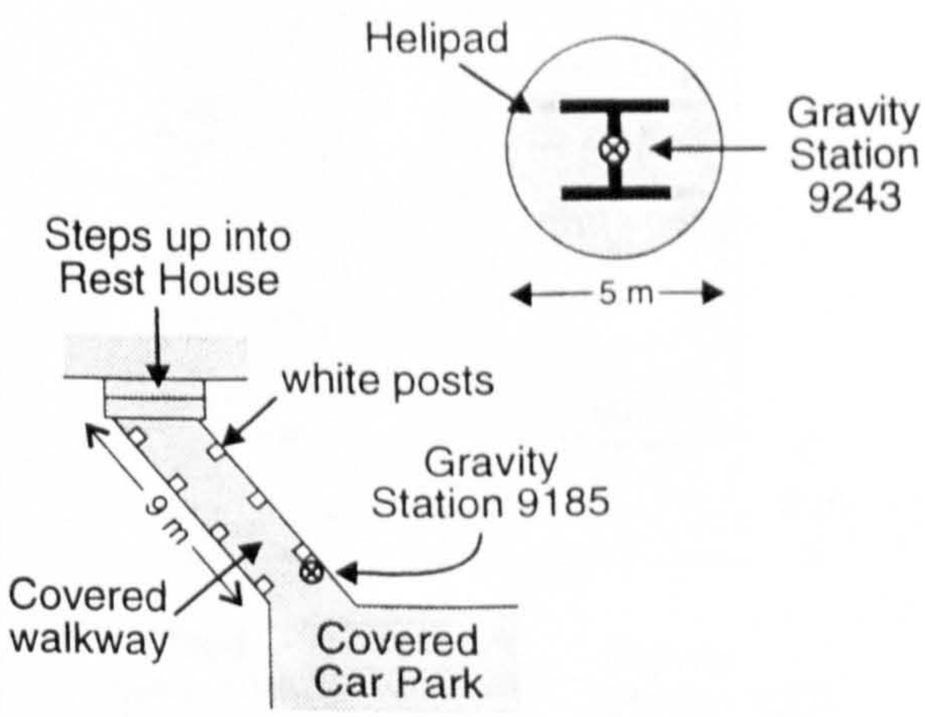

Diagram by Rob Holt **Date** 26 June 1996

STATION HISTORY

Both stations were established during the 1995 Geological Survey of Malaysia / University College London Sabah gravity survey. Stations linked to the Tawau and Telupid gravity base stations (9502.9169 and 9502.9028 respectively).

Source organisation(s) Geological Survey of Malaysia / University College London

GRAVITY STATION DESCRIPTION

Station number and name: 9502.9301 Tambunan, Sabah

Nearest City	State / Province / County	Country
Tambunan	Sabah	Malaysia

Latitude	Longitude	Source
5° 40.17' N	116° 21.93' E	Magellan GPS Fix

Elevation	Source
575.3m	Barometer tie to sea level

Observed gravity (IGSN 71)	Free-air gravity	Bouguer gravity ($\rho = 2.67$ Mg.m^{-3})
977939.97 mGal ±0.11	35.12 mGal	-78.05 mGal

DESCRIPTION

On tiled pavement on south side of shopping complex south of the centre of Tambunan and west of the main road between Ranau and Keningau. The station is equidistant from the SE and SW corners of the western building of the complex, immediately outside the Sabah Bank Berhad branch and equidistant from the wall and the edge of the pavement.

Described by Rob Holt — **Date** 11 November 1996

DIAGRAM

GENERAL

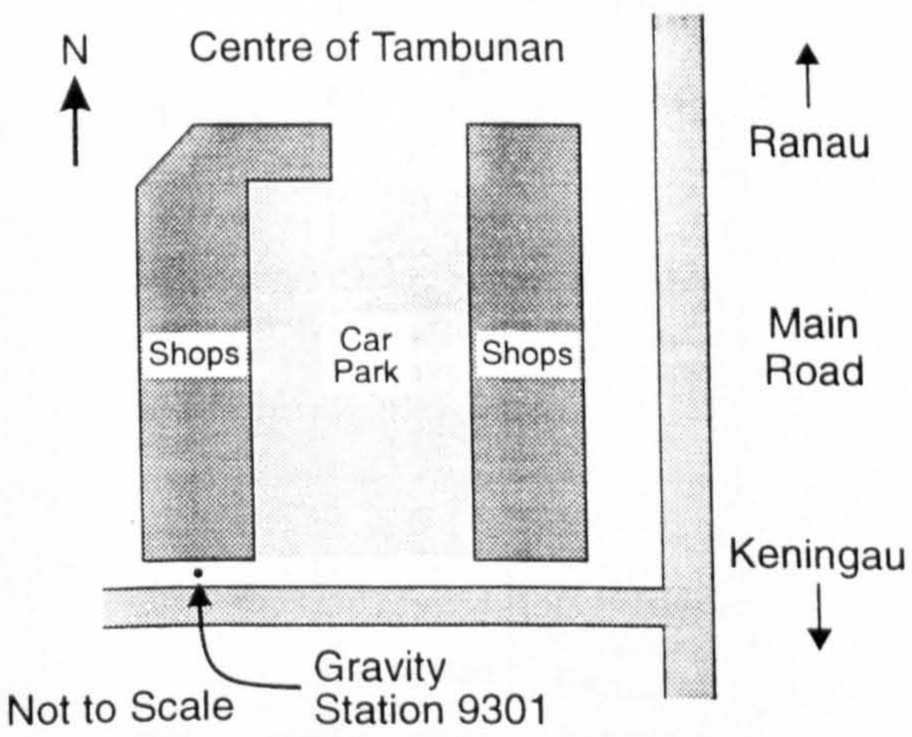

DETAIL

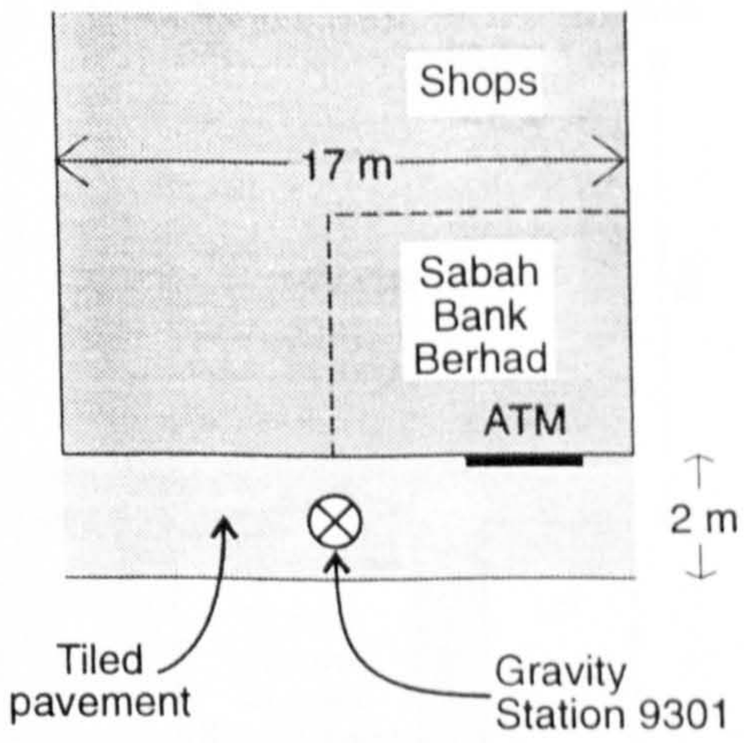

Diagram by Rob Holt — **Date** 26 June 1996

STATION HISTORY

The station was established in the course of the 1995 Geological Survey of Malaysia / University College London Sabah gravity survey, and is linked directly to the Geological Survey of Malaysia gravity base station in Kota Kinabalu (9502.9002).

Source organisation(s) Geological Survey of Malaysia / University College London

GRAVITY STATION DESCRIPTION

Station number and name
SWB0 Hotel Sungei Wang, Kuala Lumpur

Nearest City	State / Province / County	Country
Kuala Lumpur	Selangor	Malaysia

Latitude	Longitude	Source
3° 00.6' N	101° 40.8' E	Magellan GPS Fix

Elevation	Source
.	-

Observed gravity (IGSN 71)	Free-air gravity	Bouguer gravity ($\rho = 2.67$ Mg.m^{-3})
978026.00 mGal	-	-

DESCRIPTION

The station is located in the foyer of the Hotel Sungei Wang, Kuala Lumpur. The station lies 1 m from the rear, right-hand corner of the hotel foyer when entered from Jalan Bukit Bintang, approximately 4 m from the hotel lift door.

Described by	Rob Holt	Date	23 November 1996

DIAGRAM

GENERAL

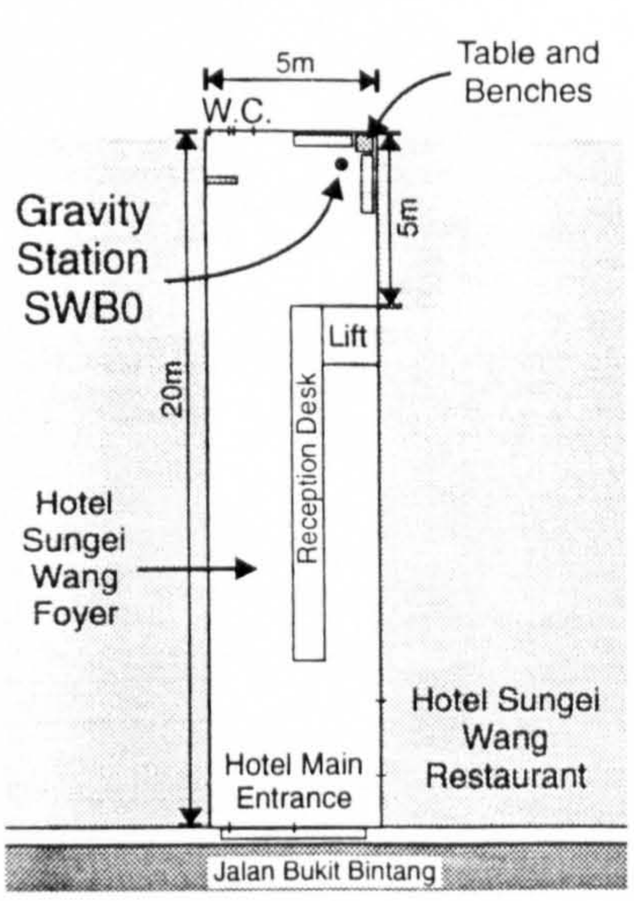

DETAIL

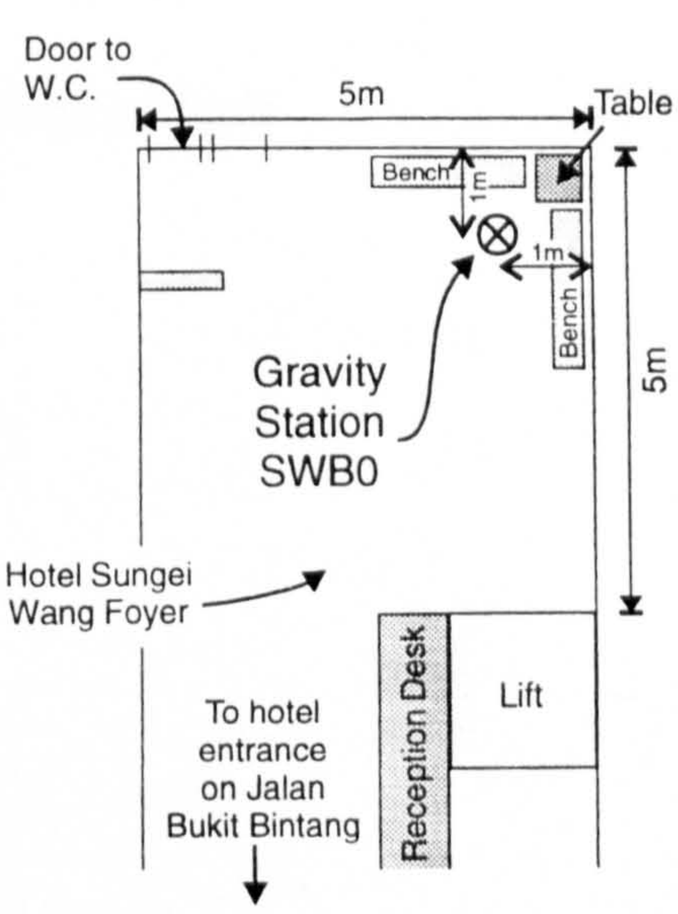

Diagram by	Rob Holt	Date	23 November 1996

STATION HISTORY

The station was established in the course of the 1995 Geological Survey of Malaysia / University College London Sabah gravity survey. It is linked to the main Malaysian gravity base station in the Physics Department, University of Malaya in Kuala Lumpur by three A-B-A ties. The reference value at the University base (G4/76) has been taken as 978034.45 mGal.

Source organisation(s)	Geological Survey of Malaysia / University College London

APPENDIX 3

Gravity meter G-90 calibration table

COPY OF GRAVITY METER CALIBRATION TABLE

Milligal values for LaCoste & Romberg, Inc. Model G Gravity Meter #G-90

Counter Reading	Value in Milligals	Factor for Interval	Counter Reading	Value in Milligals	Factor for Interval
000	000.00	1.03148			
100	103.15	1.03134	3600	3715.43	1.03403
200	206.28	1.03125	3700	3818.84	1.03415
300	309.41	1.03121	3800	3922.25	1.03427
400	412.53	1.03119	3900	4025.68	1.03439
500	515.65	1.03117	4000	4129.12	1.03448
600	618.76	1.03116	4100	4232.56	1.03459
700	721.88	1.03117	4200	4336.02	1.03470
800	825.00	1.03118	4300	4439.49	1.03480
900	928.12	1.03120	4400	4542.97	1.03488
1000	1031.24	1.03123	4500	4646.46	1.03496
1100	1134.36	1.03128	4600	4749.96	1.03501
1200	1237.49	1.03134	4700	4853.46	1.03507
1300	1340.62	1.03139	4800	4956.97	1.03512
1400	1443.76	1.03145	4900	5060.48	1.03518
1500	1546.90	1.03151	5000	5164.00	1.03523
1600	1650.06	1.03158	5100	5267.52	1.03525
1700	1753.21	1.03167	5200	5371.04	1.03526
1800	1856.38	1.03176	5300	5474.57	1.03524
1900	1959.56	1.03186	5400	5578.09	1.03521
2000	2062.74	1.03196	5500	5631.61	1.03516
2100	2165.94	1.03207	5600	5785.13	1.03510
2200	2269.15	1.03217	5700	5888.64	1.03503
2300	2372.36	1.03228	5800	5992.14	1.03495
2400	2475.59	1.03242	5900	6095.64	1.03485
2500	2578.83	1.03256	6000	6199.12	1.03471
2600	2682.09	1.03271	6100	6302.59	1.03453
2700	2785.36	1.03288	6200	6406.05	1.03435
2800	2888.65	1.03301	6300	6509.48	1.03414
2900	2991.95	1.03316	6400	6612.90	1.03393
3000	3095.26	1.03330	6500	6716.29	1.03369
3100	3198.59	1.03344	6600	6819.66	1.03345
3200	3301.94	1.03357	6700	6923.00	1.03316
3300	3405.30	1.03368	6800	7026.32	1.03282
3400	3508.66	1.03379	6900	7129.60	1.03197
3500	3612.04	1.03390	7000	7232.80	

Note: Right-hand wheel on counter indicates approximately 0.1 milligal.

1-25-82

APPENDIX 4

1995 Sabah Gravity Survey Full Results Listing

SABAH LAND GRAVITY SURVEY JULY-AUGUST 1996

GRAVITY DATA PROCESSING, NOVEMBER 1996

GRAVITY BASE STATION IN UNIVERSITY OF MALAYA, MALAYSIA (G4/76) IS 978034.46 mGAL

DATE	DAY	TIME		STATION NUMBER	LATITUDE	LONGITUDE	ELEVATION	GRAVITY READING	EQUIVALENT	TIDE CORRECTION	TIDE CORRECTED	DRIFT CORRECTION	DRIFT CORRECTED	G Observed	G Normal	FAC	FAA	[illegible]	[illegible]	TC	[illegible]
		HR	MIN		(Degrees)	(Degrees)	(Metres)		(mGal)	(mGal)	(mGal)	(mGal)	(mGal)	(mGal)	(mGal)	(mGal)	(mGal)	(mGal)	(mGal)	(mGal)	(mGal)
July, 5	1	13	56	SWB0	3.0100	101.6800	50.0	153904.0	1587.17	-0.055	1587.12	0.09	1587.02	978026.02	978046.10	15.43	-4.65	-9.84	-14.48	0	-14.48
July, 5	1	15	15	SWB0	3.0100	101.6800	50.0	153900.0	1587.13	-0.029	1587.10	0.11	1586.99	978025.99	978046.10	15.43	-4.67	-9.84	-14.51	0	-14.51
July, 6	2	5	56	SWB0	3.0100	101.6800	50.0	153904.0	1587.17	0.058	1587.23	0.23	1587.00	978026.00	978046.10	15.43	-4.67	-9.84	-14.50	0	-14.50
August, 4	31	13	58	SWB0	3.0100	101.6800	50.0	154057.0	1588.75	0.051	1588.80	1.80	1587.00	978026.00	978046.10	15.43	-4.66	-9.84	-14.50	0	-14.50
August, 7	34	14	27	SWB0	3.0100	101.6800	50.0	154053.0	1588.71	-0.030	1588.68	1.66	1587.01	978026.01	978046.10	15.43	-4.65	-9.84	-14.49	0	-14.49
August, 7	34	15	28	SWB0	3.0100	101.6800	50.0	154055.0	1588.73	-0.076	1588.65	1.66	1586.99	978025.99	978046.10	15.43	-4.68	-9.84	-14.51	0	-14.51
August, 7	34	16	29	SWB0	3.0100	101.6800	50.0	154058.0	1588.76	-0.103	1588.66	1.66	1587.00	978026.00	978046.10	15.43	-4.67	-9.84	-14.51	0	-14.51
July, 5	1	14	39	G4/76	3.0100	101.6800	50.0	154722.0	1595.61	-0.044	1595.56	0.10	1595.46	978034.46	978046.10	15.43	3.79	-9.84	-6.04	0	-6.04
August, 7	34	14	51	G4/76	3.0100	101.6800	50.0	154872.0	1597.16	-0.050	1597.11	1.66	1595.44	978034.44	978046.10	15.43	3.77	-9.84	-6.06	0	-6.06
August, 7	34	16	1	G4/76	3.0100	101.6800	50.0	154877.0	1597.21	-0.094	1597.11	1.66	1595.45	978034.45	978046.10	15.43	3.78	-9.84	-6.05	0	-6.05
July, 6	2	10	58	1	5.9775	116.0758	16.9	162383.0	1674.64	-0.024	1674.62	0.27	1674.35	978113.35	978068.03	5.20	30.52	-3.31	27.21	0	27.21
July, 6	2	13	45	1	5.9775	116.0758	16.9	162389.0	1674.70	-0.040	1674.66	0.29	1674.37	978113.37	978068.03	5.20	30.54	-3.31	27.23	0	27.23
July, 6	2	16	15	1	5.9775	116.0758	16.9	162381.0	1674.62	0.027	1674.65	0.31	1674.34	978113.34	978068.03	5.20	30.51	-3.31	27.19	0	27.19
July, 7	3	8	28	1	5.9775	116.0758	16.9	162380.0	1674.61	0.086	1674.70	0.34	1674.36	978113.36	978068.03	5.20	30.53	-3.31	27.21	0	27.21
July, 7	3	11	14	1	5.9775	116.0758	16.9	162386.0	1674.67	0.004	1674.68	0.34	1674.34	978113.34	978068.03	5.20	30.51	-3.31	27.19	0	27.19
July, 8	4	8	34	1	5.9775	116.0758	16.9	162378.0	1674.59	0.109	1674.70	0.35	1674.35	978113.35	978068.03	5.20	30.52	-3.31	27.21	0	27.21
July, 8	4	10	26	1	5.9775	116.0758	16.9	162380.0	1674.61	0.082	1674.69	0.35	1674.35	978113.35	978068.03	5.20	30.52	-3.31	27.20	0	27.20
July, 8	4	18	10	1	5.9775	116.0758	16.9	162383.0	1674.64	0.002	1674.64	0.35	1674.30	978113.30	978068.03	5.20	30.47	-3.31	27.15	0	27.15
July, 9	5	16	35	1	5.9775	116.0758	16.9	162399.0	1674.81	-0.100	1674.71	0.35	1674.35	978113.35	978068.03	5.20	30.52	-3.31	27.21	0	27.21
July, 9	5	17	8	1	5.9775	116.0758	16.9	162398.0	1674.80	-0.089	1674.71	0.35	1674.35	978113.35	978068.03	5.20	30.52	-3.31	27.21	0	27.21
July, 10	6	8	31	1	5.9775	116.0758	16.9	162382.0	1674.63	0.085	1674.72	0.36	1674.36	978113.36	978068.03	5.20	30.53	-3.31	27.21	0	27.21
July, 10	6	17	43	1	5.9775	116.0758	16.9	162396.0	1674.78	-0.112	1674.66	0.36	1674.30	978113.30	978068.03	5.20	30.47	-3.31	27.16	0	27.16
July, 11	7	8	46	1	5.9775	116.0758	16.9	162385.0	1674.66	0.057	1674.72	0.36	1674.36	978113.36	978068.03	5.20	30.53	-3.31	27.21	0	27.21
July, 6	2	15	24	2	5.9588	116.0723	3.4	162269.0	1673.47	0.002	1673.47	0.30	1673.16	978112.16	978067.68	1.04	25.52	-0.66	24.86	0	24.86
July, 7	3	8	40	2	5.9588	116.0723	3.4	162265.0	1673.43	0.084	1673.51	0.34	1673.17	978112.17	978067.68	1.04	25.53	-0.66	24.87	0	24.87
July, 7	3	11	1	2	5.9588	116.0723	3.4	162273.0	1673.51	0.013	1673.52	0.34	1673.18	978112.18	978067.68	1.04	25.54	-0.66	24.88	0	24.88
July, 8	4	8	45	2	5.9588	116.0723	3.4	162266.0	1673.44	0.110	1673.55	0.35	1673.20	978112.20	978067.68	1.04	25.56	-0.66	24.90	0	24.90
July, 8	4	10	8	2	5.9588	116.0723	3.4	162269.0	1673.47	0.092	1673.56	0.35	1673.21	978112.21	978067.68	1.04	25.57	-0.66	24.91	0	24.91
July, 10	6	8	44	2	5.9588	116.0723	3.4	162270.0	1673.48	0.098	1673.57	0.36	1673.22	978112.22	978067.68	1.04	25.58	-0.66	24.91	0	24.91
July, 11	7	9	3	2	5.9588	116.0723	3.4	162269.0	1673.47	0.077	1673.54	0.36	1673.18	978112.18	978067.68	1.04	25.54	-0.66	24.88	0	24.88
July, 21	17	18	50	2	5.9588	116.0723	3.4	162333.0	1674.13	0.030	1674.16	1.02	1673.14	978112.14	978067.68	1.04	25.50	-0.66	24.83	0	24.83
July, 23	19	5	21	2	5.9588	116.0723	3.4	162348.0	1674.28	-0.038	1674.24	1.08	1673.17	978112.17	978067.68	1.04	25.53	-0.66	24.86	0	24.86
July, 30	26	14	23	2	5.9588	116.0723	3.4	162403.0	1674.85	0.135	1674.98	1.80	1673.19	978112.19	978067.68	1.04	25.55	-0.66	24.88	0	24.88
July, 31	27	8	47	2	5.9588	116.0723	3.4	162428.0	1675.11	-0.088	1675.02	1.83	1673.19	978112.19	978067.68	1.04	25.55	-0.66	24.89	0	24.89
August, 2	29	9	2	2	5.9588	116.0723	3.4	162426.0	1675.09	-0.062	1675.02	1.82	1673.21	978112.21	978067.68	1.04	25.57	-0.66	24.90	0	24.90
August, 2	29	9	56	2	5.9588	116.0723	3.4	162425.0	1675.08	-0.064	1675.01	1.82	1673.19	978112.19	978067.68	1.04	25.55	-0.66	24.89	0	24.89
August, 2	29	10	35	2	5.9588	116.0723	3.4	162425.0	1675.08	-0.056	1675.02	1.82	1673.20	978112.20	978067.68	1.04	25.56	-0.66	24.90	0	24.90
August, 3	30	8	35	2	5.9588	116.0723	3.4	162421.0	1675.03	-0.014	1675.02	1.81	1673.21	978112.21	978067.68	1.04	25.57	-0.66	24.90	0	24.90
August, 3	30	14	35	2	5.9588	116.0723	3.4	162412.0	1674.94	0.039	1674.98	1.81	1673.17	978112.17	978067.68	1.04	25.53	-0.66	24.87	0	24.87
August, 4	31	8	20	2	5.9588	116.0723	3.4	162414.0	1674.96	0.037	1675.00	1.81	1673.19	978112.19	978067.68	1.04	25.55	-0.66	24.89	0	24.89
July, 8	4	11	42	3	5.4718	115.7982	9.6	160597.0	1656.22	0.079	1656.30	0.35	1655.95	978094.95	978078.95	2.97	18.97	-1.89	17.08	0	17.08
July, 8	4	14	27	3	5.4718	115.7982	9.6	160608.0	1656.33	-0.025	1656.31	0.35	1655.96	978094.96	978078.95	2.97	18.98	-1.89	17.09	0	17.09
July, 8	4	16	33	3	5.4718	115.7982	9.6	160607.0	1656.32	-0.013	1656.31	0.35	1655.96	978094.96	978078.95	2.97	18.98	-1.89	17.09	0	17.09
July, 8	4	12	3	4	5.4088	115.7505	11.3	160406.0	1654.25	0.070	1654.32	0.35	1653.97	978092.97	978077.87	3.49	18.59	-2.22	16.36	0	16.36
July, 8	4	12	29	5	5.5058	115.7795	3.5	159960.0	1649.64	0.039	1649.68	0.35	1649.33	978088.33	978079.53	1.09	9.89	-0.70	9.19	0	9.19
July, 8	4	12	43	6	5.5298	115.7447	4.2	159182.0	1641.81	0.026	1641.84	0.35	1641.29	978080.29	978079.95	1.30	1.64	-0.83	0.82	0	0.82
July, 8	4	12	57	7	5.5328	115.7005	2.5	158640.0	1636.02	0.016	1636.04	0.35	1635.69	978074.69	978080.00	0.78	-4.53	-0.50	-5.03	0	-5.03
July, 8	4	13	12	8	5.5370	115.6805	1.0	158488.0	1634.45	0.005	1634.46	0.35	1634.11	978073.11	978080.07	0.31	-6.65	-0.20	-6.85	0	-6.85
July, 8	4	13	31	9	5.5685	115.6012	0.2	159574.0	1645.66	-0.010	1645.65	0.35	1645.30	978084.30	978080.62	0.06	3.73	-0.03	3.70	0	3.70
July, 8	4	13	46	10	5.5458	115.6242	1.9	159281.0	1642.63	-0.016	1642.62	0.35	1642.27	978081.27	978080.23	0.57	1.62	-0.36	1.26	0	1.26
July, 8	4	15	25	11	5.3320	115.5912	6.7	158503.0	1634.61	-0.017	1634.59	0.35	1634.25	978073.25	978076.58	2.08	-1.25	-1.33	-2.58	0	-2.58
July, 8	4	15	39	12	5.3595	115.6095	6.9	158235.0	1631.84	-0.019	1631.83	0.35	1631.48	978070.48	978077.04	2.13	-4.43	-1.36	-5.79	0	-5.79
July, 8	4	15	50	13	5.3590	115.6473	9.1	158440.0	1633.98	-0.016	1633.94	0.35	1633.60	978072.60	978077.03	2.81	-1.62	-1.79	-3.41	0	-3.41
July, 8	4	16	4	14	5.3722	115.6985	10.8	159103.0	1640.80	-0.014	1640.78	0.35	1640.44	978079.44	978077.25	3.33	5.52	-2.12	3.39	0	3.39
July, 10	6	10	24	14	5.3722	115.6985	10.8	159082.0	1640.58	0.205	1640.79	0.36	1640.43	978079.43	978077.25	3.33	5.51	-2.12	3.38	0	3.38
July, 10	6	14	45	14	5.3722	115.6985	10.8	159102.0	1640.79	0.014	1640.80	0.36	1640.44	978079.44	978077.25	3.33	5.52	-2.12	3.40	0	3.40
July, 10	6	16	2	14	5.3722	115.6985	10.8	159102.0	1640.79	-0.046	1640.74	0.36	1640.38	978079.38	978077.25	3.33	5.46	-2.12	3.34	0	3.34
July, 8	4	16	15	15	5.3533	115.7267	10.1	160306.0	1653.22	-0.008	1653.21	0.35	1652.86	978091.86	978076.93	3.12	18.05	-1.99	16.06	0	16.06
July, 8	4	17	10	16	5.6682	115.8935	0.6	161572.0	1666.28	-0.014	1666.26	0.35	1665.92	978104.92	978082.35	0.17	22.74	-0.11	22.63	0	22.63
July, 9	5	10	13	2nd fl HA	5.9775	116.0758	23.3	162192.3	1672.68	0.127	1672.80	0.35	1672.45	978111.45	978068.03	7.21	30.63	-4.59	26.03	0	26.03
July, 9	5	10	22	2nd fl HA	5.9775	116.0758	23.3	162190.0	1672.65	0.125	1672.78	0.35	1672.42	978111.42	978068.03	7.21	30.60	-4.59	26.01	0	26.01
July, 9	5	10	29	2nd fl HA	5.9775	116.0758	23.3	162189.5	1672.65	0.123	1672.77	0.35	1672.42	978111.42	978068.03	7.21	30.59	-4.59	26.00	0	26.00
July, 9	5	10	37	2nd fl HA	5.9775	116.0758	23.3	162191.5	1672.67	0.120	1672.79	0.35	1672.43	978111.43	978068.03	7.21	30.61	-4.59	26.02	0	26.02
July, 9	5	10	43	2nd fl HA	5.9775	116.0758	23.3	162191.5	1672.67	0.118	1672.79	0.35	1672.43	978111.43	978068.03	7.21	30.61	-4.59	26.02	0	26.02
July, 9	5	10	51	2nd fl HA	5.9775	116.0758	23.3	162192.7	1672.68	0.114	1672.79	0.35	1672.44	978111.44	978068.03	7.21	30.62	-4.59	26.02	0	26.02
July, 9	5	11	0	2nd fl HA	5.9775	116.0758	23.3	162193.0	1672.68	0.110	1672.79	0.35	1672.44	978111.44	978068.03	7.21	30.62	-4.59	26.02	0	26.02
July, 9	5	11	25	2nd fl HA	5.9775	116.0758	23.3	162194.0	1672.69	0.095	1672.79	0.35	1672.44	978111.44	978068.03	7.21	30.61	-4.59	26.02	0	26.02
July, 9	5	11	36	2nd fl HA	5.9775	116.0758	23.3	162193.0	1672.68	0.087	1672.77	0.35	1672.42	978111.42	978068.03	7.21	30.59	-4.59	26.00	0	26.00
July, 9	5	11	40	2nd fl HA	5.9775	116.0758	23.3	162192.0	1672.67	0.084	1672.76	0.35	1672.40	978111.40	978068.03	7.21	30.58	-4.59	25.99	0	25.99
July, 9	5	12	46	2nd fl HA	5.9775	116.0758	23.3	162200.0	1672.75	0.027	1672.78	0.35	1672.43	978111.43	978068.03	7.21	30.60	-4.59	26.01	0	26.01
July, 9	5	13	30	2nd fl HA	5.9775	116.0758	23.3	162205.5	1672.81	-0.015	1672.80	0.35	1672.44	978111.44	978068.03	7.21	30.62	-4.59	26.03	0	26.03
July, 9	5	15	3	2nd fl HA	5.9775	116.0758	23.3	162213.0	1672.89	-0.085	1672.80	0.35	1672.45	978111.45	978068.03	7.21	30.63	-4.59	26.03	0	26.03
July, 9	5	15	32	2nd fl HA	5.9775	116.0758	23.3	162212.5	1672.88	-0.097	1672.79	0.35	1672.43	978111.43	978068.03	7.21	30.61	-4.59	26.02	0	26.02
July, 9	5	16	25	2nd fl HA	5.9775	116.0758	23.3	162214.0	1672.90	-0.102	1672.80	0.35	1672.44	978111.44	978068.03	7.21	30.62	-4.59	26.03	0	26.03
July, 9	5	16	52	17	5.9843	116.0732	2.2	162542.0	1676.28	-0.098	1676.19	0.35	1675.83	978114.83	978088.16	0.69	27.36	-0.44	26.92	0	26.92
July, 10	6	10	43	18	5.4067	115.6842	7.4	158777.0	1637.44	0.202	1637.64	0.36	1637.28	978076.28	978077.84	2.29	0.73	-1.46	-0.73	0	-0.73
July, 10	6	11	0	19	5.4260	115.6533	6.9	158408.0	1633.81	0.198	1633.81	0.36	1633.45	978072.45	978078.16	2.13	-3.58	-1.36	-4.94	0	-4.94
July, 10	6	11	18	20	5.4503	115.6237	4.4	158452.0	1634.08	0.190	1634.27	0.36	1633.91	978072.91	978078.58	1.35	-4.31	-0.86	-5.17	0	-5.17
July, 10	6	11	37	21	5.4607	115.5863	2.4	158510.0	1634.68	0.181	1634.86	0.36	1634.50	978073.50	978078.76	0.73	-4.53	-0.46	-4.99	0	-4.99
July, 10	6	12	0	22	5.4972	115.5548	2.4	159050.0	1640.25	0.164	1640.42	0.36	1640.06	978079.06	978079.39	0.73	0.40	-0.46	-0.06	0	-0.06
July, 10	6	13	3	23	5.5423	115.5808	0.7	159408.0	1643.94	0.105	1644.05	0.36	1643.69	978082.69	978080.17	0.21	2.73	-0.13	2.60	0	2.60
July, 10	6	13	34	24	5.4908	115.4857	0.0	159594.0	1645.86	0.078	1645.94	0.36	1645.58	978084.58	978079.27	0.00	5.31	0.00	5.31	0	5.31
July, 10	6	15	16	25	5.2842	115.6822	4.7	160125.0	1651.35	-0.006	1651.34	0.36	1650.98	978089.98	978075.78	1.46	15.66	-0.93	14.73	0	14.73
July, 10	6	15	31	26	5.3165	115.7083	7.6	160315.0	1653.31	-0.021	1653.29	0.36	1652.93	978091.93	978076.32	2.34	17.95	-1.49	16.46	0	16.46
July, 10	6	15	46	27	5.3430	115.7460	3.0	160048.0	1650.56	-0.034	1650.52	0.36	1650.16	978089.16	978076.76	0.94	13.34	-0.60	12.74	0	12.74
July, 11	7	15	4	26	5.6280	117.1310	100.7	166102.0	1713.01	0.006	1713.01	0.37	1712.65	978151.65	978081.67	31.07	101.04	-19.80	81.24	0	81.24
July, 29	25	14	56	26	5.6280	117.1310	100.7	166224.0	1714.27	0.122	1714.39	1.71	1712.68	978151.68	978081.67	31.07	101.07	-19.80	81.27	0	81.27
July, 30	26	8	18	26	5.6280	117.1310	100.7	166244.0	1714.47	-0.063	1714.41	1.77	1712.64	978151.64	978081.67	31.07	101.03	-19.80	81.23	0	81.23
July, 30	26	10	32	26	5.6280	117.1310	100.7	166235.0	1714.38	0.049	1714.43	1.78	1712.65	978151.65	978081.67	31.07	101.04	-19.80	81.24	0	81.24
July, 11	7	18	9	29	5.0263	118.3335	6.1	166577.0	1717.91	-0.038	1717.87	0.37	1717.50	978156.50	978071.60	1.88	86.78	-1.20	85.58	0	85.58
July, 12	8	7	56	29	5.0263	118.3335	6.1	166575.0	1717.89	0.045	1717.93	0.38	1717.55	978156.55	978071.60	1.88	86.83	-1.20	85.63	0	85.63
July, 12	8	17	7	29	5.0263	118.3335	6.1	166580.0	1717.94	-0.020	1717.92	0.40	1717.52	978156.52	978071.60	1.88	86.79	-1.20	85.60	0	85.60
July, 13	9	7	57	29	5.0263	118.3335	6.1	166584.0	1717.98	0.001	1717.98	0.44	1717.54	978156.54	978071.60	1.88	86.82	-1.20	85.62	0	85.62
July, 13	9	16	49	29	5.0263	118.3335	6.1	166584.0	1717.98	0.040	1718.02	0.46	1717.56	978156.56	978071.60	1.88	86.84	-1.20	85.64	0	85.64
July, 14	10	8	0	29	5.0263	118.3335	6.1	166593.0	1718.07	-0.020	1718.05	0.50	1717.55	978156.55	978071.60	1.88	86.83	-1.20	85.63	0	85.63
July, 14	10	17	0	29	5.0263	118.3335	6.1	166582.0	1717.96	0.077	1718.04	0.52	1717.51	978156.51	978071.60	1.88	86.79	-1.20	85.59	0	85.59
July, 15	11	7	55	29	5.0263	118.3335	6.1	166589.0	1718.13	-0.020	1718.11	0.56	1717.55	978156.55	978071.60	1.88	86.83	-1.20	85.63	0	85.63
July, 15	11	17	28	29	5.0263	118.3335	6.1	166590.0	1718.04	0.094	1718.14	0.58	1717.55	978156.55	978071.60	1.88	86.83	-1.20	85.63	0	85.63
July, 16	12	8	55	29	5.0263	118.3335	6.1	166603.0	1718.18	0.001	1718.18	0.62	1717.56	978156.56	978071.60	1.88	86.83	-1.20	85.63	0	85.63
July, 16	12	16	27	29	5.0263	118.3335	6.1	166586.0	1718.00	0.176	1718.18	0.64	1717.53	978156.53	978071.60	1.88	86.81	-1.20	85.61	0	85.61

N.B. Bouguer anomalies incorrectly calculated using -0·1967h instead of -0·1119h

SABAH LAND GRAVITY SURVEY JULY-AUGUST 1996
GRAVITY DATA PROCESSING, NOVEMBER 1996
GRAVITY BASE STATION IN UNIVERSITY OF MALAYA, MALAYSIA (G4/76) IS 978034.46 mGAL

DATE	DAY	TIME		STATION NUMBER	LATITUDE	LONGITUDE	ELEVATION	GRAVITY READING	EQUIVALENT	TIDE CORRECTION	TIDE CORRECTED	DRIFT CORRECTION	DRIFT CORRECTED	G Observed	G Normal	FAC	FAA	BC	BA	TC	BA inc TC
		HR	MIN		(Degrees)	(Degrees)	(Metres)		(mGal)	(mGal)	(mGal)	(mGal)	(mGal)	(mGal)	(mGal)	(mGal)	(mGal)	(mGal)	(mGal)	(mGal)	(mGal)
July, 17	13	8	48	29	5.0263	118.3335	6.1	166605.0	1718.20	0.021	1718.22	0.70	1717.52	978156.52	978071.80	1.88	86.79	-1.20	85.60	0	85.60
July, 17	13	17	20	29	5.0263	118.3336	6.1	166602.0	1718.18	0.154	1718.32	0.78	1717.54	978156.54	978071.80	1.88	86.82	-1.20	85.62	0	85.62
July, 18	14	7	55	29	5.0263	118.3336	6.1	166615.0	1718.30	0.079	1718.38	0.84	1717.54	978156.54	978071.80	1.88	86.82	-1.20	85.62	0	85.62
July, 18	14	16	40	29	5.0263	118.3336	6.1	166611.0	1718.26	0.162	1718.42	0.88	1717.54	978156.54	978071.80	1.88	86.82	-1.20	85.62	0	85.62
July, 19	15	7	59	29	5.0263	118.3336	6.1	166620.0	1718.35	0.111	1718.46	0.94	1717.52	978156.52	978071.80	1.88	86.80	-1.20	85.60	0	85.60
July, 21	17	10	19	29	5.0263	118.3336	6.1	166626.0	1718.41	0.117	1718.53	1.01	1717.52	978156.52	978071.80	1.88	86.80	-1.20	85.60	0	85.60
July, 21	17	13	23	29	5.0263	118.3335	6.1	166634.0	1718.50	0.050	1718.55	1.01	1717.53	978156.53	978071.80	1.88	86.81	-1.20	85.61	0	85.61
July, 23	19	7	36	29	5.0263	118.3336	6.1	166631.0	1718.46	0.141	1718.61	1.09	1717.52	978156.52	978071.80	1.88	86.80	-1.20	85.60	0	85.60
July, 12	8	8	33	30	5.0527	118.2795	36.6	166344.0	1715.50	0.087	1715.59	0.38	1715.21	978154.21	978072.02	11.29	93.48	-7.20	86.28	0	86.28
July, 12	8	8	49	31	5.0897	118.2505	41.8	164237.0	1693.77	0.104	1693.87	0.38	1693.49	978132.49	978072.61	12.91	72.79	-8.23	64.56	0	64.56
July, 12	8	9	1	32	5.1260	118.2218	31.7	162442.0	1675.25	0.116	1675.37	0.38	1674.99	978113.99	978073.19	9.78	50.58	-6.24	44.34	0	44.34
July, 12	8	9	14	33	5.1542	118.1848	45.2	162020.0	1670.90	0.130	1671.03	0.38	1670.65	978109.65	978073.65	13.95	49.94	-8.89	41.06	0	41.06
July, 12	8	15	42	33	5.1542	118.1848	45.2	162035.0	1671.05	0.056	1671.11	0.40	1670.71	978109.71	978073.65	13.95	50.01	-8.89	41.12	0	41.12
July, 12	8	9	26	34	5.1702	118.1360	49.9	162179.0	1672.54	0.143	1672.68	0.38	1672.30	978111.30	978073.91	15.40	52.79	-9.82	42.98	0	42.98
July, 12	8	9	41	35	5.2053	118.0980	40.0	160419.0	1654.38	0.157	1654.54	0.38	1654.16	978093.16	978074.48	12.33	31.01	-7.86	23.15	0	23.15
July, 12	8	9	55	36	5.2463	118.0807	36.8	159380.0	1643.66	0.168	1643.82	0.38	1643.44	978082.44	978075.15	11.34	18.63	-7.23	11.40	0	11.40
July, 12	8	12	54	36	5.2463	118.0807	36.8	159386.0	1643.72	0.225	1643.94	0.39	1643.55	978082.55	978075.15	11.34	18.74	-7.23	11.51	0	11.51
July, 12	8	10	8	37	5.2807	118.0243	31.2	158176.0	1631.24	0.176	1631.41	0.38	1631.03	978070.03	978075.72	9.63	3.93	-6.14	-2.20	0	-2.20
July, 12	8	15	20	37	5.2807	118.0243	31.2	158192.0	1631.40	0.072	1631.47	0.40	1631.08	978070.08	978075.72	9.63	3.98	-6.14	-2.15	0	-2.15
July, 12	8	10	20	38	5.3210	117.9913	31.5	157186.0	1621.02	0.185	1621.21	0.38	1620.83	978059.83	978076.39	9.73	-8.84	-6.20	-13.04	0	-13.04
July, 12	8	10	34	39	5.3577	117.9565	17.2	157380.0	1623.03	0.193	1623.22	0.38	1622.83	978061.83	978077.01	5.31	-9.87	-3.38	-13.25	0	-13.25
July, 12	8	10	49	40	5.4067	117.9500	7.8	156910.0	1618.18	0.199	1618.38	0.39	1617.99	978056.99	978077.84	2.39	-18.45	-1.53	-19.98	0	-19.98
July, 12	8	11	28	41	5.4058	117.9537	16.2	156794.0	1616.98	0.219	1617.20	0.39	1616.81	978055.81	978077.82	5.00	-17.01	-3.18	-20.20	0	-20.20
July, 12	8	11	47	41	5.4058	117.9537	16.2	156791.0	1616.95	0.223	1617.17	0.39	1616.79	978055.79	978077.82	5.00	-17.04	-3.18	-20.22	0	-20.22
July, 12	8	13	32	42	5.3243	118.0107	85.3	156046.0	1609.27	0.190	1609.46	0.39	1609.08	978048.08	978076.45	26.33	-2.05	-16.78	-18.84	0	-18.84
July, 12	8	14	19	44	5.3013	118.0327	22.9	157615.0	1625.45	0.145	1625.59	0.39	1625.20	978064.20	978076.06	7.06	-10.43	-4.58	-15.01	0	-15.01
July, 12	8	14	32	45	5.3240	118.0470	15.2	157355.0	1622.77	0.127	1622.89	0.39	1622.50	978061.50	978076.44	4.66	-10.26	-2.99	-13.24	0	-13.24
July, 12	8	15	58	46	5.1537	118.1953	57.5	161498.0	1665.51	0.037	1665.55	0.40	1665.15	978104.15	978073.84	17.74	48.26	-11.31	36.95	0	36.95
July, 12	8	16	15	47	5.1663	118.2287	91.1	159014.0	1639.88	0.017	1639.90	0.40	1639.50	978078.50	978073.83	28.10	32.77	-17.91	14.86	0	14.86
July, 13	9	8	31	48	5.0105	118.2552	30.0	167482.0	1727.24	0.036	1727.28	0.44	1726.84	978165.84	978071.35	9.26	103.75	-5.90	97.84	0	97.84
July, 15	11	8	26	49	4.9812	118.2148	128.7	166151.0	1713.51	-0.011	1713.50	0.56	1712.94	978151.94	978070.89	39.73	120.78	-25.32	95.46	0	95.46
July, 19	15	8	38	49	4.9812	118.2148	128.7	166175.0	1713.76	0.098	1713.86	0.95	1712.91	978151.91	978070.89	39.73	120.75	-25.32	95.42	0	95.42
July, 21	17	9	48	49	4.9812	118.2148	128.7	166185.0	1713.86	0.132	1714.00	1.01	1712.99	978151.99	978070.89	39.73	120.82	-25.32	95.50	0	95.50
July, 13	9	8	59	50	4.9838	118.1648	109.1	166418.0	1716.27	0.069	1716.34	0.44	1715.89	978154.89	978071.09	33.67	117.47	-21.46	96.01	0	96.01
July, 13	9	9	17	51	4.9813	118.1162	143.5	165718.0	1709.05	0.091	1709.14	0.44	1708.69	978147.69	978070.90	44.26	121.08	-28.23	92.86	0	92.86
July, 13	9	9	32	52	4.9925	118.0710	162.0	164636.0	1697.88	0.109	1697.99	0.44	1697.55	978136.55	978071.07	50.01	115.49	-31.87	83.61	0	83.61
July, 13	9	15	54	52	4.9925	118.0710	162.0	164639.0	1697.91	0.109	1698.02	0.46	1697.57	978136.57	978071.07	50.01	115.50	-31.87	83.63	0	83.63
July, 13	9	9	50	53	5.0050	118.0210	253.6	162742.0	1678.35	0.130	1678.48	0.44	1678.03	978117.03	978071.27	78.26	124.03	-49.89	74.14	0	74.14
July, 13	9	10	5	54	4.9980	117.9800	188.2	163746.0	1688.70	0.149	1688.85	0.44	1688.41	978127.41	978071.16	58.07	114.32	-37.02	77.31	0	77.31
July, 13	9	10	23	55	4.9575	117.9383	229.7	160226.0	1652.39	0.172	1652.56	0.44	1652.12	978091.12	978070.52	70.88	91.47	-45.18	46.29	0	46.29
July, 13	9	10	36	56	4.9587	117.9188	159.9	160972.0	1660.09	0.186	1660.27	0.45	1659.83	978098.83	978070.54	49.33	77.62	-31.44	46.17	0	46.17
July, 13	9	10	54	57	4.9817	117.9018	128.5	162046.0	1671.17	0.204	1671.37	0.45	1670.92	978109.92	978070.90	39.65	78.68	-25.27	53.40	0	53.40
July, 13	9	11	9	58	4.9825	117.8735	125.5	160427.0	1654.46	0.217	1654.68	0.45	1654.23	978093.23	978070.91	38.72	81.04	-24.68	56.36	0	56.36
July, 13	9	13	50	59	4.9838	117.8028	154.5	157601.0	1625.31	0.240	1625.55	0.45	1625.09	978064.09	978070.62	47.67	41.14	-30.36	10.75	0	10.75
July, 19	15	17	35	59	4.9838	117.8028	154.5	157666.0	1625.98	0.147	1626.12	0.97	1625.16	978064.16	978070.62	47.67	41.20	-30.36	10.82	0	10.82
July, 21	17	8	25	59	4.9838	117.8028	154.5	157666.0	1625.98	0.157	1626.13	1.01	1625.12	978064.12	978070.62	47.67	41.17	-30.36	10.79	0	10.79
July, 13	9	13	54	60	4.9839	117.8027	162.9	157474.0	1624.00	0.237	1624.23	0.45	1623.78	978062.78	978070.62	50.27	42.42	-32.04	10.38	0	10.38
July, 19	15	17	32	60	4.9839	117.8027	162.9	157535.0	1624.62	0.147	1624.77	0.97	1623.81	978062.81	978070.62	50.27	42.45	-32.04	10.41	0	10.41
July, 20	16	7	12	60	4.9839	117.8027	162.9	157515.0	1624.42	0.155	1624.57	0.98	1623.59	978062.59	978070.62	50.27	42.24	-32.04	10.20	0	10.20
July, 20	16	7	48	60	4.9839	117.8027	162.9	157531.0	1624.58	0.147	1624.73	0.98	1623.75	978062.75	978070.62	50.27	42.39	-32.04	10.36	0	10.36
July, 20	16	7	56	60	4.9839	117.8027	162.9	157536.0	1624.62	0.145	1624.77	0.98	1623.79	978062.79	978070.62	50.27	42.43	-32.04	10.39	0	10.39
July, 20	16	16	1	60	4.9839	117.8027	162.9	157536.0	1624.63	0.100	1624.73	0.99	1623.74	978062.74	978070.62	50.27	42.39	-32.04	10.36	0	10.36
July, 21	17	8	17	60	4.9839	117.8027	162.9	157537.0	1624.64	0.158	1624.80	1.01	1623.80	978062.80	978070.62	50.27	42.44	-32.04	10.40	0	10.40
July, 13	9	14	29	61	4.9868	117.8380	300.5	155385.0	1602.45	0.208	1602.66	0.46	1602.20	978041.20	978070.67	92.73	83.26	-59.11	4.16	0	4.16
July, 14	10	8	22	62	5.0372	118.3790	5.6	164480.0	1696.27	-0.007	1696.27	0.50	1695.77	978134.77	978071.78	1.72	64.71	-1.09	63.61	0	63.61
July, 14	10	8	37	63	5.0283	118.4277	11.1	164343.0	1694.86	0.008	1694.87	0.50	1694.37	978133.37	978071.63	3.43	65.17	-2.19	62.98	0	62.98
July, 14	10	8	51	64	5.0082	118.4877	8.7	164858.0	1700.17	0.020	1700.19	0.50	1699.69	978138.69	978071.32	2.68	70.05	-1.71	68.35	0	68.35
July, 14	10	13	18	64	5.0082	118.4877	8.7	164834.0	1699.93	0.251	1700.18	0.51	1699.66	978138.66	978071.32	2.68	70.03	-1.71	68.32	0	68.32
July, 14	10	13	47	64	5.0082	118.4877	8.7	164834.0	1699.93	0.248	1700.17	0.51	1699.66	978138.66	978071.32	2.68	70.02	-1.71	68.31	0	68.31
July, 14	10	9	4	65	4.9978	118.5588	28.8	164360.0	1695.04	0.033	1695.07	0.50	1694.57	978133.57	978071.15	8.90	71.31	-5.67	65.64	0	65.64
July, 14	10	9	18	66	4.9782	118.6225	143.8	162786.0	1678.80	0.050	1678.85	0.50	1678.35	978117.35	978070.85	44.39	90.89	-28.29	62.60	0	62.60
July, 14	10	9	31	67	4.9733	118.6805	234.9	161276.0	1663.22	0.064	1663.29	0.50	1662.78	978101.78	978070.77	72.49	103.50	-46.20	57.30	0	57.30
July, 14	10	9	44	68	4.9572	118.7453	11.3	165813.0	1710.03	0.080	1710.11	0.50	1709.60	978148.60	978070.52	3.49	81.57	-2.22	79.35	0	79.35
July, 14	10	10	8	69	4.9927	118.8092	18.7	163755.0	1688.80	0.107	1688.90	0.51	1688.40	978127.40	978071.07	5.78	82.10	-3.68	58.42	0	58.42
July, 14	10	10	20	70	5.0222	118.8738	16.2	162237.0	1673.14	0.120	1673.26	0.51	1672.75	978111.75	978071.54	5.00	45.21	-3.18	42.02	0	42.02
July, 14	10	11	52	70	5.0222	118.8736	16.2	162226.0	1673.02	0.215	1673.24	0.51	1672.73	978111.73	978071.54	5.00	45.19	-3.18	42.00	0	42.00
July, 14	10	10	42	71	5.0850	118.9265	8.1	161393.0	1664.43	0.143	1664.57	0.51	1664.07	978103.07	978072.22	2.50	33.35	-1.59	31.76	0	31.76
July, 14	10	10	58	72	5.1127	118.9740	10.3	160530.0	1655.53	0.156	1655.68	0.51	1655.18	978094.18	978072.98	3.17	24.37	-2.02	22.35	0	22.35
July, 14	10	11	9	73	5.1578	119.0142	32.2	159992.0	1649.97	0.166	1650.13	0.51	1649.63	978068.63	978073.71	9.95	24.87	-6.34	18.53	0	18.53
July, 17	13	10	7	73	5.1578	119.0142	32.2	160019.0	1650.26	0.017	1650.27	0.71	1649.56	978068.56	978073.71	9.95	24.80	-6.34	18.46	0	18.46
July, 17	13	15	59	73	5.1578	119.0142	32.2	160020.0	1650.27	0.175	1650.44	0.77	1649.67	978068.67	978073.71	9.95	24.92	-6.34	18.57	0	18.57
July, 14	10	11	43	74	5.0197	118.8893	3.4	162459.0	1675.43	0.208	1675.63	0.51	1675.13	978114.13	978071.50	1.04	43.67	-0.66	43.00	0	43.00
July, 14	10	12	49	75	4.9567	118.5865	0.2	166705.0	1719.23	0.249	1719.48	0.51	1718.96	978157.96	978070.51	0.05	87.51	-0.03	87.47	0	87.47
July, 14	10	14	14	76	5.0210	118.6015	27.3	163125.0	1682.30	0.237	1682.53	0.52	1682.02	978121.02	978071.52	8.43	57.93	-5.37	52.56	0	52.56
July, 14	10	14	41	77	5.0542	118.6222	45.9	161388.0	1664.38	0.218	1664.60	0.52	1664.08	978103.08	978072.04	14.15	45.19	-9.02	36.17	0	36.17
July, 14	10	15	43	78	5.0483	118.4880	32.6	162233.0	1673.10	0.162	1673.26	0.52	1672.74	978111.74	978071.95	10.06	49.84	-6.41	43.43	0	43.43
July, 14	10	16	0	79	5.0792	118.4655	100.4	159327.0	1643.11	0.141	1643.25	0.52	1642.73	978081.73	978072.44	30.96	40.26	-19.74	20.52	0	20.52
July, 15	11	8	41	80	4.9118	118.1472	11.5	167746.0	1729.97	-0.002	1729.96	0.56	1729.40	978168.4	978069.81	3.56	102.14	-2.26	99.88	0	99.88
July, 15	11	8	56	81	4.8647	118.0980	11.0	165082.0	1702.28	0.008	1702.29	0.56	1701.72	978140.7.	978069.09	3.38	75.02	-2.16	72.86	0	72.86
July, 15	11	9	17	82	4.7477	118.1192	31.4	162374.0	1674.55	0.024	1674.57	0.56	1674.01	978113.01	978067.32	9.71	55.39	-6.19	49.21	0	49.21
July, 15	11	9	49	84	4.6747	118.2155	53.5	163567.0	1686.88	0.051	1686.91	0.57	1686.34	978145.51	978067.12	1.25	79.64	-0.80	78.84	0	78.84
July, 15	11	10	2	85	4.6115	118.1952	93.3	161500.0	1665.53	0.082	1665.60	0.57	1665.03	978125.34	978066.24	16.50	75.60	-10.51	65.08	0	65.08
July, 15	11	10	13	86	4.5468	118.1918	58.5	162664.0	1677.54	0.071	1677.61	0.57	1677.05	978116.05	978064.39	18.04	69.70	-11.50	58.20	0	58.20
July, 15	11	10	24	87	4.4775	118.1902	36.0	163908.0	1690.35	0.079	1690.43	0.57	1689.87	978128.87	978063.40	11.12	78.59	-7.09	60.50	0	60.50
July, 15	11	10	35	88	4.4255	118.1840	35.6	164394.0	1695.39	0.088	1695.48	0.57	1694.91	978133.91	978062.67	10.98	82.21	-7.00	75.22	0	75.22
July, 15	11	15	41	88	4.4255	118.1840	35.6	164384.0	1695.28	0.197	1695.48	0.58	1694.90	978133.90	978062.67	10.98	82.21	-7.00	75.21	0	75.21
July, 25	21	9	42	88	4.4255	118.1840	35.6	164451.0	1695.98	0.189	1696.16	1.33	1694.83	978133.83	978062.67	10.98	82.14	-7.00	75.14	0	75.14
July, 15	11	10	49	89	4.4437	118.2525	3.2	164389.0	1695.13	0.104	1695.23	0.57	1694.67	978133.67	978062.93	0.99	71.73	-0.63	71.10	0	71.10
July, 15	11	11	2	90	4.4140	118.3208	12.8	164352.0	1694.95	0.116	1695.07	0.57	1694.50	978133.50	978062.51	3.95	74.94	-2.52	72.42	0	72.42
July, 15	11	11	12	91	4.3783	118.3643	40.1	165159.0	1703.28	0.125	1703.40	0.57	1702.84	978141.84	978062.02	12.38	92.20	-7.89	84.31	0	84.31
July, 15	11	11	23	92	4.3825	118.4260	41.8	165258.0	1704.30	0.137	1704.44	0.57	1703.87	978142.87	978062.22	12.91	93.56	-8.23	85.33	0	85.33
July, 15	11	11	38	93	4.4228	118.4880	31.2	165386.0	1705.41	0.155	1705.57	0.57	1705.00	978144.00	978062.84	9.63	90.99	-6.14	84.85	0	84.85
July, 15	11	11	49	94	4.4455	118.5500	32.0	164738.0	1698.94	0.167	1699.10	0.57	1698.53	978137.53	978062.96	9.89	84.47	-6.30	78.16	0	78.16
July, 15	11	12	8	95	4.4782	118.6147	-1.9	164196.0	1693.35	0.186	1693.53	0.57	1692.96	978131.96	978063.41	-0.57	67.97	0.36	68.34	0	68.34
July, 15	11	12	22	96	4.4795	118.6157	-0.5	164142.0	1692.79	0.198	1692.99	0.57	1692.41	978131.41	978063.43	-0.16	67.83	0.10	67.93	0	67.93
July, 15	11	13	5	95	4.4782	118.6147	-1.9	164198.0	1693.37	0.225	1693.59	0.57	1693.02	978132.02	978063.41	-0.57	68.03	0.36	68.40	0	68.40
July, 15	11	13	25	97	4.4192	118.6172	0.8	166301.0	1715.06	0.229	1715.29	0.57	1714.71	978153.71	978062.59	0.26	91.39	-0.17	91.22	0	91.22
July, 15	11	13	33	98	4.4230	118.6048	1.0	166194.0	1713.96	0.232	1714.19	0.57	1713.61	978152.61	978062.64	0.31	90.29	-0.20	90.09	0	90.09

SABAH LAND GRAVITY SURVEY JULY-AUGUST 1996
GRAVITY DATA PROCESSING, NOVEMBER 1996
GRAVITY BASE STATION IN UNIVERSITY OF MALAYA, MALAYSIA (G4/76) IS 978034.46 mGAL

DATE	DAY	TIME		STATION NUMBER	LATITUDE	LONGITUDE	ELEVATION	GRAVITY READING	EQUIVALENT	TIDE CORRECTION	TIDE CORRECTED	DRIFT CORRECTION	DRIFT CORRECTED	G Observed	G Normal	F AC	F AA	BC	BA	TC	BA inc TC
		HR	MIN		(Degrees)	(Degrees)	(Metres)		(mGal)	(mGal)	(mGal)	(mGal)	(mGal)	(mGal)	(mGal)	(mGal)	(mGal)	(mGal)	(mGal)	(mGal)	(mGal)
July, 15	11	13	58	99	4.5210	118.5323	2.7	164045.0	1691.79	0.240	1692.03	0.58	1691.45	978130.45	978064.02	0.83	67.27	-0.53	66.74	0	66.74
July, 15	11	14	21	100	4.5147	118.5828	-3.7	164185.0	1693.23	0.238	1693.47	0.58	1692.89	978131.89	978063.93	-1.14	66.82	0.73	67.55	0	67.55
July, 16	12	11	4	101	5.0853	118.4675	44.0	160207.0	1652.20	0.074	1652.27	0.63	1651.64	978090.64	978072.54	13.58	31.68	-8.68	23.00	0	23.00
July, 16	12	11	19	102	5.1182	118.4823	35.7	159264.0	1642.46	0.085	1642.54	0.63	1641.91	978080.91	978073.07	11.03	18.88	-7.03	11.85	0	11.85
July, 16	12	11	34	103	5.1513	118.4943	71.8	158172.0	1631.19	0.098	1631.29	0.63	1630.66	978069.66	978073.60	22.17	18.23	-14.13	4.10	0	4.10
July, 16	12	11	46	104	5.1897	118.5003	40.3	158079.0	1630.24	0.104	1630.34	0.63	1629.71	978068.71	978074.23	12.44	6.92	-7.93	-1.01	0	-1.01
July, 16	12	14	34	104	5.1897	118.5003	40.3	158073.0	1630.17	0.200	1630.37	0.64	1629.74	978068.74	978074.23	12.44	6.95	-7.93	-0.98	0	-0.98
July, 16	12	12	20	105	5.2160	118.5050	128.3	156184.0	1610.69	0.131	1610.82	0.63	1610.19	978049.19	978074.68	39.60	14.13	-25.24	-11.11	0	-11.11
July, 16	12	12	41	106	5.2463	118.5122	17.0	159034.0	1640.09	0.145	1640.23	0.63	1639.60	978078.60	978075.15	5.26	8.70	-3.35	5.35	0	5.35
July, 16	12	12	58	107	5.2813	118.5182	14.3	159644.0	1646.38	0.154	1646.53	0.63	1645.90	978084.90	978075.73	4.42	13.59	-2.82	10.77	0	10.77
July, 16	12	13	33	108	5.3337	118.5273	8.1	160591.0	1656.16	0.169	1656.33	0.64	1655.69	978094.69	978076.61	2.50	20.58	-1.59	18.99	0	18.99
July, 16	12	13	45	109	5.3130	118.5315	100.8	158526.0	1634.85	0.176	1635.02	0.64	1634.39	978073.39	978076.26	31.12	28.25	-19.83	8.41	0	8.41
July, 16	12	15	16	110	5.0928	118.4367	39.5	159954.0	1649.58	0.204	1649.78	0.64	1649.14	978088.14	978072.66	12.18	27.66	-7.76	19.90	0	19.90
July, 17	13	10	21	111	5.1407	119.0678	54.1	159321.0	1643.05	0.024	1643.07	0.72	1642.35	978081.35	978073.43	16.70	24.63	-10.65	13.98	0	13.98
July, 17	13	10	35	112	5.1610	119.1303	29.8	159636.0	1646.30	0.029	1646.33	0.72	1645.61	978084.61	978073.76	9.21	20.06	-5.87	14.19	0	14.19
July, 17	13	10	48	113	5.1990	119.1863	15.3	160005.0	1650.11	0.032	1650.14	0.72	1649.42	978088.42	978074.38	4.74	18.78	-3.02	15.76	0	15.76
July, 17	13	11	4	114	5.2723	119.2093	18.4	160028.0	1650.35	0.034	1650.38	0.73	1649.66	978088.66	978075.58	5.67	18.75	-3.62	15.13	0	15.13
July, 17	13	13	51	114	5.2723	119.2093	18.4	160007.0	1650.13	0.144	1650.28	0.76	1649.52	978088.52	978075.58	5.67	18.61	-3.62	14.99	0	14.99
July, 17	13	11	17	115	5.3338	119.1935	38.8	160672.0	1656.99	0.036	1657.03	0.73	1656.30	978095.30	978076.61	11.97	30.66	-7.63	23.03	0	23.03
July, 17	13	11	33	116	5.3440	119.1233	28.7	161656.0	1667.14	0.045	1667.19	0.73	1666.46	978105.46	978076.78	8.86	37.53	-5.64	31.89	0	31.89
July, 17	13	12	7	117	5.3640	119.0920	32.4	162381.0	1674.62	0.067	1674.69	0.74	1673.95	978112.95	978077.11	9.99	45.83	-6.37	39.46	0	39.46
July, 17	13	12	31	118	5.3942	119.0803	4.2	163618.0	1687.38	0.081	1687.46	0.74	1686.72	978125.72	978077.62	1.30	49.40	-0.83	48.57	0	48.57
July, 17	13	13	15	119	5.3283	119.0742	20.1	161887.0	1669.53	0.118	1669.64	0.75	1668.89	978107.89	978076.51	6.19	37.57	-3.95	33.62	0	33.62
July, 17	13	14	33	120	5.0817	119.0690	10.3	160677.0	1657.04	0.177	1657.22	0.77	1656.46	978095.46	978072.48	3.17	26.15	-2.02	24.12	0	24.12
July, 17	13	15	3	120	5.0817	119.0690	10.3	160678.0	1657.05	0.183	1657.24	0.77	1656.47	978095.47	978072.48	3.17	26.16	-2.02	24.14	0	24.14
July, 17	13	15	22	121	5.0823	119.0980	0.2	161192.0	1662.36	0.184	1662.54	0.77	1661.77	978100.77	978072.49	0.05	28.33	-0.03	28.30	0	28.30
July, 18	14	9	14	122	4.7255	118.0743	81.3	160387.0	1654.05	0.056	1654.11	0.85	1653.26	978092.26	978066.99	25.08	50.36	-15.99	34.37	0	34.37
July, 18	14	9	41	123	4.7450	118.0240	96.1	159684.0	1646.79	0.050	1646.84	0.85	1645.99	978084.99	978067.28	29.86	47.37	-18.91	28.47	0	28.47
July, 18	14	10	23	124	4.7210	117.9898	94.3	159884.0	1648.86	0.048	1648.90	0.85	1648.05	978087.05	978066.93	29.09	49.22	-18.54	30.67	0	30.67
July, 18	14	10	45	125	4.7252	117.9552	99.8	159660.0	1646.54	0.050	1646.59	0.85	1645.74	978084.74	978066.99	30.81	48.56	-19.64	28.92	0	28.92
July, 18	14	11	2	126	4.7218	117.9100	293.7	155722.0	1605.92	0.053	1605.98	0.85	1605.12	978044.12	978066.94	90.65	67.84	-57.78	10.06	0	10.06
July, 18	14	11	29	127	4.6975	117.8820	417.7	152606.0	1573.78	0.081	1573.84	0.86	1572.99	978011.99	978066.58	128.90	74.31	-82.16	-7.85	0	-7.85
July, 18	14	11	48	128	4.6948	117.9200	113.1	158754.0	1637.20	0.068	1637.27	0.86	1636.41	978075.41	978066.54	34.92	43.79	-22.28	21.51	0	21.51
July, 18	14	12	10	129	4.6723	117.9403	118.7	158476.0	1634.33	0.078	1634.41	0.86	1633.55	978072.55	978066.21	36.63	42.98	-23.36	19.63	0	19.63
July, 18	14	12	33	130	4.6313	117.8977	257.2	155623.0	1604.90	0.089	1604.99	0.86	1604.13	978043.13	978065.61	79.36	56.88	-50.58	6.30	0	6.30
July, 18	14	13	29	131	4.7078	117.9382	113.1	159031.0	1640.08	0.119	1640.17	0.86	1639.31	978078.31	978066.73	34.92	46.50	-22.26	24.24	0	24.24
July, 18	14	15	19	132	4.8700	118.0725	15.0	164445.0	1695.91	0.163	1696.08	0.87	1695.21	978134.21	978069.17	4.63	69.66	-2.95	66.71	0	66.71
July, 18	14	16	25	133	5.0350	118.3690	88.7	164149.0	1692.86	0.163	1693.02	0.88	1692.15	978131.15	978071.74	27.37	86.78	-17.45	69.33	0	69.33
July, 19	15	8	53	134	5.0023	118.1728	83.8	166815.0	1720.36	0.088	1720.45	0.95	1719.50	978158.50	978071.22	25.86	113.14	-16.48	96.66	0	96.66
July, 19	15	9	59	135	4.9865	117.9623	162.4	160342.0	1653.59	0.065	1653.66	0.95	1652.70	978091.70	978070.98	50.11	70.84	-31.94	38.90	0	38.90
July, 19	15	10	29	136	5.0098	117.9595	170.1	162539.0	1676.25	0.056	1676.31	0.95	1675.35	978114.35	978071.34	52.51	95.52	-33.47	62.05	0	62.05
July, 19	15	10	58	137	4.9892	117.9438	217.7	161504.0	1665.57	0.054	1665.63	0.96	1664.67	978103.67	978071.02	67.18	99.84	-42.82	57.01	0	57.01
July, 19	15	12	22	138	4.9793	117.8837	173.5	159008.0	1639.80	0.061	1639.86	0.96	1638.90	978077.90	978070.86	53.53	60.57	-34.12	26.45	0	26.45
July, 19	15	12	43	139	4.9502	117.8508	254.3	156764.0	1616.67	0.067	1616.74	0.96	1615.78	978054.78	978070.41	78.47	62.84	-50.02	12.82	0	12.82
July, 19	15	13	6	140	4.9227	117.8475	314.3	156505.0	1614.00	0.076	1614.08	0.96	1613.11	978052.11	978069.98	97.00	79.13	-61.83	17.30	0	17.30
July, 19	15	13	29	141	4.9342	117.8750	246.2	157736.0	1626.70	0.083	1626.78	0.96	1625.82	978064.82	978070.16	75.98	70.83	-48.43	22.21	0	22.21
July, 19	15	13	50	142	4.9545	117.8932	163.1	160077.0	1650.85	0.090	1650.94	0.96	1649.98	978088.98	978070.48	50.32	68.83	-32.07	36.75	0	36.75
July, 19	15	14	26	143	4.9567	117.8707	174.2	158975.0	1639.48	0.104	1639.58	0.96	1638.62	978077.62	978070.51	53.75	60.86	-34.26	26.60	0	26.60
July, 19	15	15	18	144	4.9120	117.8255	396.8	155732.0	1606.03	0.125	1606.15	0.96	1605.19	978044.19	978069.82	122.44	96.81	-78.05	18.77	0	18.77
July, 20	16	8	28	145	4.9987	117.8303	256.3	156335.0	1612.25	0.133	1612.38	0.96	1611.40	978050.40	978071.14	79.10	58.36	-50.42	7.94	0	7.94
July, 20	16	8	46	146	5.0078	117.7915	177.2	157663.0	1625.94	0.125	1626.07	0.98	1625.09	978064.09	978071.31	54.69	47.47	-34.88	12.61	0	12.61
July, 20	16	9	1	147	5.0413	117.7828	216.3	157223.0	1621.41	0.118	1621.52	0.98	1620.54	978059.54	978071.84	66.76	54.47	-42.56	11.91	0	11.91
July, 20	16	9	12	148	5.0590	117.7445	203.5	156441.0	1613.34	0.112	1613.45	0.98	1612.47	978051.47	978072.12	62.81	42.16	-40.03	2.12	0	2.12
July, 20	16	9	25	149	5.0728	117.7135	144.8	156674.0	1615.74	0.106	1615.85	0.98	1614.87	978053.87	978072.34	44.70	26.23	-28.49	-2.27	0	-2.27
July, 20	16	9	43	150	5.0935	117.6815	297.1	152790.0	1575.68	0.097	1575.78	0.98	1574.79	978013.79	978072.87	91.69	32.81	-58.44	-25.63	0	-25.63
July, 20	16	9	56	151	5.0908	117.6432	125.0	156058.0	1609.39	0.092	1609.48	0.98	1608.50	978047.50	978072.83	38.56	13.43	-24.58	-11.15	0	-11.15
July, 20	16	10	8	152	5.0733	117.6072	136.8	155813.0	1606.86	0.088	1606.95	0.98	1605.97	978044.97	978072.35	42.20	14.82	-26.90	-12.08	0	-12.08
July, 20	16	10	22	153	5.0415	117.5687	207.7	154940.0	1597.86	0.085	1597.94	0.98	1596.96	978035.96	978071.84	64.11	28.22	-40.86	-12.64	0	-12.64
July, 20	16	10	41	154	5.0135	117.5395	184.0	155458.0	1603.20	0.080	1603.28	0.98	1602.30	978041.30	978071.40	56.77	26.67	-36.19	-9.52	0	-9.52
July, 20	16	11	0	155	4.9905	117.5382	352.6	152187.0	1569.46	0.075	1569.53	0.98	1568.55	978007.56	978071.04	106.81	45.32	-69.36	-24.03	0	-24.03
July, 20	16	11	20	156	4.9895	117.5087	676.7	148494.0	1500.43	0.071	1500.50	0.99	1499.51	977938.51	978070.71	208.83	76.83	-133.11	-56.47	0	-56.47
July, 20	16	11	40	157	4.9712	117.4775	577.4	147296.0	1519.01	0.066	1519.08	0.99	1518.10	977957.10	978070.74	178.18	64.54	-113.57	-49.03	0	-49.03
July, 20	16	12	6	158	4.9740	117.4538	299.8	152330.0	1570.93	0.061	1571.00	0.99	1570.01	978009.01	978070.78	92.52	30.75	-58.97	-28.22	0	-28.22
July, 20	16	12	24	159	4.9590	117.4662	293.2	152054.0	1568.09	0.060	1568.15	0.99	1567.16	978006.16	978070.55	90.49	26.11	-57.68	-31.57	0	-31.57
July, 20	16	13	12	160	5.0147	117.5187	276.7	153692.0	1584.98	0.056	1585.04	0.99	1584.05	978023.05	978071.42	86.39	37.03	-54.43	-17.40	0	-17.40
July, 20	16	14	43	161	5.0217	117.6700	148.2	157600.0	1625.29	0.072	1625.37	0.99	1624.38	978063.38	978071.53	45.74	37.59	-29.16	8.43	0	8.43
July, 21	17	11	8	162	5.0072	118.1977	37.9	167889.0	1731.44	0.097	1731.54	1.01	1730.53	978169.53	978071.30	11.68	109.91	-7.45	102.46	0	102.46
July, 21	17	11	23	163	5.0117	118.1775	121.1	167078.0	1723.08	0.090	1723.17	1.01	1722.15	978161.15	978071.37	37.36	127.15	-23.82	103.33	0	103.33
July, 21	17	12	14	1163	4.9217	118.1200	30.4	167143.0	1723.75	0.074	1723.82	1.01	1722.81	978161.81	978069.97	9.37	101.21	-5.97	95.24	0	95.24
July, 21	17	13	13	164	5.0283	118.3283	14.3	166109.0	1713.06	0.052	1713.13	1.01	1712.12	978151.12	978071.63	4.42	83.91	-2.82	81.09	0	81.09
July, 23	19	9	40	165	5.0238	118.2050	80.1	167220.0	1724.54	0.179	1724.72	1.10	1723.62	978162.62	978071.56	24.72	115.78	-15.78	100.02	0	100.02
July, 23	19	10	39	166	4.9292	118.1095	66.4	165804.0	1709.93	0.174	1710.11	1.10	1709.01	978148.01	978070.08	20.50	98.42	-13.07	85.36	0	85.36
July, 23	19	11	56	168	4.8277	118.2068	127.3	160866.0	1658.99	0.139	1659.13	1.11	1658.02	978097.02	978065.55	39.29	70.76	-25.04	45.72	0	45.72
July, 23	19	14	23	169	4.2467	117.8822	1.9	162418.0	1675.00	0.027	1675.03	1.12	1673.91	978112.91	978060.23	0.57	53.25	-0.36	52.89	0	52.89
July, 23	19	16	40	169	4.2467	117.8822	1.9	162425.0	1675.08	0.009	1675.08	1.13	1673.95	978112.95	978060.23	0.57	53.29	-0.36	52.93	0	52.93
July, 24	20	7	54	169	4.2467	117.8822	1.9	162414.0	1674.96	0.119	1675.08	1.21	1673.86	978112.86	978060.23	0.57	53.21	-0.36	52.85	0	52.85
July, 24	20	16	28	169	4.2467	117.8822	1.9	162437.0	1675.20	-0.010	1675.19	1.25	1673.94	978112.94	978060.23	0.57	53.28	-0.36	52.92	0	52.92
July, 25	21	7	59	169	4.2467	117.8822	1.9	162431.0	1675.14	0.097	1675.23	1.32	1673.91	978112.91	978060.23	0.57	53.25	-0.36	52.89	0	52.89
July, 25	21	17	39	169	4.2467	117.8822	1.9	162453.0	1675.36	-0.018	1675.35	1.37	1673.98	978112.98	978060.23	0.57	53.31	-0.36	52.95	0	52.95
July, 26	22	8	26	169	4.2467	117.8822	1.9	162442.0	1675.25	0.095	1675.35	1.43	1673.92	978112.92	978060.23	0.57	53.25	-0.36	52.89	0	52.89
July, 23	19	16	27	170	4.2620	117.8840	14.3	162224.0	1673.00	0.008	1673.01	1.13	1671.88	978110.88	978060.44	4.42	54.86	-2.82	52.04	0	52.04
July, 24	20	16	19	170	4.2620	117.8840	14.3	162239.0	1673.16	-0.008	1673.15	1.25	1671.90	978110.90	978060.44	4.42	54.89	-2.82	52.07	0	52.07
July, 24	20	8	9	171	4.3075	117.8842	17.4	161981.0	1670.29	0.135	1670.42	1.21	1669.22	978108.22	978061.05	5.36	52.52	-3.42	49.11	0	49.11
July, 24	20	8	21	172	4.3320	117.8485	21.2	161487.0	1665.40	0.145	1665.54	1.21	1664.34	978103.34	978061.39	6.56	48.51	-4.18	44.33	0	44.33
July, 24	20	8	37	173	4.3782	117.8183	16.7	160765.0	1657.95	0.158	1658.11	1.21	1656.90	978095.90	978062.02	5.15	39.03	-3.28	35.75	0	35.75
July, 24	20	8	49	174	4.4140	117.7790	16.5	160265.0	1652.79	0.168	1652.96	1.21	1651.75	978090.75	978062.51	5.10	33.34	-3.25	30.09	0	30.09
July, 24	20	9	0	175	4.4625	117.7665	27.1	160236.0	1652.49	0.176	1652.67	1.21	1651.46	978090.46	978063.19	8.38	35.65	-5.34	30.31	0	30.31
July, 24	20	9	13	176	4.4883	117.7307	24.8	159934.0	1649.37	0.183	1649.55	1.21	1648.34	978087.34	978063.56	7.65	31.44	-4.88	26.56	0	26.56
July, 24	20	9	25	177	4.5185	117.7013	22.3	159774.0	1647.72	0.189	1647.91	1.21	1646.70	978086.70	978063.98	6.87	28.58	-4.38	24.20	0	24.20
July, 24	20	9	37	178	4.5132	117.6495	92.4	158307.0	1632.59	0.193	1632.78	1.21	1631.57	978070.57	978063.91	28.52	35.18	-18.18	17.00	0	17.00
July, 24	20	9	50	179	4.5025	117.6083	43.2	159186.0	1641.65	0.195	1641.85	1.21	1640.64	978079.64	978063.76	13.32	29.20	-8.49	20.71	0	20.71
July, 24	20	10	4	180	4.5203	117.5703	13.0	159744.0	1647.41	0.198	1647.61	1.22	1646.39	978086.39	978064.01	4.01	25.39	-2.55	22.84	0	22.84
July, 24	20	10	24	181	4.5175	117.5136	124.3	157471.0	1623.98	0.199	1624.16	1.22	1622.95	978061.95	978063.97	36.35	36.33	-24.45	11.88	0	11.88
July, 24	20	10	37	182	4.5578	117.4895	132.7	156849.0	1617.55	0.199	1617.75	1.22	1616.53	978055.53	978064.54	40.95	31.94	-26.10	5.83	0	5.83
July, 24	20	10	49	183	4.6068	117.4548	150.6	155638.0	1605.08	0.199	1605.28	1.22	1604.04	978043.04	978066.25	46.47	24.26	-29.62	-5.36	0	-5.36
July, 24	20	11	1	184	4.6122	117.4105	207.2	154271.0	1590.98	0.196	1591.15	1.22	1589.93	978028.93	978066.33	63.96	27.56	-40.78	-13.21	0	-13.21
July, 24	20	11	20	185	4.6100	117.3952	134.1	155579.0	1604.45	0.190	1604.64	1.22	1603.42	978042.42	978066.30	41.37	18.49	-26.37	-7.88	0	-7.88
July, 27	23	8	22	185	4.6100	117.3952	134.1	155628.0	1604.93	0.078	1605.01	1.52	1603.49	978042.49	978066.30	41.37	18.57	-26.37	-7.80	0	-7.80
July, 26	22	17	8	186	4.6100	117.3952	134.1	155628.0	1604.95	-0.005	1604.95	1.46	1603.49	978042.49	978066.30	41.37	18.56	-26.37	-7.81	0	-7.81

SABAH LAND GRAVITY SURVEY JULY-AUGUST 1996

GRAVITY DATA PROCESSING, NOVEMBER 1996

GRAVITY BASE STATION IN UNIVERSITY OF MALAYA, MALAYSIA (G4/76) IS 978034.46 mGAL

DATE	DAY	TIME		STATION NUMBER	LATITUDE	LONGITUDE	ELEVATION	GRAVITY READING	EQUIVALENT	TIDE CORRECTION	TIDE CORRECTED	DRIFT CORRECTION	DRIFT CORRECTED	G Observed	G Normal	FAC	FAA	BC	BA	TC	BA inc TC
		HR	MIN		(Degrees)	(Degrees)	(Metres)		(mGal)	(mGal)	(mGal)	(mGal)	(mGal)	(mGal)	(mGal)	(mGal)	(mGal)	(mGal)	(mGal)	(mGal)	(mGal)
July, 27	23	17	32	185	4.6100	117.3952	134.1	155628.0	1604.95	-0.008	1604.95	1.55	1603.40	978042.40	978065.30	41.37	18.47	-26.37	-7.90	0	-7.90
July, 27	23	17	41	185	4.6100	117.3952	134.1	155630.0	1604.97	-0.011	1604.96	1.55	1603.41	978042.41	978065.30	41.37	18.49	-26.37	-7.88	0	-7.88
July, 28	24	7	56	185	4.6100	117.3952	134.1	155633.0	1605.00	0.026	1605.03	1.60	1603.43	978042.43	978065.30	41.37	18.50	-26.37	-7.87	0	-7.87
July, 28	24	16	44	185	4.6100	117.3952	134.1	155639.0	1605.07	0.041	1605.11	1.63	1603.48	978042.48	978065.30	41.37	18.56	-26.37	-7.82	0	-7.82
July, 29	25	7	37	185	4.6100	117.3952	134.1	155646.0	1605.14	-0.004	1605.14	1.69	1603.45	978042.45	978065.30	41.37	18.52	-26.37	-7.85	0	-7.85
July, 24	20	12	18	186	4.4820	117.4910	122.3	157543.0	1624.71	0.154	1624.86	1.23	1623.63	978062.63	978063.47	37.73	36.90	-24.06	12.86	0	12.86
July, 24	20	12	46	187	4.3975	117.4922	3.4	160126.0	1651.36	0.128	1651.49	1.23	1650.26	978089.26	978062.29	1.04	28.01	-0.66	27.35	0	27.35
July, 26	22	11	33	187	4.3975	117.4922	3.4	160135.0	1651.45	0.217	1651.67	1.44	1650.23	978089.23	978062.29	1.04	27.98	-0.66	27.32	0	27.32
July, 24	20	14	1	188	4.4838	117.5890	11.6	159956.0	1649.60	0.074	1649.67	1.23	1648.44	978087.44	978063.49	3.59	27.54	-2.29	25.25	0	25.25
July, 24	20	14	59	189	4.4538	117.7787	13.8	160465.0	1654.86	0.033	1654.89	1.24	1653.65	978092.65	978063.07	4.27	33.95	-2.72	31.13	0	31.13
July, 24	20	15	25	190	4.4655	117.8022	176.9	157250.0	1621.68	0.021	1621.71	1.24	1620.46	978059.46	978063.23	54.59	50.82	-34.79	16.02	0	16.02
July, 24	20	15	36	191	4.4578	117.7955	125.6	158180.0	1631.28	0.016	1631.29	1.24	1630.05	978069.05	978063.13	38.77	44.69	-24.71	19.98	0	19.98
July, 25	21	8	27	192	4.2552	117.9438	12.8	162228.0	1673.04	0.123	1673.17	1.32	1671.84	978110.84	978060.36	3.95	54.45	-2.52	51.93	0	51.93
July, 25	21	8	40	193	4.2702	117.9972	55.3	162567.0	1676.54	0.135	1676.68	1.33	1675.35	978114.35	978060.56	17.07	70.87	-10.88	59.99	0	59.99
July, 25	21	8	51	194	4.2743	118.0542	39.6	162711.0	1678.03	0.144	1678.17	1.33	1676.84	978115.84	978060.61	12.23	67.47	-7.79	59.67	0	59.67
July, 25	21	9	3	195	4.3233	118.0930	40.3	162432.0	1675.15	0.158	1675.31	1.33	1673.98	978112.98	978061.27	12.44	84.15	-7.93	56.22	0	56.22
July, 25	21	9	20	196	4.3778	118.1313	7.3	163813.0	1689.39	0.173	1689.57	1.33	1688.24	978127.24	978062.01	2.24	67.46	-1.43	68.04	0	68.04
July, 25	21	9	30	197	4.4032	118.1778	53.6	163985.0	1690.96	0.181	1691.14	1.33	1689.81	978128.81	978062.36	16.55	83.00	-10.55	72.45	0	72.45
July, 25	21	10	26	198	4.5825	118.2287	77.6	162117.0	1671.90	0.212	1672.11	1.33	1670.78	978109.78	978064.90	23.94	68.81	-15.26	53.56	0	53.56
July, 25	21	10	49	199	4.5898	118.2812	51.6	162778.0	1678.72	0.215	1678.93	1.34	1677.60	978116.60	978065.00	15.92	67.52	-10.15	57.37	0	57.37
July, 25	21	11	38	200	4.6110	118.2550	120.1	161821.0	1668.85	0.207	1669.05	1.34	1667.71	978106.71	978065.31	37.05	78.45	-23.82	54.84	0	54.84
July, 25	21	12	1	201	4.6167	118.2987	46.2	163426.0	1685.40	0.197	1685.60	1.34	1684.26	978123.26	978065.39	14.26	72.12	-9.09	63.03	0	63.03
July, 25	21	12	42	202	4.5485	118.2863	50.9	162819.0	1677.08	0.170	1677.25	1.35	1675.90	978114.90	978064.38	15.72	86.24	-10.02	56.22	0	56.22
July, 25	21	13	19	203	4.4943	118.2737	79.1	162229.0	1673.05	0.137	1673.19	1.35	1671.84	978110.84	978063.64	24.41	71.61	-15.56	56.05	0	56.05
July, 25	21	13	33	204	4.4435	118.2708	42.3	163356.0	1684.68	0.122	1684.80	1.35	1683.45	978122.45	978062.93	13.06	72.59	-8.33	64.26	0	64.26
July, 25	21	14	0	204	4.4435	118.2708	42.3	163361.0	1684.73	0.098	1684.83	1.35	1683.48	978122.48	978062.93	13.06	72.61	-8.33	64.29	0	64.29
July, 25	21	14	49	205	4.3590	118.1868	0.0	164956.0	1701.19	0.050	1701.24	1.36	1699.88	978138.88	978061.76	0.00	77.12	0.00	77.12	0	77.12
July, 25	21	15	8	206	4.3677	118.2080	8.4	164786.0	1699.43	0.035	1699.47	1.36	1698.11	978137.11	978061.88	2.60	77.84	-1.66	76.18	0	76.18
July, 25	21	15	31	207	4.3187	118.1993	6.6	164508.0	1696.58	0.015	1696.58	1.36	1695.22	978134.22	978061.21	2.03	75.04	-1.29	73.75	0	73.75
July, 25	21	15	51	208	4.3145	118.2143	3.2	164685.0	1698.39	0.004	1698.39	1.36	1697.03	978136.03	978061.15	0.99	75.87	-0.63	75.24	0	75.24
July, 26	22	9	41	209	4.5681	117.7384	171.3	156706.0	1616.07	0.183	1616.26	1.43	1614.82	978053.82	978064.69	52.87	42.00	-33.70	8.30	0	8.30
July, 26	22	9	55	210	4.6017	117.7212	155.1	156865.0	1617.71	0.194	1617.91	1.44	1616.47	978055.47	978065.18	47.87	38.17	-30.52	7.65	0	7.65
July, 26	22	10	3	211	4.6244	117.7267	114.7	157545.0	1624.73	0.200	1624.93	1.44	1623.49	978062.49	978065.51	35.39	32.37	-22.55	9.82	0	9.82
July, 26	22	11	51	212	4.4300	117.4393	24.3	159694.0	1646.89	0.217	1647.11	1.44	1645.67	978084.67	978062.74	7.49	29.43	-4.78	24.65	0	24.65
July, 26	22	12	8	213	4.4622	117.3840	65.3	158509.0	1634.67	0.214	1634.89	1.44	1633.44	978072.44	978063.19	20.14	29.39	-12.84	16.56	0	16.56
July, 26	22	12	21	214	4.5025	117.3347	42.8	158089.0	1630.34	0.211	1630.55	1.44	1629.11	978068.11	978063.76	13.22	17.57	-8.42	9.14	0	9.14
July, 26	22	12	34	215	4.5080	117.2793	51.3	157072.0	1619.85	0.205	1620.05	1.45	1618.61	978057.61	978063.81	15.82	9.62	-10.08	-0.46	0	-0.46
July, 26	22	12	47	216	4.5230	117.2200	96.1	155976.0	1608.54	0.198	1608.74	1.45	1607.30	978046.30	978064.05	29.66	11.91	-18.91	-7.00	0	-7.00
July, 26	22	13	4	217	4.5330	117.1617	53.1	149755.0	1544.38	0.187	1544.56	1.45	1543.12	977982.12	978064.19	16.39	-65.68	-10.45	-76.13	0	-76.13
July, 26	22	13	23	218	4.5950	117.1708	163.2	153632.0	1584.36	0.174	1584.54	1.45	1583.09	978022.09	978065.06	50.37	7.38	-32.11	-24.72	0	-24.72
July, 26	22	13	43	219	4.6055	117.2278	138.4	154582.0	1594.16	0.157	1594.32	1.45	1592.87	978031.87	978065.23	42.72	9.36	-27.23	-17.87	0	-17.87
July, 26	22	14	0	220	4.5993	117.2638	120.9	155168.0	1600.21	0.141	1600.35	1.45	1598.90	978037.90	978065.14	37.31	10.07	-23.78	-13.71	0	-13.71
July, 26	22	14	16	221	4.5882	117.3043	108.8	155467.0	1603.29	0.125	1603.42	1.45	1601.97	978040.97	978064.98	33.56	9.55	-21.39	-11.84	0	-11.84
July, 26	22	14	32	222	4.6282	117.3423	109.0	155370.0	1602.29	0.110	1602.40	1.45	1600.95	978039.95	978065.56	33.62	8.01	-21.43	-13.42	0	-13.42
July, 26	22	16	20	223	4.3979	117.5582	2.5	159795.0	1647.94	0.006	1647.94	1.46	1646.48	978086.48	978062.29	0.79	23.98	-0.50	23.48	0	23.48
July, 27	23	9	17	224	4.6715	117.3058	114.3	154908.0	1597.51	0.136	1597.64	1.52	1596.12	978035.12	978066.19	35.28	4.21	-22.49	-18.28	0	-18.28
July, 27	23	9	31	225	4.7138	117.2828	265.9	151247.0	1559.76	0.151	1559.91	1.52	1558.39	977997.39	978066.82	82.06	12.64	-52.31	-39.67	0	-39.67
July, 27	23	9	44	226	4.7708	117.2622	294.9	149483.0	1541.57	0.164	1541.74	1.52	1540.22	977979.22	978067.67	91.01	2.56	-58.01	-55.45	0	-55.45
July, 27	23	9	57	227	4.8245	117.2365	170.6	152489.0	1572.57	0.175	1572.75	1.52	1571.23	978010.23	978068.48	52.66	-5.59	-33.57	-39.16	0	-39.16
July, 27	23	10	12	228	4.8832	117.2210	211.5	152567.0	1573.38	0.186	1573.56	1.52	1572.04	978011.04	978069.37	65.26	6.92	-41.59	-34.67	0	-34.67
July, 27	23	10	27	229	4.9203	117.1920	138.8	154235.0	1590.58	0.197	1590.78	1.52	1589.26	978028.26	978069.95	42.83	1.14	-27.30	-26.16	0	-26.16
July, 27	23	10	47	230	4.9695	117.1528	171.3	153874.0	1586.86	0.208	1587.07	1.52	1585.54	978024.54	978070.71	52.87	6.70	-33.70	-27.00	0	-27.00
July, 27	23	11	7	231	5.0127	117.1075	283.1	152110.0	1568.68	0.217	1568.88	1.53	1567.36	978006.36	978071.39	87.37	22.34	-55.69	-33.35	0	-33.35
July, 27	23	11	18	232	5.0318	117.1080	207.7	153650.0	1584.55	0.220	1584.77	1.53	1583.24	978022.24	978071.69	54.11	14.66	-40.86	-26.20	0	-26.20
July, 27	23	11	46	233	5.0837	117.0930	135.6	155296.0	1601.53	0.223	1601.75	1.53	1600.22	978039.22	978072.51	41.84	8.56	-26.67	-18.12	0	-18.12
July, 27	23	12	10	234	5.1408	117.0747	90.7	156588.0	1614.86	0.220	1615.08	1.53	1613.55	978052.55	978073.43	28.00	7.11	-17.84	-10.73	0	-10.73
July, 27	23	12	27	235	5.1647	117.1000	75.4	157283.0	1622.02	0.215	1622.24	1.53	1620.71	978059.71	978073.82	23.26	9.15	-14.83	-5.67	0	-5.67
July, 27	23	12	43	236	5.2205	117.0930	51.3	159072.0	1640.48	0.205	1640.68	1.53	1639.15	978078.15	978074.73	15.82	19.24	-10.08	9.16	0	9.16
July, 27	23	13	0	237	5.2770	117.0885	41.8	159827.0	1648.27	0.192	1648.46	1.53	1646.93	978086.93	978075.66	12.91	23.17	-8.23	14.95	0	14.95
July, 27	23	13	22	238	5.3050	117.0723	73.0	159722.0	1647.18	0.175	1647.36	1.53	1645.82	978084.82	978076.13	22.53	31.23	-14.36	16.87	0	16.87
July, 29	25	11	52	238	5.3050	117.0723	73.0	159742.0	1647.39	0.188	1647.58	1.70	1645.88	978084.88	978076.13	22.53	31.28	-14.36	16.92	0	16.92
July, 29	25	17	37	238	5.3050	117.0723	73.0	159764.0	1647.62	-0.005	1647.61	1.72	1645.89	978084.89	978076.13	22.53	31.30	-14.36	16.94	0	16.94
July, 30	26	8	58	238	5.3050	117.0723	73.0	159770.0	1647.68	-0.037	1647.64	1.77	1645.87	978084.87	978076.13	22.53	31.28	-14.36	16.92	0	16.92
July, 27	23	14	2	239	5.2202	117.0357	83.5	157180.0	1620.96	0.151	1621.11	1.54	1619.58	978058.58	978074.72	25.76	9.61	-16.42	-6.81	0	-6.81
July, 27	23	14	8	240	5.2173	117.0442	140.8	156156.0	1610.40	0.146	1610.55	1.54	1609.01	978048.01	978074.68	43.45	16.78	-27.70	-10.91	0	-10.91
July, 27	23	14	42	241	5.1385	117.0982	298.3	152828.0	1576.07	0.118	1576.19	1.54	1574.65	978013.65	978073.39	92.06	32.31	-58.68	-26.36	0	-26.36
July, 27	23	15	22	242	5.1163	117.0788	279.6	152862.0	1576.42	0.078	1576.50	1.54	1574.96	978013.96	978073.04	86.28	27.20	-54.99	-27.79	0	-27.79
July, 27	23	17	36	243	4.6100	117.3946	134.1	155635.0	1605.03	-0.009	1605.02	1.55	1603.47	978042.47	978065.30	41.37	18.54	-26.37	-7.83	0	-7.83
July, 27	23	17	49	243	4.6100	117.3946	134.1	155636.0	1605.04	-0.011	1605.02	1.55	1603.48	978042.48	978065.30	41.37	18.55	-26.37	-7.82	0	-7.82
July, 28	24	9	38	245	4.6003	117.1727	160.7	153604.0	1584.08	0.127	1584.20	1.61	1582.60	978021.60	978065.16	49.59	6.03	-31.61	-25.58	0	-25.58
July, 28	24	10	3	246	4.5712	117.1290	535.4	146005.0	1505.70	0.153	1505.85	1.61	1504.24	977943.24	978064.74	165.22	43.73	-105.31	-61.58	0	-61.58
July, 28	24	10	17	247	4.5527	117.0662	448.4	146592.0	1511.75	0.166	1511.92	1.61	1510.31	977949.31	978064.47	138.37	23.21	-88.20	-64.99	0	-64.99
July, 28	24	10	29	248	4.5500	117.0678	305.0	149379.0	1540.50	0.178	1540.68	1.61	1539.07	977978.07	978064.43	94.14	7.77	-60.00	-52.23	0	-52.23
July, 28	24	10	42	249	4.5822	116.9662	352.1	147995.0	1526.22	0.190	1526.41	1.61	1524.80	977963.80	978064.89	108.65	7.56	-69.26	-61.69	0	-61.69
July, 28	24	10	52	250	4.5800	116.9015	482.6	144837.0	1493.85	0.198	1493.85	1.61	1492.24	977931.24	978064.86	148.93	15.31	-94.93	-79.62	0	-79.62
July, 28	24	11	10	251	4.5917	116.8440	450.1	145937.0	1505.00	0.212	1505.21	1.61	1503.60	977942.60	978065.03	138.89	16.45	-86.53	-72.07	0	-72.07
July, 28	24	11	23	252	4.6145	116.7923	412.1	146446.0	1510.25	0.221	1510.47	1.61	1508.86	977947.86	978065.36	127.18	9.67	-81.06	-71.39	0	-71.39
July, 28	24	11	40	253	4.6118	116.7512	407.9	146279.0	1508.52	0.230	1508.75	1.61	1507.14	977946.14	978065.32	125.88	6.70	-80.23	-73.54	0	-73.54
July, 28	24	11	55	254	4.6043	116.6973	412.1	146207.0	1507.78	0.236	1508.02	1.61	1506.40	977945.40	978065.21	127.18	7.37	-81.06	-73.69	0	-73.69
July, 28	24	12	9	255	4.6020	116.6486	355.8	146898.0	1514.91	0.240	1515.15	1.62	1513.53	977952.53	978065.18	109.80	-2.85	-69.99	-72.83	0	-72.83
July, 28	24	12	27	256	4.6107	116.7233	372.7	146980.0	1515.76	0.243	1516.00	1.62	1514.38	977953.38	978065.31	115.00	3.08	-73.30	-70.22	0	-70.22
July, 28	24	12	45	257	4.6263	116.7795	404.9	146445.0	1510.24	0.242	1510.48	1.62	1508.86	977947.86	978065.53	124.94	7.27	-79.64	-72.37	0	-72.37
July, 28	24	12	59	258	4.6657	116.7772	572.1	142968.0	1474.37	0.240	1474.61	1.62	1472.99	977911.99	978066.11	176.56	22.45	-112.54	-90.09	0	-90.09
July, 28	24	13	32	259	4.5902	116.8777	535.6	143894.0	1483.92	0.225	1484.15	1.62	1482.53	977921.53	978065.01	166.27	21.70	-106.34	-83.56	0	-83.56
July, 28	24	13	43	260	4.5532	116.8407	487.0	145197.0	1497.36	0.218	1497.58	1.62	1495.96	977934.96	978064.48	150.28	20.77	-96.79	-75.02	0	-75.02
July, 28	24	13	57	261	4.5270	116.8085	519.7	145044.0	1495.79	0.207	1495.99	1.62	1494.37	977933.37	978064.10	160.38	29.66	-102.23	-72.58	0	-72.58
July, 28	24	14	8	262	4.5117	116.7577	488.2	145583.0	1501.35	0.198	1501.54	1.62	1499.92	977938.92	978063.89	150.85	25.88	-96.02	-70.34	0	-70.34
July, 28	24	15	12	263	4.5743	116.9947	298.5	149482.0	1541.56	0.138	1541.70	1.63	1540.07	977979.07	978064.78	92.11	6.40	-58.71	-52.31	0	-52.31
July, 29	25	8	55	264	4.9315	117.2258	421.6	149187.0	1538.52	0.046	1538.57	1.69	1536.88	977975.88	978070.12	130.09	35.86	-82.92	-47.07	0	-47.07
July, 29	25	9	9	265	4.9555	117.2427	189.0	153844.0	1586.55	0.058	1586.61	1.69	1584.92	978023.92	978070.49	58.33	11.76	-37.18	-25.42	0	-25.42
July, 29	25	9	24	266	4.9803	117.2720	232.2	153195.0	1579.86	0.073	1579.93	1.69	1578.24	978017.24	978070.57	71.66	18.33	-45.67	-27.36	0	-27.36
July, 29	25	12	46	267	5.3220	117.1022	221.1	157575.0	1625.04	0.208	1625.24	1.70	1623.54	978062.54	978076.41	68.22	54.36	-43.48	10.87	0	10.87
July, 29	25	13	0	268	5.3352	117.1603	64.4	160775.0	1658.05	0.209	1658.26	1.70	1656.56	978096.56	978076.83	19.88	38.81	-12.67	26.14	0	26.14
July, 29	25	13	12	269	5.3905	117.1773	61.5	163944.0	1690.75	0.202	1690.95	1.71	1689.24	978128.24	978077.56	18.99	69.67	-12.11	57.57	0	57.57
July, 29	25	13	24	270	5.4297	117.2087	61.7	164277.0	1694.18	0.196	1694.38	1.71	1692.67	978131.67	978078.23	19.06	72.49	-12.14	60.36	0	60.36
July, 29	25	13	34	271	5.4652	117.2352	75.4	163754.0	1688.79	0.190	1688.98	1.71	1687.27	978126.27	978078.83	23.26	70.70	-14.83	55.87	0	55.87
July, 29	25	13	50	272	5.5043	117.2273	90.0	163782.0	1689.07	0.180	1689.25	1.71	1687.55	978126.55	978079.51	27.79	74.83	-17.71	57.12	0	57.12
July, 29	25	14	3	273	5.5677	117.2212	96.6	162889.0	1679.86	0.167	1680.03	1.71	1678.32	978117.32	978080.61	29.82	66.53	-19.01	47.52	0	47.52
July, 29	25	14	14	274	5.6102	117.2250	105.9	162380.0	1674.61	0.156	1674.77	1.71	1673.06	978112.06	978081.36	32.68	63.38	-20.83	42.55	0	42.55
July, 29	25	14	29	275	5.6503	117.2472	80.3	162417.0	1674.99	0.141	1675.13	1.71	1673.42	978112.42	978082.06	24.77	55.13	-15.79	39.34	0	39.34

SABAH LAND GRAVITY SURVEY JULY-AUGUST 1995																				
GRAVITY DATA PROCESSING, NOVEMBER 1995																				
GRAVITY BASE STATION IN UNIVERSITY OF MALAYA, MALAYSIA (G4/76) IS 978034.46 mGAL																				
DATE	DAY	TIME		STATION NUMBER	LATITUDE	LONGITUDE	ELEVATION	GRAVITY READING	EQUIVALENT	TIDE CORRECTION	TIDE CORRECTED	DRIFT CORRECTION	DRIFT CORRECTED	G Observed	G Normal	FAC	FAA	BC	BA	TC	BA inc TC
		HR	MIN		(Degrees)	(Degrees)	(Metres)		(mGal)	(mGal)	(mGal)	(mGal)	(mGal)	(mGal)	(mGal)	(mGal)	(mGal)	(mGal)	(mGal)	(mGal)	(mGal)
July, 29	25	14	44	276	5.6422	117.1840	92.6	165071.0	1702.37	0.131	1702.50	1.71	1700.79	978139.79	978081.92	28.57	86.44	-18.21	68.23	0	68.23
July, 29	25	15	35	277	5.6208	117.1433	98.6	165685.0	1708.71	0.084	1708.79	1.71	1707.08	978146.08	978081.54	30.44	94.98	-19.40	75.57	0	75.57
July, 29	25	15	48	278	5.6208	117.1063	78.1	166763.0	1719.83	0.070	1719.90	1.71	1718.18	978157.18	978081.54	24.09	99.73	-15.36	84.38	0	84.38
July, 29	25	16	7	279	5.6137	117.1720	120.2	164704.0	1698.59	0.050	1698.64	1.72	1696.92	978135.92	978081.42	37.10	91.81	-23.65	67.96	0	67.96
July, 29	25	16	21	280	5.6130	117.2170	102.9	162784.0	1678.78	0.035	1678.81	1.72	1677.10	978116.10	978081.40	31.74	66.44	-20.23	46.20	0	46.20
July, 30	26	8	48	281	5.8087	117.1045	117.4	166153.0	1713.53	-0.045	1713.49	1.78	1711.71	978150.71	978081.33	36.22	105.60	-23.09	82.52	0	82.52
July, 30	26	8	57	282	5.5978	117.0783	134.2	165886.0	1710.57	-0.037	1710.54	1.78	1708.76	978147.76	978081.14	41.42	108.04	-26.40	81.64	0	81.64
July, 30	26	9	4	283	5.5745	117.0613	138.1	165880.0	1710.51	-0.030	1710.48	1.78	1708.70	978147.70	978080.73	42.62	109.59	-27.17	82.43	0	82.43
July, 30	26	9	20	284	5.6170	117.0595	148.1	165786.0	1709.75	-0.021	1709.73	1.78	1707.95	978146.95	978081.47	45.69	111.16	-29.12	82.04	0	82.04
July, 30	26	9	52	285	5.6227	117.0760	120.1	166134.0	1713.34	0.008	1713.35	1.78	1711.57	978150.57	978081.58	37.05	106.04	-23.62	82.43	0	82.43
July, 30	26	10	0	286	5.6562	117.0703	116.5	166406.0	1716.14	0.012	1716.16	1.78	1714.38	978153.38	978082.17	35.96	107.17	-22.92	84.25	0	84.25
July, 30	26	10	7	287	5.6640	117.0380	128.8	164683.0	1698.37	0.019	1698.39	1.78	1696.61	978135.61	978082.31	39.76	93.06	-25.34	67.72	0	67.72
August, 2	29	9	36	288	5.9425	116.0508	4.6	162525.0	1676.11	-0.064	1676.04	1.82	1674.23	978113.23	978087.38	1.41	27.25	-0.90	26.36	0	26.36
August, 2	29	10	18	288	5.9425	116.0508	4.6	162526.0	1676.12	-0.060	1676.06	1.82	1674.24	978113.24	978087.38	1.41	27.27	-0.90	26.37	0	26.37
August, 3	30	14	19	288	5.9425	116.0508	4.6	162512.0	1675.97	0.032	1676.01	1.81	1674.19	978113.19	978087.38	1.41	27.22	-0.90	26.33	0	26.33
August, 3	30	8	54	289	5.9160	116.0988	8.4	161772.0	1668.34	-0.020	1668.32	1.81	1666.51	978105.51	978086.88	2.60	21.22	-1.66	19.57	0	19.57
August, 3	30	9	5	290	5.9087	116.1375	16.5	161008.0	1660.46	-0.024	1660.43	1.81	1658.62	978097.62	978086.75	5.10	15.97	-3.25	12.72	0	12.72
August, 3	30	9	17	291	5.9082	116.1782	55.1	159595.0	1645.87	-0.029	1645.84	1.81	1644.03	978083.03	978086.74	17.02	13.31	-10.86	2.46	0	2.46
August, 3	30	9	28	292	5.8998	116.2167	166.9	156695.0	1615.96	-0.033	1615.93	1.81	1614.11	978053.11	978086.58	51.52	18.06	-32.84	-14.79	10	-4.79
August, 3	30	9	39	293	5.8793	116.2410	441.6	151043.0	1557.66	-0.035	1557.62	1.81	1555.81	977994.81	978086.21	136.29	44.89	-86.87	-41.98	20	-21.98
August, 3	30	9	58	294	5.8647	116.2597	852.7	142831.0	1472.96	-0.038	1472.92	1.81	1471.11	977910.11	978085.94	263.15	87.33	-167.73	-80.41	30	-50.41
August, 3	30	10	16	295	5.8552	116.2978	1282.1	134089.0	1382.79	-0.041	1382.75	1.81	1380.94	977819.94	978085.76	395.64	129.82	-252.18	-122.36	40	-82.36
August, 3	30	10	29	296	5.8390	116.3243	1571.4	128167.0	1321.72	-0.041	1321.68	1.81	1319.87	977758.87	978085.46	484.94	158.34	-309.10	-150.76	50	-100.76
August, 3	30	10	47	297	5.8130	116.3386	1722.7	124887.0	1287.89	-0.039	1287.85	1.81	1286.04	977725.04	978084.99	531.62	171.67	-338.86	-167.18	50	-117.18
August, 3	30	11	9	298	5.7643	116.3580	1159.8	135345.0	1395.75	-0.033	1395.71	1.81	1393.90	977832.90	978084.10	357.92	106.71	-228.13	-121.42	40	-81.42
August, 3	30	11	22	299	5.7393	116.3728	811.8	141681.0	1461.10	-0.029	1461.07	1.81	1459.26	977898.26	978083.66	250.51	85.11	-159.67	-94.56	30	-64.56
August, 3	30	11	33	300	5.7193	116.4077	643.8	144255.0	1487.65	-0.025	1487.62	1.81	1485.81	977924.81	978083.29	198.68	40.20	-126.64	-86.44	25	-61.44
August, 3	30	11	54	301	5.6895	116.3855	575.3	145724.0	1502.80	-0.014	1502.79	1.81	1500.97	977939.97	978082.40	177.55	36.12	-113.17	-78.05	20	-58.05

Key

G Normal = 978031.8.(1+0.0053024sin(lat)^2-0.000005sin(2lat)^4), FAC = Free Air Correction +0.3086h, h = Station Elevation, FAA = Free Air Anomaly

BC = Bouguer Correction -0.1967h, BA = Bouguer Anomaly excluding Terrain Correction, TC = Terrain Correction, BA inc TC = Bouguer Anomaly + Terrain Correction

APPENDIX 5

1995 Sabah Gravity Survey Results Summary

1995 SABAH GRAVITY SURVEY RESULTS SUMMARY

STATION	LATITUDE (°N)	LONGITUDE (°E)	ELEVATION (m)	FAA (mGal)	~~BA (mGal)~~	TC (mGal)	~~BA inc TC (mGal)~~
SWB0	3.0100	101.6800	50.0	-4.67	-14.50	0	-14.50
G4/76	3.0100	101.6800	50.0	3.78	-6.05	0	-6.05
1	5.9775	116.0758	16.9	30.51	27.20	0	27.20
2	5.9588	116.0723	3.4	25.55	24.89	0	24.89
3	5.4718	115.7962	9.6	18.98	17.09	0	17.09
4	5.4088	115.7505	11.3	18.59	16.36	0	16.36
5	5.5058	115.7795	3.5	9.89	9.19	0	9.19
6	5.5298	115.7447	4.2	1.64	0.82	0	0.82
7	5.5328	115.7005	2.5	-4.53	-5.03	0	-5.03
8	5.5370	115.6605	1.0	-6.65	-6.85	0	-6.85
9	5.5685	115.6012	0.2	3.73	3.70	0	3.70
10	5.5458	115.6242	1.9	1.62	1.25	0	1.25
11	5.3320	115.5912	6.7	-1.25	-2.58	0	-2.58
12	5.3595	115.6095	6.9	-4.43	-5.79	0	-5.79
13	5.3590	115.6473	9.1	-1.62	-3.41	0	-3.41
14	5.3722	115.6985	10.8	5.50	3.38	0	3.38
15	5.3533	115.7267	10.1	18.05	16.06	0	16.06
16	5.6662	115.8935	0.6	22.74	22.63	0	22.63
17	5.9843	116.0732	2.2	27.36	26.92	0	26.92
18	5.4067	115.6842	7.4	0.73	-0.73	0	-0.73
19	5.4260	115.6533	6.9	-3.58	-4.94	0	-4.94
20	5.4503	115.6237	4.4	-4.31	-5.17	0	-5.17
21	5.4607	115.5863	2.4	-4.53	-4.99	0	-4.99
22	5.4972	115.5548	2.4	0.40	-0.06	0	-0.06
23	5.5423	115.5808	0.7	2.73	2.60	0	2.60
24	5.4908	115.4857	0.0	5.31	5.31	0	5.31
25	5.2842	115.6822	4.7	15.66	14.73	0	14.73
26	5.3165	115.7083	7.6	17.95	16.46	0	16.46
27	5.3430	115.7460	3.0	13.34	12.74	0	12.74
28	5.6280	117.1310	100.7	101.06	81.26	0	81.26
29	5.0263	118.3335	6.1	86.81	85.61	0	85.61
30	5.0527	118.2795	36.6	93.48	86.28	0	86.28
31	5.0897	118.2505	41.8	72.79	64.56	0	64.56
32	5.1260	118.2218	31.7	50.58	44.34	0	44.34
33	5.1542	118.1848	45.2	49.94	41.06	0	41.06
33	5.1542	118.1848	45.2	50.01	41.12	0	41.12
34	5.1702	118.1360	49.9	52.79	42.98	0	42.98
35	5.2053	118.0980	40.0	31.01	23.15	0	23.15
36	5.2463	118.0607	36.8	18.69	11.46	0	11.46
37	5.2807	118.0243	31.2	3.97	-2.17	0	-2.17
38	5.3210	117.9913	31.5	-6.84	-13.04	0	-13.04
39	5.3577	117.9565	17.2	-9.87	-13.25	0	-13.25
40	5.4067	117.9500	7.8	-18.45	-19.98	0	-19.98
41	5.4058	117.9537	16.2	-17.03	-20.21	0	-20.21
42	5.3243	118.0107	85.3	-2.05	-18.84	0	-18.84
43	5.3312	118.0292	23.3	-10.43	-15.01	0	-15.01
44	5.3013	118.0327	22.9	-4.79	-9.30	0	-9.30
45	5.3240	118.0470	15.2	-10.26	-13.24	0	-13.24

N.B. Bouguer anomalies incorrectly calculated using -0·1967h instead of -0·1119h

46	5.1537	118.1953	57.5	48.26	36.95	0	36.95
47	5.1653	118.2287	91.1	32.77	14.86	0	14.86
48	5.0105	118.2552	30.0	103.75	97.84	0	97.84
49	4.9812	118.2148	128.7	120.79	95.46	0	95.46
50	4.9938	118.1648	109.1	117.47	96.01	0	96.01
51	4.9813	118.1162	143.5	121.08	92.86	0	92.86
52	4.9925	118.0710	162.0	115.49	83.61	0	83.61
52	4.9925	118.0710	162.0	115.50	83.63	0	83.63
53	5.0050	118.0210	253.6	124.03	74.14	0	74.14
54	4.9980	117.9800	188.2	114.32	77.31	0	77.31
55	4.9575	117.9363	229.7	91.47	46.29	0	46.29
56	4.9587	117.9188	159.9	77.62	46.17	0	46.17
57	4.9817	117.9018	128.5	78.68	53.40	0	53.40
58	4.9825	117.8735	125.5	61.04	36.36	0	36.36
59	4.9638	117.8028	154.5	41.16	10.78	0	10.78
60	4.9639	117.8027	162.9	42.40	10.35	0	10.35
61	4.9668	117.8360	300.5	63.26	4.16	0	4.16
62	5.0372	118.3790	5.6	64.71	63.61	0	63.61
63	5.0283	118.4277	11.1	65.17	62.98	0	62.98
64	5.0082	118.4877	8.7	70.03	68.32	0	68.32
65	4.9978	118.5568	28.8	71.31	65.64	0	65.64
66	4.9782	118.6225	143.8	90.89	62.60	0	62.60
67	4.9733	118.6805	234.9	103.50	57.30	0	57.30
68	4.9572	118.7453	11.3	81.57	79.35	0	79.35
69	4.9927	118.8092	18.7	62.10	58.42	0	58.42
70	5.0222	118.8738	16.2	45.20	42.01	0	42.01
71	5.0650	118.9265	8.1	33.35	31.76	0	31.76
72	5.1127	118.9740	10.3	24.37	22.35	0	22.35
73	5.1578	119.0142	32.2	24.87	18.52	0	18.52
74	5.0197	118.8893	3.4	43.67	43.00	0	43.00
75	4.9567	118.5865	0.2	87.51	87.47	0	87.47
76	5.0210	118.6015	27.3	57.93	52.56	0	52.56
77	5.0542	118.6222	45.9	45.19	36.17	0	36.17
78	5.0483	118.4860	32.6	49.84	43.43	0	43.43
79	5.0792	118.4655	100.4	40.26	20.52	0	20.52
80	4.9118	118.1472	11.5	102.14	99.88	0	99.88
81	4.8647	118.0980	11.0	75.02	72.86	0	72.86
82	4.7477	118.1192	31.4	55.39	49.21	0	49.21
83	4.7340	118.1997	4.0	79.64	78.84	0	78.84
84	4.6747	118.2155	53.5	75.60	65.08	0	65.08
85	4.6115	118.1952	93.3	67.51	49.16	0	49.16
86	4.5468	118.1918	58.5	69.70	58.20	0	58.20
87	4.4775	118.1902	36.0	76.59	69.50	0	69.50
88	4.4255	118.1840	35.6	82.19	75.19	0	75.19
89	4.4437	118.2525	3.2	71.73	71.10	0	71.10
90	4.4140	118.3208	12.8	74.94	72.42	0	72.42
91	4.3783	118.3643	40.1	92.20	84.31	0	84.31
92	4.3925	118.4260	41.8	93.56	85.33	0	85.33
93	4.4228	118.4860	31.2	90.99	84.85	0	84.85
94	4.4455	118.5500	32.0	84.47	78.16	0	78.16
95	4.4782	118.6147	-1.9	68.00	68.37	0	68.37
96	4.4795	118.6157	-0.5	67.83	67.93	0	67.93
97	4.4192	118.6172	0.8	91.39	91.22	0	91.22
98	4.4230	118.6048	1.0	90.29	90.09	0	90.09

99	4.5210	118.5323	2.7	67.27	66.74	0	66.74
100	4.5147	118.5828	-3.7	66.82	67.55	0	67.55
101	5.0853	118.4675	44.0	31.68	23.03	0	23.03
102	5.1182	118.4823	35.7	18.88	11.85	0	11.85
103	5.1513	118.4943	71.8	18.23	4.10	0	4.10
104	5.1897	118.5003	40.3	6.94	-0.99	0	-0.99
105	5.2160	118.5050	128.3	14.13	-11.11	0	-11.11
106	5.2463	118.5122	17.0	8.70	5.35	0	5.35
107	5.2813	118.5162	14.3	13.59	10.77	0	10.77
108	5.3337	118.5273	8.1	20.58	18.99	0	18.99
109	5.3130	118.5315	100.8	28.25	8.41	0	8.41
110	5.0928	118.4367	39.5	27.66	19.90	0	19.90
111	5.1407	119.0678	54.1	24.63	13.98	0	13.98
112	5.1610	119.1303	29.8	20.06	14.19	0	14.19
113	5.1990	119.1863	15.3	18.78	15.76	0	15.76
114	5.2723	119.2093	18.4	18.68	15.06	0	15.06
115	5.3338	119.1935	38.8	30.66	23.03	0	23.03
116	5.3440	119.1233	28.7	37.53	31.89	0	31.89
117	5.3640	119.0920	32.4	45.83	39.46	0	39.46
118	5.3942	119.0803	4.2	49.40	48.57	0	48.57
119	5.3283	119.0742	20.1	37.57	33.62	0	33.62
120	5.0817	119.0690	10.3	26.16	24.14	0	24.14
121	5.0823	119.0980	0.2	28.33	28.30	0	28.30
122	4.7255	118.0743	81.3	50.35	34.37	0	34.37
123	4.7450	118.0240	96.1	47.37	28.47	0	28.47
124	4.7210	117.9898	94.3	49.22	30.67	0	30.67
125	4.7252	117.9552	99.8	48.56	28.92	0	28.92
126	4.7218	117.9100	293.7	67.84	10.06	0	10.06
127	4.6975	117.8820	417.7	74.31	-7.85	0	-7.85
128	4.6948	117.9200	113.1	43.79	21.53	0	21.53
129	4.6723	117.9403	118.7	42.98	19.63	0	19.63
130	4.6313	117.8977	257.2	56.88	6.30	0	6.30
131	4.7078	117.9382	113.1	46.50	24.24	0	24.24
132	4.8700	118.0725	15.0	69.66	66.71	0	66.71
133	5.0350	118.3690	88.7	86.78	69.33	0	69.33
134	5.0023	118.1728	83.8	113.14	96.66	0	96.66
135	4.9865	117.9623	162.4	70.84	38.90	0	38.90
136	5.0098	117.9595	170.1	95.52	62.05	0	62.05
137	4.9892	117.9438	217.7	99.84	57.01	0	57.01
138	4.9793	117.8637	173.5	60.57	26.45	0	26.45
139	4.9502	117.8508	254.3	62.84	12.82	0	12.82
140	4.9227	117.8475	314.3	79.13	17.30	0	17.30
141	4.9342	117.8750	246.2	70.63	22.21	0	22.21
142	4.9545	117.8932	163.1	68.83	36.75	0	36.75
143	4.9567	117.8707	174.2	60.86	26.60	0	26.60
144	4.9120	117.8255	396.8	96.81	18.77	0	18.77
145	4.9967	117.8303	256.3	58.36	7.94	0	7.94
146	5.0078	117.7915	177.2	47.47	12.61	0	12.61
147	5.0413	117.7828	216.3	54.47	11.91	0	11.91
148	5.0590	117.7445	203.5	42.16	2.12	0	2.12
149	5.0728	117.7135	144.8	26.23	-2.27	0	-2.27
150	5.0935	117.6815	297.1	32.81	-25.63	0	-25.63
151	5.0908	117.6432	125.0	13.43	-11.15	0	-11.15
152	5.0733	117.6072	136.8	14.82	-12.08	0	-12.08

153	5.0415	117.5687	207.7	28.22	-12.64	0	-12.64
154	5.0135	117.5395	184.0	26.67	-9.52	0	-9.52
155	4.9905	117.5382	352.6	45.32	-24.03	0	-24.03
156	4.9695	117.5087	676.7	76.63	-56.47	0	-56.47
157	4.9712	117.4775	577.4	64.54	-49.03	0	-49.03
158	4.9740	117.4538	299.8	30.75	-28.22	0	-28.22
159	4.9590	117.4692	293.2	26.11	-31.57	0	-31.57
160	5.0147	117.5187	276.7	37.03	-17.40	0	-17.40
161	5.0217	117.6700	148.2	37.59	8.43	0	8.43
162	5.0072	118.1977	37.9	109.91	102.46	0	102.46
163	5.0117	118.1775	121.1	127.15	103.33	0	103.33
1163	4.9217	118.1200	30.4	101.21	95.24	0	95.24
164	5.0283	118.3283	14.3	83.91	81.09	0	81.09
165	5.0238	118.2050	80.1	115.78	100.02	0	100.02
166	4.9292	118.1095	66.4	98.42	85.36	0	85.36
167	4.9278	118.1157	37.1	98.60	91.30	0	91.30
168	4.6277	118.2068	127.3	70.76	45.72	0	45.72
169	4.2467	117.8822	1.9	53.27	52.90	0	52.90
170	4.2620	117.8840	14.3	54.87	52.05	0	52.05
171	4.3075	117.8842	17.4	52.52	49.11	0	49.11
172	4.3320	117.8465	21.2	48.51	44.33	0	44.33
173	4.3782	117.8183	16.7	39.03	35.75	0	35.75
174	4.4140	117.7790	16.5	33.34	30.09	0	30.09
175	4.4625	117.7665	27.1	35.65	30.31	0	30.31
176	4.4883	117.7307	24.8	31.44	26.56	0	26.56
177	4.5185	117.7013	22.3	28.58	24.20	0	24.20
178	4.5132	117.6495	92.4	35.18	17.00	0	17.00
179	4.5025	117.6063	43.2	29.20	20.71	0	20.71
180	4.5203	117.5703	13.0	25.39	22.84	0	22.84
181	4.5175	117.5135	124.3	36.33	11.88	0	11.88
182	4.5578	117.4895	132.7	31.94	5.83	0	5.83
183	4.6068	117.4548	150.6	24.26	-5.36	0	-5.36
184	4.6122	117.4105	207.2	27.56	-13.21	0	-13.21
185	4.6100	117.3952	134.1	18.52	-7.85	0	-7.85
186	4.4820	117.4910	122.3	36.90	12.85	0	12.85
187	4.3975	117.4922	3.4	28.00	27.34	0	27.34
188	4.4838	117.5890	11.6	27.54	25.25	0	25.25
189	4.4538	117.7787	13.8	33.85	31.13	0	31.13
190	4.4655	117.8022	176.9	50.82	16.02	0	16.02
191	4.4578	117.7955	125.6	44.69	19.98	0	19.98
192	4.2552	117.9438	12.8	54.45	51.93	0	51.93
193	4.2702	117.9972	55.3	70.87	59.99	0	59.99
194	4.2743	118.0542	39.6	67.47	59.67	0	59.67
195	4.3233	118.0930	40.3	64.15	56.22	0	56.22
196	4.3778	118.1313	7.3	67.46	66.04	0	66.04
197	4.4032	118.1778	53.6	83.00	72.45	0	72.45
198	4.5825	118.2287	77.6	68.81	53.56	0	53.56
199	4.5898	118.2812	51.6	67.52	57.37	0	57.37
200	4.6110	118.2550	120.1	78.45	54.84	0	54.84
201	4.6167	118.2987	46.2	72.12	63.03	0	63.03
202	4.5465	118.2853	50.9	66.24	56.22	0	56.22
203	4.4943	118.2737	79.1	71.61	56.05	0	56.05
204	4.4435	118.2708	42.3	72.61	64.28	0	64.28
205	4.3590	118.1868	0.0	77.12	77.12	0	77.12

206	4.3677	118.2060	8.4	77.84	76.18	0	76.18
207	4.3187	118.1993	6.6	75.04	73.75	0	73.75
208	4.3145	118.2143	3.2	75.87	75.24	0	75.24
209	4.5681	117.7384	171.3	42.00	8.30	0	8.30
210	4.6017	117.7212	155.1	38.17	7.65	0	7.65
211	4.6244	117.7267	114.7	32.37	9.82	0	9.82
212	4.4300	117.4393	24.3	29.43	24.65	0	24.65
213	4.4622	117.3840	65.3	29.39	16.56	0	16.56
214	4.5025	117.3347	42.8	17.57	9.14	0	9.14
215	4.5060	117.2793	51.3	9.62	-0.46	0	-0.46
216	4.5230	117.2200	96.1	11.91	-7.00	0	-7.00
217	4.5330	117.1617	53.1	-65.68	-76.13	0	-76.13
218	4.5950	117.1708	163.2	7.38	-24.72	0	-24.72
219	4.6055	117.2278	138.4	9.36	-17.87	0	-17.87
220	4.5993	117.2638	120.9	10.07	-13.71	0	-13.71
221	4.5882	117.3043	108.8	9.55	-11.84	0	-11.84
222	4.6282	117.3423	109.0	8.01	-13.42	0	-13.42
223	4.3979	117.5582	2.5	23.98	23.48	0	23.48
224	4.6715	117.3058	114.3	4.21	-18.28	0	-18.28
225	4.7138	117.2828	265.9	12.64	-39.67	0	-39.67
226	4.7708	117.2622	294.9	2.56	-55.45	0	-55.45
227	4.8245	117.2365	170.6	-5.59	-39.16	0	-39.16
228	4.8832	117.2210	211.5	6.92	-34.67	0	-34.67
229	4.9203	117.1920	138.8	1.14	-26.16	0	-26.16
230	4.9695	117.1528	171.3	6.70	-27.00	0	-27.00
231	5.0127	117.1075	283.1	22.34	-33.35	0	-33.35
232	5.0318	117.1060	207.7	14.66	-26.20	0	-26.20
233	5.0837	117.0930	135.6	8.55	-18.12	0	-18.12
234	5.1408	117.0747	90.7	7.11	-10.73	0	-10.73
235	5.1647	117.1000	75.4	9.15	-5.67	0	-5.67
236	5.2205	117.0930	51.3	19.24	9.16	0	9.16
237	5.2770	117.0885	41.8	23.17	14.95	0	14.95
238	5.3050	117.0723	73.0	31.28	16.91	0	16.91
239	5.2202	117.0357	83.5	9.61	-6.81	0	-6.81
240	5.2173	117.0442	140.8	16.78	-10.91	0	-10.91
241	5.1385	117.0982	298.3	32.31	-26.36	0	-26.36
242	5.1163	117.0788	279.6	27.20	-27.79	0	-27.79
243	4.6100	117.3946	134.1	18.55	-7.82	0	-7.82
245	4.6003	117.1727	160.7	6.03	-25.58	0	-25.58
246	4.5712	117.1290	535.4	43.73	-61.58	0	-61.58
247	4.5527	117.0662	448.4	23.21	-64.99	0	-64.99
248	4.5500	117.0678	305.0	7.77	-52.23	0	-52.23
249	4.5822	116.9662	352.1	7.56	-61.69	0	-61.69
250	4.5800	116.9015	482.6	15.31	-79.62	0	-79.62
251	4.5917	116.8440	450.1	16.45	-72.07	0	-72.07
252	4.6145	116.7923	412.1	9.67	-71.39	0	-71.39
253	4.6118	116.7512	407.9	6.70	-73.54	0	-73.54
254	4.6043	116.6973	412.1	7.37	-73.69	0	-73.69
255	4.6020	116.6488	355.8	-2.85	-72.83	0	-72.83
256	4.6107	116.7233	372.7	3.08	-70.22	0	-70.22
257	4.6263	116.7795	404.9	7.27	-72.37	0	-72.37
258	4.6657	116.7772	572.1	22.45	-90.09	0	-90.09
259	4.5902	116.8777	535.6	21.79	-83.55	0	-83.55
260	4.5532	116.8407	487.0	20.77	-75.02	0	-75.02

261	4.5270	116.8065	519.7	29.65	-72.58	0	-72.58
262	4.5117	116.7577	488.2	25.68	-70.34	0	-70.34
263	4.5743	116.9947	298.5	6.40	-52.31	0	-52.31
264	4.9315	117.2258	421.6	35.85	-47.07	0	-47.07
265	4.9555	117.2427	189.0	11.76	-25.42	0	-25.42
266	4.9603	117.2720	232.2	18.33	-27.35	0	-27.35
267	5.3220	117.1022	221.1	54.35	10.87	0	10.87
268	5.3352	117.1603	64.4	38.81	26.14	0	26.14
269	5.3905	117.1773	61.5	69.67	57.57	0	57.57
270	5.4297	117.2067	61.7	72.49	60.35	0	60.35
271	5.4652	117.2352	75.4	70.70	55.87	0	55.87
272	5.5043	117.2273	90.0	74.83	57.12	0	57.12
273	5.5677	117.2212	96.6	66.53	47.52	0	47.52
274	5.6102	117.2250	105.9	63.38	42.55	0	42.55
275	5.6503	117.2472	80.3	55.13	39.34	0	39.34
276	5.6422	117.1840	92.6	86.44	68.23	0	68.23
277	5.6208	117.1433	98.6	94.98	75.57	0	75.57
278	5.6208	117.1063	78.1	99.73	84.38	0	84.38
279	5.6137	117.1720	120.2	91.61	67.96	0	67.96
280	5.6130	117.2170	102.9	66.44	46.20	0	46.20
281	5.6087	117.1045	117.4	105.60	82.52	0	82.52
282	5.5978	117.0783	134.2	108.04	81.64	0	81.64
283	5.5745	117.0613	138.1	109.59	82.43	0	82.43
284	5.6170	117.0595	148.1	111.16	82.04	0	82.04
285	5.6227	117.0760	120.1	106.04	82.43	0	82.43
286	5.6562	117.0703	116.5	107.17	84.25	0	84.25
287	5.6640	117.0380	128.8	93.06	67.72	0	67.72
288	5.9425	116.0508	4.6	27.25	26.35	0	26.35
289	5.9160	116.0988	8.4	21.22	19.57	0	19.57
290	5.9087	116.1375	16.5	15.97	12.72	0	12.72
291	5.9082	116.1782	55.1	13.31	2.46	0	2.46
292	5.8998	116.2167	166.9	18.05	-14.79	10	-4.79
293	5.8793	116.2410	441.6	44.89	-41.98	20	-21.98
294	5.8647	116.2597	852.7	87.33	-80.41	30	-50.41
295	5.8552	116.2978	1282.1	129.82	-122.36	40	-82.36
296	5.8390	116.3243	1571.4	158.34	-150.76	50	-100.76
297	5.8130	116.3385	1722.7	171.67	-167.18	50	-117.18
298	5.7643	116.3580	1159.8	106.71	-121.42	40	-81.42
299	5.7393	116.3728	811.8	65.11	-94.56	30	-64.56
300	5.7193	116.4077	643.8	40.20	-86.44	25	-61.44
301	5.6695	116.3655	575.3	35.12	-78.05	20	-58.05

Key

FAA = Free-Air Anomaly, BA = Bouguer Anomaly (excluding Terrain Correction),
TC = Terrain Correction, BA inc TC = Bouguer Anomaly including Terrain Correction

APPENDIX 6

Corrected Darvel Bay Gravity Data

CORRECTED DARVEL BAY GRAVITY DATA

Station	Latitude (°N)	Longitude (°E)	Elevation (m)	Bouguer Anomaly (mGal)
Darvel Bay				
1	4.9788	118.3437	2.4	116.46
2	4.9925	118.3467	1.1	108.80
3	4.9920	118.3583	1.8	107.39
4	4.9758	118.3810	0.4	108.19
5	4.9628	118.3475	0.6	115.08
6	4.9540	118.3180	0.7	121.00
7	4.9618	118.3008	1.2	116.32
8	4.9670	118.3223	0.9	116.82
9	4.9250	118.2628	1.8	109.27
10	4.9475	118.2502	1.8	108.55
11	4.9523	118.2928	1.5	119.07
12	4.9428	118.2348	1.6	106.94
13	4.9250	118.1988	1.7	108.24
14	4.9410	118.2143	1.8	103.00
15	4.9647	118.2135	0.9	109.50
16	4.9307	118.2320	1.5	107.85
17	4.8142	118.2862	1.8	106.42
18	4.8105	118.3070	1.5	108.01
19	4.7902	118.2848	1.8	108.41
20	4.8228	118.2728	1.8	103.82
21	4.8785	118.1535	0.6	90.10
22	4.9003	118.2040	0.4	102.75
23	4.9085	118.2387	0.6	108.30
24	4.9377	118.2722	0.3	116.32
25	4.9847	118.3165	1.7	111.11
26	5.0220	118.3278	2.7	85.87
27	4.6868	118.2503	2.5	71.37
28	4.7705	118.2338	1.6	100.02
29	4.8015	118.3240	1.8	109.64
30	4.8067	118.3558	2.0	108.93
31	4.7892	118.3683	1.0	111.55
32	4.7665	118.3065	1.3	105.66
33	4.7573	118.3840	1.7	110.75
34	4.7748	118.3787	1.8	112.25
35	4.7963	118.3783	1.7	109.59
36	4.8062	118.3747	1.8	107.82
37	4.7915	118.4048	1.4	112.40
38	4.7833	118.4132	1.4	113.03
39	4.7617	118.4743	-	109.00
40	4.7467	118.5123	1.8	110.37
41	4.7263	118.4575	1.5	102.01
42	4.7097	118.3960	1.4	98.67
43	4.7283	118.2280	0.9	82.44
44	4.6572	118.3190	1.5	67.76
45	4.6708	118.3510	1.8	76.62
46	4.6727	118.3747	1.7	80.24
47	4.6263	118.3290	3.6	66.94
48	4.6462	118.3730	3.0	74.40
49	4.6308	118.4090	1.6	75.07
50	4.6015	118.4202	1.6	74.08
51	4.6072	118.4630	1.5	79.35

52	4.5945	118.4830	0.7	77.77
53	4.6262	118.3680	1.5	71.36
54	4.9353	118.4315	0.4	117.38
55	4.9260	118.4668	1.0	113.79
56	4.9497	118.4648	1.8	101.22
57	4.9565	118.4465	1.7	103.77
58	4.9512	118.3225	1.2	121.31
59	4.9972	118.4123	4.8	87.61
60	5.0098	118.4175	1.5	77.86
61	5.0280	118.3757	1.5	71.80
62	5.0117	118.3175	1.6	90.04
Lahad Datu - Kunak				
0	5.0297	118.3233	14	80.69
101	5.0283	118.2967	13	86.57
102	5.0137	118.2788	7	96.23
103	5.0083	118.2467	6	98.75
104	4.9835	118.2320	126	103.33
105	4.9445	118.1800	39	99.41
106	4.9122	118.1433	12	98.63
107	4.8878	118.1010	8	82.67
108	4.8645	118.0922	9	71.47
109	4.8312	118.0978	8	59.29
110	4.8188	118.1000	155	56.91
111	4.7888	118.0895	36	<54.00
112	4.7488	118.1145	31	<53.6
113	4.7305	118.1620	8	70.5
114	4.7223	118.1888	7	73.02
115	4.6895	118.2102	29	70.77
116	4.7383	118.1218	64	<60.42
117	5.0608	118.2937	23	<55.41

APPENDIX 7

Corrected USAMS(FE) Sabah Gravity Data Set

CORRECTED USAMS(FE) SABAH GRAVITY DATA SET

Longitude (°E)	Latitude (°N)	Height (m)	Original Bouguer Gravity (mGal)	Corrected Bouguer Gravity (mGal)
115.7432	5.3448	9.1	29.1	15.4
115.7898	5.3427	13.7	20.6	6.9
115.7960	5.2865	15.2	11.5	-2.2
115.8498	5.2387	45.7	6.2	-7.5
115.8750	5.1352	115.8	-11.6	-25.3
115.8765	5.1882	57.9	-16.0	-29.7
115.9065	4.8882	355.4	-52.8	-66.5
115.9082	4.9415	233.1	-50.8	-64.5
115.9178	5.0192	220.1	-46.3	-60.0
115.9413	5.1232	182.0	-32.7	-46.4
115.9677	5.1832	214.3	-32.0	-45.7
115.9893	5.7088	100.0	30.3	16.6
115.9955	5.2427	195.4	-21.8	-35.5
116.0288	5.2873	353.9	-16.6	-30.3
116.0602	5.2915	518.2	-24.5	-38.2
116.0723	5.9693	2.1	39.9	26.2
116.0740	5.3165	426.7	-25.5	-39.2
116.0748	5.9873	2.7	41.7	28.0
116.0832	5.9748	2.7	40.2	26.5
116.0915	5.9618	74.1	36.0	22.3
116.0943	5.9027	113.4	29.8	16.1
116.1165	5.9915	2.1	36.8	23.1
116.1332	5.9943	2.7	35.0	21.3
116.1443	6.0178	3.0	35.7	22.0
116.1538	6.0282	6.7	35.2	21.5
116.1577	5.3090	337.1	-20.8	-34.5
116.1653	6.0538	7.9	36.2	22.5
116.1720	5.3623	314.9	-23.1	-36.8
116.1720	5.9822	76.8	27.3	13.6
116.1832	5.1998	308.5	-24.8	-38.5
116.1832	5.2482	455.1	-25.5	-39.2
116.1943	6.0943	11.0	35.9	22.2
116.2053	6.1165	3.4	36.8	23.1
116.2138	6.1512	31.1	38.6	24.9
116.2165	5.4165	326.7	-26.7	-40.4
116.2165	6.1415	2.4	38.3	24.6
116.2193	6.1498	3.0	38.4	24.7
116.2193	6.1638	3.0	39.2	25.5
116.2365	5.1648	375.5	-17.0	-30.7
116.2633	6.1348	5.8	30.9	17.2
116.2725	5.5000	609.6	-26.0	-39.7
116.2763	6.1307	29.6	31.5	17.8
116.2778	5.5748	773.0	-16.2	-29.9
116.2900	6.1720	153.3	30.1	16.4
116.2922	5.1393	342.0	-13.9	-27.6
116.2943	6.1237	213.4	27.7	14.0
116.3027	6.1217	401.1	18.4	4.7
116.3027	6.1238	304.8	19.4	5.7

116.3107	6.2182	97.2	34.6	20.9
116.3110	6.1165	426.7	17.6	3.9
116.3162	5.6157	602.9	-17.4	-31.1
116.3220	6.1117	487.7	14.9	1.2
116.3302	6.1160	552.6	7.5	-6.2
116.3410	6.1098	697.7	10.6	-3.1
116.3415	6.2693	82.3	36.8	23.1
116.3482	5.6898	778.2	-18.3	-32.0
116.3527	6.1090	759.6	10.5	-3.2
116.3595	5.2310	355.4	-5.5	-19.2
116.3695	5.1347	360.9	-2.5	-16.2
116.3760	5.2815	361.5	-5.8	-19.5
116.3823	6.1087	855.6	11.8	-1.9
116.3887	6.1185	762.0	7.6	-6.1
116.4180	6.3553	9.1	38.6	24.9
116.4182	5.3265	389.2	-2.7	-16.4
116.4193	6.1090	670.6	8.5	-5.2
116.4265	6.3553	9.7	41.1	27.4
116.4332	5.0990	464.2	-0.2	-13.9
116.4332	6.0915	823.0	9.0	-4.7
116.4535	5.0232	447.8	-1.8	-15.5
116.4582	4.7118	259.7	-18.7	-32.4
116.4647	6.0322	944.9	-6.0	-19.7
116.4700	6.4153	119.2	43.8	30.1
116.4712	4.9448	443.9	-6.8	-20.5
116.4753	6.0138	1074.1	-10.1	-23.8
116.4828	4.8832	448.1	-4.7	-18.4
116.4858	4.7498	350.5	-21.6	-35.3
116.5015	5.3273	356.3	7.5	-6.2
116.5135	4.7982	457.2	-8.7	-22.4
116.5165	5.8405	998.5	-25.4	-39.1
116.5527	5.9860	1359.4	-16.7	-30.4
116.5557	5.8782	1332.9	-34.3	-48.0
116.5832	5.9882	1218.9	-14.3	-28.0
116.6498	5.9465	793.1	-16.4	-30.1
116.6665	5.9553	518.2	-13.2	-26.9
116.6762	5.9582	502.9	-10.9	-24.6
116.6822	6.5423	420.3	37.4	23.7
116.6898	6.7493	404.8	41.1	27.4
116.6937	6.6415	476.1	40.2	26.5
116.7053	6.0335	548.0	-7.8	-21.5
116.7053	6.9375	155.1	47.8	34.1
116.7178	5.9595	832.7	-8.5	-22.2
116.7270	5.3212	899.8	4.4	-9.3
116.7363	6.9202	57.3	52.7	39.0
116.7435	6.6327	15.2	45.0	31.3
116.7500	6.8332	15.2	32.5	18.8
116.7500	6.9248	3.0	56.2	42.5
116.7612	6.0532	274.3	-5.1	-18.8
116.7647	6.9073	93.9	43.8	30.1
116.7778	6.7110	389.5	49.4	35.7
116.7953	6.0715	233.8	6.8	-6.9
116.7960	5.9627	692.5	-2.4	-16.1
116.8007	5.8695	240.5	16.3	2.6

116.8080	5.7527	410.0	1.7	-12.0
116.8168	5.7665	222.5	12.7	-1.0
116.8193	6.9657	18.3	56.7	43.0
116.8315	5.2097	65.5	-2.0	-15.7
116.8457	6.8807	1.5	58.5	44.8
116.8535	6.5815	0.9	46.9	33.2
116.8715	6.1378	139.3	4.0	-9.7
116.8818	5.2893	45.7	6.4	-7.3
116.8832	7.2215	0.3	61.2	47.5
116.8873	5.7420	156.4	27.2	13.5
116.9190	6.6582	6.1	50.1	36.4
116.9353	6.1582	102.4	20.0	6.3
116.9452	5.4028	97.8	29.4	15.7
116.9607	5.3750	97.5	29.3	15.6
116.9655	5.7340	130.1	60.4	46.7
116.9670	5.2655	45.7	11.3	-2.4
116.9720	5.2698	125.6	9.6	-4.1
116.9720	6.0927	79.9	27.2	13.5
116.9832	7.2432	0.1	45.9	32.2
116.9862	5.3190	94.8	24.1	10.4
116.9865	5.4862	146.0	56.3	42.6
116.9918	6.7612	0.1	63.7	50.0
117.0228	7.0748	24.4	87.1	73.4
117.0315	6.8932	0.1	78.2	64.5
117.0403	6.1072	48.5	40.6	26.9
117.0452	5.5540	89.9	103.6	89.9
177.0455	7.3425	0.3	60.7	47.0
117.0555	7.0865	3.7	95.1	81.4
117.0565	7.2090	6.7	95.8	82.1
117.0682	6.9870	1.5	100.4	86.7
117.0693	5.2822	30.5	27.7	14.0
117.0745	5.7203	91.1	101.6	87.9
117.0957	6.1082	50.9	51.1	37.4
117.1332	5.6443	71.0	100.2	86.5
117.1485	5.3082	821.1	19.3	5.6
117.1528	6.1323	29.3	61.7	48.0
177.1582	7.3427	0.3	94.4	80.7
117.1602	5.2678	33.8	41.5	27.8
117.1665	7.1498	0.1	107.3	93.6
117.1927	5.6648	49.7	74.7	61.0
117.1965	6.1652	23.5	63.8	50.1
117.2005	6.9815	0.1	93.3	79.6
117.2220	5.8395	20.4	91.1	77.4
117.2353	6.8740	123.4	87.9	74.2
117.2442	6.7905	2.4	82.7	69.0
117.2472	5.8998	36.0	99.8	86.1
117.2485	6.2027	0.9	63.5	49.8
117.2738	7.2215	0.1	87.6	73.9
117.2840	5.3068	31.7	30.5	16.8
177.2855	7.3348	3.7	91.7	78.0
117.2915	7.0328	0.3	82.3	68.6
117.2927	6.6682	18.6	71.3	57.6
117.2998	5.9503	9.1	92.3	78.6
117.3110	5.6528	66.9	50.2	36.5

117.3177	6.2323	0.9	63.4	49.7
117.3282	6.9405	0.1	88.4	74.7
117.3448	6.8232	0.9	83.0	69.3
117.3565	5.9193	159.1	75.7	62.0
117.3687	6.2490	3.4	61.8	48.1
117.3707	5.2682	10.4	2.7	-11.0
117.3882	6.5782	0.1	68.0	54.3
117.3888	6.7352	110.3	69.2	55.5
117.3910	6.2442	88.1	59.9	46.2
117.3915	5.6680	135.0	41.1	27.4
117.3952	5.9798	3.0	52.3	38.6
117.4185	6.2873	1.8	63.1	49.4
117.4262	5.2218	19.5	-10.6	-24.3
117.4345	5.8265	1.5	50.5	36.8
117.4482	5.9653	2.1	45.1	31.4
117.4515	5.6857	30.1	31.8	18.1
117.4632	5.2832	328.9	-6.6	-20.3
117.4692	6.7582	0.1	72.0	58.3
117.4717	6.8865	45.1	73.6	59.9
117.4732	5.8668	0.6	41.3	27.6
117.4760	5.2232	35.7	-9.4	-23.1
117.4805	5.2553	18.3	-6.0	-19.7
117.4877	6.2712	0.9	60.1	46.4
117.4965	5.6893	25.1	23.0	9.3
117.5190	6.6298	0.1	63.9	50.2
117.5360	6.2732	2.7	56.4	42.7
117.5480	5.2842	14.6	-1.8	-15.5
117.5532	5.8980	51.2	23.5	9.8
117.5548	6.5537	0.1	60.5	46.8
117.5757	5.6977	81.6	16.5	2.8
117.5887	6.2802	179.2	42.5	28.8
117.6323	5.3307	14.9	-5.7	-19.4
117.6343	6.1035	0.3	39.9	26.2
117.6440	6.2327	0.9	45.8	32.1
117.6445	5.7170	82.2	13.0	-0.7
117.6457	6.2073	0.1	43.9	30.2
117.6498	5.9220	0.1	22.0	8.3
117.6815	5.3623	5.5	-0.8	-14.5
117.6867	6.5315	0.1	51.0	37.3
117.7015	5.7382	108.4	9.8	-3.9
117.7140	6.0327	0.1	21.7	8.0
117.7173	5.4287	8.2	2.7	-11.0
117.7240	6.2912	0.3	36.7	23.0
117.7318	6.4337	0.3	37.4	23.7
117.7545	5.9330	0.1	13.2	-0.5
117.7698	5.7777	82.1	3.4	-10.3
117.7840	5.4170	2.4	4.9	-8.8
117.7905	5.4907	88.7	10.1	-3.6
117.8112	6.0365	0.1	5.5	-8.2
117.8252	5.8368	45.5	2.4	-11.3
117.8977	5.7437	0.9	-2.9	-16.6
117.8980	5.9743	0.3	0.3	-13.4
117.9045	5.8845	6.5	-5.4	-19.1
117.9073	5.7915	0.6	-6.6	-20.3

117.9102	5.4977	3.4	-4.3	-18.0
117.9165	5.3877	245.7	-14.6	-28.3
117.9253	5.6898	0.1	-13.4	-27.1
117.9612	6.0708	45.7	9.5	-4.2
117.9723	5.8498	169.8	-14.0	-27.7
117.9920	5.8078	0.1	-1.2	-14.9
117.9980	5.6827	0.3	-10.7	-24.4
118.0348	6.0368	5.4	16.5	2.8
118.0515	6.1518	0.1	23.5	9.8
118.0573	6.1775	0.6	24.7	11.0
118.0632	5.7198	21.6	-9.7	-23.4
118.0668	5.9602	0.1	15.5	1.8
118.0682	5.5282	221.3	-20.1	-33.8
118.0748	5.8110	3.0	-15.8	-29.5
118.1077	5.7818	0.9	0.6	-13.1
118.1138	5.8387	3.0	2.7	-11.0
118.1343	5.6073	1.2	-10.2	-23.9
118.1378	5.7128	15.2	4.0	-9.7
118.1385	5.6403	0.3	-6.5	-20.2
118.1465	5.8698	179.5	1.0	-12.7
118.1853	5.8177	0.1	17.8	4.1
118.1870	5.7465	4.9	13.3	-0.4
118.2027	5.5082	162.5	-18.7	-32.4
118.2337	5.8420	0.3	31.5	17.8
118.2873	5.5077	1.8	4.4	-9.3
118.3440	5.5927	1.5	25.3	11.6
118.3465	5.7305	0.1	43.3	29.6
118.3663	5.6562	1.2	40.7	27.0